International Journal of Photoenergy

TiO_2 Photocatalytic Materials 2014

Guest Editors: Jiaguo Yu, Mietek Jaroniec, Wei Xiao, Christos Trapalis, and Hong Liu

TiO_2 Photocatalytic Materials 2014

International Journal of Photoenergy

TiO_2 Photocatalytic Materials 2014

Guest Editors: Jiaguo Yu, Mietek Jaroniec, Wei Xiao, Christos Trapalis, and Hong Liu

Editorial Board

Contents

Hindawi Publishing Corporation
International Journal of Photoenergy
Volume 2015, Article ID 786562, 2 pages
http://dx.doi.org/10.1155/2015/786562

Editorial
TiO_2 Photocatalytic Materials 2014

Jiaguo Yu,[1] Mietek Jaroniec,[2] Wei Xiao,[3] Christos Trapalis,[4] and Hong Liu[5]

[1]*State Key Laboratory of Advanced Technology for Material Synthesis and Processing, Wuhan University of Technology, Luoshi Road 122, Wuhan 430070, China*
[2]*Department of Chemistry, Kent State University, Kent, OH 44242, USA*
[3]*Department of Environmental Engineering, School of Resource & Environmental Sciences, Wuhan University, Wuhan 430072, China*
[4]*Institute of Materials Science, National Centre for Scientific Research "Demokritos", Agia Paraskevi Attikis, 153 10 Athens, Greece*
[5]*Chongqing Institute of Green and Intelligent Technology, Chinese Academy of Sciences, Chongqing, China*

Correspondence should be addressed to Jiaguo Yu; jiaguoyu@yahoo.com and Christos Trapalis; c.trapalis@inn.demokritos.gr

Received 21 December 2014; Accepted 21 December 2014

Semiconductor photocatalytic material and technology are of great significance in degradation of pollutant and conversion of solar energy. Among various oxide semiconductor photocatalysts, titania is the most important one up to now due to its chemical inertness, low price, nontoxicity, and strong oxidation and reduction ability under solar light. However, the photocatalytic performance of titania should be further improved from the viewpoint of practical application and commerce. To achieve this purpose, we invited investigators to contribute review and original research articles on TiO_2 photocatalytic materials. This special issue consists of 19 papers, mainly related to environmental purification of TiO_2 photocatalytic materials. Among them, 15 papers are about TiO_2 photocatalytic materials. A brief summary of all 19 accepted papers is provided below.

In "Effect of Ce Doping on RGO-TiO_2 Nanocomposite for High Photoelectrocatalytic Behavior," the paper indicates that the Ce-doped RGO-TiO_2 composite film showed higher photoelectrochemical performance than that of RGO-TiO_2 composite and pure TiO_2 under solar simulator irradiation.

The paper "Theoretical Study on Electronic Structure and Optical Performance of Nickel and Nitrogen Codoped Rutile Titanium Dioxide" reports ab initio calculations of nickel-doped, nitrogen-doped, and nickel + nitrogen-codoped rutile TiO_2 based on density functional theory.

The paper "Application of Glass Fiber-Based N-Doped Titania under Visible-Light Exposure for Photocatalytic Degradation of Aromatic Pollutants" reports fabrication of flexible glass fiber-supported nitrogen-doped TiO_2 photocatalysts by a dip-coating method followed by a low-temperature heat-treatment process and their application for the degradation of aromatic volatile organic compounds (VOCs) under visible-light irradiation.

The paper "Effects of UV-Vis Irradiation on Vanadium Etioporphyrins Extracted from Crude Oil and the Role of Nanostructured Titania" reports the use of N-TiO_2/Cu induces an important delay in the initiation of the porphyrins' photodegradation process.

The paper "Influence of Nd-Doping on Photocatalytic Properties of TiO_2 Nanoparticles and Thin Film Coatings" reports structural, optical, and photocatalytic properties of TiO_2 and TiO_2:Nd nanopowders and thin films.

The paper "Effect of Aging Time and Film Thickness on the Photoelectrochemical Properties of TiO_2 Sol-Gel Photoanodes" reports a nonaqueous based sol-gel process to produce TiO_2 based photoelectrodes for solar water splitting.

The paper "Synthesis of Submicron Hexagonal Plate-Type SnS_2 and Band Gap-Tuned $Sn_{1-x}Ti_xS_2$ Materials and Their Hydrogen Production Abilities on Methanol/Water Photosplitting" reports SnS_2 and $Sn_{1-x}Ti_xS_2$ (x = 0, 0.1, 0.3, 0.5, and 0.7 mol) materials designed using solvothermal method with the aim of enhancing hydrogen production from water/methanol aqueous solution.

The paper "Role of Platinum Deposited on TiO_2 in Photocatalytic Methanol Oxidation and Dehydrogenation Reactions" reports that the platinized titanium dioxide samples are always more active than the corresponding bare TiO_2 for both methanol oxidation and dehydrogenation processes.

The loading with various platinum amounts resulted in a significant improvement of the photocatalytic activity of TiO_2. This beneficial effect was attributed to an increased separation of the photogenerated electron-hole charge carriers.

The paper "An Overview: Recent Development of Titanium Oxide Nanotubes as Photocatalyst for Dye Degradation" presents a critical review of recent achievements in the modification of TiO_2 nanotubes for dye degradation.

The paper "TiO_2 Nanotube Arrays Composite Film as Photoanode for High-Efficiency Dye-Sensitized Solar Cell" presents a double-layered photoanode made of hierarchical TiO_2 nanotube arrays (TNT-arrays) as the overlayer and commercial-grade TiO_2 nanoparticles (P25) as the underlayer for dye-sensitized solar cells (DSSCs).

The paper "Hole-Phonon Relaxation and Photocatalytic Properties of Titanium Dioxide and Zinc Oxide: First-Principles Approach" presents first-principles calculations for the temporal characteristics of hole-phonon relaxation in the valence band of titanium dioxide and zinc oxide.

The paper "Electronic Structures of S/C-Doped TiO_2 Anatase (101) Surface: First-Principles Calculations" presents the electronic structures of sulfur- (S-) or carbon- (C-) doped TiO_2 anatase (101) surfaces investigated by density functional theory (DFT) plane-wave pseudopotential method.

The paper "Synthesis and Photocatalytic Activity of Magnetically Recoverable Core-Shell Nanoparticles" presents TiO_2/SiO_2/Fe_3O_4 (TSF) core-shell nanoparticles with good photocatalytic activity and capable of fast magnetic separation after photocatalytic reaction.

The paper "Photocatalytic Bactericidal Efficiency of Ag Doped TiO_2/Fe_3O_4 on Fish Pathogens under Visible Light" presents photocatalytic bactericidal efficiency of Ag-TiO_2/Fe_3O_4 under visible light using target pollutants that include *Aeromonas hydrophila, Edwardsiella tarda*, and *Photobacterium damselae* subsp. *piscicida*.

The paper "Boundary Layer of Photon Absorption Applied to Heterogeneous Photocatalytic Solar Flat Plate Reactor Design" presents the design of heterogeneous photocatalytic solar reactors with flat plate geometry used in treatment of effluents and conversion of biomass to hydrogen.

The paper "Antimicrobial Activity of TiO_2 Nanoparticle-Coated Film for Potential Food Packaging Applications" presents the antimicrobial activity of the films investigated by their capability to inactivate *Escherichia coli* (*E. coli*) in an actual food packaging application test under various conditions, including types of light and the exposed light time.

The paper "Preparation, Characterization, and Biotoxicity of Nanosized Doped ZnO Photocatalyst" presents preparation of five types of nondoped ZnO, iron-doped ZnO, cobalt-doped ZnO, nickel-doped ZnO, and manganese-doped ZnO materials by a wet chemical method, which were then exposed to *Daphnia magna* (*D. magna*) at low and high concentrations (50 and 250 μgL^{-1}).

The paper "Manipulation of MWCNT Concentration in MWCNT/TiO_2 Nanocomposite Thin Films for Dye-Sensitized Solar Cell" presents preparation of dye-sensitized solar cell (DSSC) using multiwalled carbon nanotube/titanium dioxide (MWCNT/TiO_2) using sol-gel method.

The paper "Oxidation of 4-Chlorophenol by Mesoporous Titania: Effect of Surface Morphological Characteristics" presents preparation of mesoporous nanocrystalline anatase via EISA employing CTAB as structure directing agent.

Acknowledgment

We wish to express our sincere thanks to all the authors for submitting their articles to this special issue.

Jiaguo Yu
Mietek Jaroniec
Wei Xiao
Christos Trapalis
Hong Liu

Hindawi Publishing Corporation
International Journal of Photoenergy
Volume 2014, Article ID 472539, 10 pages
http://dx.doi.org/10.1155/2014/472539

Research Article

Effect of Aging Time and Film Thickness on the Photoelectrochemical Properties of TiO_2 Sol-Gel Photoanodes

D. Regonini,[1] A. K. Alves,[2] F. A. Berutti,[2] and F. Clemens[1]

[1] *Laboratory for High Performance Ceramics, Swiss Federal Laboratories for Materials Science and Technology (EMPA), Überlandstrasse 129, 8600 Dübendorf, Switzerland*
[2] *Laboratory of Ceramic Materials, Federal University of Rio Grande do Sul, 99 Osvaldo Aranha Avenue, 90035-190 Porto Alegre, RS, Brazil*

Correspondence should be addressed to D. Regonini; domenico.regonini@empa.ch and F. Clemens; frank.clemens@empa.ch

Received 10 April 2014; Accepted 21 July 2014; Published 25 August 2014

Academic Editor: Jiaguo Yu

This work has focused on the investigation of a non-aqueous based sol-gel process to produce TiO_2 based photoelectrodes for solar water splitting. In particular, the effect of the aging time of the sol and TiO_2 film thickness on the photoelectrochemical properties of the photoanodes has been investigated. In order to achieve optimal performances (i.e., photocurrent density up to 570 $\mu A/cm^2$ and IPCE of 26% at 300 nm), the sol needs to be aged for 3 to 6 h, before being dip-coated to produce the photoanodes. The importance of the aging time can also be appreciated from the optical properties of the TiO_2 films; the absorbance threshold of the sol-gel aged for 3–6 h is slightly shifted towards longer wavelenghts in comparison to 0 h aging. Aging is necessary to build up a well-interconnected sol-gel network which finally leads to a photoelectrode with optimized light absorption and electron collection properties. This is also confirmed by the higher IPCE signal of aged photoelectrodes, especially below 340 nm. Among thicknesses considered, there is no apparent significant difference in the photoresponse (photocurrent density and IPCE) of the TiO_2 sol-gel films.

1. Introduction

The photoelectrochemical solar water splitting promoted by TiO_2 has been first reported in 1972 by Fujishima and Honda [1] and extensively investigated over the last 40 years [2–4]. TiO_2 is recognized as an environmentally friendly, economically accessible, photostable, and biologically inert photocatalyst [3, 4], although its large band-gap (3.0 to 3.2 eV) allows only the absorption of a small portion of the photons available from the solar spectrum [3]. To date, various attempts to modify the band-gap of TiO_2 by introducing suitable dopants within its lattice [3, 5, 6] have failed to deliver a material with an enhanced photoactivity. Such doping increases visible light absorption but increases also the probability of charge carriers recombination (i.e., new defects formed within the doped structure act as traps [7] for e^- and h^+). More promising results are instead obtained by inducing oxygen nonstoichiometry in TiO_2 via thermal treatment in a reducing atmosphere; in this case, the conductivity and to some extent the optical properties of the oxide are improved and the photoactivity is also enhanced, with the oxide remaining free from defects typically introduced whenever attempting to dope with foreign species [8–10]. It is also possible to optimize the electron transport properties of TiO_2 by selecting the most appropriate morphology for a given application [11, 12]. Concerning solar driven water splitting, Hartmann et al. [13] suggested that mesoporous TiO_2 sol-gel represents the ideal morphology to ensure good electronic interconnectivity and therefore a much more efficient collection of the photogenerated e^- than in TiO_2 nanoparticles. It should also be considered that, unlike mesoporous sol-gel films, TiO_2 nanoparticles are too small to support an inbuilt electrical field [14], meaning there is no space-charged layer [15] to assist the water splitting process. Under such conditions, the surface intermediates (Ti_s–$O^\bullet$ radicals, Ti_s–O–O–Ti_s peroxo species) involved in the photooxidation of water act as scavengers of e^- in the conduction band of TiO_2 nanoparticles; hence, the photocurrent is drastically

reduced [11]. Concerning the electron transport within a network of nanoparticles, it has been shown that it is aided by self-doping, occurring under illumination and enhancing the conductivity of the nanoparticles [16]. Therefore, Augustyński et al. [15] argue that the superior water splitting performances of sol-gel should not be ascribed to the good electronic interconnectivity but rather to the absence of a space-charged layer in the case of nanoparticles. Based on our recent studies on TiO_2 sol-gel, electrospun fibres, and nanoparticles [17], we suggest that both the absence of an inbuilt electric field in nanoparticles and the better interconnectivity (due to the Ti–O–Ti network) within the sol-gel are contributing to the better performances of sol-gel photoanodes. Among the possible sol-gel routes to obtain TiO_2 from a Ti alkoxide precursor, a better control over the structure of the sol and nanocrystallinity in the spin- (or dip-) coated films can be established, for example, by replacing water with an organic acid and an alcohol and also by using nonionic surfactants such as Triton X-100 [18] or Tween 20 [19, 20]. A similar approach is adopted and implemented within this work. As discussed later in Section 3, an added value and novelty of this work are the development of a system where the thickness of the film is not influenced by the aging time and the viscosity of the sol but only by the number of dip-coated layers. This allows a direct comparison between photoanodes aged for different times (as they have the same thickness). Furthermore, only few studies on the effect of film thickness on the photochemistry of the sol-gel are available to date. Yasumori et al. [21, 22] showed a nearly linear correlation between the thickness (up to 400 nm) of sol-gel photocatalyst and the amount of H_2 produced. Similarly, it has been recently reported that at a given wavelength (365 nm) the IPCE also increases (almost) linearly with the thickness of TiO_2 sol-gel photoanode (maximum thickness investigated was 1.3 μm) [23]. Nevertheless, further investigations are required to understand to which extent (in terms of thickness, porosity, aging, and crystallinity) a carefully chosen sol-gel synthetic route can lead to TiO_2 photoanodes with optimal electron transport properties. The aims of this work are

(i) to investigate the effect of film thickness on the photocurrent density and the IPCE response of TiO_2 sol-gel films,

(ii) to optimize the photoelectrochemical properties of our sol-gel processing method [17, 24] by investigating the influence of aging time on the performances of TiO_2 photoanodes.

As a result of this study, a robust correlation between the processing method (aging and thickness), the microstructure, and crystallinity of the sol-gel photoelectrodes and their photoelectrochemical properties is established by the use of different characterization techniques (Section 2.2) and presented in detail in Section 3.

2. Materials and Methods

2.1. Fabrication of TiO_2 Sol-Gel Photoelectrodes. The sol-gel photoelectrodes were prepared according to the following procedure: 2.84 mL (9.6 mmol) of titanium tetraisopropoxide [$Ti(OPr^i)_4$, Merck] was mixed in 2.84 mL (50 mmol) of acetic acid (Sigma-Aldrich) and kept under magnetic stirring for 10 minutes. The sol was then additionally kept in the dark for 15 minutes, before adding 0.8 mL (7.8 mmol) of acetylacetone (Acac, Sigma-Aldrich), 0.1 mL of Triton-x-100 (Sigma-Aldrich) [24], and a solution of 0.32 g (5wt.%) of PVB (Mowital B 30H, Omya) in 8 ml of dry EtOH. The sol was finally aged in the dark for different times, 0 h (i.e., no aging), 3 h, or 6 h, before being dip-coated (Compact DipMaster 50 Dip Coater, Chemat Scientific Inc.) on FTO glass substrates (Pilkington NSG TEC 8A, Xop Física) previously cleaned by sonication in isopropanol for 10 minutes, rinsed with distilled water and EtOH, and dried under an air flow. Dip coating parameters to obtain a 1-layer-thick green sol-gel photoelectrode were (a) substrate dipping/withdrawal speed of 50 mm/min and (b) dipping time of 30 s. In the case of multilayered films, the entire procedure described above was repeated to obtain 2 or 3 layers of green sol-gel photoanodes. All the photoelectrodes were left to dry for 24 h before being calcinated at 500°C in air (heating rate of 1.6°C/min, dwelling time: 2 h). In the case of multilayers photoanodes, the time interval between each dip coating was also kept for 24 h and the calcination done only once, when all the desired layers had been dip-coated on the FTO glass.

2.2. Characterization

2.2.1. Rheology. Measurements were performed using a Rheolab MC 120 (Anton Paar GmbH, Germany) rheometer. The viscosity (Pa·s) and the shear stress (Pa) of the sols were measured as a function of the shear rate (from 100 to 1000 s^{-1}) at different time intervals (0, 3, and 6 h) to monitor changes of flow behavior occurring during the aging process.

2.2.2. Morphology, Microstructure, and Crystallinity. The morphology, microstructure, and thickness of the photoelectrodes were analyzed by scanning electron microscopy (SEM, either TS5136 MM-Tescan or a Field Emission Nova NanoSEM 230-Nova FEI) and the crystal phases determined by grazing angle X-ray diffraction (GAXRD) analysis, performed on TiO_2 thin film photoelectrodes (grazing angle $\omega = 1°$, using a Panalytical, X'Pert Pro instrument (Cu-Kα1, λ = 1.5406 Å). The porosity of the thin film photoelectrodes was estimated from SEM images using the freeware ImageJ.

2.2.3. Specific Surface Area of Photoelectrodes. The surface area of the thin films was determined by dye adsorption/desorption measurements, using a commercial N719 dye (Sigma-Aldrich), assuming a dye monolayer coverage of the TiO_2 and a dye molecular footprint of 180 $Å^2$ [26]. Photoelectrodes were first left to dry at 80°C overnight and then soaked for 3 h in a 0.2 mM solution of N719 in tert-butanol/acetonitrile (1 : 1 in volume). Samples were removed

from the above solution, rinsed with EtOH and acetonitrile, and left to dry at 60°C for 1 h. The N719 dye adsorbed onto the TiO_2 films was desorbed by soaking (1 h) the films in a known volume of 0.01 M KOH in water. From UV-Vis (UV 3600 Spectrophotometer, Shimadzu) absorbance analysis and knowing the porosity of the films, it was then possible to calculate the specific surface area of the TiO_2 photoelectrodes aged for different times.

2.2.4. Photoelectrochemical and Optical Characterizations. The photocurrent measurements were performed using a 3-electrode system (working electrode: TiO_2 photoanode; counter electrode: platinum plate, XM120, Radiometer Analytical; reference electrode: Ag/AgCl/3M-KCl, XR300, Radiometer Analytical) inserted into a cappuccino cell [27] filled with 10 mL of 1 M KOH solution (pH = 13.8) and connected to a potentiostat (Voltalab80 PGZ 402, Radiometer Analytical). The cappuccino cell was irradiated by a Xe lamp (solar simulator, Oriel Lamp by LOT-Oriel AG), at an intensity correspondent to 1.5AM (1 sun, 1,000 W/m^2), and the resulting photocurrent density (J) measured as a function of a potential sweep from −900 to +600 mV (vs the Ag/AgCl ref. electrode), at a scan rate of 20 mV/sec.

Additionally, incident photon to current efficiency (IPCE) action spectra were also performed adopting a 2-electrode system, using a Xe lamp (by LOT-Oriel AG) as light source and a monochromator (Omni-λ 300, LOT-Oriel AG). A typical experiment consisted in illuminating a TiO_2 photoanode (immersed in 1 M KOH) with light of wavelength (λ) ranging from 600 nm to 300 nm (at 1 nm step). A Keithley 2450 source meter was used to provide a bias (0.00 V or 0.23 V) between the photoanode and a Pt counter electrode and to measure the photocurrent as a function of the wavelength, $J_{\text{Photo}}(\lambda)$. The power of the irradiating source, $P(\lambda)$, was recorded with a ThorLabs PM100USB power meter and the IPCE(λ)% values calculated as

$$\text{IPCE}(\lambda)\,\% = 1240 \cdot \left(\frac{J_{\text{Photo}}(\lambda)\ \left(\mu\text{A}\cdot\text{cm}^{-2}\right)}{\lambda \cdot P(\lambda)\ \left(\text{nm}\cdot\text{W}\cdot\text{m}^{-2}\right)} \right). \quad (1)$$

For the photocurrent and IPCE measurements, a minimum of 5 specimens for each different type of photoelectrodes were tested and results are given together with their relative standard deviations. UV-Visible analysis (UV 3600 Spectrophotometer, Shimadzu) was performed to determine the transmittance and diffuse reflectance of the photoelectrodes (T_{TiO_2}, R_{TiO_2}) and the FTO substrate (T_{FTO}, R_{FTO}), ranging λ from 650 to 250 nm (sampling interval 1 nm). The absorbance, that is, optical density, opt. dens. (λ), is then given by

$$\text{Opt. dens.}\ (\lambda) = -\text{Log}_{10}\left(\frac{\left(T_{TiO_2}/T_{FTO}\right)}{1-\left(\left(R_{TiO_2}-R_{FTO}\right)/100\right)} \right) = \frac{\alpha \cdot d}{2.303}, \quad (2)$$

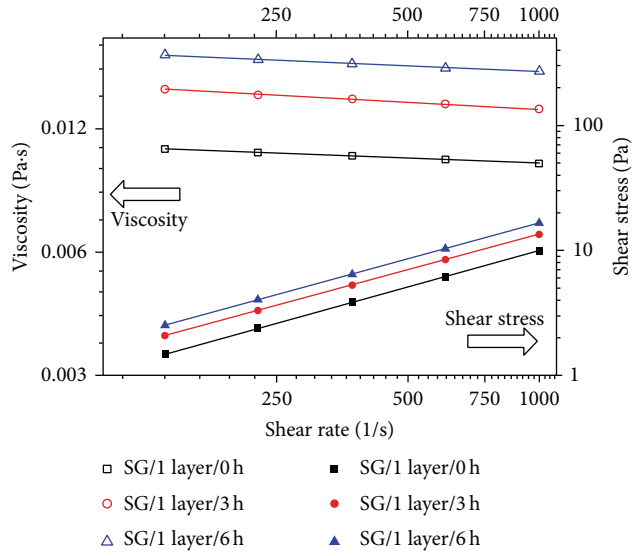

Figure 1: Rheology measurements showing how the viscosity and shear stress of the sol change during the aging process.

Table 1: Thickness of sol-gel TiO_2 photoelectrodes measured by SEM. The indirect band-gap obtained from the Tauc plot [25] applied to the optical data in Figure 3 is also given.

Photoelectrode	Thickness (d) (μm)	Indirect band-gap (eV)
0 h aging, 1 layer	0.6 ± 0.1	3.25 ± 0.08
3 h aging, 1 layer	0.6 ± 0.1	3.25 ± 0.06
6 h aging, 1 layer	0.6 ± 0.1	3.21 ± 0.08
6 h aging, 2 layers	1.1 ± 0.1	3.22 ± 0.06
6 h aging, 3 layers	1.6 ± 0.2	3.21 ± 0.02

where α is the absorption coefficient and d is the thickness of the film. The indirect band-gap of the photoelectrodes was extrapolated from a plot of $(\alpha h\nu)^{1/2}$ versus $h\nu$, Tauc plot [25].

3. Results and Discussion

As expected, the rheology measurements performed on the TiO_2 sol-gel system, Figure 1, are showing an increase in shear stress and viscosity occuring during the aging process of the sol, which was monitored at 0, 3, and 6 h. The increase in shear stress and viscosity is more pronounced between 0 and 3 h than between 3 and 6 h aging, suggesting that the most significant physical and chemical changes within the TiO_2 sol are occuring within the first 3 h of the aging process. This is in good agreement with previous reports on the preparation of sols using metal alkoxide based precursors [28]. The results of the SEM analysis, summarized in Table 1, reveal that aging time has no effect on the thickness of the photoanode, which remains as 0.6 ± 0.1 μm for 1 layer TiO_2 dip-coated after 0, 3, or 6 h aging. This was expected, considering there is no real gelling effect (i.e., shear thinning effect) in the TiO_2 sol; from Figure 1, it is clear that the sol behaves almost as a newtonian fluid [29]. The viscosity is almost independent of the shear rate and the shear stress shows linear behavior versus

the shear rate. It is therefore assumed that the film thickness is mainly influenced by the solid TiO_2 content (kept constant in this study) inside the sol-gel system. The TiO_2 sol system does not show a real gelling effect for the following reasons.

(i) The water required for hydrolysis of $Ti(OPr^i)_4$ is initally absent and it is only slowly released in the sol via reaction between the alcohol (EtOH) and the acetic acid. The Ti–O–Ti network can also be created by alcoholysis of the Ti alkoxide precursor, which again is slower than hydrolysis and easier to control [18].

(ii) It has been previously shown that chelating agent such as Acac, used in this study, despite causing the Ti alkoxide precoursor to be more prone to hydrolysis/alcoholysis, is in fact slowing down (or preventing) gelation because it offers alternative paths to the polymerization reaction [30].

(iii) An excess of acetic acid is used in our system and this is also known to retard the gelation of Ti alkoxides by promoting the formation of stabilized dimeric complexes (the coordination of Ti also changes from 4 to 6 upon addition of acetic acid) [29].

Our study shows that it is possible to prepare films with thickness independent of aging time; as previously mentioned, this allows evaluating the impact of aging time on the ability of the photoelectrodes to sustain electron transport.

The results of the GAXRD analysis of the photoelectrodes (after calcination at 500°C) are summarized in Figure 2. Anatase is the dominant phase (>95%) in all the photoelectrodes, although a small amount of rutile is also present. An additional and important fact emerging from Figure 2 is the impact of the sol-gel aging process on the crystallinity of the film. By comparing the XRD spectra of 1-layer-thick photoelectrodes (i.e., same thickness) without aging (0 h) and aged for 3 or 6 h, the anatase peaks appear to be more pronounced in the case of aged films. In other terms, when the aging step is not performed (0 h), the XRD signals of the FTO substrates dominate over the TiO_2 peaks. This is best appreciated when comparing the anatase peak at 25.4° and the FTO peak at 26.6°. Crystallinity is indeed a very important requirement towards the design of effective photocatalysts for the formation of H_2 via solar water splitting [31]. Additionally, the analysis of the crystalline particles size by applying the Scherrer equation [32] to the anatase peak (101) at 2θ = 25.3 – 25.4°, Figure 2, reveals that they are sufficiently big to allow efficient electron transport. The size of the crystalline domains for all the different photoelectrodes is approximately 30 nm and sufficiently larger domains (at least >15 nm) are generally suggested to be required to facilitate transport of electrons during the water splitting process [13].

Despite having no significant effect on the thickness of TiO_2 films, aging time appears to influence the optical properties of the photoanodes, as shown in Figure 3; the absorbance threshold of the sol-gel aged for 3 and 6 h is slightly shifted towards higher wavelenghts in comparison to 0 h aging. Furthermore, for a given wavelenght, by comparing

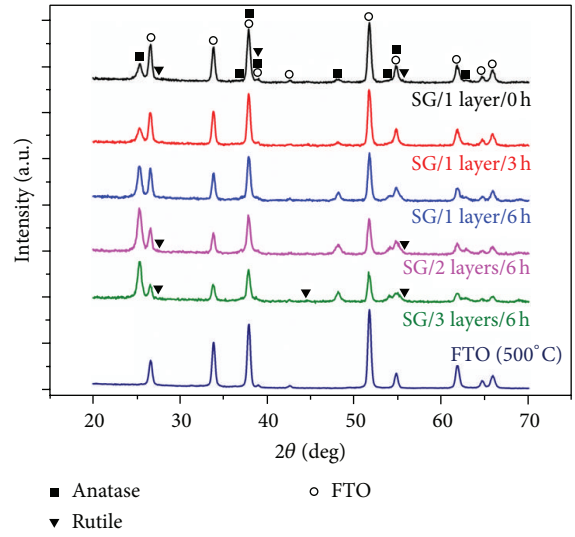

Figure 2: GA-XRD analysis of the different TiO_2 sol-gel photoelectrodes. The crystallinity of aged sol-gel is improved in comparison with the gel without aging (0 h). Anatase is the dominant phase in all the photoelectrodes, although a small amount of rutile is also present.

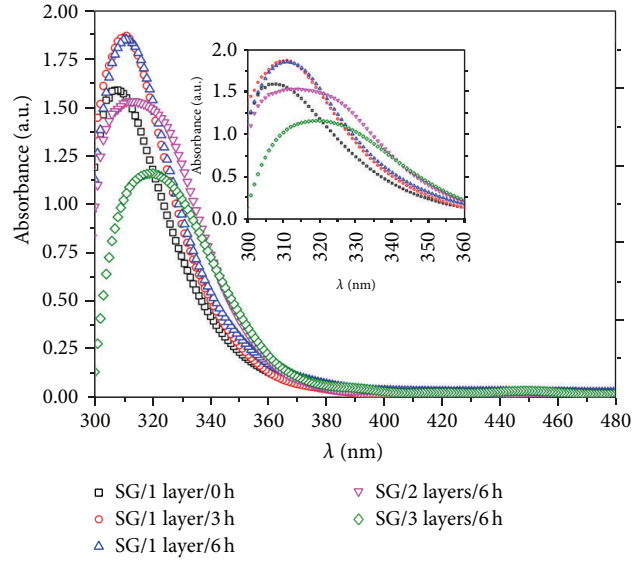

Figure 3: Absorbance (optical density) of the different sol-gel photoelectrodes. The slight changes in the optical properties induced by the aging time, as well as by the dip coating of multilayer photoelectrodes, are better appreciated in the inset.

the 1-layer photoelectrodes aged for difference times, it is evident that the absorbance intensity is higher in 6 h aged films. This is best appreciated in the region 300–320 nm, Figure 3, and must be a consequence of the chemical and physical changes [33] occuring within the sol. As previously discussed, the sizes of crystalline domains are very similar (approximately 30 nm) in all the photoelectrodes and cannot explain the differences in their optical properties. However, XRD analysis, Figure 2, has shown that aged photoelectrodes

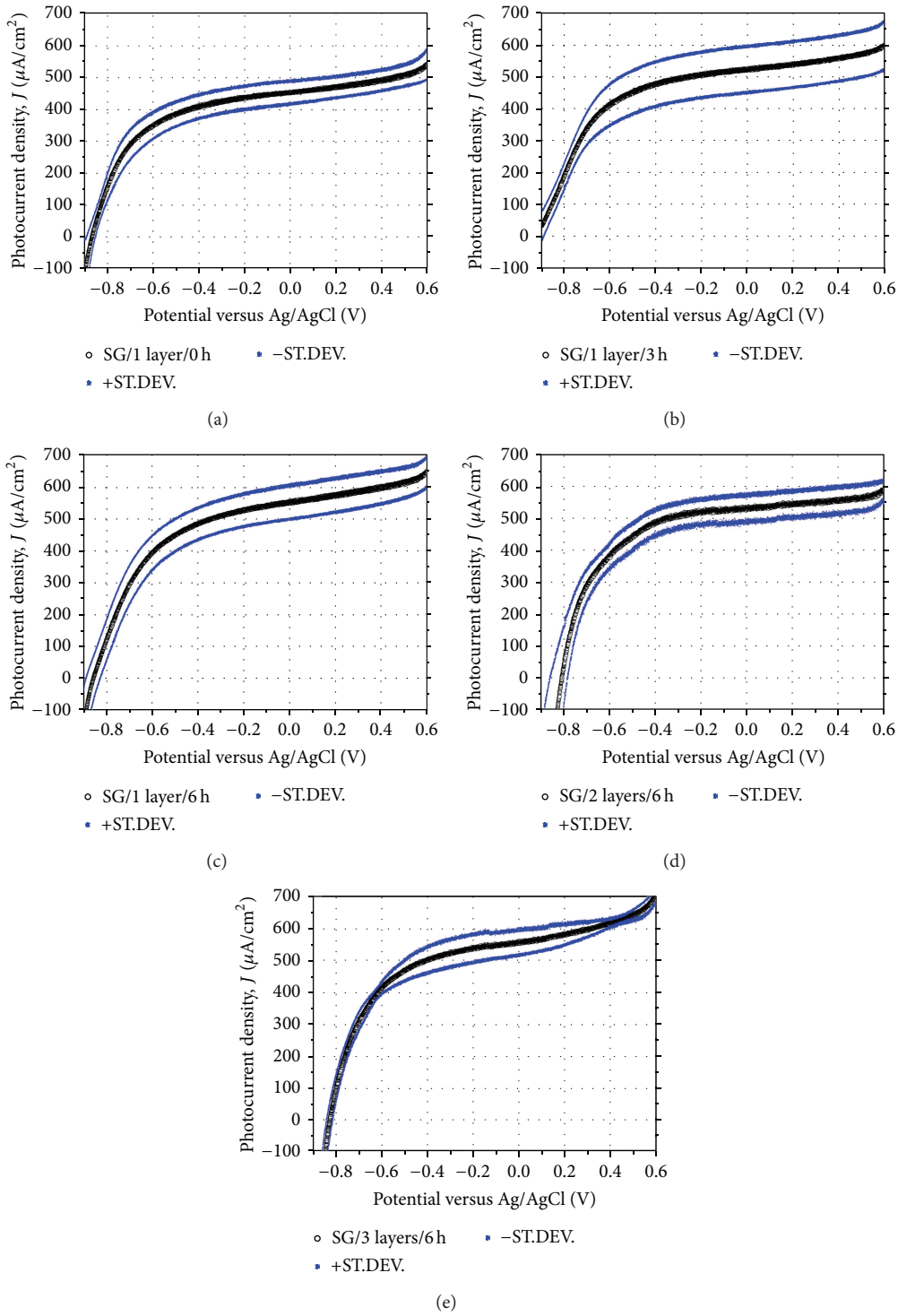

FIGURE 4: Effect of aging time on the photocurrent of TiO_2 sol-gel photoelectrodes: (a) SG/1 layer/0 h, (b) SG/1 layer/3 h, and (c) SG/1 layer/6 h. The effect of the thickness of TiO_2 on the photocurrent density is also reported; see (d) SG/2 layers/6 h and (e) SG/3 layers/6 h.

have a higher degree of crystallinity than nonaged films and, as a result, may interact differently with the incident light. We therefore tentatively assign the shift of the absorbance threshold to differences in the light scattering phenomena occuring within films aged for different times.

The optical properties are also in good agreement with the photocurrent measurements, reported in Figures 4(a)–4(c) for different aging times, 0, 3, and 6 h. By taking the value of the photocurrent density at 0.23 V versus Ag/AgCl (i.e., 1.23 V vs RHE in 1 M KOH), the reponse increases from

460 μA/cm^2 for 0 h aging time to 550 and 570 μA/cm^2 in the case of 3 and 6 h aging time, respectively. The standard deviation between the photocurrent measurements for a given aging time is typically in the order of ±10% and it can be concluded that there is no significant difference between the photoresponses of the sol-gel aged after 3 and 6 h, whereas the sol-gel with no aging (i.e., 0 h) clearly has the lowest performance. We ascribe the shift observed in the absorbance, Figure 3, and the enhanced photocurrent density in aged photoelectrodes, Figure 4, to the building-up of the sol-gel network occuring during the aging process. Clearly, the formation of such network has an impact on both the crystallinity and the optical properties as well as ability to collect the photogenerated electrons.

Additional information on the photoelectrochemical properties of sol-gel films is provided by the IPCE analysis in Figures 5(a)–5(c). The study of the IPCE curve, particularly in the region 300–340 nm, provides information on the electron transport properties of the photoelectrodes. What clearly emerges from the IPCE analysis, in good agreement with the photocurrent density measured previously discussed (Figures 4(a)–4(c)), is the superior ability of aged films (see comparison between 0 h aging, Figure 4(a), and 3 h, Figure 4(b), and 6 h aging, Figure 4(c)) to absorb photons and collect them at the back FTO electrode. Despite having practically the same IPCE in the range of 460 to 340 nm, the SG/1 layer/6 h photoelectrodes provide higher IPCE than SG/1 layer/0 h films for $\lambda < 340$ nm: 10% versus 7% at 340 nm, 17.5% versus 12.5% at 320 nm, and 26% versus 20% at 300 nm, as shown in Figures 5(a) and 5(c). The values for SG/1-layer/3 h aging, 7.5% at 340 nm, 14% at 320 nm, and 20% at 300 nm, Figure 5(b), are in between those of 0 and 6 h aging. The reason for the higher photocurrent density of 3 and 6 h aging times in comparison with 0 h aging time can therefore be confidently linked to the superior ability of aged photoelectrodes to collect electrons photogenerated from the absorption of shorter wavelength (300 nm $\leq \lambda \leq$ 340 nm). Considering that the photoanodes were "front illuminated" and the absorption coefficient (α) of the light is a decreasing function of λ (i.e., shorter λ have higher α than longer λ), light of 300 nm $\leq \lambda \leq$ 340 nm is mostly absorbed in the 10 to 100 nm region [34] closest to the electrolyte. Therefore, in the SG/1 layer/0–6 h aged photoelectrodes, the photogenerated electrons have to diffuse through the entire film (0.6 ± 0.1 μm) in order to be collected at the FTO back contact. This requires an excellent network interconnectivity, which can be ensured by aging the photoelectrodes, as clearly shown in Figures 4(a)–4(c) and Figures 5(a)–5(c). SEM analysis also reveals an additional feature responsible for the good performances of the SG photoelectrodes: their mesoporosity, Figures 6(a)-6(b), is in fact crucial to ensure penetration of the electrolyte within the photoanode. It should be noted that Figures 6(a)-6(b) show the microstructure of 6 h aged photoelectrodes; however, no significant differences in the morphology and mesoporosity of photoelectrodes aged for 0 or 3 h were observed. From the analysis of Figures 6(a)-6(b), it is not possible to provide an exact value for the pore size within the TiO_2 films; however, it is clear that such pores are bigger than 10 nm and are very likely to allow a good contact/interface within the film and electrolyte [13]. In contrast, whenever the diameter of the pore is below 10 nm, the bulk of the film may not be in contact with the electrolyte and therefore does not contribute to the charge transfer process, limiting the film's photoactivity [23]. It is likely that the presence of 5wt.% PVB in the sol also contributes to establish such an optimal porous structure, although further studies are necessary to confirm this hypothesis.

The porosity of the thin films photoelectrodes has been estimated (from SEM micrograph) to be 21.8 ± 0.6%, 20.2 ± 0.7%, and 19.4 ± 0.5% for 0, 3, and 6 h aged photoelectrodes, respectively. As expected, considering the rather small window of investigated range of aging time (0 to 6 h), no major changes are observed. It has also been possible to estimate the specific surface area of the photoelectrodes by dye adsorption/desorption. Again, no significant differences were osberved, with values of 22 ± 3 m^2/g, 20 ± 2 m^2/g, and 19 ± 2 m^2/g for 0, 3, and 6 h aged photoelectrodes, respectively. Typically, larger modifications of surface area and porosity as a function of aging time are better appreciated by extending the aging to days or even weeks [35]. Nevertheless, there seems to be a trend suggesting a small decrease in porosity and surface area as the aging time increases; this could be due to further condensation reactions and formation of Ti–O–Ti within the sol. Such small changes of porosity and surface area (observed between 0 and 6 h aging time) may also contribute to generate differences in the light scattering behaviour and optical properties of the various photoelectrodes.

In addition to the influence of aging time, we have also investigated the effect of film thickness on the performances of the photoanodes, while keeping the aging time of the sol constant (6 h), attempting to optimize their light absorption properties. As it can be appreciated from Table 1, by increasing the number of dip-coated layers from 1 to 2 and 3, the thickness of the film increases from 0.6 ± 0.1 μm to 1.1 ± 0.1 μm and 1.6 ± 0.2 μm, respectively. As an example, the SEM cross section profile of a SG/3-layer-thick photoanode is given in Figure 6(b).

The photocurrent measurements of multilayered photoanodes are reported in Figures 4(d)-4(e). By comparison with Figure 4(c) (1 layer, 6 h aging), it can be concluded that the photocurrent is not affected by the thickness/number of layers dip-coated on the FTO substrate and remains in the order of 550 to 570 μA/cm^2 at 0.23 V vs Ag/AgCl. Likewise, the IPCE curves of SG/2 layers/6 h and films, Figures 5(d)-5(e), are very similar to the IPCE response of SG/1 layer/6 h, Figure 5(c). The IPCE values of SG/3 layers/6 h, SG/2 layers/6 h, and SG/1 layer/6 h are, respectively, 12, 11, and 10% at 340 nm, 18, 19, and 17.5% at 320 nm, and 25, 25, and 26% at 300 nm. This is in contrast with a recent report [23] on a nearly linear increase in the IPCE on TiO_2 films up to 1.3 μm thick, but once more it confirms the good electron transport properties of the photoelectrodes; the photogenerated charge carriers from light of 300 nm $\leq \lambda \leq$ 340 nm can be also successfully collected in multilayers film (up to 1.6 μm thick, Table 1).

Even at 300 nm, where the light's penetration depth is estimated to be 10–30 nm, based on the absorption spectrum

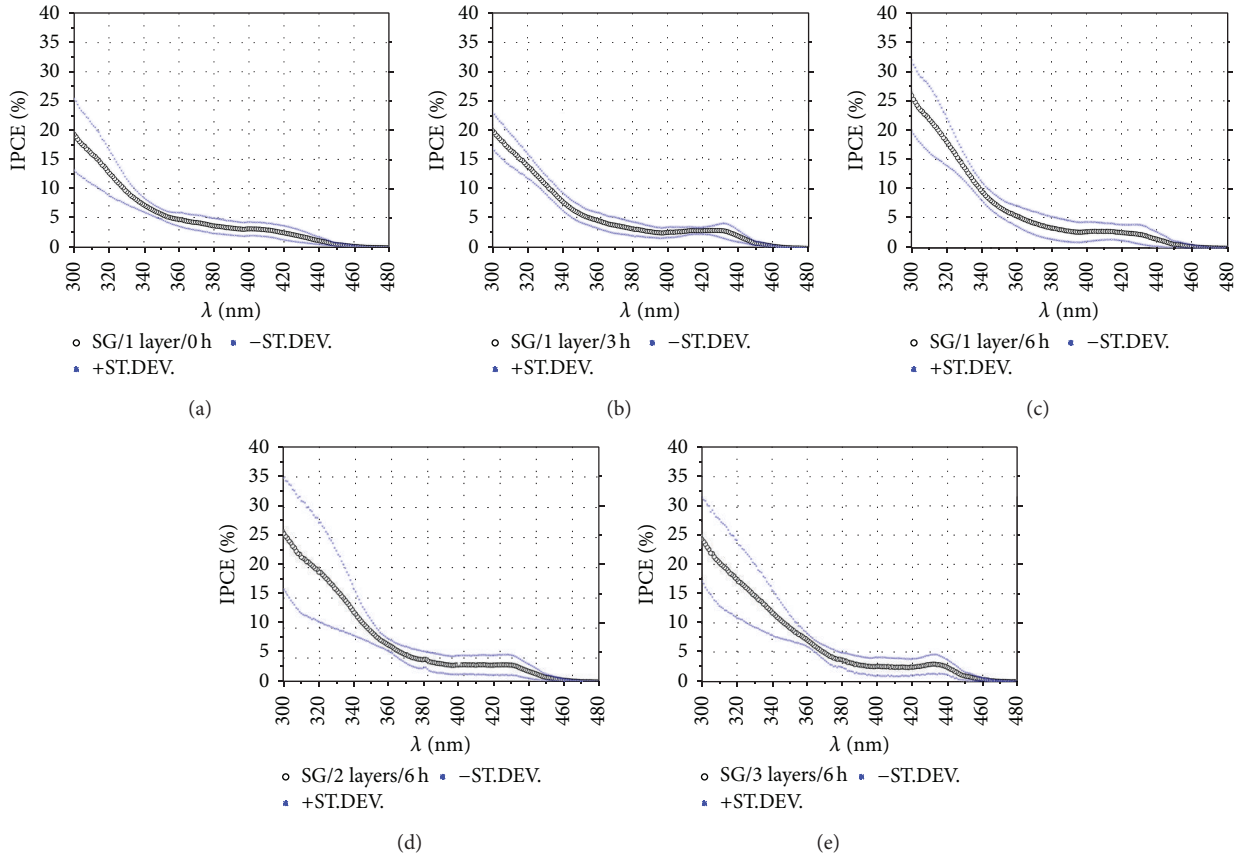

Figure 5: IPCE of the different types of sol-gel photoelectrodes investigated within this study: (a) SG/1 layer/0 h, (b) SG/1 layer/3 h, (c) SG/1 layer/6 h, (d) SG/2 layers/6 h, and(e) SG/3 layers/6 h.

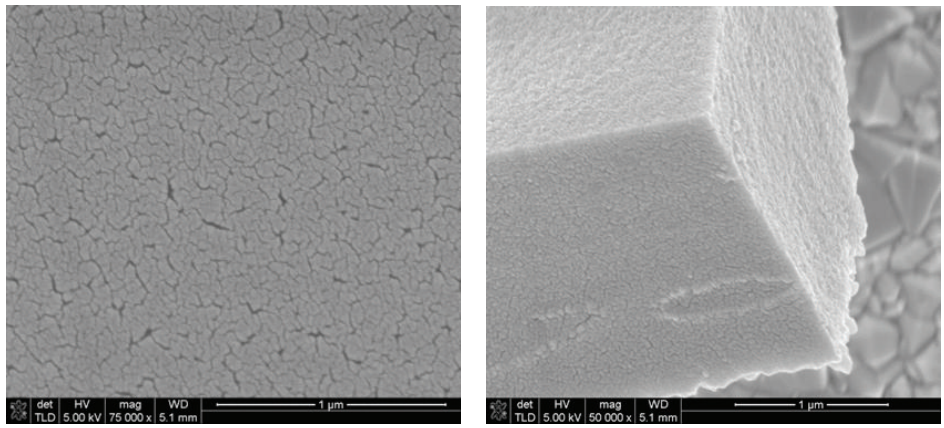

Figure 6: (a) Showing the mesoporosity of the SG photoelectrodes and (b) the view of a SG/3 layers/6 h photoelectrode. The mesoporosity of the film allows good penetration of the electrolyte within the film and it is likely to be responsible for the good photoactivity shown by the SG photoanodes.

by Eagles [34] and accounting for film's porosity and the presence of anatase [16], the IPCE is still 25% in both SG/3 layers/6 h and SG/2 layers/6 h. Films thinner than $0.6 \pm 0.1\,\mu$m (1 layer with dip coating parameter adopted within this work) were not considered in this study; it has been recently reported that $0.2\,\mu$m thick mesoporous sol-gel provides photocurrent density (related to solar water splitting) in the range of $1\,\text{mA/cm}^2$ [13] and it could be argued that also in our case thinner films may lead to an improved photoresponse. A final consideration to highlight

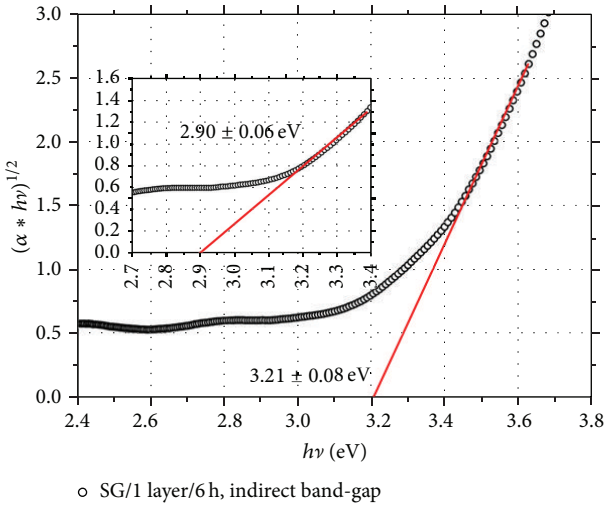

FIGURE 7: Tauc plot [25] of SG/1 layer/6 h photoelectrode. The indirect band-gap extrapolated from the plot is 3.21 ± 0.08 eV. An additional tail for a sub-band-gap of 2.9 ± 0.06 eV is also present. This indicates the presence of oxygen vacancies (shallow donors) within the photoanodes and explains the small IPCE signal observed for the photoelectrodes above 400 nm.

regarding the sol-gel photoelectrodes is their weak response in the region 400–440 nm, which can be appreciated in all the IPCE spectra, Figures 5(a)–5(e). The indirect band-gap of the photoelectrodes, Table 1, estimated by applying the Tauc plot to the optical data in Figure 3 is in the range of 3.21 to 3.25 eV, corresponding to an absorption threshold of 386.3 to 381.5 nm. The IPCE response well above the absorption threshold can be explained by the presence of shallow donor states within the TiO_2; for example, the use of carbon based precursors for the preparation of the TiO_2 sol-gel, as well as the sintering performed in air, is likely to introduce oxygen vacancies within the oxide. The presence of oxygen vacancies acting as donor states [36] also emerges from the Tauc plot of the photoelectrodes. As an example, the Tauc plot of SG/1 layer/6 h is shown in Figure 7. In addition to the indirect band-gap, extrapolated to be 3.21 ± 0.08 eV, there is a tail (Figure 7 inset) corresponding to a sub-band-gap of 2.90 ± 0.06 eV. Similar donor levels were also highlighted in a previous study on the activation energy for conduction in TiO_2 [37]. Finally, the trapping of a small amount of visible light within the photoanode could also be a consequence of the mesoporosity of the film, Figures 6(a)-6(b).

4. Conclusions

The optimization of a sol-gel process aimed at producing mesoporous TiO_2 based photoelectrodes for solar water splitting has been presented within this work. In particular, we have investigated two parameters, aging time of the sol and thickness of the TiO_2 films, and their impact on the photoelectrochemical properties of the material. Our results show that aging the sol for 3 to 6 h before the dip coating onto FTO substrates is crucial to ensure optimal performance of the photoelectrodes. It should be noticed that the aging time did not influence the thickness of the film. It is assumed that the concentration of the titanium tetraisopropoxide in the sol-gel system should instead affect the coating thickness (and should possibly also modify the long stability of the sol); this will be investigated in a separate study. The absorbance threshold of aged sol-gels is slightly shifted towards higher wavelenghts in comparison to 0 h aging and their photocurrent density (up to 570 $\mu A/cm^2$, among the highest photocurrent densities reported for TiO_2 sol-gel) and IPCE response (10% at 340 nm and 26% at 300 nm) confirm the superiority of aged films also in terms of network interconnectivity and electron collection properties. It is also evident that the crystallinity of the films is improved after aging. No significant changes of the photoresponse were instead observed by increasing the thickness of the TiO_2 films. The presence of weak IPCE signals in all TiO_2 photoelectrodes, above 400 nm, is explained in terms of donor levels (oxygen vacancies) introduced during the processing and sintering of the sol-gel. Due to its wide band-gap (above 3 eV), TiO_2 alone cannot lead towards the development of photoelectrochemical water splitting devices with a 10% solar to hydrogen (STH) efficiency (the threshold above which such technology becomes industrially viable [27]). However, considering its unique properties, the study and the optimization of the photoelectrochemical behavior of TiO_2 based mesoporous photoanodes are very important, as we believe they can be used as an efficient, stable, and robust support for materials/particles capable of harvesting visible light.

Conflict of Interests

The authors declare that there is no conflict of interests regarding the publication of this paper.

Acknowledgments

The authors gratefully thank the financial support by the Brazilian Swiss Joint Research Programme (BSJRP 0112-11) and by the Swiss National Science Foundation under Project no. R'Equip 206021-121306 (Fundamental Aspects of Photocatalysis and Photoelectrochemistry/Basic Research Instrumentation for Functional Characterization). Dr. Artur Braun (EMPA) is also kindly acknowledged for the provision of experimental facilities. The photoelectrochemical (cappuccino) cell was machined at the Empa Machine Shop based on the original design provided by the Laboratory for Photonics and Interfaces, EPFL Lausanne. Dr. Fabio La Mattina and A. Kupferschmid (Empa) are also gratefully acknowledged for their contribution to the IPCE set-up.

References

[1] A. Fujishima and K. Honda, "Electrochemical photolysis of water at a semiconductor electrode," *Nature*, vol. 238, no. 5358, pp. 37–38, 1972.

[2] A. L. Linsebigler, G. Lu, and J. T. Yates Jr., "Photocatalysis on TiO_2 surfaces: principles, mechanisms, and selected results," *Chemical Reviews*, vol. 95, no. 3, pp. 735–758, 1995.

[3] T. Bak, J. Nowotny, M. Rekas, and C. C. Sorrell, "Photo-electrochemical hydrogen generation from water using solar energy. Materials-related aspects," *International Journal of Hydrogen Energy*, vol. 27, no. 10, pp. 991–1022, 2002.

[4] M. Ni, M. K. H. Leung, D. Y. C. Leung, and K. Sumathy, "A review and recent developments in photocatalytic water-splitting using TiO2 for hydrogen production," *Renewable and Sustainable Energy Reviews*, vol. 11, no. 3, pp. 401–425, 2007.

[5] A. Fujishima, X. Zhang, and D. A. Tryk, "TiO_2 photocatalysis and related surface phenomena," *Surface Science Reports*, vol. 63, no. 12, pp. 515–582, 2008.

[6] X. Chen and S. S. Mao, "Titanium dioxide nanomaterials: synthesis, properties, modifications and applications," *Chemical Reviews*, vol. 107, no. 7, pp. 2891–2959, 2007.

[7] J. A. Anta, "Electron transport in nanostructured metal-oxide semiconductors," *Current Opinion in Colloid and Interface Science*, vol. 17, no. 3, pp. 124–131, 2012.

[8] M. Radecka, A. Trenczek-Zajac, K. Zakrzewska, and M. Rekas, "Effect of oxygen nonstoichiometry on photo-electrochemical properties of TiO_{2-x}," *Journal of Power Sources*, vol. 173, no. 2, pp. 816–821, 2007.

[9] X. Chen, L. Liu, P. Y. Yu, and S. S. Mao, "Increasing solar absorption for photocatalysis with black hydrogenated titanium dioxide nanocrystals," *Science*, vol. 331, no. 6018, pp. 746–750, 2011.

[10] G. Wang, H. Wang, Y. Ling et al., "Hydrogen-treated TiO_2 nanowire arrays for photoelectrochemical water splitting," *Nano Letters*, vol. 11, no. 7, pp. 3026–3033, 2011.

[11] J. Augustynski and R. Solarska, "To what extent do the nanostructured photoelectrodes perform better than their macrocrystalline counterparts?" *Catalysis Science and Technology*, vol. 3, no. 7, pp. 1810–1814, 2013.

[12] E. Ghadiri, N. Taghavinia, S. M. Zakeeruddin, M. Grätzel, and J. Moser, "Enhanced electron collection efficiency in dye-sensitized solar cells based on nanostructured TiO2 hollow fibers," *Nano Letters*, vol. 10, no. 5, pp. 1632–1638, 2010.

[13] P. Hartmann, D. Lee, B. M. Smarsly, and J. Janek, "Mesoporous TiO_2: comparison of classical sol-gel and nanoparticle based photoelectrodes for the water splitting reaction," *ACS Nano*, vol. 4, no. 6, pp. 3147–3154, 2010.

[14] A. Hagfeldt and M. Grätzel, "Molecular photovoltaics," *Accounts of Chemical Research*, vol. 33, no. 5, pp. 269–277, 2000.

[15] J. Augustyński, B. D. Alexander, and R. Solarska, "Metal oxide photoanodes for water splitting," *Topics in Current Chemistry*, vol. 303, pp. 1–38, 2011.

[16] A. Wahl and J. Augustynski, "Charge carrier transport in nanostructured anatase TiO_2 films assisted by the self-doping of nanoparticles," *Journal of Physical Chemistry B*, vol. 102, no. 40, pp. 7820–7828, 1998.

[17] D. Regonini, A. C. Teloeken, A. K. Alves et al., "Electrospun TiO_2 fiber composite photoelectrodes for water splitting," *ACS Applied Materials & Interfaces*, vol. 5, no. 22, pp. 11747–11755, 2013.

[18] E. Stathatos, P. Lianos, and C. Tsakiroglou, "Highly efficient nanocrystalline titania films made from organic/inorganic nanocomposite gels," *Microporous and Mesoporous Materials*, vol. 75, no. 3, pp. 255–260, 2004.

[19] Y. Chen, E. Stathatos, and D. D. Dionysiou, "Microstructure characterization and photocatalytic activity of mesoporous TiO_2 films with ultrafine anatase nanocrystallites," *Surface and Coatings Technology*, vol. 202, no. 10, pp. 1944–1950, 2008.

[20] D. Hidalgo, R. Messina, A. Sacco et al., "Thick mesoporous TiO_2 films through a sol-gel method involving a non-ionic surfactant: characterization and enhanced performance for water photo-electrolysis," *International Journal of Hydrogen Energy*, 2014.

[21] A. Yasumori, K. Ishizu, S. Hayashi, and K. Okada, "Preparation of a TiO2 based multiple layer thin film photocatalyst," *Journal of Materials Chemistry*, vol. 8, no. 11, pp. 2521–2524, 1998.

[22] A. Yasumori, H. Shinoda, Y. Kameshima, S. Hayashi, and K. Okada, "Photocatalytic and photoelectrochemical properties of TiO_2-based multiple layer thin film prepared by sol-gel and reactive-sputtering methods," *Journal of Materials Chemistry*, vol. 11, no. 4, pp. 1253–1257, 2001.

[23] J. Krýsa, M. Baudys, M. Zlámal, H. Krýsová, M. Morozová, and P. Klusoň, "Photocatalytic and photoelectrochemical properties of sol-gel TiO_2 films of controlled thickness and porosity," *Catalysis Today*, vol. 230, pp. 2–7, 2014.

[24] A. K. Alves, F. A. Berutti, F. J. Clemens, T. Graule, and C. P. Bergmann, "Photocatalytic activity of titania fibers obtained by electrospinning," *Materials Research Bulletin*, vol. 44, no. 2, pp. 312–317, 2009.

[25] J. Tauc, "Absorption edge and internal electric fields in amorphous semiconductors," *Materials Research Bulletin*, vol. 5, no. 8, pp. 721–729, 1970.

[26] A. Fattori, *Electrochemical and Spectroelectrochemical studies of dyes used in dye-sensitized solar cells [Ph.D. thesis]*, University of Bath, 2010.

[27] R. van de Krol and M. Gratzel, *Photoelectrochemical Hydrogen Production*, Springer, New York, NY, USA, 2012.

[28] L. L. Hench and J. K. West, "The Sol-Gel process," *Chemical Reviews*, vol. 90, no. 1, pp. 33–72, 1990.

[29] C. J. Brinker and G. W. Scherer, *Sol-gel Science: The Physics and Chemistry of Sol-gel Processing*, Academic Press, San Diego, Calif, USA, 1990.

[30] V. G. Kessler, G. I. Spijksma, G. A. Seisenbaeva, S. Håkansson, D. H. A. Blank, and H. J. M. Bouwmeester, "New insight in the role of modifying ligands in the sol-gel processing of metal alkoxide precursors: a possibility to approach new classes of materials," *Journal of Sol-Gel Science and Technology*, vol. 40, no. 2-3, pp. 163–179, 2006.

[31] T. Sreethawong, Y. Suzuki, and S. Yoshikawa, "Synthesis, characterization, and photocatalytic activity for hydrogen evolution of nanocrystalline mesoporous titania prepared by surfactant-assisted templating sol-gel process," *Journal of Solid State Chemistry*, vol. 178, no. 1, pp. 329–338, 2005.

[32] A. L. Patterson, "The scherrer formula for X-ray particle size determination," *Physical Review*, vol. 56, no. 10, pp. 978–982, 1939.

[33] H. Sakamoto, J. Qiu, and A. Makishima, "The preparation and properties of CeO_2-TiO_2 film by sol-gel spin-coating process," *Science and Technology of Advanced Materials*, vol. 4, no. 1, pp. 69–76, 2003.

[34] D. M. Eagles, "Polar modes of lattice vibration and polaron coupling constants in rutile (TiO_2)," *Journal of Physics and Chemistry of Solids*, vol. 25, no. 11, pp. 1243–1251, 1964.

[35] C. J. Brinker, R. Sehgal, S. L. Hietala et al., "Sol-gel strategies for controlled porosity inorganic materials," *Journal of Membrane Science*, vol. 94, pp. 85–102, 1994.

[36] A. Janotti, J. B. Varley, P. Rinke, N. Umezawa, G. Kresse, and C. G. van de Walle, "Hybrid functional studies of the oxygen vacancy in TiO_2," *Physical Review B—Condensed Matter and Materials Physics*, vol. 81, no. 8, Article ID 085212, 7 pages, 2010.

[37] D. Regonini, V. Adamaki, C. R. Bowen, S. R. Pennock, J. Taylor, and A. C. E. Dent, "AC electrical properties of TiO_2 and Magnéli phases, Ti_nO_{2n-1}," *Solid State Ionics*, vol. 229, pp. 38–44, 2012.

Hindawi Publishing Corporation
International Journal of Photoenergy
Volume 2014, Article ID 168276, 6 pages
http://dx.doi.org/10.1155/2014/168276

Research Article

Theoretical Study on Electronic Structure and Optical Performance of Nickel and Nitrogen Codoped Rutile Titanium Dioxide

Fei Wang,[1,2,3] Lei Feng,[4] Dongmei Zhang,[4] Qingguo Tang,[1,3] Jinsheng Liang,[1,3] and Dan Feng[1,3]

[1] *Institute of Power Source & Ecomaterials Science, Hebei University of Technology, Tianjin 300130, China*
[2] *Key Laboratory for Palygorskite Science and Applied Technology of Jiangsu Province, Huaiyin Institute of Technology, Huaian 223003, China*
[3] *Key Laboratory of Special Functional Materials for Ecological Environment and Information, Hebei University of Technology, Ministry of Education, Tianjin 300130, China*
[4] *Qian'an College, Hebei United University, Hebei 064400, China*

Correspondence should be addressed to Fei Wang; luckyphilip@sina.com

Received 11 April 2014; Revised 7 May 2014; Accepted 7 May 2014; Published 24 July 2014

Academic Editor: Jiaguo Yu

The nickel doped, nitrogen doped and nickel + nitrogen codoped rutile titanium dioxide have been investigated by ab initio calculations based on density functional theory. The electronic structure and optical performance of different ions doping models are researched through the obtained results, which reflects that the band gap of nickel and nitrogen codoped system declines apparently; the decrease of electron-hole pairs separation and charge carriers recombination rate becomes more desirable. Moreover, the optical absorption curves of nitrogen and nickel codoped rutile titanium dioxide demonstrate the higher photoresponse for visible-light than that of nickel or nitrogen single doped. The above results could provide theoretical basis for further developing of titanium dioxide photocatalyst and related experimental studies.

1. Introduction

Titanium dioxide has characteristics of strong catalytic activity, a long lifetime of photon-generated carrier, high chemical and thermal stability, and low cost; it has become one of the most extensively utilized ideal photocatalytic materials [1–3]. Generally, titanium dioxide has three basic crystalline phases containing brookite, anatase, and rutile titanium dioxide. Anatase titanium dioxide has been widely studied, and rutile titanium dioxide as the most stable one should be further studied and applied. Unfortunately, rutile titanium dioxide has intrinsic wide band gap value of 3.0 eV, and it can be activated only under the ultraviolet radiation from sunlight with only a small portion of the solar energy, resulting in its quite low solar energy usage [4–6]. Therefore, the high efficient usage of visible-light has become one of the most urgent purposes for the photocatalytic materials, and a large number of related theoretical and experimental studies have been performed to regulate the electronic structure and optical performance for titanium dioxide.

At present, many efforts have been made in enhancing the photocatalytic performance of titanium dioxide, including transition metal doping, nonmetal doping, noble metal loading, organic dye sensitizing, and semiconductor compounding [7–11]. Among the above methods, ion doping has been regarded as one of the most effective ways. The previous studies have mostly focused on the single ion doping for titanium dioxide [12–15], but relatively few recent experimental works show that various ions codoping into titanium dioxide can enhance the optical absorption scope and photocatalytic activity. However, the above experimental ions codoping work has disadvantages of variable experimental conditions and sample fabrication methods, resulting in the difficulty in studying the ion doping effect and modification

mechanism [16–19]. Alternatively, the computer simulation could conquer the experimental work drawback and be applied to analyzing the ion doping effects and modification mechanism deeply.

In this paper, the density functional theory plane-wave ultrasoft pseudopotentials method within the first-principles framework has been applied to investigating the electronic structure and optical performance of different ions doping models, including nitrogen and/or nickel doping rutile titanium dioxide. The corresponding properties of pure rutile titanium dioxide are also calculated as a reference. Based on the above mentioned work, the effect of these ions on the electronic structure and optical performance of rutile titanium dioxide has been also illustrated.

2. Models and Computation Details

A $2 \times 2 \times 1$ supercell containing twenty-four atoms for rutile titanium dioxide has been developed in the calculations. As shown in Figure 1, in nickel and nitrogen doped titanium dioxide model, one titanium atom and one oxygen atom were substituted by nickel and nitrogen atom, respectively. As a result, one supercell consisted of seven titanium atoms, fifteen oxygen atoms, one nickel atom, and one nitrogen atom; the atomic concentration of impurity was about 4.17% (atomic fraction) in total. The other models were developed using the almost identical way.

Ab initio calculations based on the density functional theory were performed with the Cambridge Serial Total Energy Package code in Materials Studio 5.5 provided from Accelrys Software Inc. [20, 21]. The ultrasoft pseudopotential was selected to depict the interaction between electrons and the ionic core. The electronic exchange-correlation energy was handled with Perdew-Burke-Ernzerhof (PBE) function in the generalized gradient approximation (GGA) framework. The energy cutoff for the plane-wave basis was 340 eV and Brillouin zone integrations were finished using a Monkhorst-Pack grid of $3 \times 3 \times 8$ k-points [22, 23]. To obtain stable atomic configuration and accurate results comparable with experimental data, pure and various doped models were geometrically optimized by means of the Broyden-Fletcher-Goldfarb-Shanno (BFGS) algorithm. The convergence threshold for self-consistent tolerance was set to 1×10^{-5} eV per atom and atomic relaxations were conducted until the residual forces were below 0.03 eV/Å. The above parameters were suitable for getting well-converged total energy and geometry optimization results. After the geometry optimization, the band structure, density of states, and optical properties of the optimized supercells were calculated. For optical properties calculations, polycrystalline models and "scissors operators" were adapted.

3. Results and Discussions

After the geometry optimization, the lattice parameters of the pure rutile titanium dioxide supercell are obtained as follows: $a = 9.32939$ Å, $b = 9.32939$ Å, and $c = 2.966985$ Å. The above lattice parameters are in good agreement with the experimental results [24, 25], which reflects that the chosen calculation methods are reasonable, and the authentic results could be obtained. Aiming at conveniently comparing the electronic structures of different ions doping models, the same k-points mesh is set to sample the first Brillouin zone for all models. The calculated band gap of pure rutile titanium dioxide is 1.87 eV at G (gamma point) shown in Figure 2; however, the value is much lower than 3.0 eV as the experimental value. The reason for the above phenomenon is that the discontinuity in the exchange-correlation potential is not taken into account within the framework of density functional theory, and the calculated band gap value is often lower than the experimental value [26, 27]. The calculated band structures of Ni-doped, N-doped, and Ni + N-codoped rutile titanium dioxide are shown in Figure 2, respectively.

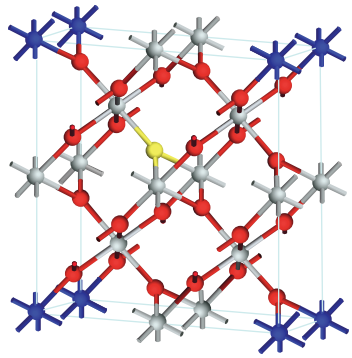

Figure 1: Supercell model for Ni + N-codoped rutile titanium dioxide in the present work (red ball represents the O atom; white ball represents the Ti atom; blue ball represents the Ni atom; yellow ball represents the N atom).

From Figure 2, we can see that the energy levels decline and are split due to the reduction of crystal symmetry degree and destruction of periodic potential field by means of doping. As a result, the valence band top and conduction band bottom of rutile titanium dioxide are both removed towards low energy. Meanwhile, the new energy levels between valence band and conduction band are introduced by electrons of impurity atoms, thus the band gap values of the doped system are all decreased. Specifically, the band gap decreases of Ni-doped, N-doped, and Ni + N-codoped rutile titanium dioxide doped system are 0.08, 0.11, and 0.44 eV, respectively. For Ni-doped rutile titanium dioxide, isolated impurity energy levels are mainly located in the middle of band gap. The above impurity energy levels overlap with valence band maximum or conduction band minimum of rutile titanium dioxide fully. For N-doped rutile titanium dioxide, the impurity energy levels mainly located above the valence band are acceptor states. These states lead to the decrease of band gap and photoelectron transition energy. For N + Ni-codoped rutile titanium dioxide, the energy levels splitting becomes more apparent due to the further decrease of crystal symmetry degree, and more impurity energy levels are developed in the band gap of rutile titanium dioxide. Compared with the single N- or Ni-doped rutile titanium dioxide, the overlapping between impurity energy

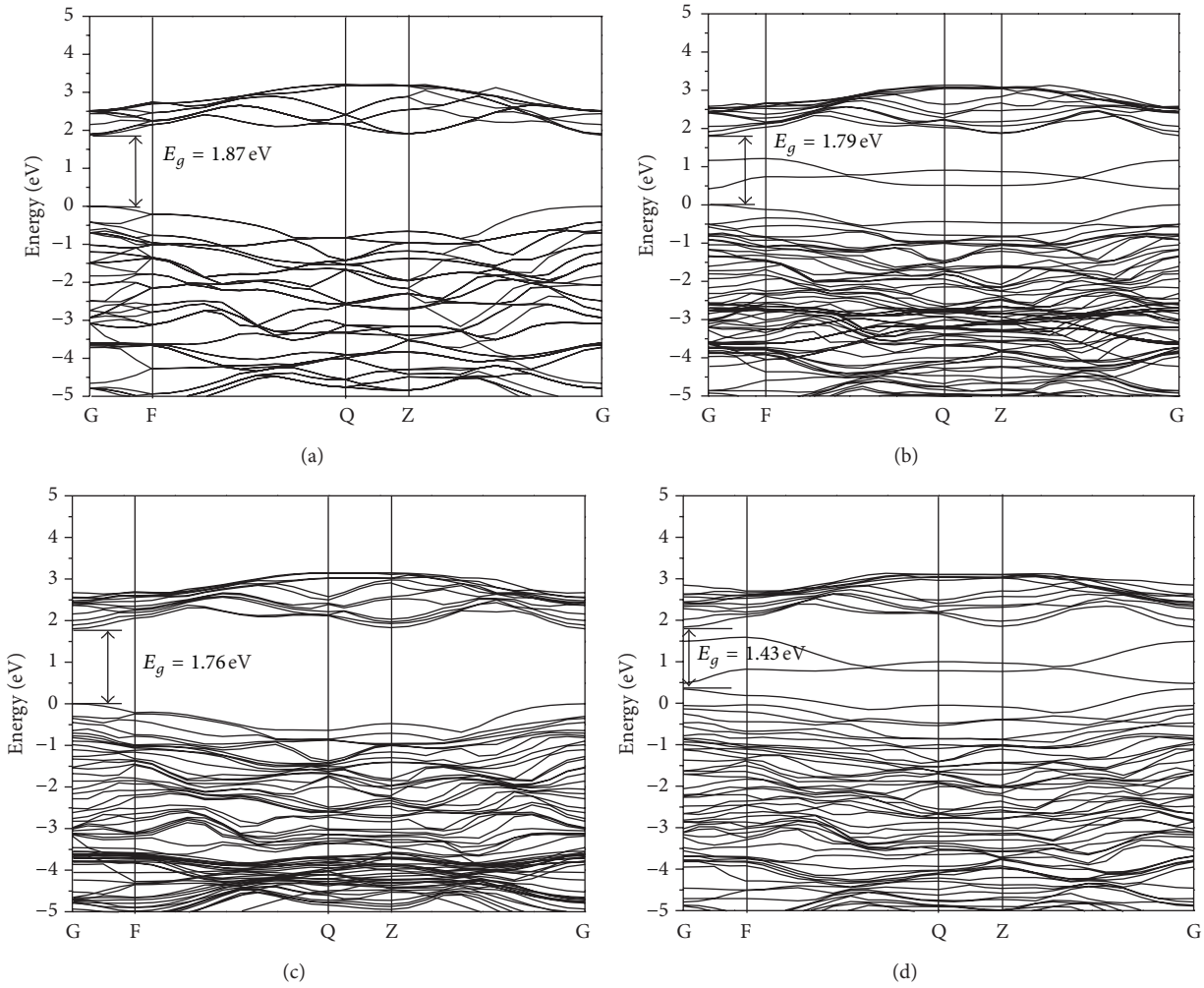

Figure 2: The calculated band structures of (a) pure rutile titanium dioxide, (b) Ni-doped rutile titanium dioxide, (c) N-doped rutile titanium dioxide, and (d) Ni + N-codoped rutile titanium dioxide.

levels and valence band maximum or conduction band minimum is more apparent. Nickel and nitrogen codoping can adjust the band structure of rutile titanium dioxide, and impurity energy levels are developed in the band gap of rutile titanium dioxide. As a result, the band gap of doped system is decreased effectively, and the separation of electron-hole pairs becomes more desirable, which has significant influence on increasing the catalytic activity and visible-light absorption of rutile titanium dioxide [28, 29].

The calculated total density of states and partial density of states of doped models are shown in Figure 3, in order to analyze the origin of the band gap change and the variation of electronic structures caused by doping. Specifically, Figure 3(a) shows the total density of states of all the models; Figures 3(b)–3(e) represent the calculated partial density of states of different doped models, and the vertical dot line at 0 eV is Fermi level.

From Figure 3, it can be seen that valence band and conduction band are mainly composed of O-2p states and Ti-3d states in all rutile titanium dioxide modles. For the pure rutile titanium dioxide, the conduction band is primarily provided by the Ti-3d states, and the valence band is primarily given by the O-2p and partial Ti-3d states. The obtained electronic structures described in the present work are consistent with the results of other theoretical methods [30]. For Ni-doped rutile titanium dioxide, the impurity states are in the middle of band gap, which are composed of O-2p and N-3d states. These states service as a "ladder" through which the electrons in the valence band can be excited to them and then excited to the conduction band. For N-doped rutile titanium dioxide, the valence band around Fermi level is composed by electrons in both the O-2p and N-2p orbit, and it is mainly composed by electrons in the O-2p orbit for pure rutile titanium dioxide. In addition, the valence band around Fermi level is wider than that of pure rutile titanium dioxide, and the valence band top has been shifted up. On the other hand, the conduction band width around Fermi level is approximate to that of pure rutile titanium dioxide, and the conduction band bottom has been shifted down. As a result, the band gap of the N-doped rutile titanium dioxide is decreased, which is consistent with the band structure calculated result. For nickel and nitrogen codoped titanium dioxide, the valence band is mainly

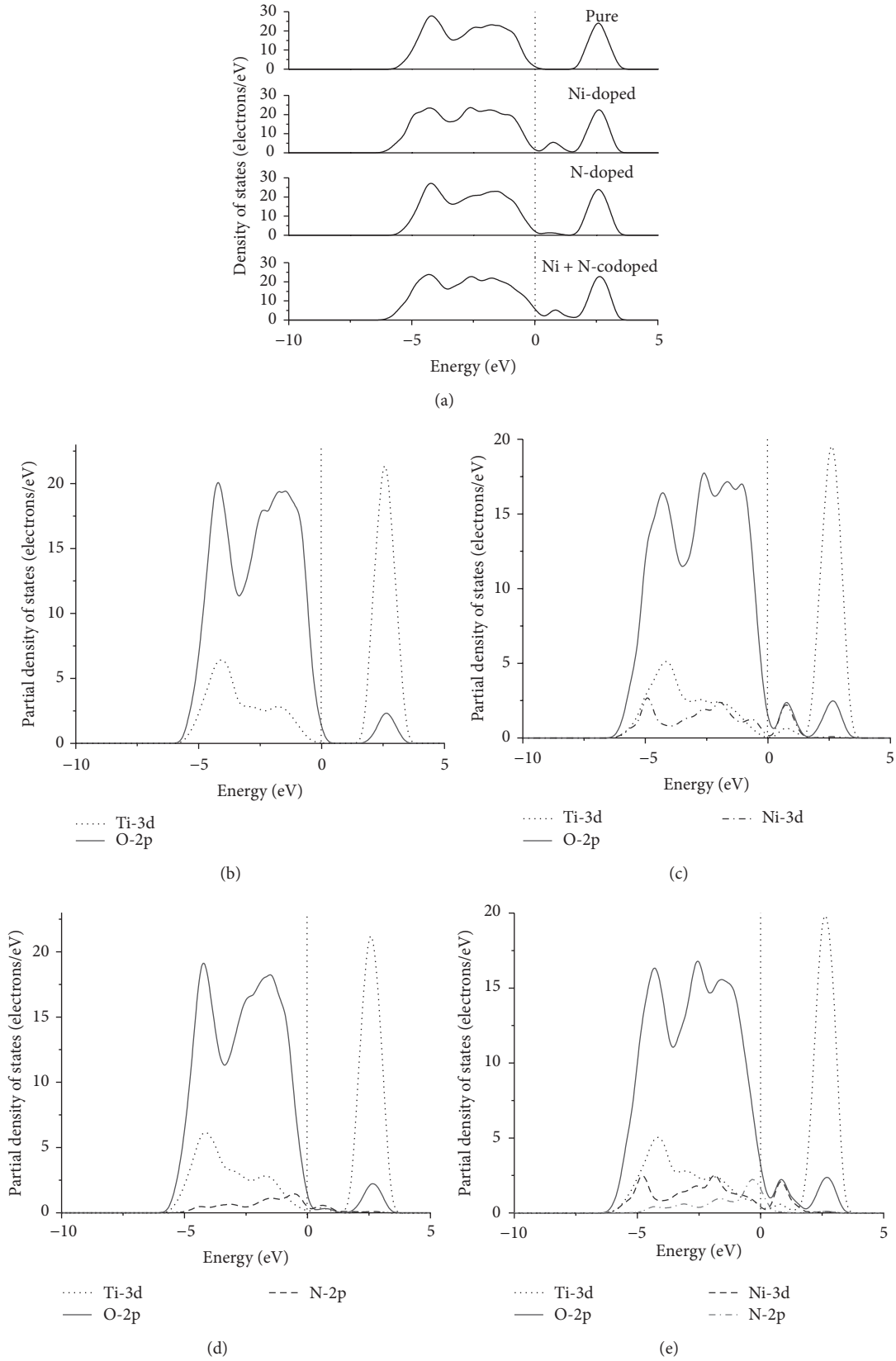

Figure 3: (a) Calculated and comparison total density of states; calculated partial density of states of (b) pure rutile titanium dioxide, (c) Ni-doped rutile titanium dioxide, (d) N-doped rutile titanium dioxide, and (e) Ni + N-codoped rutile titanium dioxide. The dot line at zero point energy is Fermi level.

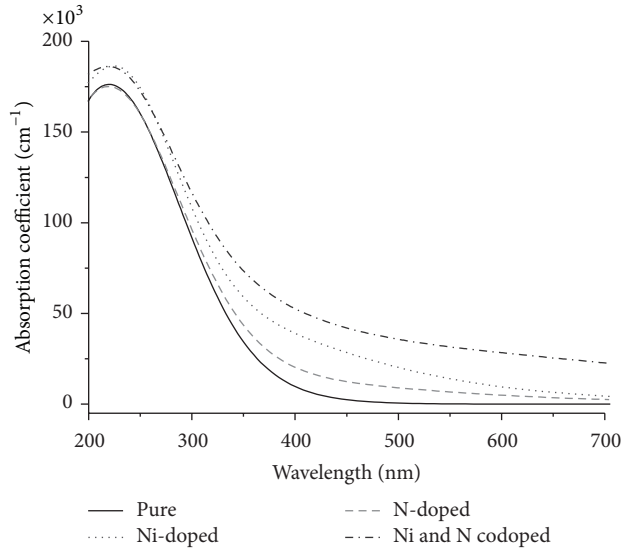

Figure 4: The calculated optical absorption curves for different kinds of rutile titanium dioxide models.

developed by O-2p states hybridization with N-2p states. The impurity energy levels developed by N-2p states overlapped with valence band maximum are situated on the valence band maximum, and the impurity energy levels developed by Ni-3d states are situated on the top of valence band, resulting in the decrease of charge carriers recombination rate and photocatalytic activity improvement of titanium dioxide [31–33]. Meanwhile, the electrons in the valence band can be excited to them and then excited to the conduction band subsequently by visible-light absorption, which is caused by the above impurity energy levels in the band gap. Therefore, these impurity energy levels have advantages on extending the sensitive light wavelength towards visible-light region.

The calculated optical absorption spectra of different doped titanium dioxide models between 200 and 700 nm are shown in Figure 4, in order to investigate the doping effect on the optical performance of rutile titanium dioxide. For all calculations, the scissors operator is chosen as 1.13 eV based on the difference between the experimental and calculated band gap, which could make the obtained results consistent with experimental values.

From Figure 4, it can be seen that the fundamental absorption edges red-shift toward visible-light region after nitrogen or nickel doping. The above phenomenon is more apparent for nitrogen and nickel codoped rutile titanium dioxide than that of nitrogen or nickel single doped rutile titanium dioxide. Therefore, the optical absorption curves of nickel and nitrogen codoped rutile titanium dioxide indicate the highest photoresponse for visible-light, which is consistent with the conclusions obtained from the electronic structure analysis.

4. Conclusion

We have developed and calculated the supercells of pure rutile titanium dioxide, nitrogen, and/or nickel doping rutile titanium dioxide, using ab initio calculations with the plane-wave ultrasoft pseudopotentials method. On the basis of the above calculational results, the electronic structure and optical performance of the above various ions doping models have been also studied. The results indicate that the energy levels splitting becomes apparent for nitrogen and nickel codoped rutile titanium dioxide, and the overlapping between impurity energy levels and valence band maximum or conduction band minimum is more apparent than that of single ion doping. Nitrogen and nickel codoping is quite useful for the decrease of charge carriers recombination rate and energy gap, thus resulting in the great photocatalytic activity increase of rutile titanium dioxide. The optical absorption curves of nitrogen and nickel codoped rutile titanium dioxide indicate that the fundamental absorption edges red-shift toward visible-light region after nitrogen or nickel doping, especially for nitrogen and nickel codoped rutile titanium dioxide. Moreover, the highest photoresponse for visible-light is consistent with the conclusions obtained from the electronic structure analysis. The above conclusions could give the theoretical advice for further developing of titanium dioxide photocatalyst and related experimental research.

Conflict of Interests

The authors declare that there is no conflict of interests regarding the publication of this paper.

Acknowledgments

This research was financially supported by the Natural Science Foundation of Hebei Province, China (Grant no. E2014202276), and the Application Foundation and Advanced Technology Research Program of Tianjin City, China (Grant no. 12JCQNJC02100).

References

[1] O. Ruzimuradov, S. Nurmanov, M. Hojamberdiev et al., "Fabrication of nitrogen-doped TiO_2 monolith with well-defined macroporous and bicrystalline framework and its photocatalytic performance under visible light," *Journal of the European Ceramic Society*, vol. 34, no. 3, pp. 809–816, 2014.

[2] J. G. Yu, C. Trapalis, P. Y. Zhang, G. S. Li, and H. G. Yu, "Environmental photocatalysis 2013," *International Journal of Photoenergy*, vol. 2013, Article ID 786806, 3 pages, 2013.

[3] M. Erol, T. Dikici, M. Toparli, and E. Celik, "The effect of anodization parameters on the formation of nanoporous TiO_2 layers and their photocatalytic activities," *Journal of Alloys and Compounds*, vol. 604, pp. 66–72, 2014.

[4] T. S. Bjørheim, A. Kuwabara, C. E. Mohn, and T. Norby, "Defects at the (1 1 0) surface of rutile TiO_2 from *ab initio* calculations," *International Journal of Hydrogen Energy*, vol. 37, no. 9, pp. 8110–8117, 2012.

[5] T. K. Jia, F. Fu, J. W. Zhao et al., "Sonochemical synthesis, characterization, and photocatalytic activity of N-Doped TiO_2 nanocrystals with mesoporous structure," *International Journal of Photoenergy*, vol. 2014, Article ID 516806, 7 pages, 2014.

[6] C. C. Pei and W. W. Leung, "Enhanced photocatalytic activity of electrospun TiO_2/ZnO nanofibers with optimal anatase/rutile ratio," *Catalysis Communications*, vol. 37, pp. 100–104, 2013.

[7] L. Ćurković, D. Ljubas, S. Šegota, and I. Bačić, "Photocatalytic degradation of Lissamine Green B dye by using nanostructured sol-gel TiO_2 films," *Journal of Alloys and Compounds*, vol. 604, pp. 309–316, 2014.

[8] A. Kusior, J. Klich-Kafel, A. Trenczek-Zajac, K. Swierczek, M. Radecka, and K. Zakrzewska, "TiO_2-SnO_2 nanomaterials for gas sensing and photocatalysis," *Journal of the European Ceramic Society*, vol. 33, no. 12, pp. 2285–2290, 2013.

[9] K. Siwińska-Stefańska, F. Ciesielczyk, M. Nowacka, and T. Jesionowski, "Influence of selected alkoxysilanes on dispersive properties and surface chemistry of titanium dioxide and TiO_2-SiO_2 composite material," *Journal of Nanomaterials*, vol. 2012, Article ID 316173, 19 pages, 2012.

[10] G. Kyung, M. Ha, and S. Ko, "Facile synthesis of solar light sensitive Ag/TiO_2 nanocatalyst wrapped with multiwalled carbon nanotubes," *Nanoscience and Nanotechnology Letters*, vol. 6, pp. 62–67, 2014.

[11] M. M. Rashad, E. M. Elsayed, M. S. Al-Kotb, and A. E. Shalan, "The structural, optical, magnetic and photocatalytic properties of transition metal ions doped TiO_2 nanoparticles," *Journal of Alloys and Compounds*, vol. 581, pp. 71–78, 2013.

[12] K. Seonghyuk, "Photochemical synthesis, characterization and enhanced visible light induced photocatalysis of Ag modified TiO_2 nanocatalyst," *Journal of Nanoscience and Nanotechnology*, vol. 14, no. 9, pp. 6923–6928, 2014.

[13] J. N. Xu, F. Wang, W. X. Liu, W. B. Cao, and J. Photoenergy, "Nanocrystalline N-doped TiO_2 powders: mild hydrothermal synthesis and photocatalytic degradation of phenol under visible light irradiation," *International Journal of Photoenergy*, vol. 2013, Article ID 616139, 7 pages, 2013.

[14] S. K. Zheng, G. H. Wu, and L. Liu, "First-principles calculations on Hg-doped anatase TiO_2 with and without O vacancy," *Solid State Communications*, vol. 165, pp. 15–18, 2013.

[15] M. Khan, J. Xu, W. Cao, and Z.-K. Liu, "Mo-doped TiO_2 with enhanced visible light photocatalytic activity: a combined experimental and theoretical study," *Journal of Nanoscience and Nanotechnology*, vol. 14, no. 9, pp. 6865–6871, 2014.

[16] X. F. Wang, K. Wang, K. W. Feng et al., "Greatly enhanced photocatalytic activity of $TiO_{2-x}N_x$ by a simple surface modification of Fe(III) cocatalyst," *Journal of Molecular Catalysis A: Chemical*, vol. 391, pp. 92–98, 2014.

[17] Y. R. Uhm, S. H. Woo, W. W. Kim, S. J. Kim, and C. K. Rhee, "The characterization of magnetic and photo-catalytic properties of nanocrystalline Ni-doped TiO_2 powder synthesized by mechanical alloying," *Journal of Magnetism and Magnetic Materials*, vol. 304, no. 2, pp. 781–783, 2006.

[18] D. Wojcieszak, M. Mazur, M. Kurnatowska et al., "Influence of Nd-doping on photocatalytic properties of TiO_2 nanoparticles and thin film coatings," *International Journal of Photoenergy*, vol. 2014, Article ID 463034, 10 pages, 2014.

[19] D. D. Sun, Y. Wu, and P. Gao, "Effects of TiO_2 nanostructure and operating parameters on optimized water disinfection processes: a comparative study," *Chemical Engineering Journal*, vol. 249, pp. 160–166, 2014.

[20] Q. S. Shao and H. Zhao, "First-principles studies on magnetic stability of SrC and BaC in rocksalt, zincblende, and nickel arsenide phases under pressure," *Journal of Superconductivity and Novel Magnetism*, vol. 25, pp. 2063–2067, 2012.

[21] X. Guo, P. Q. La, X. F. Lu, Y. P. Wei, X. L. Nan, and L. He, "Theoretical research of electronic structures and optical properties of $\beta - Si_2[Si_{(1-x)}Yb_x]N_4$ (x = 1/4, 1/2 and 3/4) based on the first-principles calculations," *Nanoscience and Nanotechnology Letters*, vol. 5, pp. 1237–1244, 2013.

[22] J. P. Perdew, K. Burke, and M. Ernzerhof, "Generalized gradient approximation made simple," *Physical Review Letters*, vol. 77, no. 18, pp. 3865–3868, 1996.

[23] J. G. Yu, Q. J. Xiang, and M. H. Zhou, "Preparation, characterization and visible-light-driven photocatalytic activity of Fe-doped titania nanorods and first-principles study for electronic structures," *Applied Catalysis B: Environmental*, vol. 90, pp. 595–602, 2009.

[24] J. M. R. Muir, D. Costa, and H. Idriss, "DFT computational study of the RGD peptide interaction with the rutile TiO_2 (110) surface," *Surface Science*, vol. 624, pp. 8–14, 2014.

[25] X. Wang, F. H. Wang, J. X. Shang, and Y. S. Zhou, "*Ab initio* studies of Nb doping effect on the formation of oxygen vacancy in rutile TiO_2," *Journal of Physics and Chemistry of Solids*, vol. 73, no. 1, pp. 84–93, 2012.

[26] J. Pascual, J. Camassel, and H. Mathieu, "Fine structure in the intrinsic absorption edge of TiO_2," *Physical Review B*, vol. 18, no. 10, pp. 5606–5614, 1978.

[27] A. Dashora, N. Patel, D. C. Kothari, B. L. Ahuja, and A. Miotello, "Formation of an intermediate band in the energy gap of TiO_2 by Cu–N-codoping: first principles study and experimental evidence," *Solar Energy Materials and Solar Cells*, vol. 125, pp. 120–126, 2014.

[28] P. Zhou, J. G. Yu, and Y. X. Wang, "The new understanding on photocatalytic mechanism of visible-light response N-S codoped anatase TiO_2 by first-principles," *Applied Catalysis B: Environmental*, vol. 142-143, pp. 45–53, 2013.

[29] J. G. Yu, P. Zhou, and Q. Li, "New insight into the enhanced visible-light photocatalytic activities of B-, C- and B/C-doped anatase TiO_2 by first-principles ," *Physical Chemistry Chemical Physics*, vol. 15, pp. 12040–12047, 2013.

[30] H. Yan, S. T. Kochuveedu, L. N. Quan, S. S. Lee, and D. H. Kim, "Enhanced photocatalytic activity of C, F-codoped TiO_2 loaded with AgCl," *Journal of Alloys and Compounds*, vol. 560, pp. 20–26, 2013.

[31] L. B. Xiong, J. L. Li, B. Yang, and Y. Yu, "Ti^{3+} in the surface of titanium dioxide: generation, properties and photocatalytic application," *Journal of Nanomaterials*, vol. 2012, Article ID 831524, 13 pages, 2012.

[32] Y. M. Lin, Z. Y. Jiang, C. Y. Zhu, X. Y. Hu, X. D. Zhang, and J. Fan, "Visible-light photocatalytic activity of Ni-doped TiO_2 from *ab initio* calculations," *Materials Chemistry and Physics*, vol. 133, pp. 746–750, 2012.

[33] F. Yuan, S. X. Lu, W. G. Xu, and H. F. Zhang, "First-principles study of structural, electronic, and optical properties of the rutile $TiO_2(011)$-2 × 1 surface," *Surface Science*, vol. 621, pp. 88–93, 2014.

Hindawi Publishing Corporation
International Journal of Photoenergy
Volume 2014, Article ID 479508, 9 pages
http://dx.doi.org/10.1155/2014/479508

Research Article

Synthesis of Submicron Hexagonal Plate-Type SnS_2 and Band Gap-Tuned $Sn_{1-x}Ti_xS_2$ Materials and Their Hydrogen Production Abilities on Methanol/Water Photosplitting

Kang Min Kim, Byeong Sub Kwak, Sora Kang, and Misook Kang

Department of Chemistry, College of Science, Yeungnam University, Gyeongsan, Gyeongbuk 712-749, Republic of Korea

Correspondence should be addressed to Misook Kang; mskang@ynu.ac.kr

Received 9 April 2014; Revised 16 May 2014; Accepted 18 May 2014; Published 7 July 2014

Academic Editor: Wei Xiao

SnS_2 and $Sn_{1-x}Ti_xS_2$ ($x = 0$, 0.1, 0.3, 0.5, and 0.7 mol) materials were designed using solvothermal method with the aim to enhance hydrogen production from water/methanol water photosplitting. Scanning electron microscopy revealed hexagonal plates with one side, 3.0 μm in length, in the SnS_2 materials. Pure SnS_2 showed absorption band edges of above 660 nm, and the absorption was shifted to low wavelengths with the insertion of Ti ions. The evolution of H_2 from MeOH/H_2O (1 : 1) photosplitting over SnS_2 hexagonal plates in the photocatalytic liquid system was 0.016 mL h^{-1} g^{-1}, and the evolutions were enhanced in $Sn_{1-x}Ti_xS_2$. In particular, 0.049 mL h^{-1} g^{-1} of H_2 gas was produced in $Sn_{0.7}Ti_{0.3}S_2$ without electrolytes and it increased significantly to more than 90.6% (0.47 mL h^{-1} g^{-1} evolutions) at higher pH using 0.1 M of KOH. Based on the UV-visible absorption spectra, the high photocatalytic activity of $Sn_{1-x}Ti_xS_2$ was attributed to the existence of an appropriate band-gap state that retarded recombination between the electrons and holes.

1. Introduction

Many attempts have been shown to produce hydrogen as a renewable energy carrier to satisfy future demands because of its versatility and friendly properties. With this in mind, the photocatalytic formation of hydrogen and oxygen on semiconductors, such as pure TiO_2 (anatase) [1, 2] and metal loaded-TiO_2 [3–6] or non-metal loaded-TiO_2 [7–9], has been studied extensively because of their relatively low band gap and high corrosion resistance. On the other hand, these materials are activated only by UV because of their large energy band gap (e.g., 3.2 eV for anatase TiO_2). To improve the utilization of solar energy, considerable research effort has focused on shifting the photocatalytic hydrogen producing activity of TiO_2 into the visible wavelength above 450 nm, which accounts for ~42% of solar energy. Recently, studies of metal sulfide photocatalysts, particularly ZnS, Bi_2S_3, and CdS-loaded TiO_2, have covered topics ranging from synthesis to applications in new photocatalytic reaction mechanisms [10–15]. A narrow band gap makes it possible to absorb longer wavelengths compared to the wide band gaps of conventional metal oxide semiconductor systems.

Some researchers have reported SnS_2 materials. In particular, nanostructures of SnS_2 often demonstrated shape and size-dependent physical and chemical properties that are of technological and scientific importance [16, 17]. Consequently, a great deal of effort has been focused on designing methods for the synthesis of SnS_2 with different characteristics [18, 19] to exploit their potential. SnS_2 has abundant optical, electrical, and photoelectric properties [20, 21] and has a band gap of 2.25 eV [22]. Owing to its photoconductivity, it is also considered a prospective candidate for solar cells and optoelectronic devices [20, 21]. Crystals of SnS_2 consist of planar triple layers (sandwiches, S–Sn–S with strong ion-covalent bonding) that are coupled weakly to one another by van der Waals forces. One of the most salient properties of layered SnS_2 is their ability to act as a host for atomic and molecular guest species, which are accommodated at the empty sites bounded by van der Waals forces between the adjacent close packed

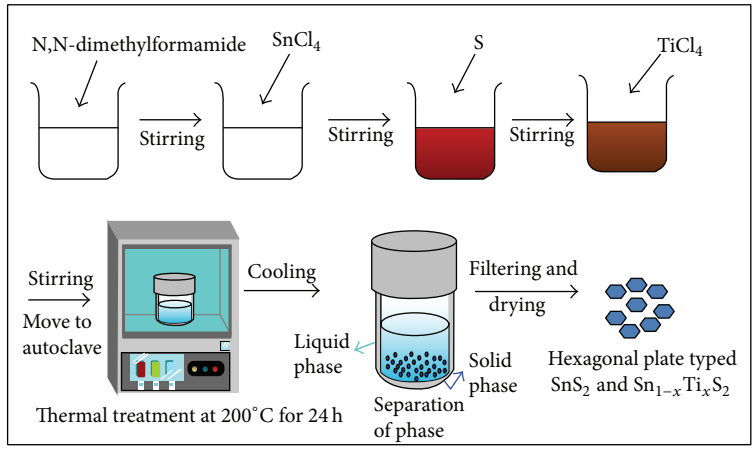

Scheme 1: Synthesis procedure of SnS_2 and $Sn_{1-x}Ti_xS_2$ by a solvothermal method.

chalcogen layers [23]. Owing to this property, lithium can be inserted into SnS_2, meaning that SnS_2 can become a promising candidate as a cathode material in the preparation of lithium batteries [24–26]. In addition, the absence of surface states associated with dangling bonds, which can act as recombination centers for photoinjected electrons, makes SnS_2 an ideal model system for dye sensitization studies and contributes to the high quantum yields [27]. Recently, the application of SnS_2 is shifting to its photocatalytic activity. Yang et al. [28] attributed the greatly enhanced photocatalytic activity of the SnS_x/TiO_2 composites to the matching band potentials and efficient charge transfer and separation at the tight-bonding interface between SnS_x and TiO_2. On the other hand, there are few reports of SnS_2 for photocatalytic hydrogen production, particularly the replacement of the SnS_2 framework with Ti ions ($Sn_{1-x}Ti_xS_2$).

In this study, the SnS_2 submicron hexagonal plate shaped particle was synthesized by a solvothermal method. Ti ions were incorporated into SnS_2 at various molar ratios ($Sn_{1-x}Ti_xS_2$) to regulate the potential energies of the valence and conduction bands for efficient hydrogen production from $MeOH/H_2O$ photosplitting. The relationship between their spectroscopic properties and the photocatalytic performance on the production of H_2 is discussed and the characteristics of SnS_2 and $Sn_{1-x}Ti_xS_2$ were determined by X-ray diffraction (XRD), transmission electron microscopy (TEM), UV-visible absorption spectroscopy, and photoluminescence (PL) spectroscopy.

2. Experimental

SnS_2 and $Sn_{1-x}Ti_xS_2$ were prepared using a solvothermal method, as shown in the experimental flowchart in Scheme 1. To prepare the sol mixture, $SnCl_4$, sulfur powder, and $TiCl_4$ were used as the Sn, S, and Ti precursors, respectively. First, $1 - x$ moles (x is Ti concentration, $x = 0$, 0.1, 0.3, 0.5, and 0.7 mol) of $SnCl_4$ were dissolved in N, N-dimethylformamide as a solvent. 2 moles of S powders and 0, 0.1, 0.3, and 0.5 moles of $TiCl_4$ were added slowly to the solution with constant stirring and stirred to homogeneity for 2 h. Subsequently, the final solution was transferred to an autoclave for the thermal treatment. Sn and Ti ions were sulfurized during thermal treatment at 200°C for 24 h in a nitrogen environment. The resulting precipitates were obtained, washed with acetone, and dried at 50°C for 24 h. Finally, four different materials, SnS_2, $Sn_{0.9}Ti_{0.1}S_2$, $Sn_{0.7}Ti_{0.3}S_2$, and $Sn_{0.5}Ti_{0.5}S_2$ were prepared.

The synthesized SnS_2 and $Sn_{1-x}Ti_xS_2$ particles were examined by XRD (X'Pert Pro MPD PANalytical 2-circle diffractometer at the Yeungnam University Instrumental Analysis Center) using nickel-filtered CuKα radiation (30 kV and 30 mA). The sizes and shapes of the SnS_2 and $Sn_{1-x}Ti_xS_2$ particles were examined by field emission scanning electron microscopy (FE-SEM, S-4100, Hitachi). The UV-visible absorption spectra of SnS_2 and $Sn_{1-x}Ti_xS_2$ particles were obtained using a Cary 500 spectrometer with a reflectance sphere. PL spectroscopy was also performed to determine the number of photoexcited electron hole pairs using a photoluminescence mapping system (LabRamHR, Sci-Tech Instruments).

Photosplitting in a $MeOH/H_2O$ solution was carried out using a liquid photoreactor designed in our laboratory, as shown in Figure 1. For water photosplitting, 0.5 g of SnS_2 or $Sn_{1-x}Ti_xS_2$ particles were added to 1.0 L distilled water in a 2.0 L Pyrex reactor. UV-lamps (6×3 W cm^{-2} = 18 W cm^{-2}, 30 cm length × 2.0 cm diameter; Shinan Com., Korea) emitting radiation of 365 nm were used. Methanol/water ($MeOH/H_2O$) photosplitting was carried out for 10 h with constant stirring, and hydrogen evolution was measured at an interval of 1 h. The concentration of each added electrolyte was 0.1 moles. The hydrogen gas (H_2) produced during water photosplitting was analyzed by TCD-type gas chromatography (GC, model DS 6200; Donam Instruments Inc., Korea). To determine the products and intermediates, the GC was connected directly to the water decomposition reactor. The following GC conditions were used: TCD detector; Carbosphere column (Alltech, Deerfield, IL, USA); 140°C injection temp: 30°C initial temp.; 150°C final temp.; 300°C detector temp.

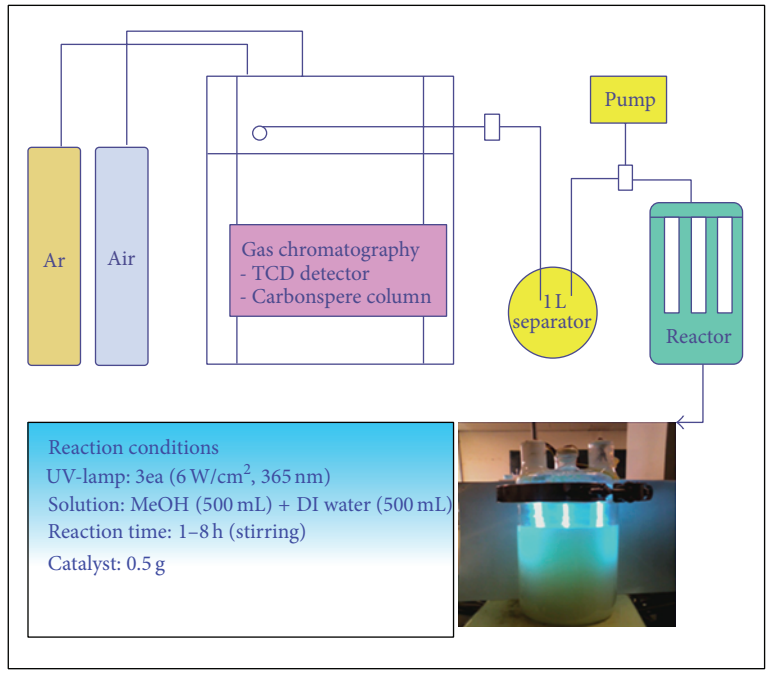

FIGURE 1: Liquid photoreactor designed in our laboratory for photosplitting in a MeOH/H_2O solution.

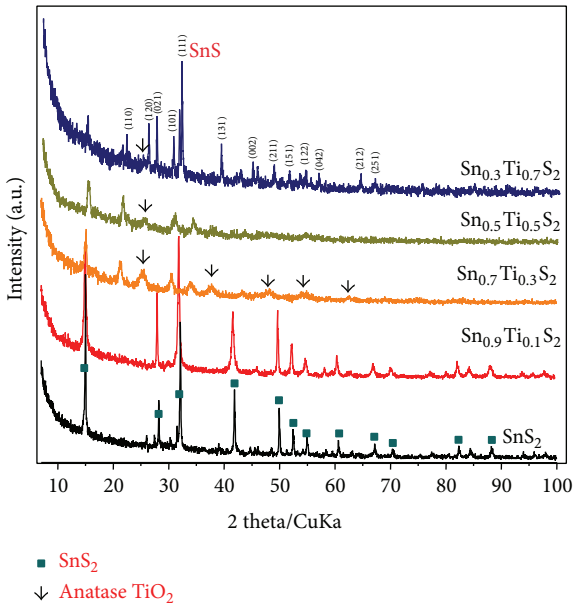

FIGURE 2: XRD patterns of the as-synthesized SnS_2 and $Sn_{1-x}Ti_xS_2$ particles.

3. Results and Discussions

Figure 2 shows XRD patterns of the SnS_2 and $Sn_{1-x}Ti_xS_2$ particles. The XRD peaks in the SnS_2 materials corresponded to pure hexagonal phase SnS_2 (Berndtite-2T, P-3m1, JCPDS card number 23-677), whereas those of $Sn_{1-x}Ti_xS_2$ revealed the formation of SnS_2 and anatase TiO_2 (tetragonal phase, JCPDS card number 65-5714) mixtures. The XRD patterns in hexagonal phase SnS_2 showed the main peaks at 15.0, 28.3, 32.2, 42.2, 50.1, 52.6, 55.3, 60.9, 67.3, 70.5, 82.4, and 88.4° 2θ, which were assigned to the (001), (100), (101), (102), (110), (111), (103), (201), (202), (113), (211), and (212) planes, respectively. In the case of $Sn_{0.9}Ti_{0.1}S_2$, although there was very little reduction in intensity, the peak positions for the SnS_2 structure were not changed and no peaks assigned to TiO_2 were observed despite the addition of Ti ions to the framework because of the very small amount. The peaks for TiO_2 at 25.38, 38.08, 48.28, 54.8, and 63.8° were assigned to the (101), (004), (200), (105), and (204) crystal planes in $Sn_{0.7}Ti_{0.3}S_2$ [29]. The peaks for $Sn_{0.5}Ti_{0.5}S_2$ were very weak, which might be caused by structural damage to the SnS_2 hexagonal phases depending on the level of substitution of Ti ions. This result can be predicted as follows more specifically. The sample nonadded Ti ingredient (SnS_2) exhibits a complete hexagonal crystal structure. However, the SnS_2 framework turns into a new crystal structure (orthorhombic SnS) with an increase of Ti concentration. $Sn_{0.9}Ti_{0.1}S_2$ including Ti 0.1 moL presented to the same framework of SnS_2; however two crystal structures (SnS_2 and SnS) coexisted in $Sn_{0.7}Ti_{0.3}S_2$ with Ti concentration increasing to be 0.3 moL. Here the crystal growth directions in two structures are different, and thus the two crystals are competitively grown, and eventually the peak intensities in XRD patterns are decreased. At this time, the anatase TiO_2 crystals rapidly formed between Ti components which not fully inserted into SnS_2 framework are shown in $Sn_{0.5}Ti_{0.5}S_2$ and $Sn_{0.7}Ti_{0.3}S_2$ samples. It is maybe attributed to too slow crystal growth of SnS_2 and SnS. The result was also similar in $Sn_{0.5}Ti_{0.5}S_2$. Otherwise, the $Sn_{0.3}Ti_{0.7}S_2$ expressed an orthorhombic SnS crystal structure; thus the crystal growth rate increased and finally the strong peak intensities in XRD patterns were

shown in $Sn_{0.3}Ti_{0.7}S_2$. On the other hand, the full width at half maximum (FWHM) of the 25.38 2θ peak for $Sn_{0.7}Ti_{0.3}S_2$ and $Sn_{0.5}Ti_{0.5}S_2$ was estimated. The Scherrer's equation was used to estimate the crystallite size [30]. The calculated crystallite sizes of the $Sn_{0.7}Ti_{0.3}S_2$ and $Sn_{0.5}Ti_{0.5}S_2$ were 13.7 and 10.0 nm, respectively. Surprisingly, the diffraction peaks of the $Sn_{0.3}Ti_{0.7}S_2$ were rather similar to the orthorhombic SnS (JCPDS card, number 01-0984, Pmcn, a = 3.99 A, b = 4.34 A, c = 11.2 A) structure. This suggests that the hexagonal SnS_2 structure can be transferred to an orthorhombic SnS structure when many Ti ions are inserted.

Figure 3 shows low-magnification SEM images of SnS_2 and $Sn_{1-x}Ti_xS_2$ particles. SEM revealed hexagonal plates of one side 3.0 μm in the SnS_2 materials. In contrast, the morphologies of the $Sn_{1-x}Ti_xS_2$ materials varied according to the level of Ti ions insertion: broken sheets, coexisting forms with TiO_2 nanoparticles, and peanut-shaped have been appeared in $Sn_{0.9}Ti_{0.1}S_2$, $Sn_{0.7}Ti_{0.3}S_2$, and $Sn_{0.5}Ti_{0.5}S_2$, respectively. Otherwise, microrods with a similar morphology to SnS were observed in $Sn_{0.3}Ti_{0.7}S_2$. On the other hand, the specific surface areas of SnS_2, $Sn_{0.9}Ti_{0.1}S_2$, $Sn_{0.7}Ti_{0.3}S_2$, $Sn_{0.5}Ti_{0.5}S_2$, and $Sn_{0.3}Ti_{0.7}S_2$ exhibited 38.72, 44.24, 54.20, 68.52, and 48.30 cm^2/g, respectively. Typically, it is well known that the surface area differs on the particle shape and size. However, the specific surface area values in this study seem to be related to the bulk pores formed by the contacts between the particles rather than the particle size and shape. Especially the larger surface area in the case of $Sn_{0.5}Ti_{0.5}S_2$ sample can be considered by bulk pores much formed between the smaller and round-shaped particles. Generally, the larger surface area has, the catalytic performance increases. However, the surface area in our study was not directly related to the catalytic activity. The surface area in $Sn_{0.7}Ti_{0.3}S_2$ was greater than $Sn_{0.5}Ti_{0.5}S_2$; however, the photocatalytic activity (hydrogen production) was more excellent in $Sn_{0.5}Ti_{0.5}S_2$. It can be concluded in this study that the proper band gap and light absorption ability of samples were more advantageously affected to the catalytic activity.

Figure 4 shows the UV-visible diffuse reflectance spectra of the as-synthesized SnS_2 and $Sn_{1-x}Ti_xS_2$ powders. All products displayed optical absorption capabilities over the entire visible light spectrum (400–700 nm). The broad spectrum response suggests that the as-synthesized SnS_2 hexagonal plates should be an excellent visible light responsive photocatalyst for $MeOH/H_2O$ splitting. With Ti ion insertion, the curves were shifted to shorter wavelengths. The optical band-gaps were determined based on the theory of optical absorption for direct band gap semiconductors [31]: $\alpha h\nu = B(h\nu - \mathrm{Eg})^{1/2}$. The curves of $(\alpha h\nu)^2$ versus $(h\nu)$ for the as-synthesized SnS_2 hexagonal plates were plotted. By extrapolating the straight line portion of the plots of $(\alpha h\nu)^2$ versus $(h\nu)$ to $\alpha = 0$, the Eg values of the as-synthesized SnS_2, $Sn_{0.9}Ti_{0.1}S_2$, $Sn_{0.7}Ti_{0.3}S_2$, and $Sn_{0.5}Ti_{0.5}S_2$ were estimated to be 1.87 (670 nm), 1.88 (660 nm), 1.90 (650 nm), and 2.25 (550 nm) eV, respectively. Generally the band gaps of SnS_2 and SnS are 2.2 and 1.08 eV [32]. However, the absorption in the visible region was attributed to the transition from the ground state to a few defect related deep states. This excitation character of the absorption spectra indicated the excellent crystal quality of the semiconductor. A red-shift is observed in the optical absorption spectra of the SnS_2 hexagonal columns, which indicates that the SnS_2 particles were too large to show quantum confinement related effects. This absorption in the visible region was attributed to the transition from the ground state to a few defect related deep states. Consequently, the band gap can be varied according to the particle size or crystal defects.

Photoluminescence (PL) spectroscopy measures the spectrum emitted by the recombination of photogene-rated minority carriers and is a direct way of measuring the band gap. On the other hand, the large quantity of impurities induces a large free carrier density in the bands. Consequently, different carrier interactions cause remarkable modifications of the line shape and spectral energy of the PL features. Figure 5 shows the PL spectra of SnS_2 and $Sn_{1-x}Ti_xS_2$ taken at room temperature. The spectra exhibited a strong emission peak at 549.9 nm corresponding to green emission. The strong PL peaks might be related to crystalline defects induced during growth. SnS_2 exhibits a luminescence peak for near band emission at 549.78 nm (2.25 eV). The intensities of PL curves of samples were smaller with an increase of Ti insertion, and those were decreased in the following order: $SnS_2 < Sn_{0.9}Ti_{0.1}S_2 < Sn_{0.5}Ti_{0.5}S_2 < Sn_{0.7}Ti_{0.3}S_2$. Otherwise, the emission bands of TiO_2 (at 420 nm) were not observed because SnS_2 is a real light sensitizer. Typically, a smaller PL intensity indicates better photoactivity [33].

Figure 6 summarizes the evolution of H_2 from $MeOH/H_2O$ photosplitting over the SnS_2, $Sn_{0.9}Ti_{0.1}S_2$, $Sn_{0.7}Ti_{0.3}S_2$, and $Sn_{0.5}Ti_{0.5}S_2$ photocatalysts in a batch-type liquid photosystem. The catalytic activity of $Sn_{1-x}Ti_xS_2$ was enhanced considerably compared to that of pure SnS_2. 0.08 mL of H_2 gas was collected over 0.5 g SnS_2 photocatalyst after $MeOH/H_2O$ photosplitting for 10 h. SnS_2 easily absorbed longer wavelengths in UV-visible absorption but the recombination between the excited electrons and holes also rapidly generated rapid catalytic deactivation. In contrast a significant amount of H_2 gas was collected over the $Sn_{1-x}Ti_xS_2$, and the amount of H_2 produced reached 0.245 mL (0.049 mL h^{-1} g^{-1}) over 0.5 g $Sn_{0.7}Ti_{0.3}S_2$. $Sn_{1-x}Ti_xS_2$ will show stronger oxidation-reduction ability than pure SnS_2 with decreased electron-hole recombination due to the wider band gap, which increases the photocatalytic performance. This can be related to the PL result. The PL intensity of $Sn_{0.9}Ti_{0.1}S_2$ sample was larger, and this fact means that the recombination between holes and electrons in $Sn_{0.9}Ti_{0.1}S_2$ sample is larger than those in $Sn_{0.5}Ti_{0.5}S_2$. The holes and electrons generated from $Sn_{0.9}Ti_{0.1}S_2$ eventually did not play well in catalytic reaction. Consequently, the recombination time between electrons and holes for sample with mixed structure is expected to be longer rather than a sample having a perfect crystal structure like as SnS or SnS_2. In particular, the catalytic performance for $MeOH/H_2O$ decomposition over $Sn_{0.7}Ti_{0.3}S_2$ was enhanced further in the alkali solution electrolytes (B). Hydrogen production was increased dramatically in the alkali solution (NaOH and KOH) due to the generation of more OH radicals from

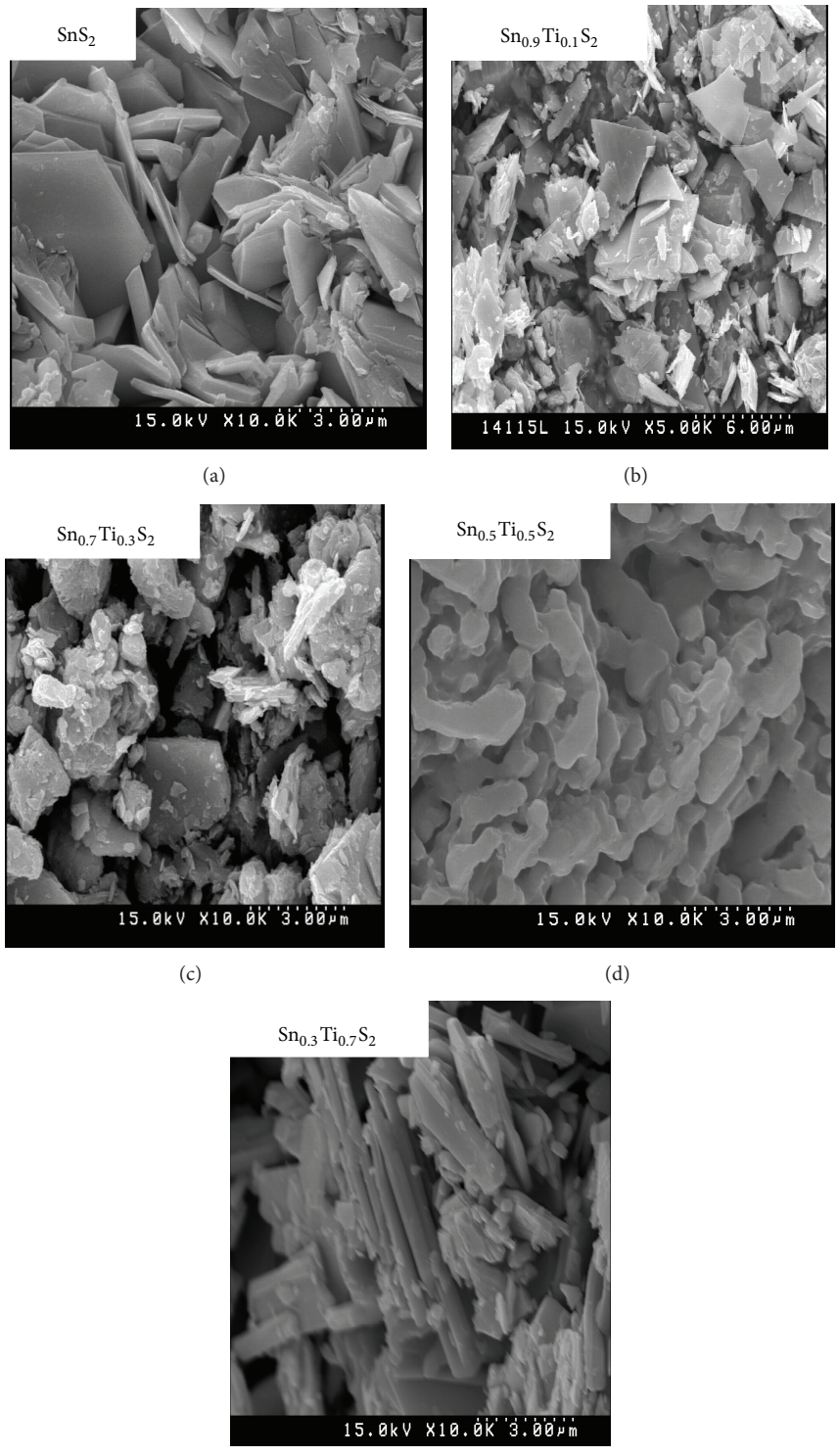

Figure 3: Low-magnification SEM images of the as-synthesized SnS_2 and $Sn_{1-x}Ti_xS_2$ particles.

alkali compounds, and it is reaching up to 0.47 mL h^{-1} g^{-1} evolution in a KOH solution. In acidic solutions as like H_2SO_4 and CH_3COOH, the hydrogen production decreased because the unstable S ions in the $Sn_{0.7}Ti_{0.3}S_2$ catalyst which dissolved in acidic solution oxidized with O ions in water and resulted in forming SO_4^{2-} ions. The ions combined with the hydrogen ions generated during the $MeOH/H_2O$ photosplitting process to form H_2SO_4, and thus the hydrogen production was decreased. Otherwise, when neutral Na_2SO_4 compounds are added into the reaction solution, there is

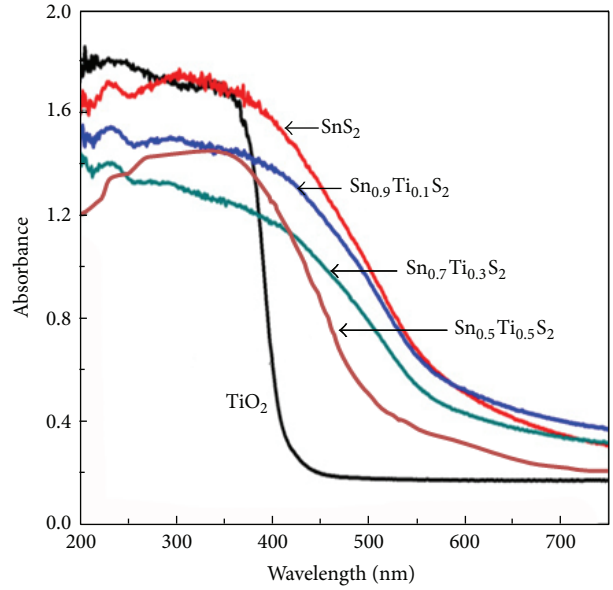

Figure 4: UV-visible diffuse reflectance spectra of the as-synthesized SnS_2 and $Sn_{1-x}Ti_xS_2$ powders.

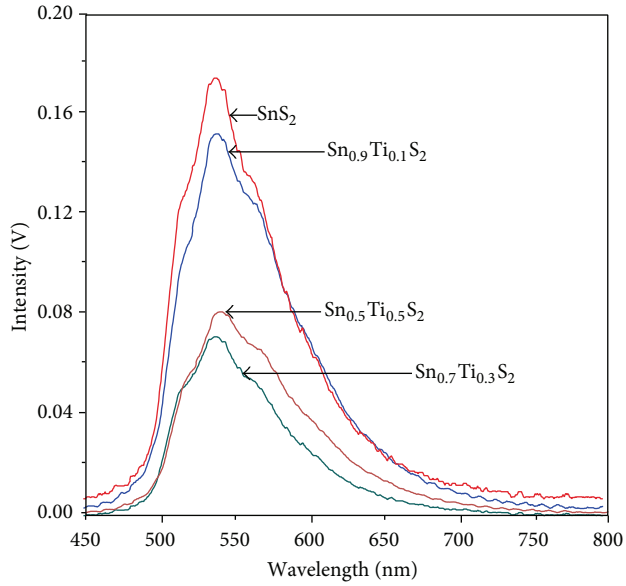

Figure 5: PL spectra of the as-synthesized SnS_2 and $Sn_{1-x}Ti_xS_2$ at room temperature.

already the excess amount of SO_4^{2-} ions, and thus SO_4^{2-} ions formations are suppressed by the principle of Le Chatelier. Consequently, the catalytic activity in Na_2SO_4 solution relatively increased compared to it in the solution with nonadditives.

The UV-visible absorption and PL spectra indicated two photocatalysis models, as shown in Scheme 2. In model (a), combination between TiO_2 and SnS_2 was perfectly formed as in the $Sn_{0.9}Ti_{0.1}S_2$ composite, despite the initial photoreaction being slower because of the larger band gap but the recombination of electrons and holes was slower, resulting in an increase in catalytic performance. In model (b), if TiO_2 particles are physically loaded on the surface of SnS_2 particles, the first electronic transition would occur in the SnS_2 semiconductors from the 365 nm radiation source, and the electrons at a higher conduction band in SnS_2 move to the TiO_2 conduction band, whereas the holes in TiO_2 move to the valence band of SnS_2, which is formed by the current recycle. Therefore, the recombination of excited electrons and holes will be suppressed during photocatalysis. These phenomena increase the evolution of OH radicals formed from the electrons and holes that will eventually enhance the photocatalytic performance of MeOH and H_2O degradation. Therefore, the $Sn_{1-x}Ti_xS_2$ composites exhibited better catalytic performance than the TiO_2 and SnS_2 monocatalysts.

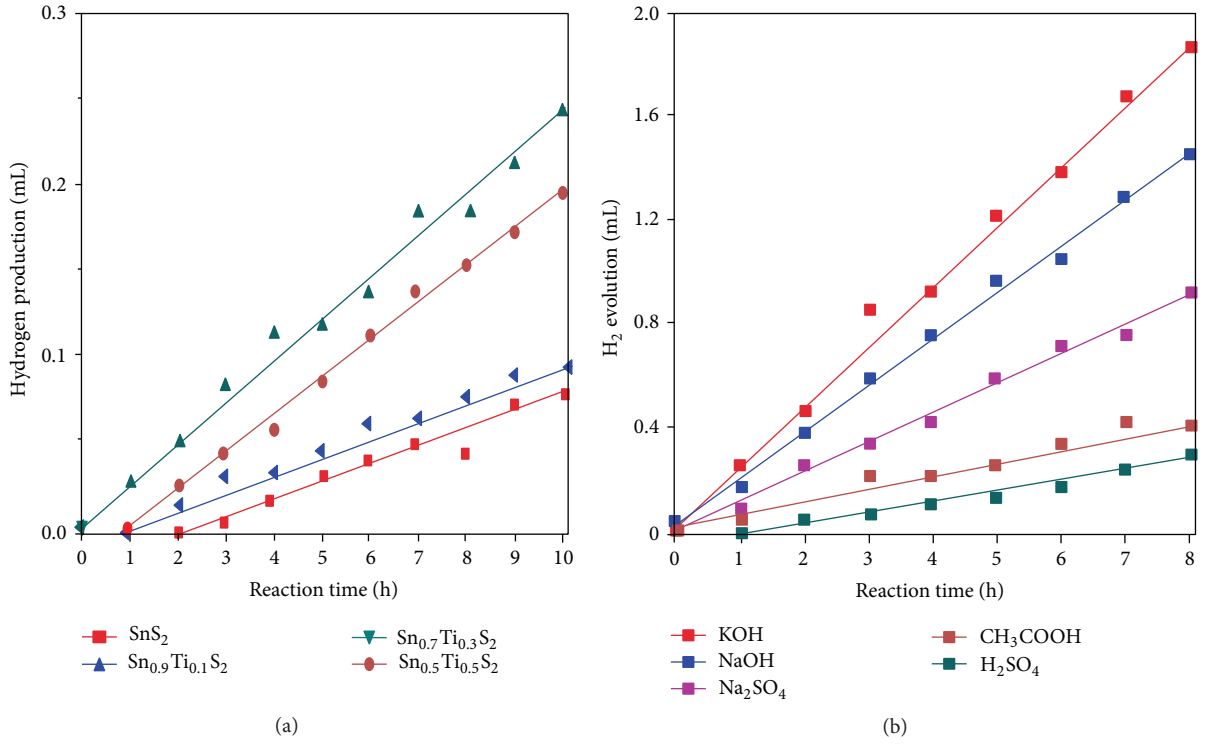

FIGURE 6: Evolution of H_2 gases from MeOH/H_2O photosplitting over the as-synthesized SnS_2, $Sn_{0.9}Ti_{0.1}S_2$, $Sn_{0.7}Ti_{0.3}S_2$, and $Sn_{0.5}Ti_{0.5}S_2$ photocatalysts. (a) On the photocatalysts without electrolytes and (b) on $Sn_{0.7}Ti_{0.3}S_2$ with various electrolytes.

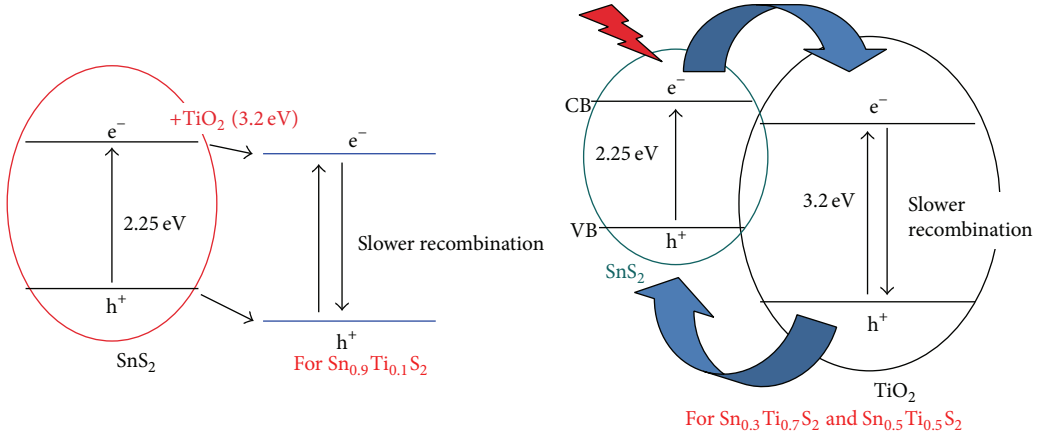

(a) If Ti ions are inserted into SnS_2 framework

(b) If TiO_2 particles are loaded on the surface of SnS_2 particles

SCHEME 2: Two photocatalysis models suggested in this study. (a) Ti ions are inserted into SnS_2 framework, and (b) TiO_2 particles are loaded on the surface of the SnS_2 particles.

4. Conclusions

This reported the development of new photocatalysts using a metal sulfide framework for hydrogen production from MeOH/H_2O splitting. SnS_2 and $Sn_{1-x}Ti_xS_2$ exhibiting activity in the visible radiation were synthesized using a solvothermal method. UV-visible absorption spectroscopy revealed estimated band gaps of 1.87, 1.88, 1.90, and 2.25 eV for the as-synthesized SnS_2, $Sn_{0.9}Ti_{0.1}S_2$, $Sn_{0.7}Ti_{0.3}S_2$, and $Sn_{0.5}Ti_{0.5}S_2$, respectively. The PL intensity of SnS_2 and $Sn_{1-x}Ti_xS_2$ decreased with the addition of Ti and was smallest in $Sn_{0.7}Ti_{0.3}S_2$. A significant amount of H_2 gas was collected over the $Sn_{0.7}Ti_{0.3}S_2$ photocatalyst, and the amount reached 0.049 mL h^{-1} g^{-1} without an electrolyte with a maximum yield of 1.88 mL after 8 h in a KOH solution. This is due most likely to the slower recombination of electrons

and holes, which enables higher catalytic performance for $Sn_{0.7}Ti_{0.3}S_2$.

Conflict of Interests

The authors declare that there is no conflict of interests regarding the publication of this paper.

Acknowledgment

This work was supported by the National Research Foundation of Korea (NRF) Grant funded by the Ministry of Education, Science and Technology (no. 2012R1A1A3005043), for which the authors are very grateful.

References

[1] S. Sakulkhaemaruethai and T. Sreethawong, "Synthesis of mesoporous-assembled TiO_2 nanocrystals by a modified urea-aided sol-gel process and their outstanding photocatalytic H_2 production activity," *International Journal of Hydrogen Energy*, vol. 36, no. 11, pp. 6553–6559, 2011.

[2] J. Yu, M. Jaroniec, G. Lu, C. Trapalis, and G. Liu, "TiO_2 photocatalytic materials 2013," *International Journal of Photoenergy*, vol. 2013, Article ID 534164, 2 pages, 2013.

[3] C. Zhao, A. Krall, H. Zhao, Q. Zhang, and Y. Li, "Ultrasonic spray pyrolysis synthesis of Ag/TiO_2 nanocomposite photocatalysts for simultaneous H_2 production and CO_2 reduction," *International Journal of Hydrogen Energy*, vol. 37, no. 13, pp. 9967–9976, 2012.

[4] X. Wu, Q. Song, L. Jia, Q. Li, C. Yang, and L. Lin, "Pd-Gardenia-TiO_2 as a photocatalyst for H_2 evolution from pure water," *International Journal of Hydrogen Energy*, vol. 37, no. 1, pp. 109–114, 2012.

[5] B.-S. Huang, F.-Y. Chang, and M.-Y. Wey, "Photocatalytic properties of redox-treated Pt/TiO_2 photocatalysts for H_2 production from an aqueous methanol solution," *International Journal of Hydrogen Energy*, vol. 35, no. 15, pp. 7699–7705, 2010.

[6] H. Bai, J. Juay, Z. Liu, X. Song, S. S. Lee, and D. D. Sun, "Hierarchical $SrTiO_3/TiO_2$ nanofibers heterostructures with high efficiency in photocatalytic H_2 generation," *Applied Catalysis B: Environmental*, vol. 125, pp. 367–374, 2012.

[7] B. Viswanathan and K. R. Krishanmurthy, "Nitrogen incorporation in TiO_2: does it make a visible light photo-active material?" *International Journal of Photoenergy*, vol. 2012, Article ID 269654, 10 pages, 2012.

[8] K. M. Parida, S. Pany, and B. Naik, "Green synthesis of fibrous hierarchical meso-macroporous N doped TiO_2 nanophotocatalyst with enhanced photocatalytic H_2 production," *International Journal of Hydrogen Energy*, vol. 38, no. 9, pp. 3545–3553, 2013.

[9] H. Bai, K. S. Y. Kwan, Z. Liu, X. Song, S. S. Lee, and D. D. Sun, "Facile synthesis of hierarchically meso/nanoporous s- and c-codoped TiO_2 and its high photocatalytic efficiency in H_2 generation," *Applied Catalysis B: Environmental*, vol. 129, pp. 294–300, 2013.

[10] J. Kim and M. Kang, "A newly designed a Tio_2-loaded spherical ZnS nano/micro-composites for high hydrogen production from methanol/water solution photo-splitting," *Bulletin of the Korean Chemical Society*, vol. 33, no. 7, pp. 2133–2139, 2012.

[11] J. Kim and M. Kang, "High photocatalytic hydrogen production over the band gap-tuned urchin-like Bi_2S_3-loaded TiO_2 composites system," *International Journal of Hydrogen Energy*, vol. 37, no. 10, pp. 8249–8256, 2012.

[12] J. Kim, Y. Sohn, and M. Kang, "New fan blade-like core-shell $Sb_2Ti_xS_y$ photocatalytic nanorod for hydrogen production from methanol/water photolysis," *International Journal of Hydrogen Energy*, vol. 38, no. 5, pp. 2136–2143, 2013.

[13] J. S. Jang, H. G. Kim, U. A. Joshi, J. W. Jang, and J. S. Lee, "Fabrication of CdS nanowires decorated with TiO_2 nanoparticles for photocatalytic hydrogen production under visible light irradiation," *International Journal of Hydrogen Energy*, vol. 33, no. 21, pp. 5975–5980, 2008.

[14] S. Peng, Y. Huang, and Y. Li, "Rare earth doped TiO_2-CdS and TiO_2-CdS composites with improvement of photocatalytic hydrogen evolution under visible light irradiation," *Materials Science in Semiconductor Processing*, vol. 16, no. 1, pp. 62–69, 2013.

[15] C. Li, J. Yuan, B. Han, L. Jiang, and W. Shangguan, "TiO_2 nanotubes incorporated with CdS for photocatalytic hydrogen production from splitting water under visible light irradiation," *International Journal of Hydrogen Energy*, vol. 35, no. 13, pp. 7073–7079, 2010.

[16] Y. C. Zhang, Z. N. Du, K. W. Li, and M. Zhang, "Size-controlled hydrothermal synthesis of SnS_2 nanoparticles with high performance in visible light-driven photocatalytic degradation of aqueous methyl orange," *Separation and Purification Technology*, vol. 81, no. 1, pp. 101–107, 2011.

[17] H. Mukaibo, A. Yoshizawa, T. Momma, and T. Osaka, "Particle size and performance of SnS_2 anodes for rechargeable lithium batteries," *Journal of Power Sources*, vol. 119–121, pp. 60–63, 2003.

[18] H. Yang, C. Huang, and X. Su, "Synthesis of homogeneous PVP-capped SnS_2 submicron particles via microwave irradiation," *Materials Letters*, vol. 60, no. 29-30, pp. 3714–3717, 2006.

[19] S. Liu, X. Yin, L. Chen, Q. Li, and T. Wang, "Synthesis of self-assembled 3D flowerlike SnS_2 nanostructures with enhanced lithium ion storage property," *Solid State Sciences*, vol. 12, no. 5, pp. 712–718, 2010.

[20] R. W. Miles, O. E. Ogah, G. Zoppi, and I. Forbes, "Thermally evaporated thin films of SnS for application in solar cell devices," *Thin Solid Films*, vol. 517, no. 17, pp. 4702–4705, 2009.

[21] R. B. V. Chalapathy, G. S. Jung, and B. T. Ahn, "Fabrication of Cu_2ZnSnS_4 films by sulfurization of Cu/ZnSn/Cu precursor layers in sulfur atmosphere for solar cells," *Solar Energy Materials and Solar Cells*, vol. 95, no. 12, pp. 3216–3221, 2011.

[22] S. C. Ray, M. K. Karanjai, and D. Dasgupta, "Structure and photoconductive properties of dip-deposited SnS and SnS_2 thin films and their conversion to tin dioxide by annealing in air," *Thin Solid Films*, vol. 350, no. 1, pp. 72–78, 1999.

[23] R. Schlaf, N. R. Armstrong, B. A. Parkinson, C. Pettenkofer, and W. Jaegermann, "Van der Waals epitaxy of the layered semiconductors $SnSe_2$ and SnS_2: morphology and growth modes," *Surface Science*, vol. 385, no. 1, pp. 1–14, 1997.

[24] T.-J. Kim, C. Kim, D. Son, M. Choi, and B. Park, "Novel SnS_2-nanosheet anodes for lithium-ion batteries," *Journal of Power Sources*, vol. 167, no. 2, pp. 529–535, 2007.

[25] T. Momma, N. Shiraishi, A. Yoshizawa et al., "SnS_2 anode for rechargeable lithium battery," *Journal of Power Sources*, vol. 97-98, pp. 198–200, 2001.

[26] Q. Wang, Y. Huang, J. Miao, Y. Zhao, and Y. Wang, "Synthesis and electrochemical characterizations of Ce doped SnS_2 anode

materials for rechargeable lithium ion batteries," *Electrochimica Acta*, vol. 93, pp. 120–130, 2013.

[27] N. Takeda and B. A. Parkinson, "The relationship between squaraine dye surface morphology and sensitization behavior on SnS_2 electrodes," *Electrochimica Acta*, vol. 45, no. 28, pp. 4559–4564, 2000.

[28] C. Yang, W. Wang, Z. Shan, and F. Huang, "Preparation and photocatalytic activity of high-efficiency visible-light-responsive photocatalyst SnS_x/TiO_2," *Journal of Solid State Chemistry*, vol. 182, no. 4, pp. 807–812, 2009.

[29] Y. Li, X. Sun, H. Li, S. Wang, and Y. Wei, "Preparation of anatase TiO_2 nanoparticles with high thermal stability and specific surface area by alcohothermal method," *Powder Technology*, vol. 194, no. 1-2, pp. 149–152, 2009.

[30] S. Modak, M. Ammar, F. Mazaleyrat, S. Das, and P. K. Chakrabarti, "XRD, HRTEM and magnetic properties of mixed spinel nanocrystalline Ni-Zn-Cu-ferrite," *Journal of Alloys and Compounds*, vol. 473, no. 1-2, pp. 15–19, 2009.

[31] X. Hu, G. Song, W. Li et al., "Phase-controlled synthesis and photocatalytic properties of SnS, SnS_2 and SnS/SnS_2 heterostructure nanocrystals," *Materials Research Bulletin*, vol. 48, no. 6, pp. 2325–2332, 2013.

[32] M. L. Toh, K. J. Tan, F. X. Wei, K. K. Zhang, H. Jiang, and C. Kloc, "Intercalation of organic molecules into SnS_2 single crystals," *Journal of Solid State Chemistry*, vol. 198, pp. 224–230, 2013.

[33] B. Liu, X. Zhao, Q. Zhao, X. He, and J. Feng, "Effect of heat treatment on the UV-vis-NIR and PL spectra of TiO_2 films," *Journal of Electron Spectroscopy and Related Phenomena*, vol. 148, no. 3, pp. 158–163, 2005.

Hindawi Publishing Corporation
International Journal of Photoenergy
Volume 2014, Article ID 930439, 8 pages
http://dx.doi.org/10.1155/2014/930439

Research Article

Boundary Layer of Photon Absorption Applied to Heterogeneous Photocatalytic Solar Flat Plate Reactor Design

Héctor L. Otálvaro-Marín,[1] Miguel Angel Mueses,[2] and Fiderman Machuca-Martínez[1]

[1] *GAOX Group, Chemical Engineering School, Universidad del Valle, A.A. 25360 Cali, Colombia*
[2] *Photocatalysis and Solar Photoreactors Engineering, Department of Chemical Engineering, Universidad de Cartagena, A.A. 1382 Cartagena, Colombia*

Correspondence should be addressed to Héctor L. Otálvaro-Marín; hector.otalvaro@correounivalle.edu.co

Received 28 February 2014; Accepted 12 May 2014; Published 5 June 2014

Academic Editor: Hong Liu

This study provides information to design heterogeneous photocatalytic solar reactors with flat plate geometry used in treatment of effluents and conversion of biomass to hydrogen. The concept of boundary layer of photon absorption taking into account the efficient absorption of radiant energy was introduced; this concept can be understood as the reactor thickness measured from the irradiated surface where 99% of total energy is absorbed. Its thickness and the volumetric rate of photons absorption (VRPA) were used as design parameters to determine (i) reactor thickness, (ii) maximum absorbed radiant energy, and (iii) the optimal catalyst concentration. Six different commercial brands of titanium dioxide were studied: Evonik-Degussa P-25, Aldrich, Merck, Hombikat, Fluka, and Fisher. The local volumetric rate of photon absorption (LVRPA) inside the reactor was described using six-flux absorption-scattering model (SFM) applied to solar radiation. The radiation field and the boundary layer thickness of photon absorption were simulated with absorption and dispersion effects of catalysts in water at different catalyst loadings. The relationship between catalyst loading and reactor thickness that maximizes the absorption of radiant energy was obtained for each catalyst by apparent optical thickness. The optimum concentration of photocatalyst Degussa P-25 was 0.2 g/l in 0.86 cm of thickness, and for photocatalyst Aldrich it was 0.3 g/l in 0.80 cm of thickness.

1. Introduction

Heterogeneous photocatalysis based on TiO_2 and modified photocatalysts is widely used in energetic and environmental applications, including water and air purification systems [1, 2], self-cleaning surfaces [3], wettability patterns, and printing applications [4], and as a clean production route of hydrogen fuel [5]. The first step of photocatalytic reaction mechanism [6] is the radiant energy absorption higher than the band gap of the semiconductor to generate electron-hole pairs on its surface, which can initiate oxidation and reduction reactions.

A clean route for hydrogen production has been proposed by photogenerated electrons at the conduction band from reduction of water in the absence of oxygen and oxidation of waste biomass using solar energy [7].

Regarding the mineralization of organic contaminants, Turchi and Ollis proposed a path based on the generation of oxidizing species (Table 1) [6]; adsorbed water on the TiO_2's surface (reactions 2a and 2b) reacts with holes to generate hydroxyl radicals (reactions 6a and 6b). The attack of the hydroxyl radical (reactions 9–12) on a C–H bond is the prevailing step for the oxidative breakdown, which is responsible for the mineralization of a wide range of pollutants (e.g., cyanide, arsenic, halogenated hydrocarbons, pesticides, endocrine disruptors, estrogens, inorganics, aromatics, emerging pollutants, and many others) [8–14]. More details of the mechanism and their considerations are in [15].

The above mentioned applications present a trend towards the use of solar energy as a sustainable source of energy, development of efficient reactors geometries, and scale-up of reactors. Therefore, rigorous methodologies have

Table 1: Heterogeneous photocatalysis reaction scheme based on semiconductor TiO_2, extracted from Turchi and Ollis [6].

Activation	$TiO_2 \xrightarrow{h\nu} e^- + h^+$	(1)
Adsorption	$O^{2-}_{Lattic} + Ti^{IV} + H_2O \rightleftharpoons O_L H^- + Ti^{IV} - OH^-$	(2a)
	$Ti^{IV} + H_2O \rightleftharpoons Ti^{IV} - H_2O$	(2b)
	$Site + R_i \rightleftharpoons R_{i,ads}$	(3)
	$OH^\bullet + Ti^{IV} \rightleftharpoons Ti^{IV} - OH^\bullet$	(4)
Recombination	$e^- + h^+ \rightarrow heat$	(5)
Hole trapping	$Ti^{IV} - OH^- + h^+ \rightleftharpoons Ti^{IV} - OH^\bullet$	(6a)
	$Ti^{IV} - H_2O + h^+ \rightleftharpoons Ti^{IV} - OH^\bullet + H^+$	(6b)
	$R_{i,ads} + h^+ \rightleftharpoons R^+_{i,ads}$	(7)
Electron trapping	$Ti^{IV} + e^- \rightleftharpoons Ti^{III}$	(8a)
	$Ti^{III} + O_2 \rightleftharpoons Ti^{IV} - O_2^{\bullet -}$	(8b)
Hydroxyl attack		
Case I	$Ti^{IV} - OH^\bullet + R_{i,ads} \rightarrow Ti^{IV} + R_{j,ads}$	(9)
Case II	$OH^\bullet + R_{i,ads} \rightarrow R_{j,ads}$	(10)
Case III	$Ti^{IV} - OH^\bullet + R_i \rightarrow Ti^{IV} + R_j$	(11)
Case IV	$OH^\bullet + R_i \rightarrow R_j$	(12)

been developed for design and optimization of photoreactors based on scientific knowledge of the photocatalytic process [8, 9, 14, 16–18], allowing a more economical and technically feasible process.

The rigorous description of photoreactor requires (i) radiation field, (ii) hydrodynamic field, and (iii) mass balance with kinetic expression whose parameters should be independent of photon absorption. The study of the radiation field provides optimal design information such as reactor geometry, catalyst selection, catalyst loading, and dimensions of the reactor [19, 20].

The variable most employed to quantify the spatial distribution of radiant energy absorbed within the reactor is the local volumetric rate of photon absorption (LVRPA); it depends on the geometry, radiation source, loading, and type of photocatalyst, in some cases on the pollutant if this presents absorption of radiant energy. A rigorous approach to determine the LVRPA is the solution of the radiative transfer equation (RTE), by the discrete ordinate method (DOM), which requires spatial, directional, and spectral discretizations inside the reactor [8, 20, 21].

A useful approach is the six-flux absorption-scattering model (SFM); it has been applied to different geometries: compound parabolic collector (CPC) photoreactors [10, 19], annular reactors [12, 13, 22–24], and flat plate reactors [25]. This model calculates the LVRPA through a system of algebraic equations, where the scattering event can occur only along the six directions of the Cartesian coordinates [25]; it reduces the mathematical complexity to an analytical system, thus saving computational time and effort.

Flat plate reactors are scalable, and these can be used with solar radiation, so they are very attractive and also provide an excellent configuration for efficient excitation of the semiconductor photocatalyst TiO_2 [26]; their modeling requires a complex analysis of the radiation field inside the photoreactor [27]. In water treatment, for a dilute pollutant is considered the photon absorption only by the solid photocatalyst particles [28, 29], therefore, the pollutant concentration and the radiation field are decoupled [20, 25] allowing us to separately study the effect of photon absorption of the water-catalyst solution.

In this study, design parameters of a flat plate photoreactor with photocatalysts based on TiO_2 and solar radiation were analyzed in terms of absorption of photons. For mathematical convenience, the variable LVRPA/I_0 was employed; it is estimated by SFM model and does not require emission model. Also, a new design parameter for selection of the optimum reactor thickness called boundary layer thickness of photon absorption is presented. The information presented might be used in kinetic models of pollutants degradation and hydrogen production.

2. Methodology

2.1. Model of Boundary Layer of Photon Absorption. This paper proposes a new concept for heterogeneous photocatalytic reactor design, which allows us to determine the best thickness. Figure 1 shows a schematic representation of a double flat plate reactor with thick H_R, located perpendicular to the source. Additionally, the figure presents a profile of LVRPA along the y-coordinate, with maximum value at the interface surface-flow ($LVRPA_s$) and minimum value at reactor bottom ($LVRPA_\infty$).

The region where there is a gradient of energy absorption has been called "boundary layer of photon absorption," and its thickness δ_{abs} is defined as y-value which satisfies the following ratio:

$$\frac{LVRPA_s - LVRPA(\delta_{abs})}{LVRPA_s - LVRPA_\infty} = 0.99. \quad (1)$$

This definition of boundary layer thickness for transport phenomena and absorption of radiant energy is analogous to the definition of thickness of hydrodynamic, thermal, and concentration boundary layer on a flat plate [30]. The δ_{abs}

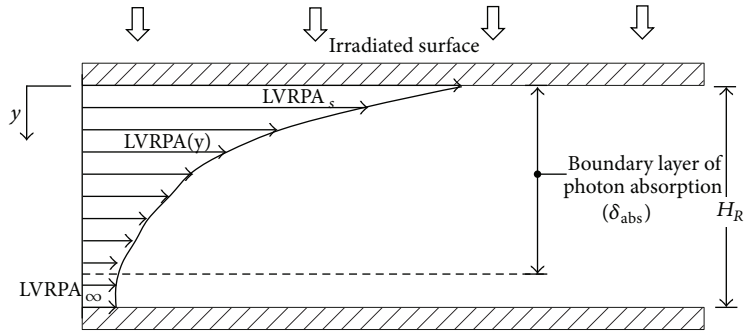

Figure 1: Boundary layer of photon absorption in a double flat plate reactor irradiated onto upper plate.

can be understood as the reactor thickness measured from the irradiated surface where 99% of total energy is absorbed. For this reason, boundary layer thickness becomes a design parameter for selection of optimum thickness of flat plate reactors. Oversizing of reactor thickness can lead to the presence of a dark sublayer, where there is no considerable photon absorption.

This design parameter is similar to the apparent optical thickness used for sizing of annular reactors and CPCs [19, 31]. The δ_{abs} uses the analogous concept of boundary layer thickness to obtain the optimal light absorption. δ_{abs} depends of catalyst (type and loading) and it can be used as a geometrical parameter equal to the optimum reactor thickness H_R (see Figure 1).

2.2. Volumetric Rate of Photon Absorption VRPA. VRPA is defined as an average value of LVRPA in the whole volume. For a flat plate reactor the VRPA is expressed as [20]

$$\mathrm{VRPA} = \langle \mathrm{LVRPA} \rangle_{V_R} = \frac{1}{H_R} \int_0^{H_R} \mathrm{LVRPA}\left(C_{m,\mathrm{cat}}, y\right) dy. \quad (2)$$

VRPA is a design parameter established and validated to determine catalyst concentrations in photocatalytic processes [20].

VRPA and boundary layer thickness presented above are design parameters of photoreactors and their calculations require a model of radiant field, which quantify LVRPA within the reactor.

2.3. Radiant Field Model. The radiation field of a reactor with incident solar radiation was modeled by six-flux absorption-scattering model (SFM) [10, 12, 14, 19, 24, 25]. LVRPA divided by flux of incident radiant energy in reactor I_0 expressed by this model is

$$\begin{aligned} \frac{\mathrm{LVRPA}}{I_0} &= \left[\left(\omega_{\mathrm{corr}} - 1 + \sqrt{1-\omega_{\mathrm{corr}}^2}\right) e^{\left(-r_p/\lambda_{\omega_{\mathrm{corr}}}\right)}\right. \\ &\quad \left. + \gamma\left(\omega_{\mathrm{corr}} - 1 - \sqrt{1-\omega_{\mathrm{corr}}^2}\right) e^{\left(r_p/\lambda_{\omega_{\mathrm{corr}}}\right)}\right] \\ &\quad \times \left(\lambda_{\omega_{\mathrm{corr}}} \omega_{\mathrm{corr}} (1-\gamma)\right)^{-1}, \end{aligned} \quad (3)$$

where r_p is the coordinate of photon, $r_p = y$ in a flat plate reactor, ω_{corr} is the corrected scattering albedo, $\lambda_{\omega_{\mathrm{corr}}}$ corresponds to the corrected value of mean free path of photons in the suspension, and γ is a SFM parameter.

The parameters of (3) are function of average values of the scattering and absorption coefficients of catalyst, which are calculated as well:

$$\begin{aligned} \langle \sigma^* \rangle &= \frac{\int_{\lambda_{\min}}^{\lambda_{\max}} \sigma_\lambda^* I(\lambda)\, d\lambda}{\int_{\lambda_{\min}}^{\lambda_{\max}} I(\lambda)\, d\lambda} \\ \langle \kappa^* \rangle &= \frac{\int_{\lambda_{\min}}^{\lambda_{\max}} \kappa_\lambda^* I(\lambda)\, d\lambda}{\int_{\lambda_{\min}}^{\lambda_{\max}} I(\lambda)\, d\lambda}, \end{aligned} \quad (4)$$

where $\lambda_{\min}$ and $\lambda_{\max}$ correspond to 280 y 395 nm, respectively, given by the interception of solar emission spectrum and TiO_2 absorption spectrum; $I(\lambda)$ is the spectrum of solar emission power [32]; σ_λ^* and κ_λ^* are the spectrums of scattering and absorption coefficients, respectively, per mass unit of catalyst, reported in [33] using a phase function with diffuse reflectance for different commercial brands of TiO_2.

Extinction coefficient β is the sum of the absorption and scattering average coefficients $\beta = \langle \kappa^* \rangle + \langle \sigma^* \rangle$. This parameter is used to calculate the scattering albedo $\omega = \langle \sigma^* \rangle / \beta$ which determines the fraction of dispersed energy.

Scattering albedo requires a correction ω_{corr} to the model of six directions [25], through probabilities of forward, backward, and sideways scattering (p_f, p_b, p_s):

$$\omega_{\mathrm{corr}} = \frac{b}{a}, \quad (5)$$

where

$$\begin{aligned} a &= 1 - \omega p_f - \frac{4\omega^2 p_s^2}{\left(1 - \omega p_f - \omega p_b - 2\omega p_s\right)} \\ b &= \omega p_b + \frac{4\omega^2 p_s^2}{\left(1 - \omega p_f - \omega p_b - 2\omega p_s\right)}; \end{aligned} \quad (6)$$

p_f, p_b, p_s values are 0.11, 0.71, and 0.045 for a phase function of great sphere with diffuse reflectance [10]. Mean free path

of photons in the suspension λ_0 and its corrected value $\lambda_{\omega_{corr}}$, which depend on catalyst concentration, are calculated as well [10]:

$$\lambda_0 = \frac{1}{\beta C_{m,cat}}$$
$$\lambda_{\omega_{corr}} = \frac{\lambda_0}{a\sqrt{1-\omega_{corr}^2}}. \quad (7)$$

Finally, the parameter γ is calculated through the following equation:

$$\gamma = \frac{1-\sqrt{1-\omega_{corr}^2}}{1+\sqrt{1-\omega_{corr}^2}} e^{(-2\tau_{app})}, \quad (8)$$

where τ_{app} is apparent optimal thickness defined as

$$\tau_{app} = \tau a \sqrt{1-\omega_{corr}^2} \quad (9)$$

and τ is the optical thickness, for a flat plate reactor $\tau = H_R/\lambda_0$ [25, 26].

To obtain the new parameter, boundary layer thickness of photon absorption δ_{abs} is proposed to minimize an objective function (10), which is obtained from the definition (1), using the Nelder-Mead optimization algorithm:

$$F_{obj}(\delta_{abs}) = \left[\left(LVRPA_s - LVRPA(\delta_{abs})\right) - 0.99\left(LVRPA_s - LVRPA_\infty\right)\right]^2, \quad (10)$$

where $LVRPA_s$ and $LVRPA_\infty$ correspond to the SFM evaluated in r_p equal to zero and H_R, respectively.

3. Results and Discussion

3.1. Optical Properties under Solar Radiation. The SFM parameters that are independent of the catalyst concentration are shown in Table 2 for six different commercial brands of TiO_2 and solar radiation using (4)–(6). Parameters of photocatalytic activity are different due to the percentage of anatase, rutile, and brookite present in each trademark.

The values reported here disagree with those reported by [10] for Degussa under the same radiation condition ($\langle\sigma^*\rangle = 1.30 \times 10^4$ and $\langle\kappa^*\rangle = 1.75 \times 10^3$) due to the use of different phase functions. Colina-Márquez et al. [10] applied optical properties described by Henyey and Greenstein phase function [34]; in contrast, this study employed optical properties of catalyst and scattering probabilities p_f, p_b, p_s from a phase function model of diffuse reflectance [22, 25].

3.2. LVRPA. Figure 2 shows the $LVRPA/I_0$ profiles (3) as a function of y-coordinate inside a flat plate photoreactor with solar radiation for catalyst Degussa and Aldrich for different catalyst concentrations. The optical properties presented in Table 2 were used. A reactor thickness H_R equal to 1 cm was considered, because it is enough for photon absorption [20, 35]. Therefore, the dimensionless optical thickness ($\tau = H_R/\lambda_0$) varies from 4 to 22 depending on loading and type of catalyst.

Table 2: Average optical properties of commercial photocatalysts based on titanium dioxide under solar radiation.

Catalyst	$\langle\sigma^*\rangle \times 10^{-4}$ ($cm^2\ g^{-1}$)	$\langle\kappa^*\rangle \times 10^{-3}$ ($cm^2\ g^{-1}$)	$\beta \times 10^{-4}$ ($cm^2\ g^{-1}$)	ω	ω_{corr}
Aldrich	3.73	2.43	3.98	0.94	0.84
Degussa	5.42	2.87	5.71	0.95	0.87
Merck	2.97	2.68	3.24	0.92	0.81
Hombikat	2.52	1.17	2.64	0.96	0.88
Fischer	1.60	2.65	1.86	0.86	0.72
Fluka	1.64	2.89	1.92	0.85	0.71

The $LVRPA/I_0$ at irradiated surface of the reactor increases with catalyst concentration due to the amount of surface-exposed catalyst and back-scattering energy absorption from internal layer inside the reactor. These results agree with the literature [20]. In addition, it was found that the distribution of LVPRA is similar when the apparent optical thickness is used in annular and CPCs reactors [31].

The change of $LVRPA/I_0$ with respect to y near the irradiated surface is associated with extinction coefficients; the total energy available in the system is quickly extinguished by increases in catalyst concentration and high extinction coefficients β.

Finally, the distance from the surface ($y = 0$) where the radiant energy is absorbed (i.e., boundary layer thickness) depends on concentration and type of catalyst. For catalyst loading greater than 0.3 g/l, the $LVRPA/I_0$ at the bottom of the reactor is negligible.

To validate the SFM in a flat plate reactor, the model was run against rigorous solution of RTE proposed by [9, 36]. The reported reactor had 1.2 cm of thickness, UV lamps as radiation source, Aldrich and Degussa P-25 as photocatalysts. The SFM parameters were calculated to the experimental conditions reported ($\langle I_0\rangle \approx 1.81 \times 10^{-8}$ Einstein $cm^{-2}\ s^{-1}$, catalyst Aldrich, $\langle\sigma\rangle = 3.60 \times 10^4\ cm^2\ g^{-1}$, and $\langle\kappa\rangle = 3.28 \times 10^3\ cm^2\ g^{-1}$) with a local percent error of LVRPA lower than 12, and 2.4 for VRPA.

3.3. Design of Reactors. Figure 3 shows the $VRPA/I_0$ profiles (2) in solid lines as a function of catalyst loading inside a flat plate reactor, for six different commercial brands of TiO_2 catalysts. The dashed lines represent the values of δ_{abs} that satisfy (1).

For all catalysts, a catalyst loading less than 0.2 g/l has low rate of photon absorption; from 0.2 to 0.4 g/l there are high values of $VRPA/I_0$ and thus the best operating conditions of the system are within this interval; loadings greater than 0.4 g/l reach some form of saturation; therefore, there is no justification for extra consumption of catalyst.

From $VRPA/I_0$ profile in Figure 3 and Table 2, it is established that the absorption of radiant energy is faster

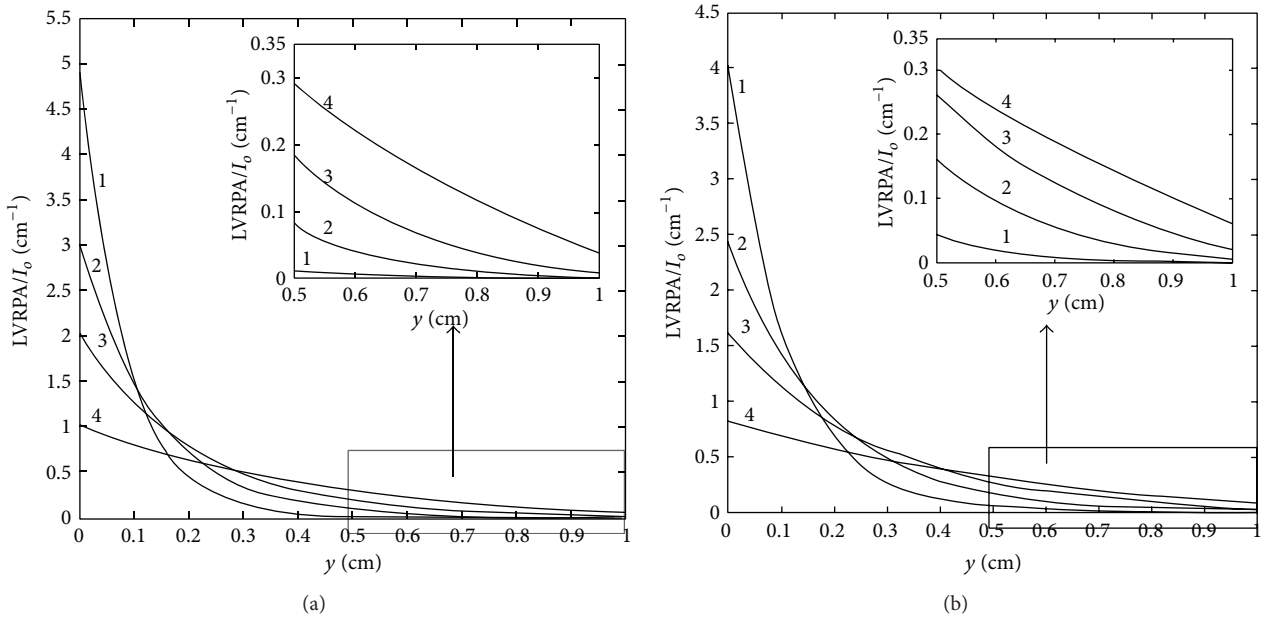

Figure 2: Profile of energy absorption rate (LVRPA/I_0) through fluid (y-coordinate) for Degussa P-25 (a) and Aldrich (b). Catalysts loading (g·l^{-1}): line 1 = 0.5; line 2 = 0.3; line 3 = 0.2; line 4 = 0.1.

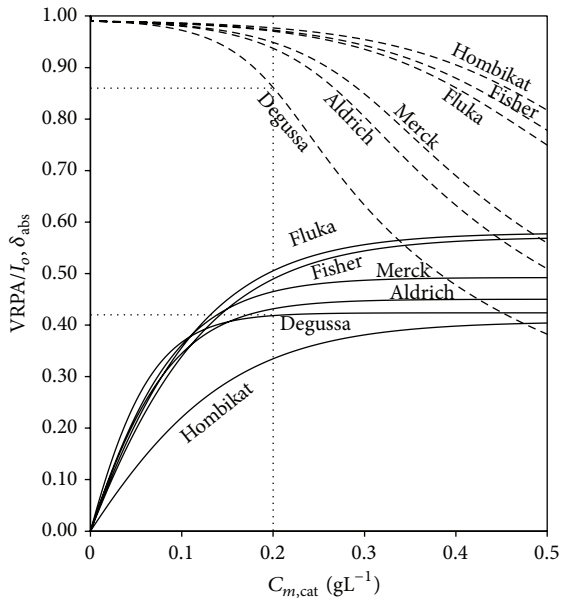

Figure 3: Design parameters of a flat plate solar photoreactor for different commercial brands of TiO_2 as a function of its loading. VRPA/I_0 (cm^{-1}): (—); boundary layer thickness of photon absorption δ_{abs} (cm): (-------).

for catalysts with a low coefficient of scattering albedo ω. In other words, high absorption coefficients and low scattering coefficients have greater absorption of photons, increasing the mathematical relationship $1 - \omega$. As a result, the absorption presents the following order: Fluka > Fischer > Merck > Aldrich > Degussa P-25 > Hombikat.

The catalyst Aldrich has a maximum VRPA 7% higher than the one presented by the catalyst Degussa. A similar trend was reported for polychromatic radiation using UV lamps, where the catalyst Aldrich is 19% more efficient than Degussa P-25 [36].

For all catalysts and loadings lower than 0.1 g/l, the absorption of photons occurs in the entire thickness of the reactor (1 cm), but the VRPA has small values. Catalyst loadings between 0.1 and 0.2 g/l employ the entire thickness of the reactor with approximately zero values of the LVRPA at the bottom of the reactor and begin to show a boundary layer of photon absorption thinner than 1 cm, due to some form of saturation between photon transport and the catalyst amount to absorb them.

For catalyst loading higher than 0.2 g/l, different boundary layer thicknesses of absorption can be seen. Catalysts with higher coefficient of photon extinction have a thinner boundary layer because the energy is quickly extinguished as it travels through the fluid.

However, Hombikat catalyst has the largest boundary layer of photon absorption, despite having an intermediate value of extinction coefficient; this is due to its low absorption coefficient κ and its high coefficient of scattering albedo ω; most of the photons are dispersed in a large layer of fluid phase with a photon absorption rate slower than other catalysts.

Profile of boundary layer thickness of photon absorption represents the best conditions of design. A point above this curve presents a dark layer inside reactor, while a point below it presents VRPA less than the maximum possible.

3.4. Optimal Configuration of Reactors. Figure 3 provides useful information to define the design thickness of a flat

plate reactor and type and loading of catalyst. For applications in very thin reactors (e.g., thin films of continuous fluid by sliding on an inclined flat plate), the catalyst with the best performance is Degussa P-25 followed by Aldrich; the catalyst selection is based on reactor thickness. On the other hand, for applications in very thick reactors, the catalyst with the best performance is Fluka followed by Fischer; the catalyst selection is based on the greater amount of energy absorbed.

To design a photoreactor using a specific catalyst, for example, Degussa P-25 (point line), the VRPA/I_0 profile in Figure 3 recommends 0.2 g/l of catalyst to take the maximum energy absorbed with the minimum consumption of catalyst. The δ_{abs} profile in the same figure suggests a design thickness of reactor equal to or slightly higher than 0.86 cm and take advantage of the entire volume within the reactor for the photon absorption. Table 3 was reported using the procedure above.

The optimum catalyst loading was calculated for catalysts water system; this increases in systems where there is absorption of radiant energy by substrate. Other authors have reported optimum values of catalyst loading similar to those reported in this paper. Brandi et al. report a loading close to 0.3 g/l based on the simulation of photon absorption for Aldrich and Degussa catalysts with radiation from UV lamps in a flat plate reactor [20, 36].

Experimental researches developed at the solar platform from Almeria obtained an optimal loading of Degussa P-25 in a plate flat solar reactor equal to 0.2 g/l [37–39]; this concentration is the same obtained by simulation in this work.

Different geometries are not comparable; however, the reported values of optimum catalyst loading have proved to be very similar in different reactors. An example of this result is the work made by Colina-Márquez and coworkers. They found optimum catalyst loadings from 0.17 to 0.4 g/l for catalysts with scattering albedo between 0.75 and 0.95 in a CPC solar reactor and catalyst loadings between 0.2 and 0.6 g/l for a tubular reactor [19]. Particularly, they obtained 0.21 g/l as optimal loading for Degussa P-25.

For thicknesses not near 1 cm, it is recommended to use the design parameter called apparent optical thickness $\tau_{app} = \tau a\sqrt{1-\omega_{corr}^2}$, where $\tau = H_R\beta C_{m,cat}$; the parameter was proposed by [19] and modified here for its application to flat plate reactor. At conditions reported in Table 2, the τ_{app} values obtained were 4.39, 4.08, 4.15, 3.77, 3.99, and 4.10 to Aldrich, Degussa, Merck, Hombikat, Fisher, and Fluka, respectively. The best design conditions for different catalyst loadings and reactor thicknesses are obtained by keeping τ_{app} constant.

Reactor design information presented in this paper is useful to determine the optimum catalyst loading, the optimal thickness of reactor, and the radiant energy absorbed. In addition, it eliminates the need of statistical analysis of experiment design which involves considerable consumption of time and resources [19]. New photocatalysts can be analyzed using the methodology presented here by varying absorption and scattering coefficients.

Table 3: Optimum catalyst loading, maximum energy absorbed, and design thickness of flat plate reactor under solar radiation.

Catalyst	Loading (g/L)	$VRPA_{max}/I_0$ (cm^{-1})	Suggested thickness of the reactor (cm)
Degussa P-25	0.2	0.42	0.86
Aldrich	0.3	0.45	0.80
Merck	0.3	0.49	0.85
Hombikat	0.4	0.40	0.90
Fisher	0.4	0.56	0.88
Fluka	0.4	0.57	0.86

4. Conclusions

This study has presented a new parameter for selection of thickness of a flat plate reactor called boundary layer thickness of photon absorption δ_{abs}, which represents an effective thickness of absorption. Its use allows the elimination of dark zones within the reactor and absorption of the largest amount of photons. Also, together with the VRPA, it provides sufficient criteria for sizing of reactor thickness, the choice of catalyst, and its loading. Its use is applicable to the scale-up of solar reactors.

The parameter was evaluated for TiO_2 semiconductors Degussa P-25, Aldrich, Merck, Hombikat, Fluka, and Fisher, as a function of reactor thickness, catalyst loading, and the maximum amount of energy absorbed getting optimal operating conditions in the catalyst loading.

Nomenclature

a : SFM parameter, dimensionless
b: SFM parameter, dimensionless
$C_{m,cat}$: Catalyst concentration, $g\,l^{-1}$
F_{obj}: Objective function, $mol^2\,cm^{-6}$
H: Thickness, cm
I: Emission spectrum of radiation source, Einstein $cm^{-2}\,s^{-1}$
I_0: Flux of radiation at surface, Einstein $cm^{-2}\,s^{-1}$
LVRPA: Local volumetric rate of photon absorption, Einstein $cm^{-3}\,s^{-1}$
p_b: Probability of backward scattering, dimensionless
p_f: Probability of forward scattering, dimensionless
p_s: Probability of side scattering, dimensionless
r_p: Auxiliary coordinate in the photon flux direction, cm
x: Cartesian coordinate, cm
y: Cartesian coordinate, cm
z: Cartesian coordinate, cm.

Greek Letters

β: Specific extinction coefficient, $cm^2\ g^{-1}$
γ: SFM parameter, dimensionless
δ_{abs}: Boundary layer thickness of photon absorption, cm
κ: Specific absorption coefficient, $cm^2\ g^{-1}$
λ: Radiation wavelength, nm
λ_0: Mean free path of photons, cm
$\lambda_{\omega_{corr}}$: Extinction length, cm
σ: Specific scattering coefficient, $cm^2\ g^{-1}$
τ: Optical thickness, dimensionless
τ_{app}: Apparent optical thickness, dimensionless
ω: Scattering albedo, dimensionless
ω_{corr}: Scattering albedo corrected, adimensional.

Subscripts

corr: Corrected
max: Maximum
min: Minimum
R: Reactor
s: Irradiated surface
∞: Bottom of reactor.
λ: Spectral.

Superscripts

$*$: Specific.

Special Symbols

$\langle\rangle$: Average value.

Conflict of Interests

The authors declare that there is no conflict of interests regarding the publication of this paper.

Acknowledgments

The authors are grateful to Universidad del Valle for the financial support to produce this work and to Colciencias for the financial support during their Ph.D. studies. M. A. Mueses thanks Universidad de Cartagena for the financial support. Finally, the authors thank Fernando Otálvaro for the English revision.

References

[1] A. C. Affam and M. Chaudhuri, "Degradation of pesticides chlorpyrifos, cypermethrin and chlorothalonil in aqueous solution by TiO_2 photocatalysis," *Journal of Environmental Management*, vol. 130, pp. 160–165, 2013.

[2] M. Tanveer and G. Tezcanli Guyer, "Solar assisted photo degradation of wastewater by compound parabolic collectors: review of design and operational parameters," *Renewable and Sustainable Energy Reviews*, vol. 24, pp. 534–543, 2013.

[3] J. Ângelo, L. Andrade, L. M. Madeira, and A. Mendes, "An overview of photocatalysis phenomena applied to NO_x abatement," *Journal of Environmental Management*, vol. 129, pp. 522–539, 2013.

[4] K. Nakata and A. Fujishima, "TiO_2 photocatalysis: design and applications," *Journal of Photochemistry and Photobiology C: Photochemistry Reviews*, vol. 13, no. 3, pp. 169–189, 2012.

[5] Z. Xing, X. Zong, J. Pan, and L. Wang, "On the engineering part of solar hydrogen production from water splitting: photoreactor design," *Chemical Engineering Science*, vol. 104, pp. 125–146, 2013.

[6] C. S. Turchi and D. F. Ollis, "Photocatalytic degradation of organic water contaminants: mechanisms involving hydroxyl radical attack," *Journal of Catalysis*, vol. 122, no. 1, pp. 178–192, 1990.

[7] D. I. Kondarides, V. M. Daskalaki, A. Patsoura, and X. E. Verykios, "Hydrogen production by photo-induced reforming of biomass components and derivatives at ambient conditions," *Catalysis Letters*, vol. 122, no. 1-2, pp. 26–32, 2008.

[8] J. Marugán, R. van Grieken, A. E. Cassano, and O. M. Alfano, "Intrinsic kinetic modeling with explicit radiation absorption effects of the photocatalytic oxidation of cyanide with TiO_2 and silica-supported TiO_2 suspensions," *Applied Catalysis B: Environmental*, vol. 85, no. 1-2, pp. 48–60, 2008.

[9] C. S. Zalazar, R. L. Romero, C. A. Martín, and A. E. Cassano, "Photocatalytic intrinsic reaction kinetics I: mineralization of dichloroacetic acid," *Chemical Engineering Science*, vol. 60, no. 19, pp. 5240–5254, 2005.

[10] J. Colina-Márquez, F. Machuca-Martínez, and G. Li Puma, "Photocatalytic mineralization of commercial herbicides in a pilot-scale solar CPC reactor: photoreactor modeling and reaction kinetics constants independent of radiation field," *Environmental Science and Technology*, vol. 43, no. 23, pp. 8953–8960, 2009.

[11] M. L. Satuf, R. J. Brandi, A. E. Cassano, and O. M. Alfano, "Photocatalytic degradation of 4-chlorophenol: a kinetic study," *Applied Catalysis B: Environmental*, vol. 82, no. 1-2, pp. 37–49, 2008.

[12] G. Li Puma, V. Puddu, H. K. Tsang, A. Gora, and B. Toepfer, "Photocatalytic oxidation of multicomponent mixtures of estrogens (estrone (E1), 17β-estradiol (E2), 17α-ethynylestradiol (EE2) and estriol (E3)) under UVA and UVC radiation: photon absorption, quantum yields and rate constants independent of photon absorption," *Applied Catalysis B: Environmental*, vol. 99, no. 3-4, pp. 388–397, 2010.

[13] G. Li Puma, B. Toepfer, and A. Gora, "Photocatalytic oxidation of multicomponent systems of herbicides: scale-up of laboratory kinetics rate data to plant scale," *Catalysis Today*, vol. 124, no. 3-4, pp. 124–132, 2007.

[14] M. A. Mueses, F. Machuca-Martinez, and G. Li Puma, "Effective quantum yield and reaction rate model for evaluation of photocatalytic degradation of water contaminants in heterogeneous pilot-scale solar photoreactors," *Chemical Engineering Journal*, vol. 215-216, pp. 937–947, 2013.

[15] O. M. Alfano, M. I. Cabrera, and A. E. Cassano, "Photocatalytic reactions involving hydroxyl radical attack: I. Reaction kinetics formulation with explicit photon absorption effects," *Journal of Catalysis*, vol. 172, no. 2, pp. 370–379, 1997.

[16] M. Á. Mueses and F. Machuca-Martínez, "Mathematical model for non-intrinsic photonic yields in heterogeneous photocatalytic reactions," *Información Tecnológica*, vol. 23, no. 3, pp. 43–50, 2012.

[17] G. E. Imoberdorf, A. E. Cassano, H. A. Irazoqui, and O. M. Alfano, "Simulation of a multi-annular photocatalytic reactor for degradation of perchloroethylene in air: parametric analysis of radiative energy efficiencies," *Chemical Engineering Science*, vol. 62, no. 4, pp. 1138–1154, 2007.

[18] M. L. Satuf, R. J. Brandi, A. E. Cassano, and O. M. Alfano, "Scaling-up of slurry reactors for the photocatalytic degradation of 4-chlorophenol," *Catalysis Today*, vol. 129, no. 1-2, pp. 110–117, 2007.

[19] J. Colina-Márquez, F. MacHuca-Martínez, and G. L. Puma, "Radiation absorption and optimization of solar photocatalytic reactors for environmental applications," *Environmental Science and Technology*, vol. 44, no. 13, pp. 5112–5120, 2010.

[20] R. J. Brandi, O. M. Alfano, and A. E. Cassano, "Modeling of radiation absorption in a flat plate photocatalytic reactor," *Chemical Engineering Science*, vol. 51, no. 11, pp. 3169–3174, 1996.

[21] J. J. Duderstadt and E. R. Martín, *Transport Theory*, Wiley, New York, NY, USA, 1979.

[22] B. Toepfer, A. Gora, and G. Li Puma, "Photocatalytic oxidation of multicomponent solutions of herbicides: reaction kinetics analysis with explicit photon absorption effects," *Applied Catalysis B: Environmental*, vol. 68, no. 3-4, pp. 171–180, 2006.

[23] G. Li Puma, J. N. Khor, and A. Brucato, "Modeling of an annular photocatalytic reactor for water purification: oxidation of pesticides," *Environmental Science and Technology*, vol. 38, no. 13, pp. 3737–3745, 2004.

[24] G. Li Puma and A. Brucato, "Dimensionless analysis of slurry photocatalytic reactors using two-flux and six-flux radiation absorption-scattering models," *Catalysis Today*, vol. 122, no. 1-2, pp. 78–90, 2007.

[25] A. Brucato, A. E. Cassano, F. Grisafi, G. Montante, L. Rizzuti, and G. Vella, "Estimating radiant fields in flat heterogeneous photoreactors by the six-flux model," *AIChE Journal*, vol. 52, no. 11, pp. 3882–3890, 2006.

[26] G. Li Puma, "Dimensionless analysis of photocatalytic reactors using suspended solid photocatalysts," *Chemical Engineering Research and Design*, vol. 83, no. 7, pp. 820–826, 2005.

[27] A. E. Cassano, C. A. Martín, R. J. Brandi, and O. M. Alfano, "Photoreactor analysis and design: fundamentals and applications," *Industrial and Engineering Chemistry Research*, vol. 34, no. 7, pp. 2155–2201, 1995.

[28] J. Blanco Gálvez, S. Malato Rodríguez, J. Peral, B. Sánchez, and A. I. Cardona, "Diseño de reactores para fotocatálisis: evaluación comparativa de las distintas opciones," in *Eliminación De Contaminantes Por Fotocatálisis Heterogénea*, pp. 243–266, 2004.

[29] G. Li Puma and P. L. Yue, "Modelling and design of thin-film slurry photocatalytic reactors for water purification," *Chemical Engineering Science*, vol. 58, no. 11, pp. 2269–2281, 2003.

[30] F. P. Incropera and D. P. DeWitt, *Fundamentals of Heat and Mass Transfer*, John Wiley & Sons, New York, NY, USA, 4th edition, 1996.

[31] J. Moreira, B. Serrano, A. Ortiz, and H. De Lasa, "Evaluation of photon absorption in an aqueous TiO_2 slurry reactor using Monte Carlo simulations and macroscopic balance," *Industrial and Engineering Chemistry Research*, vol. 49, no. 21, pp. 10524–10534, 2010.

[32] "Standard Tables for Reference Solar Spectral Irradiances: Direct Normal and Hemispherical on 37° Tilted Surface. ASTM G173 03," ASTM International, 2012.

[33] M. I. Cabrera, O. M. Alfano, and A. E. Cassano, "Absorption and scattering coefficients of titanium dioxide participate suspensions in water," *Journal of Physical Chemistry*, vol. 100, no. 51, pp. 20043–20050, 1996.

[34] M. L. Satuf, R. J. Brandi, A. E. Cassano, and O. M. Alfano, "Experimental method to evaluate the optical properties of aqueous titanium dioxide suspensions," *Industrial and Engineering Chemistry Research*, vol. 44, no. 17, pp. 6643–6649, 2005.

[35] R. J. Brandi, G. Rintoul, O. M. Alfano, and A. E. Cassano, "Photocatalytic reactors—reaction kinetics in a flat plate solar simulator," *Catalysis Today*, vol. 76, no. 2–4, pp. 161–175, 2002.

[36] R. J. Brandi, O. M. Alfano, and A. E. Cassano, "Rigorous model and experimental verification of the radiation field in a flat-plate solar collector simulator employed for photocatalytic reactions," *Chemical Engineering Science*, vol. 54, no. 13-14, pp. 2817–2827, 1999.

[37] S. Malato Rodríguez, J. Blanco Gálvez, M. I. Maldonado Rubio et al., "Engineering of solar photocatalytic collectors," *Solar Energy*, vol. 77, no. 5, pp. 513–524, 2004.

[38] J. Giménez, D. Curcó, and M. A. Queral, "Photocatalytic treatment of phenol and 2,4-dichlorophenol in a solar plant in the way to scaling-up," *Catalysis Today*, vol. 54, no. 2-3, pp. 229–243, 1999.

[39] S. Malato, J. Blanco, A. Vidal et al., "New large solar photocatalytic plant: set-up and preliminary results," *Chemosphere*, vol. 47, no. 3, pp. 235–240, 2002.

Hindawi Publishing Corporation
International Journal of Photoenergy
Volume 2014, Article ID 816234, 7 pages
http://dx.doi.org/10.1155/2014/816234

Research Article

Electronic Structures of S/C-Doped TiO_2 Anatase (101) Surface: First-Principles Calculations

Qili Chen,[1] Min Liu,[2] Kaihua He,[1] and Bo Li[3]

[1] *School of Mathematics and Physics, China University of Geosciences, Wuhan 430074, China*
[2] *Central China Normal University Press, Wuhan 430074, China*
[3] *Faculty of Mechanical and Electronic Information, China University of Geosciences, Wuhan 430074, China*

Correspondence should be addressed to Bo Li; lbchql@sina.com

Received 18 February 2014; Accepted 10 March 2014; Published 2 June 2014

Academic Editor: Jiaguo Yu

The electronic structures of sulfur (S) or carbon (C)-doped TiO_2 anatase (101) surfaces have been investigated by density functional theory (DFT) plane-wave pseudopotential method. The general gradient approximation (GGA) + U (Hubbard coefficient) method has been adopted to describe the exchange-correlation effects. All the possible doping situations, including S/C dopants at lattice oxygen (O) sites (anion doping), S/C dopants at titanium (Ti) sites (cation doping), and the coexisting of anion and cation doping, were studied. By comparing the formation energies, it was found that the complex of anion and cation doping configuration forms easily in the most range of O chemical potential for both S and C doping. The calculated density of states for various S/C doping systems shows that the synergistic effects of S impurities at lattice O and Ti sites lead a sharp band gap narrowing of 1.35 eV for S-doped system comparing with the pure TiO_2 system.

1. Introduction

Many researchers have paid much attention on titanium dioxide (TiO_2). As a promising photocatalytic semiconductor for environmental treatment, it has excellent functionality, long-term stability, and nanotoxicity [1]. However, TiO_2 is a kind of wide band gap semiconductor (3.2 eV for anatase phase and 3.0 eV for rutile phase [2]). It needs ultraviolet (UV) radiation to excite the electrons from valence band (VB) to conduction band (CB). Unfortunately, the energy of UV light accounts for only small fraction of the sunlight. Then, how to enhance the ability of visible light (VIS) absorption of TiO_2 is critical to enable the utility of TiO_2 photocatalyst materials.

Many efforts have been made to achieve this purpose, including introducing metal or nonmetal species for doping. S and C species are special among nonmetal species. For these two species, both cation and anion doping could be formed in TiO_2. The group of Umebayashi [3, 4] have synthesized S-doped TiO_2 by ion implantation and oxidation annealing of TiS_2. They found that the S atoms occupied oxygen sites to form Ti-S bonds and lead a decrease in the band-gap energy. Based on the theoretical analyses using ab initio band calculations, they thought that mixing of the S 3p states with the valence band contributes to the band gap narrowing. Ohno's group [5] have synthesized S-doped TiO_2 photocatalysts chemically in which S (S^{4+}) substitute some of the lattice titanium atoms, which showed strong absorption for visible light and high activities for degradation of methylene blue, 2-propanol in aqueous solution, and partial oxidation of adamantane under irradiation at wavelengths longer than 440 nm. Long et al. [6] have discussed the structural and electronic properties of S-doping configurations by substitution and adsorption at the rutile TiO_2 (110) surface with first-principles density functional theory calculations. Their results indicate that S dopants replace surface O atoms or bind to Ti atoms preferentially. S-cation doping led to relatively small reductions of the photon transition energy, while S-anion doping and adsorption on the surface resulted in significant red shifts of the optical absorption edge. For

C-doped TiO_2, some experimental researches have been done by Nakano et al. [7]. They have prepared C-doped TiO_2 film by oxidative annealing of sputtered TiC films at 550°C in flowing O_2 gas. Deep-level optical spectroscopy measurements revealed three deep levels located at 0.86, 1.30, and 2.34 eV below the CB. They thought the 2.34 eV band introduced by the C-doping contributes to band gap narrowing by mixing with the O 2p valence band. Both anion doping and cation doping have been studied by Kamisaka et al. [8] for C-doped TiO_2. It was found that neither in-gap impurity states nor visible-light absorbance were observed in the case of cation doping, while a density-of-states analysis revealed three in-gap impurity states for anion doping. Kesong et al. [9] have also discussed the structural and electronic properties of two possible substitutional carbon-doped structures of anatase and rutile TiO_2. They found that the band gap changes slightly for C-anion doping and the optical absorption energy is reduced by about 0.18 and 0.3 eV for cation C-doped anatase and rutile TiO_2, respectively. Lee et al. [10] presented first-principles density-functional calculations for the electronic properties anion C-doped TiO_2. They found that three C 2p bands appear in the band gap; they were located at 0.52, 0.96, and 1.48 eV away from the VB maximum of TiO_2. The energy gap between the highest O 2p band and the lowest Ti 3d band is 2.42 eV, close to 2.39 eV in undoped TiO_2.

However, these theoretical and experimental studies are not enough to give a clear insight of the real mechanism for VIS sensitivity of S/C-doped TiO_2. In this paper, we demonstrated a relatively more comprehensive investigation on the effects of S/C impurities on the electronic structures of TiO_2. Firstly, the surface models were adopted to calculate the band structure of S/C-doped TiO_2 anatase. To our opinion, the surface model is more suitable to simulate synthesized powder or film samples than bulk model. Of the anatase single-crystalline surfaces, the (101) surface is the predominant face that is exposed on anatase minerals and polycrystalline powders, and theory calculations also show that it is thermodynamically the low-energy surface [1, 11]. Moreover, besides the isolated anion and cation doping that have been discussed in our calculations, the case of anion and cation codoping with two S/C atoms (lattice O and Ti atoms are replaced by S/C atoms synchronously) has also been studied. Furthermore, because the local density approximation (LDA) and general gradient approximation (GGA) which are generally used to describe the exchange-correlation effects always lead to a severe underestimation of the band gap [12] for transition metal oxides, GGA + U (Hubbard coefficient) was used in this present work to compensate for the limitation for those strongly correlated systems [13] which introduces an additional term based on a simple Hubbard model for electron on-site repulsion.

2. Methods and Models

2.1. Computational Details. The computational calculations have been performed by density-functional theory (DFT) plane-wave pseudopotential method [14], as implemented in the CASTEP 5.0 codes [15]. GGA + U was used for describing the exchange-correlation effects. Within GGA + U, the Coulomb correlation interaction of Ti 3d electrons has been taken into account. The U = 8.50 eV of Ti 3d electrons was adopted in all energy calculations which has been confirmed by our previous works [16–18]. The ultrasoft pseudopotential was used to describe electron-ion interactions. The kinetic energy cutoff for the plane-wave basis was chosen as 380.0 eV. The Brillouin zone sampling was restricted to the point in surface geometry optimization. In energy calculations, it was set to $1 \times 2 \times 4$. Structure optimization was performed by minimizing the total energy and the ionic force, until all the components of the residual forces were less than 0.01 eV·Å^{-1}. The energy and the displacement tolerance were set to 5.0×10^{-6} eV·atom^{-1} and 5.0×10^{-4} Å, respectively.

2.2. Models. The TiO_2 (hereafter referring to the anatase structure exclusively) (101) surfaces were modeled by vacuum slabs. According to our previous computational results [19] and some references [20, 21], we have selected a slab of $Ti_{24}O_{48}$(TO) with surface area of 11.15×7.55 Å^2 and slab thickness of 3 layers (see Figure 1(a)). The surface species, namely, the bridging two-fold coordinated oxygen atom (O_{2C}), three types of three-fold coordinated oxygen atom (O^1_{3C}, O^2_{3C}, and O^3_{3C}), and five/six-fold coordinated titanium atoms (Ti_{5C} and Ti_{6C}), are denoted in Figure 1(a) as well.

The models of anion doping surfaces $Ti_{24}O_{47}S$(A-STO) and $Ti_{24}O_{47}C$(A-CTO) were built by replacing a surface oxygen atom with a sulfur or carbon atom in the slab of TO (the configuration of an S or C atom substituting an O atom is denoted S_O or C_O). There are four types of surface oxygen site, namely, the O_{2C}, O^1_{3C}, O^2_{3C}, and O^3_{3C} site (as shown in Figure 1(a)), for a sulfur or carbon atom to substitute. For the models of cation doping surfaces $Ti_{23}SO_{48}$(C-STO) and $Ti_{23}CO_{48}$(C-CTO), there are two possible surface sites, Ti_{5C} and Ti_{6C} site, for a sulfur or carbon atom to substitute (the configuration of a S or C atom substituting a Ti atom is denoted S_{Ti} or C_{Ti}). By comparing the total energy of the optimized slabs for S/C doping (the values are shown in Table 1), it was clear that the O_{2C} site and Ti_{5C} site are energetically favored for anion and cation doping, respectively. Long's results also show that S dopants replace surface O atoms preferentially [6].

Figures 2(a), 2(b), 2(d) and 2(e) exhibit the relaxed configurations of S_O, C_O and S_{Ti}, C_{Ti}. It can be seen from the structures that S atom substituting Ti atom at Ti_{5C} site (see Figure 2(d)) and C substituting O atom at O_{2C} site (see Figure 2(b)) do not lead significant lattice distortion, while substitutional S atom at O_{2C} site extends upwards and tends to leave the surface (see Figure 2(a)) and substitutional C atom at Ti_{5C} site seems to be attracted by O atoms at O_{2C} and O^3_{3C} site strongly (see Figure 2(e)), forming two short C–O bond with distance of 1.360 and 1.387 Å, which is consistent with [6].

According to the above discussions, the model of anion and cation codoping surface with two S atoms, $Ti_{23}SO_{47}S$ (AC-STO), or that with two C atoms, $Ti_{23}CO_{47}C$(AC-CTO), was created by one S or C atom substituting an O atom at O_{2C} site and the other S or C atom substituting a Ti atom

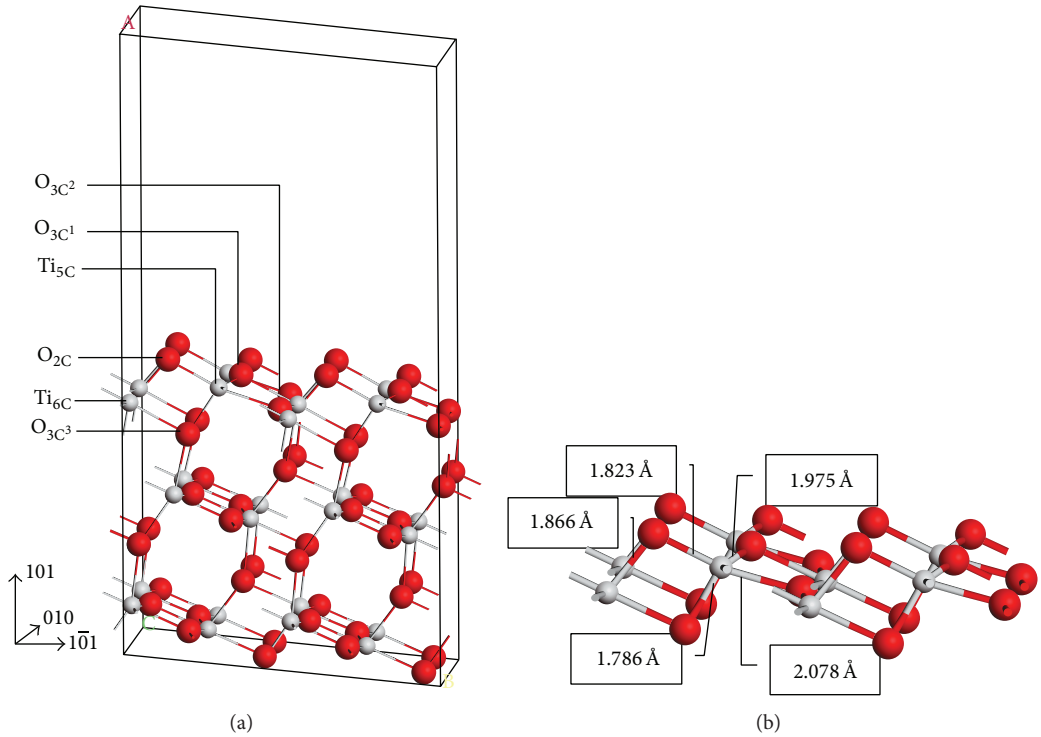

Figure 1: (a) Relaxed structure of $Ti_{24}O_{48}$ surface cell (TO) with surface area of 11.15×7.55 Å^2, the first layer is in the dashed line. (b) Relaxed structure of the first layer of TO, the bond length of Ti_{5C} with its neighboring O atoms and O_{2C} with its neighboring Ti atoms are labeled. Ti and O atoms are represented by grey and red spheres, respectively.

Table 1: Energy differences for S and C dopant at different substitutional doping site on TiO_2 anatase (101) surface. A-STO and A-CTO denote anion doping surfaces $Ti_{24}O_{47}S$ and $Ti_{24}O_{47}C$; C-STO and C-CTO denote cation doping surfaces $Ti_{23}SO_{48}$ and $Ti_{23}CO_{48}$, respectively.

	Substitutional doping site					
	O_{2C}	$O_{3C}{}^1$	$O_{3C}{}^2$	$O_{3C}{}^3$	Ti_{5C}	Ti_{6C}
A-STO	0.00	0.45	1.51	2.47	—	—
A-CTO	0.00	0.06	0.17	0.21	—	—
C-STO	—	—	—	—	0.00	1.16
C-CTO	—	—	—	—	0.00	1.13

Unit: eV.

at Ti_{5C} site in the slab of TO. For the case of coexistent S_O and S_{Ti}(S_O + S_{Ti}) or C_O and C_{Ti}(C_O + C_{Ti}) on TO surface, there are four Ti_{5C} sites around a O_{2C} site, which could be distinguished by distance, namely, the nearest one, the next nearest one, the next next nearest one, and the farthest one. For S doping, the total energy differences are 0.14, 0.08, 0.07, and 0.00 eV of the optimized slabs, for C doping, and the total energy differences are 0.00, 0.04, 0.07, and 0.12 eV of each optimized configuration. It was found that S_O and S_{Ti} tend to be apart, while C_O and C_{Ti} tend to be close; the optimized C–C bond length is only 1.360 Å. Figures 2(c) and 2(f) exhibit the relaxed configuration of S_O + S_{Ti} and C_O + C_{Ti}.

3. Results and Discussion

3.1. Defect Formation Energy. In order to evaluate the relative stability of various doping configurations under deferent oxygen atmosphere, the defect formation energies (E_f) of each doping configuration as a function of O chemical potential ($\mu(O)$) has been calculated and the results were exhibited in Figure 3. Taking S doping, for example, the calculation scheme was displayed as follows.

Firstly, for the neutral S_O, S_{Ti} defect, and the complex S_O + S_{Ti} defect, the substitutional formation energies are calculated as the following equations [22]:

$$\begin{aligned} E_f(S_O) &= E(\text{A-STO}) - E(\text{TO}) - \mu(S) + \mu(O) \\ E_f(S_{Ti}) &= E(\text{C-STO}) - E(\text{TO}) - \mu(S) + \mu(Ti) \\ E_f(S_O + S_{Ti}) &= E(\text{AC-STO}) - E(\text{TO}) \\ &\quad - 2\mu(S) + \mu(Ti) + \mu(O), \end{aligned} \tag{1}$$

where E(TO), E(A-STO), E(C-STO), and E(AC-STO) are the total energies of TO, A-STO, C-STO, and AC-STO, respectively. μ(S), μ(Ti), and μ(O) are the chemical potentials of S, Ti, and O atom, respectively.

Nextly, the atom chemical potentials of Ti and O must satisfy the boundary conditions $\mu(O) \le 1/2\mu(O_2)$ and $\mu(Ti) \le \mu(\text{Ti metal})$, where $\mu(O_2)$ and $\mu(\text{Ti metal})$ are the chemical potentials of oxygen gas and titanium metal, respectively.

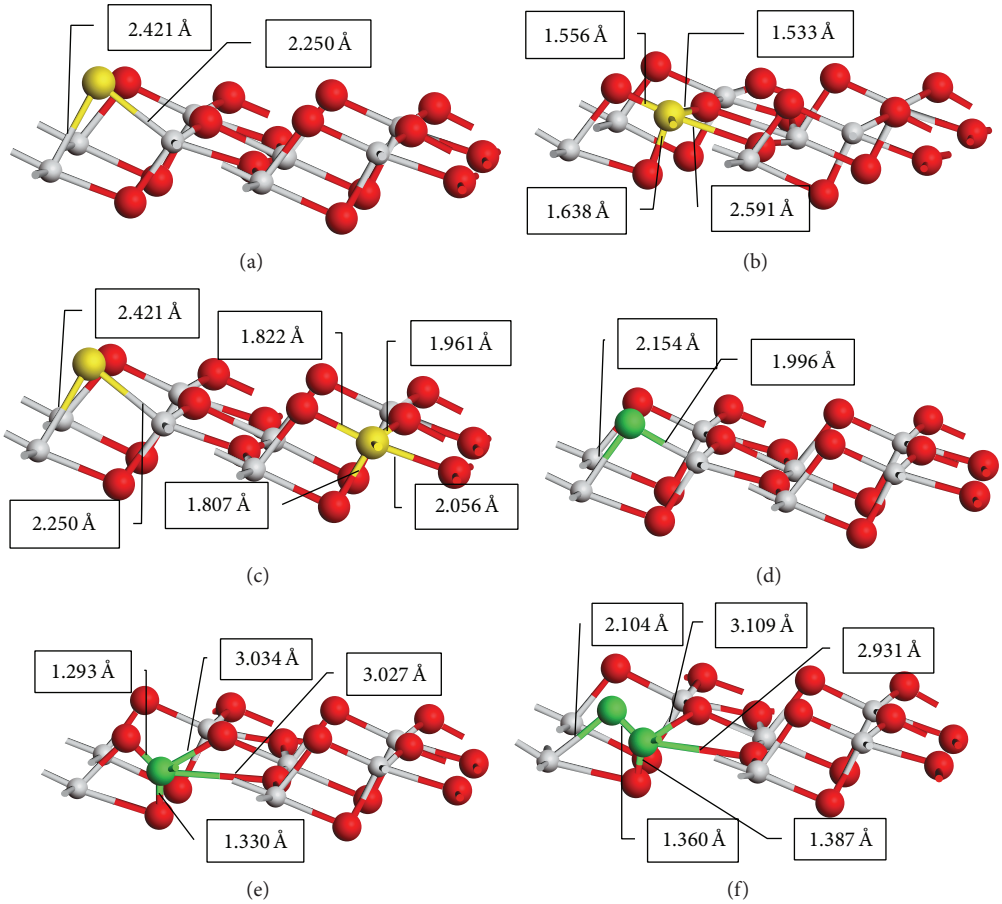

FIGURE 2: Relaxed structure of the first layer of S/C-doped surfaces: (a) $Ti_{24}O_{47}S$(A-STO), (b) $Ti_{23}SO_{48}$(C-STO), (c) $Ti_{23}SO_{47}S$(AC-STO), (d) $Ti_{24}O_{47}C$(A-CTO), (e) $Ti_{23}CO_{48}$(C-CTO), and (f) $Ti_{23}CO_{47}C$(AC-CTO). The bond length of S or C dopants with its neighboring Ti or O atoms is labeled. Ti and O atoms are represented by grey and red black spheres, respectively. Substitutional S and C dopants are represented by yellow and green spheres.

Under the oxygen-rich (metal-poor) condition, μ(O) is set as $1/2\mu(O_2)$. While, under the oxygen-poor (metal-rich) condition, μ(Ti) = μ(Ti metal). Correspondingly μ(Ti) or μ(O) is derived from the relation $\mu(Ti) + 2\mu(O) = \mu(TiO_2$ bulk) [23–25]. $\mu(TiO_2$ bulk) is the chemical potentials of TiO_2 anatase bulk.

Figure 3(a) exhibits the formation energies of S_O, S_{Ti} and the complex $S_O + S_{Ti}$, as a function of μ(O), with the zero of the vertical scale corresponding to the formation energy of S_{Ti}. $E_f(S_O + S_{Ti})$ is always lower than $E_f(S_{Ti})$, only under the sufficient O-poor (Ti-rich) growth condition; $E_f(S_O + S_{Ti})$ is larger than $E_f(S_O)$, which indicates that in the most range of μ(O), the complex $S_O + S_{Ti}$ forms much more easily. Thus, S_O and S_{Ti} could be created synchronously in S-doped TiO_2 samples.

For the case of C doping, the defect formation energies are calculated in the same way. Figure 3(b) shows the formation energies of C_O, C_{Ti} and the complex $C_O + C_{Ti}$, as a function of μ(O), with the zero of the vertical scale corresponding to the formation energy of C_{Ti}. Namely, in the most range of μ(O), $E_f(C_{Ti})$ is lower than $E_f(C_O)$ and $E_f(C_O + C_{Ti})$ is always the lowest in all the range of μ(O), which shows that isolated C_{Ti} forms more easily than isolated C_O and $C_O + C_{Ti}$ has the most possibility to be on the C-doped TiO_2 surfaces.

3.2. Electronic Structures of Substitutional S/C-Doped Surfaces. The density of the states (DOS) for TO is shown in Figure 4, with the Fermi level being 0 eV on the energy axis. For the pure surface TO, the calculated band gap energy is about 2.64 eV which is smaller than 3.2 eV calculated for bulk structure. The valence band (VB) consists of Ti 3d and O 2p orbits with the width of 5.40 eV, and the conductive band (CB) consists of Ti 3d states mainly.

The calculated partial density of the states (PDOS) of S-doped surfaces is shown in Figure 5. In the PDOS of A-STO (Figure 5(a)), S 3p states are localized; a part of them are lying at the Femi level and adjacent to the TiO_2 VB maximum, which leads an expansion of VB from 5.40 to 5.80 eV. The electron excitation energy from the occupied VB states to the CB minimum shortens to 2.00 eV. However, in the PDOS of C-STO (see Figure 5(b)), the majority of S 3p states locates far away from the Femi level; only a few of them disperse and mix with O 2p and Ti 3d VB states. There is a slight change for

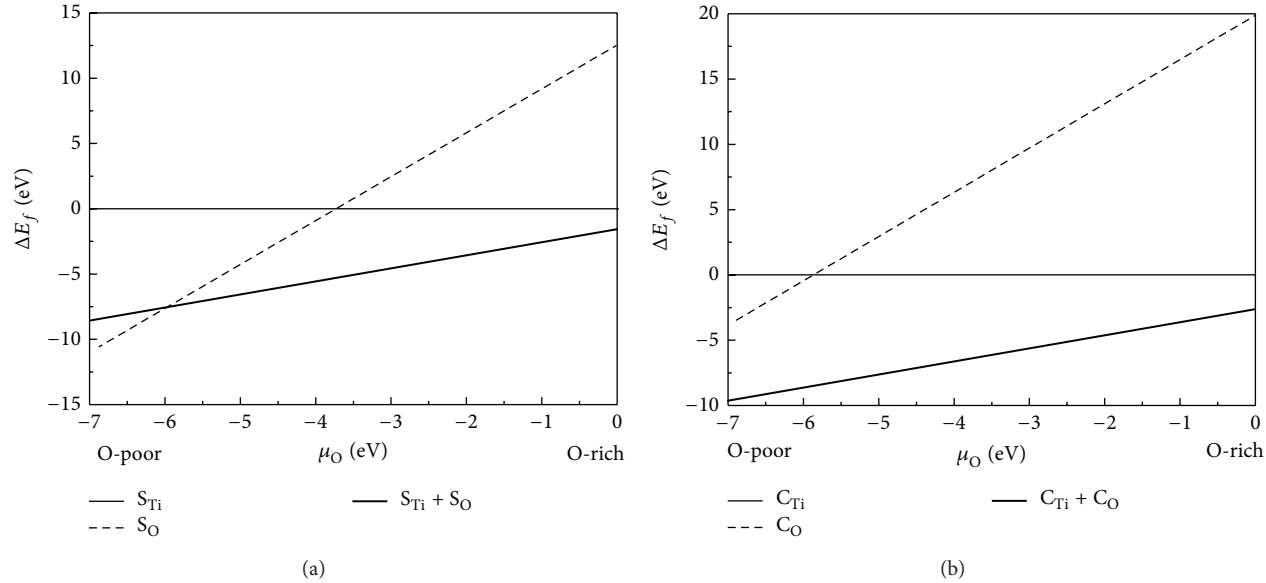

FIGURE 3: (a) The formation energies of the S_{Ti}, S_O, and $S_{Ti} + S_O$ complexes as a function of O chemical potential. The zero in the vertical axis corresponds to the formation energy of S_{Ti}. (b) The formation energies of the C_{Ti}, C_O, and $C_{Ti} + C_O$ complexes as a function of O chemical potential. The zero in the vertical axis corresponds to the formation energy of C_{Ti}.

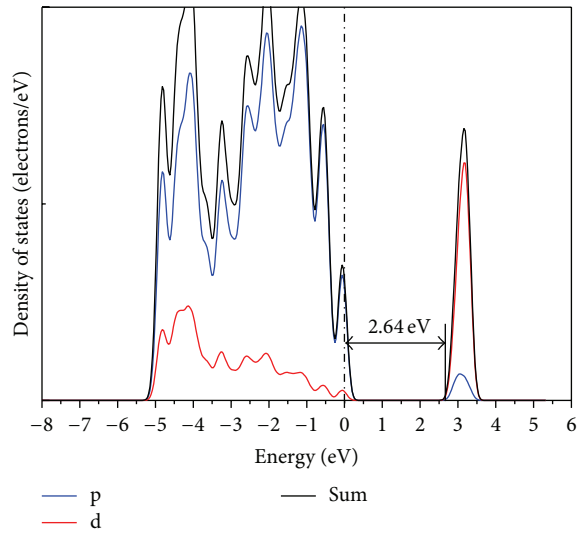

FIGURE 4: Density of the states (DOS) calculated for the pure surface $Ti_{24}O_{48}$(TO). Fermi level is at 0 eV and U is 8.50 eV for Ti 3d electrons.

the band gap energy from 2.64 eV to 2.45 eV. The conclusion accords with [6] that S-anion doping leads significant red shifts of the optical absorption edge.

For the AC-STO, the PDOS (Figure 5(c)) shows that the localized S 3p states introduced by S dopant at O_{2C} site still appear at the top of VB, and S dopant at Ti_{5C} site provides some localized 3p states at the bottom of CB; thus the width of VB states expands to 6.10 eV and the band gap energy decreases to 1.45 eV, which indicates a great decrease of excited energy for electronic transition and a red shift of the optical absorption for S-doped TiO_2. Obviously, the electronic properties of codoped systems are not a mechanical mixture of those of both single-doped systems, but the coupling contribution of surface S impurities at O_{2C} and Ti_{5C} sites, which is consistent with [26, 27].

The calculated PDOSs of C-doped surfaces are shown in Figure 6. Figure 6(a) exhibits the PDOS of A-CTO. A part of localized C 2p states locate at the TiO_2 VB maximum, which leads a slight expansion of VB from 5.40 to 5.50 eV, the band gap energy has a very small shortness of 0.14 eV. Additionally, another part of localized C 2p is lying in the gap and 1.70 eV away from the Femi level. In the PDOS of C-CTO (Figure 5(b)), C dopants do not introduce any states around the Femi level, and the calculated band gap energy is almost equal to that of TO. These conclusions are similar with [8].

For the AC-CTO, the PDOS (Figure 6(c)) shows that the C dopant at O_{2C} site still provides two parts of localized 2p states: one is at the bottom of VB and the other is in the gap, 1.23 eV away from the Femi level. The band gap energy decreases from 2.64 eV to 2.23 eV, and the VIS absorption of C-doped TiO_2could be improved by the decrease of intrinsic absorption energy. On the other hand, extrinsic absorption from VB states to unoccupied gap states contributes to the VIS sensitivity of C-doped TiO_2, either. However, the gap states may also act as the electron-cavity recombination centers, thus reducing the photocatalytic efficiency.

4. Conclusions

In this present work, all spin-polarized density-functional theory plane-wave pseudopotential method has been adopted to investigate the electronic properties of TiO_2 anatase (101) surfaces with S and C doping. GGA + U (Hubbard

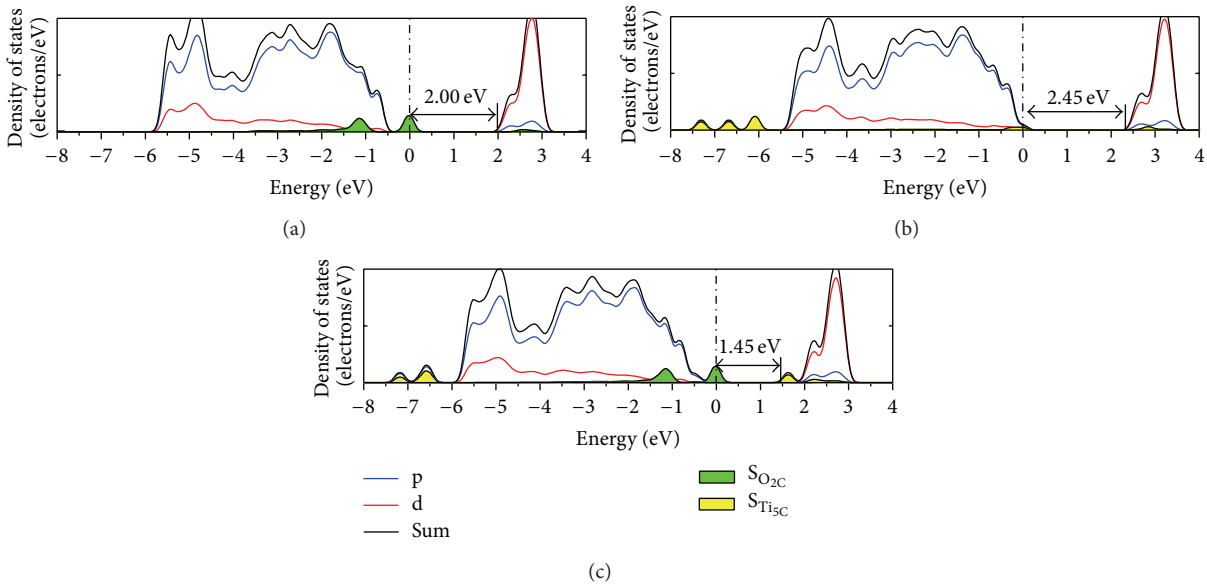

FIGURE 5: Density of the states (DOS) calculated for S-doped surfaces: (a) $Ti_{24}O_{47}S$(A-STO), (b) $Ti_{23}SO_{48}$(C-STO), and (c) $Ti_{23}SO_{47}S$(AC-STO). Fermi level is at 0 eV and U is 8.50 eV for Ti 3d electrons. The 3p states of S dopant at O_{2C} site and that of S dopant at Ti_{5C} site are represented by dark grey and black area, respectively.

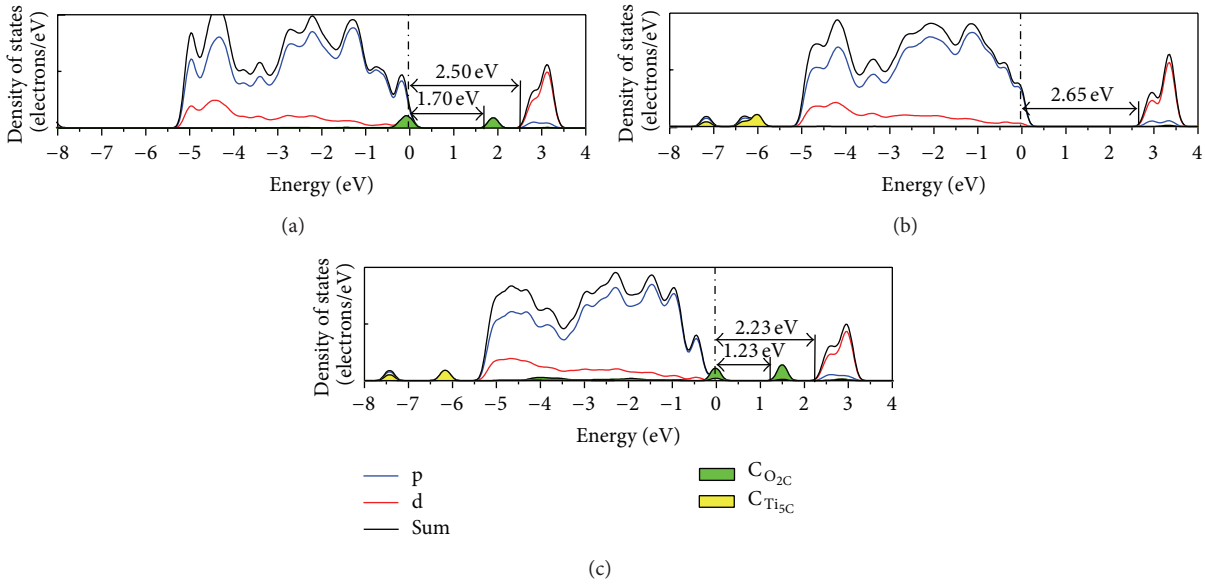

FIGURE 6: Density of the states (DOS) calculated for C-doped surfaces: (a) $Ti_{24}O_{47}C$(A-CTO), (b) $Ti_{23}CO_{48}$(C-CTO), and (c) $Ti_{23}CO_{47}C$(AC-CTO). Fermi level is at 0 eV and U is 8.50 eV for Ti 3d electrons. The 2p states of C dopant at O_{2C} site and that of C dopant at Ti_{5C} site are represented by dark grey and black area, respectively.

coefficient) method has been used to describe exchange-correlation effects. For the case of S doping, our calculations demonstrated that the formation energy of the complex S_O + S_{Ti} is lower than that of the isolated S_{Ti} or S_O in the most range of chemical potentials of O, which indicates that the complex $S_O + S_{Ti}$ may form more easily under most of conditions for S-doped TiO_2. The calculated density of the states of anion and cation codoping surface AC-STO shows that there is a sharp decrease for the band gap energy from 2.64 to 1.45 eV due to the synergistic effect of S_O and S_{Ti} defects. Thus, the ability of VIS absorption for S-doped TiO_2 could be improved greatly. For the case of C doping, the formation energy of the complex C_O + C_{Ti} is the lowest in all the range of chemical potentials of O. The calculated density of the states of anion and cation codoping surface AC-CTO also shows a decrease for the band gap energy from 2.64 to 2.23 eV and the VIS absorption could be improved by the decrease of intrinsic absorption energy appreciably, but the gap states induced by C_O defect may act

as the electron-cavity recombination centers, thus reducing the photocatalytic efficiency.

Conflict of Interests

The authors declare that there is no conflict of interests regarding the publication of this paper.

Acknowledgments

The project was supported by the National Natural Science Foundation of China (41340048), and the Fundamental Research Funds for the Central Universities (CUG120110).

References

[1] U. Diebold, "The surface science of titanium dioxide," *Surface Science Reports*, vol. 48, no. 5–8, pp. 53–229, 2003.

[2] D. P. Norton, "Synthesis and properties of epitaxial electronic oxide thin-film materials," *Materials Science and Engineering R*, vol. 43, no. 5-6, pp. 139–247, 2004.

[3] T. Umebayashi, T. Yamaki, S. Yamamoto et al., "Sulfur-doping of rutile-titanium dioxide by ion implantation: photocurrent spectroscopy and first-principles band calculation studies," *Journal of Applied Physics*, vol. 93, no. 9, pp. 5156–5160, 2003.

[4] T. Umebayashi, T. Yamaki, H. Itoh, and K. Asai, "Band gap narrowing of titanium dioxide by sulfur doping," *Applied Physics Letters*, vol. 81, no. 3, pp. 454–456, 2002.

[5] T. Ohno, M. Akiyoshi, T. Umebayashi, K. Asai, T. Mitsui, and M. Matsumura, "Preparation of S-doped TiO_2 photocatalysts and their photocatalytic activities under visible light," *Applied Catalysis A*, vol. 265, no. 1, pp. 115–121, 2004.

[6] R. Long, N. J. English, and Y. Dai, "First-principles study of s doping at the rutile TiO_2 (110) surface," *Journal of Physical Chemistry C*, vol. 113, no. 40, pp. 17464–17470, 2009.

[7] Y. Nakano, T. Morikawa, T. Ohwaki, and Y. Taga, "Electrical characterization of band gap states in C-doped TiO_2 films," *Applied Physics Letters*, vol. 87, no. 5, Article ID 052111, 2005.

[8] H. Kamisaka, T. Adachi, and K. Yamashita, "Theoretical study of the structure and optical properties of carbon-doped rutile and anatase titanium oxides," *Journal of Chemical Physics*, vol. 123, no. 8, Article ID 084704, 2005.

[9] Y. Kesong, D. Ying, H. Baibiao, and W. Myung-Hwan, "Density functional characterization of the visible-light absorption in substitutional C-anion- and C-cation-doped TiO_2," *Journal of Physical Chemistry C*, vol. 113, no. 6, pp. 2624–2629, 2009.

[10] J. Y. Lee, J. Park, and J. H. Cho, "Electronic properties of N- and C-dopedTiO_2," *Applied Physics Letters*, vol. 87, Article ID 011904, 2005.

[11] T. Ihara, M. Miyoshi, Y. Iriyama, O. Matsumoto, and S. Sugihara, "Visible-light-active titanium oxide photocatalyst realized by an oxygen-deficient structure and by nitrogen doping," *Applied Catalysis B*, vol. 42, no. 4, pp. 403–409, 2003.

[12] C. Stampfl and C. G. Van De Walle, "Density-functional calculations for III-V nitrides using the local-density approximation and the generalized gradient approximation," *Physical Review B*, vol. 59, no. 8, pp. 5521–5535, 1999.

[13] S. L. Dudarev, G. A. Botton, S. Y. Savrasov, C. J. Humphreys, and A. P. Sutton, "Electron-energy-loss spectra and the structural stability of nickel oxide: an LSDA+U study," *Physical Review B*, vol. 57, no. 3, pp. 1505–1509, 1998.

[14] M. C. Payne, M. P. Teter, D. C. Allan, T. A. Arias, and J. D. Joannopoulos, "Iterative minimization techniques for ab initio total-energy calculations: molecular dynamics and conjugate gradients," *Reviews of Modern Physics*, vol. 64, no. 4, pp. 1045–1097, 1992.

[15] S. J. Clark, M. D. Segall, C. J. Pickard et al., "First principles methods using CASTEP," *Zeitschrift für Kristallographie*, vol. 220, no. 4, pp. 567–570, 2005.

[16] Q. L. Chen, G. Zheng, K. H. He, and B. Le, "First-principles calculations on electronic structures of TiO_2 anatase (101) surfaces with N impurities," *Modern Physics Letters B*, vol. 25, p. 119, 2011.

[17] Q.-L. Chen and C.-Q. Tang, "First-principles calculations on electronic structures of N/F-doped and N-F-codoped TiO_2 anatase (101) surfaces," *Acta Physico-Chimica Sinica*, vol. 25, no. 5, pp. 915–920, 2009.

[18] Q. Chen, C. Tang, and G. Zheng, "First-principles study of TiO_2 anatase (101) surfaces doped with N," *Physica B*, vol. 404, no. 8-11, pp. 1074–1078, 2009.

[19] Q. L. Chen, B. Li, G. Zheng, K. H. He, and A. S. Zheng, "First-principles calculations on electronic structures of Fe-vacancy-codoped TiO_2 anatase (101) surface," *Physica B*, vol. 406, no. 20, pp. 3841–3846, 2011.

[20] E. Finazzi, C. Di Valentin, A. Selloni, and G. Pacchioni, "First principles study of nitrogen doping at the anatase TiO_2 (101) surface," *Journal of Physical Chemistry C*, vol. 111, no. 26, pp. 9275–9282, 2007.

[21] Y. W. Xu, K. Chen, S. H. Liu, M. J. Cao, and J. Q. Li, "Interaction of photoactive catechol with TiO_2 anatase (101) surface: a periodic density functional theory study," *Chemical Physics*, vol. 331, pp. 275–282, 2007.

[22] X. Y. Cui, J. E. Medvedeva, B. Delley, A. J. Freeman, and C. Stampfl, "Spatial distribution and magnetism in poly-Cr-doped GaN from first principles," *Physical Review B*, vol. 75, no. 15, Article ID 155205, 2007.

[23] F. Wang, Z. Pang, L. Lin, S. Fang, Y. Dai, and S. Han, "Theoretical study of the magnetic interaction of Cr-doped ZnO with and without vacancies," *Journal of Magnetism and Magnetic Materials*, vol. 321, no. 19, pp. 3067–3070, 2009.

[24] F. Gao, J. Hu, J. Wang, C. Yang, and H. Qin, "Ferromagnetism induced by intrinsic defects and carbon substitution in single-walled ZnO nanotube," *Chemical Physics Letters*, vol. 488, no. 1–3, pp. 57–61, 2010.

[25] A. Debernardi and M. Fanciulli, "The magnetic interaction of Fe doped ZnO with intrinsic defects: a first principles study," *Physica B*, vol. 401-402, pp. 451–453, 2007.

[26] J. Yu, P. Zhou, and Q. Li, "New insight into the enhanced visible-light photocatalytic activities of B-, C- and B/C-doped anatase TiO_2 by first-principles," *Physical Chemistry Chemical Physics*, vol. 15, no. 29, pp. 12040–12047, 2013.

[27] P. Zhou, J. G. Yu, and Y. X. Wang, "The new understanding on photocatalytic mechanism of visible-light response N–S codoped anatase TiO_2 by first-principles," *Applied Catalysis B*, vol. 142-143, pp. 45–53, 2013.

Hindawi Publishing Corporation
International Journal of Photoenergy
Volume 2014, Article ID 903612, 8 pages
http://dx.doi.org/10.1155/2014/903612

Research Article

Photocatalytic Bactericidal Efficiency of Ag Doped TiO_2/Fe_3O_4 on Fish Pathogens under Visible Light

Ekkachai Kanchanatip,[1,2] Nurak Grisdanurak,[3] Naichia Yeh,[4] and Ta Chih Cheng[5]

[1] *International Postgraduate Program in Environmental and Hazardous Waste Management, Chulalongkorn University, Bangkok 10330, Thailand*
[2] *National Center of Excellence for Environmental and Hazardous Waste Management, Chulalongkorn University, Bangkok 10330, Thailand*
[3] *Department of Chemical Engineering, Faculty of Engineering, Thammasat University, Bangkok 12120, Thailand*
[4] *Center of General Education, MingDao University, Changhua 52345, Taiwan*
[5] *Department of Tropical Agriculture and International Cooperation, National Pingtung University of Science and Technology, Pingtung 91201, Taiwan*

Correspondence should be addressed to Nurak Grisdanurak; gnurak@engr.tu.ac.th and Ta Chih Cheng; cheng.tachih@gmail.com

Received 22 February 2014; Revised 27 April 2014; Accepted 8 May 2014; Published 27 May 2014

Academic Editor: Hong Liu

This research evaluates photocatalytic bactericidal efficiencies of Ag-TiO_2/Fe_3O_4 in visible light using target pollutants that include *Aeromonas hydrophila, Edwardsiella tarda*, and *Photobacterium damselae* subsp. *piscicida*. The investigation started with Ag-TiO_2/Fe_3O_4 synthesis and calcination followed by a series of product tests that include the examination of crystallite phase, light absorption, element composition morphology, and magnetic properties. The results of the experiment indicate that Ag and Fe_3O_4 significantly enhanced the light absorption capacity of TiO_2 in the entire visible light range. The Ag-TiO_2/Fe_3O_4 prepared in this study displays significantly enhanced visible light absorption and narrowed band gap energy. The magnetic property of Ag-TiO_2/Fe_3O_4 made it easy for retrieval using a permanent magnet bar. The photocatalytic activity of Ag-TiO_2/Fe_3O_4 remains above 85% after three application cycles, which indicates high and favorable efficiency in bactericidal evaluation. The experiments have proved that the Ag-TiO_2/Fe_3O_4 magnetic photocatalyst is a promising photocatalyst for antibacterial application under visible light.

1. Introduction

Bacterial pathogens are a main cause of fish mortalities in cultured fish and occasionally in wild fish. As facultative pathogen exists for both fish and human [1, 2], human infections caused by pathogens transmitted from fish or aquatic environment are quite general. Such infection varies by seasons, dietary habits, and the immune system status of the exposed individual. Traditional methods such as chlorination are chemical intensive and have many disadvantages. For example, chlorine used in water treatment for disinfection can react with organic material to generate carcinogenic chloroorganic compounds. Moreover, certain pathogens, bacteria, and protozoans have been known to be resistant to chlorine disinfection [3].

Applications of photocatalytic processes are viable solutions to environmental problems. Heterogeneous photocatalytic oxidation (PCO) has been proposed as one of the advanced oxidation techniques for mineralization of hydrocarbon pollutants. PCO helps to create strong oxidation agents that breakdown organics to CO_2 in the presence of the photocatalyst, H_2O, and light. Heterogeneous systems also have the advantages of minimal waste generation and reusability of catalysts.

TiO_2, one of the most promising semiconductor photocatalysts for removing pollutant and cleaning water, is of low cost, nontoxic, and physically and chemically stable. TiO_2 particles are both photocatalytic and antimicrobial [4]. Anatase TiO_2 is superior to rutile and brookite for organic compound removal. However, its wide band gap (3.2 eV)

allows it to be activated only by UV. Also, the high rate of electron-hole (e^--h^+) recombination in TiO_2 particles results in low photocatalytic efficiency. Doping TiO_2 with various transition metal ions narrows the band gap [5] and expands the photoresponse of TiO_2 into visible spectrum [6]. Also, electron transfer between those metal ions and TiO_2 can alter e^--h^+ recombination as the metal ions are incorporated into the TiO_2 lattice. Feng et al. [7] have studied the antibacterial mechanism of Ag^+ on bacteria and found that Ag^+ deprives DNA molecules' replication abilities. In addition, Ag^+ increases visible light absorption and holds up the e^--h^+ recombination of TiO_2.

Many of the particles used in the separation technology are superparamagnetic, which can be magnetized with an external magnetic field and redispersed upon the removal of magnet [8, 9]. For example, the magnetic property Fe_3O_4 helps to enhance the recovery of the catalyst via external magnetic field. Magnetic Fe_3O_4 particles suspended in carrier fluids are referred to as magnetic fluids. Additionally, Fe_3O_4 also enhances the visible light absorption which resulted from the band gap reduction [10].

2. Materials and Methods

2.1. Materials. The chemicals used in this study include titanium (IV) isopropoxide (98% Acros Organics), isopropyl alcohol (99.9% Carlo Erba), acetylacetone (99.5% Carlo-Erba), silver nitrate (99.8% Sigma-Aldrich), ferric chloride anhydrous (98% Katayama Chemical Inc.), ferrous chloride (97% Katayama Chemical Inc.), and sodium hydroxide (97% Katayama Chemical Inc.). These chemicals are analytical reagent grades and used without further modification.

2.2. Synthesis of Ag-TiO_2/Fe_3O_4. The Ag-TiO_2/Fe_3O_4 magnetic photocatalyst was synthesized in two steps. First, magnetite (Fe_3O_4) nanoparticles were synthesized via coprecipitation method, in which $FeCl_3$ anhydrous and $FeCl_2{\cdot}4H_2O$ salts in the molar ratio of 2 : 1 were dissolved and vigorously stirred in double-distilled water. NaOH was then dropped slowly into the solution until a large amount of black precipitates formed. The resulting precipitates were collected using a magnet and washed several times with double-distilled water and ethanol. The reaction in this process is as follows:

$$2FeCl_3 + FeCl_2 + 8NaOH \longrightarrow Fe_3O_4 + 8NaCl + 4H_2O \quad (1)$$

In the second step, Ag-TiO_2/Fe_3O_4 composite particles were prepared using modified sol-gel method. Acetylacetone (Acac), as a chelating agent, was added into isopropyl alcohol and stirred magnetically. Titanium isopropoxide (TTIP) was then added gradually to the mixture with Acac : IPA : TTIP in molar ratio of 2.84 : 23.64 : 1. An appropriate volume of aqueous silver nitrate was added to the titanium solution to attain 1 wt% of Ag on TiO_2 and stirred vigorously for 30 minutes. Meanwhile, Fe_3O_4 particles were dispersed in isopropyl alcohol and sonicated in an ultrasonic apparatus for 10 minutes. Thereafter, slowly add the mixture of Ag-TiO_2 into Fe_3O_4 suspension with TTIP : Fe_3O_4 ratio of 10 (weight basis) and stir the mixture at room temperature for 3 hours to ensure uniform composition. The obtained suspension was placed in a hot air oven at 90°C for the particles to dry. Finally, the composite particles were calcinated in oxygen at 450°C for 3 hours to form Ag-TiO_2/Fe_3O_4.

2.3. Characterization of Ag-TiO_2/Fe_3O_4. The properties of Ag-TiO_2/Fe_3O_4 magnetic photocatalyst were characterized with various instruments. The crystal structure of the particles was characterized with X-ray diffraction (XRD) on a Bruker AXS diffractometer with CuKα radiation. The X-ray was generated with a current of 40 mA and a potential of 40 kV in angular range (2θ) from 10° to 80°. The UV-Visible diffuse reflectance spectra in the range of 320–800 nm were acquired from a Hitachi U3501UV-visible diffuse reflectance spectrophotometer (UV-Vis DRS) equipped with integrating sphere. Pure $BaSO_4$ powder was used as a reflectance standard. Transmission electron microscopy (TEM) observation of the samples was performed on a HITACHI 7500 transmission electron microscope operated at 80 kV. The magnetization of photocatalyst was measured using superconducting quantum interference device (SQUID).

2.4. Evaluation of Photocatalytic Bactericidal Activities. The research team has evaluated photocatalytic bactericidal activities using modified antibacterial drop test. In order to differentiate the effect of TiO_2 and silver, the experiment was conducted both under visible light and in dark to block photocatalytic process to assure that the bactericidal activity is exclusively from silver. Fish pathogens used in the experiment included *Aeromonas hydrophila* (BCRC13018), *Edwardsiella tarda* (BCRC10670), and *Photobacterium damselae* subsp. *piscicida* (BCRC17065). Bacterial cells were collected via centrifugation at 9500 rpm for 10 minutes to remove supernatants. The pellets were then rinsed twice with 15 mL phosphate buffer saline (PBS, 137 mM sodium chloride; 10 mM phosphate; 2.7 mM potassium chloride; pH 7.4). Ten mL of pathogens in PBS was added to each 6 cm diameter sterilized glass Petri dish containing various amounts of Ag-TiO_2/Fe_3O_4 and irradiated with visible fluorescence light (FL40S·N-EDL·NU, Mitsubishi/Osram, Japan, $\lambda > 420$ nm, 1040 lux) for various time intervals. The control groups were without photocatalyst. All control and experimental groups had 3 replicates. At each time interval, 20 μL of such solution was transferred from each Petri dish to 96-well plate containing 180 μL of 0.05% 2,3,5-triphenyl tetrazolium chloride (TTC) and incubated at 28°C for 10 hours. The absorbance of each tube at 540 nm was measured with ELISA reader after adding 50 μL of isopropanol to the tubes to terminate reaction [11].

The inhibition efficiencies to fish pathogen were calculated as

$$\frac{[\mathrm{Abs}]_i - [\mathrm{Abs}]_t}{[\mathrm{Abs}]_i} \times 100\%, \quad (2)$$

where $[\mathrm{Abs}]_i$ is the absorbance of control group at certain time interval and $[\mathrm{Abs}]_t$ is the absorbance of experimental group at the same time interval.

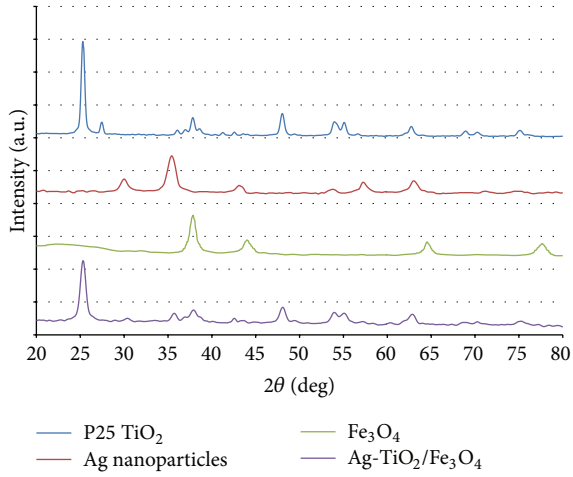

Figure 1: XRD spectra of Ag-TiO_2/Fe_3O_4.

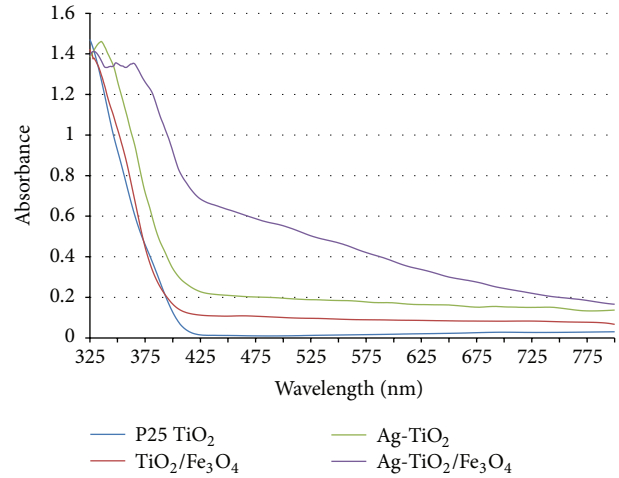

Figure 2: UV-Vis diffuse reflectance spectra for the as-synthesized samples.

3. Results and Discussion

Figure 1 displays the XRD patterns of P25 TiO_2, Fe_3O_4, and Ag-TiO_2/Fe_3O_4. The main peaks of Ag-TiO_2/Fe_3O_4 are present at 25.3, 38, 48, and 54° corresponding to (101), (004), (200), and (211) planes of TiO_2, respectively (JCPDS, number 21-1272). With no evidence of its correspondence to the rutile phase, the patterns correspond to the anatase phase exclusively at the calcination temperature of 450°C. These results help to conclude that the presence of the iron oxide has no accelerating effect on the anatase-rutile phase transformation of the TiO_2. In addition, there is no characteristic peak of Ag presented in the pattern, which implies that the amount of Ag particles is not adequate to present their characteristic patterns [12, 13]. The pattern of Fe_3O_4 does not appear in the XRD, which may indicate that Fe_3O_4 is encapsulated by Ag-TiO_2. However, the broadened patterns suggest that Ag^+ doping suppresses the growth of TiO_2 crystals.

The average crystallite size (D) of catalyst is estimated using Scherrer's equation:

$$D = \frac{k\lambda}{\beta \cos\theta}, \quad (3)$$

where D is crystallite size (nm), k is crystallite shape factor (0.90), λ is X-ray wavelength, for CuKα (0.15418 nm), β is the full-width-half-maximum (FWHM) of the peak, and θ is Bragg angle.

The crystallite size can be measured via the diffraction data in Figure 1 according to the Scherrer equation for the peak at 25.3°. The estimated size is about 12.53 nm.

Figure 2 shows the influence of Ag and Fe_3O_4 on the UV-Visible light absorption. Fe_3O_4 slightly enhances the visible light absorption of TiO_2. With the modification of Ag, the shifting of Ag-TiO_2 absorption spectrum to longer wavelengths is noticeable, which is due to the interaction between Ag and TiO_2 matrix. In addition, Ag-TiO_2/Fe_3O_4 demonstrates significantly higher absorption in the 400–800 nm range.

Table 1: Estimated band gap energy of as-synthesized samples.

Sample	Band gap energy (eV)	Band edge wavelength (nm)[a]
TiO_2/Fe_3O_4	2.9	428
Ag-TiO_2	2.7	460
Ag-TiO_2/Fe_3O_4	2.35	528

[a] $E_{bg} = hc/\lambda$.

As shown in Figure 3, UV-Vis absorption spectra are converted to the Tauc plot of $(\alpha h\nu)^{1/2}$ and photon energy, and the linear extrapolations are made by drawing a tangent line through the maximum slope and taking its intersection with X-axis at $(\alpha h\nu)^{1/2} = 0$ [14].

The calculated energy band gaps of TiO_2/Fe_3O_4, Ag-TiO_2, and Ag-TiO_2/Fe_3O_4 are 2.9, 2.7, and 2.35 eV, respectively (Figure 3). Compared to the original anatase TiO_2 band gap of 3.2 eV, Fe_3O_4 and Ag dopants have improved the photocatalytic activity under visible light via narrowing the band gap and enhancing the visible light absorption of TiO_2 (Table 1).

Figure 4 shows the XPS spectra for Ag3d region of Ag-TiO_2/Fe_3O_4. The spectra consist of two peaks at around 367 and 373 eV, which correspond to $Ag3d_{5/2}$ and $Ag3d_{3/2}$, respectively. The peaks are slightly broadened and can be considered as the sum of multiple overlapping peaks. As the XPS infers, the silver species on the Ag-TiO_2/Fe_3O_4 photocatalyst are metallic silver and silver ions coexisting in terms of the bonding energy corresponding to $Ag3d_{5/2}$ of metallic Ag (Ag^0, 368 eV), Ag_2O (Ag^+, 367.5 eV), and AgO (Ag^{2+}, 367 eV), respectively [15, 16].

Figure 5 shows the morphology of the sample under TEM. The Ag-TiO_2/Fe_3O_4 particle connects tightly to one another. The diameter of the particles is in the range of 14–40 nm.

Figure 6 displays the energy dispersive X-ray (EDX) spectra analysis of Ag-TiO_2/Fe_3O_4 and Table 2 lists the

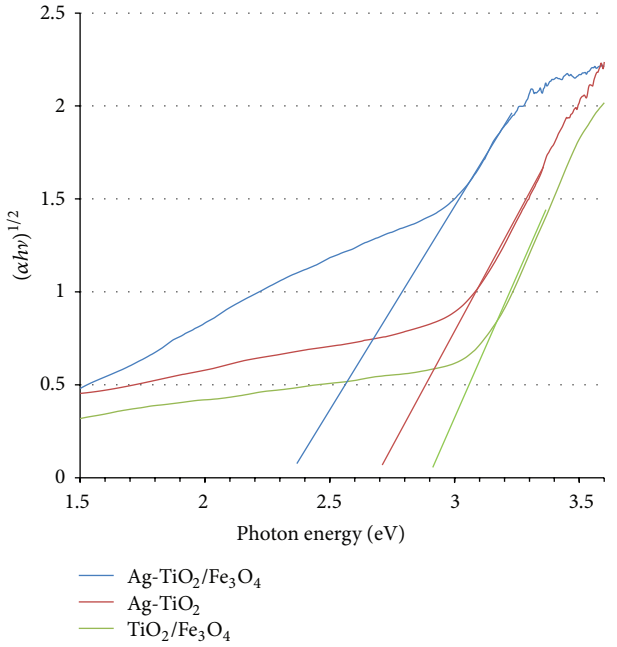

Figure 3: Tauc plot for the determination of band gap for the as-synthesized samples.

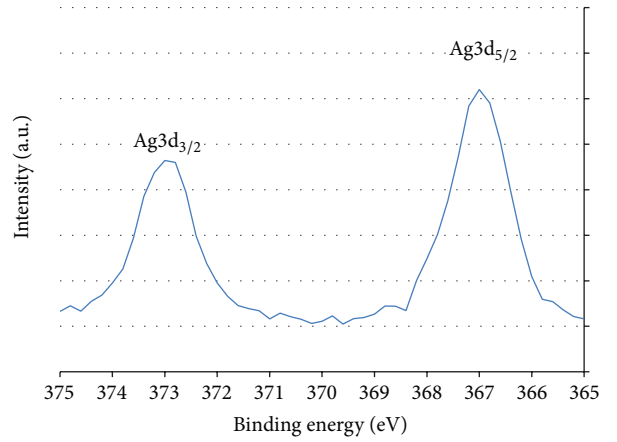

Figure 4: X-ray photoelectron spectra (XPS) of the as-synthesized Ag-TiO_2/Fe_3O_4 in the Ag3d region.

composition of the prepared photocatalyst. Among the four elements (Ti, Fe, O, and Ag) presented, higher Ti content compared to magnetite could be resulting from the formation of TiO_2 layer coated on Fe_3O_4 particles. The Ag signals are around 2.8 keV, which may indicate the existence of Ag particles in catalyst.

Figure 7 displays the magnetic property of Ag-TiO_2/Fe_3O_4 measured at 25°C. The absence of hysteresis loop of the sample indicates the superparamagnetic character of the material [17]. Figure 8 shows the synthesized Ag-TiO_2/Fe_3O_4 (with a saturation magnetization of 2.7 emu/g) being recollected from the solution with a magnet.

Figure 9 shows the indigo carmine decolorization efficiency of TiO_2, Ag-TiO_2, TiO_2/Fe_3O_4, and Ag-TiO_2/Fe_3O_4, in visible light. Ag-TiO_2 exhibits the highest photocatalytic

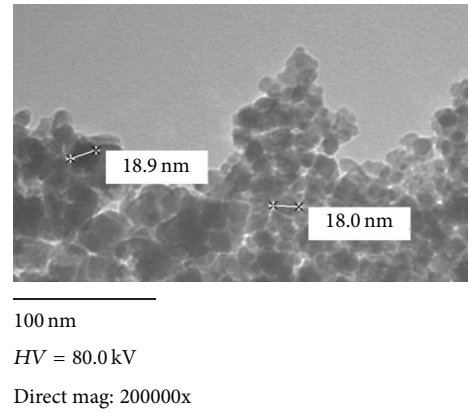

Figure 5: TEM photograph for the as-synthesized Ag-TiO_2/Fe_3O_4.

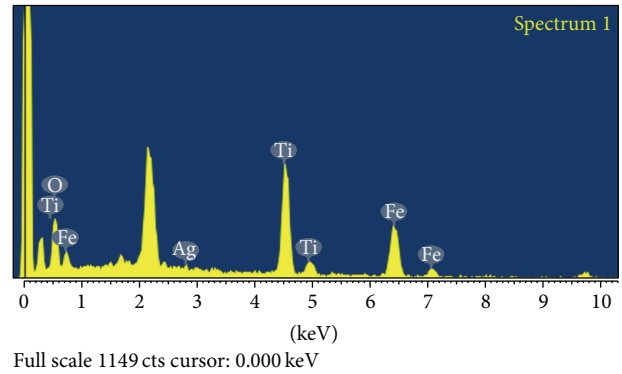

Figure 6: Energy dispersive X-ray spectra for the as-synthesized Ag-TiO_2/Fe_3O_4.

Table 2: Characterization data of EDX for Ag-TiO_2/Fe_3O_4.

Element	Weight (%)	Atomic (%)
O K	26.55	54.12
Ti K	33.85	23.05
Fe K	38.59	22.53
Ag L	1.01	0.3
Total	100.00	

activity (near 100% indigo carmine degradation within 2 hours). No decolorization has been found in undoped TiO_2. The decolorization efficiencies of TiO_2/Fe_3O_4 and Ag-TiO_2/Fe_3O_4 are ~68% and ~85%, respectively, after 5 hours. The results suggest that Ag deposition has enhanced the visible light photocatalytic activity of TiO_2. Such enhancement may be attributed to the electron interaction at the contact between the metal deposits and the semiconductor surface. The Ag deposits act as e^- traps that immobilize the photogenerated electrons. The trapped electrons are then transferred to oxygen to form highly oxidative species such as O_2^-. The Fe_3O_4 in the photocatalyst helps to enhance the visible light activity of TiO_2. As TiO_2 is the active site of the catalyst, substituting Ag-TiO_2 with Fe_3O_4 may decrease the photocatalytic activity. Although Ag-TiO_2 demonstrates higher decolorization efficiency than Ag-TiO_2/Fe_3O_4, yet Ag-TiO_2 is not recollectable with magnet after dispersing in

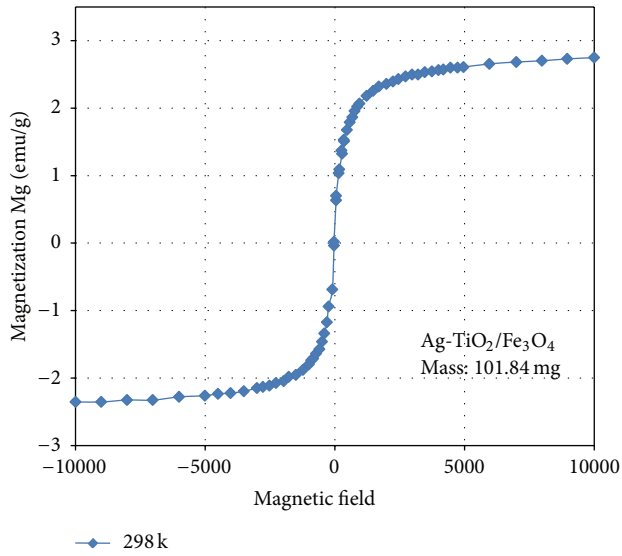

Figure 7: Magnetization curves of Ag-TiO_2/Fe_3O_4 at room temperature.

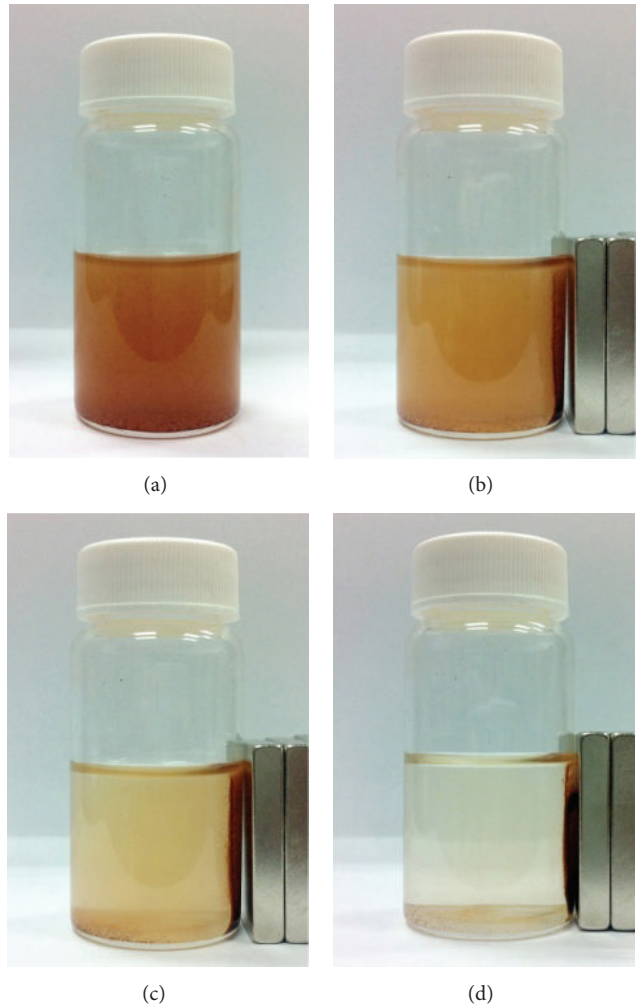

Figure 8: Photographs of Ag-TiO_2/Fe_3O_4 dispersed in water after sonication (a) along with its response to the presence of magnet at 10 seconds (b), 1 minute (c), and 5 minutes (d).

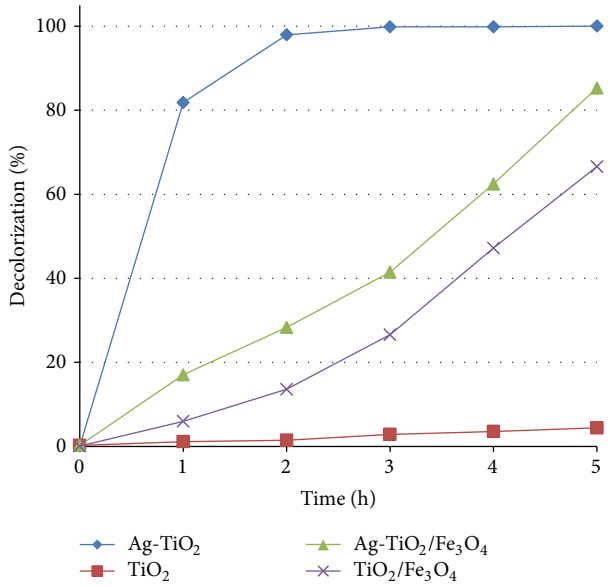

FIGURE 9: Photocatalytic activity in decolorization of indigo carmine (O.D.620 = 0.1) under visible light irradiation at room temperature.

water. As a result, only Ag-TiO_2/Fe_3O_4 is used for bactericidal efficiency evaluation.

The catalyst reusability is an important parameter for practical applications. The repetitive use of as-synthesized Ag-TiO_2/Fe_3O_4 was studied for different cycles of indigo carmine decolorization under visible light irradiation. The catalyst was recovered using a permanent magnet bar and used for three cycles with all other parameters kept constant. The results demonstrate that Ag-TiO_2/Fe_3O_4 maintains good activity in three runs, with only a small loss. The drop in decolorization might be due to the loss or aggregation of the particles during the recycling process. The decolorization after 6 h irradiation at the third run (Figure 10) was around 85%, which indicates that Ag-TiO_2/Fe_3O_4 sustains well from recycling and has good potential for practical applications.

The research team tested three Ag-TiO_2/Fe_3O_4 loadings (i.e., 3.5 mg, 2.7 mg, and 1.8 mg) to select its suitable one in 10 mL of phosphate buffer saline (PBS) containing fish pathogens. As displayed in Figure 11, the antibacterial efficiencies are less than 10% in all loadings for all catalysts within the first 30 minutes. After that, the specimen of 3.5 mg Ag-TiO_2/Fe_3O_4 load demonstrates sharp efficiency increase to reach ~100% after 90 minutes. The specimen of 2.7 mg load demonstrates increased antibacterial efficiency after 60 minutes to reach 95% after 120 minutes. The specimen of 1.8 mg load demonstrates very low antibacterial efficiency, only 18% fish pathogens degradation. Therefore, 2.7 mg load was chosen for further study.

The experiment uses *Aeromonas hydrophila* (BCRC-13018), *Edwardsiella tarda* (BCRC10670), and *Photobacterium damselae* subsp. *piscicida* (BCRC17065) as target bacteria. These bacteria, which cause losses in wild and farmed fish stocks, are gram negative fish pathogens that inhabit in freshwater as well as seawater. As shown in Figure 12, the effects have been slow in the first 30 minutes and then start to increase more significantly. Almost all bacteria were

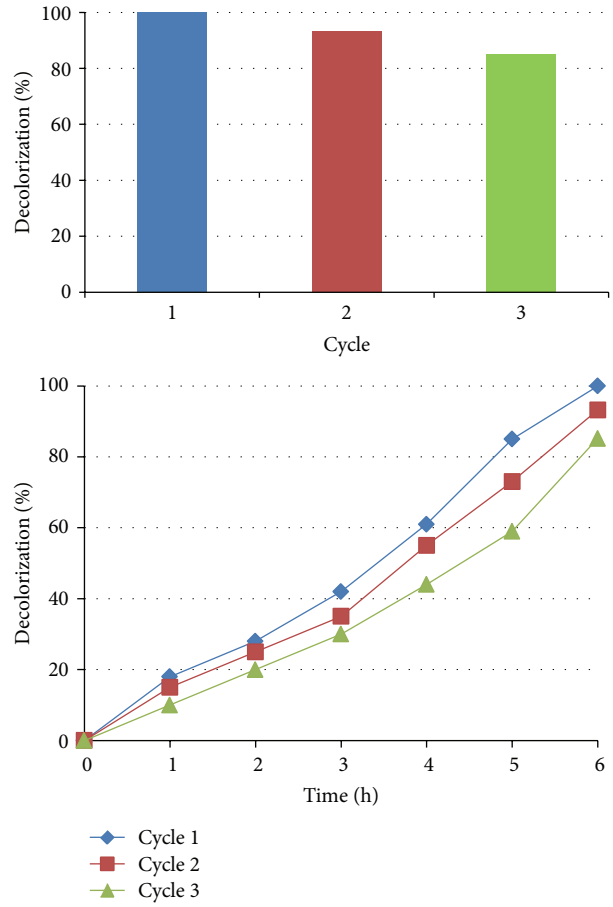

FIGURE 10: The reusability of Ag-TiO_2/Fe_3O_4 as demonstrated in decolorization of indigo carmine under visible light irradiation.

destroyed by Ag-TiO_2/Fe_3O_4 after 120 minutes irradiation. The bactericidal efficiency is about 20% for both BCRC13018 and BCRC17065 after 60 minutes of visible light irradiation. No significant difference has been found between these two pathogens. After 120 minutes, the bactericidal efficiencies increase to 93% for BCRC13018 and 81% for BCRC17065. The results suggest that *Photobacterium damselae* subsp. *piscicida* is more resistant to Ag-TiO_2/Fe_3O_4 among these three pathogens.

Figure 13 shows that in the dark, where no photocatalysis process occurs, *Aeromonas hydrophila* and *Photobacterium damselae* subsp. *piscicida* degrade ~15% after 120 minutes, while *Edwardsiella tarda* degrades more quickly and reach 100% within 120 minutes. The bactericide effect seems to be exclusive due to the presence of Ag^+. Such findings indicate that *Edwardsiella tarda* is a very sensitive microorganism and more susceptible to silver particle. These results suggest that Ag-TiO_2/Fe_3O_4's photocatalytic bactericidal effect is species dependent.

4. Conclusions

Ag-TiO_2/Fe_3O_4 magnetic photocatalyst has demonstrated strong antimicrobial properties through a mechanism including photocatalytic production of reactive oxygen species

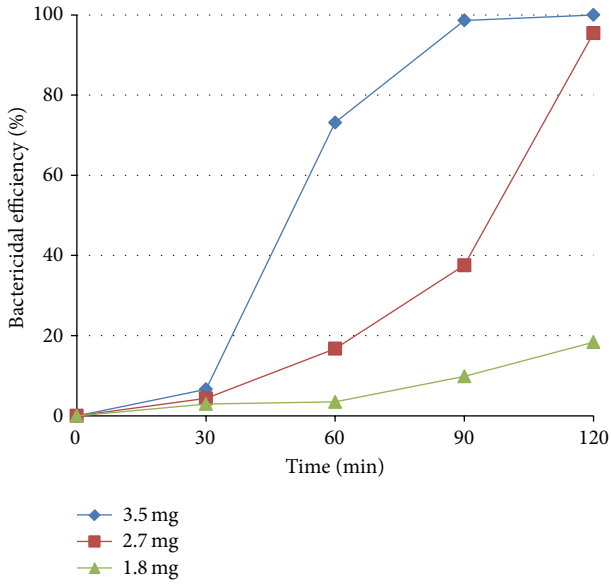

FIGURE 11: Photocatalytic bactericidal efficiency for *Aeromonas hydrophila* (BCRC13018) at different loadings of Ag-TiO_2/Fe_3O_4 under visible light irradiation.

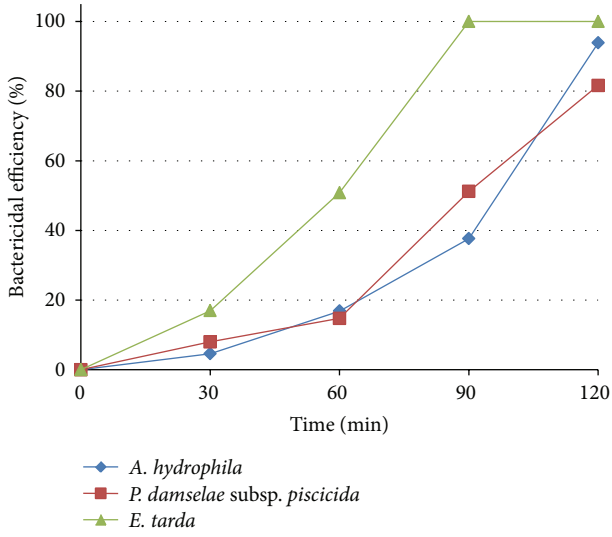

FIGURE 12: Bactericidal efficiency of 2.7 mg Ag-TiO_2/Fe_3O_4 to *Aeromonas hydrophila* (♦), *Edwardsiella tarda* (▲), and *Photobacterium damselae* subsp. *piscicida* (■) under visible light.

that damage cell components and viruses [18]. The holes on the valence band of TiO_2 can react with either H_2O or OH^- absorbed on the surface to produce hydroxyl radicals and with the electrons on the conduction band to reduce O_2 to produce superoxide anion. The detection of other reactive oxygen species such as H_2O_2 and singlet oxygen has also been reported. Hydroxyl radical and superoxide anions, both known to be highly reactive with biological samples, are considered the main species generated in the anodic and cathodic pathways, respectively, of photocatalytic processes in the presence of oxygen. The XPS data indicated different silver species coexisting in the $Ag3d_{5/2}$ region of

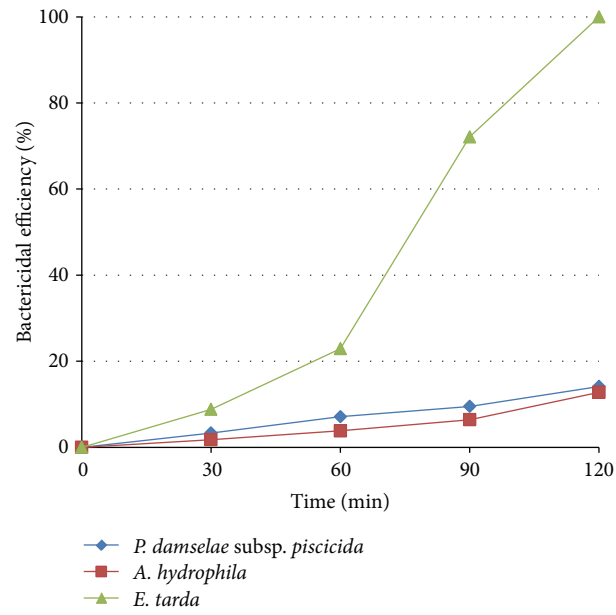

FIGURE 13: Bactericidal efficiency of 2.7 mg Ag-TiO_2/Fe_3O_4 to *Aeromonas hydrophila* (■), *Edwardsiella tarda* (▲), and *Photobacterium damselae* subsp. *piscicida* (♦) in the dark.

photocatalyst with binding energies at around 367 eV and 368 eV, assigned to silver ion (Ag^+ and/or Ag^{2+}) and metallic silver (Ag^0), respectively. Ag^+ can cause severe alterations to bacteria via binding to bacterial denatured DNA and RNA so as to inhibit the replication. The modifications of membrane structure that include changes in membrane-bound enzyme activities, metabolic pathways, transport systems, and permeability alterations lead to cell death. Ag^+ from Ag-TiO_2 inactivates membrane proteins and respiratory enzymes. Reactive oxygen species damage cell membrane when cell comes into contact with catalyst surface. Ag also acts as the trap of photogenerated electrons to prevent the e^--h^+ pairs from recombining rapidly after photoexcitation.

As a final remark, the research team intend to use light emitting diodes (LEDs) of different colors as the light source to identify the most responsive spectrum of Ag-TiO_2/Fe_3O_4 for the future study since high intensity LEDs have become prominent light sources for scientific research [19–21].

Conflict of Interests

The authors declare that there is no conflict of interests regarding the publication of this paper.

Acknowledgments

The authors thank the National Science Council, Taiwan, for sponsoring this research under Project no. NSC: 102-2313-B-020-004. They also thank the Office of International Affairs, National Pingtung University of Science and Technology, Taiwan, for part of the financial support. The advice on the experiment provided by The Faculty of Engineering, Thammasat University, Thailand, is also appreciated.

References

[1] V. S. Blazer, "Bacterial fish pathogens," *Environmental Biology of Fishes*, vol. 21, no. 1, pp. 77–79, 1988.

[2] L. Novotny, L. Dvorska, A. Lorencova, V. Beran, and I. Pavlik, "Fish: a potential source of bacterial pathogens for human beings," *Veterinarni Medicina*, vol. 49, no. 9, pp. 343–358, 2004.

[3] Z. Zhang and J. Gamage, "Applications of photocatalytic disinfection," *International Journal of Photoenergy*, vol. 2010, Article ID 764870, 11 pages, 2010.

[4] K. S. Yao, T. C. Cheng, S. J. Li et al., "Comparison of photocatalytic activities of various dye-modified TiO_2 thin films under visible light," *Surface and Coatings Technology*, vol. 203, no. 5–7, pp. 922–924, 2008.

[5] W. Choi, A. Termin, and M. R. Hoffmann, "The role of metal ion dopants in quantum-sized TiO_2: correlation between photoreactivity and charge carrier recombination dynamics," *Journal of Physical Chemistry*, vol. 98, no. 51, pp. 13669–13679, 1994.

[6] M. Maeda and T. Yamada, "Photocatalytic activity of metal-doped titanium oxide films prepared by sol-gel process," *Journal of Physics: Conference Series*, vol. 61, no. 1, article 151, pp. 755–759, 2007.

[7] Q. L. Feng, J. Wu, G. Q. Chen, F. Z. Cui, T. N. Kim, and J. O. Kim, "A mechanistic study of the anti-bacterial effect of silver ions on *Escherichia coli* and *Staphylococcus aureus*," *Journal of Biomedical Materials Research*, vol. 52, pp. 662–668, 2000.

[8] W. Wu, Q. He, and C. Jiang, "Magnetic iron oxide nanoparticles: synthesis and surface functionalization strategies," *Nanoscale Research Letter*, vol. 3, no. 11, pp. 397–415, 2008.

[9] B. Tural, N. Özkan, and M. Volkan, "Preparation and characterization of polymer coated superparamagnetic magnetite nanoparticle agglomerates," *Journal of Physics and Chemistry of Solids*, vol. 70, no. 5, pp. 860–866, 2009.

[10] Q. He, Z. Zhang, J. Xiong, Y. Xiong, and H. Xiao, "A novel biomaterial—Fe_3O_4:TiO_2 core-shell nano particle with magnetic performance and high visible light photocatalytic activity," *Optical Materials*, vol. 31, no. 2, pp. 380–384, 2008.

[11] T. C. Cheng, K. S. Yao, N. Yeh et al., "Bactericidal effect of blue LED light irradiated TiO_2/Fe_3O_4 particles on fish pathogen in seawater," *Thin Solid Films*, vol. 519, no. 15, pp. 5002–5006, 2011.

[12] S. A. Amin, M. Pazouki, and A. Hosseinnia, "Synthesis of TiO_2-Ag nanocomposite with sol-gel method and investigation of its antibacterial activity against *E. coli*," *Powder Technology*, vol. 196, no. 3, pp. 241–245, 2009.

[13] K. Loganathan, P. Bommusamy, P. Muthaiahpillai, and M. Velayutham, "The syntheses, characterizations, and photocatalytic activities of silver, platinum, and gold doped TiO_2 nanoparticles," *Environmental Engineering Research*, vol. 16, no. 2, pp. 81–90, 2011.

[14] E. Kanchanatip, N. Grisdanurak, R. Thongruang, and A. Neramittagapong, "Degradation of paraquat under visible light over fullerene modified V-TiO_2 ," *Reaction Kinetics, Mechanisms and Catalysis*, vol. 103, no. 1, pp. 227–237, 2011.

[15] I. M. Arabatzis, T. Stergiopoulos, M. C. Bernard, D. Labou, S. G. Neophytides, and P. Falaras, "Silver-modified titanium dioxide thin films for efficient photodegradation of methyl orange," *Applied Catalysis B: Environmental*, vol. 42, no. 2, pp. 187–201, 2003.

[16] P. Prieto, V. Nistor, K. Nouneh, M. Oyama, M. Abd-Lefdil, and R. Díaz, "XPS study of silver, nickel and bimetallic silver-nickel nanoparticles prepared by seed-mediated growth," *Applied Surface Science*, vol. 258, no. 22, pp. 8807–8813, 2012.

[17] Z. Teng, X. Su, G. Chen et al., "Superparamagnetic high-magnetization composite microspheres with Fe_3O_4@SiO_2 core and highly crystallized mesoporous TiO_2 shell," *Colloids and Surfaces A: Physicochemical and Engineering Aspects*, vol. 402, pp. 60–65, 2012.

[18] Q. Li, S. Mahendra, D. Y. Lyon et al., "Antimicrobial nanomaterials for water disinfection and microbial control: potential applications and implications," *Water Research*, vol. 42, no. 18, pp. 4591–4602, 2008.

[19] N. Yeh and J.-P. Chung, "High-brightness LEDs-Energy efficient lighting sources and their potential in indoor plant cultivation," *Renewable and Sustainable Energy Reviews*, vol. 13, no. 8, pp. 2175–2180, 2009.

[20] N. G. Yeh, C.-H. Wu, and T. C. Cheng, "Light-emitting diodes—their potential in biomedical applications," *Renewable and Sustainable Energy Reviews*, vol. 14, no. 8, pp. 2161–2166, 2010.

[21] N. Yeh, P. Yeh, N. Shih, O. Byadgi, and T. C. Cheng, "Applications of light-emitting diodes in researches conducted in aquatic environment," *Renewable and Sustainable Energy Reviews*, vol. 32, pp. 611–618, 2014.

Hindawi Publishing Corporation
International Journal of Photoenergy
Volume 2014, Article ID 602692, 8 pages
http://dx.doi.org/10.1155/2014/602692

Research Article

TiO_2 Nanotube Arrays Composite Film as Photoanode for High-Efficiency Dye-Sensitized Solar Cell

Jinghua Hu,[1,2,3] Li Zhao,[1,2] Yingping Yang,[3] Hong Liao,[3] Shimin Wang,[1,2] Xiaodong Sun,[3] Jiejie Cheng,[3] and Binghai Dong[1,2]

[1] *Hubei Collaborative Innovation Center for Advanced Organic Chemical Materials, Wuhan 430062, China*
[2] *Ministry of Education Key Laboratory for the Green Preparation and Application of Functional Materials, Faculty of Materials Science and Engineering, Hubei University, Wuhan 430062, China*
[3] *School of Science, Wuhan University of Technology, Wuhan 430070, China*

Correspondence should be addressed to Li Zhao; zhaoli7376@163.com, Yingping Yang; y.p.yang@126.com and Shimin Wang; shiminwang@126.com

Received 7 April 2014; Revised 9 May 2014; Accepted 12 May 2014; Published 25 May 2014

Academic Editor: Wei Xiao

A double-layered photoanode made of hierarchical TiO_2 nanotube arrays (TNT-arrays) as the overlayer and commercial-grade TiO_2 nanoparticles (P25) as the underlayer is designed for dye-sensitized solar cells (DSSCs). Crystallized free-standing TNT-arrays films are prepared by two-step anodization process. For photovoltaic applications, DSSCs based on double-layered photoanodes produce a remarkably enhanced power conversion efficiency (PCE) of up to 6.32% compared with the DSSCs solely composed of TNT-arrays (5.18%) or nanoparticles (3.65%) with a similar thickness (24 μm) at a constant irradiation of 100 mW cm^{-2}. This is mainly attributed to the fast charge transport paths and superior light-scattering ability of TNT-arrays overlayer and good electronic contact with F-doped tin oxide (FTO) glass provided from P25 nanoparticles as a bonding layer.

1. Introduction

Currently, dye-sensitized solar cells (DSSCs) have attracted considerable attention as a potential alternative to conventional silicon-related solar cells owing to the high efficiency and low cost since 1991 [1]. Their overall conversion efficiencies have reached 11.2%, which was still low as compared to that of 13–25% usually reparted in the silicon-based solar cells [2]. Nanocrystalline TiO_2 photoelectrode, as one of the major components of DSSCs, is critical for the photovoltaic performance. It is well known that the DSSCs efficiency is strongly dependent on a dynamic competition between the electron transportation in TiO_2 and the interfacial charge recombination. So much effort has been made up to now on the photoanode to facilitate electron transport and retard electron recombination.

To satisfy these requirements, one-dimensional (1D) TiO_2 materials, such as nanowire [3], nanorods [4], nanofiber [5], and nanotube [6], have been successively synthesized and applied on the DSSCs. From all morphological forms of titanium dioxide for solar energy conversion, TiO_2 nanotube arrays (TNT-arrays) appear highly ordered and vertically aligned, offering electron transport properties comparable to nanoparticles. It not only exhibits few grain boundaries but also provides direct pathways for electron transportation, leading to the suppressed electron-hole recombination [7]. TNT-arrays have been fabricated by using various methods, such as sol-gel [8, 9], hydrothermal [10, 11] and chemical vapor deposition [12], and electrochemical anodization [13–16]. Electrochemical anodization has been recognized as more convenient and simpler approach to produce integrative vertically and highly ordered TNT-arrays with controllable structural morphologies [17]. However, the performance of DSSCs based TNT-arrays on Ti substrate is restricted due to the presence of opaque Ti substrate. TNT-arrays/Ti-based DSSCs required back-side illumination [18, 19] which is not an optimal approach for increasing the power conversion efficiency. Hence, the fabrication of TNT-arrays on a transparent conductive substrate for front-side illuminated DSSCs is desired and will be expected to improve photovoltaic

performance [20]. Transparent TNT-arrays/FTO glass was prepared via an anodic oxidation of titanium thin film that was sputtered onto FTO conductive glass [21], which involves the sputtering of Ti films onto FTO glass, thus leading to a high fabrication cost. Hyeoká Park and GuáKang transferred and adhered TNT-arrays onto the FTO glass using Ti isopropoxide solution as a paste [22]; however, the TNT-arrays/FTO has a very small area (0.03–0.15 cm^2) owing to the structural destruction during one step annealing. Hence, a simple process of fabricating large-scale TNT-arrays film on FTO glass is very desirable.

Herein, we fabricated a novel double-layered TiO_2 photoanode consisting of hierarchical TNT-arrays and TiO_2 nanoparticle on a FTO glass substrate. Specially, the overlayer consisting of TNT-arrays plays a dual role for both stronger light-scattering capability and fast electron transport paths, and the underlayer made of TiO_2 nanoparticles serves as a bonding layer, which offers good contact between TNT-arrays and FTO glass. As a result, the photoelectronic conversion efficiency (PCE) of 6.32% was achieved in double-layered composite film. The performance improvement is almost attributed to the stronger light-scattering capability and fast electron paths of TNT-arrays films, resulting in decreased recombination of the electron-hole. Meanwhile, it is related to the good electronic contact between TiO_2 film and the F-doped tin oxide (FTO) glass.

2. Experiment

2.1. Preparation of the TNT-Arrays/Ti Foils Substrate. TNT-arrays films were prepared by anodization of Ti foils (99.7%, 0.25 um, Aldrich) in an NH_4F/ethylene glycol electrolyte solution by using a DC power source (PPS-1206, Motech) at room temperature, while a Pt foil was used as the counter electrode. The Ti foils were first physically polished, then degreased by sonication in acetone, ethanol, and DI water. Anodization was carried out in an ethylene glycol based on electrolyte containing NH_4F (0.5 wt%) and deionized water (2 vol%) under a constant voltage of 40 V. After the anodic oxidation, the Ti foil with the TNT-arrays grown on one side of its surfaces was thoroughly washed with a large amount of DI water and ethanol.

2.2. Preparation of the P25/TNT-Arrays/FTO Glass Photoanode. In order to achieve free-standing TNT-arrays films, the grown TNT-arrays were detached from the metallic Ti substrate as described in the following. The as-anodized TNT-arrays films were annealed at 450°C for 30 min to crystallize and then reanodized in the same electrolyte at corresponding potential for 3 h to form an amorphous TiO_2 layer between the crystallized TNT-arrays and the Ti foil. Finally, the resulting film was soaked in an H_2O_2 solution (35.5 wt%). A free-standing TiO_2 nanotube layer was obtained, as it can be easily handled with tweezers. TiO_2 nanoparticle viscous paste was spin-coated onto FTO glass substrates, and the free-standing TNT-arrays membranes were transferred onto the paste layers immediately. After being dried in air, the films were sintered at 450°C for 30 min.

2.3. Preparation of the TNT-Arrays/FTO Glass Photoanode. The as-prepared TNT-arrays were transferred onto FTO glass and two drops of 0.1 M Ti-isopropoxide were subsequently added to the TiO_2 nanotube films to form interconnections between the TNT-arrays and the FTO glass. In this work, three kinds of different TiO_2 films (TNT-arrays film, P25 nanoparticle film, and P25/TNT-arrays double-layered composite film) as photoelectrodes were fabricated and their photovoltaic conversion performances were investigated and compared.

2.4. Fabrication Dye-Sensitized Solar Cells. Three kinds of different TiO_2 films were immersed into a 0.3 mM solution of N719 in anhydrous ethanol and kept at room temperature for 24 h. The sensitized electrodes were further sandwiched with the sputtered-Pt FTO glass, separated by a 40 um thick hotmelt spacer. The intervening space was filled with an electrolyte made with 0.3 M LiI, 0.05 M I_2, 0.6 M 1-propyl-3-methylimidazolium iodide, and 0.5 M *tert*-butylpyridine in dry acetonitrile, and the assembled cell was tested immediately. The photographs of the TNT-arrays films at the different stages of the fabrication process are shown in Figure 1.

2.5. Characterization and Measurement. The morphologies of the obtained free-standing TNT-arrays films were characterized using a S-4800 field emission SEM (FESEM, Hitachi, Japan). X-ray diffraction (XRD) patterns were obtained using a D/MAX-IIIC X-ray diffractometer (Akishima-shi, Tokyo, Japan). UV-Vis absorbed spectra of different films were measured by a UV-visible spectrometer (UV2550, Shimadzu, Japan). In order to estimate the dye adsorbed amount on the three kinds of TiO_2 photoelectrodes, we immersed, respectively, the sensitized electrodes into a 0.1 M NaOH solution in a mixed solvent (water : ethanol = 1 : 1, in volume fraction), and afterwards the absorption spectra of the solutions were obtained and the concentration of adsorbed dye was evaluated spectrophotometrically.

The photocurrent-voltage characteristics (J-V curves) of the DSSCs were performed under AM 1.5 G solar simulator (Oriel Sol3A, Newport Corporation, Irvine, CA, USA) at a light intensity of 100 mW cm^{-2}. The electrochemical impedance spectroscopy (EIS) measurements of all the DSSCs were recorded using electrochemical workstation (IM6, Germany) under 100 mW cm^{-2} light illumination condition. The frequency range was explored from 0.1 Hz to 100 kHz, and the applied bias voltage and ac amplitude were set at open-circuit voltage of the DSSCs and 10 mV, respectively.

3. Results and Discussion

3.1. Phase Structures and Morphology. It is well known that the phase structure and crystallinity of TiO_2 are of great influence on its photoelectrochemical properties. Therefore, XRD was used to characterize the changes of phase structures of the prepared TNT-arrays before and after annealing. Figure 2 shows XRD patterns of as-annealed TNT-arrays and annealed TNT-arrays on Ti foil at 450°C, respectively. No peaks were shown in Figure 2(a) because the as-annealed

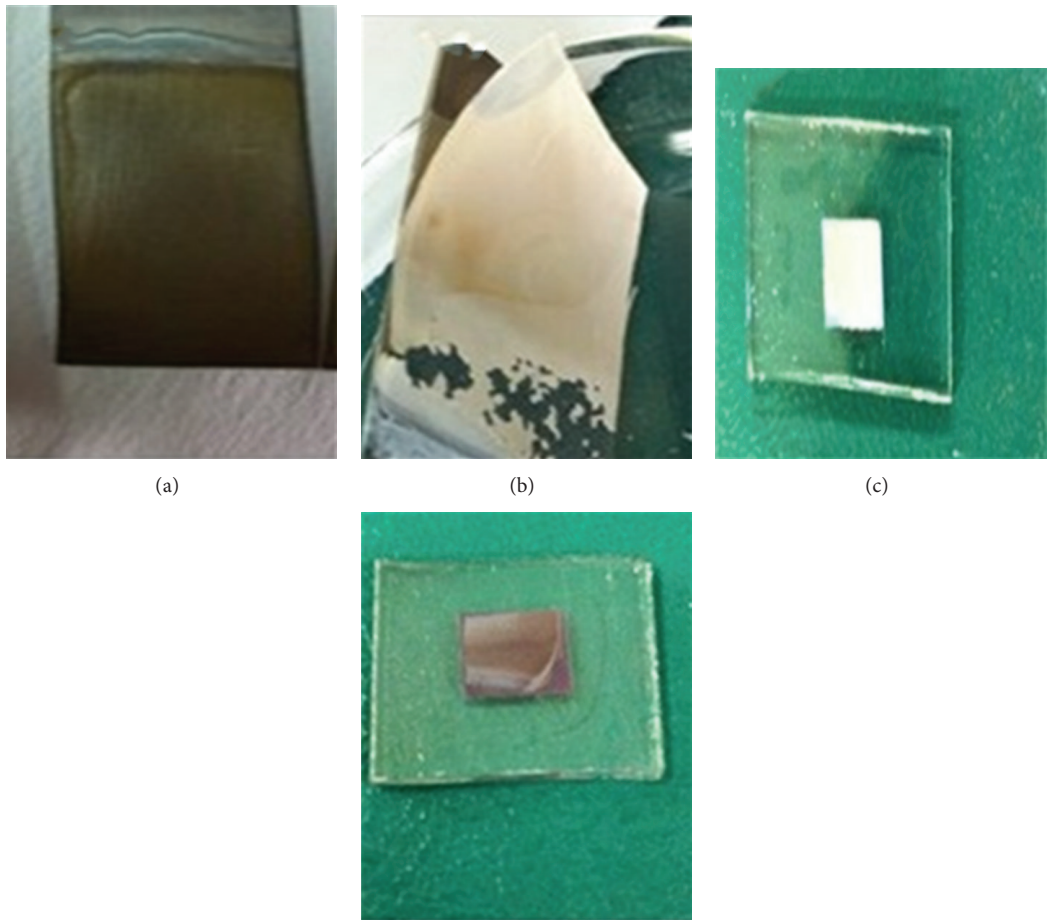

Figure 1: Photographs of TNT-arrays at different fabrication stages: TNT-arrays on the Ti substrate via anodization method (a), TNT-arrays membrane detached from the Ti substrate via a secondary anodization method (b), crystalline TNT-arrays/FTO film after heat treatment before dye loading (c), and N719 dye loaded TNT-arrays/FTO film (d).

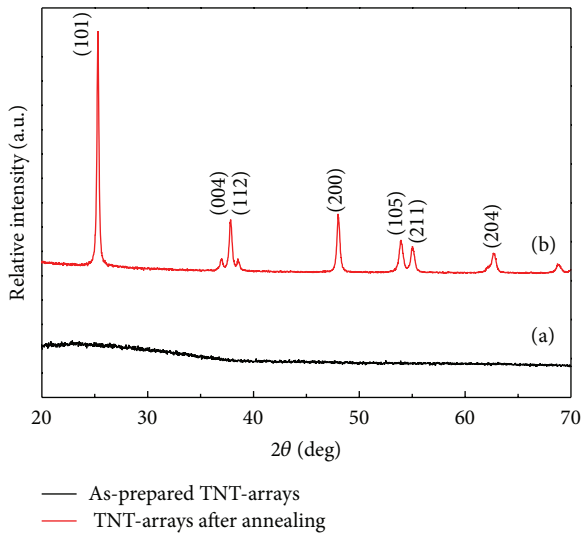

Figure 2: XRD patterns of as-prepared TNT-arrays (a) and TNT-arrays after annealing process at 450°C for 30 min (b).

TNT-arrays have an amorphous structure. However, after annealing process at 450°C for 30 min (as shown in Figure 2(b)), all the diffraction peaks are indexed to the anatase phase of TiO_2, which is consistent with the pure anatase phase of TiO_2 (space group: $I4_1/amd$ (141); JPCDS No. 21-1272).

Figure 3 shows the typical SEM images of TNT-arrays in a top-view, bottom-view, and cross-sectional-view, respectively, which were prepared by anodization of titanium foils at 40 V for 12 h in an ethyl glycol based electrolyte containing NH_4F (0.5 wt%) and deionized water (2 vol%) solution. It can be seen that the closely packed highly ordered nanotube arrays were obtained, which have an average pore diameter of around 120 nm and wall thickness of ca. 20 nm. Figures 3(a) and 3(b) show that the nanotubes opened on the top but closed on the bottom. Figure 3(c) exhibits a cross-sectional SEM image of the TNT-arrays, indicating that the TNT-arrays contain well-aligned nanotubes about 10.7 μm in length which grow vertically from a Ti substrate.

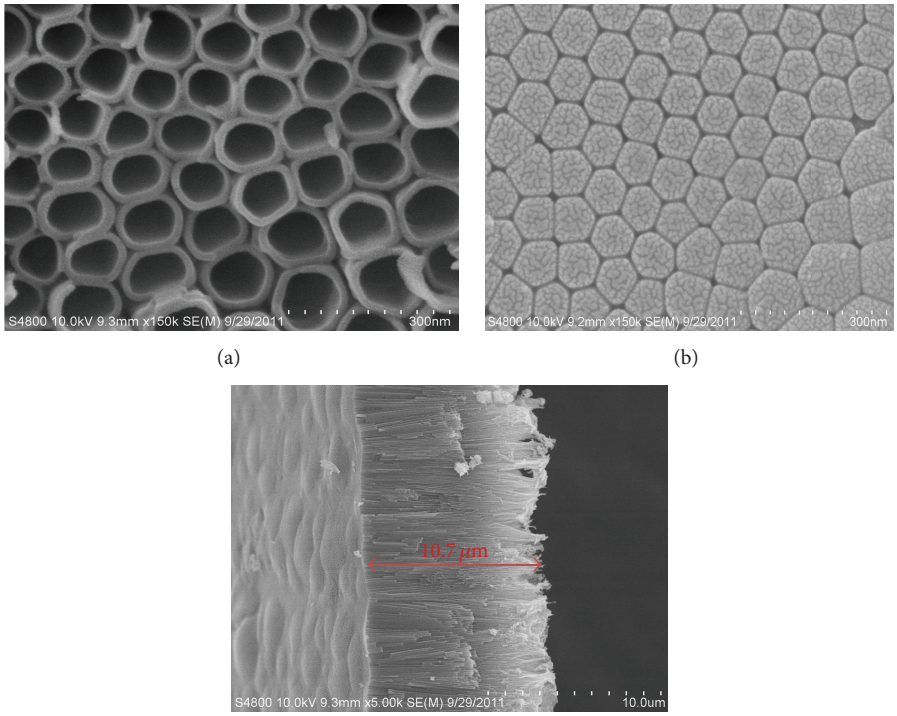

(a) (b)

(c)

Figure 3: SEM images of TNT-arrays in top-view (a), in bottom-view (b), and in cross-sectional-view (c).

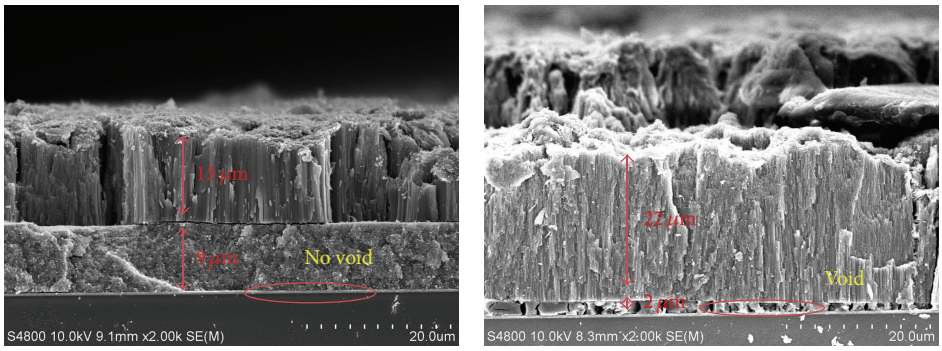

(a) (b)

Figure 4: SEM images of cross-section of double-layer composite film (a) and TNT-arrays film (b).

The cross-sectional SEM images of double-layer film and TNT-arrays film were shown in Figures 4(a) and 4(b). As shown in Figure 4(a), one can clearly recognize the double-layer structure with a 15 μm thick TNT-arrays overlayer and a 9 μm thick TiO_2 nanoparticle underlayer. Compact P25 nanoparticle underlayer will enlarge contact area between the TiO_2 film and FTO glass; meanwhile, it may cut off the direct contact between I_3^- ions and FTO glass. Charge recombination at FTO/TiO_2 interfaces has been prevented and the bonding strength between TiO_2 film and FTO glass has been improved. However, some voids can be seen on the FTO surface in the TNT-arrays film. As shown in Figure 4(b), it cannot cover the FTO surface smoothly in comparison with double-layered film. Consequently, some of I_3^- ions can reach the FTO glass between the interfaces of TNT-arrays film and FTO glass. As a result, the electrons would be back transported from the TNT-arrays photoelectrode to the I_3^- ions.

3.2. UV-Visible Absorbed Spectra and Dye Adsorption Measurements. Figure 5 shows diffuse reflection spectra (DRS) for three photoanodes. The DRS reveals stronger scattering for the pure TNT-arrays films in comparison with that of P25 particle films in the visible and near-infrared region, suggesting better light-scattering capabilities for TNT-arrays films compared with P25 nanoparticles films. The light-scattering capability of the double-layered films is placed in the middle.

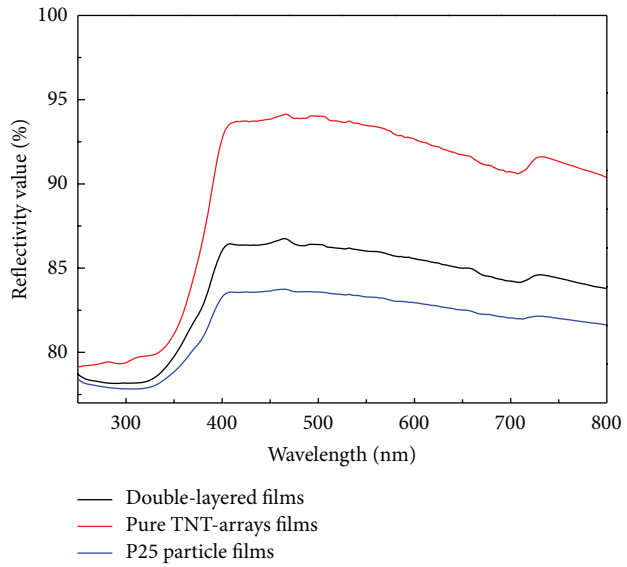

Figure 5: Diffused reflectance spectra of DSSCs based on a nanoparticle film, a TNT-arrays film, and a double-layered film with a similar thickness.

This is because the double-layered film is made of the two different morphological forms of titanium dioxide. The highest light-scattering capability of TNT-arrays is almost attributed to its homogeneous, highly ordered electronic transport paths, in which the incident light can reflect repeatedly to prolong effectively the optical transfer length of photoanode, resulting in enhanced light harvesting efficiency.

The dye adsorption amount in these films is displayed in Table 1. Obviously, the adsorbed amount of dye in double-layered films (4.43×10^{-8} mol cm^{-2}) is slightly higher compared with TNT-arrays (3.54×10^{-8} mol cm^{-2}) or P25 films (3.75×10^{-8} mol cm^{-2}). This is largely attributed to the presence of lots of interfaces between TNT-arrays and particle films in double-layered films, which facilitates the absorption of more amounts of dye molecules in the double-layered films. Meanwhile, it can be seen that both TNT-arrays films and P25 films have almost the same dye adsorption amount. This is because the surface area of TNT-arrays films is the same as that of P25 particle films.

3.3. Photovoltaic Performances of DSSCs. Figure 6(a) shows the dark current-voltage characteristics of DSSCs for three kinds of photoanodes. It is noted that the pure TNT-arrays photoelectrode produces the highest dark current, while the double-layered and P25 photoanode produces the lowest dark current at the same potential of about 0.55 V. These observations reflect a higher recombination at the pure TNT-arrays films than the double-layered films and P25 films. The dark current measurement indicated that the double-layered photoanode had a slower photoelectrons recombination rate, which is more contributed to the photoelectronic performance of DSSCs.

Under illumination, the typical photocurrent density-photovoltage (J-V) curves of the cells made from three kinds of photoanode are shown in Figure 6(b). The detailed photovoltaic parameters are summarized in Table 1. As shown in Table 1, DSSCs based on double-layered film attained a short-circuit current density (J_{sc}) of 15.88 mA cm^{-2} and an open-circuit voltage (V_{oc}) of 0.65 V, leading to a higher PCE of 6.32%. Meanwhile, DSSCs based on pure TNT-arrays film only got a short-circuit current density (J_{sc}) of 12.78 mA cm^{-2}, an open-circuit voltage (V_{oc}) of 0.67 V, and thus a PCE of 5.18%. And then DSSCs based on P25 nanoparticle film only got a short-circuit current density (J_{sc}) of 10.66 mA cm^{-2}, an open-circuit voltage (V_{oc}) of 0.60 V, and thus a lower PCE of 3.65%. Evidently, the PCE of DSSCs based double-layered composite photoanode is 42.4% higher than that of TNT-arrays photoanode, and it is also 49% higher than that of P25 nanoparticle photoelectrode. As a result, the remarkable enhancement of PCE for double-layered photoanode compared to the others is mainly attributed to the improvement of the J_{sc}. The enhanced J_{sc} of the former can be attributed to the lower electronic recombination rate from P25 nanoparticle underlayer and fast electronic transport paths provided by TNT-arrays overlayer. More detailed explanations for the enhancement of η for double-layer TiO_2 photoelectrode will be discussed later.

Table 1: Comparisons of the photovoltaic performances and adsorbed dye amount of DSSCs made from P25 nanoparticle film, TNT-arrays films, and double-layer composite film. All measurements were performed under AM 1.5 one-sun light intensity of mW cm^{-2}, and the thickness of all the films was controlled to be similar (ca. 24 μm).

Photoanode	J_{sc} (mA cm^{-2})	V_{oc} (V)	FF	η (%)	Adsorbed dye amount ($\times 10^{-8}$ mol cm^{-2})
P25 particle	10.66	0.60	0.64	3.65	3.75
TNT-arrays	12.78	0.67	0.52	5.18	3.54
Double-layer	15.88	0.65	0.61	6.32	4.43

3.4. EIS Analyses. The electrochemical impedance spectroscopy (EIS) analysis of DSSCs fabricated with the three different TiO_2 photoanodes noted above was performed to elucidate the characteristics of electron transport in the DSSCs. The EIS measurements were carried out at the frequency range of 10^{-1}–10^5 Hz at V_{oc} under one-sun illumination to determine impedance of solar cells. The Nyquist plots and the equivalent circuit diagram are shown in Figure 7(a) and in the inset of Figure 7(a). According to the EIS model for TiO_2 reported in our previous work [23], the Nyquist plots exhibit a large semicircle at low frequencies and a small one at high frequencies. The smaller semicircle in the high frequency represents the redox charge transfer at the counter electrode and the larger semicircle in the low frequency denotes the electron transfer at the TiO_2-dye-electrolyte interface, which were fitted as R_{ct} and R_w using Z-view software, whereas R_s represents the sheet resistance of FTO and the contact resistance between the FTO and TiO_2 film. The R_s, R_{ct}, and R_w data are collected in Table 2. Obviously, the TNT-arrays films show

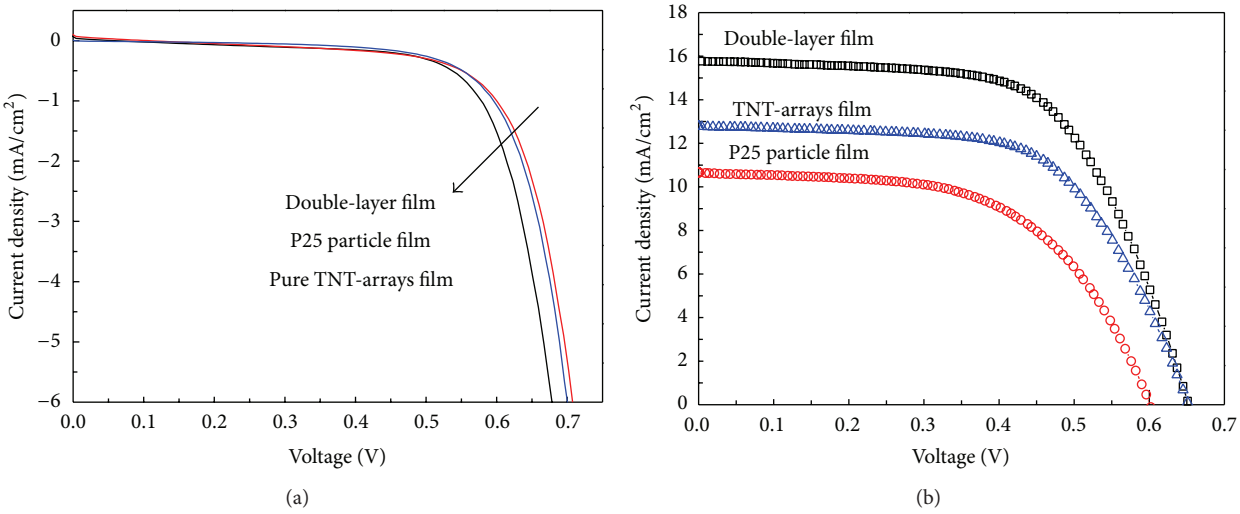

FIGURE 6: *I-V* performance of the DSSCs based on P25 nanoparticle film, TNT-arrays films, and double-layer composite film in the dark (a) and under AM 1.5 illuminations (b).

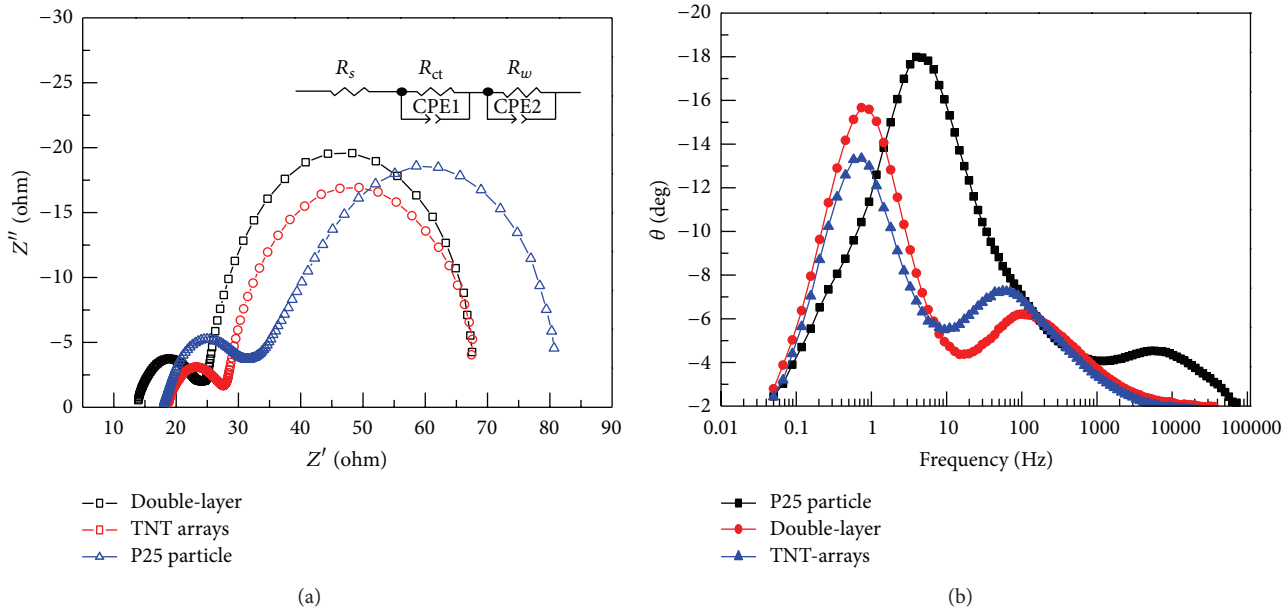

FIGURE 7: EIS spectra of DSSCs based on double-layer composite film, TNT-arrays film, and P25 nanoparticle film. (a) Nyquist plots and (b) Bode phase plots.

the lowest values for R_{ct} and R_w resistance among three cells, suggesting that more efficient charge-transfer process at the Pt counter electrode/redox electrolyte interface and the dye-coated TNT-arrays/electrolyte interface occurs. However, the TNT-arrays films also display the poor contact between TNT-arrays films and FTO conducting glass due to the highest value of R_s resistance. Therefore, the double-layered films possess the lowest value of R_s and slightly lower values for R_{ct} and R_w resistance, resulting in the optimal conversion efficiency among the three cells, which corresponds well with the aforementioned *J-V* characterization data. The Bode phase plots (Figure 7(b)) of EIS spectra display the frequency peaks of the charge-transfer process at different interfaces for three kinds of cells. The electron lifetime (τ_e) in DSSCs can be calculated from the maximum frequency of the low-frequency peak (f_{max}) value following the equation $\tau_e = 1/2\pi f_{max}$ [24]. As is shown in Table 2, both TNT-arrays films and the double-layered films indicate the relatively longer electron lifetime compared to P25 nanoparticle films. Hence the decrease in the transport resistance and increase in electronic lifetime are observed in the double-layered films. Especially, it is worth noting that the value for the R_s is almost a critical role for PCE for solar cells, which means that better electronic contact between TiO_2 film and FTO conducting glass is very important for DSSCs, leading to the enhancement of power conversion efficiency.

Table 2: Parameters obtained by fitting the impedance spectra of DSSCs using the equivalent circuit in Figure 6.

Sample	R_s (Ω)	R_{ct} (Ω)	R_w (Ω)	τ (ms)
P25 particle	17.84	15.84	59.86	42.2
TNT-arrays	18.33	10.21	43.38	60.1
Double-layer	12.33	12.38	46.42	59.5

4. Conclusions

In conclusion, we successfully fabricated a TiO_2 double-layer composite film consisting of hierarchical TNT-arrays as overlayer and P25 nanoparticles as underlayer for applications as improved dye-sensitized solar cells. The XRD patterns of the double-layered films are indexed to the excellent anatase phase of TiO_2. The microscopy technique confirms the TNT-arrays structure is highly ordered and vertically aligned on the substrate, which offers effective transport paths for electron. DSSCs based on the double-layered films exhibit 6.32% power conversion efficiency (PCE), which is 73% higher than that of P25 nanoparticle films (3.65%) and 22% higher than that of TNT-arrays films (5.18%) under similar film thickness (ca. 24 μm) at a constant irradiation of 100 mW cm^{-2}. The enhanced PCE of DSSCs based double-layered films is attributed to the good contact with FTO, fast electron transport, superior light-scattering ability and slower charge recombination. Thus, the double-layered films applied in DSSCs open up a new route to fabricate the low-cost, environmentally safe, and improved solar-to-electric efficiency.

Conflict of Interests

The authors declare that there is no conflict of interests regarding the publication of this paper.

Acknowledgments

This work was supported by the NSFC (51102087, 11172221, and 11205066) and the Fundamental Research Funds for the Central Universities (WUT: 2014-Ia-028). This work was also financially supported by the Ph.D. Programs Foundation of Ministry of Education of China (20114208110004) and Wuhan Science and Technology Bureau of Hubei Province of China (201051730551 and 2013010501010143).

References

[1] B. O. 'Regan and M. Grazel, "A low-cost, high-efficiency solar cell based on dye-sensitized colloidal TiO_2 films," *Nature*, vol. 353, pp. 737–740, 1991.

[2] A. Yella, H. W. Lee, H. N. Tsao et al., "Porphyrin-sensitized solar cells with cobalt (II/III)-based redox electrolyte exceed 12 percent efficiency," *Science*, vol. 334, no. 6056, pp. 629–634, 2011.

[3] X. Feng, K. Shankar, O. K. Varghese, M. Paulose, T. J. Latempa, and C. A. Grimes, "Vertically aligned single crystal TiO_2 nanowire arrays grown directly on transparent conducting oxide coated glass: synthesis details and applications," *Nano Letters*, vol. 8, no. 11, pp. 3781–3786, 2008.

[4] H. S. Kim, Y. J. Kim, W. Lee, and S. H. Kang, "One-pot synthesis of peacock-shaped TiO_2 light scattering layer with TiO_2 nanorods film for dye-sensitized solar cells," *Applied Surface Science*, vol. 273, pp. 226–232, 2013.

[5] A. S. Nair, R. Jose, Y. Shengyuan, and S. Ramakrishna, "A simple recipe for an efficient TiO_2 nanofiber-based dye-sensitized solar cell," *Journal of Colloid and Interface Science*, vol. 353, no. 1, pp. 39–45, 2011.

[6] K. Zhu, N. R. Neale, A. Miedaner, and A. J. Frank, "Enhanced charge-collection efficiencies and light scattering in dye-sensitized solar cells using oriented TiO_2 nanotubes arrays," *Nano Letters*, vol. 7, no. 1, pp. 69–74, 2007.

[7] S. P. Albu, A. Ghicov, J. M. Macak, R. Hahn, and P. Schmuki, "Self-organized, free-standing TiO_2 nanotube membrane for flow-through photocatalytic applications," *Nano Letters*, vol. 7, no. 5, pp. 1286–1289, 2007.

[8] T. Maiyalagan, B. Viswanathan, and U. V. Varadaraju, "Fabrication and characterization of uniform TiO_2 nanotube arrays by sol-gel template method," *Bulletin of Materials Science*, vol. 29, no. 7, pp. 705–708, 2006.

[9] T. S. Kang, A. P. Smith, B. E. Taylor, and M. F. Durstock, "Fabrication of highly-ordered TiO_2 nanotube arrays and their use in dye-sensitized solar cells," *Nano Letters*, vol. 9, no. 2, pp. 601–606, 2009.

[10] K. P. Yu, W. Y. Yu, M. C. Kuo, Y. C. Liou, and S. H. Chien, "Pt/titania-nanotube: a potential catalyst for CO_2 adsorption and hydrogenation," *Applied Catalysis B: Environmental*, vol. 84, no. 1-2, pp. 112–118, 2008.

[11] S. Sreekantan and L. C. Wei, "Study on the formation and photocatalytic activity of titanate nanotubes synthesized via hydrothermal method," *Journal of Alloys and Compounds*, vol. 490, no. 1-2, pp. 436–442, 2010.

[12] C. T. Hsieh, M. H. Lai, and C. Pan, "Synthesis and visible-light-derived photocatalysis of titania nanosphere stacking layers prepared by chemical vapor deposition," *Journal of Chemical Technology and Biotechnology*, vol. 85, no. 8, pp. 1168–1174, 2010.

[13] D. Gong, C. A. Grimes, O. K. Varghese et al., "Titanium oxide nanotube arrays prepared by anodic oxidation," *Journal of Materials Research*, vol. 16, no. 12, pp. 3331–3334, 2001.

[14] J. M. Macak and P. Schmuki, "Anodic growth of self-organized anodic TiO_2 nanotubes in viscous electrolytes," *Electrochimica Acta*, vol. 52, no. 3, pp. 1258–1264, 2006.

[15] S. Sreekantan, R. Hazan, and Z. Lockman, "Photoactivity of anatase-rutile TiO_2 nanotubes formed by anodization method," *Thin Solid Films*, vol. 518, no. 1, pp. 16–21, 2009.

[16] A. El Ruby Mohamed and S. Rohani, "Synthesis of titania nanotube arrays by anodization," *AIDIC Conference Series*, vol. 9, pp. 121–129, 2009.

[17] A. El Ruby Mohamed and S. Rohani, "Modified TiO_2 nanotube arrays (TNTAs): progressive strategies towards visible light responsive photoanode, a review," *Energy and Environmental Science*, vol. 4, no. 4, pp. 1065–1086, 2011.

[18] D. Kuang, J. Brillet, P. Chen et al., "Application of highly ordered TiO_2 nanotube arrays in flexible dye-sensitized solar cells," *ACS Nano*, vol. 2, no. 6, pp. 1113–1116, 2008.

[19] C. J. Lin, W. Y. Yu, and S. H. Chien, "Rough conical-shaped TiO_2-nanotube arrays for flexible backilluminated dye-sensitized solar cells," *Applied Physics Letters*, vol. 93, Article ID 133107, 2008.

[20] P. T. Hsiao, Y. J. Liou, and H. Teng, "Electron transport patterns in TiO_2 nanotube arrays based dye-sensitized solar cells under frontside and backside illuminations," *Journal of Physical Chemistry C*, vol. 115, no. 30, pp. 15018–15024, 2011.

[21] G. K. Mor, K. Shankar, M. Paulose, O. K. Varghese, and C. A. Grimes, "Use of highly-ordered TiO_2 nanotube arrays in dye-sensitized solar cells," *Nano Letters*, vol. 6, no. 2, pp. 215–218, 2006.

[22] J. Hyeoká Park and M. GuáKang, "Employment information," *Chemical Communications*, vol. 25, no. 39, pp. 2867–2869, 2008.

[23] G. Dai, L. Zhao, S. Wang et al., "Double-layer composite film based on sponge-like TiO_2 and P25 as photoelectrode for enhanced efficiency in dye-sensitized solar cells," *Journal of Alloys and Compounds*, vol. 539, pp. 264–270, 2012.

[24] S. M. Park and J. S. Yoo, "Peer reviewed: electrochemical impedance spectroscopy for better electrochemical measurements," *Analytica Chemistry*, vol. 75, no. 21, pp. 455–461, 2003.

Hindawi Publishing Corporation
International Journal of Photoenergy
Volume 2014, Article ID 475825, 8 pages
http://dx.doi.org/10.1155/2014/475825

Research Article

Preparation, Characterization, and Biotoxicity of Nanosized Doped ZnO Photocatalyst

Lingling Liu, XiangRui Wang, Xiuping Yang, Wenhong Fan, Xiaolong Wang, Ning Wang, Xiaomin Li, and Feng Xue

Key Laboratory of Bio-Inspired Smart Interfacial Science and Technology of Ministry of Education, Department of Environmental Science and Engineering, School of Chemistry and Environment, Beihang University, Beijing 100191, China

Correspondence should be addressed to Wenhong Fan; fanwh@buaa.edu.cn

Received 4 April 2014; Accepted 29 April 2014; Published 22 May 2014

Academic Editor: Jiaguo Yu

Metal-doped nanosized ZnO (nZnO) photocatalyst has been widely used for its typical properties and has thus gained considerable attention. In this study, five types of nZnO (nondoped nZnO, iron- (Fe-) doped nZnO, cobalt- (Co-) doped nZnO, nickel- (Ni-) doped nZnO, and manganese- (Mn-) doped nZnO) materials were prepared through a wet chemical method and then exposed to *Daphnia magna* (*D. magna*) at low and high concentrations (50 and 250 $\mu g\,L^{-1}$). Results showed that the different metal-doped nZnOs had a variety of shapes and sizes and exhibited diverse dissolubility. After exposure tests, Zn accumulation, metallothionein (MT), and malondialdehyde (MDA) contents in *D. magna* under 250 $\mu g\,L^{-1}$ were significantly higher than those in the 50 $\mu g\,L^{-1}$ groups. Compared with nondoped nZnO, Co-doped and Ni-doped nZnO enhanced Zn accumulation in *D. magna* whereas Mn-doped nZnO reduced such accumulation. MT and MDA contents in metal-doped nZnO (except Ni-nZnO) treatments were lower than those in nondoped nZnO. Zn accumulation showed a negative relationship with dissolved Zn percentage, which can be explained by the swallowing of nZnO particles as an important pathway of *D. magna* ingestion. Sizes, dissolubility, and physiological functions of doping metals were the influencing factors on metal-doped nZnO biotoxicity to *D. magna*.

1. Introduction

ZnO is an excellent photocatalyst because of its high electrical conductivity and optical transmittance in the solar spectrum. Particularly in a nanometer scale, nanosized ZnO (nZnO) exhibits numerous novel characteristics, such as high ratio of surface area to volume, high electron conductivity, and transmission capability, which provides more opportunities for potential applications in the areas of paint industry, biomedicine, and environmental engineering [1, 2].

However, the photocatalytic activity of nZnO is highly dependent on its crystallite size, specific surface area, morphologies, and UV irradiation wavelengths [3, 4]. Numerous studies had proven that modified nZnOs with other elements improve photocatalytic properties. N-containing ZnO showed higher visible-light photocatalytic activity than pure ZnO [5]. ZnO-coated steel mesh has been repeatedly used for over 10 cycles without significant loss of catalyst mass [6]. The photocatalytic properties of the Co-doped ZnO had also been found to have improved significantly, and the degradation ratio of an organic dye (methyl orange) reached 78% when the doping concentration was 3% [7]. Mn-doped ZnO bleached methylene blue considerably faster than nondoped ZnO upon exposure to visible light [8].

Widespread use has caused these doped nZnO photocatalysts to enter the environment inevitably, thus resulting in intentional and unintentional exposures and giving rise to environmental and health risks [9]. Zn^{2+} ion dissolution, nanoscale size, and oxidative damage comprise the widely accepted potential mechanism of nZnO toxicity [10]. To the best of our knowledge, only the toxicity of Fe-doped nZnO was evaluated by Xia et al. [11], who revealed that Fe doping reduced nZnO dissolution, thus preventing its toxicity to animals and the environment. However, these findings are insufficient to facilitate understanding of the effect of doping on nZnO toxicity.

In this study, we synthesized five doped nZnO photocatalysts (nondoped, Fe-doped, Co-doped, Ni-doped, and Mn-doped) through a wet chemical method. The morphology and dissolubility of these photocatalysts in natural water were characterized. Zn accumulation, metallothionein, and lipid peroxidation contents of *Daphnia magna* (*D. magna*) in response to five nZnO exposures were quantified to evaluate the biotoxicity of nZnO photocatalysts. The influence and relationships of metal-doped nZnO, as well as the toxic effects to *D. magna*, were analyzed and discussed. These results facilitated understanding of the effects of element doping on nZnO photocatalyst toxicity.

2. Materials and Methods

2.1. Preparation of Doped nZnO Photocatalysts. The metal-doped nZnO (M-nZnO) powders were obtained by using a wet chemical method in aqueous solutions as reported previously [12]. First, zinc nitrate hexahydrate [$Zn(NO_3)_2{\cdot}6H_2O$] and hexamethylenetetramine ($C_6H_{12}N_4$) with a certain concentration of Fe (Co, Ni, and Mn) nitrate hexahydrate were separately dissolved in 100 mL of deionized water. The concentrations of each metal dopant were 5% in molarity. Subsequently, the mixture was placed into glass vials and heated at 95°C for several hours to grow metal-doped nZnO. Thereafter, the containers were taken out and cooled naturally to room temperature. The samples were rinsed thoroughly with deionized water and dried at 100°C for 2 h. Finally, metal-doped nZnO (Fe, Co, Ni, and Mn) powders were obtained. The nondoped nZnO samples were synthesized through the same process without adding other metals.

2.2. Characterization of nZnO Photocatalysts. The morphology of five types of nZnO (nondoped nZnO, Fe-nZnO, Co-nZnO, Ni-nZnO, and Mn-nZnO) particles in water was observed by using a JEOL transmission electron microscope (TEM) (JEOL, JEM-2100F), which was operated at 100 kV. The nZnO stocks were under ultrasonic treatment for better dispersion before making TEM samples. Several droplets of nZnO stock solution were injected into the Formvar-coated (Electron Microscopy Sciences, Fort Washington, PA, USA) copper grids using a capillary tube. After drying at room temperature, the samples were placed in the TEM for imaging.

The dissolubility of the five types of nZnO in natural water was investigated through dissolution tests. The nZnOs were dissolved in pH 8.5 natural water contained in 100 mL Erlenmeyer flasks. The concentration of nZnO was 100 $\mu g\,L^{-1}$. Three replicates were set up for each kind of nZnO. After rapid mixing, the flasks were placed on a shaker at 150 rpm. Then, a 10 mL aliquot was removed at 30, 60, 120, 180, and 240 min. These samples were centrifuged at 12 000 rpm for 10 min with a versatile compact centrifuge (Himac CF 16RX, Hitachi, Tokyo, Japan) to separate nZnO particles. The Zn^{2+} concentration in the supernatant was determined by using inductively coupled plasma mass spectrometry (ICP-MS) and then used to calculate the quantity of dissolved nZnO in the water. The water that was used in both the dissolubility and toxicity experiments was collected near Huo Qi Ying Bridge (116° 16′ 732 E, 39° 58′ 401 N).

2.3. Biotoxicity Test of Doped nZnO Photocatalysts

2.3.1. Toxicity Exposure of D. magna to nZnO Photocatalysts. The test organism was *D. magna*, an ecologically important freshwater zooplankton widely used in toxicity tests. NZnO stock suspension was prepared with natural water and dispersed evenly through ultrasonic treatment. NZnO concentrations of stocks were determined according to the metal concentrations of Zn, Fe, Co, Ni, and Mn in the suspension by utilizing inductively coupled plasma atomic emission spectrometry (ICP-AES). The suspension was then diluted with natural water, and two treatment concentrations (50 and 250 $\mu g\,L^{-1}$) of each nZnO were used in the experiments. The natural water sample without nZnO was used as the control. Two replicates were set up for each treatment, each containing 50 daphnids (1 individual/10 mL) aged 14 d to 21 d. The daphnids were not fed, and the water was not changed during exposure.

2.3.2. Determination of Toxic Effects in D. magna. After 48 h of exposure, living daphnids were collected from each treatment and treated similar to the treatment in our previous study [13]. Ten to fifteen daphnids were subsequently dried at 80°C to a constant weight and then digested in 68% nitric acid (HNO_3, Aristar grade) at 110°C. The digestion solution was used to determine Zn accumulation in *D. magna* by using ICP-MS. The remaining 15 to 20 daphnids were immediately weighed on a wet basis. The daphnid tissues were homogenized through ultrasonication in 0.5 mL of sucrose buffer (0.25 mol L^{-1} sucrose, 0.1 mol L^{-1} Tris-HCl, and pH 8.6) and then centrifuged at 12 000 ×g in a refrigerated centrifuge for 20 min. The supernatant was collected and diluted with a homogenate of 1.5 mL. The 0.5 mL of diluted supernatant fluid was mixed with Ag^+ solution for MT measurement according to the modified silver saturation method [14]. Thereafter, 0.2 mL of the aforementioned diluted supernatant fluid was used to measure MDA by using a spectrophotometer according to the manufacturer's instructions. MDA contents in *D. magna* were assayed using commercially available kits according to the manufacturer's protocol (Nanjing Jiancheng Bioengineering Institute, China). The analysis of MT and MDA contents was completed within 3 d after 48 h of exposure.

3. Results and Discussion

3.1. Characterization of Five nZnO Photocatalysts

3.1.1. Morphology of Five nZnO Photocatalysts. Images of nZnO dispersion in water were characterized by TEM, as shown in Figure 1. The Mn-nZnO was a rod with nano-sized diameter and microsized length. The remaining nZnO materials were particles. Fe-nZnO had the smallest particle size (approximately 20 nm) with a uniform shape. The sizes of Co-nZnO, Ni-nZnO, and nondoped nZnO were between

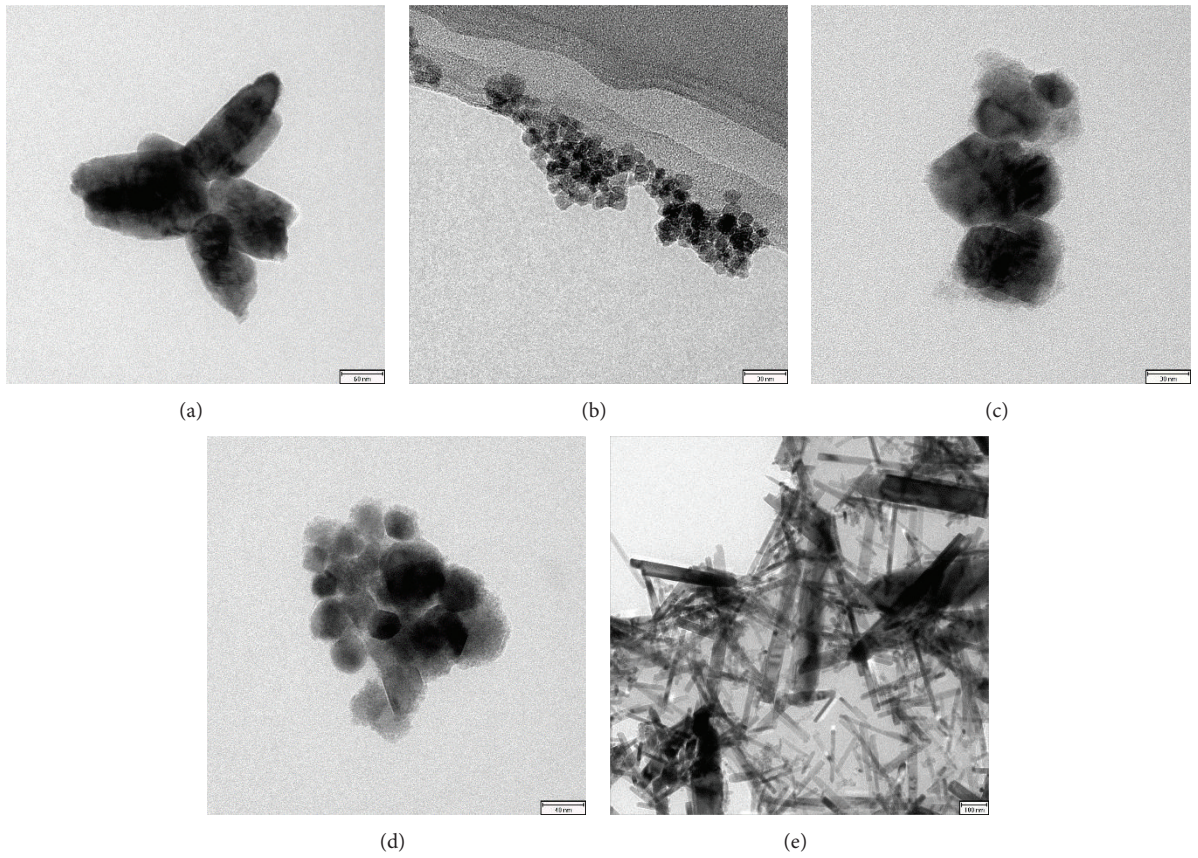

Figure 1: TEM images of different doped nZnO photocatalysts. (a) Nondoped nZnO, (b) Fe-nZnO, (c) Co-nZnO, (d) Ni-nZnO, and (e) Mn-nZnO.

40 and 100 nm. All the five types of nZnO materials tended to aggregate in water, especially for Mn-nZnO. The table of ionic radius showed that the radius of Zn^{2+} was 0.074 nm, that of Fe^{3+} was 0.0645 nm, that of Co^{2+} was 0.074 nm, that of Ni^{2+} was 0.072 nm, and that of Mn^{2+} was 0.08 nm. These results may explain why Fe-nZnO had the smallest particle size, whereas Mn-nZnO had the largest. Xia et al. [11] also proved that Fe doping can reduce nZnO size.

3.1.2. Dissolubility of Five nZnO Photocatalysts in Natural Water. Figure 2 shows the percentage content of dissolved Zn^{2+} in the supernatant of each natural water sample, which indicated that nZnO exhibited certain solubility in water. However, the dissolved Fe, Co, Ni, and Mn were not detected because their contents were under the detection limit of ICP-MS. When the nZnO concentration was 100 $\mu g\,L^{-1}$, the dissolved Zn^{2+} content of each sample was lower than 2% at 240 min. This solubility was considerably lower than that in Franklin's study, which determined the solubility of nZnO in natural water at 100 $mg\,L^{-1}$ in 72 h [15]. The solubility of nZnO might be influenced by nominal nZnO concentration and testing period. Moreover, the solubility of Mn-nZnO and Fe-nZnO was significantly higher than that of other nZnO. Nevertheless, the solubility of Ni-nZnO was similar to that of the nondoped nZnO. In addition, the solubility of Co-nZnO

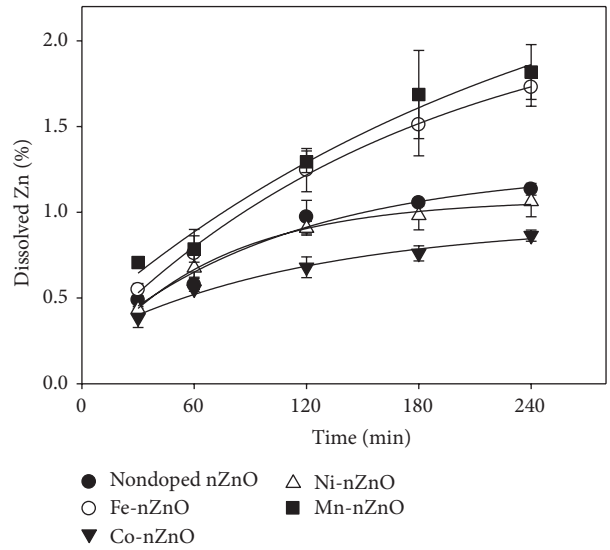

Figure 2: Dissolution of different doped nZnO photocatalysts in natural water. Mean ± standard deviation (n = 2).

was lower than 1%, which was the lowest among the five kinds of nZnO. These results indicate that different doped metals changed the solubility of nZnO. However, the solubility of Fe-doped nZnO from this study was different from that in the

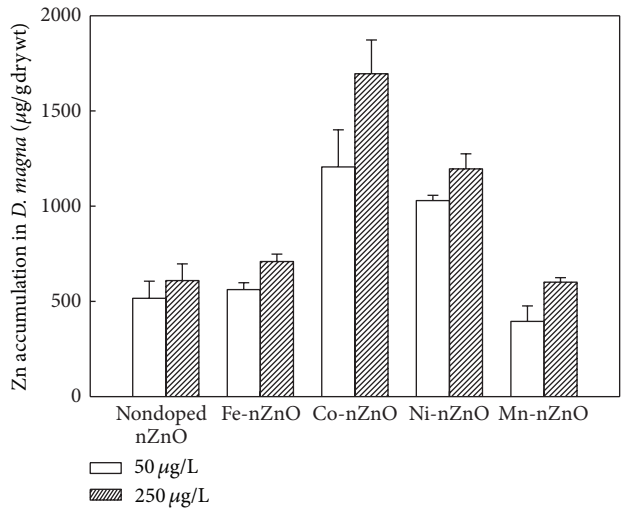

Figure 3: Zn accumulation in *D. magna* after exposure to different doped nZnO photocatalysts. Mean ± standard deviation ($n = 2$).

study of Xia et al. [11]. This condition might be attributed to the different synthesis nZnO methods. The synthesis method of Xia et al. was flame spray pyrolysis, whereas our method was a wet chemical method. Miao's study also indicated that several physicochemical factors have to be considered in nZnO dissolution behavior.

3.2. Biotoxicity of Five nZnO Photocatalysts to D. magna

3.2.1. Bioaccumulation of Zn in D. magna. Zn accumulation in *D. magna* after exposure to five different nZnO photocatalysts was measured, as shown in Figure 3. The high-concentration exposure groups of all types of nZnO had higher Zn accumulation than the low-concentration exposure groups. Zn accumulation was 156 μg/g dry wt in nonexposure *D. magna*, significantly lower than that in the nZnO exposure groups. No apparent difference was observed in the Zn accumulation in *D. magna* after exposure to nondoped nZnO, Fe-nZnO, and Mn-nZnO (400–700 μg/g dry wt). While exposed to Co-nZnO and Ni-nZnO, the Zn accumulation in *D. magna* was higher than 1,000 μg/g dry wt. *D. magna* is a filter feeding organism that can swallow a range of sizes of nanoparticle clusters [17]. Nano-ZnO, especially Mn-nZnO rods, tended to aggregate in water. Mn-nZnO, which had a larger size and poorer dispersion, more easily sank to the bottom of the container and was not conducive for *D. magna* to adsorb, which might be the reason why Mn-nZnO treatment exhibited the least accumulation in daphnids after 48 h of exposure. Zn accumulation in Co-doped exposure groups was significantly higher than that in the other groups because of the large intestinal particle aggregation, which was difficult to excrete (Figure 4(c)).

To explore the states of existence of nZnO in *D. magna*, intestinal slices of daphnids exposed to nZnO particles were observed by SEM (JSM-6380) with an EDAX-Genesis-2000 energy X-ray dispersive spectrometer. *D. magna* was prepared before dissection according to the method described by Tervonen et al. [18]. As shown in Figure 4, the existing particles at the root of the *D. magna* intestinal villi were observed. Energy dispersive X-ray spectroscopy (EDS) elemental analysis showed that these particles are the exposed ZnO nanoparticles. The doping elements Fe, Co, and Mn were identified in the corresponding intestinal slice samples. In the intestinal slice sample of Ni-nZnO treatment, Fe was detected instead of Ni because the proportion of Ni was low at the detected point and the Fe content was high in air and natural water.

3.2.2. Induction of Metallothioneins by Five nZnOs. MT is a cysteine-rich metal binding protein with low molecular weight, which can combine some essential trace metals, such as Zn and Cu, as well as nonessential toxic metals, such as Cd, Hg, and Ag in cells [19]. Therefore, MT regulates the intracellular metal concentration and protects cells from toxic effects. As a biomarker, the MT contents of *D. magna*, in response to nZnO exposure, are shown in Figure 5. MT inductions were between 30 and 40 μg/g wet wt in the low-concentration exposure groups and 40 and 50 μg/g wet wt in the high-concentration exposure groups. A minor difference was observed between the two concentration groups, which was similar to the results obtained by Wong et al. [20]. Comparing five different nZnOs, MT inductions caused by Ni-nZnO were slightly higher than those by nondoped nZnO exposure groups, whereas Fe-, Co-, and Mn-doped nZnO decreased such inductions in the daphnids to a small degree. Binding to the excess metal ions was usually believed to be a protection mechanism of MT during metal exposure. Low dissolubility of the five types of nZnO might be a reason for the lack of a significant difference in MT content.

3.2.3. MDA Levels in D. magna after Exposure to Five nZnOs. MDA is a product of lipid oxidation caused by reactive oxygen species (ROS) attacking unsaturated fatty acids (PUFA) in biofilms [21]. The amount of MDA reflected the body lipid peroxidation levels, thus indirectly reflecting the degree of cell damage [22]. MDA contents of *D. magna* without nanomaterials exposure were measured to be approximately 10 nmol/mgprot. Figure 6 shows the MDA contents of *D. magna* after exposure to nZnO particles. The MDA contents were between 20 and 30 nmol/mgprot in 50 μg L^{-1} exposure groups (i.e., twice to thrice that of the control) and between 40 and 50 nmol/mgprot in 250 μg L^{-1} exposure groups (i.e., four to five times that of the control). That is, the MDA contents of the high-concentration groups were 1.5 to two times that of the low-concentration groups after nZnO exposure. These results indicated that these five types of nZnO can cause serious lipid peroxidation, and this extent of damage expanded rapidly with increasing exposure concentration. At the same concentration, the Ni-doped nZnO exposure group has similar MDA levels to the nondoped nZnO exposure group, whereas the doping of Fe, Co, and Mn reduced MDA contents. This finding indicates that the doping elements changed the bioeffects of nZnO. Previous studies found that doping of Co [23] and Mn [24] in ZnO influenced the antibacterial property of nZnO.

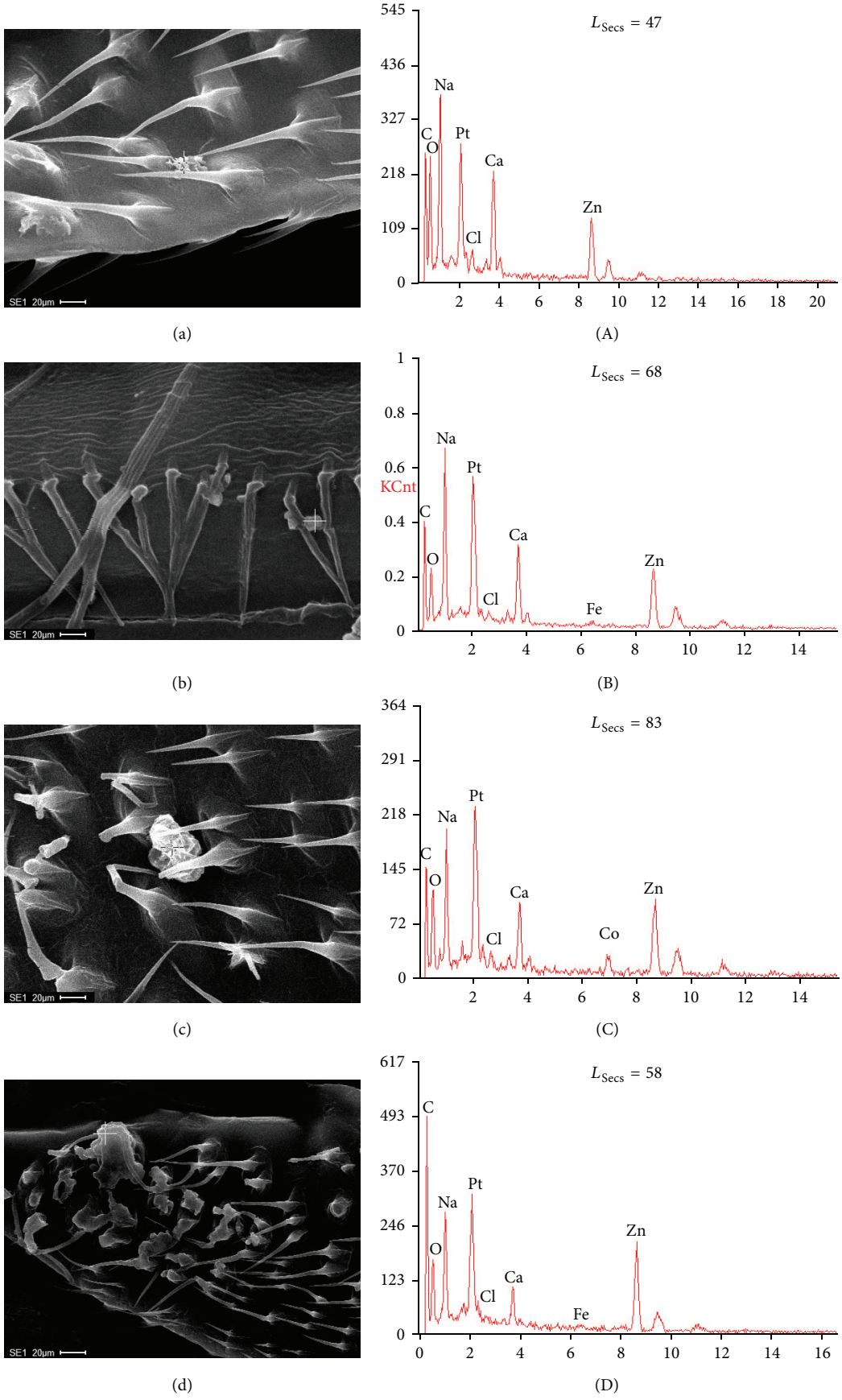

Figure 4: Continued.

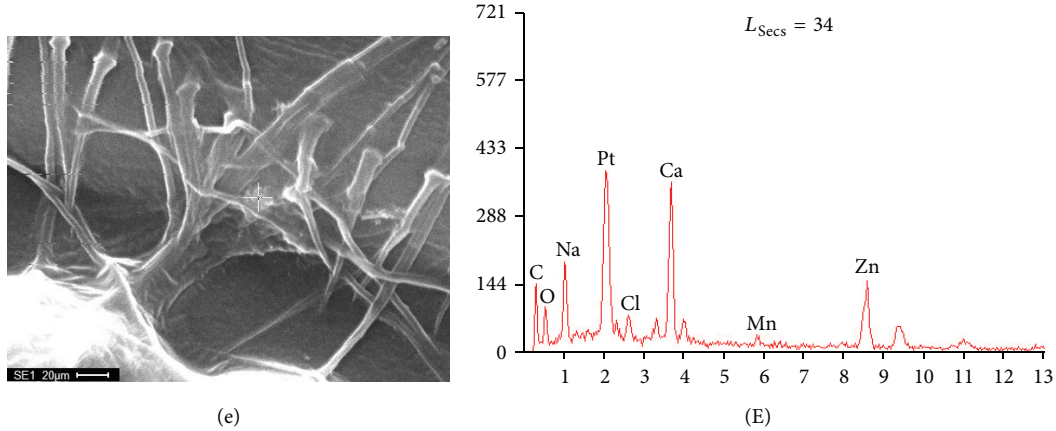

FIGURE 4: SEM images and microanalysis by an energy dispersive spectrometer of accumulated nZnO in the intestines of *D. magna* after 2 d exposure. (A, a) Nondoped nZnO, (B, b) Fe-nZnO, (C, c) Co-nZnO, (D, d) Ni-nZnO, and (E, e) Mn-nZnO.

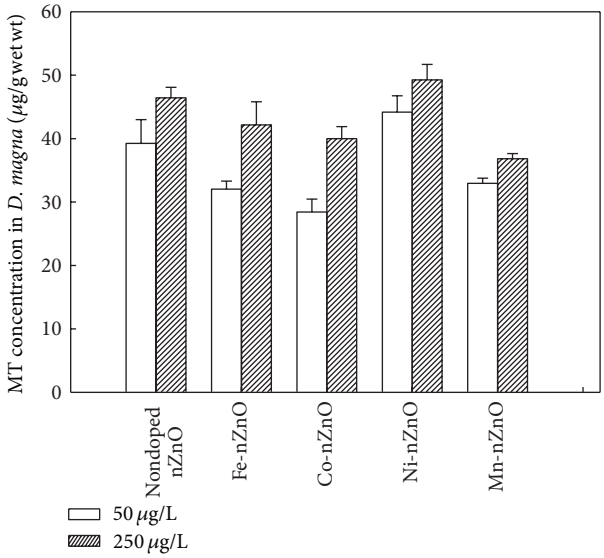

FIGURE 5: MT induction of *D. magna* after exposure to different doped nZnO photocatalysts. Mean ± standard deviation (n = 2).

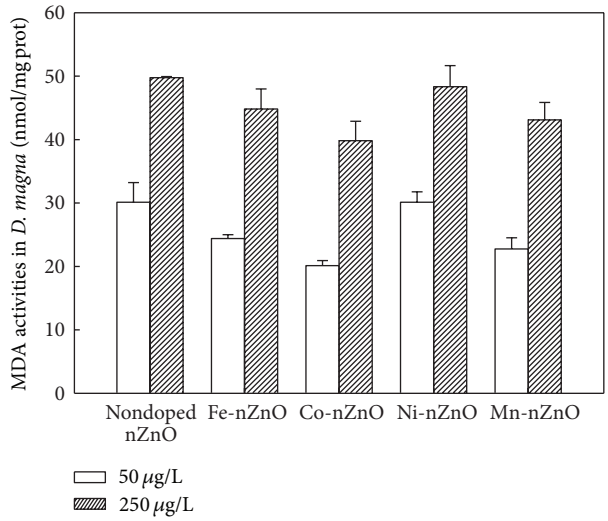

FIGURE 6: MDA activities of *D. magna* after exposure to different doped nZnO photocatalysts. Mean ± standard deviation (n = 2).

3.3. Relationship of the Dissolubility of Five nZnO Photocatalysts with the Biotoxicity to D. magna. As previously discussed, five nZnO (nondoped nZnO, Fe-nZnO, Co-nZnO, Ni-nZnO, and Mn-nZnO) photocatalysts showed varying dissolubility in natural water and toxic effects to *D. magna*, and their relationships were investigated in Figure 7. A negative relationship was observed between dissolved Zn percentage and Zn accumulation in *D. magna*, as shown in Figure 7(a). This finding indicates that the ingestion of Zn^{2+} from aqueous phase was not the main uptake behavior in this study. Zn accumulation was distinctive under different metal-doped nZnO, which might be because of the dissolved Zn^{2+}, different aggregation clusters of M-nZnO, and particularities of doping metals. As for soluble Ag nanoparticles, the results of the uptake experiments showed that water drinking was an important pathway to obtain AgNPs in the medium for *D. magna* [25]. On the contrary, MT and MDA contents were independent of the dissolved Zn percentage in the medium (Figures 7(b) and 7(c)). Among all the metals in this study, only Zn can induce the generation of MT. Thus, the MT contents were correlated with the concentration of free Zn^{2+} in the body instead of external mediums. One important toxicity mechanism of nZnO photocatalysts was oxidative damage by ROS. Meanwhile, MDA reflected the degree of lipid peroxidation and was influenced by many factors. In this study, physiological functions of doping metals might alleviate the biotoxicity of M-nZnO photocatalysts to various extents. Fe, Co, Zn, and Mn are essential elements that have important effects on the growth of organisms [26]. During the experiment process, parts of the doped Fe, Co, and Mn dissolved into the medium despite being undetected. The release of trace metals can supply nutrition for *D. magna* under short-term exposure.

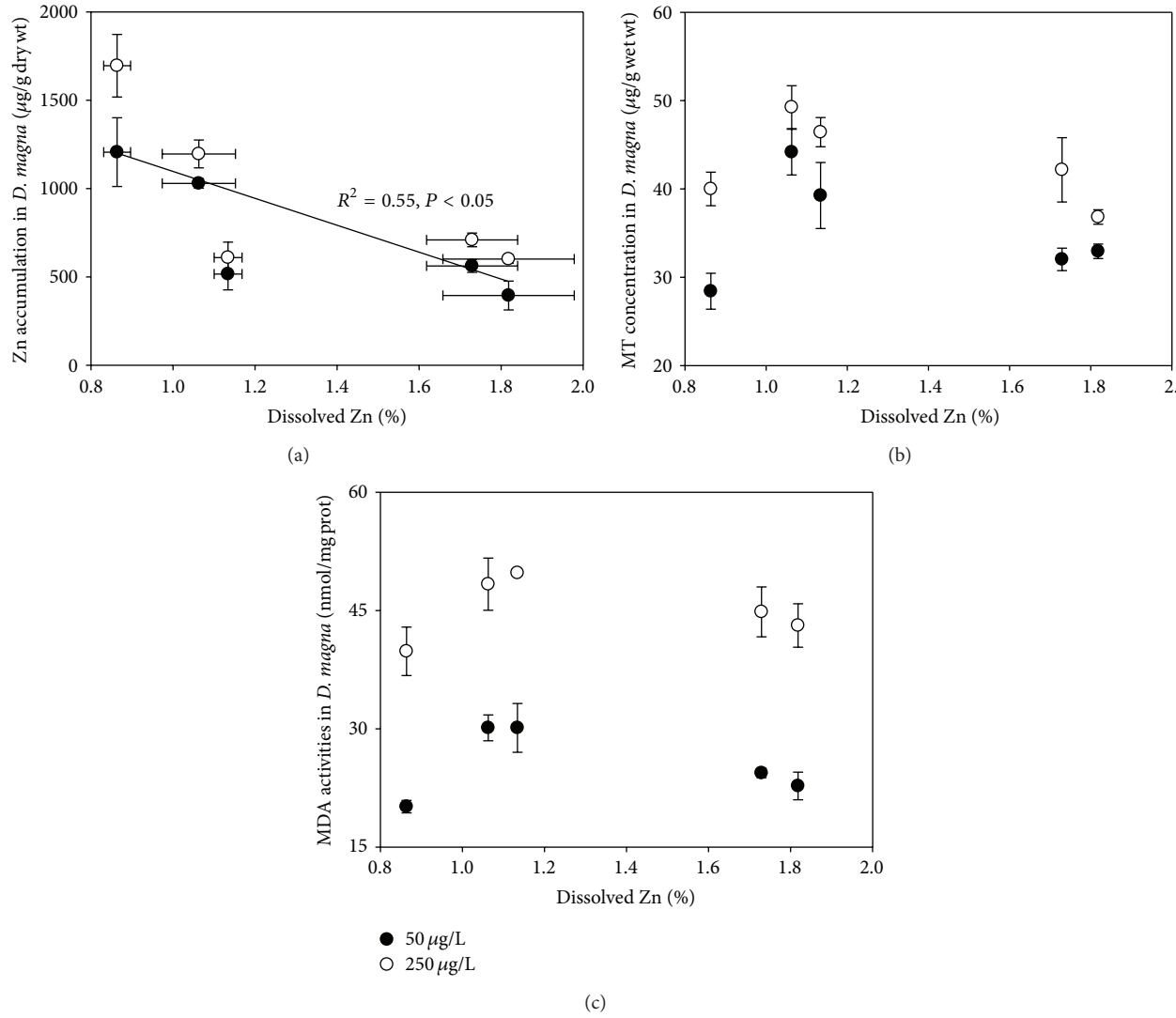

Figure 7: Relationships between dissolubility of five nZnO photocatalysts and toxic effects in *D. magna*. (a) Zn accumulation, (b) MT concentration, and (c) MDA activity.

4. Conclusions

Metal-doped nZnO (Fe-nZnO, Co-nZnO, Ni-nZnO, and Mn-nZnO) and nondoped nZnO photocatalysts were prepared through hydrothermal method of zinc nitrate, hexamethylenetetramine, and various metal ions. The morphologies and dissolubility of five nZnO photocatalysts were diverse because of the doping metals. Moreover, metal-doped nZnO photocatalysts changed toxic effects in *D. magna* compared with nondoped nZnO. Co-doped and Ni-doped nZnO enhanced Zn accumulation in daphnids, whereas Mn-doped nZnO reduced such accumulation. Biomarkers, such as MT and MDA contents, in metal-doped nZnO treatments, except for Ni-nZnO, were lower than those in nondoped nZnO. Zn accumulation showed a negative relationship with dissolved Zn percentage, which indicated that Zn^{2+} was not the only pathway of *D. magna* ingestion. By contrast, MT and MDA contents in organisms were dependent on the dose of nZnO exposure rather than on dissolubility. When considering the biotoxicity of metal-doped nZnO photocatalysts, physiological functions of doping metals should not be ignored.

Conflict of Interests

The authors declare that there is no conflict of interests regarding the publication of this paper.

Authors' Contribution

Both Lingling Liu and XiangRui Wang contributed equally to this work.

Acknowledgments

This work was supported by the National Natural Science Foundation of China (nos. 51378041 and 51290283) and

Specialized Research Fund for the Doctoral Program of Higher Education (no. 20131102110035).

References

[1] Z. Fan and J. G. Lu, "Zinc oxide nanostructures: synthesis and properties," *Journal of Nanoscience and Nanotechnology*, vol. 5, no. 10, pp. 1561–1573, 2005.

[2] Z. L. Wang, "Zinc oxide nanostructures: growth, properties and applications," *Journal of Physics Condensed Matter*, vol. 16, no. 25, pp. 829–858, 2004.

[3] Z. S. Seddigi, S. A. Ahmed, S. P. Ansari, E. Danish, A. A. Alkibash, and S. Ahmed, "Kinetics and photodegradation study of aqueous methyl tert-butyl ether using zinc oxide: the effect of particle size," *International Journal of Photoenergy*, vol. 2013, Article ID 206129, 7 pages, 2013.

[4] J. G. Yu and X. X. Yu, "Hydrothermal synthesis and photocatalytic activity of zinc oxide hollow spheres," *Environmental Science and Technology*, vol. 42, no. 13, pp. 4902–4907, 2008.

[5] C. Shifu, Z. Wei, Z. Sujuan, and L. Wei, "Preparation, characterization and photocatalytic activity of N-containing ZnO powder," *Chemical Engineering Journal*, vol. 148, no. 2-3, pp. 263–269, 2009.

[6] M. C. Chang, H. Y. Shu, T. H. Tseng, and H. W. Hsu, "Supported zinc oxide photocatalyst for decolorization and mineralization of orange G dye wastewater under UV365 irradiation," *International Journal of Photoenergy*, vol. 2013, Article ID 595031, 12 pages, 2013.

[7] C. Xu, L. X. Cao, G. Su, W. Liu, X. F. Qu, and Y. Q. Yu, "Preparation, characterization and photocatalytic activity of Co-doped ZnO powders," *Journal of Alloys and Compounds*, vol. 497, no. 1-2, pp. 373–376, 2010.

[8] R. Ullah and J. Dutta, "Photocatalytic degradation of organic dyes with manganese-doped ZnO nanoparticles," *Journal of Hazardous Materials*, vol. 156, no. 1–3, pp. 194–200, 2008.

[9] S. J. Klaine, P. J. J. Alvarez, G. E. Batley et al., "Nanomaterials in the environment: behavior, fate, bioavailability, and effects," *Environmental Toxicology and Chemistry*, vol. 27, no. 9, pp. 1825–1851, 2008.

[10] H. Ma, P. L. Williams, and S. A. Diamond, "Ecotoxicity of manufactured ZnO nanoparticles—a review," *Environmental Pollution*, vol. 172, pp. 76–85, 2013.

[11] T. Xia, Y. Zhao, T. Sager et al., "Decreased dissolution of ZnO by iron doping yields nanoparticles with reduced toxicity in the rodent lung and zebrafish embryos," *ACS Nano*, vol. 5, no. 2, pp. 1223–1235, 2011.

[12] A. Wang, B. Zhang, X. Wang et al., "Nano-structure, magnetic and optical properties of Co-doped ZnO films prepared by a wet chemical method," *Journal of Physics D: Applied Physics*, vol. 41, no. 21, Article ID 215308, 2008.

[13] W. H. Fan, Z. W. Shi, X. P. Yang et al., "Bioaccumulation and biomarker responses of cubic and octahedral Cu_2O micro/nanocrystals in *Daphnia magna*," *Water Research*, vol. 46, no. 18, pp. 5981–5988, 2012.

[14] W. H. Fan, G. Tang, C. M. Zhao, Y. Duan, and R. Zhang, "Metal accumulation and biomarker responses in *Daphnia magna* following cadmium and zinc exposure," *Environmental Toxicology and Chemistry*, vol. 28, no. 2, pp. 305–310, 2009.

[15] N. M. Franklin, N. J. Rogers, S. C. Apte, G. E. Batley, G. E. Gadd, and P. S. Casey, "Comparative toxicity of nanoparticulate ZnO, bulk ZnO, and ZnCl2 to a freshwater microalga (Pseudokirchneriella subcapitata): the importance of particle solubility," *Environmental Science and Technology*, vol. 41, no. 24, pp. 8484–8490, 2007.

[16] A. J. Miao, X. Y. Zhang Z. Luo et al., "Zinc oxide-engineered nanoparticles: dissolution and toxicity to marine phytoplankton," *Environmental Toxicology and Chemistry*, vol. 29, no. 12, pp. 2814–2822, 2010.

[17] C. Tan, W. H. Fan, and W. X. Wang, "Role of titanium dioxide nanoparticles in the elevated uptake and retention of cadmium and zinc in *Daphnia magna*," *Environmental Science and Technology*, vol. 46, no. 1, pp. 469–476, 2012.

[18] K. Tervonen, G. Waissi, E. J. Petersen, J. Akkanen, and J. V. K. Kukkonen, "Analysis of fullerene-C60 and kinetic measurements for its accumulation and depuration in *Daphnia magna*," *Environmental Toxicology and Chemistry*, vol. 29, no. 5, pp. 1072–1078, 2010.

[19] J. C. Amiard, C. Amiard-Triquet, S. Barka, J. Pellerin, and P. S. Rainbow, "Metallothioneins in aquatic invertebrates: their role in metal detoxification and their use as biomarkers," *Aquatic Toxicology*, vol. 76, no. 2, pp. 160–202, 2006.

[20] S. W. Y. Wong, P. T. Y. Leung, A. B. Djurišić, and K. M. Y. Leung, "Toxicities of nano zinc oxide to five marine organisms: influences of aggregate size and ion solubility," *Analytical and Bioanalytical Chemistry*, vol. 396, no. 2, pp. 609–618, 2010.

[21] J. Pilz, I. Meineke, and C. H. Gleiter, "Measurement of free and bound malondialdehyde in plasma by high-performance liquid chromatography as the 2,4-dinitrophenylhydrazine derivative," *Journal of Chromatography B: Biomedical Sciences and Applications*, vol. 742, no. 2, pp. 315–325, 2000.

[22] W. H. Fan, X. L. Wang, M. M. Cui et al., "Differential oxidative stress of octahedral and cubic Cu_2O micro/nanocrystals to *Daphnia magna*," *Environmental Science and Technology*, vol. 46, pp. 10255–10262, 2012.

[23] M. G. Nair, M. Nirmala, K. Rekha, and A. Anukaliani, "Structural, optical, photo catalytic and antibacterial activity of ZnO and Co doped ZnO nanoparticles," *Materials Letters*, vol. 65, no. 12, pp. 1797–1800, 2011.

[24] K. Rekha, M. Nirmala, M. G. Nair, and A. Anukaliani, "Structural, optical, photocatalytic and antibacterial activity of zinco xide and manganese doped zinc oxide nanoparticles," *Physica B: Condensed Matter*, vol. 405, no. 15, pp. 3180–3185, 2010.

[25] C. M. Zhao and W. X. Wang, "Size-dependent uptake of silver nanoparticles in *Daphnia magna*," *Environmental Science and Technology*, vol. 46, pp. 11345–11351, 2012.

[26] M. N. Hughes and R. K. Poole, "Metal speciation and microbial growth—the hard (and soft) facts," *Journal of General Microbiology*, vol. 137, no. 4, pp. 725–734, 1991.

Hindawi Publishing Corporation
International Journal of Photoenergy
Volume 2014, Article ID 463034, 10 pages
http://dx.doi.org/10.1155/2014/463034

Research Article

Influence of Nd-Doping on Photocatalytic Properties of TiO_2 Nanoparticles and Thin Film Coatings

Damian Wojcieszak,[1] Michal Mazur,[1] Michalina Kurnatowska,[2] Danuta Kaczmarek,[1] Jaroslaw Domaradzki,[1] Leszek Kepinski,[2] and Kamil Chojnacki[1]

[1] *Faculty of Microsystem Electronics and Photonics, Wroclaw University of Technology, Janiszewskiego 11/17, 50-372 Wroclaw, Poland*
[2] *Institute of Low Temperature and Structure Research, Polish Academy of Sciences, Okólna 2, 50-422 Wroclaw, Poland*

Correspondence should be addressed to Damian Wojcieszak; damian.wojcieszak@pwr.wroc.pl

Received 28 January 2014; Revised 7 April 2014; Accepted 8 April 2014; Published 6 May 2014

Academic Editor: Mietek Jaroniec

Structural, optical, and photocatalytic properties of TiO_2 and TiO_2:Nd nanopowders and thin films composed of those materials have been compared. Titania nanoparticles with 1, 3, and 6 at. % of Nd-dopant were synthesized by sol-gel method. Additionally, thin films with the same material composition were prepared with the aid of spin-coating method. The analysis of structural investigations revealed that all as-prepared nanopowders were nanocrystalline and had TiO_2-anatase structure. The average size of crystallites was ca. 4-5 nm and the correlation between the amount of neodymium and the size of TiO_2 crystallites was observed. It was shown that the dopant content influenced the agglomeration of the nanoparticles. The results of photocatalytic decomposition of MO showed that doping with Nd (especially in the amount of 3 at. %) increased self-cleaning activity of the prepared titania nanopowder. Similar effect was received in case of the thin films, but the decomposition rate was lower due to their smaller active surface area. However, the as-prepared TiO_2:Nd photocatalyst in the form of thin films or nanopowders seems to be a very attractive material for various applications.

1. Introduction

The removal of inorganic and nonbiodegradable organic compounds is a crucial ecological problem. Dyes are an important class of synthetic organic compounds used mainly in the textile industry and therefore they are common industrial pollutants. Since the discovery of synthetic products, the global amount of dyes has been increasing year by year. Water wastes generated by the textile industry are known to contain considerable amounts of nonfixed dyes and azo dyes. Around 15% of the total world production of dyes is lost during the dyeing process and is released in textile effluents [1]. The release of those colored compounds into the ecosystem is a dramatic source of esthetic pollution and of perturbations in the aquatic life. Unfortunately, for the environment, they are very stable molecules and many efforts must be carried out for their decomposition [2].

Photocatalysis was well described in the literature [3–10]. Degradation of pollutants is a consequence of oxidation and reduction reactions due to photo-generation of charge carriers (electron-hole pairs) [3, 11–18]. There are a lot of materials that could be considered as effective photocatalysts, for example, ZnO [19], ZrO_2 [20, 21], CdS [22], MoS_2, Fe_2O_3, and WO_3 [3, 11–14]. However, the most widely used is titanium dioxide. Titania can be manufactured in a form of, for example, various kinds of layers, nanoparticles, nanotubes, solutions, or gels [14]. Photocatalytic activity of TiO_2 is related to many factors such as the method of preparation, amount and type of dopant, crystalline structure, surface properties, surface area, density of surface OH^- group, and parameters of postprocess treatment (e.g., temperature of annealing) [23]. One of the ways to increase its photocatalytic activity is manufacturing TiO_2 in the nanocrystalline form because the crystallite size reduction has a positive effect on this property

[24, 25]. Numerous scientific works have studied the effect of titania structure modification on photocatalysis [26, 27], for example, materials with the two-phase structure (anatase-rutile) [28, 29]. Another way to improve the self-cleaning properties of TiO_2 is doping, for example, with lanthanide ions having 4f configuration, such as Nd, Eu, or Tb [29–39]. Among them, neodymium doping has attracted considerable interest due to comparatively large size of Nd^{3+} ion, which causes a localized charge perturbation during substitutional doping into TiO_2-lattice to increase its photocatalytic activity [40, 41]. Usually, higher activity of Nd-doped materials can be explained by the electronic character of neodymium with the partially filled atomic d or f shells [42]. The absorption of equivalent energy during UV-Vis light exposure results in electron excitation and transition from $Nd^{3+}4f^3$ orbital. The surrounding of Nd^{3+} can react with Nd^{4+} ions obtained from the self-sensitization process and form the positively charged neodymium clusters $(Nd_n)^{m+}(m > 3n)$. Nd-clusters have empty energy levels (subbands) below the conduction band of TiO_2 (Figure 1). Therefore, the charge transfer from the TiO_2 matrix to the empty Nd^{3+} levels may occur [42]. Such transition requires less energy than the transfer valence-conduction band in TiO_2 and can also proceed in the visible light [43]. The schematic representation of the photo-induced process of pollutant decomposition is shown in Figure 1. According to authors of previous works [39], the photo-induced electrons are transferred to $^4F_{3/2}$ level of Nd^{3+} ions via matrix defect states (DS), which are located below the titania conduction band. The authors suggest that electrons from neodymium energy levels or from DS are trapped (EC: electron capturing) by O_2 (acceptors) which results in the creation of superoxides $O_2^{\bullet}$ (radical anions) that participate in the formation of hydroxyl radicals ($OH^{\bullet}$). During the light exposure also holes (positively charged vacancies) are created in the TiO_2 valance band. They are responsible for the extraction of electrons from water and hydroxyl species to produce $OH^{\bullet}$, which oxidizes (decomposes) dye molecules on the surface. The phenomenon of higher photocatalytic activity of Nd-doped nanomaterials can be explained as a higher efficiency of indirect energy transfer from the conduction band of TiO_2 to O_2 via DS or energy levels of Nd^{3+} and higher number of oxygen vacancies in DS near the valence band of TiO_2. Both phenomena are responsible for creation of $OH^{\bullet}$ that fulfill a key role in the decomposition process.

Similar conclusions about photocatalytic activity of TiO_2:Nd were presented in the works by Hewer et al. [29], Wang et al. [44], Shah et al. [45], and Li et al. [46]. The authors suggested that ions of Nd-dopant can act as electron and/or hole traps. This kind of traps may decrease the recombination rate of e^-/h^+ pairs and therefore it may increase the lifetime of charge carriers, which causes that the photocatalytic activity is more efficient [29]. An explanation of the effect of neodymium dopant on the photocatalytic activity of titania requires a consideration of the role of Ti–O–Nd bonds in the mechanism of indirect transfer of photo-generated carriers. According to Hewer et al. [29] these bonds are created on the surface of the TiO_2 nanocrystals in the

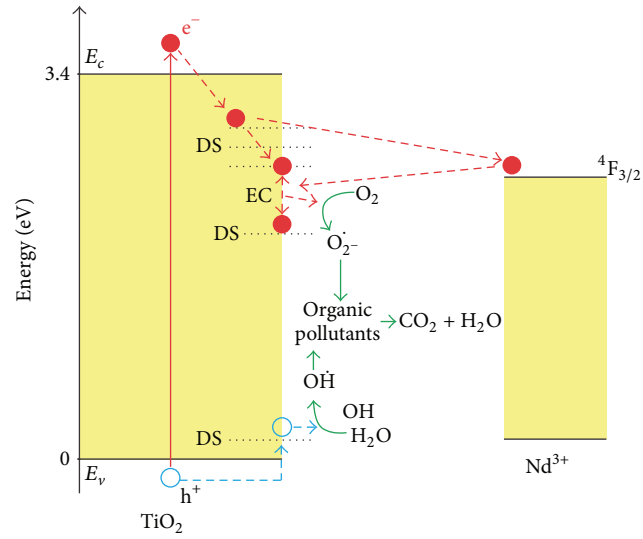

Figure 1: Schematic representation of photo-induced decomposition of organic pollutants with TiO_2:Nd. Designations: EC: electron capturing, DS: defect states, e^-: electron, h^+: hole, E_c: conduction band, and E_v: valence band.

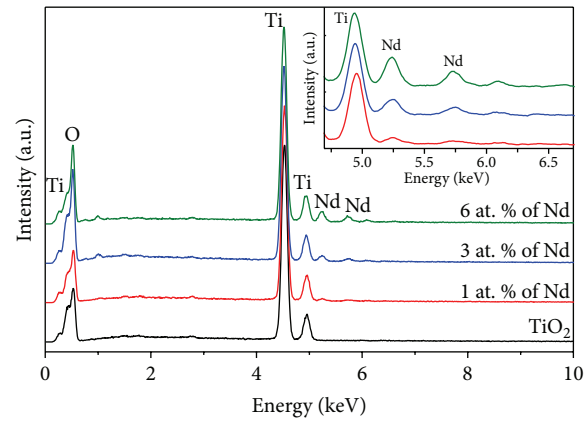

Figure 2: EDS spectra of TiO_2 nanoparticles doped with different amounts of neodymium.

surrounding of Nd_2O_3. Our earlier research on thin film coatings based on TiO_2:Nd also showed that Nd^{3+} ions were probably located on the surface of TiO_2 nanocrystallites in a form of small Nd_2O_3 agglomerates [39]. Similar conclusions were also presented in other works [29, 33–35]. Moreover, our previous investigations on TiO_2 thin films doped with lanthanides (Tb and Nd) showed that very effective direct and/or indirect energy transfer of excited electrons may occur due to such location of RE-oxides agglomerates [39, 47]. In case of TiO_2:Nd, the energy levels of titania matrix are localized above $^4F_{3/2}$ level of Nd^{3+}. Therefore, an increase in the titania DS would probably have a positive impact on the photocatalytic efficiency of TiO_2:Nd due to more probable indirect transitions. Moreover, as reported by Kralchevska et al. [33], the formation of RE clusters with discrete empty multienergy levels below the conduction band of TiO_2

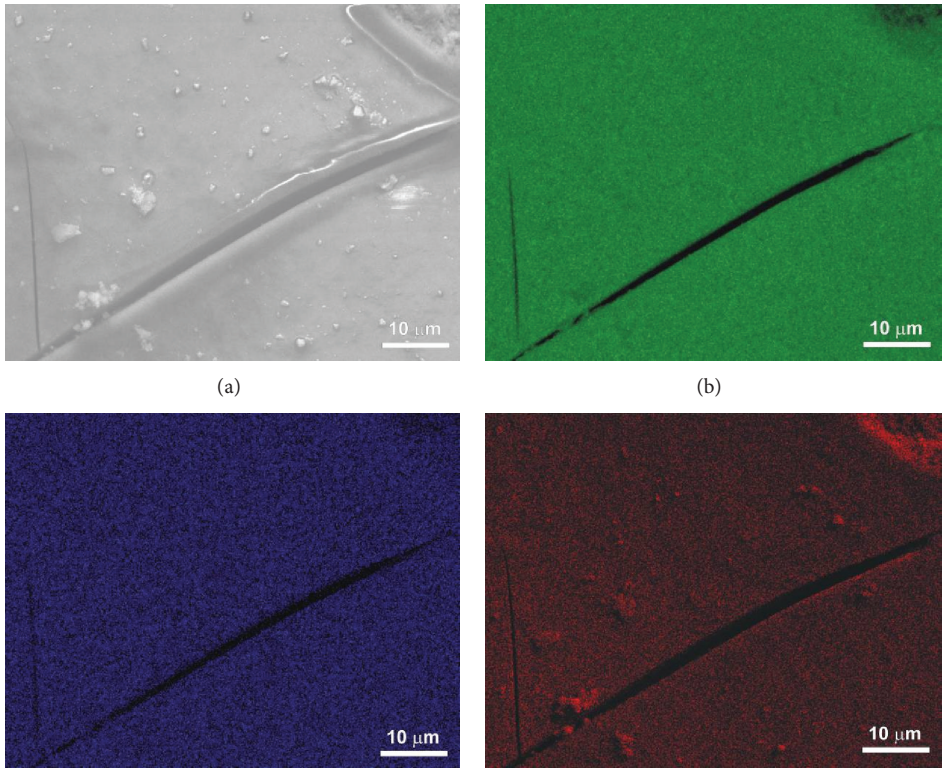

FIGURE 3: Results of X-ray microanalysis: (a) secondary electron image of selected area of TiO_2:Nd (3 at. %), (b) Ti, (c) Nd, and (d) O elements concentration distribution.

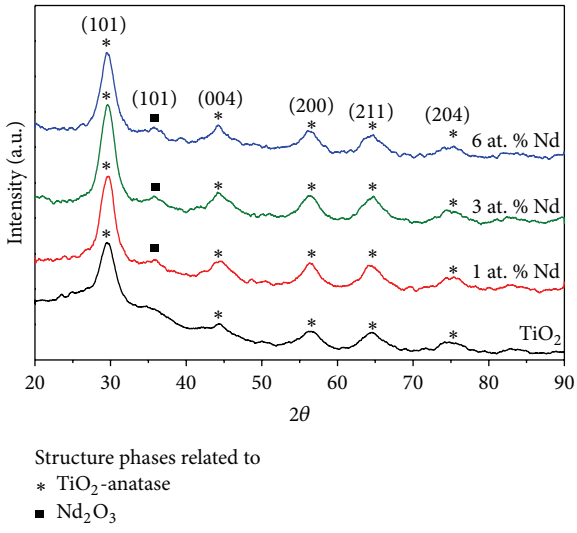

FIGURE 4: XRD patterns (Co Kα radiation) of TiO_2 and TiO_2:Nd nanoparticles prepared by sol-gel method.

allows transitions from the titania valence band to these levels. Thanks to this process, the ability of visible light absorption by titania increases, which results in slightly better performance of Nd-doped catalyst under solar irradiation. According to Yang et al. [34], certain amount of Nd_2O_3 on the surface of TiO_2 results in more efficient separation of charge carriers, prolongation of their lifetime, and inhibition of the recombination process. However, when the Nd-dopant content exceeds a certain level, an excessive amount of Nd_2O_3 on the surface of titania would inhibit the adsorption of the dye and decrease the light absorption, thus decreasing the photocatalytic activity. From this reason, titanium dioxide doped with an adequate amount of neodymium could have higher photocatalytic activity and would be much better suited to the role of commercial photocatalyst as compared to undoped TiO_2.

In this study, undoped and neodymium doped titanium dioxide nanoparticles were synthesized by sol-gel method. As-prepared samples were used for the photocatalytic degradation of the methyl orange (MO). Additionally, the thin films were prepared using spin-coating method and their photocatalytic properties were also determined in order to compare self-cleaning activity of prepared nanoparticles and thin films.

2. Experimental

Chemical reagents and solvents used in this study were of analytical or reagent grade and used as received, without further purifications. In a typical synthesis, 75 mL of (acidic) distilled water (pH = 1, adjusted with nitric acid, Baker, 65%, d = 1.40 g/mL) was added dropwise to 2 mL of

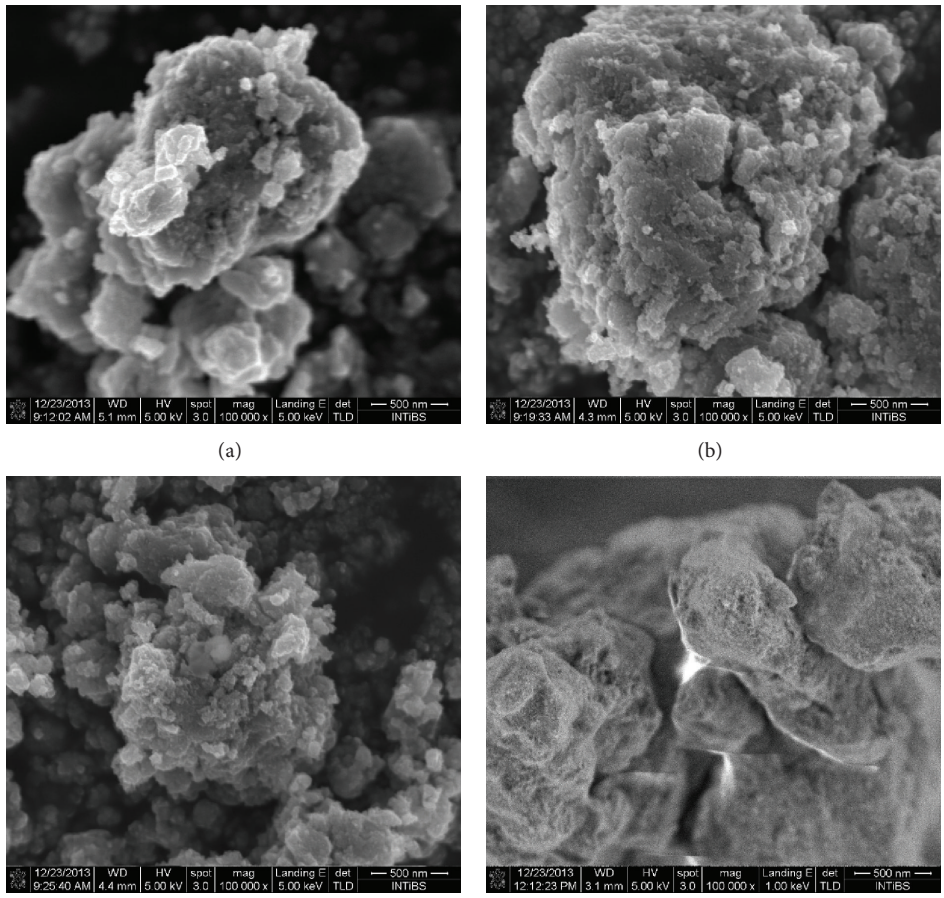

Figure 5: SEM images of (a) TiO_2, (b) TiO_2:Nd (1 at. %), (c) TiO_2:Nd (3 at. %), and (d) TiO_2:Nd (6 at. %) nanoparticles.

titanium tetraisopropoxide (TTIP, Sigma Aldrich, ≥ 98%, d = 0.96 g/mL), dissolved in 25 mL of 2-propanol (Lab-Scan, ≥ 99.7%, d = 0.78 g/mL) under vigorous magnetic stirring and heated at 80°C for 6 hours. Hydrolysis of titanium precursor occurred immediately, as indicated by the appearance of white turbidity. This resulted in a transparent translucent/milky-white colloidal system with a TiO_2 concentration of about 5 g/L (stable for several days at room temperature, without coagulation): $Ti[OCH(CH_3)_2]_4 + 2H_2O \rightarrow TiO_2 + 4(CH_3)_2CHOH$. The colloidal solution was dried in an oven in air atmosphere. This led to the formation of a white/yellowish powder. Finally the samples were annealed at 120°C for 2 hours in air for further characterization and MO photocatalytic degradation. Neodymium doped TiO_2 nanoparticles were prepared using modified version of the above procedure. An appropriate amount of pure neodymium salt ($N_d(NO_3)_3 \cdot 6H_2O$) was added to obtain a doping level of 1.0, 3.0, and 6.0 at. % (nominal atomic concentration based upon the assumption of quantitative incorporation of the dopants).

Structural properties of synthesized TiO_2 and TiO_2:Nd nanoparticles were determined based on the results of the X-ray diffraction (XRD) method. For the measurements, Siemens 5005 powder diffractometer with Co Kα X-ray (λ = 1.78897 Å) was used. The XRD studies were performed using Co lamp filtered by Fe (30 mV, 25 mA) and step size was equal to 0.02° of/in 2θ range, while time-per-step was 5 s. The correction for the broadening of the XRD instrument was accounted and the crystallite sizes were calculated using Scherrer's equation [49].

The surface morphology of the thin films was investigated with the aid of a FESEM FEI Nova NanoSEM 230 scanning electron microscope (SEM) with 30 kV of acceleration voltage. Moreover, this system was equipped with EDAX EDS microanalyzer for investigation of material composition.

High resolution transmission electron microscopy (HRTEM) as well as selected area electron diffraction (SAED) studies was performed using a Philips CM20 SuperTwin transmission electron microscope with 200 kV of acceleration voltage, which provided a resolution of 0.24 nm. A drop of each TiO_2 and TiO_2:Nd (3 at. %) nanopowders (suspension in methanol) was loaded on carbon coated copper grids and dried under a lamp. Average size of TiO_2 and TiO_2:Nd (3 at. %) crystallites was calculated from TEM

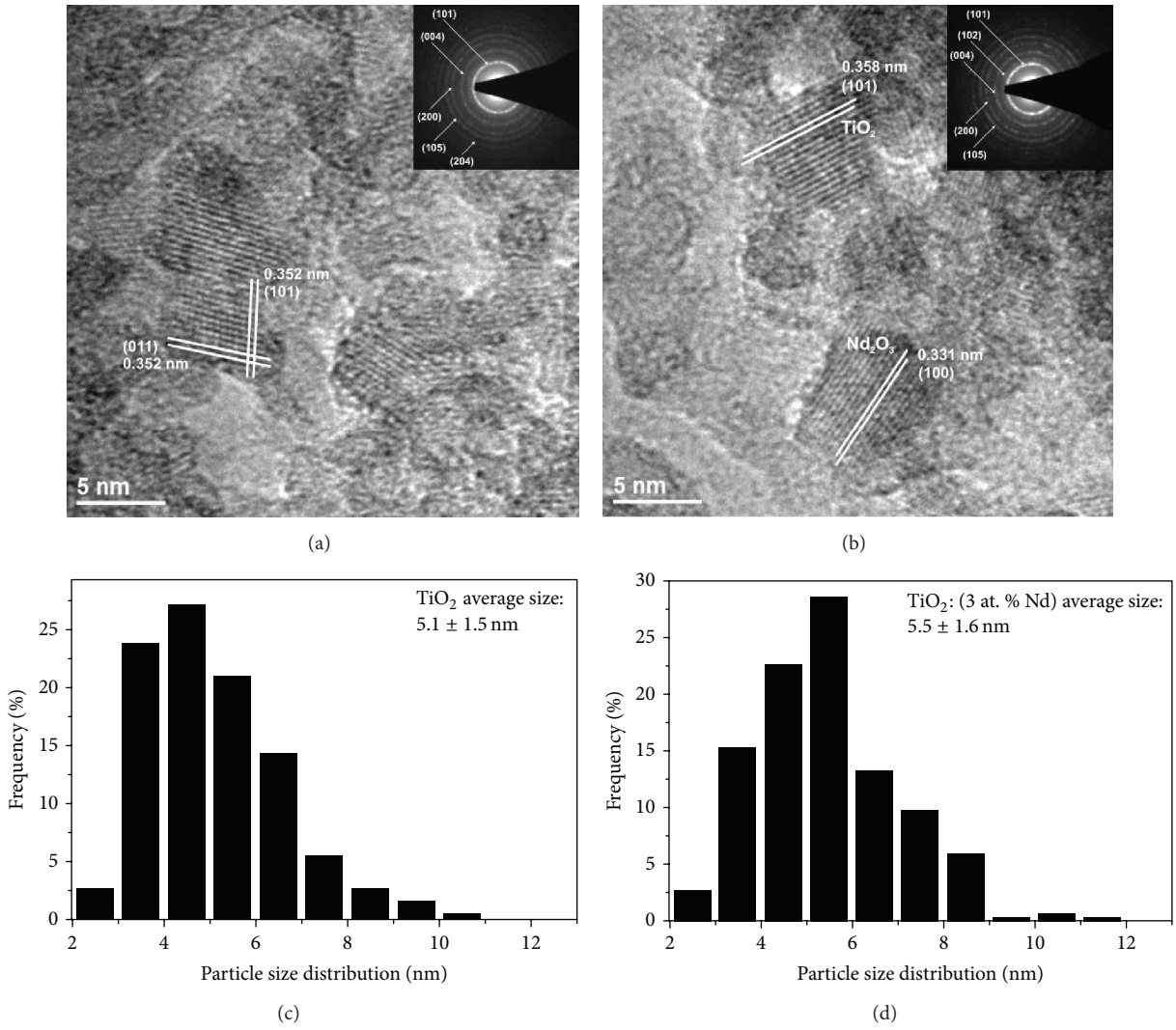

Figure 6: HRTEM images and particles size distribution of (a) TiO_2 and (b) TiO_2:Nd (3 at. %) nanoparticles.

images with the aid of ImageJ program [50]. Received values were obtained based on about two hundred particles in each case.

The influence of neodymium doping on photocatalytic properties of nanocrystalline TiO_2 nanoparticles was estimated based on methyl orange decomposition reaction. The experimental setup consisted of a UV-Vis light source (6×20 W Phillips lamps with intensity of UV and Vis radiation: 183 W/m^2 and 167 W/m^2, resp.) and cylindrical reservoir, which contained 200 mL of solution with MO concentration of 25 mg/L and 100 mg of the photocatalyst. To avoid the heating of the solution, the reaction temperature was controlled by circulation of water through the jacket at a constant temperature of ca. 15°C. All experiments were carried out under agitation with a magnetic stirrer, operating at 500 rpm, in order to provide a good mixing of the suspension. No external oxygen supply was used. No measurable degradation of the methyl orange occurred in the absence of TiO_2 nanoparticles. 30 minutes of premixing at a constant temperature in a dark condition was enough to achieve an adsorption/desorption equilibrium and after that time the light was switched onto initiate the reaction. To determine the change in MO concentration, the samples containing its solutions were withdrawn from the reactor regularly every 60 minutes for 5 hours. The solutions were poured into a quartz cuvette and analyzed by OceanOptics QE 65000 UV-Vis spectrophotometer coupled with Mikropack DH-2000-BAL deuterium-halogen light source, in the wavelength range of 300–700 nm. MO concentration was calculated from the absorption peak at ca. 466 nm by means of a calibration curve.

In this study, TiO_2 and TiO_2:Nd thin films were additionally manufactured with the aid of spin-coating method. The coatings were deposited using previously prepared solutions by sol-gel technique on Corning 7059 type substrates. For this purpose, a Spincoat SCS G3P-8 centrifuge was used. All samples (twice coated substrates) were dried at 120°C for 2 hours. The photocatalytic activity of thin films was also examined and the test procedure was the same as in the case of nanopowders. Surface morphology of manufactured coatings

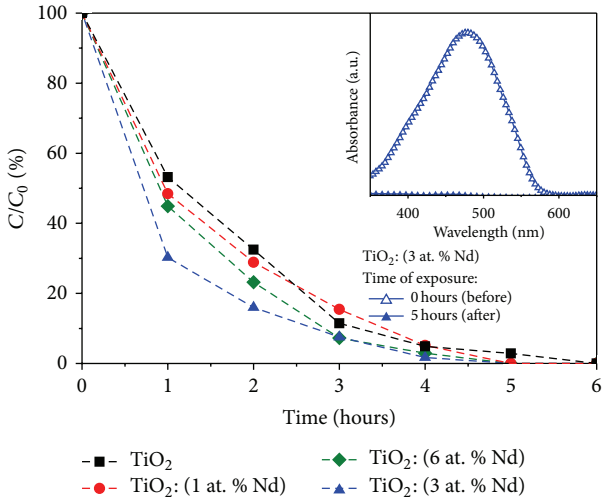

FIGURE 7: Photocatalytic activity of TiO_2 and TiO_2:Nd (1, 3, and 6 at. % of neodymium) nanoparticles after exposure to the UV-Vis light. Designations: C_0: initial concentration and C: concentration of methyl orange after time t.

was investigated with the aid of optical profiler Talysurf CCI Lite (Taylor Hobson), while the optical properties were determined on the basis of transmittance spectra in the wavelength range of 300 to 1000 nm.

3. Results and Discussion

3.1. Material Composition. Material composition of nanoparticles was measured using energy dispersive spectroscopy and the amount of neodymium dopant was in a good correlation with the quantitative assumption. The amount of dopant was ca. 1, 3, and 6 at. % (Figure 2). Results of X-ray microanalysis (Figure 3) show that the concentration distribution of each investigated element (Ti, Nd, and O) is homogenous. The area of investigation was ca. 50 μm × 65 μm.

3.2. X-Ray Diffraction of Nanopowders. XRD results of undoped and neodymium doped TiO_2 nanoparticles are shown in Figure 4. Broad peaks which are present in the patterns testify the nanocrystalline anatase structure of prepared samples. The average size of crystallites is in the range of 4.2 to 4.6 nm for TiO_2 and TiO_2:(6 at. % Nd), respectively. The doping of titanium dioxide with neodymium caused an increase in the crystallites sizes. Similar effect was observed by Khalid et al. [51], where a change in the amount of neodymium from 0.6 to 2 at. % resulted in an increase in the TiO_2-anatase nanoparticles sizes from 7 to 13 nm, respectively. However, TiO_2 doping with neodymium can also give opposite results. According to Bokare et al. [52], an increase in the amount of Nd-dopant resulted in the decrease in the sizes of TiO_2:Nd nanoparticles. In the XRD patterns of doped TiO_2 (Figure 4), a broad and very weak peak at 35.9° of 2θ range is observed. This peak is the strongest reflex from the hexagonal Nd_2O_3-structure. The difference in ion radiuses (1.13 nm for Nd^{3+} and 0.64 nm for Ti^{4+}) suggests that the neodymium ion is unable to effectively incorporate into the crystal lattice position of TiO_2. Therefore, it is more reasonable to assume that Nd-containing particles are localized at the surface of TiO_2 nanocrystals.

3.3. SEM Investigations of Nanoparticles. SEM images obtained for the prepared nanoparticles (Figure 5) show that undoped titania nanoparticles formed agglomerates, whose shape and size are irregular. It seems that for TiO_2 doped with neodymium in the amount of 1 at. % and 3 at. % the agglomerates are a bit smaller. Incorporation of the neodymium dopant in the amount of 6 at. % resulted in a significant change in morphology of the grains. Similar results of SEM investigations of TiO_2 and TiO_2:Nd (1 at. %) were obtained by Bokare et al. [52]. According to those studies, undoped titanium dioxide nanoparticles had irregular shapes and various sizes of the grains. In case of doping with neodymium Bokare et al. obtained nanoparticles with more uniform shape and size.

3.4. TEM Investigations of Nanoparticles. HRTEM images with SAED insets of TiO_2 and TiO_2:Nd (3 at. %) nanoparticles are shown in Figure 6. All diffraction rings on both SAED patterns correspond to the TiO_2-anatase structure. Figure 6(a) presents pure TiO_2 nanoparticles with marked (0 1 1) and (1 0 1) planes. For TiO_2:Nd (3 at. %) nanopowder (Figure 6(b)) the TiO_2 and Nd_2O_3 nanoparticles can be observed. The values of lattice distances 3.58 Å and 3.31 Å correspond to (1 0 1) plane of TiO_2-anatase and (1 0 1) plane of Nd_2O_3 structure, respectively. Particles size distributions of pure and doped TiO_2 are similar and in the range of 2–12 nm (Figure 6). The average sizes of nanoparticles are 5.1 nm and 5.5 nm for TiO_2 and TiO_2:Nd (3 at. %) samples, respectively. These sizes are in good agreement with XRD results (Figure 4, Table 1).

Results of TEM investigation by Bokare et al. [52] also revealed that doped titania particles were small, but their shape was irregular. Moreover, the distribution of the nanoparticles size was in the range from 5 nm to 14 nm, while most of them were in size of 7-8 nm [52]. Additionally, TEM studies performed by Khalid et al. [51] revealed that the TiO_2:Nd nanoparticles were homogenous in shape and their size was in the range of 8 nm to 12 nm. Presented studies showed that preparation of Nd-doped powder by sol-gel method enabled one to obtain nanocrystalline material with the particles of much smaller size than pure titania.

3.5. Photocatalytic Investigations of Nanopowders. The results of photocatalytic reactions showed that all nanopowders prepared by the sol-gel technique were active (Figure 7). Moreover, it was found that an appropriate amount of Nd-dopant had a beneficial effect on the level of MO decomposition by titania nanoparticles. In case of the nanopowder containing 3 at. % of neodymium the decomposition of the dye was the most dynamic and this sample had the highest photocatalytic activity. Slightly worse results were obtained for the TiO_2:(6 at. % Nd), TiO_2:(1 at. % Nd) and undoped TiO_2, respectively. This means that there is an optimum amount of Nd-dopant,

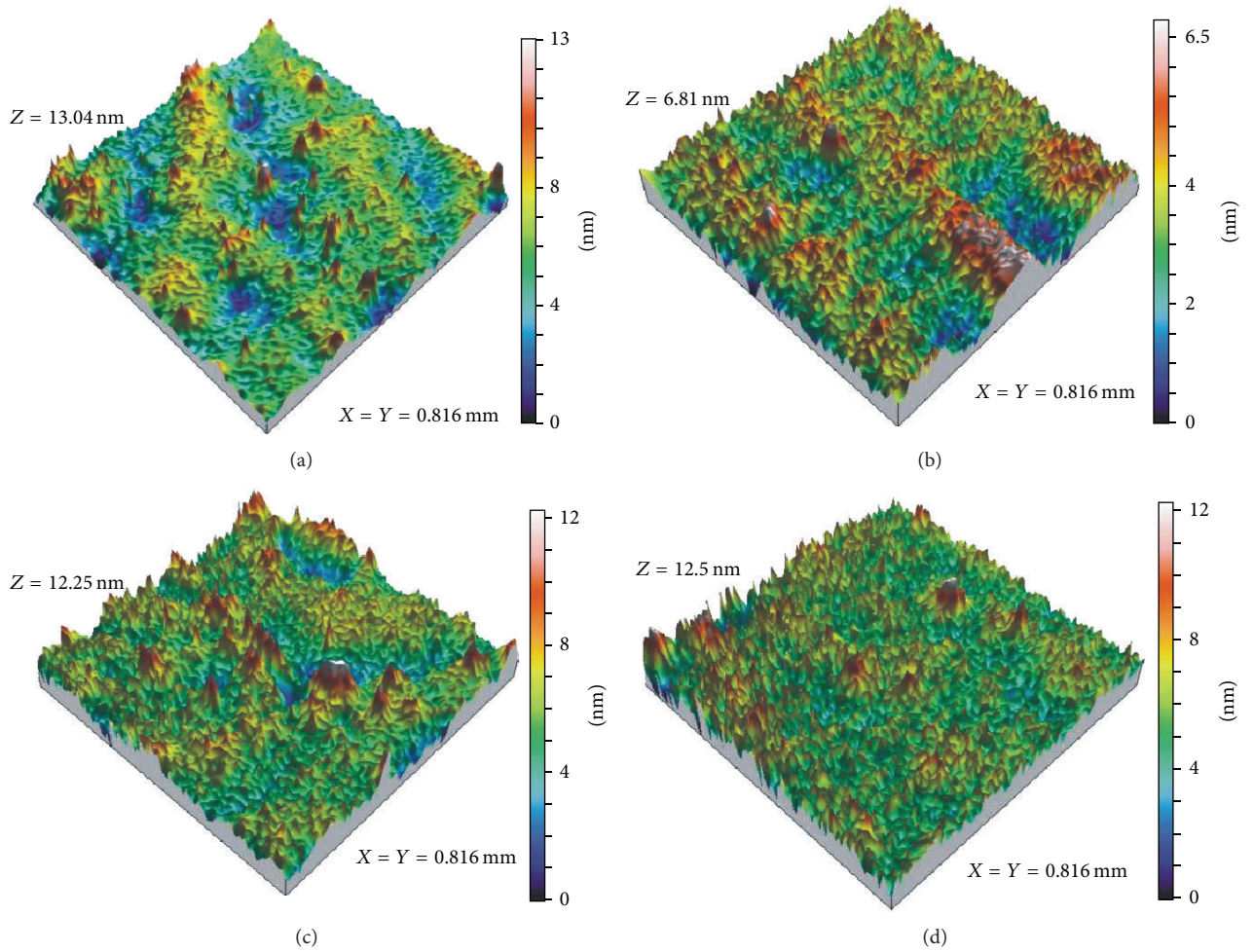

FIGURE 8: 3D surface topography profiles of prepared thin films: (a) TiO_2, (b) TiO_2:(1 at. % Nd), (c) TiO_2:(3 at. % Nd), and (d) TiO_2:(6 at. % Nd).

TABLE 1: Influence of Nd-dopant on structural parameters of titanium dioxide nanoparticles, based on XRD results.

Nanoparticles	Phase	(hkl)	2θ	d (nm)	d_{PDF} (nm)	D (nm)
TiO_2	Anatase	(101)	29.59	0.3503	0.3520 [48]	4.2
TiO_2 : Nd						
1 at. % Nd			29.64	0.3497		4.4
3 at. % Nd			29.62	0.3499		4.5
6 at. % Nd			29.58	0.3504		4.6

Designations: d: interplanar distance, d_{PDF}: standard interplanar distance, D: average crystallites size.

while too much Nd adversely affects the efficiency of MO decomposition. Similar effect was revealed by Bokare et al. [52], but, in case of their TiO_2:Nd nanopowders, the optimal value of Nd was 1 at. %, which resulted in 30% higher activity of that nanopowder as compared to undoped one. Similar results were obtained by Khalid et al. [51]. In their studies 1 at. % of Nd was also an optimum value for the photocatalysis, but the efficiency of reaction was only 20% better than for pure titania.

We suggest that high activity of our powders was directly related to small size of nanoparticles, which were in the range of ca. 4-5 nm (according to XRD and TEM results). Thanks to this fact, very large surface area per gram of the nanopowders was obtained. However, due to similar sizes of the nanoparticles their optimal size cannot be clearly determined. In our opinion the mechanism of indirect energy transfer via energy levels of neodymium ions fulfills a key role in heterogeneous photocatalysis phenomenon.

To exclude the possibility that the decoloration was caused by the UV-Vis light itself, some experiments were carried out without the photocatalyst. The differences in the UV-Vis spectra before and after irradiation for five hours were

negligible, which indicated that no decomposition of MO in the absence of TiO_2 nanopowders was observed or the rate of this reaction was very low.

3.6. Thin Films Investigations Results. Thin films were prepared from the same sol-gel solutions as the ones used for nanopowders manufacturing. Their photocatalytic activity was compared to nanoparticles. In Figure 8 three-dimensional (3D) surface profiles of the films are presented. These studies have shown that the prepared coatings are homogeneous. Their surface roughness (Sa, the arithmetic mean height of the film) is very small, in the range of 0.9 to 1.4 nm, so it means that the surface is very smooth. Moreover, based on the recorded transmittance spectra (Figure 9) one can observe that all prepared thin films are transparent. However, the doping of titanium dioxide with neodymium caused the decrease in the average transmittance from ca. 86% for TiO_2 to ca. 76% for TiO_2:(6 at. % Nd). Additionally, it can be also observed that the doping with neodymium shifted the cutoff wavelength from ca. 293 nm to 304 nm for TiO_2 and TiO_2:Nd (6 at. %), respectively. Therefore, the absorption edge of the TiO_2:Nd thin films has been shifted towards visible light range, what means that these coatings could absorb light in the wider range.

Results of photocatalytic decomposition of methyl orange during the reaction carried out in the presence of thin films are shown in Figure 10. The results clearly indicate that all manufactured films are photocatalytically active. Much lower activity of the thin films (ca. 2% after 5 hours), as compared to the full decomposition of the dye which was obtained in the case of nanoparticles, is associated primarily with the significant difference between the active area of the films and the nanoparticles. Despite the diametrical difference between them, both types of the samples were made from nanoparticles of the same size. In case of nanopowders, active surface area is often given even in tens of square meters. On the contrary, thin films were deposited on substrates that had the area of 12 square centimeters. Therefore, decomposition efficiency in range of about 2.5% can be considered as successful. It is worth to emphasize that after photocatalysis the material from which the thin films were formed was still on the substrate to which it was applied. Therefore, such films would not create problems for the environment, which are associated with nanoparticles recovering from the solution.

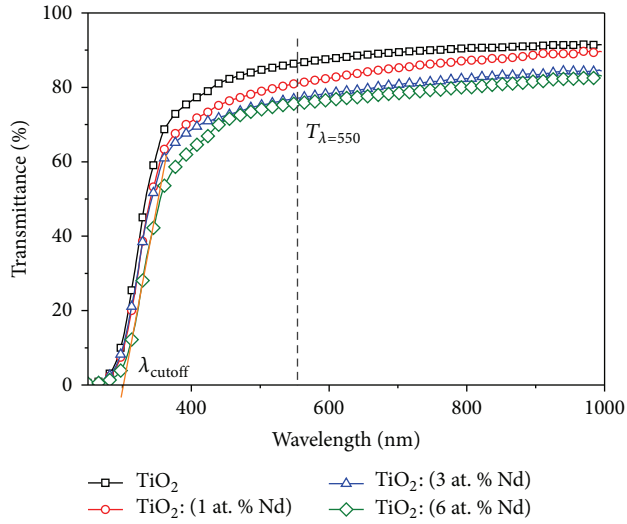

FIGURE 9: Transmittance spectra of TiO_2 and TiO_2:Nd thin films prepared by spin-coating method.

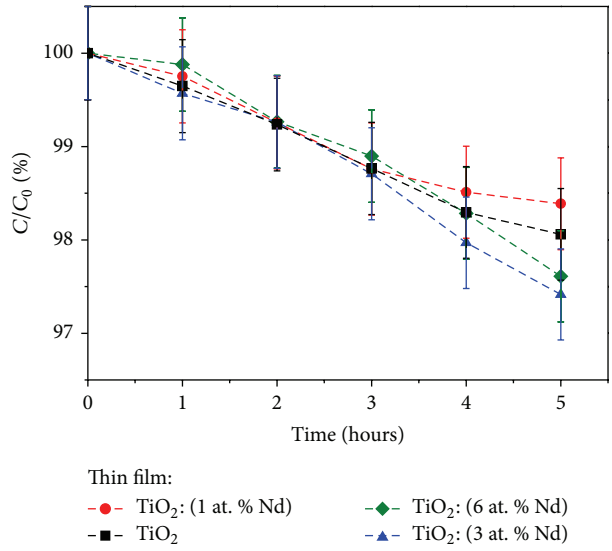

FIGURE 10: Photocatalytic activity of TiO_2 and TiO_2:Nd (1, 3, and 6 at. % of neodymium) thin films after exposure to the UV-Vis light. Designations: C_0: initial concentration and C: concentration of methyl orange after time t.

4. Conclusions

The analysis of structural investigations revealed that all as-prepared powders were nanocrystalline and had anatase structure. According to XRD and TEM results the average size of crystallites was ca. 4-5 nm. The relation between the amount of neodymium and the size of TiO_2 crystallites was observed and an increase in Nd-content resulted in an increase in crystallites size. Moreover, the correlation between the amount of Nd-dopant and the agglomeration level of nanoparticles was observed. Thanks to Nd-doping, the efficiency of photocatalytic decomposition of MO dye was considerably increased. The optimum amount of the dopant was established as 3 at. %. The dynamics of the reaction with this powder was the highest and after 4 hours the dye was completely decomposed. Similar effect was received in case of thin films prepared from the same material. However, due to their much smaller active surface area, as compared to the nanopowder, the decomposition rate was much lower. These results seem to be quite promising in spite of some disadvantages because as-prepared thin film coatings have high transparency in visible light range and very smooth surface with the roughness of ca. 1 nm. This means that such photocatalytically active material could find application as a

self-cleaning coating but in a form of a nanopowder it is also very attractive.

Conflict of Interests

The authors declare that there is no conflict of interests regarding the publication of this paper.

Acknowledgment

This work was financed from the sources granted by the NCN as a research Project no. DEC-2012/05/N/ST7/00173 and as a Ph.D. Scholarship no. DEC-2013/08/T/ST7/00131.

References

[1] H. Zollinger, Ed., *Color Chemistry. Synthesis, Properties and Applications of Organic Dyes and Pigments*, VCH, 2nd edition, 1991.

[2] M. A. Brown and S. C. de Vito, "Predicting azo dye toxicity," *Critical Reviews in Environmental Science and Technology*, vol. 23, no. 3, pp. 249–324, 1993.

[3] A. Fujishima, T. N. Rao, and D. A. Tryk, "Titanium dioxide photocatalysis," *Journal of Photochemistry and Photobiology C: Photochemistry Reviews*, vol. 1, no. 1, pp. 1–21, 2000.

[4] M. A. Fox and M. T. Dulay, "Heterogeneous photocatalysis," *Chemical Reviews*, vol. 93, no. 1, pp. 341–357, 1993.

[5] T. L. Thompson and J. T. Yates Jr., "Surface science studies of the photoactivation of TIO_2: new photochemical processes," *Chemical Reviews*, vol. 106, no. 10, pp. 4428–4453, 2006.

[6] A. Fujishima and X. Zhang, "Titanium dioxide photocatalysis: present situation and future approaches," *Comptes Rendus Chimie*, vol. 9, no. 5-6, pp. 750–760, 2006.

[7] X. Chen and S. S. Mao, "Titanium dioxide nanomaterials: synthesis, properties, modifications and applications," *Chemical Reviews*, vol. 107, no. 7, pp. 2891–2959, 2007.

[8] N. Serpone and E. Pelizetti, *Photocatalysis: Fundamentals and Application*, Wiley, 1989.

[9] M. Schiavello, *Photocatalysis and Environment Trends and Applications*, Kluwer Academic Publishers, 1988.

[10] M. Schiavello, *Heterogeneous Photocatalysis*, vol. 3, John Wiley & Sons, 1997.

[11] A. Fujishima, X. Zhang, and D. A. Tryk, "TIO_2 photocatalysis and related surface phenomena," *Surface Science Reports*, vol. 63, no. 12, pp. 515–582, 2008.

[12] K. Nakata and A. Fujishima, "TiO_2 photocatalysis: design and applications," *Journal of Photochemistry and Photobiology C: Photochemistry Reviews*, vol. 13, pp. 169–189, 2012.

[13] K. Nakata, T. Ochiai, T. Murakami, and A. Fujishima, "Photoenergy conversion with TIO_2 photocatalysis: new materials and recent applications," *Electrochimica Acta*, vol. 84, pp. 103–111, 2012.

[14] U. I. Gaya and A. H. Abdullah, "Heterogeneous photocatalytic degradation of organic contaminants over titanium dioxide: a review of fundamentals, progress and problems," *Journal of Photochemistry and Photobiology C: Photochemistry Reviews*, vol. 9, no. 1, pp. 1–12, 2008.

[15] H. Al-Ekabi and N. Serpone, "Kinetic studies in heterogeneous photocatalysis," *Journal of Physical Chemistry*, vol. 92, no. 20, pp. 5726–5731, 1988.

[16] M. R. Prairie, L. R. Evans, B. M. Stange, and S. L. Martinez, "Treatment of water contaminated with metals and organic chemicals," *Environmental Science and Technology*, vol. 27, no. 9, pp. 1776–1782, 1993.

[17] M. Sadeghi, W. Liu, T.-G. Zhang, P. Stavropoulos, and B. Levy, "Role of photoinduced charge carrier separation distance in heterogeneous photocatalysis: oxidative degradation of CH_3OH vapor in contact with Pt/TIO_2 and cofumed TIO_2-Fe_2O_3," *Journal of Physical Chemistry*, vol. 100, no. 50, pp. 19466–19474, 1996.

[18] Y. Ohko, D. A. Tryk, K. Hashimoto, and A. Fujishima, "Autoxidation of acetaldehyde initiated by TIO_2 photocatalysis under weak UV illumination," *Journal of Physical Chemistry B*, vol. 102, no. 15, pp. 2699–2704, 1998.

[19] O. Seven, B. Dindar, S. Aydemir, D. Metin, M. A. Ozinel, and S. Icli, "Solar photocalytic disinfection of a group of bacteria and fungi aqueous suspensions with TIO_2, ZnO and sahara desert dust," *Journal of Photochemistry and Photobiology A: Chemistry*, vol. 165, no. 1–3, pp. 103–107, 2004.

[20] B. K. Moon, J. H. Jeong, S.-S. Yi et al., "Luminous properties of Tb^{3+} in the ZrO_2 and TIO_2 nanoparticles," *Journal of Luminescence*, vol. 122-123, no. 1-2, pp. 873–875, 2007.

[21] J. Qiu, S. Zhang, and H. Zhao, "Recent applications of TIO_2 nanomaterials in chemical sensing in aqueous media," *Sensors and Actuators B: Chemical*, vol. 160, no. 1, pp. 875–890, 2011.

[22] A. H. Zyoud, N. Zaatar, I. Saadeddin et al., "CdS-sensitized TIO_2 in phenazopyridine photo-degradation: catalyst efficiency, stability and feasibility assessment," *Journal of Hazardous Materials*, vol. 173, no. 1–3, pp. 318–325, 2010.

[23] S.-K. Lee, P. K. J. Robertson, A. Mills, and D. McStay, "Modification and enhanced photocatalytic activity of TIO_2 following exposure to non-linear irradiation sources," *Journal of Photochemistry and Photobiology A: Chemistry*, vol. 122, no. 1, pp. 69–71, 1999.

[24] W. Choi, "Pure and modified TIO_2 photocatalysts and their environmental applications," *Catalysis Surveys from Asia*, vol. 10, no. 1, pp. 16–28, 2006.

[25] M. Fernández-García, A. Martínez-Arias, J. C. Hanson, and J. A. Rodriguez, "Nanostructured oxides in chemistry: characterization and properties," *Chemical Reviews*, vol. 104, no. 9, pp. 4063–4104, 2004.

[26] M. Fei, Y. Zhijie, W. Linzhang, Z. Yuanming, and Z. Danming, "Influence of annealing temperature on structure and photocatalytic activity of TiO_2 thin films prepared by DC reactive magnetron sputtering method," *Wuhan University Journal of Natural Sciences*, vol. 17, no. 4, pp. 309–314, 2012.

[27] A. Burns, G. Hayes, W. Li, J. Hirvonen, J. D. Demaree, and S. I. Shah, "Neodymium ion dopant effects on the phase transformation in sol-gel derived titania nanostructures," *Materials Science and Engineering B: Solid-State Materials for Advanced Technology*, vol. 111, no. 2-3, pp. 150–155, 2004.

[28] L. Chen, M. E. Graham, G. Li, and K. A. Gray, "Fabricating highly active mixed phase TIO_2 photocatalysts by reactive DC magnetron sputter deposition," *Thin Solid Films*, vol. 515, no. 3, pp. 1176–1181, 2006.

[29] T. L. R. Hewer, E. C. C. Souza, T. S. Martins, E. N. S. Muccillo, and R. S. Freire, "Influence of neodymium ions on photocatalytic activity of TIO_2 synthesized by sol-gel and precipitation methods," *Journal of Molecular Catalysis A: Chemical*, vol. 336, no. 1-2, pp. 58–63, 2011.

[30] J. Liqiang, S. Xiaojun, X. Baifu, W. Baiqi, C. Weimin, and F. Honggang, "The preparation and characterization of la doped

TIO_2 nanoparticles and their photocatalytic activity," *Journal of Solid State Chemistry*, vol. 177, no. 10, pp. 3375–3382, 2004.

[31] H. R. Kim, T. G. Lee, and Y.-G. Shul, "Photoluminescence of La/Ti mixed oxides prepared using sol-gel process and their pCBA photodecomposition," *Journal of Photochemistry and Photobiology A: Chemistry*, vol. 185, no. 2-3, pp. 156–160, 2007.

[32] J. Liqiang, Q. Yichun, W. Baiqi et al., "Review of photoluminescence performance of nano-sized semiconductor materials and its relationships with photocatalytic activity," *Solar Energy Materials and Solar Cells*, vol. 90, no. 12, pp. 1773–1787, 2006.

[33] R. Kralchevska, M. Milanova, T. Tišler, A. Pintar, G. Tyuliev, and D. Todorovsky, "Photocatalytic degradation of the herbicide iodosulfuron by neodymium or nitrogen doped TIO_2," *Materials Chemistry and Physics*, vol. 133, no. 2-3, pp. 1116–1126, 2012.

[34] L. Yang, P. Liu, X. Li, and S. Li, "The photo-catalytic activities of neodymium and fluorine doped TIO_2 nanoparticles," *Ceramics International*, vol. 38, pp. 4791–4796, 2012.

[35] V. Gomez, A. M. Balu, J. C. Serrano-Ruiz et al., "Microwave-assisted mild-temperature preparation of neodymium-doped titania for the improved photodegradation of water contaminants," *Applied Catalysis A: General*, vol. 441-442, pp. 47–53, 2012.

[36] J. Domaradzki, D. Wojcieszak, E. Prociow, and D. Kaczmarek, "Characterization of transparent and nanocrystalline TIO_2:Nd thin films prepared by magnetron sputtering," *Acta Physica Polonica A*, vol. 116, pp. S75–S77, 2009.

[37] D. Kaczmarek, J. Domaradzki, A. Borkowska, A. Podhorodecki, J. Misiewicz, and K. Sieradzka, "Optical emission from Eu, Tb, Nd luminescence centers in TIO_2 prepared by magnetron sputtering," *Optica Applicata*, vol. 37, no. 4, pp. 433–438, 2007.

[38] M. Mazur, D. Kaczmarek, J. Domaradzki et al., "Structural and surface properties of TiO_2 thin films doped with neodymium deposited by reactive magnetron sputtering," *Materials Science-Poland*, vol. 31, no. 1, pp. 71–79, 2013.

[39] D. Wojcieszak, D. Kaczmarek, J. Domaradzki et al., "Photocatalytic properties of transparent TiO_2 coatings doped with neodymium," *Polish Journal of Chemical Technology*, vol. 14, no. 3, pp. 1–7, 2012.

[40] S. Rengaraj, S. Venkataraj, J.-W. Yeon, Y. Kim, X. Z. Li, and G. K. H. Pang, "Preparation, characterization and application of Nd-TIO_2 photocatalyst for the reduction of Cr(VI) under UV light illumination," *Applied Catalysis B: Environmental*, vol. 77, no. 1-2, pp. 157–165, 2007.

[41] V. Štengl, S. Bakardjieva, and N. Murafa, "Preparation and photocatalytic activity of rare earth doped TIO_2 nanoparticles," *Materials Chemistry and Physics*, vol. 114, no. 1, pp. 217–226, 2009.

[42] Y. Xie and C. Yuan, "Photocatalysis of neodymium ion modified TIO_2 sol under visible light irradiation," *Applied Surface Science*, vol. 221, no. 1–4, pp. 17–24, 2004.

[43] I. Nakamura, N. Negishi, and S. Kutsuna, "Preparation of high quality nitrogen doped TiO_2 thin film as a photocatalyst using a pulsed laser deposition method," *Journal of Molecular Catalysis A: Chemical*, vol. 161, no. 1-2, pp. 205–212, 2000.

[44] Y. Wang, H. Cheng, L. Zhang et al., "The preparation, characterization, photoelectrochemical and photocatalytic properties of lanthanide metal-ion-doped TIO_2 nanoparticles," *Journal of Molecular Catalysis A: Chemical*, vol. 151, no. 1-2, pp. 205–216, 2000.

[45] S. I. Shah, W. Li, C.-P. Huang, O. Jung, and C. Ni, "Study of Nd^{3+}, Pd^{2+}, Pt^{4+}, and Fe^{3+} dopant effect on photoreactivity of TIO_2 nanoparticles," *Proceedings of the National Academy of Sciences of the United States of America*, vol. 99, no. 2, pp. 6482–6486, 2002.

[46] W. Li, A. I. Frenkel, J. C. Woicik, C. Ni, and S. I. Shah, "Dopant location identification in Nd^{3+}-doped TIO_2 nanoparticles," *Physical Review B. Condensed Matter and Materials Physics*, vol. 72, no. 15, Article ID 155315, 2005.

[47] D. Wojcieszak, D. Kaczmarek, J. Domaradzki, and M. Mazur, "Correlation of photocatalysis and photoluminescence effect in relation to the surface properties of TiO_2:Tb thin films," *International Journal of Photoenergy*, vol. 2013, Article ID 526140, 9 pages, 2013.

[48] Powder Diffraction File, "Joint Committee on Powder Diffraction Standards," Philadelphia, Pa, USA, Card 21-1272, 1967.

[49] H. P. Klug and L. E. Alexander, *X-Ray Diffraction Procedures for Polycrystalline and Amorphous Materials*, John Wiley and Sons, New York, 2nd edition, 1974.

[50] W. Rasband, ImageJ, U.S. National Institutes of Health, Bethesda, Md, USA, 1997–2007, http://rsb.info.nih.gov/ij/.

[51] N. R. Khalid, E. Ahmed, and Z. Hong, "Graphene modified Nd/TiO_2 photocatalyst for methyl orange degradation under visible light irradiation," *Ceramics International*, vol. 39, pp. 3569–3575, 2013.

[52] A. Bokare, A. Sanap, M. Pai, S. Sabharwal, and A. A. Athawale, "Antibacterial activities of Nd doped and Ag coated TiO_2 nanoparticles under solar light irradiation," *Colloids and Surfaces B: Biointerfaces*, vol. 102, pp. 273–280, 2013.

Hindawi Publishing Corporation
International Journal of Photoenergy
Volume 2014, Article ID 210751, 10 pages
http://dx.doi.org/10.1155/2014/210751

Research Article

Oxidation of 4-Chlorophenol by Mesoporous Titania: Effect of Surface Morphological Characteristics

Osmín Avilés-García,[1] Jaime Espino-Valencia,[1] Rubí Romero,[2] José Luis Rico-Cerda,[1] and Reyna Natividad[2]

[1] *Facultad de Ingeniería Química, Universidad Michoacana de San Nicolás de Hidalgo, Edifico V1, Ciudad Universitaria, 58060 Morelia, MICH, Mexico*
[2] *Centro Conjunto de Investigación en Química Sustentable, UAEMéx-UNAM, Km 14.5 Carretera Toluca-Atlacomulco, San Cayetano, Piedras Blancas, Toluca, MEX, Mexico*

Correspondence should be addressed to Jaime Espino-Valencia; jespinova@yahoo.com.mx and Reyna Natividad; reynanr@gmail.com

Received 28 February 2014; Accepted 1 April 2014; Published 27 April 2014

Academic Editor: Wei Xiao

Mesoporous nanocrystalline anatase was prepared via EISA employing CTAB as structure directing agent. The drying rate was used as a key synthesis parameter to increase the average pore diameter. The resultant mesoporous crystalline phases exhibited specific surface areas between 55 and 150 $m^2\ g^{-1}$, average unimodal pore sizes of about 3.4 to 5.6 nm, and average crystallite size of around 7 to 13 nm. These mesophases were used as photocatalysts for the degradation of 4-chlorophenol (4CP) with UV light. Under the studied conditions, the mesoporous anatase degraded 100% 4CP. This was twice faster than Degussa P-25. 57% reduction of chemical oxygen demand (COD) value was achieved.

1. Introduction

TiO_2 is well known as the photocatalyst by excellence. It has been successfully applied to degrade and mineralize a vast amount of hazardous compounds in both air and water [1–5], under mild reaction conditions (low temperature and atmospheric pressure). Within photocatalysis area, it has been widely accepted that the catalyst feature determining its activity is the crystalline structure. Although this is true, other surface characteristics should not be completely left aside. This work aims to report the effect of surface morphological characteristics on mesoporous nanocrystalline anatase activity. The synthesis of the material was conducted by evaporation induced self-assembly approach (EISA). This method was elected since it is a powerful synthesis method to design technologically relevant and functional oxides in the fiber, particle, and film form at the nanoscale [6–9]. The method relies on using very dilute surfactant initial concentration from which a liquid crystalline mesophase is gradually developed upon solvent evaporation. The slow coassembly between the inorganic network and the liquid crystalline phase leads to the formation of long-range order of well-defined mesostructures. The preparation of mesoporous titania particles by EISA has been studied by independent research groups [10–13]. It is expected that a change in size, shape, and dimensions of the mesopore TiO_2 modifies the accessibility, adsorption, and diffusion of guest molecules within the pore network, thereby achieving further degradation. The photocatalytic activity of the synthesized TiO_2 was tested in the degradation of 4-chlorophenol (4CP).

Chlorinated aromatic compounds are a class of compounds widely used and constitute a particular group of priority pollutants. This is mainly due to their numerous origins (pesticide, paint, solvent, pharmaceutics, wood preserving chemicals, coke oven, and pulp industries) [14, 15] and toxic effects. They can be found in ground water, wastewater, and soil. In particular, chlorophenols (CPs) pose serious ecological problems as environmental pollutants due to their

high toxicity, recalcitrance, bioaccumulation, strong odor emission and persistence in environment, and suspected carcinogen and mutagen effect on the living [16, 17]. The photocatalytic degradation of chlorinated phenols in TiO_2 suspensions has been studied by many investigators [18–24]. The results show that phenolic compounds are degraded completely to CO_2 and H_2O through a mechanism involving hydroxylation of the aromatic ring. In particular, 4-chlorophenol (4CP) has been accepted as the standard pollutant for heterogeneous photocatalysis. The photocatalytic degradation of 4CP has been the topic of many investigations [25–29], and the kinetics of the photocatalytic degradation has been extensively studied [30–36]. Despite this vast literature, it still remains unclear whether there is an interaction or not between 4CP degradation and surface morphological characteristics of the employed photocatalyst. Therefore, it is relevant to conduct this study not only in the context of 4CP degradation but also in general within photocatalysis area.

2. Experimental

2.1. Materials and Synthesis. Titanium (IV) ethoxide ($C_8H_{20}O_4Ti$, 80% Aldrich) and titanium (IV) butoxide ($C_{16}H_{36}O_4Ti$, 97% Aldrich) were used as precursors. Hexadecyltrimethylammonium bromide, denoted as CTAB ($C_{19}H_{42}NBr$, 99% Sigma), was used as the structure directing agent (SDA). Ethanol (99.6%, Sigma-Aldrich) was used as organic solvent. Nitric acid (65.2%, Sigma-Aldrich) was used as catalyst.

The synthesis was performed as follows. An alcoholic solution of the precursor was prepared. This solution was added to the SDA under vigorous stirring, and then nitric acid was added dropwise. The resultant solution was stirred at room temperature for 3 h and then was dried at room temperature. Samples with different drying rates were placed in a rotary evaporator at 100 rpm (Heidolph G3 model) using oil as a heating medium. The synthesized powders were then calcined at 350°C and 400°C. It is worth clarifying that samples calcined at 350°C were first calcined at 300°C for 1 hour and then at 350°C for 4 hours with controlled heating and cooling rate of 1°C min^{-1} to remove the SDA. The same heating rate was used for the samples calcined at 400°C. The molar ratio of the as prepared samples was 1 precursor : 3.55 HNO_3 : 0.018 CTAB : 18.71 ethanol.

2.2. Characterization. Mesoporous titania samples were analyzed by X-ray diffraction (XRD) in a Bruker D8 Advanced diffractometer with Cu Kα radiation and a LynxEYE detector. BET surface areas and N_2 adsorption-desorption isotherms were obtained in an Autosorb-1 Quantachrome. Before measurements, samples were degassed at 250°C for 2 h. TEM images were taken with a JEOL-2100 200 kV LaB6 filament. The morphology and particle size of the mesophases were inspected with a SEM JEOL JSM-6510LV.

2.3. Heterogeneous Photocatalytic Oxidation of 4CP. Photocatalytic degradation studies of 4CP were performed in a batch photoreactor of cylindrical shape (see Figure 1). The photoreactor was provided with ports in the lower and upper section for the inlet and outlet of gases and for sampling. Mesoporous titania samples were placed in the glass reactor under continuous stirring (1000 rpm). The total reaction volume was 30 mL. Tests were performed using 0.8 g L^{-1} of mesoporous titania at an initial pH value of 2 and 4CP initial concentration $[4CP]_0$ was 0.233 mmol L^{-1}. The pH adjustment was made by using 0.003 M HCl solution. The temperature throughout the experiment was kept constant at 20°C. The UV lamp was placed at the center of the reactor as the source of UV radiation (254 nm at 0.786 watts cm^{-2}). Oxygen flow of 50 mL min^{-1} was constantly fed at the bottom of the reactor and an oxygen trap was used to increase its residence time. Aliquots samples (0.5 mL) were withdrawn from the system every 30 minutes during 3 hours. Catalyst was removed before analysis.

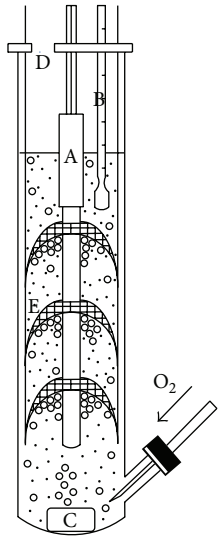

Figure 1: Experimental set-up. (A) UV lamp, (B) thermometer, (C) magnetic stirrer, (D) gas outlet and sampling, and (E) oxygen trap.

At all experiments, the concentration of 4CP (C_{4CP}) was determined using UV/Vis spectroscopy in a Perkin-Elmer Model Lambda 25 UV/Vis spectrophotometer with a wavelength range of 200–360 nm, where the characteristic absorption peak for 4-chlorophenol is located at 280 nm. A calibration curve was constructed from 0 to 0.311 mmol L^{-1}. A determination coefficient of $r^2 = 0.9994$ and a slope of $\varepsilon b = 0.0119$ were obtained. The experiments were repeated three times to verify results reliability.

The chemical oxygen demand (COD) value was analyzed with a Hach UV/Vis Model DR-5000 spectrophotometer in order to determine the degree of oxidation of the 4-chlorophenol after the photocatalytic tests.

3. Results and Discussion

3.1. Catalysts Characterization. The textural properties of the synthesized mesoporous titania with different type of drying are summarized in Table 1. The mesoporous samples that were dried at room temperature exhibited specific

Table 1: Specific surface area, average pore size, and average crystallite size of mesoporous titania samples with different type of drying.

Drying	Precursor	Sample ID	Calcination (°C)	Specific surface area (m^2/g)	Average pore size (nm)	Average crystallite size (nm)
Room temperature	Titanium ethoxide	AE3	350	117	3.4	7
		AE4	400	71	3.4	11
	Titanium butoxide	AB3	350	99	3.4	9
		AB4	400	55	3.4	13
Rotary evaporator	Titanium ethoxide	RE3	350	115	3.8	9
		RE4	400	87	4.3	11
	Titanium butoxide	RB3	350	145	4.3	8
		RB4	400	108	4.9	10

Table 2: Specific surface area, average pore size, and average crystallite size of mesoporous titania samples with different drying rate in rotary evaporator.

Drying rate	Calcination (°C)	Sample ID	Specific surface area (m^2/g)	Average pore size (nm)	Average crystallite size (nm)
Fast	350	FR3	150	3.8	8
	400	FR4	103	4.3	10
Medium	350	MR3 (RB3)	145	4.3	8
	400	MR4 (RB4)	108	4.9	10
Slow	350	SR3	147	4.9	8
	400	SR4	108	5.6	10

surface areas of around 117 $m^2\,g^{-1}$ and average pore size of approximately 3.4 nm. Furthermore, it was observed that the pore diameter remains constant and independent of the calcination temperature. However, the calcination conducted at 400°C decreases the specific surface area. Mesoporous samples dried in rotary evaporator exhibited specific surface areas of approximately 145 $m^2\,g^{-1}$ and average pore size of around 4.9 nm. Furthermore, it was observed that the calcination temperature modifies both the specific surface area and average pore diameter. For this type of drying, the best textural properties were obtained using titanium butoxide as precursor. The reactivity of the precursor determines the rates of hydrolysis and condensation to generate the final inorganic oxide structure. Also, the time used in these processes must be sufficient to allow proper interaction between the SDA and the inorganic precursor and generate assembly and organization in regular structures that finally will lead to an ordered mesoporous structure. For this reason, the titanium butoxide as precursor provides a more controlled reactivity and easy handling, thus allowing control of the hydrolysis and condensation reactions, as well as the dimensions of the pores directly related to the size of the alkoxy groups [37, 38].

The textural properties of the mesoporous titania phases synthesized with titanium butoxide as precursor and different drying rate in a rotary evaporator are summarized in Table 2. Specific surface areas and average pore size of samples were around 150 $m^2\,g^{-1}$ and 5.6 nm, respectively. When the drying rate became slower (at the same calcination temperature), the average pore diameter is observed to increase. Furthermore, the calcination temperature is found to be the only variable that modifies the specific surface area for these samples. Thus, the influence of the evaporation rate of volatile entities is a key parameter that determines the final mesostructure. The slow and gradual evaporation of the solvent promotes progressive increase in the concentration of the SDA by obtaining the critical micellar concentration (CMC), surfactant micelle formation, and their self-assembly with inorganic species at a specific time where the network is flexible enough leads to greater micellar arrangement [39].

The average crystallite size for all samples was estimated using the Scherrer equation and the FWHM of anatase (1 0 1) reflection. Crystal growth increases with a calcination temperature of 400°C for all samples. With increasing calcination temperature, the peak intensity of anatase increases (Figure 2), and the width of the (101) peak becomes narrower due to the growth of anatase crystallites. The pore diameter increase is caused by shrinkage of the mesoporous framework at higher temperatures [40].

The XRD patterns of all the mesophases exhibited only the characteristic reflections of anatase at approximately 2θ of 25°, 38°, 48°, 54°, 55°, and 63°. These correspond to the (1 0 1), (0 0 4), (2 0 0), (1 0 5), (2 1 1), and (2 0 4) planes, respectively, of tetragonal titania [13, 41] as shown in Figure 2.

Nitrogen adsorption-desorption isotherms and the Barrett-Joyner-Halenda (BJH) pore size distribution of synthesized samples are shown in Figure 3. All of these samples show a IV type isotherm with H_2 hysteresis loop, which is representative of mesoporous materials [42].

The TEM images of the mesoporous anatase samples AB4 (dried at room temperature) and SR4 (slow drying rate in rotary evaporator) are shown in Figure 4. For these samples,

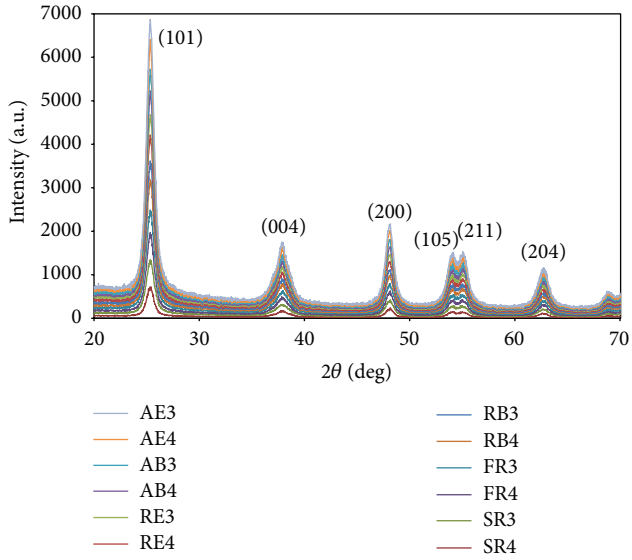

Figure 2: XRD patterns of the prepared mesoporous anatase samples.

Table 3: Initial reaction rates and removal of 4CP with the titania samples and Degussa P-25.

Sample ID	4CP degradation rate $-r_{4CF0} \times 10^8$ (mol/g seg)	Removal of 4CP (%)
AE3	6.30	69
AE4	2.47	62
AB3	8.85	67
AB4	3.93	60
RE3	3.92	75
RE4	7.00	80
RB3	10.27	86
RB4	4.68	93
FR3	5.94	77
FR4	4.42	82
SR3	10.46	95
SR4	13.54	100
Degussa P-25	6.97	57

the anatase crystals were determined to be approximately 13 and 10 nm in size, respectively. The spacing of 0.35 nm, measured for these two sets of fringes, coincides with 0.352 nm, that is, with the d-spacing of (1 0 1) type planes in the anatase form of titania, and this was confirmed by XRD data (Figure 2).

Figure 5 shows SEM images of the mesoporous anatase samples SR4 and AB4. The synthesized mesophase SR4 exhibited clusters of approximately 5–10 μm while the synthesized mesophase AB4 resulted in the formation of larger clusters of approximately 5–14 μm with irregular shapes.

The reference material Degussa P-25 contains anatase and rutile phases in a ratio of about 3 : 1. Anatase and rutile particles separately form their agglomerates and the average sizes of the anatase and rutile elementary particles are 85 and 25 nm, respectively [43]. Furthermore, their specific surface area is 52 $m^2 g^{-1}$ and the average crystallite size is 30 nm [44].

3.2. 4CP Degradation. The mesoporous anatase phases were evaluated in the photodegradation of 4CP. The photoactivity of these samples was compared to that of the reference material Degussa P-25. Figure 6 shows the photocatalytic degradation profiles of 4CP over the mesoporous titania samples and Degussa P-25. All synthesized titania samples showed a higher percentage of degradation than titania Degussa P-25. This may be related to the smaller crystallite size and relatively ordered pore structure of the obtained mesophases. Also, the enhanced photocatalytic activity of the mesoporous titania samples can be partially attributed to the presence of pure anatase phase which is the primary photoactive phase [45].

The mesoporous samples dried at room temperature (Figure 6(a)) and the ones dried in a rotary evaporator (Figure 6(b)) degraded approximately 60–69% and 75–93% of 4CP, respectively, after 180 min. Degussa P-25 degraded only 57% of 4CP after the same time of exposure to UV irradiation. Although mesoporous titania samples dried at room temperature showed the same average pore diameter of 3.4 nm, in Figure 6(a) it is evident that there are differences in the percentages of 4CP degradation due to different specific surface areas. For mesoporous titania samples dried in a rotary evaporator, the highest percentage of degradation (approximately 93%) was obtained with the highest average pore diameter of 4.9 nm (sample RB4), despite not having the largest specific surface area.

The mesoporous titania samples synthesized with different drying rate in a rotary evaporator (Figure 6(c)) degraded approximately 77–100% of 4CP. In Figure 6(c) it is evident that the increase in the percentage of degradation of 4CP is related to the increase in average pore diameters of synthesized samples, since the sample SR4 (average pore diameter of 5.6 nm and specific surface area of 108 $m^2 g^{-1}$) achieves 100% of 4CP degradation in 180 minutes and the sample SR3 achieved only 95% of degradation at the same time, despite having higher specific surface area (147 $m^2 g^{-1}$) and smaller average pore diameter of 4.9 nm. The ordered pore architecture of the mesoporous samples as compared to Degussa P-25 may result in higher diffusion rates of the guest molecules, and therefore the photocatalytic reaction rate increases. The benefits of having an ordered mesopore structure for photocatalytic applications have been demonstrated by independent research groups [46–48].

Table 3 shows the initial rates of degradation of 4CP for all samples synthesized and Degussa P-25. No effect of the average pore diameter was observed on the initial rate of degradation for the samples dried at room temperature. This may be due to several factors such as crystal size, because, when this decreases, the surface density of active sites available for substrate adsorption increases, thus increasing the photocatalytic reaction rate [49, 50].

Figure 7 shows the removal of 4CP by photocatalysis, adsorption, and photolysis using mesoporous titania sample

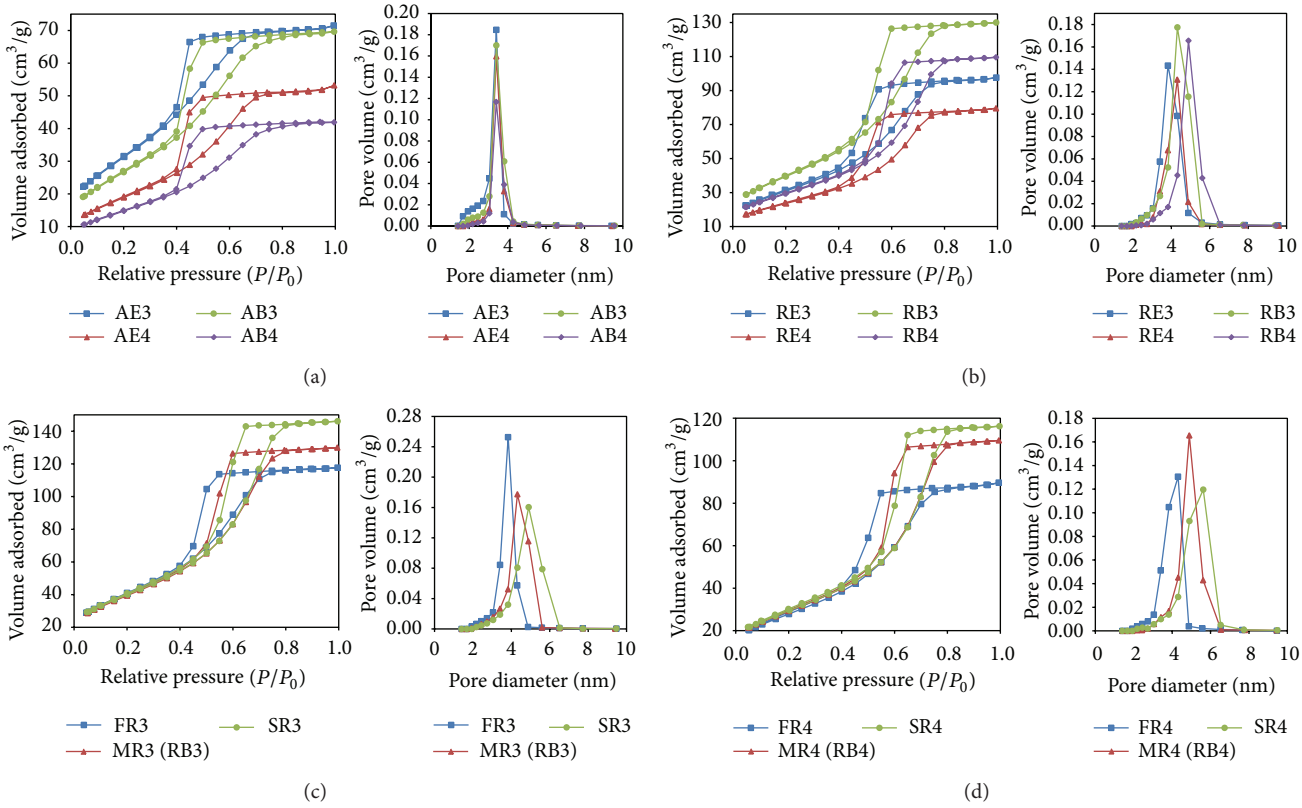

Figure 3: N_2 adsorption-desorption isotherms and pore size distribution of the mesoporous anatase phases dried (a) at room temperature (b) in rotary evaporator (c) with different rate in rotary evaporator and calcined at 350°C (d) with different rate in rotary evaporator calcined at 400°C.

Table 4: Apparent constant, half-life, and linearization coefficient for the Langmuir-Hinshelwood model for 4CP photodegradation.

Sample ID	k_{ap}	$t_{1/2}$ (min)	r^2
AE3	6.60	105.0	0.948
AE4	5.69	121.8	0.968
AB3	5.50	126.0	0.895
AB4	5.46	127.0	0.920
RE3	7.79	89.0	0.996
RE4	8.52	81.3	0.968
RB3	11.02	63.0	0.981
RB4	14.68	47.2	0.997
FR3	8.57	80.9	0.976
FR4	9.53	72.7	0.970
SR3	15.85	43.7	0.987
SR4	27.07	25.6	0.996
Degussa P-25	4.40	157.5	0.864

SR4 since 100% of 4CP degradation was achieved in 180 minutes. The effect of photolysis was studied by carrying out the experiment only in the presence of oxygen and UV light without mesoporous titania. The degradation of 4CP by direct photolysis is negligible, and the increase in concentration is due to an electronic effect that modifies the UV absorbance spectrum and appears as if it was an increase in concentration (Figure 8). This phenomenon has been described as a photoinduction period associated with reactions involving the formation of free radicals [51–53]. Furthermore, the removal of 4CP by adsorption is considered negligible (Figure 7).

The kinetics of photocatalytic reactions of organic compounds are usually adequately described by the Langmuir-Hinshelwood model [29, 51]. It relates the degradation rate

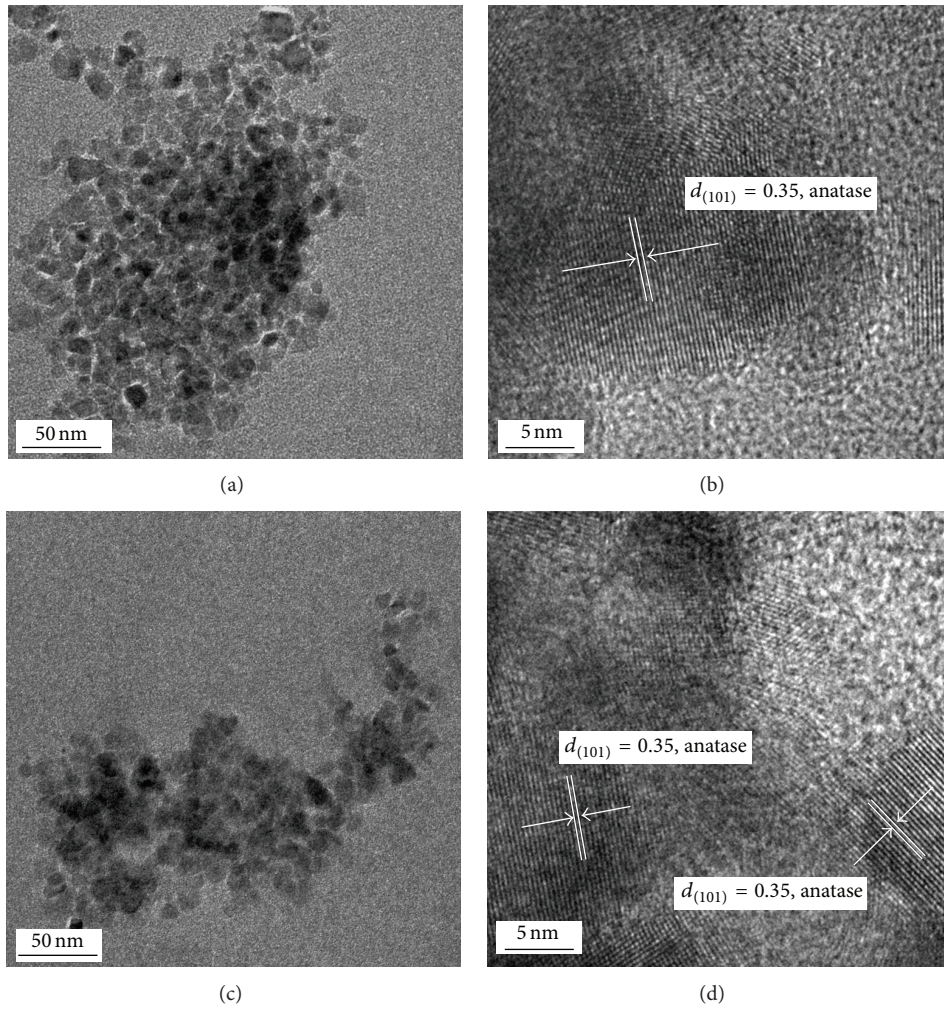

Figure 4: (a) and (c) TEM images of mesoporous nanocrystalline anatase samples AB4 and SR4. (b) A magnified image of (a) and (d) a magnified image of (c) with the d-spacing (1 0 1) of anatase form of titania.

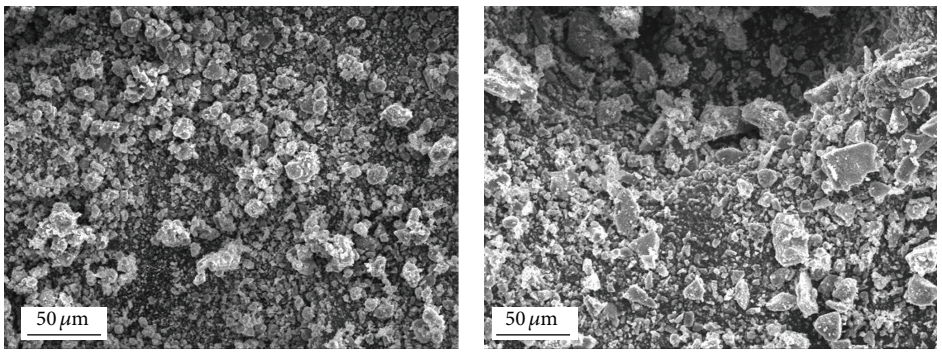

Figure 5: SEM images of the mesoporous anatase phases (a) SR4 (b) AB4.

r and the concentration of organic compound C and is expressed as follows:

$$r = -\frac{dC}{dt} = \frac{k_r K_{ad} C}{1 + K_{ad} C}, \quad (1)$$

where k_r is the intrinsic rate constant and K_{ad} is the adsorption equilibrium constant. If adsorption is weak and concentration of organic compounds is low, the factor $K_{ad}C$ is negligible, and thus (1) can be simplified to the first-order kinetics with an apparent rate constant ($K_{ap} = k_r K_{ad}$),

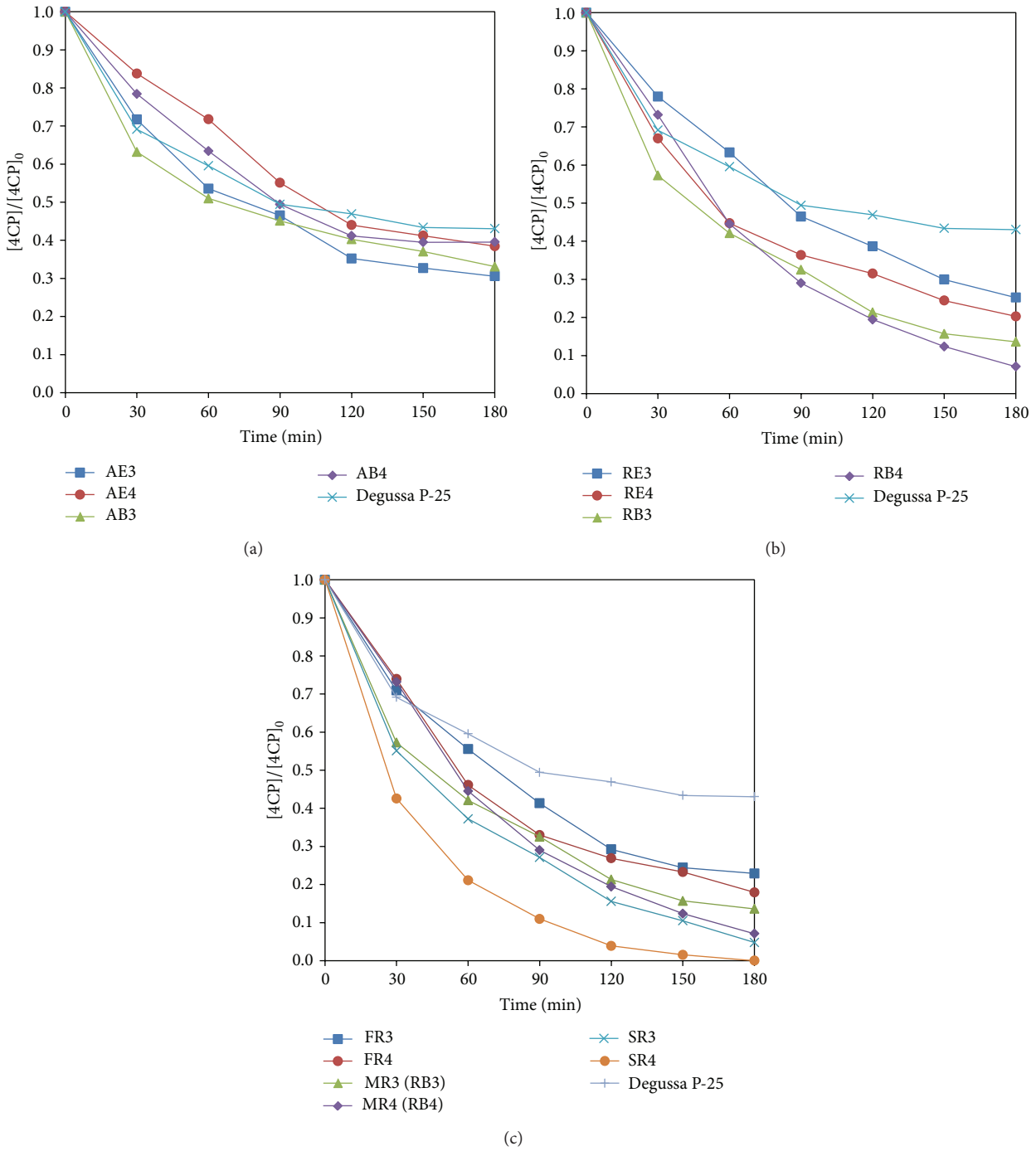

FIGURE 6: Photocatalytic degradation profiles of 4CP over the mesoporous titania samples synthesized with (a) room temperature, (b) rotary evaporator, (c) drying rate in rotary evaporator, and Degussa P-25.

which gives the following, after integration in the interval $[C, C_0]$:

$$\ln \frac{C_0}{C} = K_{ap} t. \quad (2)$$

Plotting $\ln(C_0/C)$ versus reaction time t yields a straight line, where the slope is the apparent rate constant. The half-life of the degraded organic compound can then be easily calculated. Figure 9 shows the lineal plot of 4CP photodegradation, which adjusts well to a pseudo-first-order kinetic behavior. Apparent constant K_{ap}, 4CP half-life, and the linearization coefficient r^2 are summarized in Table 4. 4CP half-life is as short as 25.6 min, with mesoporous titania sample SR4, and nearly 80% of initial 0.233 mmol L^{-1} is degraded in 60 minutes.

Table 5: COD values of the aqueous solution before and after photocatalytic tests, adsorption, and photolysis.

Sample	COD value (mg/L)	
	Initial (0 minutes)	Final (180 minutes)
SR4 (photocatalysis)	47	20
SR4 (adsorption)	47	47
Degussa P-25 (photocatalysis)	47	36
Photolysis	47	47

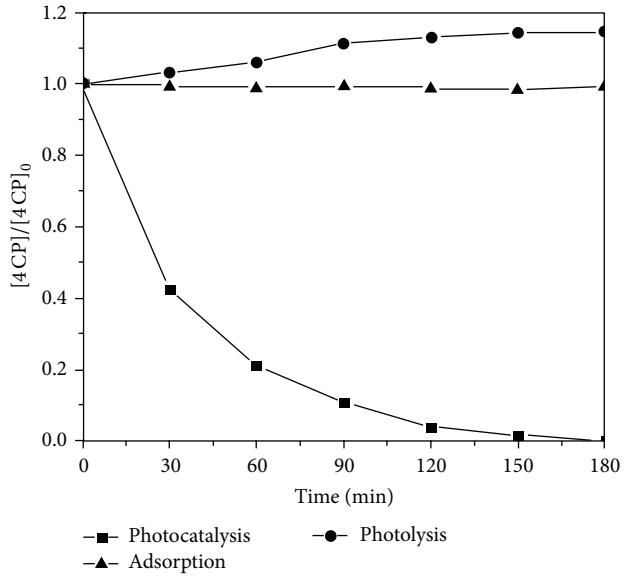

Figure 7: Effect of photocatalysis, adsorption, and photolysis on the removal of 4CP as a function of time using mesoporous titania sample SR4.

Table 5 shows the COD values to identify the presence of organic matter in the aqueous solution after photocatalytic tests. 4CP photodegradation using sample SR4 reduced the initial value of COD by 57%, whereas Degussa P-25 reduced the initial value of COD by 23% after the same time of exposure to UV irradiation. These results support the removal of 4CP by adsorption and photolysis shown in Figure 7, without reduction in initial values of COD. Therefore, it is demonstrated that the organic compound is mineralized. In specialized literature [34, 36], hydroquinone (HQ), benzoquinone (BQ), and 4-chlorocatechol (4CC) have been reported as the major aromatic intermediates, identified by HPLC, LC-MS, and GC-MS techniques. Although interesting, such characterization is beyond the scope of this paper.

4. Conclusions

Mesoporous nanocrystalline anatase was found to provide a faster degradation rate than Degussa P-25 as consequence of different surface morphological characteristics. Among the studied variables, different drying rate in rotary evaporator

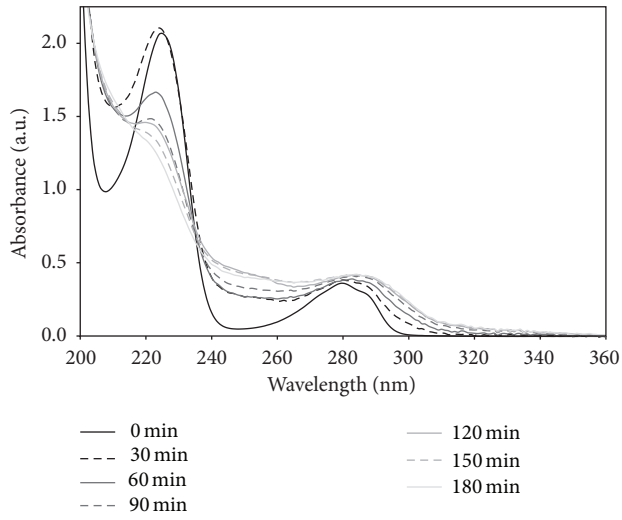

Figure 8: UV/Vis spectra of the 4CP degradation under photolysis.

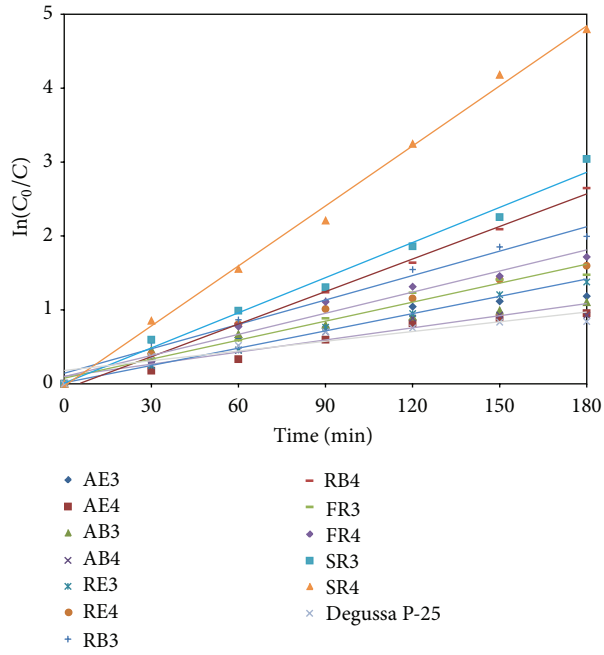

Figure 9: Pseudo-first-order kinetics degradation of 4CP, by the Langmuir-Hinshelwood model.

was determined to be the one that affects the increase in average pore diameter, and this affects both the percentage of photodegradation and the chemical oxygen demand (COD) value. The diffusion towards the active sites and the accessibility of the active sites for adsorption due to the presence of large pores are key parameters for the photocatalytic degradation of 4CP. The photodegradation process was found to be controlled by the Langmuir-Hinshelwood model. The mesoporous anatase degraded 100% 4CP, while Degussa P-25 degraded 57%. The enhanced photocatalytic activity of the

mesoporous titania samples when compared to Degussa P-25 was related to smaller crystallite size, presence of pure anatase phase, higher average pore diameter, and surface area. The reduction of 57% COD with mesoporous anatase compared with 23% Degussa P-25 shows that 4CP is mineralized.

Conflict of Interests

The authors declare that there is no conflict of interests regarding the publication of this paper.

Acknowledgments

The authors are grateful to PROMEP for financial support through Project 103.5/13/S257. Osmín Avilés-García thanks CONACYT for scholarship 290649 and CCIQS from UAEM for the granted support.

References

[1] R. W. Matthews, "Kinetics of photocatalytic oxidation of organic solutes over titanium dioxide," *Journal of Catalysis*, vol. 111, pp. 264–272, 1988.

[2] C. S. Turchi and D. F. Ollis, "Photocatalytic degradation of organic water contaminants: mechanisms involving hydroxyl radical attack," *Journal of Catalysis*, vol. 122, no. 1, pp. 178–192, 1990.

[3] D. W. Bahnemann, J. Cunningham, M. A. Fox, E. Pelizzetti, P. Pichat, and N. Serpone, "Photocatalytic treatment of waters," in *Aquatic Surface and Photochemistry*, R. G. Zepp, G. R. Helz, and D. G. Crosby, Eds., pp. 261–316, Lewis, Boca Raton, Fla, USA, 1994.

[4] M. R. Hoffmann, S. T. Martin, W. Choi, and D. W. Bahnemann, "Environmental applications of semiconductor photocatalysis," *Chemical Reviews*, vol. 95, no. 1, pp. 69–96, 1995.

[5] J.-M. Herrmann, "Heterogeneous photocatalysis: fundamentals and applications to the removal of various types of aqueous pollutants," *Catalysis Today*, vol. 53, no. 1, pp. 115–129, 1999.

[6] H. Yang, A. Kuperman, N. Coombs, S. Mamiche-Afara, and G. A. Ozin, "Synthesis of oriented films of mesoporous silica on mica," *Nature*, vol. 379, no. 6567, pp. 703–705, 1996.

[7] H. Yang, N. Coombs, I. Sokolov, and G. A. Ozin, "Free-standing and oriented mesoporous silica films grown at the air-water interface," *Nature*, vol. 381, no. 6583, pp. 589–592, 1996.

[8] Y. Lu, R. Ganguli, C. A. Drewien et al., "Continuous formation of supported cubic and hexagonal mesoporous films by sol-gel dip-coating," *Nature*, vol. 389, no. 6649, pp. 364–368, 1997.

[9] M. A. Carreon and V. V. Guliants, "Mesostructuring of metal oxides through EISA: fundamentals and applications," in *Ordered Porous Solids*, Chapter 16, pp. 413–439, 2009.

[10] G. J. D. A. A. Soler-Illia, A. Louis, and C. Sanchez, "Synthesis and characterization of mesostructured titania-based materials through evaporation-induced self-assembly," *Chemistry of Materials*, vol. 14, no. 2, pp. 750–759, 2002.

[11] K. De Witte, A. M. Busuioc, V. Meynen et al., "Influence of the synthesis parameters of TiO_2-SBA-15 materials on the adsorption and photodegradation of rhodamine-6G," *Microporous and Mesoporous Materials*, vol. 110, no. 1, pp. 100–110, 2008.

[12] M. A. Carreon, S. Y. Choi, M. Mamak, N. Chopra, and G. A. Ozin, "Pore architecture affects photocatalytic activity of periodic mesoporous nanocrystalline anatase thin films," *Journal of Materials Chemistry*, vol. 17, no. 1, pp. 82–89, 2007.

[13] M. L. Carreon, H. G. Carreon, J. Espino-Valencia, and M. A. Carreon, "Photocatalytic degradation of organic dyes by mesoporous nanocrystalline anatase," *Materials Chemistry and Physics*, vol. 125, no. 3, pp. 474–478, 2011.

[14] R. Andreozzi and R. Marotta, "Ozonation of p-chlorophenol in aqueous solution," *Journal of Hazardous Materials*, vol. 69, no. 3, pp. 303–317, 1999.

[15] C. H. Kuo and C. H. Huang, "Aqueous phase ozonation of chlorophenols," *Journal of Hazardous Materials*, vol. 41, no. 1, pp. 31–45, 1995.

[16] Y. Pi, L. Zhang, and J. Wang, "The formation and influence of hydrogen peroxide during ozonation of para-chlorophenol," *Journal of Hazardous Materials*, vol. 141, no. 3, pp. 707–712, 2007.

[17] M. L. Satuf, R. J. Brandi, A. E. Cassano, and O. M. Alfano, "Photocatalytic degradation of 4-chlorophenol: a kinetic study," *Applied Catalysis B: Environmental*, vol. 82, no. 1-2, pp. 37–49, 2008.

[18] J.-C. D'Oliveira, G. Al-Sayyed, and P. Pichat, "Photodegradation of 2- and 3-chlorophenol in TiO_2 aqueous suspensions," *Environmental Science and Technology*, vol. 24, no. 7, pp. 990–996, 1990.

[19] T. Pandiyan, O. M. Rivas, J. O. Martínez, G. B. Amezcua, and M. A. M. Carrillo, "Comparison of methods for the photochemical degradation of chlorophenols," *Journal of Photochemistry and Photobiology A: Chemistry*, vol. 146, pp. 149–155, 2002.

[20] J.-C. D'Oliveira, C. Minero, E. Pelizzetti, and P. Pichat, "Photodegradation of dichlorophenols and trichlorophenols in TiO_2 aqueous suspensions: kinetic effects of the positions of the Cl atoms and identification of the intermediates," *Journal of Photochemistry and Photobiology A: Chemistry*, vol. 72, no. 3, pp. 261–267, 1993.

[21] K. H. Wang, Y. H. Hsieh, M. Y. Chou, and C. Y. Chang, "Photocatalytic degradation of 2-chloro and 2-nitrophenol by titanium dioxide suspensions in aqueous solution," *Applied Catalysis B: Environmental*, vol. 21, pp. 1–8, 1999.

[22] Y.-C. Chan, J.-N. Chen, and M.-C. Lu, "Intermediate inhibition in the heterogeneous UV-catalysis using a TiO_2 suspension system," *Chemosphere*, vol. 45, no. 1, pp. 29–35, 2001.

[23] A. M. Peiró, J. A. Ayllón, J. Peral, and X. Doménech, "TIO_2-photocatalyzed degradation of phenol and *ortho*-substituted phenolic compounds," *Applied Catalysis B: Environmental*, vol. 30, pp. 359–373, 2001.

[24] U. Stafford, K. A. Gray, and P. V. Kamat, "Photocatalytic degradation of 4-chlorophenol: the effects of varying TiO_2 concentration and light wavelength," *Journal of Catalysis*, vol. 167, no. 1, pp. 25–32, 1997.

[25] U. Stafford, K. A. Gray, and P. V. Kamat, "Radiolytic and TiO_2-assisted photocatalytic degradation of 4-chlorophenol. A comparative study," *Journal of Physical Chemistry*, vol. 98, no. 25, pp. 6343–6351, 1994.

[26] A. Mills and J. Wang, "Photomineralisation of 4-chlorophenol sensitised by TiO_2 thin films," *Journal of Photochemistry and Photobiology A: Chemistry*, vol. 118, pp. 53–63, 1998.

[27] X. Li, J. W. Cubbage, T. A. Tetzlaff, and W. S. Jenks, "Photocatalytic degradation of 4-chlorophenol. 1. The hydroquinone pathway," *Journal of Organic Chemistry*, vol. 64, no. 23, pp. 8509–8524, 1999.

[28] X. Li, J. W. Cubbage, and W. S. Jenks, "Photocatalytic degradation of 4-chlorophenol. 2. The 4-chlorocatechol pathway,"

Journal of Organic Chemistry, vol. 64, no. 23, pp. 8525–8536, 1999.

[29] E. M. Campo, J. S. Valente, T. Pavón, R. Romero, Á. Mantilla, and R. Natividad, "4-chlorophenol oxidation photocatalyzed by a calcined Mg–Al–Zn layered double hydroxide in a co-current downflow bubble column," *Industrial & Engineering Chemistry Research*, vol. 50, pp. 11544–11552, 2011.

[30] H. Al-Ekabi, N. Serpone, E. Pelizzetti, C. Minero, M. A. Fox, and R. B. Draper, "Kinetic studies in heterogeneous photocatalysis. 2. TiO_2-mediated degradation of 4-chlorophenol alone and in a three-component mixture of 4-chlorophenol, 2,4-dichlorophenol, and 2,4,5-trichlorophenol in air-equilibrated aqueous media," *Langmuir*, vol. 5, no. 1, pp. 250–255, 1989.

[31] R. W. Matthews, "Purification of water with near-U.V. illuminated suspensions of titanium dioxide," *Water Research*, vol. 24, no. 5, pp. 653–660, 1990.

[32] G. Al-Sayyed, J. C. D'Oliveira, and P. Pichat, "Semiconductor-sensitized photodegradation of 4-chlorophenol in water," *Journal of Photochemistry and Photobiology A: Chemistry*, vol. 58, pp. 99–114, 1991.

[33] A. Mills, S. Morris, and R. Davies, "Photomineralisation of 4-chlorophenol sensitised by titanium dioxide: a study of the intermediates," *Journal of Photochemistry and Photobiology A: Chemistry*, vol. 70, pp. 183–191, 1993.

[34] A. Mills and S. Morris, "Photomineralization of 4-chlorophenol sensitized by titanium dioxide: a study of the initial kinetics of carbon dioxide photogeneration," *Journal of Photochemistry and Photobiology A: Chemistry*, vol. 71, pp. 75–83, 1993.

[35] J. Theurich, M. Lindner, and D. W. Bahnemann, "Photocatalytic degradation of 4-chlorophenol in aerated aqueous titanium dioxide suspensions: a kinetic and mechanistic study," *Langmuir*, vol. 12, no. 26, pp. 6368–6376, 1996.

[36] M. Hügül, I. Boz, and R. Apak, "Photocatalytic decomposition of 4-chlorophenol over oxide catalysts," *Journal of Hazardous Materials*, vol. 64, no. 3, pp. 313–322, 1999.

[37] M. Fröba, O. Muth, and A. Reller, "Mesostructured TiO_2: ligand-stabilized synthesis and characterization," *Solid State Ionics*, vol. 101–103, no. 1, pp. 249–253, 1997.

[38] S. Cabrera, J. El Haskouri, A. Beltrán-Porter, D. Beltrán-Porter, M. D. Marcos, and P. Amorós, "Enhanced surface area in thermally stable pure mesoporous TiO_2," *Solid State Sciences*, vol. 2, pp. 513–518, 2000.

[39] A. Gibaud, D. Grosso, B. Smarsly et al., "Evaporation-controlled self-assembly of silica surfactant mesophases," *Journal of Physical Chemistry B*, vol. 107, no. 25, pp. 6114–6118, 2003.

[40] T. Hongo and A. Yamazaki, "Thermal influence on the structure and photocatalytic activity of mesoporous titania consisting of TiO_2(B)," *Microporous and Mesoporous Materials*, vol. 142, no. 1, pp. 316–321, 2011.

[41] E. L. Crepaldi, G. J. D. A. A. Soler-Illia, D. Grosso, F. Cagnol, F. Ribot, and C. Sanchez, "Controlled formation of highly organized mesoporous titania thin films: from mesostructured hybrids to mesoporous nanoanatase TiO_2," *Journal of the American Chemical Society*, vol. 125, no. 32, pp. 9770–9786, 2003.

[42] K. S. W. Sing, D. H. Everett, R. A. W. Haul et al., "Reporting physisorption data for gas/solid systems with special reference to the determination of surface area and porosity (Recommendations 1984)," *Pure and Applied Chemistry*, vol. 57, pp. 603–619, 1985.

[43] T. Ohno, K. Sarukawa, K. Tokieda, and M. Matsumura, "Morphology of a TiO_2 photocatalyst (Degussa, P-25) consisting of anatase and rutile crystalline phases," *Journal of Catalysis*, vol. 203, no. 1, pp. 82–86, 2001.

[44] A. Katti, S. R. Venna, and M. A. Carreon, "Self-assembly hydrothermal assisted synthesis of mesoporous anatase in the presence of ethylene glycol," *Catalysis Communications*, vol. 10, no. 15, pp. 2036–2040, 2009.

[45] A. Mills and S. LeHunte, "An overview of semiconductor photocatalysis," *Journal of Photochemistry and Photobiology A: Chemistry*, vol. 108, pp. 1–35, 1997.

[46] Y. Sakatani, D. Grosso, L. Nicole, C. Boissiere, G. J. D. A. A. Soller-Illia, and C. Sanchez, "Optimised photocatalytic activity of grid-like mesoporous TiO_2 films: effect of crystallinity, pore size distribution, and pore accessibility," *Journal of Materials Chemistry*, vol. 16, pp. 77–82, 2006.

[47] K. De Witte, S. Ribbens, V. Meynen et al., "Photocatalytic study of P25 and mesoporous titania in aqueous and gaseous environment," *Catalysis Communications*, vol. 9, no. 8, pp. 1787–1792, 2008.

[48] E. Beyers, P. Cool, and E. F. Vansant, "Stabilisation of mesoporous TiO_2 by different bases influencing the photocatalytic activity," *Microporous and Mesoporous Materials*, vol. 99, no. 1-2, pp. 112–117, 2007.

[49] J. W. Moon, C. Y. Yun, and K. W. Chung, "Photocatalytic activation of TiO_2 under visible light using Acid Red 44," *Catalysis Today*, vol. 87, pp. 77–86, 2003.

[50] E. P. Reddy, B. Sun, and P. G. Smiriniotis, "Transition metal modified TiO_2-loaded MCM-41 catalysts for visible- and UV-light driven photodegradation of aqueous organic pollutants," *The Journal of Physical Chemistry B*, vol. 108, pp. 17198–17205, 2004.

[51] J. S. Valente, F. Tzompantzi, J. Prince, J. G. H. Cortez, and R. Gomez, "Adsorption and photocatalytic degradation of phenol and 2,4 dichlorophenoxiacetic acid by Mg-Zn-Al layered double hydroxides," *Applied Catalysis B: Environmental*, vol. 90, no. 3-4, pp. 330–338, 2009.

[52] J. S. Valente, F. Tzompantzi, and J. Prince, "Highly efficient photocatalytic elimination of phenol and chlorinated phenols by CeO_2/MgAl layered double hydroxides," *Applied Catalysis B: Environmental*, vol. 102, no. 1-2, pp. 276–285, 2011.

[53] G. Sivalingam, M. H. Priya, and G. Madras, "Kinetics of the photodegradation of substituted phenols by solution combustion synthesized TiO_2," *Applied Catalysis B: Environmental*, vol. 51, no. 1, pp. 67–76, 2004.

Hindawi Publishing Corporation
International Journal of Photoenergy
Volume 2014, Article ID 141368, 8 pages
http://dx.doi.org/10.1155/2014/141368

Research Article

Effect of Ce Doping on RGO-TiO_2 Nanocomposite for High Photoelectrocatalytic Behavior

Md. Rakibul Hasan, Chin Wei Lai, Sharifah Bee Abd Hamid, and Wan Jeffrey Basirun

Nanotechnology and Catalysis Research Centre (NANOCAT) and Institute of Postgraduate Studies, University of Malaya, Level 3, Block A, 50603 Kuala Lumpur, Malaysia

Correspondence should be addressed to Chin Wei Lai; cwlai@um.edu.my and Sharifah Bee Abd Hamid; sharifahbee@um.edu.my

Received 14 December 2013; Revised 13 January 2014; Accepted 13 January 2014; Published 15 April 2014

Academic Editor: Jiaguo Yu

Ce doped RGO-TiO_2 composite films on ITO substrates were prepared by sol-gel process using tetrabutyl titanate and reduced graphene oxide (RGO) as the starting materials. The sample was designed for the photoelectrocatalytic applications. The obtained samples were characterized by X-ray diffraction, UV-vis absorption spectroscopy, scanning electron microscopy, and Fourier transformed infrared spectroscopy. The results showed that doping of Ce on RGO-TiO_2 composite film inhibited the TiO_2 anatase-rutile phase transformation. In this case, Ce atoms could serve as dispersion oxide and suppress the recombination of photoinduced electron-hole pairs. Besides, the change in absorbance from UV to visible region was observed in Ce doped RGO-TiO_2 nanocomposite films. The Ce doped RGO-TiO_2 composite film showed higher photoelectrochemical performance than that of RGO-TiO_2 composite and pure TiO_2 under solar simulator irradiation. The main reason might be attributed to the optimum content of Ce that could act as electrons acceptor to hinder the recombination loss and facilitate the better transportation for photoinduced charge carriers.

1. Introduction

Today, high performance photoactive electrode is considered to be one of the probable solutions for utilization of solar energy. Efficient photoelectrocatalysis (PEC) process is greatly dependent on such an electrode surface which shows high photon absorption, less photocorrosion, mesoporous surface structure, and highly dispersed uniform active sites [1]. Various metal oxides, carbon nanomaterials, and so forth have been extensively investigated for photocatalytic applications such as H_2 production from water splitting, pollutants degradation, dye sensitized solar cells, and CO_2 photoreduction [2, 3]. But the overall photocatalytic performance under visible irradiation is still not satisfactory. Photocatalytic redox reaction under visible light irradiation can be enhanced by applying little bias potential and this electroassisted photocatalysis is called the photoelectrocatalysis (PEC) process.

After the invention of graphene in 2004, this two-dimensional sp2 bonded honeycomb-like carbon nanomaterial brought a massive change in electronics and solar and energy management devices. Reduced graphene oxide (RGO) support on photoelectrodes showed high electron mobility and high thermal resistivity and stability [4]. On the other hand, TiO_2, which is already commercially established as a photocatalyst material, shows better performance as catalyst support due to stability in chemical solution and its tunable textural properties. Although TiO_2 possesses excellent optoelectronic properties under UV irradiation, it shows poor absorption under visible light due to its wide band gap value of 3.2 eV. However, recent research showed that RGO-TiO_2 composite material can show higher photocatalytic activity under visible light [5–7]. This is due to broad expanse of the electronic state of RGO-TiO_2 coupling. Moreover, this coupling possesses high adsorption capacity, extended light absorption range, and enhanced charge separation and transportation properties [8].

Nevertheless, the difficulties of catalyst recovery, low visible light absorption, and fast recombination of electron-hole pairs are still the main pitfalls of using powder photocatalyst in aqueous media [9]. These drawbacks are crucial indeed

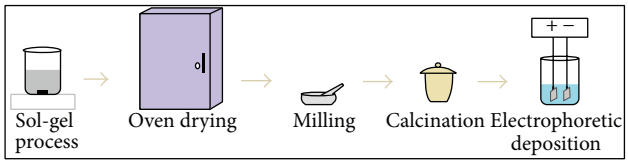

Figure 1: Schematic diagram of the experimental procedure.

for viable large scale applications like H_2 production from water and CO_2 conversion into useful fuels. However, the catalyst recovery and recycling difficulties can be avoided to a great extent using thin film photocatalysts. And the process when assisted with electrochemical bias can help to improve the overall efficiency of the photocatalytic process [10, 11]. Other than RGO-TiO_2 composite film, some other transition metal oxides such as ZnO, ZrO_2, NbO_5, and V_2O_5 also showed promising outcome in photocatalytic process [12, 13]. But in terms of stability and longtime functionality, both of the materials RGO and TiO_2 got benchmark performance in different photocatalytic activities like water splitting and dye degradation [14, 15]. It is noted that, even though RGO-TiO_2 can enhance their synergistic effects over a photocatalysis process, the electron-hole separation upon visible light irradiation is energetically unstable and recombination rates are very fast on the order of nanoseconds [16]. Experimental results showed that controlled charge separation in photoelectrocatalysis process rectifies electron transfer on the photocatalyst film and it also increases the electron availability on the conducting substrates.

The photocatalytic activity of RGO-TiO_2 composite can be more enhanced either by promoting the light absorption or by suppressing the electron-hole recombination rate through the incorporation of other species to the binary composites [17]. Some rare earth oxides show polymorphism, good thermal stability and good light absorption, and so forth due to their multielectron atoms including f orbital electrons. Previous experiments proved that, Ce ion, a rare earth metal which has the ability to enhance the photocatalytic activity of TiO_2 [18, 19]. This is due to the presence of different electronic structures (Ce^{3+}/Ce^{4+}) of cerium ion which show different electronic and optical properties of the catalyst. Thus, RGO-TiO_2 composite photocatalyst doped with Ce can act as exciton trap and might retard the fast electron/hole recombination. In essence, it can help to increase available photoelectrons on the surface. In the present study, we prepared Ce doped RGO-TiO_2 composite powder via sol-gel method and thin film photocatalyst was prepared via electrophoretic deposition method (Figure 1). Solar simulator was used to stimulate the thin film photocatalyst and studied in the PEC process. The photoelectrocatalytic conversion performance of the films as-prepared was examined, and the interesting results were obtained.

2. Experimental Methods

2.1. Catalyst Powder Preparation. Tetra-n-butyl orthotitanate (TBOT) was procured from Sigma-Aldrich and all other chemicals used in this work were of analytical grade. The indium tin oxide (ITO) coated conducting glass plates (0.7 mm thickness) were procured from Osaka, Japan. Graphene oxide was prepared via modified Hummer's method [20, 21]. Hydrazine treatment was done to obtain reduced graphene oxide (RGO) [22]. For the preparation of TiO_2, 4 mL TBOT was added with 20 mL of absolute ethanol and kept under stirring. This solution was added dropwise to a mixture of 2 mL of DI water and 1 wt% of cerium nitrate hexahydrate. Acetic acid was added to the mixture to keep the pH <3. This was followed by the addition of 1 wt% RGO, 2 mL of deionized water, and 5 mL ethanol and kept under sonication for 1 hour. This solution was added gradually with the previous solution. The total mixture was stirred for 30 minutes and kept for 24 hours for gel formation. The gel was dried at 70°C overnight. The dry porous gel was milled using mortar and pestle. The dried catalyst powder was calcined at 550°C for 4 h. The same procedure was followed to prepare RGO-TiO_2 composite and pure TiO_2 powder.

2.2. Thin Film Preparation. ITO coated glass substrate was cleaned with acetone, dehydrated alcohol, and ultrapure water, respectively. The powder photocatalyst was deposited on the ITO coated substrate via electrophoretic deposition method [23]. A DC power supply was used for the necessary current-voltage application. The substrate was cut into a 1 cm × 1 cm working area and used as both anode and cathode. The electrolyte composition was prepared at 1 mg/mL powder catalyst by sonication before the deposition process. The applied voltage was 60 V and deposition time was 1 min.

2.3. Characterizations of Catalysts. XRD spectra were recorded with a powder X-ray diffractometer (type Bruker D8 Advance equipped with EVA diffract software, Germany) over the range $20^\circ \leq 2\theta \leq 80^\circ$, operating at 40 kV and 40 mA, using Cu Kα radiation (k = 1.5418 A). A scanning electron microscope (SEM, Quanta FEI 200) was used to probe the coating materials on the surface of ITO coated glass substrates. A UV-vis spectrophotometer from PerkinElmer, Lambda 35 series, equipped with a 10 mm path length quartz cell was used for UV spectroscopic measurement. Fourier transformed infrared (FTIR) spectroscopy was recorded using a Bruker IFS 66V/S using a KBr technique.

All photoelectrochemical experiments were carried out with an Autolab PGSTAT302N potentiostat/galvanostat (EcoChemie, The Netherlands) with a three-electrode quartz cell. Ce-RGO-TiO_2/ITO, RGO-TiO_2/ITO, and TiO_2/ITO modified electrodes were used as the working electrode. A saturated calomel electrode (SCE) was used as the reference and a platinum wire was used as the counter electrode. A 0.1 M Na_2SO_4 solution was used as a supporting electrolyte. An active area of 1.0 cm^2 working electrodes for each sample was used in the photocurrent experiments. A 150 W solar simulator was used as a light source to study the photoelectrochemical response (Figure 2). The photocurrent was measured for the Ce-RGO-TiO_2 and the RGO-TiO_2 modified composite electrode at an applied potential of 0.02 V (SCE).

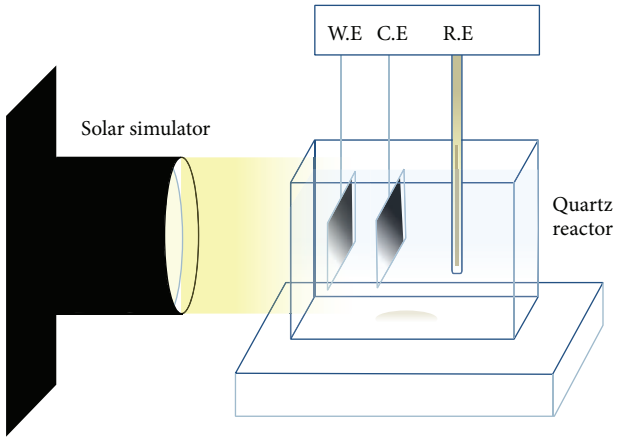

Figure 2: Quartz made photoelectrocatalytic (PEC) reactor with solar simulator.

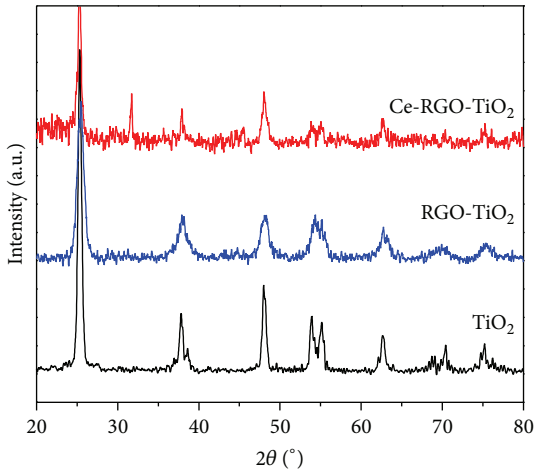

Figure 3: XRD pattern of pure TiO_2, RGO-TiO_2, and Ce-RGO-TiO_2.

3. Results and Discussion

The samples were collected by scraping off the pure TiO_2, RGO-TiO_2, and Ce doped RGO-TiO_2 from the ITO coated electrodes for XRD measurements to confirm that the samples are well crystallized. According to JCPDS data (reference code 832243), the peaks at 25.4° (1 0 1), 38.5° (1 1 2), and 48.6° (2 0 0) are the characteristic diffraction pattern of the anatase phase. The diffraction patterns are shown in Figure 3. No phase change from anatase to rutile was found in the samples although the calcination temperature was 550°C. In fact, the phase transformation can occur from anatase to rutile at 500–700°C [24]. Thus, the presence of Ce atoms can block the anatase-rutile phase transformation for TiO_2 [25]. The average crystallite size was calculated using Scherrer's formula (1) with respect to the anatase peaks. Consider

$$D = \frac{0.89\lambda}{\beta \cos\theta}, \quad (1)$$

where D = crystallite size, λ = wavelength of X-ray, β = full width at half maximum of the peak (in radians), and θ = angle of diffraction (in degrees) [26].

The crystallite size for the RGO-TiO_2 was between 40 and 62 nm which is similar to the pure TiO_2 nanoparticles. So, it can be concluded that RGO has no effect on the crystal structure of TiO_2 [27]. But, for Ce-RGO-TiO_2, the crystallite size was between 35 and 45 nm with respect to the Ti-anatase peaks which is lower than the RGO-TiO_2 or pure TiO_2. Thus, Ce atoms can suppress the growth of TiO_2 crystallite size. Moreover, due to the large difference in atomic radius between Ce and Ti (204 and 160 pm, resp.), the cations cannot be incorporated with each other. It is assumed that Ce atoms are dispersed on the surface of TiO_2. The XRD pattern for 1% Ce doped RGO-TiO_2 shows a characteristic peak for Ce at 33.09°. According to JCPDS reference code 340394, the peak is attributed to CeO_2 (2 0 0) plane. other peaks are not obvious due to high dispersion of CeO_2 on RGO-TiO_2 surface.

Figure 4 shows the SEM images of Ce-RGO-TiO_2 and RGO-TiO_2. It could be observed that while Ce-RGO-TiO_2 composite approximately exists in the form of spherical particles, RGO-TiO_2 exists mostly as granular structure. RGO could help the TiO_2 nanoparticles to disperse more smooth and uniform whereas Ce particles can improve the stability of the active phase. And, hence, the film surface was even and the film strength was observed to be higher than pure TiO_2. The thickness of the films was found to be roughly 2 μm. 1% RGO loading showed more homogeneous dispersion and electrochemical stability than higher percentage of RGO loading. Cerium atom dispersion with the RGO-TiO_2 structure has made the material more porous and hence the available active sites for redox reactions have increased. The average size was about ~40 nm, according to the value determined by XRD.

The morphology of Ce-RGO-TiO_2 was also observed with TEM. Figure 5 shows the porous structure with crystallite size below 50 nm which is well suited with XRD and SEM results. Agglomeration over the grain boundaries was observed in TiO_2 nanoparticles due to Ce doping.

The optical absorption spectra of the samples are shown in Figure 6. The RGO-TiO_2 and Ce doped RGO-TiO_2 showed higher photoabsorption in the visible region (>400 nm) compared to the pure TiO_2. Pure titania anatase showed an absorption edge at ~387 nm, while RGO incorporated TiO_2 also showed absorption at the same wavelength but with higher intensity. More photon absorption was observed for Ce-RGO-TiO_2 as well. Band gap values were determined by the following equation:

$$E_{bg} = \frac{1240}{\lambda}\ (\text{eV}), \quad (2)$$

where E_{bg} = band gap energy of the photocatalyst material and λ = maximum wavelength in nm.

A reduced band gap value was expected but no significant change in band gap energy was observed. This could be due to the aggregation of RGO material and the electron trap effect of ceria nanoparticles. The band gap energy was not much reduced and maximum absorption was still in the UV region for the modified TiO_2 samples. Nevertheless, more

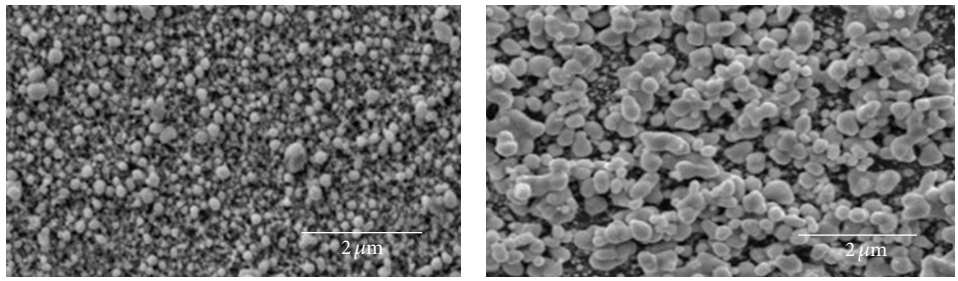

(a) (b)

Figure 4: SEM image of (a) RGO-TiO_2 and (b) Ce-RGO-TiO_2 coated ITO substrate.

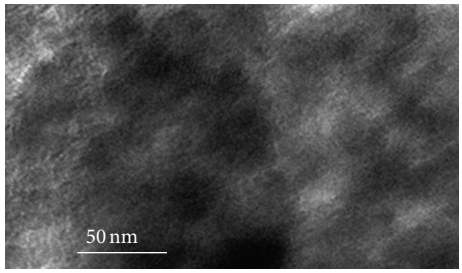

Figure 5: TEM image of Ce-RGO-TiO_2.

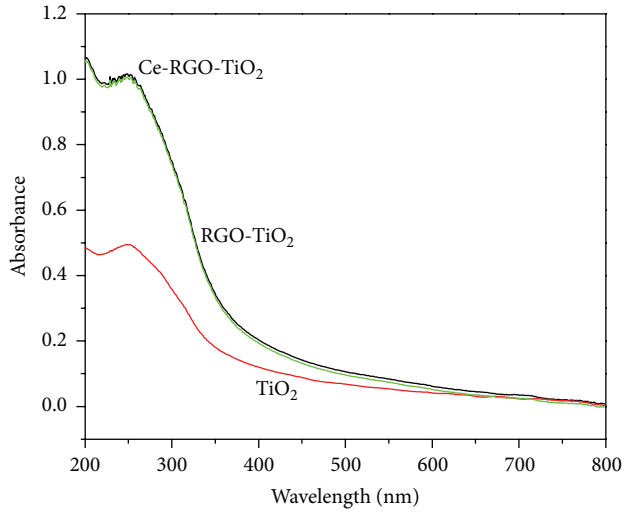

Figure 6: Effect of Ce loading on UV absorbance in RGO-TiO_2 photocatalysts.

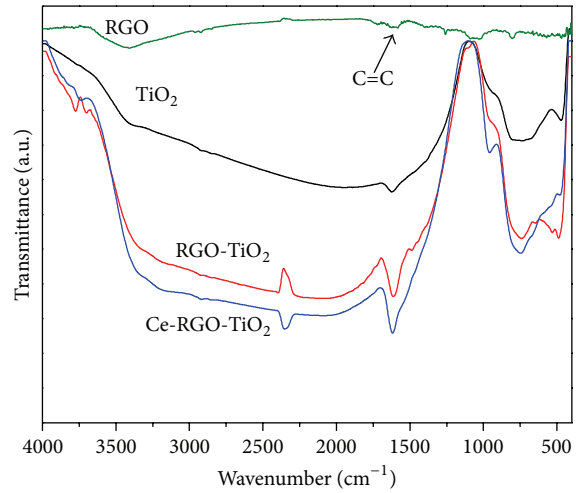

Figure 7: FTIR spectra of Ce doped RGO-TiO_2 composites.

photoelectrons can be produced using UV light source and it will ease the photocatalytic reduction process due to available electrons on the catalyst surface. It is clear that both RGO and Ce particles showed an enhanced photon absorption property in this respect.

The FTIR spectra of the samples were presented in Figure 7. It can be observed that, in RGO, most of the peaks for oxygen functional groups were eliminated whereas C=C skeletal vibration of graphene sheet is obvious at 1580 cm^{-1} [28]. It confirms that graphene oxide was reduced well and the surface became hydrophobic. In TiO_2, the broad peaks at 580 and 1050 cm^{-1} can be attributed to Ti–O–Ti and Ti–O stretching vibrations [29]. A band that slightly shifted from 1500 cm^{-1} in both RGO-TiO_2 and Ce-RGO-TiO_2 was also observed. It is attributed to the graphene sheet skeletal vibrations. The broad bands below 1000 to 600 cm^{-1} in TiO_2 composites can be assigned to Ti–O stretching vibrations [30]. The weak peak below 500 cm^{-1} in Ce-RGO-TiO_2 sample denotes Ce-O vibrational stretch [31].

The cyclic voltammetry for RGO-TiO_2/ITO and Ce-RGO-TiO_2/ITO modified electrodes are shown in Figure 8. The scan rate was fixed at 50 mV/s in the range of −1 V to +1 V. It is observed that both positive extraction peak and negative injection peak for RGO-TiO_2 and Ce-RGO-TiO_2 are obvious with little peak current. In the dark, both samples showed almost same characteristic peaks with a very small peak current (Table 1). But under visible light irradiation, both extraction and injection peaks are enhanced obviously. The Ce-RGO-TiO_2 showed the highest peak current while illumination, although Ce doping in RGO-TiO_2 did not enhance current efficiency in dark.

It can be concluded that Ce atoms can absorb photons and transfer to the electrons that gain more energy to produce photocurrent. 1% Ce doping showed an optimal

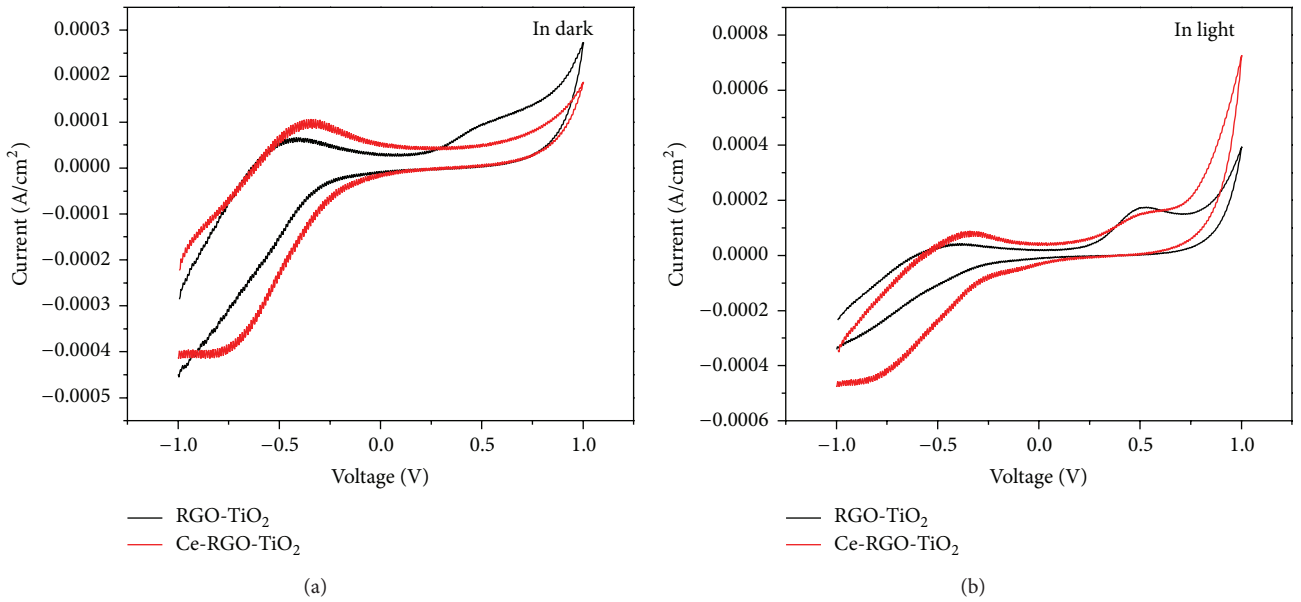

Figure 8: Cyclic voltammogram of catalytic activity with RGO-TiO_2/ITO and Ce-RGO-TiO_2/ITO modified electrodes in both dark and visible light irradiation.

Table 1: Peak current table for RGO-TiO_2 and Ce doped RGO-TiO_2 thin films (values in mA/cm^2).

Peak current	RGO-TiO_2 thin film		Ce doped RGO-TiO_2 thin film	
	Dark	Light	Dark	Light
+ve extraction peak current	0.3	0.3	0.2	0.7
−ve injection peak current	0.4	0.4	0.4	0.6

photocurrent value of 0.74 mA/cm^2. The RGO-TiO_2 sample showed another minor peak at 0.58 V both in dark and under light illumination. But that peak vanished in Ce-RGO-TiO_2 sample. The reason behind this could be due to the defect formation in octahedral TiO_2 structure from the doping with Ce. The regular TiO_2 octahedron structure became distorted and highly amorphous. This structure provided more open spaces in the crystal lattice and facilitated electron trapping. That could hide the minor peak current formation.

The photoelectrochemical performance is largely dependent on charge transfer and recombination properties of a photocatalyst material. In this case, electrochemical impedance spectrum (EIS) is very useful tool to investigate the charge carriers transfer and recombination processes at semiconductor/electrolyte interfaces. The samples were investigated for EIS responses and the components of complex impedance Z were plotted as Z'' (imaginary part) versus Z' (real part) in Nyquist plot (Figure 9).

The values were measured at open circuit potential for both dark and light irradiation periods. It can be observed that the samples formed pseudoarcs in the Nyquist plot for both dark and light irradiation periods. Under light irradiation, the photogenerated electrons moved from the electrode surface to the outer circuit. This phenomenon helped to reduce the interface resistance. Thus, the diameter of the loops was also reduced under light irradiation. The diameter of the loops was reduced for Ce doped RGO-TiO_2 samples as well. In fact, graphene can also show synergistic effect with doped metal atoms (here Ce) in terms of reducing charge transfer resistance [32]. In this case, the hybridization of Ce on RGO-TiO_2 composites leads to high-speed charge transport properties. This is due to the excellent Ce light absorption and ultrahigh electron mobility in graphene structures. The diameter actually reflects the rate of electron transfer which also indicates the photocatalytic reaction rate [1]. The equivalent circuit with the corresponding Nyquist plot is shown in Figure 10.

It can be simulated with Warburg semi-infinite diffusion model where a double layer capacitance and a charge transfer impedance are added with Warburg diffusion impedance. Here, polarization that occurred was influenced by the kinetic and diffusion processes and it can be interpreted by the Warburg model simulation. Here, R_s denotes the solution resistance. It showed the resistance value literally where the semicircle intercepts with the real axis at high frequency region. In this model, the passivation reaction was proposed and the resistance between the space charge layer and open Helmholtz layer was considered dependent on the double layer capacitance (C_{dl}) and charge transfer resistance (R_{ct}).

A simple mechanism of photoelectron excitation was illustrated in Figure 11. When light was illuminated with sufficient photon energy, the electron transfer happens from O (2p) valence band to Ti (3d) conduction band. The Ce

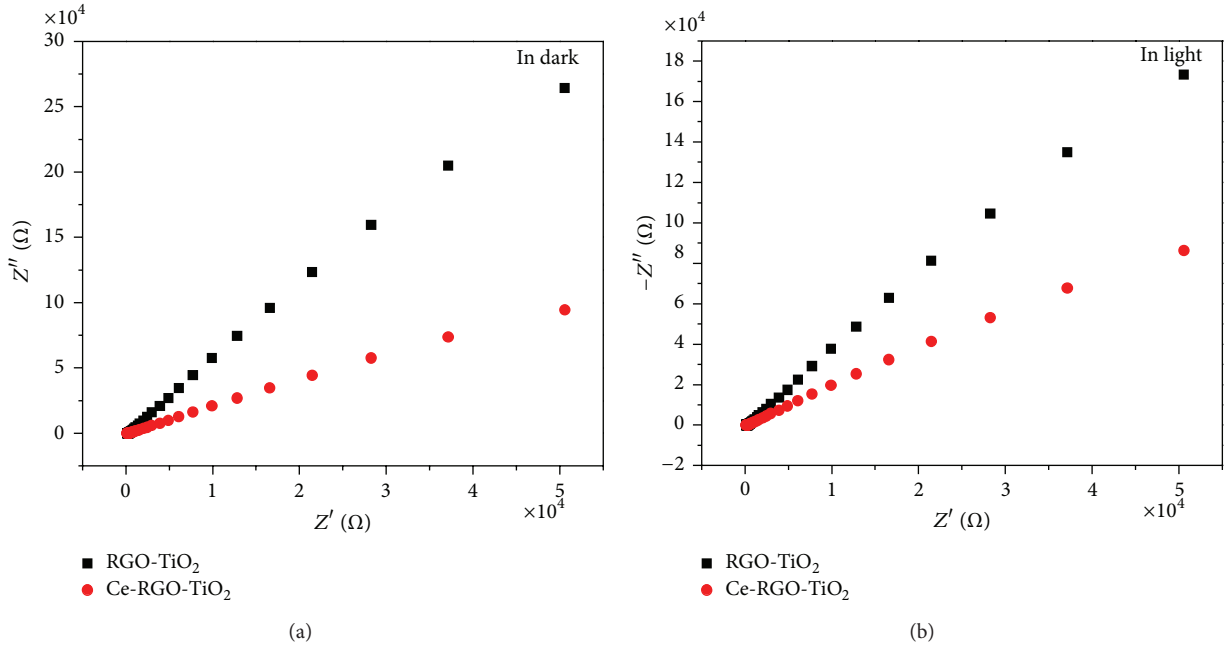

Figure 9: The EIS responses (Nyquist plots) of the RGO-TiO_2 and Ce doped RGO-TiO_2 film electrodes with and without light irradiation at open circuit potential (in dark) and at open circuit potential under visible light irradiation.

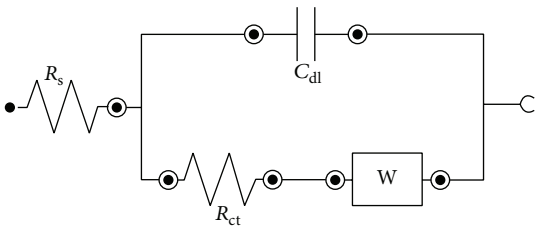

Figure 10: Warburg impedance simulation cell (equivalent circuit with mixed kinetic and charge transfer control).

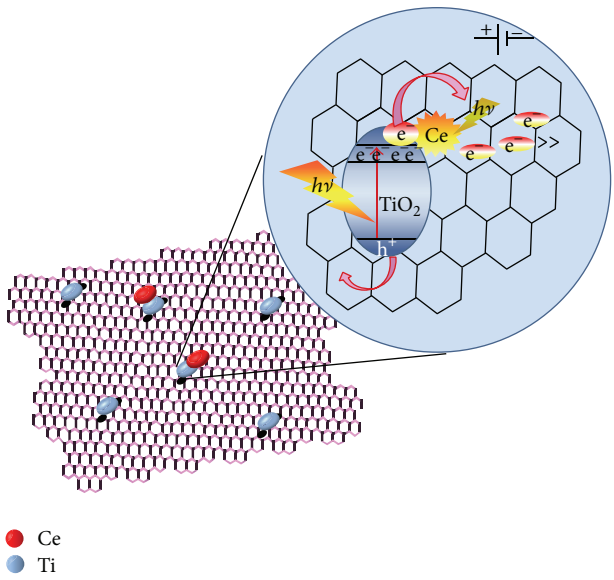

Figure 11: A schematic diagram of Ce doped RGO-TiO_2 composite and a rough presentation of photoelectron release mechanism.

atoms also absorb photon energy and transfer it to the photoelectrons. This incident drives the electrons intensely and it helps to reduce the recombination of electron-hole pairs.

The Ce atoms also act as a charge carrier trap. And finally, with the help of a little outer circuit bias, the electrons move steadily towards counter electrode. RGO π-electron conjugation structure favors the electron movement in this regard. Thus, electrons become available on counter electrode for redox species to be reduced, leaving the holes for the other species to be oxidized. Thus, the photocatalytic reaction proceeds and the photocurrent generated from the reaction becomes the driving force for the reaction. The whole process is still unclear to the researchers and we are lacking great deal of information about different behaviors of catalyst material towards different redox species. However, a combination of both theoretical and experimental results will help to understand in detail the PEC process.

When a semiconductor is dipped into an electrolyte containing redox species, the chemical potentials of electrons on both semiconductor and redox species will try to be in equilibrium. The charge transfer across the semiconductor surface will generate a space charge layer and band bending will occur. This is to minimize the effect of space charge layer in the semiconductor. Eventually, a potential barrier

is established so that further electron transfer could not occur. Under illumination, the space charge layer is weakened due to electron-hole separation [1]. The photons push the electrons inside the bulk of the semiconductor and thus the holes come out on the surface. Ultimately, the band bending decreases and it facilitates the movement of electrons towards outer circuit that is to the counter electrode. Thus, the photocurrent develops when the holes start to react with the redox species present in the electrolyte. The electron-hole separation can be enhanced by applying a small bias voltage to form overpotential on the electrode. This overpotential changes the width of the space charge layer and hinders the recombination of electron-hole pairs. Thus, more and more active species are oxidized on the semiconductor surface and photoelectrocatalytic process continues.

4. Conclusions

Ce doped RGO-TiO_2 composite thin films were prepared by sol-gel and electrophoretic deposition method. The sample showed enhanced photoelectrocatalytic activity compared to pure TiO_2 and RGO-TiO_2 composite films. The experiment was conducted under visible light irradiation. ITO immobilized Ce doped RGO-TiO_2 composite film can be an effective photocatalyst material with the assistance of electrochemical activity. Cerium atom absorbs photon at a higher degree and active photogenerated holes and electrons can be produced by applying an external bias. The excitons can be rectified towards efficient oxidation-reduction reaction. ITO glass substrate can provide a better route for the redox reactions to take place. Above all, the sample showed better stability even after 5-hour irradiation period. Further study is needed to understand the enhanced material efficiency.

Conflict of Interests

The authors declare that there is no conflict of interests regarding the publication of this paper.

Acknowledgment

The authors would like to thank University of Malaya for sponsoring this work under National Nanotechnology Directorate (NND-53-02031090), High Impact Research (HIR-F-000032) and IPPP grant (PG043-2012B) for their cordial support to complete this work.

References

[1] X. Meng, J. Yao, F. Liu et al., "Preparation of SnO_2@C-doping TiO_2 nanotube arrays and its electrochemical and photoelectrochemical properties," *Journal of Alloys and Compounds*, vol. 552, pp. 392–397, 2013.

[2] S. Morales-Torres, L. M. Pastrana-Martínez, J. L. Figueiredo, J. L. Faria, and A. M. T. Silva, "Design of graphene-based TiO_2 photocatalysts—a review," *Environmental Science and Pollution Research*, no. 19, pp. 3676–3687, 2012.

[3] Q. Xiang, J. Yu, and M. Jaroniec, "Graphene-based semiconductor photocatalysts," *Chemical Society Reviews*, vol. 41, no. 2, pp. 782–796, 2012.

[4] Q. Xiang and J. Yu, "Graphene-based photocatalysts for hydrogen generation," *The Journal of Physical Chemistry Letters*, vol. 4, no. 5, pp. 753–759, 2013.

[5] Z. Huimin, S. Fang, F. Xinfei, Y. Hongtao, W. Dan, and Q. Xie, "Graphene-TiO_2 Composite Photocatalyst with Enhanced Photocatalytic Performance," *Chinese Journal of Catalysis*, no. 33, pp. 777–782, 2012.

[6] W. Geng, H. Liu, and X. Yao, "Enhanced photocatalytic properties of titania-graphene nanocomposites: a density functional theory study," *Physical Chemistry Chemical Physics*, vol. 15, no. 16, pp. 6025–6033, 2013.

[7] Y. Zhang, N. Zhang, Z. R. Tang, and Y. J. Xu, "Improving the photocatalytic performance of graphene-TiO_2 nanocomposites via a combined strategy of decreasing defects of graphene and increasing interfacial contact," *Physical Chemistry Chemical Physics*, vol. 14, no. 25, pp. 9167–9175, 2012.

[8] L. Zhang, H. H. Mohamed, R. Dillert, and D. Bahnemann, "Kinetics and mechanisms of charge transfer processes in photocatalytic systems: a review," *Journal of Photochemistry and Photobiology C: Photochemistry Reviews*, vol. 13, no. 4, pp. 263–276, 2012.

[9] A. Panniello, M. L. Curri, D. Diso et al., "Nanocrystalline TiO_2 based films onto fibers for photocatalytic degradation of organic dye in aqueous solution," *Applied Catalysis B: Environmental*, vol. 121-122, pp. 190–197, 2012.

[10] M. Zhang, S. Yuan, Z. Wang, Y. Zhao, and L. Shi, "Photoelectrocatalytic properties of Cu2+-doped TiO_2 film under visible light," *Applied Catalysis B: Environmental*, vol. 134-135, pp. 185–192, 2013.

[11] G. Li, Y. Zhang, H. Sun et al., "Photocatalytic and photoelectrocatalytic degradation of small biological compounds: a case study of uridine," *Catalysis Today*, vol. 201, pp. 167–174, 2013.

[12] T. Inoue, A. Fujishima, S. Konishi, and K. Honda, "Photoelectrocatalytic reduction of carbon dioxide in aqueous suspensions of semiconductor powers," *Nature*, vol. 277, no. 5698, pp. 637–638, 1979.

[13] H. Inoue, H. Moriwaki, K. Maeda, and H. Yoneyama, "Photoreduction of carbon dioxide using chalcogenide semiconductor microcrystals," *Journal of Photochemistry and Photobiology A*, vol. 86, no. 1–3, pp. 191–196, 1995.

[14] Q. Xiang, J. Yu, and M. Jaroniec, "Enhanced photocatalytic H_2-production activity of graphene-modified titania nanosheets," *Nanoscale*, vol. 3, no. 9, pp. 3670–3678, 2011.

[15] C. Zhai, M. Zhu, F. Ren, Z. Yao, Y. Du, and P. Yang, "Enhanced photoelectrocatalytic performance of titanium dioxide/carbon cloth based photoelectrodes by graphene modification under visible-light irradiation," *Journal of Hazardous Materials*, vol. 263, part 2, pp. 291–298, 2013.

[16] X. Y. Zhang, H. P. Li, X. L. Cui, and Y. Lin, "Graphene/TiO_2 nanocomposites: synthesis, characterization and application in hydrogen evolution from water photocatalytic splitting," *Journal of Materials Chemistry*, vol. 20, no. 14, pp. 2801–2806, 2010.

[17] M. R. Hoffmann, S. T. Martin, W. Choi, and D. W. Bahnemann, "Environmental applications of semiconductor photocatalysis," *Chemical Reviews*, vol. 95, no. 1, pp. 69–96, 1995.

[18] T. D. Nguyen, C. T. Dinh, and T. O. Do, "A general procedure to synthesize highly crystalline metal oxide and mixed oxide

nanocrystals in aqueous medium and photocatalytic activity of metal/oxide nanohybrids," *Nanoscale*, vol. 3, no. 4, pp. 1861–1873, 2011.

[19] Y. Xie and C. Yuan, "Visible-light responsive cerium ion modified titania sol and nanocrystallites for X-3B dye photodegradation," *Applied Catalysis B: Environmental*, vol. 46, no. 2, pp. 251–259, 2003.

[20] W. S. Hummers Jr. and R. E. Offeman, "Preparation of graphitic oxide," *Journal of the American Chemical Society*, vol. 80, no. 6, p. 1339, 1958.

[21] N. Huang, H. Lim, C. Chia, M. Yarmo, and M. Muhamad, "Simple room-temperature preparation of high-yield large-area graphene oxide," *International Journal of Nanomedicine*, vol. 6, pp. 3443–3448, 2011.

[22] S. Stankovich, D. A. Dikin, R. D. Piner et al., "Synthesis of graphene-based nanosheets via chemical reduction of exfoliated graphite oxide," *Carbon*, vol. 45, no. 7, pp. 1558–1565, 2007.

[23] H. Zhang, X. Zhang, D. Zhang et al., "One-step electrophoretic deposition of reduced graphene oxide and $Ni(OH)_2$ composite films for controlled syntheses supercapacitor electrodes," *The Journal of Physical Chemistry B*, vol. 117, no. 6, pp. 1616–1627, 2013.

[24] S. Ngamta, N. Boonprakob, N. Wetchakun, K. Ounnunkad, S. Phanichphant, and B. Inceesungvorn, "A facile synthesis of nanocrystalline anatase TiO_2 from $TiOSO_4$ aqueous solution," *Materials Letters*, vol. 105, pp. 76–79, 2013.

[25] Y. H. Xu, H. R. Chen, Z. X. Zeng, and B. Lei, "Investigation on mechanism of photocatalytic activity enhancement of nanometer cerium-doped titania," *Applied Surface Science*, vol. 252, no. 24, pp. 8565–8570, 2006.

[26] M. Hamadanian, A. Reisi-Vanani, and A. Majedi, "Synthesis, characterization and effect of calcination temperature on phase transformation and photocatalytic activity of Cu,S-codoped TiO_2 nanoparticles," *Applied Surface Science*, vol. 256, no. 6, pp. 1837–1844, 2010.

[27] S. Liu, H. Sun, S. Liu, and S. Wang, "Graphene facilitated visible light photodegradation of methylene blue over titanium dioxide photocatalysts," *Chemical Engineering Journal*, no. 214, pp. 298–303, 2012.

[28] C. Nethravathi and M. Rajamathi, "Chemically modified graphene sheets produced by the solvothermal reduction of colloidal dispersions of graphite oxide," *Carbon*, vol. 46, no. 14, pp. 1994–1998, 2008.

[29] F. Q. Tang, L. P. Hou, and G. S. Guo, "Preparation of TiO_2 nanometer powders," *Journal of Inorganic Materials*, vol. 16, no. 4, pp. 615–619, 2001.

[30] J. Shen, B. Yan, M. Shi, H. Ma, N. Li, and M. Ye, "One step hydrothermal synthesis of TiO_2-reduced graphene oxide sheets," *Journal of Materials Chemistry*, vol. 21, no. 10, pp. 3415–3421, 2011.

[31] X. H. Liao, J. M. Zhu, J. J. Zhu, J. Z. Xu, and H. Y. Chen, "Preparation of monodispersed nanocrystalline CeO_2 powders by microwave irradiation," *Chemical Communications*, no. 10, pp. 937–938, 2001.

[32] J. Low, J. Yu, Q. Li, and B. Cheng, "Enhanced visible-light photocatalytic activity of plasmonic Ag and graphene co-modified Bi_2WO_6 nanosheets," *Physical Chemistry Chemical Physics*, vol. 16, no. 3, pp. 1111–1120, 2014.

Hindawi Publishing Corporation
International Journal of Photoenergy
Volume 2014, Article ID 867565, 8 pages
http://dx.doi.org/10.1155/2014/867565

Research Article

Synthesis and Photocatalytic Activity of Magnetically Recoverable Core-Shell Nanoparticles

Zhen Peng,[1] Hua Tang,[1] Yao Tang,[2] Ke Fu Yao,[2] and Hong Hong Shao[1]

[1] *School of Materials Science and Engineering, Jiangsu University, Zhenjiang 212013, China*
[2] *School of Materials Science and Engineering, Tsinghua University, Beijing 100084, China*

Correspondence should be addressed to Zhen Peng; peng@ujs.edu.cn and Ke Fu Yao; kfyao@tsinghua.edu.cn

Received 7 March 2014; Accepted 25 March 2014; Published 14 April 2014

Academic Editor: Jiaguo Yu

$TiO_2/SiO_2/Fe_3O_4$ (TSF) core-shell nanoparticles with good photocatalytic activity that are capable of fast magnetic separation have been successfully prepared by chemical coprecipitation and two-step sol-gel process. The as-prepared TSF nanoparticles were calcined at high temperature in order to transform the amorphous titanium dioxide into a photoactive crystalline phase. The calcined nanoparticles are composed of a Fe_3O_4 core with a strong response to external magnetic fields, a SiO_2 intermediary layer, and a TiO_2 outshell. Vibration sample magnetometer (VSM) analysis confirms the superparamagnetism of calcined nanoparticles, which can enhance the recoverable properties of the novel photocatalyst. When the $TiO_2/SiO_2/Fe_3O_4$ core-shell nanoparticles are added to the crude oily wastewater, they exhibit high photocatalytic activity in the degradation of crude oily wastewater. The oil concentration could be reduced to lower than 30 ppm within 20 minutes for the case of initial oil concentration less than 350 ppm. It has been found that the TSF nanoparticles could be easily separated from the wastewater and withdrawn by using an external magnetic field. The recovered TSF nanoparticles possess high efficiency in the degradation of crude oily wastewater even after three times successive reuse. The present results indicate that TSF core-shell nanoparticles possess great application perspectives in the degradation of crude oily wastewater.

1. Introduction

Photocatalytic technology offers a facile and cheap method for removing inorganic and organic pollutants from wastewater [1–4], since most pollutants could be degraded or mineralized by use of photocatalytic degradation technology [5–7]. Photocatalysts used in UV or near-UV light activated processes are semiconductor materials such as TiO_2, ZnO, and CdS [8, 9]: among them, the nanosized titanium dioxide is one of the most widely used photocatalysts due to its high photocatalytic activity, low cost, good stability, and nontoxic nature [10–12].

When TiO_2 photocatalyst is employed in the degradation of wastewater by photocatalytic process, it could be suspended in wastewater directly or be supported on substrate materials firstly and then immersed in wastewater with substrates. Nanosized TiO_2 photocatalyst can either be suspended in wastewater or be supported on substrate materials. Nanosized TiO_2 photocatalyst immobilized on substrate materials (such as glass, zeolite, silica, and ceramic) would benefit its separation from the wastewater. However, the activity of TiO_2 photocatalyst in the fixed state is reduced to a considerable extent because the effective surface area of TiO_2 photocatalyst decreases dramatically after the immobilization of TiO_2. In addition, TiO_2 photocatalyst may easily fall off the substrate materials, which make their complete recovery from wastewater difficult [13, 14]. So developing recoverable TiO_2 photocatalysts with high photocatalytic activity is meaningful and imperative. It has been reported that magnetic separation provides a suitable solution of this problem for removing TiO_2 photocatalysts from wastewater and reusing by applying external magnetic field [15–21]. The combination of TiO_2 photocatalyst and magnetic oxide nanoparticles (Fe_3O_4, γ-Fe_2O_3, and α-Fe_2O_3)

may enhance the separation and recoverable property of nanosized TiO_2 photocatalyst. However, compared with nanosized TiO_2, the magnetic oxide nanoparticles are much more unstable, especially under acidic conditions. Beydoun et al. [22, 23] reported a photo-dissolution phenomenon, which was found in the coating anatase TiO_2 directly onto magnetite. Electronic interactions will occur between TiO_2 and magnetite core, which not only deteriorates the photocatalytic activity of TiO_2, but also changes the magnetic properties of magnetite core. Furthermore, the preparing process of TiO_2 photocatalyst usually involves a high temperature annealing, magnetic oxide nanoparticles such as Fe_3O_4 or γ-Fe_2O_3, if treated concurrently, may transform to antiferromagnetic α-Fe_2O_3, which will reduce the property of magnetic response [24]. A suitable solution of this problem is the utilization of a passive interlayer SiO_2 between the magnetic core and TiO_2 shell. It has been found the SiO_2 layer promotes the photocatalytic activity of the catalyst by decreasing the negative effect of magnetic core [25, 26]. However, in prior studies the photocatalytic activity of combined photocatalysts did not show much improvement when compared with anatase-form nanoparticles, probably because the size of TiO_2 shell and magnetic core was not controlled reasonably.

In present study, the TSF core-shell magnetic nanoparticles, which constitute a Fe_3O_4 layer, a SiO_2 intermediary layer, and a TiO_2 outer shell, have been successfully prepared. The TSF core-shell magnetic photocatalysts exhibit high photocatalytic efficiency, which is the same as the well-known commercial photocatalyst P25, a mixture of 80% anatase and 20% rutile form of TiO_2 produced by Degussa Chemical Company (Germany). As a result, the TSF core-shell magnetic photocatalysts can be efficiently recovered from the solution by using external magnetic field for many times without significant loss of photocatalysts and photocatalytic activity. The photocatalytic activity of the as-prepared TSF core-shell magnetic nanoparticles and the recovered ones has been studied by photocatalytic experiments in the degradation of crude oily wastewater.

2. Experiment

2.1. Synthesis of Fe_3O_4 Core. The Fe_3O_4 superparamagnetic cores were prepared by the chemical coprecipitation method. The Fe_3O_4 cores were synthesized with the mixed solution of ferric chloride hexahydrate ($FeCl_3{\cdot}6H_2O$) and ferric chloride tetrahydrate ($FeCl_2{\cdot}4H_2O$) at 80°C for 1 h, together with a suitable amount of ammonia (NH_4OH). The solution was centrifuged and washed with distilled water, and the Fe_3O_4 cores were dried for 12 h. The average size of the prepared Fe_3O_4 cores is around 8–10 nm.

2.2. Synthesis of SiO_2/Fe_3O_4 Nanoparticle. The SiO_2 intermediary layer was prepared by using the sol-gel method. The above Fe_3O_4 cores were mixed with ethanol (50 mL) and ammonia under vigorous magnetic stirring. TEOS was added into the solution slowly and then aged for 5 h. After being washed with ethanol three times, SiO_2/Fe_3O_4 (SF) nanoparticle was dispersed in ethanol for using.

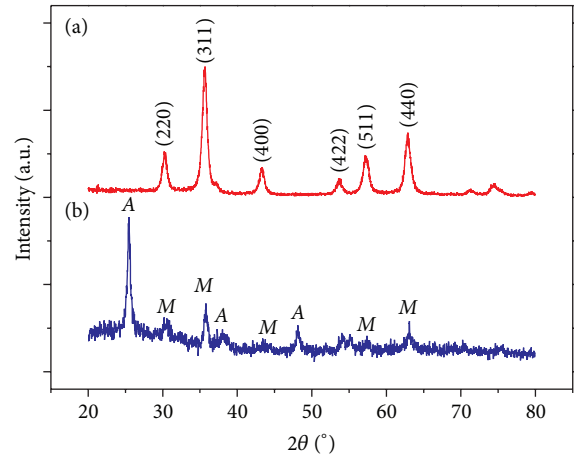

FIGURE 1: (a) XRD patterns of Fe_3O_4 core and (b) TSF photocatalyst. *A*: anatase and *M*: magnetite.

2.3. Synthesis of $TiO_2/SiO_2/Fe_3O_4$ Photocatalyst. The outer layer TiO_2 was prepared by using the sol-gel method. The SiO_2/Fe_3O_4 (SF) nanoparticles were mixed with ethanol (50 mL) and ammonia under ultrasonic dispersion for 30 min. An appropriate amount of TBOT was added into the solution drop by drop. The final photocatalysts were washed with ethanol three times, dried at 60°C for 48 h, and finally were calcined at 450°C for 3 h.

2.4. Characterization. The crystalline structure of particles was examined by using a Rigaku *D*/max-RB X-ray diffraction (XRD) spectrometry with Cu-Ka radiation. The size and microstructure of samples have been characterized with JEM 200CX transmission electron microscope (TEM) with 200 kV operating voltage and JEOL-2011 high resolution transmission electron microscopy (HRTEM). The magnetic property of samples was measured with Lakeshore 7307 vibration sample magnetometer (VSM). The porosity of samples was measured by the nitrogen adsorption-desorption isotherm and BJH methods on the micromeritics ASAP 2000 specific surface area instrument. A UV-2802PC ultraviolet-visible spectrometer was used to measure the UV/Vis absorption spectrum of the solutions to monitor the concentration of crude oil at different time intervals.

2.5. Photocatalytic Degradation of Crude Oily Wastewater. Photocatalytic activities of the nanoparticles have been evaluated by degradation experiments of modulated crude oily wastewater in a self-made photocatalytic reactor. An 8 W UV lamp was used as the ultraviolet light source and air-blowing apparatus has been used; 0.2 g/L TSF and 0.067 g/L commercial TiO_2 were suspended in the modulated crude

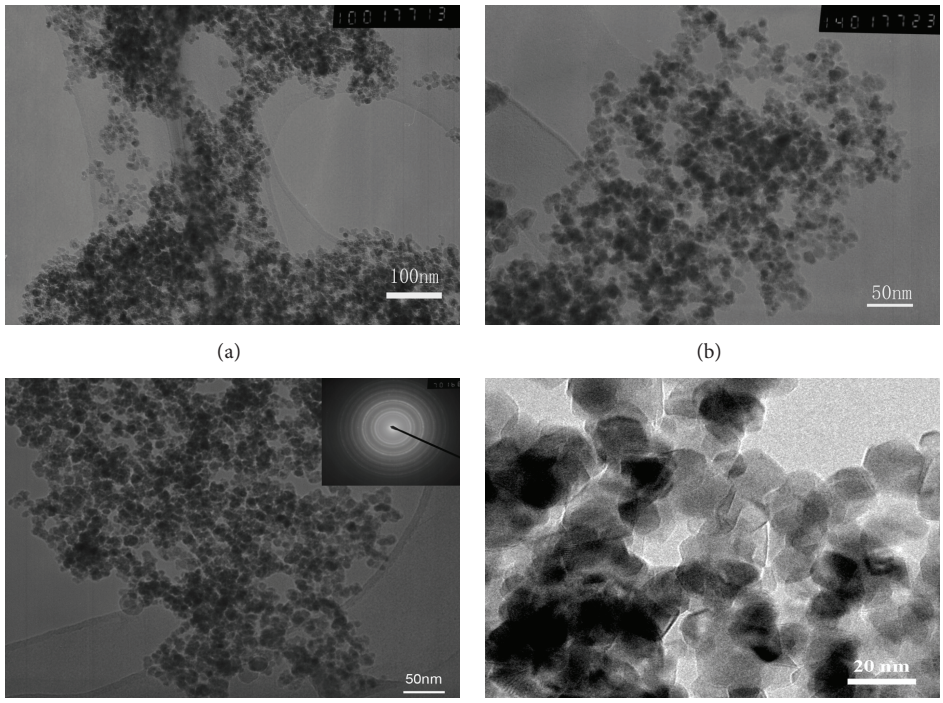

Figure 2: (a) TEM images of Fe_3O_4. (b) TEM images of SF. (c) TEM images of TSF. (d) HRTEM images of TSF. The inset in (c) is the electronic diffraction of TSF.

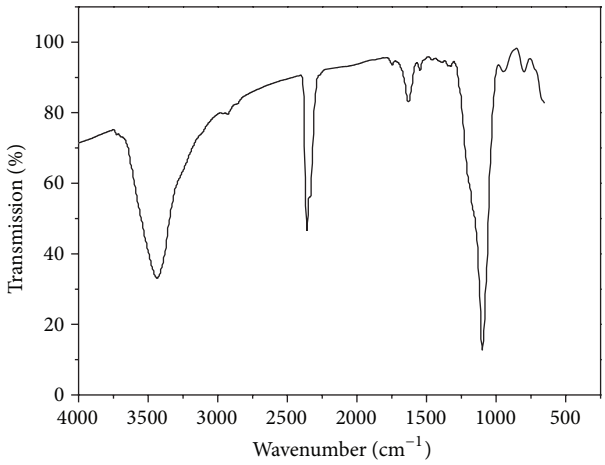

Figure 3: FTIR spectrum of TSF core-shell nanoparticles.

oily wastewater. To determine the change of crude oil concentration during photocatalysis process, a few milliliters of solution was taken from the mixture at different time. Then, the nanoparticles were separated from the solution with a magnetic bar. The solution was subsequently mixed with $CHCl_3$, followed by centrifugation. Finally, $CHCl_3$ solution was taken out and the oil concentration was measured with UV-Vis spectrometer (UV-2802PC Unico). According to the measurement, the oil concentration was calculated based on the concentration-absorbance curve obtained by a standard measurement.

3. Results and Discussion

3.1. Characterization of the Nanoparticles. The successful preparation of Fe_3O_4 magnetic nanoparticles and the TSF core-shell magnetic photocatalysts have been confirmed by X-ray diffraction analysis (Figure 1). Figure 1(a) shows X-ray diffraction patterns of Fe_3O_4 core. The diffraction peaks located at 30.0°, 35.4°, 43.0°, 53.6°, 57.2°, and 62.5° can be perfectly indexed to the crystal planes (220), (311), (400), (422), (511), and (440) of magnetite phase Fe_3O_4, respectively. The average crystal size of Fe_3O_4 was calculated by using Scherrer's formula $D_{hkl} = 0.89\lambda/(\beta\cos\theta)$, where β is the width of the XRD peak at the half-peak height, λ is the X-ray wavelength in nanometers, and θ is the half diffraction angle of 2θ in degrees. The average crystal size of Fe_3O_4, determined by the data from D_{311}, is around 11.7 nm, which is approximately consistent with the TEM observation mentioned later. After two-step sol-gel processes and calcination, the X-ray spectra confirm the transformation of amorphous TiO_2 to anatase, as shown in Figure 1(b). The diffraction peaks indicated by *A* in Figure 1(b) are indexed as anatase TiO_2, while diffraction peaks indicated by *M* in Figure 1(b) are indexed as the magnetite Fe_3O_4. The wave packet that appears in the range of 20°~ 30° might result from the interlayer of amorphous SiO_2. No clear glassy sharp peak has been observed due to the fact that the thickness of the coated SiO_2 layer is very small and the diffraction peak of amorphous structures is very weak if compared with the crystalline diffraction peaks. It approves that the coating layer of Fe_3O_4 is amorphous SiO_2. "*A*" peak is the diffraction peak of TiO_2 (25.38°, 48.04°, and

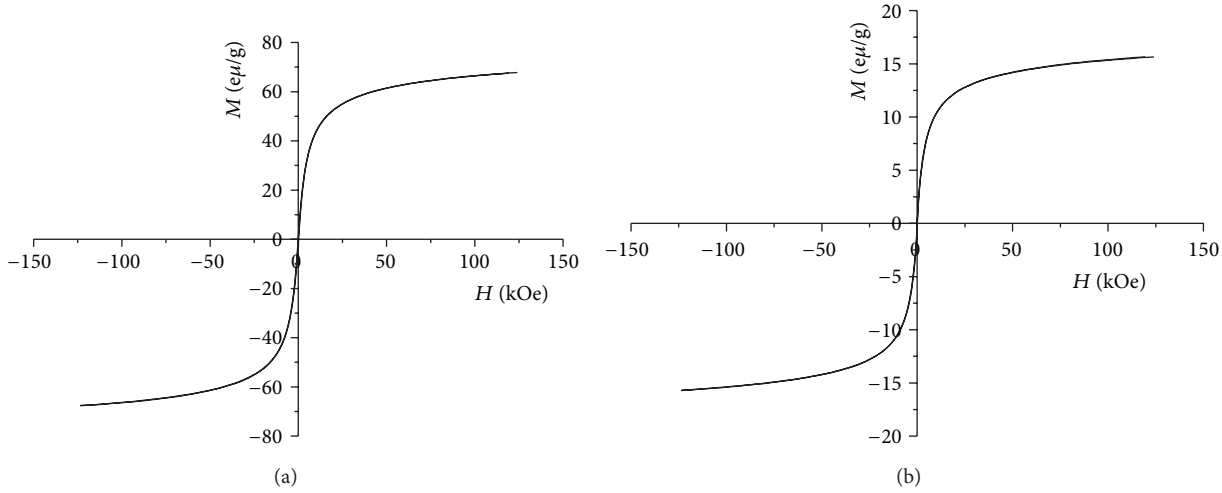

Figure 4: The magnetization curve of (a) Fe_3O_4 core and (b) TSF photocatalyst.

37.80°), and it is the coincidence of three diffraction peaks of anatase, so it approves that the coating of SF nanoparticles is anatase TiO_2. According to Scherrer's formula, the average TSF photocatalyst size was around 19.1 nm.

The structure characterization of the as-prepared nanoparticles has been examined with transmission electron microscope (TEM) and high resolution transmission electron microscope (HRTEM). Figure 2(a) shows the morphology of Fe_3O_4 nanoparticles, and the size of Fe_3O_4 nanoparticles is around 5–20 nm, which agreed with the result obtained from XRD analysis. The direct coating of silicon oxide onto the surface of the magnetite core was carried out by the hydrolysis of TEOS using sol-gel method, which can be seen from Figure 2(b). The SF nanoparticles had a core-shell structure in which magnetite was predominantly concentrated in the center of the SF nanoparticles. The direct coating of titanium oxide onto the surface of the SF nanoparticles was carried out by the hydrolysis of TBOT using sol-gel method, as can be seen from Figures 2(c) and 2(d). Before calcination, titanium oxide was amorphous and after calcination at 450°C for 3 h, the amorphous TiO_2 transformed to the anatase phase, which is confirmed by the peaks in the XRD pattern (Figure 1(b)). By using Scherrer's formula, the size of TSF photocatalyst is around 10–30 nm, which matches the results of XRD analysis.

The Fourier transform infrared (FTIR) spectroscopy spectrum of the calcined sample was investigated to confirm the structure of core-shell nanoparticles. As shown in Figure 3, TSF core-shell nanoparticles show more signals than P25. The band at ca. 1620 cm^{-1} can be assigned to the H-O-H stretching vibration, and the band at ca. 1100 cm^{-1} and 800 cm^{-1} corresponds to the asymmetric vibration and symmetric vibration of Si-O-Si. The presence of water is proved by the stretching mode at 3400 cm^{-1}. This surface hydroxylation will benefit the photocatalytic degradation of organic contaminants. Notably, no absorption peaks corresponding to Fe_3O_4 core are revealed, suggesting that it was totally coated by outer shell.

The magnetic properties of the Fe_3O_4 nanoparticles and TSF core-shell magnetic nanoparticles have been measured by use of the vibration sample magnetometer. The magnetization curves of Fe_3O_4 nanoparticles and TSF core-shell nanoparticles are shown in Figures 4(a) and 4(b), respectively. According to Figure 4, the saturation magnetization and the residual magnetization of Fe_3O_4 nanoparticles are 67.7 emu/g and 1.6 emu/g, respectively, while the coercivity of Fe_3O_4 core is close to zero, indicating the existence of superparamagnetism characteristics. After two-step coating and calcination, the saturation magnetization and the residual magnetization of TSF photocatalyst are 16.7 emu/g and 0.74 emu/g, respectively, while the coercivity of TSF photocatalyst is 5.78 Gs, which is still close to zero, confirming the superparamagnetism nature of TSF photocatalyst. Due to the superparamagnetism nature, TSF photocatalyst can demagnetize easily. When additional magnetic field intensity decreases to zero, the residual magnetization of TSF photocatalyst also drops to zero quickly, which would benefit the removal and demagnetization of TSF photocatalyst. It would provide the feasibility of the recovery and reusing of TSF photocatalyst.

The surface area of TSF photocatalyst and P25 was investigated by using nitrogen adsorption-desorption isotherms. The calculated BET surface area of TSF photocatalyst and P25 is 40.5 m^2/g and 50 m^2/g, respectively. It is known that large specific surface area is beneficial to the photocatalytic activity.

3.2. Photocatalytic Activity. We further demonstrated the photocatalytic performance of TSF photocatalyst by the removal of crude oil from oily wastewater. For comparison, we also evaluated the photocatalytic performance of P25 anatase TiO_2. Figure 5(a) shows the absorption spectra of oily wastewater exposed to UV light for different time intervals. The typical absorption peak at 245 nm gradually decreases as the time increases and completely disappears after 40 min, implying the complete degradation of crude

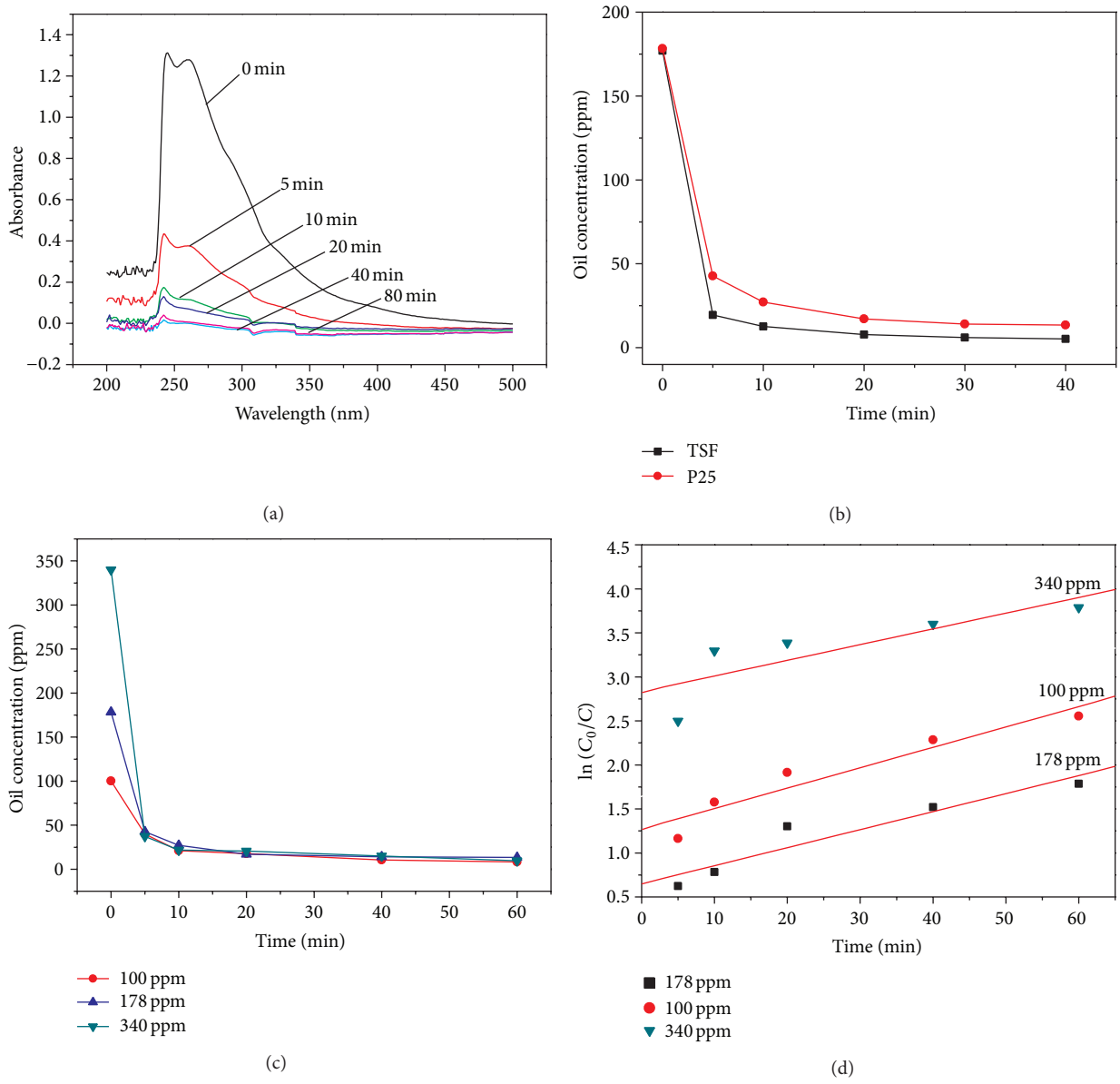

Figure 5: (a) Absorption spectra of oily wastewater exposed to UV light. (b) Photocatalytic performance of TSF and P25. (c) The effect of initial oil concentration on the photocatalysis process of TSF. (d) Pseudo-first-order model fitting of (c) in degrading crude oily wastewater with the oil concentration less than 350 ppm.

oil by the photocatalysts. Figure 5(b) shows that the oil concentration of oily wastewater varies with the photocatalytic degrading time. It shows that with the increase of degrading time the oil concentration decreases rapidly. After 10 min photocatalytic degradation, the oil concentration is reduced from 176 to 20 ppm. It indicates that the TSF core-shell magnetic nanoparticles possess high photocatalytic activity and can purify the crude oily wastewater efficiently. While keeping the amount of TiO_2 in TSF photocatalyst and P25 TiO_2 the same, we found that TSF photocatalyst and P25 TiO_2 show similar photocatalytic activity under identical conditions, as shown in Figure 5(b). The good photocatalytic activity of TSF photocatalyst may be caused by two reasons. One reason is the small size of anatase phase formed during the calcination process. Some previous papers pointed out the optimal size of anatase for photocatalysis is around 10 nm [27–29]. The other reason is the formation of Ti-O-Si bond, which has been reported in many papers to enhance the photocatalytic efficiency [30–32]. Meanwhile, SiO_2 intermediary layer inhibits electrical contact and prevents photogenerated electrons from transferring into the lower lying conduction band of the iron oxide core, thus eliminating the possible photodissolution of iron oxide in the reaction process.

Figure 5(c) shows that the curves of oil concentration vary with photocatalytic degradation time for different initial oil concentration in the wastewater. It has been found that

Table 1: Kinetic parameter of oil degradation.

Initial oil concentration C_0 (ppm)	Pseudo-first-order kinetics equation	Kinetic constant k_{obs} (min^{-1})	Correlation coefficient R^2
100	$\ln(C_0/C) = 1.2730 + 0.0231t$	0.0231	0.9554
178	$\ln(C_0/C) = 0.6504 + 0.0204t$	0.0204	0.9566
340	$\ln(C_0/C) = 2.8314 + 0.0178t$	0.0178	0.8227

even the initial oil concentration is as high as 340 ppm, the crude oily wastewater could be purified quickly and the oil concentration can be reduced to less than 30 ppm within 20 minutes. It indicates that TSF nanoparticles exhibit high efficiency. It has been shown that the photocatalytic degradation of crude oil follows pseudo-first-order kinetics according to Langmuir-Hinshelwood model, and the photocatalytic reaction can be described simply by $\ln(C_0/C) = kt$, where C and C_0 are the actual and initial oil concentration and k is the degradation rate parameter. The kinetic parameter and pseudo-first-order model fitting are summarized in Table 1 and Figure 5(d). The sample with initial oil concentration 100 ppm exhibits the highest photocatalytic efficiency; its kinetic constant K_{obs} is 0.0231 min^{-1}, which is much higher than that with initial oil concentration of 178 ppm or 340 ppm. The increase of oil concentration leads to a decrease in photocatalytic activity.

3.3. Recovery Properties. After photocatalytic degradation experiments, the TSF core-shell magnetic nanoparticles within the wastewater in the container could be easily withdrawn with an external magnetic field (NdFeB magnet). When the magnet is located at the bottom outside of the container, all of the TSF core-shell magnetic nanoparticles could be separated from the wastewater and attracted to the bottom of the container within only 5 minutes. The photocatalytic activity of the recovered photocatalysts has not noticeably changed after three successive cycles under UV-Vis irradiation indicating that magnetically recoverable photocatalyst is stable and effective for the degradation of crude oil. The photocatalytic performance of TSF after three cycles under UV-Vis irradiation is illustrated in Figure 6. The slight decrease in photocatalytic activity might result from the absorbance of crude oil, but it could be recovered by a high temperature calcination of the contaminant. Present results indicate that the magnetically recoverable TSF core-shell nanoparticles are stable and effective for the degradation of crude oily wastewater.

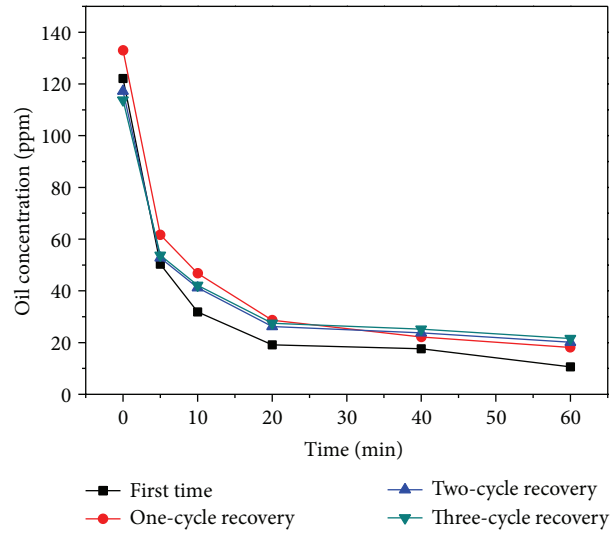

Figure 6: Photocatalytic performance of TSF after three cycles.

4. Conclusions

In summary, TSF core-shell magnetic nanoparticles, which are constituted by a Fe_3O_4 core, a SiO_2 protective intermediary layer, and a TiO_2 outshell, have been prepared by use of chemical coprecipitation and sol-gel processes. The as-prepared TSF core-shell magnetic nanoparticles display superparamagnetic behavior with saturated magnetization of 16.7 eum/g, residue magnetization of 0.74 eum/g, and coercivity of 5 Gs. It has been found that the TSF core-shell magnetic nanoparticles possess high photocatalytic activity in the degradation of crude oily wastewater. With the addition of 0.2 g/L TSF core-shell magnetic nanoparticles, the oil concentration in the crude oily wastewater could be reduced to lower than 30 ppm within 20 minutes for the initial oil concentration less than 350 ppm. After photocatalytic experiments, the TSF core-shell magnetic nanoparticles could be easily separated from the wastewater and withdrawn back by use of external magnetic field (a NdFeB magnet). It has been found that recovered TSF core-shell magnetic nanoparticles also exhibit high efficiency in the degradation of crude oily wastewater even for three cycles. Present results indicate that magnetically recoverable TSF core-shell magnetic nanoparticles are promising nanomaterials for degrading the crude oily wastewater.

Conflict of Interests

The authors declare that there is no conflict of interests regarding the publication of this paper.

Acknowledgments

This work is supported by the Jiangsu University Scientific Research Foundation for Advanced Talents (Grant no. 12JDG095) and the National Natural Science Foundation of China (Grant no. 51302112).

References

[1] M. R. Hoffmann, S. T. Martin, W. Choi, and D. W. Bahnemann, "Environmental applications of semiconductor photocatalysis," *Chemical Reviews*, vol. 95, no. 1, pp. 69–96, 1995.

[2] O. Carp, C. L. Huisman, and A. Reller, "Photoinduced reactivity of titanium dioxide," *Progress in Solid State Chemistry*, vol. 32, no. 1-2, pp. 33–177, 2004.

[3] A. L. Linsebigler, G. Lu, and J. T. Yates Jr., "Photocatalysis on TiO_2 surfaces: principles, mechanisms, and selected results," *Chemical Reviews*, vol. 95, no. 3, pp. 735–758, 1995.

[4] H. G. Yu, R. Liu, X. F. Wang, P. Wang, and J. Yu, "Enhanced visible-light photocatalytic activity of Bi_2WO_6 nanoparticles by Ag_2O cocatalyst," *Applied Catalysis B: Environmental*, vol. 111-112, pp. 326–333, 2012.

[5] P. Wang, J. Wang, X. F. Wang, H. G. Yu, J. G. Yu, and M. Lei, "One-step synthesis of easy-recycling TiO_2-rGO nanocomposite photocatalysts with enhanced photocatalytic activity," *Applied Catalysis B: Environmental*, vol. 132-133, pp. 452–459, 2013.

[6] J. G. Yu, Y. Wang, and W. Xiao, "Enhanced photoelectrocatalytic performance of SnO_2/TiO_2 rutile composite films," *Journal of Materials Chemistry A*, vol. 1, no. 36, pp. 10727–10735, 2013.

[7] R. Wang, K. Hashimoto, A. Fujishima et al., "Light-induced amphiphilic surfaces," *Nature*, vol. 388, no. 6641, pp. 431–432, 1997.

[8] R. Liu, P. Wang, X. F. Wang, H. G. Yu, and J. G. Yu, "UV- and visible-light photocatalytic activity of simultaneously deposited and doped Ag/Ag(I)-TiO_2 photocatalyst," *Journal of Physical Chemistry C*, vol. 116, no. 33, pp. 17721–17728, 2012.

[9] P. Zhou, J. Yu, and Y. X. Wang, "The new understanding on photocatalytic mechanism of visible-light response N-S codoped anatase TiO_2 by first- principles," *Applied Catalysis B: Environmental*, vol. 142, pp. 45–53, 2013.

[10] S. C. Roy, O. K. Varghese, M. Paulose, and C. A. Grimes, "Toward solar fuels: photocatalytic conversion of carbon dioxide to hydrocarbons," *ACS Nano*, vol. 4, no. 3, pp. 1259–1278, 2010.

[11] X. Chen and S. S. Mao, "Titanium dioxide nanomaterials: synthesis, properties, modifications and applications," *Chemical Reviews*, vol. 107, no. 7, pp. 2891–2959, 2007.

[12] D. Chen and J. Ye, "Hierarchical WO_3 hollow shells: dendrite, sphere, dumbbell, and their photocatalytic properties," *Advanced Functional Materials*, vol. 18, no. 13, pp. 1922–1928, 2008.

[13] S. Watson, J. Scott, D. Beydoun, and R. Amal, "Studies on the preparation of magnetic photocatalysts," *Journal of Nanoparticle Research*, vol. 7, no. 6, pp. 691–705, 2005.

[14] J. M. Lee, M. S. Kim, and B. W. Kim, "Photodegradation of bisphenol-A with TiO_2 immobilized on the glass tubes including the UV light lamps," *Water Research*, vol. 38, no. 16, pp. 3605–3613, 2004.

[15] D. Beydoun, R. Amal, G. K.-C. Low, and S. McEvoy, "Novel photocatalyst: titania-coated magnetite. Activity and photodissolution," *Journal of Physical Chemistry B*, vol. 104, no. 18, pp. 4387–4396, 2000.

[16] R. Guo, L. Fang, W. Dong, F. Zheng, and M. Shen, "Magnetically separable $BiFeO_3$ nanoparticles with a γ-Fe_2O_3 parasitic phase: controlled fabrication and enhanced visible-light photocatalytic activity," *Journal of Materials Chemistry*, vol. 21, no. 46, pp. 18645–18652, 2011.

[17] S. Watson, D. Beydoun, and R. Amal, "Synthesis of a novel magnetic photocatalyst by direct deposition of nanosized TiO_2 crystals onto a magnetic core," *Journal of Photochemistry and Photobiology A: Chemistry*, vol. 148, no. 1–3, pp. 303–313, 2002.

[18] N. Quici, M. E. Morgada, R. T. Gettar, M. Bolte, and M. I. Litter, "Photocatalytic degradation of citric acid under different conditions: TiO_2 heterogeneous photocatalysis against homogeneous photolytic processes promoted by Fe(III) and H_2O_2 ," *Applied Catalysis B: Environmental*, vol. 71, no. 3-4, pp. 117–124, 2007.

[19] S.-K. Li, F.-Z. Huang, Y. Wang et al., "Magnetic Fe_3O_4@C@Cu2O composites with bean-like core/shell nanostructures: synthesis, properties and application in recyclable photocatalytic degradation of dye pollutants," *Journal of Materials Chemistry*, vol. 21, no. 20, pp. 7459–7466, 2011.

[20] S. Xu, W. Shangguan, J. Yuan, M. Chen, J. Shi, and Z. Jiang, "Synthesis and performance of novel magnetically separable nanospheres of titanium dioxide photocatalyst with egg-like structure," *Nanotechnology*, vol. 19, no. 9, Article ID 095606, 2008.

[21] Y. S. Chung, S. B. Park, and D. Kang, "Magnetically separable titania-coated nickel ferrite photocatalyst," *Materials Chemistry and Physics*, vol. 86, no. 2-3, pp. 375–381, 2004.

[22] D. Beydoun, R. Amal, G. Low, and S. McEvoy, "Occurrence and prevention of photodissolution at the phase junction of magnetite and titanium dioxide," *Journal of Molecular Catalysis A: Chemical*, vol. 180, no. 1-2, pp. 193–200, 2002.

[23] D. Beydoun and R. Amal, "Implications of heat treatment on the properties of a magnetic iron oxide-titanium dioxide photocatalyst," *Materials Science and Engineering B: Solid-State Materials for Advanced Technology*, vol. 94, no. 1, pp. 71–81, 2002.

[24] Y. Gao, B. Chen, H. Li, and Y. Ma, "Preparation and characterization of a magnetically separated photocatalyst and its catalytic properties," *Materials Chemistry and Physics*, vol. 80, no. 1, pp. 348–355, 2003.

[25] D. Beydoun, R. Amal, J. Scott, G. Low, and S. McEvoy, "Studies on the mineralization and separation efficiencies of a magnetic photocatalyst," *Chemical Engineering & Technology*, vol. 24, no. 7, pp. 745–748, 2001.

[26] F. Chen, Y. Xie, J. Zhao, and G. Lu, "Photocatalytic degradation of dyes on a magnetically separated photocatalyst under visible and UV irradiation," *Chemosphere*, vol. 44, no. 5, pp. 1159–1168, 2001.

[27] S. Y. Chae, M. K. Park, S. K. Lee, T. Y. Kim, S. K. Kim, and W. I. Lee, "Preparation of size-controlled TiO_2 nanoparticles and derivation of optically transparent photocatalytic films," *Chemistry of Materials*, vol. 15, no. 17, pp. 3326–3331, 2003.

[28] J. Grzechulska and A. W. Morawski, "Photocatalytic labyrinth flow reactor with immobilized P25 TiO_2 bed for removal of phenol from water," *Applied Catalysis B: Environmental*, vol. 46, no. 2, pp. 415–419, 2003.

[29] S. Anandan and M. Yoon, "Photocatalytic activities of the nanosized TiO_2-supported Y-zeolites," *Journal of Photochemistry and Photobiology C: Photochemistry Reviews*, vol. 4, no. 1, pp. 5–18, 2003.

[30] K. Qi, X. Chen, Y. Liu, J. H. Xin, C. L. Mak, and W. A. Daoud, "Facile preparation of anatase/SiO_2 spherical nanocomposites and their application in self-cleaning textiles," *Journal of Materials Chemistry*, vol. 17, no. 33, pp. 3504–3508, 2007.

[31] L. Zhou, S. Yan, B. Tian, J. Zhang, and M. Anpo, "Preparation of TiO_2-SiO_2 film with high photocatalytic activity on PET substrate," *Materials Letters*, vol. 60, no. 3, pp. 396–399, 2006.

[32] A. Matsuda, T. Matoda, Y. Kotani, T. Kogure, M. Tatsumisago, and T. Minami, "Evaluation of photocatalytic activity of transparent anatase nanocrystals-dispersed silica films prepared by the sol-gel process with hot water treatment," *Journal of Sol-Gel Science and Technology*, vol. 26, no. 1–3, pp. 517–521, 2003.

Hindawi Publishing Corporation
International Journal of Photoenergy
Volume 2014, Article ID 738921, 12 pages
http://dx.doi.org/10.1155/2014/738921

Research Article

Hole-Phonon Relaxation and Photocatalytic Properties of Titanium Dioxide and Zinc Oxide: First-Principles Approach

V. P. Zhukov,[1,2] V. G. Tyuterev,[3,4] E. V. Chulkov,[2,5,6] and P. M. Echenique[2,5]

[1] *Institute of Solid State Chemistry, Urals Branch of the Russian Academy of Sciences, Pervomayskaya 91, Yekaterinburg 620990, Russia*
[2] *Donostia International Physics Center (DIPC), P. Manuel de Lardizabal 4, 20018 San Sebastián, Spain*
[3] *Tomsk State Pedagogical University, Kievskaya 60, Tomsk 634041, Russia*
[4] *National Research Tomsk State University, Lenin Street 36, Tomsk 634050, Russia*
[5] *Departamento de Física de Materiales, Facultad de Ciencias Químicas, UPV/EHU and CFM-MPC, Apartado 1072, 20080 San Sebastián, Spain*
[6] *Tomsk State University, Lenina 36, Tomsk 634050, Russia*

Correspondence should be addressed to V. P. Zhukov; zhukov_vladlen@mail.ru

Received 27 February 2014; Accepted 17 March 2014; Published 14 April 2014

Academic Editor: Jiaguo Yu

First-principles calculations for the temporal characteristics of hole-phonon relaxation in the valence band of titanium dioxide and zinc oxide have been performed. A first-principles method for the calculations of the quasistationary distribution function of holes has been developed. The results show that the quasistationary distribution of the holes in TiO_2 extends to an energy level approximately 1 eV below the top of the valence band. This conclusion in turn helps to elucidate the origin of the spectral dependence of the photocatalytic activity of TiO_2. Analysis of the analogous data for ZnO shows that in this material spectral dependence of photocatalytic activity in the oxidative reactions is unlikely.

1. Introduction

The relaxation of excited holes in the photocatalytic oxides is manifested in the transfer of holes to the highest valence band states and in trapping them on defects or surface states, the processes that profoundly affect the properties of the oxides [1–10]. Recently, Henderson published a review studies concerning the relaxation [11]; therefore, we restrict our introduction only to studies associated with the relaxation of holes that occurs via interactions with phonons and that terminates when holes ascend to the top of the valence band.

In photocatalytic oxides, the thermalization of excited electrons via electron-phonon interaction occurs very rapidly, within several hundreds of femtoseconds; see references in [12, 13]. It is natural to suppose that the relaxation of excited holes in the valence band also occurs rapidly. Since the electron-hole recombination is a much slower process, one can assume that the efficiency of a photocatalyst should not depend on the energy of the exciting photon [11]. However, this assumption is not true.

The dependence of photocatalytic activity on the energy of excitation has been observed for the first time by Grela et al. [1] who studied the photocatalytic oxidation of salicylate (S) in presence of aqueous sols containing nanoparticles of TiO_2. The authors found that the photons absorbed through nanoparticles at 254 nm were 8-times more efficient than those absorbed at 366 nm. The authors proposed that the thermalization of holes in nanoclusters occurs in the nanosecond timescale compared with the timescale of hole transitions to the molecules absorbed on the surface. The authors subsequently studied the photocatalysis of salicylate, phthalate (P), and resorcinol (R) [3]. It is well known that the effective mass of excited electrons is greater than the mass of holes, so the authors suggested that the excess photon energy is channeled into holes. An essential finding of this work is that the quantum yield of the oxidative reaction suddenly increases when the excess energy increases above ~0.2 eV. The maximum quantum yield is achieved at 0.5 eV for P, but the yield rises permanently for S and remains constant for R. These trends are explained by the Marcus theory [14–16], and

these results suggest that hole relaxation is a slower process compared with hole transfer from a solid to a molecular state; otherwise the variation of the quantum yield with the excess energy would be impossible.

Emeline et al. [5] studied the effects of photodegradation of phenol and 4-chlorophenol on the nanoparticles of the standard Degussa photocatalyst, confirming the spectral dependence of the photocatalytic activity. These authors observed that the quantum yield of the reactions varies with changes in the photon energy, as the variation of quantum yield has at least three maxima at energies corresponding to direct and indirect electron excitations in bulk TiO_2. Authors related these changes to the mobility and lifetimes of the holes generated at different excitation energies in different points of the Brillouin zone. Notably, the photocatalyst nanoparticles obtained in the experiments of Emeline et al. (~30 nm) were markedly larger than the nanoparticles obtained in the studies of Grela et al. (5 nm). These circumstances imply that spectral dependence of the photocatalytic activity can be a property of both nanoparticles and bulk photocatalysts.

Although the authors of the cited papers emphasized the important role of the hole-phonon relaxation, they did not evaluate the temporal characteristics of these processes. To our knowledge, only Morishita et al. [4] have attempted such evaluations. In their work the two-photon femtosecond transient reflecting grating (TRG) method was applied to determine the dynamics of the currents for the degradation of KSCN on the (001) surface of TiO_2. The authors showed that the dependence of the probe TRG-signal on the delay between the pump and probe pulses reflects changes in the concentration of holes excited by the pump. They fitted the signal to two exponential curves, a slow and a quick one. The slow component, with a time constant from 150 to 173 ps, has been attributed to electron-hole recombination. The quick component, whose intensity depends on the surface concentration of KSCN and intensity of irradiation, was attributed to the decrease in the hole concentration due to electron transfer from KSCN to the holes in TiO_2. With increasing pump power intensity the time constant of the quick component varied from 110 to 690 fs. The time constant of the hole-phonon relaxations cannot be less than the time constant of the quick component; otherwise the quick component is absent. So these results help to estimate the time constant of the hole relaxation.

In the remaining papers cited at the onset [6, 8–10], the processes of carrier trapping on the defects or on the surface states have been discussed, although these processes are too slow to be compared with the time of the hole-phonon relaxation. Hence, despite the important role of the hole-phonon relaxation, the available data on the timing of these processes are scanty and insufficiently accurate. The number of theoretical works on this subject is limited and incomparable to the numerous studies of relaxation time in metals [17–19]. The formerly developed methods and computer codes for the solid state theory [20] facilitate first-principle calculations for the temporal characteristics of the relaxation processes. However, to our knowledge, only in the works [12, 13, 21] the calculations for the relaxation time of excited electrons in TiO_2 and ZnO have been performed.

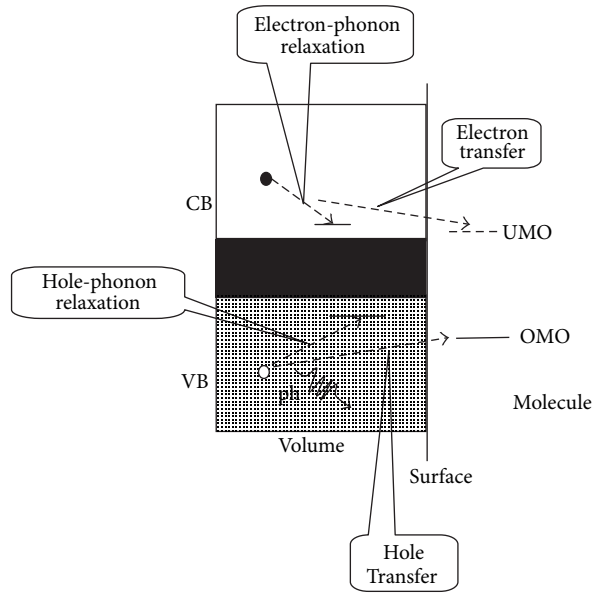

Figure 1: The scheme of the processes that occur after the excitation of the electron-hole pairs near the surface of a photocatalyzer. The notations have the following sense: VB is the band of valence states, CB is the band of conduction states, and OMO and UMO are the occupied and unoccupied molecular states, respectively.

The calculated times of electron-phonon relaxation in these studies are fairly consistent with the experimental data, and the distinctions are explained through the specificity of the performed experiments.

Therefore, we have carried out a first-principles study for the processes of relaxation of the nonequilibrated holes in TiO_2 and ZnO. In what follows we outline the physical foundations of the method and the details of the calculations and discuss the results and conclusions important for a better understanding of the photocatalytic properties of these oxides.

2. Theory

2.1. The Rate of Hole-Phonon Relaxation and the Time of Energy Loss. In Figure 1 we show the scheme of the processes that occur near the surface of a photo-catalyzer just after an electron-hole pair has been excited by the light. Both the excited hole in the valence band and the electron in the conduction band lose their energy by phonon emission. Simultaneously, the electron and hole transfer from the volume of the photo-catalyzer to the molecules adsorbed on the surface can take place. It has been shown in the work [2] that more than 98% of the photon energy goes into excitation of the holes, so we discuss in the following the rate of the hole-phonon scattering. One of our aims is to evaluate the time of the hole energy loss. The spectral dependence of the photocatalytic activity can be observed if only this time is longer than the time of hole transfer to the molecule. So the time of hole energy loss is the high limit of the hole transfer time.

Our evaluation of the hole energy loss time is based on the "golden Fermi rule" of the perturbation theory. Consistent with this rule, the probability, per unit of time, of an elementary transition of a single electron from the state with the wave-vector $\mathbf{k}$ and energy $e_{\mathbf{k},i}$ to the state with the wave-vector $\mathbf{k}+\mathbf{q}$ and energy $e_{\mathbf{k}+\mathbf{q},j}$, without considering the thermodynamic factors, can be written as

$$P^{\mathbf{q}\nu}_{\mathbf{k},i;\mathbf{k}+\mathbf{q},j} = \left(\frac{2\pi}{\hbar}\right)\left|\left\langle \mathbf{k}, i\left|\Delta V_{\mathbf{q}\nu}\right|\mathbf{k}+\mathbf{q}, j\right\rangle\right|^2 \times \delta\left(e_{\mathbf{k},i} - e_{\mathbf{k}+\mathbf{q},j} \pm \hbar\omega^{\nu}_{\mathbf{q}}\right). \tag{1}$$

Here, + and − represent the transitions accompanied by the absorption or the emission, respectively, of a phonon, $|\mathbf{k}, i\rangle$ and $|\mathbf{k}+\mathbf{q}, j\rangle$ are the wave functions of the electronic states, $\mathbf{q}$ and ν are the wave vector and polarization of the phonon, and $\Delta V_{\mathbf{q}\nu}$ is the variation of the self-consistent potential in the crystal caused by the displacement mode of the phonon. The value $\langle \mathbf{k}, i|\Delta V_{\mathbf{q}\nu}|\mathbf{k}+\mathbf{q}, j\rangle$ is the matrix element of the electron-phonon interaction; the ways of calculating this matrix element have been widely discussed [20]. The energy of phonon is typically neglected, as this value is small compared with the energies of electronic states $e_{\mathbf{k}+\mathbf{q},j}$ and $e_{\mathbf{k},j}$, representing the so-called quasielastic approximation. After integrating over all wave vectors and polarizations of the phonons and energies of electronic states, the probability is obtained, satisfying the momentum and energy conservation, for the electron to leave the state $|\mathbf{k}, i\rangle$, losing the energy $\hbar\omega$:

$$\Phi_{\mathbf{k},i}(\omega) = \left(\frac{2\pi}{\hbar}\right)\sum_j\sum_\nu\int_{BZ}\delta\left(\omega^{\nu}_{\mathbf{q}} - \omega\right)\left|\left\langle \mathbf{k}, i\left|\Delta V_{\mathbf{q}\nu}\right|\mathbf{k}+\mathbf{q}, j\right\rangle\right|^2 \times \delta\left(e_{\mathbf{k}+\mathbf{q},j} - e_{\mathbf{k},i}\right) d^3\mathbf{q}. \tag{2}$$

Function $\Phi_{\mathbf{k},i}(\omega)$ is an analog of the well-known Eliashberg function $\alpha^2 F_{\mathbf{k},i}(\omega)$ [22]. The difference is in a constant,

$$\alpha^2 F_{\mathbf{k},i}(\omega) = \frac{\Phi_{\mathbf{k},i}(\omega)}{(2\pi/\hbar)}. \tag{3}$$

In addition, the conventional Eliashberg function is defined at the Fermi energy of metals, whereas $\Phi_{\mathbf{k},i}(\omega)$ is defined at arbitrary energy inside the valence band. The Eliashberg function is connected with a constant of electron-phonon coupling λ, calculated as

$$\lambda_{\mathbf{k},i} = 2\int\frac{\alpha^2 F_{\mathbf{k},i}(\omega)}{\omega}d\omega. \tag{4}$$

When the thermodynamic equilibrium exists, the change in the population of the state at energy $e_{\mathbf{k},i}$ is determined by the effects of the four kinds of electron transitions that occur between the $e_{\mathbf{k},i}$-state and the states at $e_{\mathbf{k},i} \pm \hbar\omega$ and are accompanied by the phonon absorption or emission. The probability of these processes, hereafter U, is determined by the probability of the elementary process and Bose statistics $Q(\hbar\omega, T)$:

$$U^{\mathbf{q}\nu}_{\mathbf{k},i;\mathbf{k}+\mathbf{q},j} = P^{\mathbf{q}\nu}_{\mathbf{k},i;\mathbf{k}+\mathbf{q},j}\left[Q\left(\hbar\omega_{\mathbf{q}\nu}, T\right) + I\right] \times \delta\left(e_{\mathbf{k},i} - e_{\mathbf{k}+\mathbf{q},j} \pm \hbar\omega_{\mathbf{q}\nu}\right), \tag{5}$$

where $I = 0$ represents the absorption of phonon and 1 represents the emission. Considering this statistic for phonons and Fermi statistics for electrons, hereafter R, and assuming, for the dynamics of holes, that the initial population of the level is zero, an expression for the change of population rate (see details in [23]) can be obtained:

$$\Gamma_{\mathbf{k},i} = \int d\omega\Phi_{\mathbf{k},i}(\omega)\left[1 + 2Q\left(\hbar\omega, T\right) + R\left(e_{\mathbf{k},i} + \hbar\omega, T\right) - R\left(e_{\mathbf{k},i} - \hbar\omega, T\right)\right]. \tag{6}$$

If the electron population is $n(e_{\mathbf{k},i})$, then the number of holes in the state is $n_h(e_{\mathbf{k},i}) = 1 - n(e_{\mathbf{k},i})$, and so expression (6) also determines the rate of the hole relaxations. At low temperatures, this value is reduced with high precision to

$$\Gamma_{\mathbf{k},i} = \int d\omega\Phi_{\mathbf{k},i}(\omega)\left[2Q\left(\hbar\omega, T\right) + 1\right] = \left(\frac{2\pi}{\hbar}\right) \times \sum_j\sum_\nu\int d\omega\int_{BZ} d^3\mathbf{q}\,\delta\left(\omega_{\mathbf{q}\nu} - \omega\right) \times\left|\left\langle \mathbf{k}, i\left|\Delta V_{\mathbf{q}\nu}\right|\mathbf{k}+\mathbf{q}, j\right\rangle\right|^2 \times \delta\left(e_{\mathbf{k}+\mathbf{q},j} - e_{\mathbf{k},i}\right)\left[2Q\left(\hbar\omega, T\right) + 1\right]. \tag{7}$$

In the real calculations described below we neglect the Q factor; hence we perform evaluations for the case of low temperatures.

Having calculated the rate of hole-phonon relaxation, we can evaluate the relaxation time of the hole defined as the time from the moment of its emergence to the moment of transition to a higher level, owing to the filling of the hole-containing state with an electron that emits phonon:

$$\tau_{\mathbf{k},i} = \frac{\hbar}{\Gamma_{\mathbf{k},i}}. \tag{8}$$

Based on the calculations of the relaxation rate, one can evaluate for the state $|\mathbf{k}, i\rangle$ the energy loss per unit of time, defined by the first moment of the probability function $\Phi_{\mathbf{k},i}$:

$$\Delta\widetilde{e}_{\mathbf{k},i} = \int d\omega\Phi_{\mathbf{k},i}(\omega)\,\hbar\omega\left[2Q\left(\hbar\omega, T\right) + 1\right] = 2\pi\int d\omega\alpha^2 F_{\mathbf{k},i}(\omega)\,\hbar\omega\left[2Q\left(\hbar\omega, T\right) + 1\right]$$

$$= 2\pi \int d\omega\hbar\omega \times \sum_j \sum_\nu \int_{BZ} d^3\mathbf{q}\delta\left(\omega_{\mathbf{q}}^\nu - \omega\right) \left|\left\langle \mathbf{k}, i \left| \Delta V_{\mathbf{q}\nu} \right| \mathbf{k}+\mathbf{q}, j \right\rangle\right|^2 \times \delta\left(e_{\mathbf{k}+\mathbf{q},j} - e_{\mathbf{k},i}\right) \times \left[2Q\left(\hbar\omega_{\mathbf{q}\nu}, T\right) + 1\right]. \quad (9)$$

We calculated the characteristics averaged over the wave vectors as

$$\lambda(E) = \left[\frac{1}{N}(E)\right] \sum_i \int d^3\mathbf{k}\delta\left(e_{\mathbf{k},i} - E\right) \lambda_{\mathbf{k},i} \quad (10)$$

$$\Gamma(E) = \left[\frac{1}{N}(E)\right] \sum_i \int d^3\mathbf{k}\delta\left(e_{\mathbf{k},i} - E\right) \Gamma_{\mathbf{k},i} \quad (11)$$

$$\Delta\widetilde{e}(E) = \left[\frac{1}{N}(E)\right] \sum_i \int d^3\mathbf{k}\delta\left(e_{\mathbf{k},i} - E\right) \Delta\widetilde{e}_{\mathbf{k},i}, \quad (12)$$

where $N(E)$ are the densities of electronic states. Employing the calculated $\Gamma_{\mathbf{k},i}$ and $\Delta\widetilde{e}_{\mathbf{k},i}$, we can also evaluate the mean energy of the emitted phonons:

$$\Delta e(E) = \frac{\sum_i \int d^3\mathbf{k}\delta\left(e_{\mathbf{k},i} - E\right) \Delta\widetilde{e}_{\mathbf{k},i}}{\sum_i \int d^3\mathbf{k}\delta\left(e_{\mathbf{k},i} - E\right) \Gamma_{\mathbf{k},i}}. \quad (13)$$

In the theory of photocatalytic processes, the energy loss time $\tau_{\text{en}}(E', E)$ can also be useful that we define as the average time necessary for a hole to pass from its initial energy level E to the level E'. If at any intermediate energy E'', the average relaxation time is $\tau(E'')$ and the average energy loss is $\Delta e(E'')$, then the rate of the energy loss at this energy level is $\Delta e(E'')/\tau(E'') = \Delta e(E'')\Gamma(E'')$. Then the energy loss time is

$$\tau_{\text{en}}\left(E', E\right) = \int_{E'}^{E} \frac{dE''}{\Delta e\left(E''\right)\Gamma\left(E''\right)}. \quad (14)$$

2.2. Quasistationary Distribution of Holes inside the Valence Band. Initially, we consider the temporal evolution of the mean population $n(t, E)$ of a single state at the energy level E. Considering the four aforementioned processes, this population can be written as (here $\epsilon \equiv \hbar\omega$)

$$\frac{\partial n(t,E)}{\partial t} = [1 - n(t,E)] \int_0^{\hbar\omega_m} d\epsilon n(t, E+\epsilon) F(E+\epsilon, E) [Q(\epsilon) + 1] + [1 - n(t,E)] \int_0^{\hbar\omega_m} d\epsilon n(t, E-\epsilon) F(E-\epsilon, E) Q(\epsilon) - n(t,E) \int_0^{\hbar\omega_m} d\epsilon [1 - n(t, E+\epsilon)] F(E, E+\epsilon) Q(\epsilon) - n(t,E) \int_0^{\hbar\omega_m} d\epsilon [1 - n(t, E-\epsilon)] F(E, E-\epsilon) [Q(\epsilon) + 1] + \frac{\partial n^{\text{ext}}(t,E)}{\partial t}. \quad (15)$$

In this equation the term $\partial n^{\text{ext}}(t, E)/\partial t$ describes the instantaneous hole distribution in the valence band produced by the source of light; its form is specified below. Function $F(E, E')$ (not to mix with the Eliashberg function!) is the probability of the elementary process of electron transition from the energy level E to the level E' accompanied by the emission or absorption of the quantum $\epsilon = |E' - E|$ summarized over all the states at these levels. It can be represented as

$$F\left(E, E'\right) = \sum_{\mathbf{q}\mathbf{k}\mathbf{k}' nn'\sigma} \sum \delta\left(E - e_{\mathbf{k},n}\right) P^{\mathbf{q}\sigma}_{\mathbf{k},n;\mathbf{k}',n'} \delta_{\mathbf{k}-k'+\mathbf{q}} \times \delta\left(E' - E \mp \epsilon_{\mathbf{q}\sigma}\right) \delta\left(E' - e_{\mathbf{k}',n'}\right). \quad (16)$$

We neglect the probability of the electron-hole recombination, as this process is to some extent slower. Besides, we apply the effective phonon approximation to these equations; that is, we approve that the phonon emission at all the same frequency with the same probability takes place; then

$$F(E, E \pm \epsilon) = N(E) N(E \pm \epsilon) P(E) \delta\left(\epsilon - \hbar\omega_0\right), \quad (17)$$

where $\hbar\omega_0$ is the energy of effective phonon. For the value we can use the average energy of the emitted phonon: $\hbar\omega_0(E) = \Delta e(E)$. Studies [12, 13] have shown based on first-principle evaluations that in the cases of excited electrons in anatase, rutile, and zinc oxide the energy dependence of this value is unimportant, and this energy is close to the energy of the optic phonons. We will show below that for holes in the valence band the energy dependence is also insignificant.

Looking for an approximation for averaged transition probability $P(E)$ we use (1). This equation includes summation over electronic states only in narrow interval near the energy $e_{\mathbf{k},n}$. Neglecting this energy interval, we assume that the mean transition probability can be approximated by

$$P(E) = \frac{\Gamma(E)}{N(E)}. \quad (18)$$

We define the total distribution function of electrons as the population of all the states at an energy level; hence it is $f(t, E) = N(E)n(t, E)$. When we neglect the terms proportional to Q, that is, when we consider the case of low temperatures, and linearize (15) with respect to the small parameter ϵ, then we derive the equation for $f(t, E)$

$$\frac{\partial f(t,E)}{\partial t} = \frac{\partial}{\partial E}\left[N^{-1}(E) f(t,E) B(E)\right] + \frac{\partial f^{\text{ext}}(t,E)}{\partial t}. \quad (19)$$

Here the function

$$B(E) = \int_0^{\omega_m} \hbar\omega F(E, E+\hbar\omega) d\omega \quad (20)$$

describes the energy loss of electrons on the level E through the phonon emission, connected with the Δe-value by the relation $\Delta e(E) = B(E)/N^2(E)$. Because the hole distribution function, defined in a similar way, is $f_h(t,E) = N(E) - f(t,E)$, then (20) is also applicable to the calculations of the hole distribution. However, the term $\partial f_h^{\text{ext}}(t,E)/\partial t$ analogous to the last term of (15) should also be defined; we accept for this term the approximation

$$\frac{\partial f_h^{\text{ext}}(t,E)}{\partial t} = S_0(t)\, S_h(E). \tag{21}$$

Here the factor $S_0(t)$, which is time-dependent, describes the concentration of the holes excited by light, and the function $S_h(E)$, hereafter named as instantaneous hole distribution function (IDF), describes the probability of hole excitations depending on the excess energy of hole E. Naturally, it should be normalized to unity: $\int_0^{E_{\text{exc}}} S_h(E)dE = 1$ where E_{exc} is the photon energy. Admitting that the rate of change of the $S_0(t)$-function is small, that is, excluding the case of pulse irradiation and assuming that $\partial f_h(t,E)/\partial t = 0$ we come to the quasistationary solution for (20):

$$f_h(t,E) = S_0(t)\, \frac{1}{\Delta e(E)\, N(E)} \int_E^{E_m} S_h\left(E'\right) dE', \tag{22}$$

where E_m is the maximum excess energy of the excited holes.

The IDF-function can be obtained from the electronic band structure calculations. In order to calculate this, one should summarize the probabilities of all possible direct excitations from the states at the E level to the states at the $E + E_{\text{exc}}$ level. Thus, the unnormalized IDF can be written as

$$S_h(E) = \sum_{\mathbf{k}nn'} \delta\left(E - e_{n\mathbf{k}}\right) T\left(n\mathbf{k}, n'\mathbf{k}\right) \delta\left(e_{n\mathbf{k}} + E_{\text{exc}} - e_{n'\mathbf{k}}\right), \tag{23}$$

where $T(n\mathbf{k}, n'\mathbf{k})$ is the probability of transitions between the $|n\mathbf{k}\rangle$ and $|n'\mathbf{k}\rangle$ states. In calculations we replace the δ-functions with the normalized Gaussian functions whose width at the half-maximum is 0.01 eV.

In order to calculate the probabilities of excitations, we apply the atomic sphere approximation [24]. The essence of this approximation resides in replacing the integration over whole space with the integrations over atomic spheres whose total volume covers the total space of crystal. To describe the interaction between the crystal and the light, we apply to every atomic sphere the so-called dipole approximation [25]. With such an approximation, the Hamiltonian of interaction of an atom S with electric field of the light $\mathbf{E}(\omega)$ has the form

$$H_S = e\mathbf{D}_S\mathbf{E}(\omega), \tag{24}$$

where $e\mathbf{D}_S = e\sum_t \mathbf{r}_t^S$ is the operator of the dipole moment of atom, and $\mathbf{r}_t^S$ is the radius of an electron with respect to the center of atomic sphere. That is, the interaction of electrons with the field is

$$H(\omega) = e\sum_{t,S} \mathbf{r}_t^S \epsilon_{\mathbf{E}} E(\omega). \tag{25}$$

We consider the case of a polycrystal, so after averaging over the angles we have

$$T\left(n\mathbf{k}, n'\mathbf{k}\right) = \frac{2\pi}{\hbar} \cdot e^2 \cdot (E(\omega))^2 \frac{1}{3} \left| \sum_{t,S} \left\langle \mathbf{k}, i \left| \mathbf{r}_t^S \right| \mathbf{k}, j \right\rangle \right|^2. \tag{26}$$

The details of this derivation have been previously described [25]. Formerly we employed such an approach in the studies of radiative trapping of excited electrons on B-, C-, and N-impurities in anatase [26].

The numerical evaluations for the electron-phonon coupling have been done using the density-functional perturbation theory [20] implemented in the pseudopotential Quantum Espresso (QE) computer code [27], version 4.0.4. We have inserted in the code all the modifications necessary for our purposes. A plane-wave basis set with the energy cutoff of 50 Ry was employed which is sufficient for the successful calculations of the phonon frequencies in rutile [28]. Before the calculations of the phonons and electron-phonon interactions, the crystal structures were optimized. The perfectness of the crystal structure optimization is characterized by the final variations of the total force and total energy of the compounds. In our case these variations were no more than 0.0001 Ry/at.un. and 0.00003 Ry for the force and energy, respectively. The precision of the phonon calculations is affected also by the choice of the atomic pseudopotentials. Normally, in the calculations for the compounds containing 3d-atoms the semicore 3s- and 3p-states are treated as valence ones. With such basis sets, the calculations of the momentum-averaged characteristics of electron-phonon coupling are extremely time-consuming. An effective way to accelerate the calculations is to eliminate the semicore bands. So we have generated for titanium the ultrasoft Rabe-Rappe-Kaxiras-Joannopoulos pseudopotential with Purdew-Burke-Ernzerhof exchange and correlation (RRKJ-PBE) and only with the 3d- and 4s-states in basis set. The standard RRKJ-PBE pseudopotential was employed also for oxygen atoms. The details of the calculations with such pseudopotentials have been described in our previous paper on the excited *electron* relaxation in rutile and anatase [12]. They demonstrate that our modifications lead only to the changes in the calculated phonon spectra and electron-phonon coupling constants insignificant in the context of our discussions.

The electron excitation probabilities $T(n\mathbf{k}, n'\mathbf{k})$ were calculated based on the linear method of muffin-tin orbitals for the band structure calculations (LMTO-TB) computer code [29]. A well-known underestimation of the band gap inherent in this approach has been amended through the application of a single-site coulomb and exchange correction terms [30]. In order to calculate matrix elements of dipole moment the integration, procedures implemented in the GW computer code [31] have been employed.

3. Results and Discussions

In Figures 2, 3, and 4 we show the calculated values of λ, Γ, and Δe as functions of the excess energy of the hole E

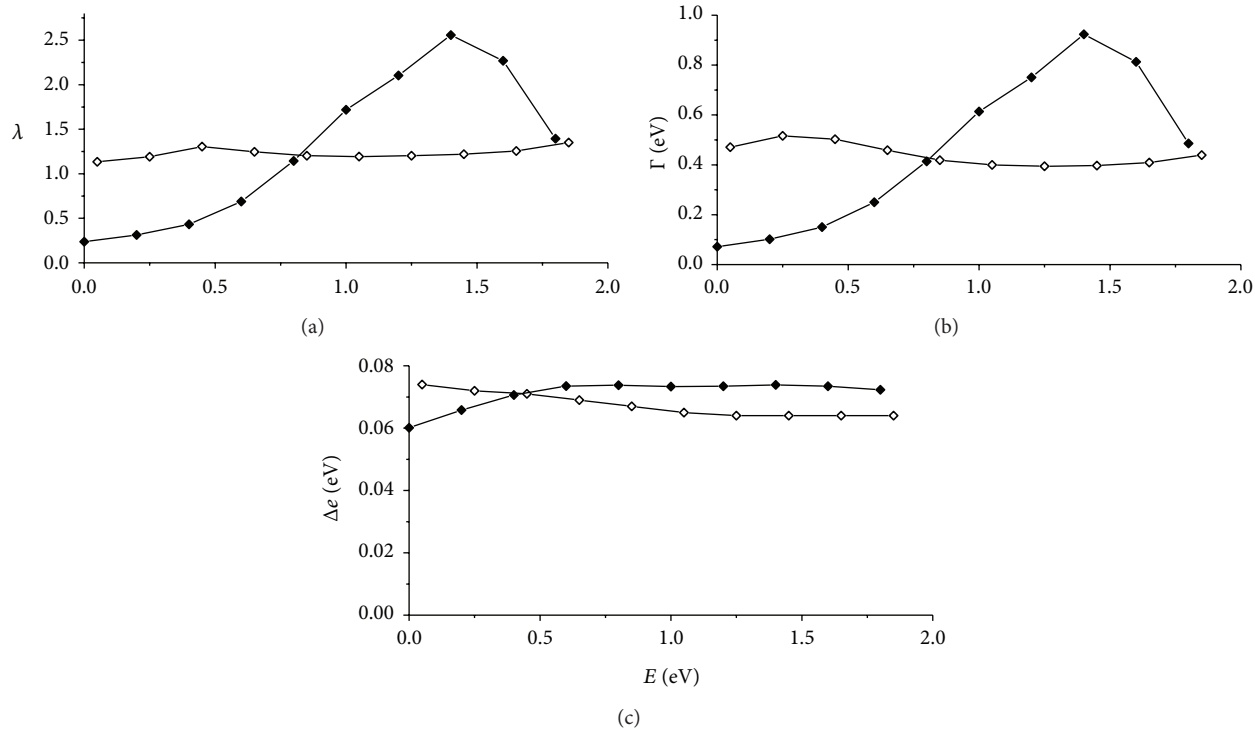

Figure 2: The mean characteristics of the hole-phonon (empty rhombus) and electron-phonon (black rhombus) relaxation for anatase as functions of the excess energy E. Here λ is the constant of interaction, Γ is the rate of energy loss according to (7) and (11), and Δe is the mean energy lost with emission of one phonon, in accordance with (9), (12), and (13).

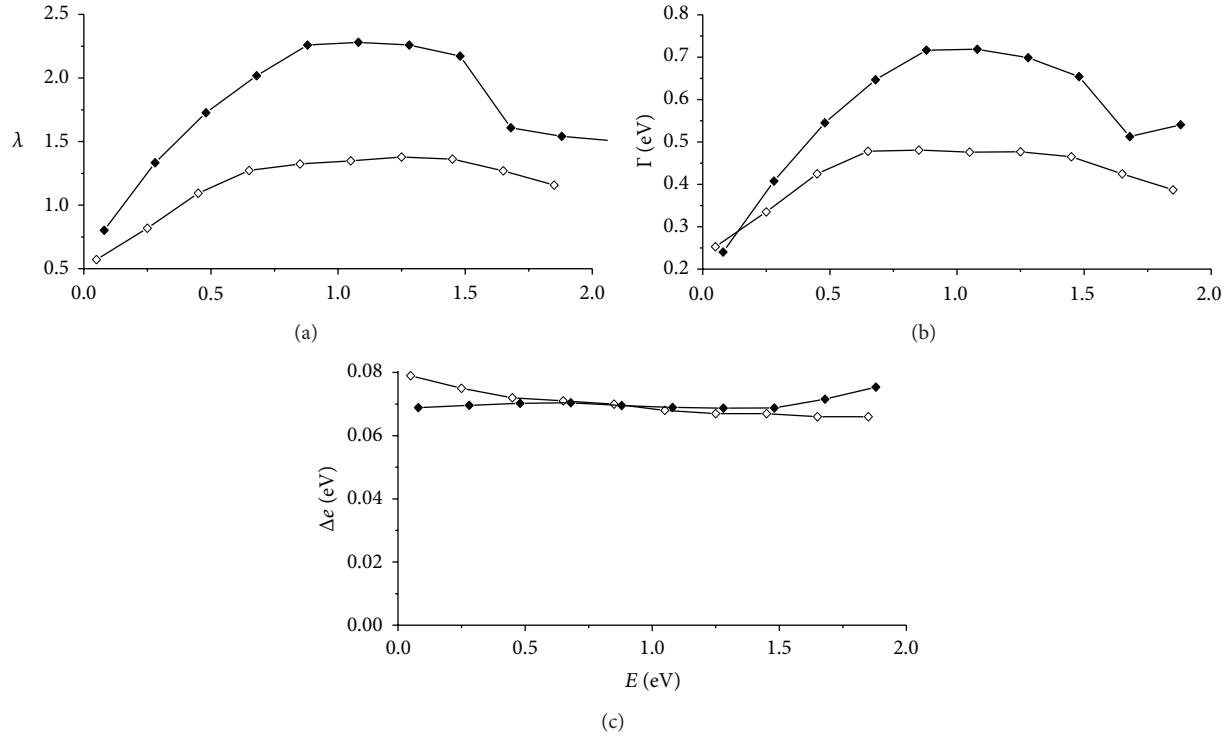

Figure 3: The characteristics of the hole-phonon and electron-phonon relaxation for rutile depending on the excess energy E. The sense of the plots is the same as in Figure 2.

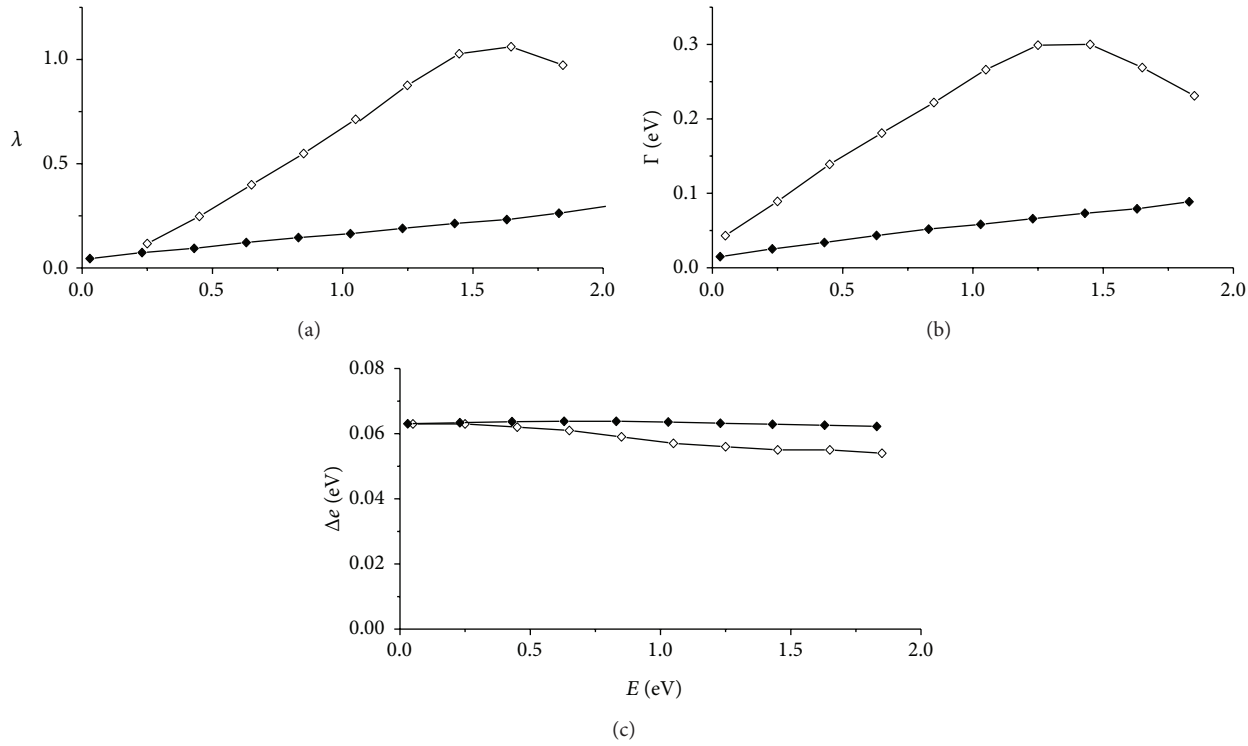

Figure 4: The characteristics of the hole-phonon and electron-phonon relaxation for ZnO depending on the excess energy E. The sense of the plots is the same as in Figure 2.

and compare them with the analogous values for excited electrons. For rutile, our results confirm the previously proposed assumption [1, 11] that the hole-phonon relaxation is a process slower than the electron-phonon relaxation. For anatase, however, the hole relaxation is slower than the electron relaxation only when the excess energy is higher than 0.7 eV. For ZnO the situation is strikingly different, as the rate of the hole relaxation is higher. In all the three cases the mean energy of the emitted phonon Δe is close to the analogous value for electrons, and this value changes insignificantly with changes in the excess energy. Therefore, we admit in the calculations for the energy loss time and distribution function that this value is constant and equal to 70 meV for anatase and rutile and 55 meV for ZnO.

In Figure 5 we show the time of energy loss of a hole, depending on its final energy E', as calculated using (14). This value has been calculated for the initial excess energy of the hole $E = 2$ eV that was the highest energy in the experiments [1]. For holes in rutile, the energy loss time $\tau_{\text{en}}(E', E)$ is at any excess energy ~30% longer than that for electrons. For holes in anatase the energy loss time is higher only when the excess energy is more than 0.5 eV. For holes in ZnO the energy loss time at any excess energy is about 3 times less than the electron energy loss time. So our results do not support the assumption that in the case of TiO_2 the hole relaxation time is much longer than the electron relaxation time, and that was proposed in earlier papers in order to explain the existence of the spectral dependence of photocatalytic activity.

Results of our calculations for the distribution functions of holes are shown in Figure 6. For anatase, the concentration of holes near zero excess energy is accompanied with a tail that extends to the energy of approximately 1 eV, the concentration of holes takes place both near the top of the valence band and in the lower states as well. This effect is even more pronounced in rutile which exhibits a sharp rise in the distribution at the energy of 0.4-0.5 eV. In the case of ZnO the rise of the distribution function appears only below 0.2 eV, and the hole concentration in the states below the top of the valence band is rather weak. In particular, the hole distribution differs in a crucial way from the analogous distribution for electrons, inasmuch as the calculations demonstrate that the concentration of excited electrons takes place only near the edge of the conduction band [21].

It has been shown [1, 3] that the quantum yield of the processes of photodegradation of a series of aromatic compounds on the surface of TiO_2 nanoparticles depends on the energy of the photon. In particular, with the rise of the excess energy an increase of the quantum yield is observed beginning from $E \sim 0.2$ eV. At higher energy, depending on the type of molecule, this rise converts to a plateau or a maximum. These results definitely demonstrate that the holes with excess energy higher than 0.2–0.5 eV participate in the oxidative reactions. This fact squares with the presence in our calculations of the distribution function that extend to ~1 eV.

Because the specimens studied in experiments were mixtures of the anatase and rutile phases, the question did not arise concerning which phase was responsible for the

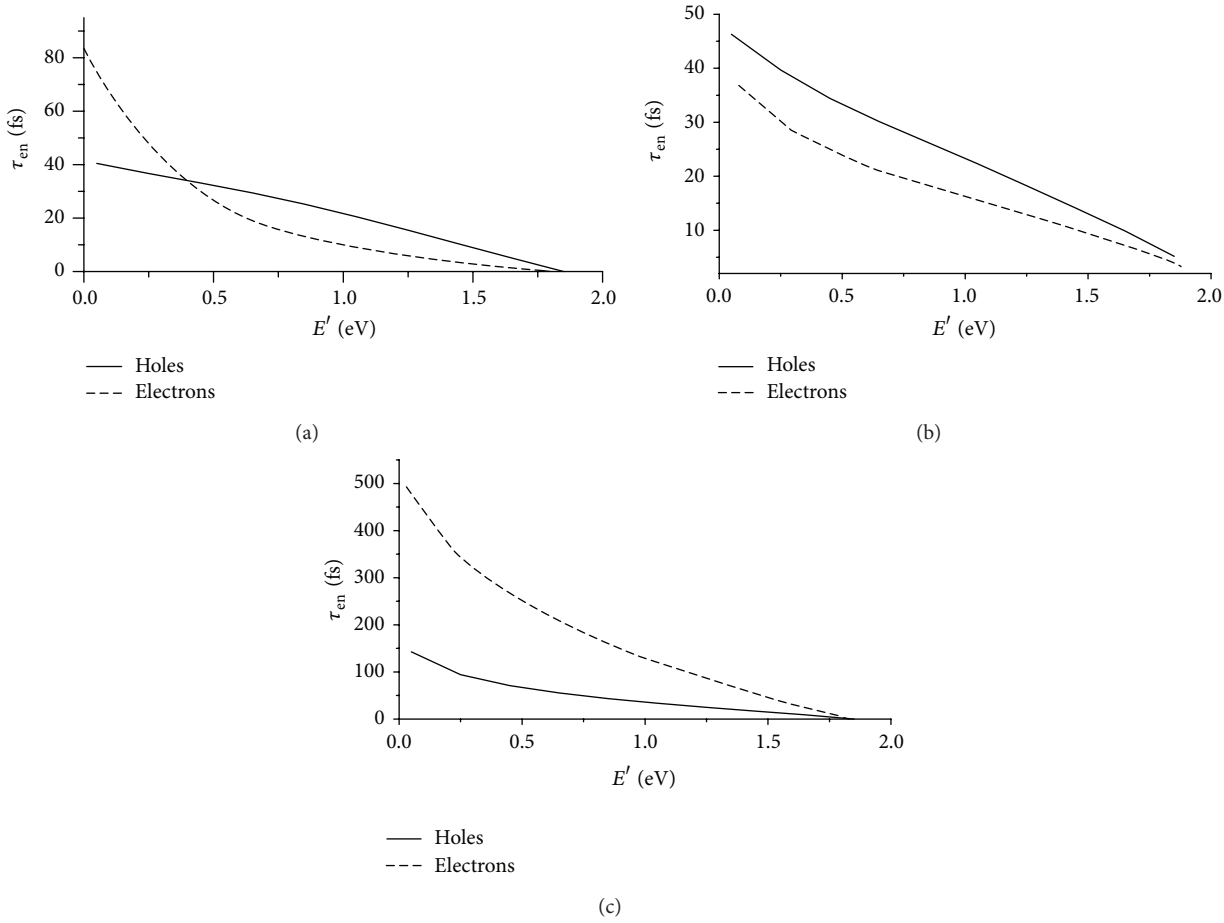

FIGURE 5: The time of energy loss of a hole (solid lines) depending on the final value of the excess energy E' for anatase (a), rutile (b), and zinc oxide (c). It is assumed that in the initial moment the hole was excited to the level $E = 2$ eV. For comparison, the analogous data are shown (dashed lines) for the energy loss time of excited electrons as calculated based on the results of the works [12, 13].

spectral dependence of the quantum yield. We can now turn our attention to the difference in the distribution functions of holes in the energy interval 0.2–0.7 eV. Here the value of this function is for rutile substantially higher than that for anatase. This difference indicates that rutile is the phase mostly responsible for the spectral dependence. To explain the differences in the distribution functions of anatase and rutile, let us examine the total densities of the states near the top of the valence band; see Figure 7. It is evident that, within the interval from 0 to 0.5 eV, the density of the states in anatase is much higher than that in rutile, consistently with (21), which generates smaller values for the distribution function. Physically, the higher distribution function of rutile reflects a much worse number of electrons that can drop to a hole state thus indicating its relaxation.

Our data indicate that zinc oxide is least favorable for the manifestation of spectral dependence of photocatalysis. The distribution function of holes in ZnO has a peak only below 0.2 eV, with no tail at a higher excess energy. The origin of the difference in the distribution functions of TiO_2 and ZnO is concealed in the details of the IDF-function $S_h(E)$, (21). In Figure 8 we show the IDF calculated for photon energies from 3.4 to 4.6 eV. These results demonstrate that in the case of anatase and rutile the holes are produced in both the lower states and the states near the top of the valence band. In both cases, with increase in photon energy, the maxima of the IDF shift to higher excess energy. In the case of anatase, the main feature of the distribution is a high peak located near the excess energy E that changes with the photon energy E_{exc} approximately as $E = -2.0 + 0.66E_{exc}$. This change is accompanied by spikes at lower E that are much lower in height. In the case of rutile, the analogous dependence is more complicated. At excitation energies above 3.5 eV, up to seven peaks of comparable height, are observed. Thus, in this case, the holes are produced with comparable probability in many states below the top of the valence band.

In contrast, in the case of ZnO, the holes are produced only in states near the top of the valence band. The IDF dependence has only one peak, which does not appear beyond 0.2 eV. In accordance with (22), the quasistationary distribution function also does not appear at the energy beyond this limit. Given this, the absence of excitations from the low-energy valence band states and spectral dependence of the oxidative reactions are unlikely in ZnO.

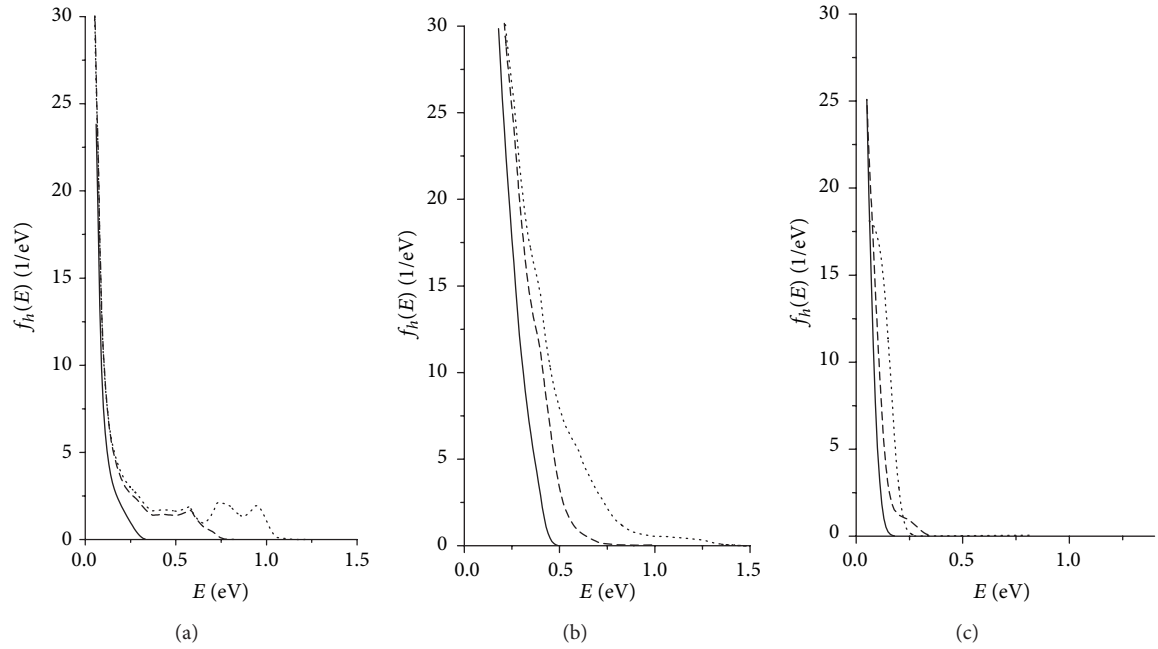

Figure 6: The calculated distribution function of holes in anatase (a), rutile (b), and zinc oxide (c). In solid lines the data are shown for the photon energy of 3.5 eV, in dashed lines the data are shown for 4.0 eV, and in point lines the data are shown for 4.5 eV. It is assumed that $S_0(t) = 1$.

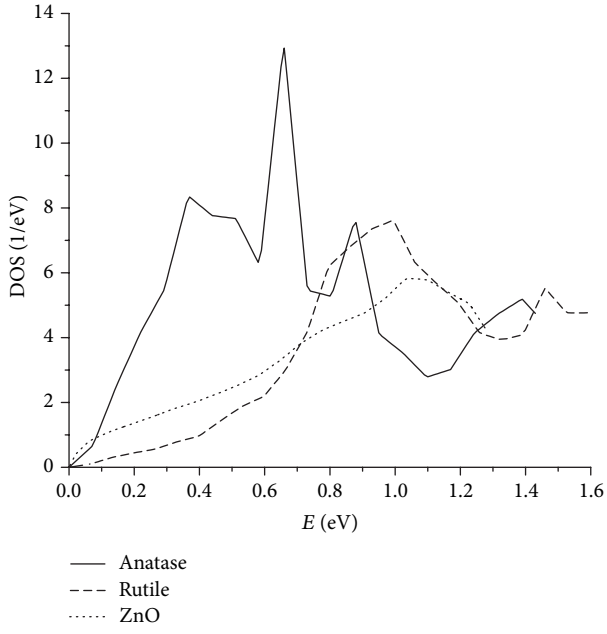

Figure 7: The total density of states near the top of the valence band versus the excess energy. The solid line is for anatase, the dashed line is for rutile, and the dotted line is for zinc oxide.

The results of our calculations make it possible to estimate the timescale of hole transfer from the bulk of the crystals to absorbed molecules. The experimental data [2, 3] demonstrate an increase in the rate of oxidative reactions when the excess energy of holes exceeds 0.2–0.5 eV. Our calculations for the hole distribution functions for TiO_2 show that the holes can emerge in many states lower than the top of the valence band. If the time of the hole transfer to molecules is less than the time of the energy loss via coupling with phonons, the holes in the states below the top of the valence band cannot participate in oxidative reactions. Hence one can expect that the time of hole transfer should be less than ~50 fs.

In order to compare this result with the experimental data of Morishita et al. [4], we need to take into account the essential differences between our first-principle and Morishita's experimental approach. We evaluate the relaxation rate of a single hole, but the results of Morishita et al. definitely demonstrate the dependence of the hole transfer time on the pump power intensity, that is, on the number of excited holes. Hence one should compare our estimation with the extrapolation of the Morishita's results to zero pump power. Because of the shortage of experimental data for low pump power, this extrapolation cannot be reliably performed. It is clear, however, that the extrapolated data should be lower than 100 fs.

Unfortunately, the experimental data on the hole relaxation rate in ZnO are absent. Also the absence of experimental data on the spectral dependence of the photocatalytic yields makes the evaluation of the hole transfer time in ZnO impossible now.

Note that first-principles calculations for the hole transfer time have not been performed.

4. Conclusions

We have performed first-principles calculations for characteristics of electron-phonon relaxation of excited holes in the valence band of TiO_2 and ZnO. These values are

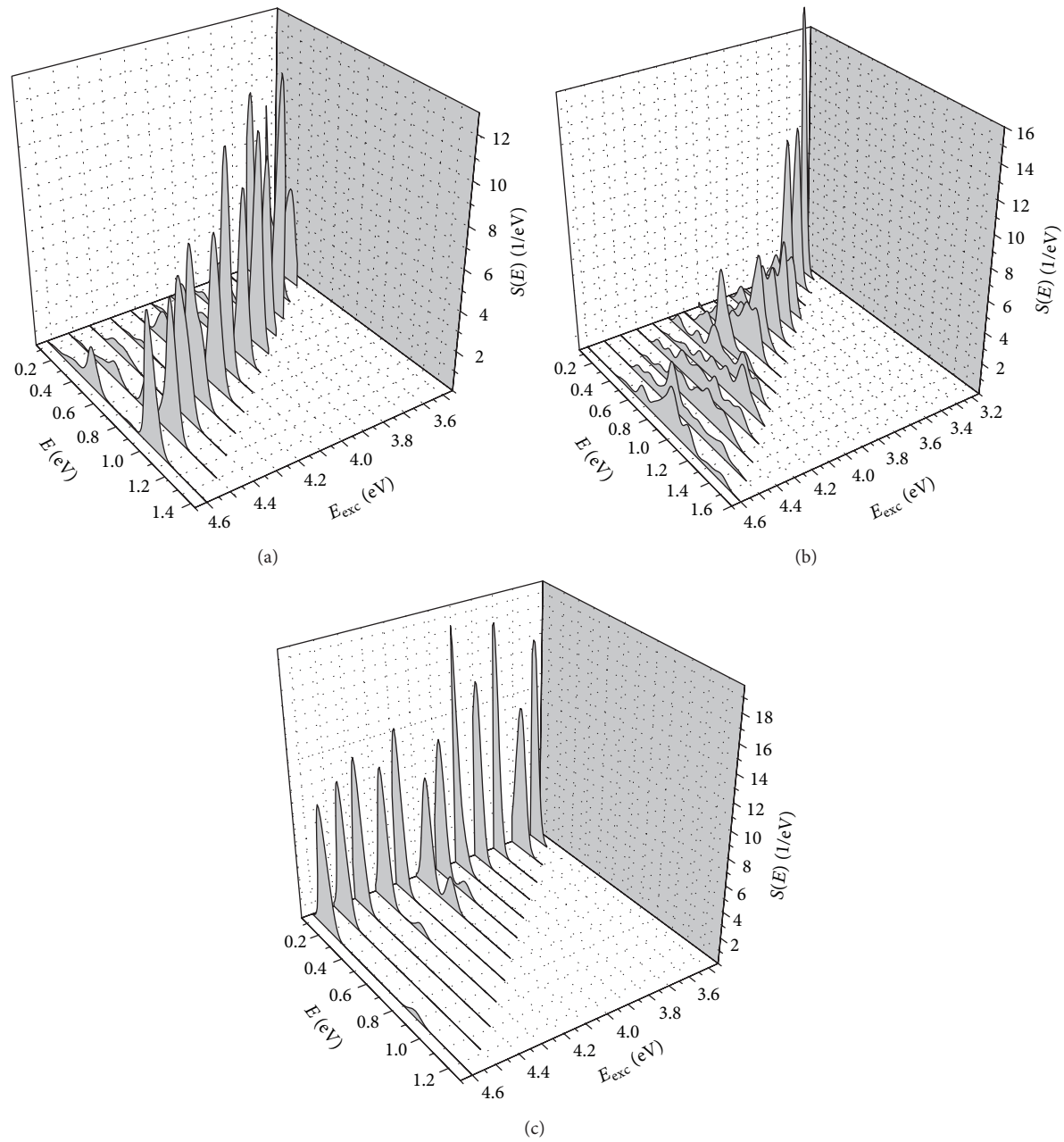

Figure 8: Instantaneous distribution function for anatase (a), rutile (b), and zinc oxide (c) depending on the excess energy of hole E, as calculated for the photon energy E_{exc} from 3.4 eV to 4.6 eV.

the constant of electron-phonon coupling, the rate of energy loss, the mean energy of the emitted phonon, and the time of energy loss of a hole. In the case of rutile we find that the time of energy loss of a hole is about 30% higher than that of an electron. For anatase the time of energy loss of a hole is higher than that of an electron only when excess energy exceeds 0.4 eV. Since these data do not directly correlate with experimental results on the rate of oxidative reactions, we conclude that the time of energy loss of a hole is not a major factor in the emergence of the spectral dependence of photocatalytic activity.

In order to elucidate the origin of the spectral dependence of oxidative reactions, we calculated the instantaneous and quasistationary distribution functions of the holes. These functions differ significantly from the analogous functions of excited electrons. The electron distribution functions demonstrate the concentration of excited electrons near zero excess energy that is in the states near the bottom of the conduction band. The distribution functions of holes in anatase reveal the presence of holes in the states more than ~0.8 eV below the top of the valence band. The distribution of holes in rutile shows a significant increase at excess energy above 0.4 eV,

thus reflecting a phenomenon favorable for photocatalytic activity, as this energy increases the oxidative potential of TiO_2. The presence of holes in the states below the top of the valence band is consistent with the available experimental data which indicate an increase in the photocatalytic activity at excess energy above 0.2 eV. We thus conclude that the major factor responsible for the spectral dependence of photocatalytic activity in TiO_2 is a high probability of excitations from the states below the top of the valence band.

We obtained different results for ZnO which make us conclude that the probability of finding spectral dependence of the photocatalytic activity is less for ZnO than for TiO_2. The major argument in favor of this conclusion is that the calculated distribution function of holes in ZnO does not extend above the excess energy of 0.2 eV.

Conflict of Interests

The authors declare that there is no conflict of interests regarding the publication of this paper.

Acknowledgments

The authors acknowledge financial support from the Spanish MICINN (Grant no. FIS2010-19609-C02-01), the Departamento de Educacíon del Gobierno Vasco, the University of the Basque Country (Grant no. GIC07-IT-366-07), and the Presidium of the Ural Branch of Russian Academy of Sciences (Grant no. 12-U-3-1001). The help of Professor L. Baker in the preparation of the paper is also greatly acknowledged. The calculations were performed using the URAN cluster of the Institute of Mathematics and Mechanics of the Russian Academy of Sciences, Yekaterinburg.

References

[1] M. A. Grela, M. A. Brusa, and A. J. Colussi, "Harnessing excess photon energy in photoinduced surface electron transfer between salicylate and illuminated titanium dioxide nanoparticles," *The Journal of Physical Chemistry B*, vol. 101, no. 51, pp. 10986–10989, 1997.

[2] M. A. Grela and A. J. Colussi, "Photon energy and photon intermittence effects on the quantum efficiency of photoinduced oxidations in crystalline and metastable TiO_2 colloidal nanoparticles," *The Journal of Physical Chemistry B*, vol. 103, no. 14, pp. 2614–2619, 1999.

[3] M. A. Grela, M. A. Brusa, and A. J. Colussi, "Efficiency of hot carrier trapping by outer-sphere redox probes at quantum dot interfaces," *The Journal of Physical Chemistry B*, vol. 103, no. 31, pp. 6400–6402, 1999.

[4] T. Morishita, A. Hibara, T. Sawada, and I. Tsuyumoto, "Ultrafast charge transfer at TiO_2/SCN^- (aq) interfaces investigated by femtosecond transient reflecting grating method," *The Journal of Physical Chemistry B*, vol. 103, no. 29, pp. 5984–5987, 1999.

[5] A. Emeline, A. Salinaro, and N. Serpone, "Spectral dependence and wavelength selectivity in heterogeneous photocatalysis. I. Experimental evidence from the photocatalyzed transformation of phenols," *The Journal of Physical Chemistry B*, vol. 104, no. 47, pp. 11202–11210, 2000.

[6] Y. Tamaki, A. Furube, R. Katoh et al., "Trapping dynamics of electrons and holes in a nanocrystalline TiO_2 film revealed by femtosecond visible/near-infrared transient absorption spectroscopy," *Comptes Rendus Chimie*, vol. 9, no. 2, pp. 268–274, 2006.

[7] Y. Tamaki, A. Furube, M. Murai, K. Hara, R. Katoh, and M. Tachiya, "Dynamics of efficient electron-hole separation in TiO_2 nanoparticles revealed by femtosecond transient absorption spectroscopy under the weak-excitation condition," *Physical Chemistry Chemical Physics*, vol. 9, no. 12, pp. 1453–1460, 2007.

[8] Y. Tamaki, A. Furube, M. Murai, K. Hara, R. Katoh, and M. Tachiya, "Direct observation of reactive trapped holes in TiO_2 undergoing photocatalytic oxidation of adsorbed alcohols: evaluation of the reaction rates and yields," *Journal of the American Chemical Society*, vol. 128, no. 2, pp. 416–417, 2006.

[9] Q. Shen, K. Katayama, M. Yamaguchi, T. Sawada, and T. Toyoda, "Study of ultrafast carrier dynamics of nanostructured TiO_2 films with and without CdSe quantum dot deposition using lens-free heterodyne detection transient grating technique," *Thin Solid Films*, vol. 486, no. 1-2, pp. 15–19, 2005.

[10] Q. Shen, K. Katayama, T. Sawada, M. Yamaguchi, Y. Kumagai, and T. Toyoda, "Photoexcited hole dynamics in TiO_2 nanocrystalline films characterized using a lens-free heterodyne detection transient grating technique," *Chemical Physics Letters*, vol. 419, no. 4-6, pp. 464–468, 2006.

[11] M. A. Henderson, "A surface science perspective on TiO_2 photocatalysis," *Surface Science Reports*, vol. 66, no. 6-7, pp. 185–297, 2011.

[12] V. Zhukov, E. Chulkov, and J. Phys, "*Ab initio* approach to the excited electron dynamics in rutile and anatase TiO_2," *Journal of Physics: Condensed Matter*, vol. 22, no. 43, Article ID 435802, 2010.

[13] V. P. Zhukov, P. M. Echenique, and E. V. Chulkov, "Two types of excited electron dynamics in zinc oxide," *Physical Review B—Condensed Matter and Materials Physics*, vol. 82, no. 9, Article ID 094302, 2010.

[14] R. Marcus, "On the theory of electron-transfer reactions. VI. Unified treatment for homogeneous and electrode reactions," *The Journal of Chemical Physics*, vol. 43, pp. 679–701, 1965.

[15] R. A. Marcus, "Reorganization free energy for electron transfers at liquid-liquid and dielectric semiconductor-liquid interfaces," *The Journal of Physical Chemistry*, vol. 94, no. 3, pp. 1050–1055, 1990.

[16] R. A. Marcus, "Electron transfer reactions in chemistry: theory and experiment (Nobel Lecture)," *Angewandte Chemie International Edition in English*, vol. 32, no. 8, pp. 1111–1121, 1993.

[17] J. M. Pitarke, V. P. Zhukov, R. Keyling, E. V. Chulkov, and P. M. Echenique, "Ultrafast electron dynamics in metals," *ChemPhysChem*, vol. 5, no. 9, pp. 1284–1300, 2004.

[18] V. P. Zhukov, E. V. Chulkov, and P. M. Echenique, "Lifetimes of excited electrons in Fe and Ni: first-principles GW and the T-matrix theory," *Physical Review Letters*, vol. 93, no. 9, Article ID 096401, 4 pages, 2004.

[19] E. V. Chulkov, A. G. Borisov, J. Gauyacq et al., "Electronic excitations in metals and at metal surfaces," *Chemical Reviews*, vol. 106, no. 10, pp. 4160–4206, 2006.

[20] S. Baroni, S. de Gironcoli, A. dal Corso, and P. Giannozzi, "Phonons and related crystal properties from density-functional perturbation theory," *Reviews of Modern Physics*, vol. 73, no. 2, pp. 515–562, 2001.

[21] V. Zhukov, V. Tyuterev, and E. Chulkov, "Electron-phonon relaxation and excited electron distribution in zinc oxide and anatase," *Journal of Physics: Condensed Matter*, vol. 24, no. 40, Article ID 405802, 2012.

[22] G. M. Eliashberg, "The low temperature specific heat of metals," *Soviet Physics, The Journal of Experimental and Theoretical Physics*, vol. 16, no. 3, pp. 780–781, 1963.

[23] G. Grimvall, *The Electron-Phonon Interactions in Metals*, North-Holland Publisher, Amsterdam, The Netherlands, 1981.

[24] O. Andersen, O. Jepsen, and M. Sob, "Linearized band structure methods," in *Electronic Band Structure and Its Applications*, M. Yussouff, Ed., vol. 283 of *Lecture Notes in Physics*, Springer, 1987.

[25] R. Loudon, *The Quantum Theory of Light*, Oxford University Press, New York, NY, USA, 1983.

[26] V. P. Zhukov and E. V. Chulkov, "*Ab initio* approach to the rate of radiative electron trapping and electron-hole recombination in B-, C-, and N-doped anatase," *Physica Status Solidi B: Basic Research*, vol. 249, no. 5, pp. 1063–1071, 2012.

[27] 2010, http://www.quantum-espresso.org and http://www.pwscf.org.

[28] R. Sikora, "*Ab initio* study of phonons in the rutile structure of TiO_2," *Journal of Physics and Chemistry of Solids*, vol. 66, no. 6, pp. 1069–1073, 2005.

[29] O. Jepsen, G. Krier, A. Burkhardt, and O. K. Andersen, *The TB-LMTO-ASA program, Max-Planck-Institut für Festkörperforschung, Heisen-bergstr*, Federal Republic of Germany, Stuttgart, Germany, 1994.

[30] V. I. Anisimov, J. Zaanen, and O. K. Andersen, "Band theory and Mott insulators: Hubbard U instead of Stoner I," *Physical Review B*, vol. 44, no. 3, pp. 943–954, 1991.

[31] F. Aryasetiawan and O. Gunnarsson, "Product-basis method for calculating dielectric matrices," *Physical Review B*, vol. 49, no. 23, pp. 16214–16222, 1994.

Hindawi Publishing Corporation
International Journal of Photoenergy
Volume 2014, Article ID 945930, 6 pages
http://dx.doi.org/10.1155/2014/945930

Research Article

Antimicrobial Activity of TiO_2 Nanoparticle-Coated Film for Potential Food Packaging Applications

Siti Hajar Othman, Nurul Raudhah Abd Salam, Norhazlizam Zainal, Roseliza Kadir Basha, and Rosnita A. Talib

Department of Process and Food Engineering, Faculty of Engineering, University Putra Malaysia, 43400 Serdang, Selangor, Malaysia

Correspondence should be addressed to Siti Hajar Othman; s.hajar@upm.edu.my

Received 29 January 2014; Revised 12 March 2014; Accepted 12 March 2014; Published 2 April 2014

Academic Editor: Jiaguo Yu

Recent uses of titanium dioxide (TiO_2) have involved various applications which include the food industry. This study aims to develop TiO_2 nanoparticle-coated film for potential food packaging applications due to the photocatalytic antimicrobial property of TiO_2. The TiO_2 nanoparticles with varying concentrations (0–0.11 g/100 mL organic solvent) were coated on food packaging film, particularly low density polyethylene (LDPE) film. The antimicrobial activity of the films was investigated by their capability to inactivate *Escherichia coli* (*E. coli*) in an actual food packaging application test under various conditions, including types of light (fluorescent and ultraviolet (UV)) and the length of time the film was exposed to light (one–three days). The antimicrobial activity of the TiO_2 nanoparticle-coated films exposed under both types of lighting was found to increase with an increase in the TiO_2 nanoparticle concentration and the light exposure time. It was also found that the antimicrobial activity of the films exposed under UV light was higher than that under fluorescent light. The developed film has the potential to be used as a food packaging film that can extend the shelf life, maintain the quality, and assure the safety of food.

1. Introduction

There has been a growing amount of research undertaken into the applications of titanium dioxide (TiO_2) photocatalyst due to the high photocatalytic activity of this material. Currently, there is considerable interest in the antimicrobial property of TiO_2 for applications in the food industry. TiO_2 is nontoxic and the American Food and Drug Administration (FDA) has approved TiO_2 for use in human food, drugs, cosmetics, and food contact materials. The photocatalytic reaction of TiO_2 has been used to inactivate a wide spectrum of microorganisms [1–3]. The bactericidal and fungicidal effects of TiO_2 on, for example, *Escherichia coli* (*E. coli*), *Staphylococcus aureus*, and *Pseudomonas putida* have been widely reported [4, 5]. The development of TiO_2-coated or incorporated food packaging has also received attention [6–9].

For food packaging applications, the main purpose of the antimicrobial agent is to act against microorganisms and enhance the functions of conventional food packaging, namely, shelf life extension, maintenance of quality, and safety assurance [10]. The antimicrobial agent inhibits spoilage and reduces pathogenic microorganisms [11]. The antimicrobial agent also helps extend the shelf life of foods by extending the lag period of microorganisms, thereby diminishing their growth and number. Although there are numerous studies of coatings or antimicrobials incorporated into food packaging [6–9], the coating of nanometre sized antimicrobial particles, particularly TiO_2 nanoparticles, onto food packaging film has not been studied extensively.

The advent of nanotechnology has greatly improved the photocatalytic properties of TiO_2. The TiO_2 nanoparticles have attracted considerable attention because they exhibit unique and improved properties compared to their bulk material counterparts [12]. They show quantum size effects in which the physical and chemical properties of materials are strongly dependent on particle size. At the nanoscale level, the particle size decreases and the surface area of the particles

increase dramatically. This is one of the desired features for the nanoparticles to be used and exploited for photocatalytic applications.

Microorganisms can be killed by TiO_2 upon illumination of light due to its photocatalytic properties. Hydroxyl radicals and reactive oxygen species generated on the illuminated TiO_2 surface play a role in inactivating microorganism by oxidising the polyunsaturated phospholipid components of the cell membrane of the microbes [13, 14]. The use of nanometre sized TiO_2 particles has the potential to further enhance the antimicrobial activity of TiO_2. Effective antimicrobial film that can extend the shelf life, maintain the quality, and assure the safety of the food can be developed by coating TiO_2 nanoparticles onto food packaging materials. This creates a large commercial potential for TiO_2 nanoparticles applications in food industry.

The aim of this study is to develop TiO_2 nanoparticle-coated film, particularly low density polyethylene (LDPE) film, by investigating the effect of TiO_2 nanoparticle concentrations (0–0.11 g/100 mL organic solvent), types of light (fluorescent and ultraviolet (UV)), and light exposure time (one–three days) on the antimicrobial activity of the film for potential food packaging applications. The study was undertaken on lettuce packed with uncoated and TiO_2 nanoparticle-coated films against *E. coli*. This research work offers knowledge for developing antimicrobial nanoparticle-coated food packaging film with consideration for advancement in industrial applications.

2. Experimental

2.1. Preparation of TiO_2 Nanoparticle-Coated Films. Commercial TiO_2 nanoparticles, Aeroxide P25, were obtained from Evonik Industries (average particle size: 25 nm, purity: ≥99.5% trace metals basis, crystalline phase: 80% anatase + 20% rutile). An amount of TiO_2 nanoparticles (0.05, 0.08, and 0.11 g) was mixed with 100 mL organic solvent, particularly ethyl methyl ketone (MEK), to produce TiO_2 nanoparticle concentrations of 0.05 g/100, 0.08 g/100, and 0.11 g/100 mL MEK. The suspensions were ultrasonically irradiated using an ultrasonic probe homogeniser equipped with a temperature controller (Cole-Parmer) for 30 minutes [4]. Based on our previous study related to dispersion and stabilisation of photocatalytic TiO_2 nanoparticles in aqueous suspension, it was expected that the nanoparticles would form agglomerates and that there would be a change in cluster size before and after the ultrasonication [4]. However, note that in this work, changes in cluster size were not measured.

The suspension was then manually coated onto one side of low density polyethylene (LDPE) packaging film (dimensions: 16.5 cm × 17.8 cm, thickness: 0.01 mm) using a K bar coater (RK Print Instruments, UK) at room temperature and dried in air for 10 minutes. A cleanroom was utilised to reduce any possible contamination that could be adsorbed or chemisorbed on to the surface of the coated films. Note that there were no significant changes in the thickness of the film after the coating process, probably due to the nanometre-sized TiO_2 particles suspension being too small to make a measurable difference to the thickness.

2.2. Preparation of E. coli Cells. *E. coli* is a Gram-negative, rod-shaped bacterium that is usually found in the human intestine. Most *E. coli* strains are harmless, but some variations can cause serious food poisoning in their hosts such as *E. coli* O157 : H7. In this work, *E. coli* O157 : H7 was obtained from the Laboratory of Microbiology, Faculty of Food Science and Technology, University Putra Malaysia. The *E. coli* cells were grown in a conical glass flask (Schott Duran) containing 500 mL Luria-Bertani broth (Becton, Dickinson & Co.). The flask was incubated on a rotary shaker (New Brunswick Scientific Co.) at 37°C for 24 hours at 150 rpm. After incubation, the *E. coli* cells were harvested by centrifugation (FinePCR) at 4000 ×g for 20 minutes and washed twice with distilled water. Microbial stock solution was prepared by suspending the final pellets in distilled water. Serial dilution was undertaken to obtain the desired initial concentration of microbial solution. The initial population of *E. coli* (CFU/mL) was determined using a colony count method and was found to be $7.33 \times 10^8 \pm 1.13$ CFU/mL or 8.86 ± 0.12 log CFU/mL (mean value ± standard deviation).

2.3. Actual Antimicrobial Test of Uncoated and TiO_2 Nanoparticle-Coated Films. Fresh lettuce was used in this experiment and cooled overnight at 4°C. The damaged part and outer parts of the lettuce were discarded. Then 25 g lettuce was cut and dipped in 10% sodium hypochlorite solution (PC Laboratory Reagent) for about two minutes for the purpose of cleaning. The cut lettuce was then dip-inoculated with *E. coli* with a concentration of about $7.33 \times 10^8 \pm 1.13$ CFU/mL for two minutes at room temperature and the excess solution was shaken off. The concentration of *E. coli* inoculated on the lettuce was assumed constant. Subsequently, about 25 g of cut lettuce pieces were taken out and packed in the uncoated or the TiO_2 nanoparticle-coated films.

The packages were placed in a dark box complete with an 8W lamp (fluorescent or UV lamp) at room temperature. Then, the packages were exposed to different types of light, namely, fluorescent at a wavelength of 425 nm or UV at a wavelength of 365 nm. An amount of 25 g of lettuce was taken after each light exposure at designated interval times (1, 2, or 3 days) for the determination of the *E. coli* colony whereby the lettuce was placed into 225 mL of distilled water and mixed using a stomacher bag for two minutes. Serial dilution was made in distilled water solution to produce countable *E. coli* colony dilutions and 0.1 mL of the undiluted and diluted solutions were plated onto Luria-Bertani agar (Becton, Dickinson & Co.) in petri dishes using the spread plate technique. A glass rod was utilised to ensure the uniformity of the spread area on the agar plates. The agar plates were then incubated in an incubator at 37°C for 24 hours. Two replicate plates were used for each dilution. After 24 hours, the colonies formed on the agar were calculated using a colony counter machine. The number of viable *E. coli* cells was presented as CFU/g lettuce. The initial concentration of *E. coli* was 9.70 ± 0.10 log CFU/g (mean value ± standard deviation).

The procedures were repeated for different light exposure times (1, 2, and 3 days). The actual antimicrobial test was

Table 1: The *E. coli* colony values (CFU/g) of the uncoated and coated films for various TiO_2 concentrations (0.05, 0.08, and 0.11 g/100 mL MEK) at designated interval times (1, 2, 3 days) exposed under fluorescent and UV light.

Light	Sample film	Day	Log CFU/g
Fluorescent	Uncoated	1	10.06 ± 0.11
		2	10.18 ± 0.18
		3	10.31 ± 0.13
Fluorescent	Coated—0.05 g TiO_2/100 mL MEK	1	9.08 ± 0.15
		2	8.38 ± 0.13
		3	8.67 ± 0.20
Fluorescent	Coated—0.08 g TiO_2/100 mL MEK	1	7.96 ± 0.10
		2	7.72 ± 0.11
		3	7.47 ± 0.15
Fluorescent	Coated—0.11 g TiO_2/100 mL MEK	1	7.44 ± 0.14
		2	7.30 ± 0.17
		3	7.07 ± 0.09
UV	Uncoated	1	9.36 ± 0.18
		2	9.94 ± 0.12
		3	10.04 ± 0.12
UV	Coated—0.05 g TiO_2/100 mL MEK	1	7.16 ± 0.11
		2	7.02 ± 0.20
		3	6.86 ± 0.16
UV	Coated—0.08 g TiO_2/100 mL MEK	1	6.96 ± 0.07
		2	6.94 ± 0.22
		3	6.44 ± 0.15
UV	Coated—0.11 g TiO_2/100 mL MEK	1	6.82 ± 0.10
		2	6.68 ± 0.09
		3	6.29 ± 0.17

repeated at least twice for all the conditions (different concentrations of TiO_2, different light exposure times, and different types of light). Note that all the procedures were undertaken inside a cleanroom to minimise any possible contamination.

3. Results and Discussion

The effect of various TiO_2 concentrations (0–0.11 g/100 mL MEK), types of light (fluorescent and UV), and the time of exposure to light of the films (one–three days) on the antimicrobial activity of the films was determined and plotted in Figure 1. For purposes of clarity, the *E. coli* colony values (log CFU/g) obtained are also tabulated in Table 1. Note that the initial *E. coli* colony value determined using the colony count method was 9.70 ± 0.10 log CFU/g.

As expected, Figure 1 and Table 1 show that the *E. coli* colony for lettuce packed with TiO_2 nanoparticle-coated films decreased over time after being exposed to both fluorescent and UV light. This is attributed to the antimicrobial property of the TiO_2 nanoparticles. For instance, the *E. coli* colony for film coated with 0.05 g TiO_2/100 mL MEK reduced from an initial value of 9.70 ± 0.10 log CFU/g to 8.67 ± 0.20 and 6.86 ± 0.16 log CFU/g after being exposed for three days to fluorescent and UV light, respectively. Moreover, although not significant, it seems that the *E. coli* colony values decreased with an increase in the light exposure time due

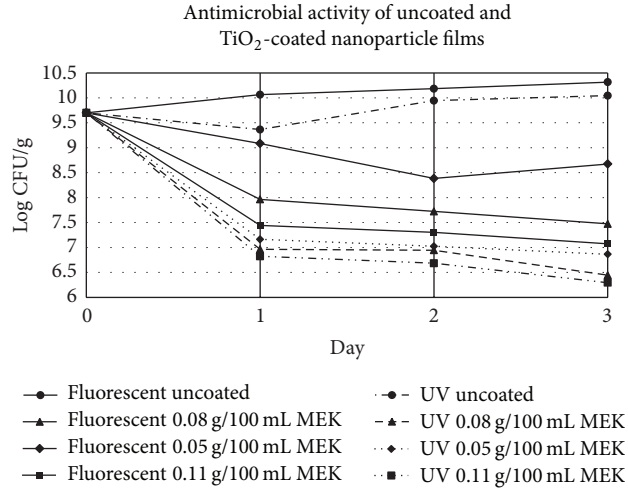

Figure 1: Antimicrobial activity of uncoated and coated films for various TiO_2 concentrations (0.05, 0.08, and 0.11 g/100 mL MEK) at designated interval times (1, 2, and 3 days) exposed to fluorescent and UV light.

to the higher chances for TiO_2 to photocatalytically react at longer light exposure time. For example, the *E. coli* colony for film coated with 0.08 g TiO_2/100 mL MEK reduced from an initial value of 9.70 ± 0.10 log CFU/g to 7.96 ± 0.10,

7.72 ± 0.11, and 7.47 ± 0.15 log CFU/g after being exposed for, respectively, 1, 2, and 3 days to fluorescent light.

In contrast, the *E. coli* colony for the lettuce packed with uncoated films increased from 9.70 ± 0.10 log CFU/g to 10.31 ± 0.13 and 10.04 ± 0.12 log CFU/g after being exposed for three days to fluorescent and UV light. The result occurred due to the absence of the TiO_2 antimicrobial agent, thus proving that the uncoated films did not exhibit any antimicrobial effect. This finding is consistent with the work of Chawengkijwanich and Hayata [9] who found that after two days, the number of cells of *E. coli* from cut lettuce which packed in uncoated film was higher than the initial concentration of *E. coli*, whereas the number of cells from TiO_2-coated polypropylene film was lower than the initial concentration. This result implies that the TiO_2 nanoparticle-coated film has the ability to decrease the microbial contamination on food products as well as decrease the risk of microbial growth in food packaging.

Note that for the uncoated film under UV light illumination, the *E. coli* colony decreased slightly from an initial value of 9.70 ± 0.10 log CFU/g to 9.36 ± 0.18 log CFU/g (day 1) possibly due to the sterile property of the UV light whereby UV light impairs microorganism cells by means of oxidative stress caused by oxygen radicals inside the cells [15]. However, UV light alone, without the presence of an antimicrobial agent is not capable of adequately inactivating the *E. coli*. The *E. coli* colony for the uncoated film under UV light illumination increased from 9.36 ± 0.18 log CFU/g to 10.04 ± 0.12 log CFU/g from day 1 to day 3.

The mechanism for the events occurring on the TiO_2 nanoparticle coating can be explained as follows. When TiO_2 nanoparticles are irradiated with light suitable to their bandgap energy of 3.2 eV or higher (wavelengths below 385 nm), they have a tendency to experience all of the physical phenomena that include absorption, reflection, and scattering of light. Apart from that, TiO_2 nanoparticles will also be involved in photophysical and photochemical processes. In a photophysical process, the absorbed photons of light will excite the electrons (e^-) from the valence band to the conduction band leaving holes (h^+) in the valence band which generate electron and hole pairs (1). These energised electron and hole pairs can either recombine and dissipate the energy as heat (2) or dissociate because of charge trapping thus producing charge carriers available for the redox reactions ((3) and (4)) in the photochemical processes [16].

$$TiO_2 + h\nu \longrightarrow e^- + h^+ \quad \text{(Photogeneration of electron and hole pairs)} \tag{1}$$

$$e^- + h^+ \longrightarrow \text{light or phonon emission} - \text{heat} \quad \text{(Electron and hole recombination)} \tag{2}$$

$$D + h^+ \longrightarrow D^{\bullet +} \quad \text{(Oxidation)} \tag{3}$$

$$A + e^- \longrightarrow A^{\bullet -} \quad \text{(Reduction)} \tag{4}$$

A portion of the photoexcited electron and hole pairs will diffuse to the surface of the TiO_2 nanoparticles and take part in the chemical reaction with the adsorbed electron donors (D) or adsorbed electron acceptors (A). The holes can oxidise adsorbed electron donors (3), whereas the electrons can reduce appropriately adsorbed electron acceptors (4) [17].

The water in the air acts as an electron donor to react with the holes to produce the highly reactive hydroxyl radical ($OH^\bullet$) (5). Oxygen that is omnipresent on the surface of the particles acts as an electron acceptor by forming the superoxide ion (O_2^-) (6). The holes, the hydroxyl radicals, and superoxide ion are very powerful oxidants that can be used to oxidise and naturally decompose common organic matters such as odour molecules, bacteria, and viruses to water and carbon dioxide (7). Among them, hydroxyl radicals play the most important role in inactivating microorganism by oxidising the polyunsaturated phospholipid component of the cell membrane of microbes

$$H_2O + h^+ \longrightarrow OH^\bullet + H^+ \quad \text{(Formation of hydroxyl radicals)} \tag{5}$$

$$O_2 + e^- \longrightarrow O_2^- \quad \text{(Formation of superoxide ion)} \tag{6}$$

$$OH^\bullet + \text{organic contaminants} \longrightarrow xCO_2 + yH_2O \quad \text{(Radical oxidation of organic compound)} \tag{7}$$

Furthermore, Figure 1 also shows that the trend of the antimicrobial activity of the coated films is the same despite different concentrations of TiO_2 nanoparticle and different types of light being used whereby the *E. coli* colony decreased over time after being exposed to both types of lighting. However, it can be clearly observed from Figure 1 that the antimicrobial effect becomes more pronounced as the TiO_2 concentration was increased from 0.05 to 0.11 g/100 mL MEK. After three days of fluorescent light exposure, the *E. coli* colony for the film coated with 0.05 g TiO_2/100 mL MEK was 8.67 ± 0.20 log CFU/g compared to 7.07 ± 0.09 log CFU/g for the film coated with 0.11 g TiO_2/100 mL MEK. Meanwhile, after three days of exposure to UV light, the *E. coli* colony for film coated with 0.05 g TiO_2/100 mL MEK was 6.86 ± 0.16 log CFU/g compared to 6.29 ± 0.17 log CFU/g for film coated with 0.11 g TiO_2/100 mL MEK, respectively. This finding is consistent with the fact that the higher the concentration of TiO_2 used as a coating, the higher the chances of photocatalytic reaction to occur, thus more *E. coli* can be inactivated.

This finding can also be evidenced from Figures 2(a)–2(c) which compares the *E. coli* colony on agar plates for lettuce packed inside uncoated and coated films of 0.05 and 0.08 g TiO_2/100 mL MEK. Note that Figure 2 is for visualisation purposes only to differentiate the effect of uncoated and coated films on the number cells in the *E. coli* colonies. Further serial dilution was undertaken in order to count the colony forming unit. From Figures 2(a)–2(c), it can be obviously seen that the *E. coli* colony area for lettuce packed with TiO_2 nanoparticle-coated films is much smaller compared to that packed with uncoated film, which demonstrates the antimicrobial activity of the coated films. Moreover, the colony area for 0.08 g TiO_2/100 mL MEK coated film (Figure 2(c))

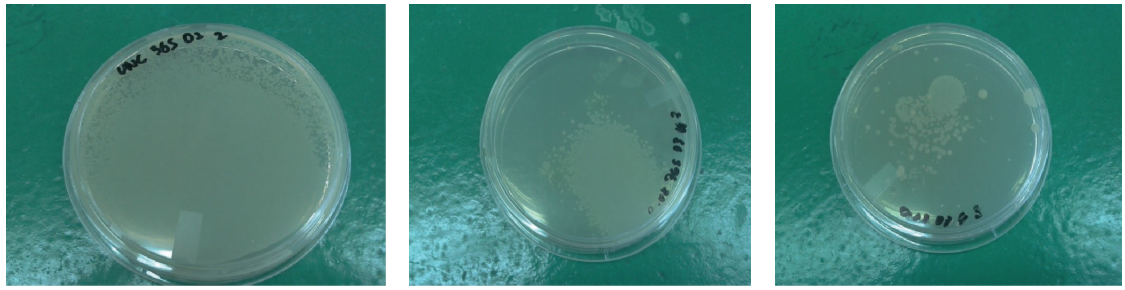

(a) (b) (c)

Figure 2: *E. coli* colony on agar plate for lettuce packed inside (a) uncoated (b) 0.05 g TiO_2/100 mL MEK and (c) 0.08 g TiO_2/100 mL MEK coated films after three days of UV light illumination.

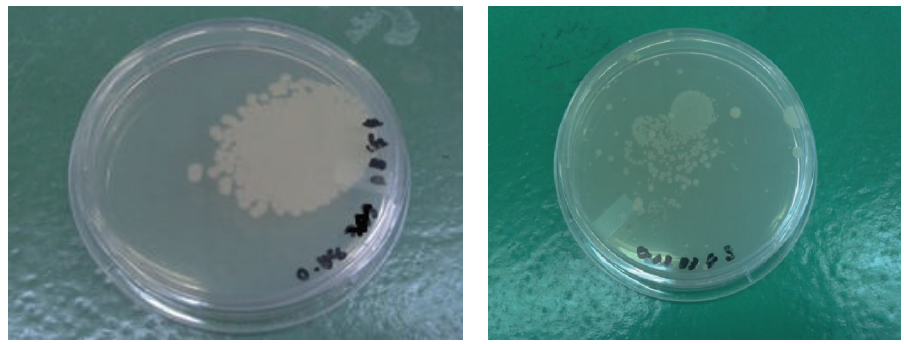

(a) (b)

Figure 3: *E. coli* colony on agar plate for lettuce packed inside 0.08 g TiO_2/100 mL MEK films after three days of (a) fluorescent and (b) UV light illumination.

is smaller than for the 0.05 g TiO_2/100 mL MEK coated film (Figure 2(b)) revealing improved antimicrobial activity of the 0.08 g TiO_2/100 mL MEK coated film. This supports the previous findings whereby antimicrobial activity becomes more pronounced with the increase in TiO_2 concentration. Thus, it can be deduced that it is vital to determine the right concentration of TiO_2 nanoparticles in order to ensure the effectiveness of the packaging application.

Moreover, from Figure 1 and Table 1 a comparison of the antimicrobial activity under UV and fluorescent light showed that the UV light was more effective at inactivating the *E. coli* than the fluorescent light. It was found that film coated with 0.05 g TiO_2/100 mL MEK managed to reduce the *E. coli* colony up to 8.67 ± 0.20 log CFU/g after three days of fluorescent illumination compared to 6.86 ± 0.16 log CFU/g after three days of UV illumination. Similarly, film coated with 0.08 g TiO_2/100 mL MEK managed to reduce the *E. coli* colony up to 7.47 ± 0.15 log CFU/g after three days of fluorescent illumination compared to 6.44 ± 0.15 log CFU/g after three days of UV illumination. Lastly, film coated with 0.11 g TiO_2/100 mL MEK managed to reduce the *E. coli* colony up to 7.07 ± 0.09 log CFU/g after three days of fluorescent illumination compared to 6.29 ± 0.17 log CFU/g after three days of UV illumination. This outcome is most likely related to the bandgap energy of TiO_2 nanoparticles (3.2 eV ≈ 385 nm) which is more suitable and closer to the wavelength of the UV light (365 nm) than fluorescent light (420 nm). The bandgap energy can be converted to wavelength by applying the following equation [18]:

$$\lambda\,(\text{nm}) = \frac{1240}{\text{bandgap}\,(\text{eV})}. \tag{8}$$

Apart from that, Horie et al. [19] who compared the photocatalytic sterilisation rates of *E. coli* cells in TiO_2 slurry irradiated with various light sources found that the inactivation rate of *E. coli* was dependent on the intensity of UVA light. Since the UVA light intensity of the UV light was much higher than the fluorescent light, more OH radicals formed on the surface of the TiO_2 coated films under UV light illumination, resulting in an increase in antimicrobial activity of the coated film under UV rather than fluorescent light. Cho et al. [14] in their study reported the linear correlation between inactivation of *E. coli* and hydroxyl radical concentration in TiO_2 photocatalytic disinfection. Photocatalytic disinfection was significant for higher hydroxyl radical concentration.

This result can also be evidently seen from Figures 3(a) and 3(b) in which the figures show the *E. coli* colony on agar plate for lettuce packed inside 0.08 TiO_2 g/100 mL MEK coated films exposed to both fluorescent and UV light for three days. Note that Figure 3 is for visualisation purposes only to differentiate the effect of the type of light on the number of cells in the *E. coli* colonies. Further serial dilution was done in order to count the colony forming unit. It can

be clearly seen from Figure 3 that the *E. coli* colony area for lettuce packed with coated film exposed to UV light is much smaller compared to that exposed to fluorescent light. This finding implies that selecting a suitable light in terms of wavelength and UVA intensity is important in order for the TiO_2 to work efficiently as a photocatalyst or antimicrobial agent.

4. Conclusion

This study demonstrated that the produced TiO_2 nanoparticle-coated films exhibited potential for antimicrobial applications in food packaging. The actual test revealed that the antimicrobial activity of the films exposed to both fluorescent and UV light increased with an increase in the TiO_2 nanoparticle concentration. The UV light was found to be more effective in expediting the antimicrobial activity of TiO_2 compared to fluorescent light due to the suitable bandgap energy of UV light and the higher hydroxyl radical concentration on the surface of the coated films. It is believed that the films can not only be used for food packaging but also other packaging applications that demand a hygienic environment. The use of nanometre sized TiO_2 has the prospect for further enhancing the antimicrobial activity of TiO_2 especially for applications in the food industry for which the antimicrobial agent is important in order to ensure food safety.

Conflict of Interests

The authors declare that there is no conflict of interests regarding the publication of this paper.

Acknowledgment

This work was financially supported by Research University Grant, University Putra Malaysia (Project no. 05-02-12-2221RU and Vote no. 9379100).

References

[1] M. Long, J. Wang, H. Zhuang, Y. Zhang, H. Wu, and J. Zhang, "Performance and mechanism of standard nano-TiO_2 (P-25) in photocatalytic disinfection of foodborne microorganisms—*Salmonella typhimurium* and *Listeria monocytogenes*," *Food Control*, vol. 39, no. 1, pp. 68–74, 2014.

[2] T. Altin and M. Sökmen, "Preparation of TiO_2-polystyrene photocatalyst from waste material and its usability for removal of various pollutants," *Applied Catalysis B: Environmental*, vol. 144, pp. 694–701, 2014.

[3] K. Gupta, R. P. Singh, A. Pandey, and A. Pandey, "Photocatalytic antibacterial performance of TiO_2 and Ag-doped TiO_2 against *S. aureus.P. aeruginosa*," *Beilsten Journal of Nanotechnology*, vol. 4, no. 1, pp. 345–351, 2013.

[4] S. Bonetta, S. Bonetta, F. Motta, A. Strini, and E. Carraro, "Photocatalytic bacterial inactivation by TiO_2-coated surfaces," *AMB Express*, vol. 3, no. 1, pp. 1–8, 2013.

[5] N. Yao and K. Lun Yeung, "Investigation of the performance of TiO_2 photocatalytic coatings," *Chemical Engineering Journal*, vol. 167, no. 1, pp. 13–21, 2011.

[6] J. J. Zhou, S. Y. Wang, and S. Gunasekaran, "Preparation and characterization of whey protein film incorporated with TiO_2 nanoparticles," *Journal of Food Science*, vol. 74, no. 7, pp. N50–N56, 2009.

[7] Z. -S. Luo, Q. -Y Ye, and D. - Li, "Influence of nano-TiO_2 modified LDPE film packaging on quality of strawberry," *Modern Food Science and Technology*, vol. 29, no. 10, pp. 2340–2344, 2537, 2013.

[8] M. Gumiero, D. Peressini, A. Pizzariello et al., "Effect of TiO_2 photocatalytic activity in a HDPE-based food packaging on the structural and microbiological stability of a short-ripened cheese," *Food Chemistry*, vol. 138, no. 2-3, pp. 1633–1640, 2013.

[9] C. Chawengkijwanich and Y. Hayata, "Development of TiO_2 powder-coated food packaging film and its ability to inactivate *Escherichia coli* in vitro and in actual tests," *International Journal of Food Microbiology*, vol. 123, no. 3, pp. 288–292, 2008.

[10] L. Bastarrachea, S. Dhawan, and S. S. Sablani, "Engineering properties of polymeric-based antimicrobial films for food packaging," *Food Engineering Reviews*, vol. 3, no. 2, pp. 79–93, 2011.

[11] J. H. Han, "Antimicrobial food packaging," in *Novel Food Packaging Techniques*, pp. 50–565, CRC Press, Boca Raton, Fla, USA, 2003.

[12] R. W. Siegel, "Cluster-assembled nanophase materials," *Annual Review of Materials Science*, vol. 21, no. 1, pp. 559–578, 1991.

[13] D. M. A. Alrousan, P. S. M. Dunlop, T. A. McMurray, and J. A. Byrne, "Photocatalytic inactivation of *E. coli* in surface water using immobilised nanoparticle TiO_2 films," *Water Research*, vol. 43, no. 1, pp. 47–54, 2009.

[14] M. Cho, H. Chung, W. Choi, and J. Yoon, "Linear correlation between inactivation of *E. coli* and OH radical concentration in TiO_2 photocatalytic disinfection," *Water Research*, vol. 38, no. 4, pp. 1069–1077, 2004.

[15] C. Bock, H. Dittmar, H. Gemeinhardt, E. Bauer, and K.-O. Greulich, "Comet assay detects cold repair of UV-A damages in a human B-lymphoblast cell line," *Mutation Research—DNA Repair*, vol. 408, no. 2, pp. 111–120, 1998.

[16] N. Serpone and A. Salinaro, "Terminology, relative photonic efficiencies and quantum yields in Heterogeneous photocatalysis. Part I: suggested protocol (Technical Report)," *Pure and Applied Chemistry*, vol. 71, no. 2, pp. 303–320, 1999.

[17] R. Benedix, F. Dehn, J. Quaas, and M. Orgass, "Application of titanium dioxide photocatalysis to create self-cleaning building materials," *Lacer*, vol. 5, pp. 157–167, 2000.

[18] C.-T. Hsieh, W.-S. Fan, W.-Y. Chen, and J.-Y. Lin, "Adsorption and visible-light-derived photocatalytic kinetics of organic dye on co-doped titania nanotubes prepared by hydrothermal synthesis," *Separation and Purification Technology*, vol. 67, no. 3, pp. 312–318, 2009.

[19] Y. Horie, M. Taya, and S. Tone, "Evaluation of photocatalytic sterilization rates of *Escherichia coli* cells in titanium dioxide slurry irradiated with various light sources," *Journal of Chemical Engineering of Japan*, vol. 31, no. 4, pp. 577–584, 1998.

Hindawi Publishing Corporation
International Journal of Photoenergy
Volume 2014, Article ID 401239, 9 pages
http://dx.doi.org/10.1155/2014/401239

Research Article

Effects of UV-Vis Irradiation on Vanadium Etioporphyrins Extracted from Crude Oil and the Role of Nanostructured Titania

Debra Jene Kirkconnell Reyes,[1] Andrés García Saravia Ortiz de Montellano,[1] Rudy Amilcar Trejo Tzab,[2] Gerko Oskam,[1] and Juan José Alvarado Gil[1]

[1] *Department of Applied Physics, CINVESTAV-Unidad Mérida, Antigua Carretera a Progreso Km. 6, 97310 Mérida, YUC, Mexico*
[2] *Facultad de Ingeniería Química, Universidad Autónoma de Yucatán, Periférico Norte Km. 33.5, Tablaje Catastral 13615, Col. Chuburná de Hidalgo Inn, 97310 Mérida, YUC, Mexico*

Correspondence should be addressed to Debra Jene Kirkconnell Reyes; debrakirkconnell@gmail.com

Received 14 December 2013; Revised 7 February 2014; Accepted 8 February 2014; Published 2 April 2014

Academic Editor: Wei Xiao

The role of UV-irradiation on oil and its derivatives is particularly important for analyzing the degradability of specific oil compounds. Also, nanostructured-TiO_2 is one of the most promising photocatalysts so it is expected to be useful in their degradation. However the complexity of crude oil, as well as that of the reactions involved, is such that the effect of the presence of TiO_2 under illumination is not well understood. In this paper, the influence of UV-Vis irradiation on vanadium etioporphyrins, extracted from crude oil from Dos Bocas, Tabasco, Mexico, is studied using UV-Vis spectrophotometry in the absence and presence of nanostructured TiO_2 or nitrogen-doped TiO_2 modified with copper (N-TiO_2/Cu). It is shown that the addition of water shortens the time to start photodegradation. However, once this process has initiated, the system enters a second stage, that is very similar for samples with or without water. It is also shown that the use of N-TiO_2/Cu induces an important delay in the initiation of the porphyrins' photodegradation process. Additionally, it has been found that the presence of TiO_2 in samples extracted with water induces a small reduction in the photodegradation duration and, hence, that TiO_2 can catalyze the degradation of petroporphyrins.

1. Introduction

The many substances forming part of crude oil can have a limited lifetime due to various external factors. One of the most important degrading factors affecting oil is UV light. The photochemical transformation of a given molecule into lower molecular weight fragments occurs usually via an oxidation process [1]. Photodegradation of petroleum products both in laboratory and the field have been extensively explored [2]. In particular, the effect of photolysis has been studied for a variety of pure hydrocarbons under solar and simulated solar conditions [3, 4]. It has been shown that, depending on temperature and using light intensities in the range from 200 to 750 W/m^2, some water-soluble compounds such as naphthalenes and phenanthrenes can degrade rapidly. In contrast, other aromatic compounds such as alkylated benzenes did not exhibit photodegradation under these conditions [4].

In general, it is important to know under which conditions certain substances remain in the oil, stable or not, under UV illumination. This can be helpful in the development of efficient methods to attend the problems generated by spills, and the vulnerability of specific components is also important for commercial or industrial purposes [5–7]. However, a large number of substances still remain to be explored and understood under diverse conditions.

Porphyrins are among the most interesting substances forming part of crude oil. In particular, the specific chemical structure of the porphyrins provides a fingerprint of the origin of the oil. They are mainly present as vanadyl and nickel chelated compounds, although metal-free porphyrins have also been isolated from immature sediments [8].

The identification and characterization of metalloporphyrins in crude oils and source rock are of fundamental interest within a geochemical context, because they may provide a better understanding of the geochemical origin of the petroleum via diagenetic and catagenetic oil formation and maturation of organic matter. Another interesting feature related to metalloporphyrins is their significant presence in heavy crude oil, which can cause problems as these metals have a deleterious effect on the hydrogenation catalysts used in upgrading and refining processes [9].

A common material used in cleaning the environment is titania (TiO_2), one of the best-known photocatalytic materials due to its high photoactivity and photostability. The photocatalytic activity of titania depends on its physical properties, such as crystal structure, surface area, particle size, particle shape, among others [10]. One of the main disadvantages of TiO_2 is its large band gap of 3.2 eV (anatase), which implies that it only absorbs UV light, corresponding to about 5% of the solar spectrum. However, nanostructured TiO_2 is expected to be useful in the degradation of crude oil as well as some of their compounds [11]. On the other hand, there are strong limitations in degrading crude oil; maybe the most important limitation is related to the opacity of crude oil to UV light, which does not allow light to successfully degrade oil even if adequate photocatalysts are present. When crude oil is mixed with solvents, a partial extraction of some components occurs; however, the effects of light and catalysts on the extracts are not well understood. Oil extracts containing porphyrins are common, and the analysis of their degradability using TiO_2 nanoparticles is an interesting challenge.

In recent years, it has been shown that the photocatalytic action of TiO_2 can be enhanced by impregnation with metals such as copper. For example, the degradation of methylene blue is accelerated using nitrogen-doped TiO_2 modified with copper (N-TiO_2/Cu) nanomaterials prepared by plasma discharge techniques in the presence of metallic copper and gaseous nitrogen [12]. In this paper, the effects of UV-Vis irradiation on crude oil extracts containing petroporphyrins are analyzed in the absence and presence of nanostructured TiO_2. In addition, the degradation of the metalloporphyrins in the presence of N-TiO_2/Cu nanomaterials is determined, and the role of water in the degradation processes is considered.

2. Materials and Methods

For the experiments we used Maya crude oil from Dos Bocas, Tabasco, Mexico, which is an oil with °API = 21.57, 3.4 wt% sulfur, and 0.32 wt% nitrogen. The following two extraction methods were used.

In the first method, 1.7 mL of heavy crude oil was mixed with 60 mL of acetone in a beaker, and then the following procedure was performed.

(a) The mixture was stirred during 2 minutes, using a Sonics ultrasonic vibrating cell (model TM VCX130PB) operating at 10 W.

(b) The obtained sample was covered with a black metallic foil and a plastic bag and left for 24 hours to obtain the extract.

(c) The supernatant, now with a yellow color, was transferred to a second beaker labeled COE (crude oil extract).

The second extraction procedure was performed by mixing 1.7 mL of heavy crude oil in a beaker with 60 mL of acetone and 5 mL of distilled water, maintaining the proportion 12 : 1 of acetone to distilled water. Afterwards, the sample was treated following the same procedure as described in steps (a), (b), and (c). The solution obtained in the second extraction procedure was labeled COEW (crude oil extract with water). Additionally, a standard solution was prepared by dissolving 0.1 mg of vanadium (IV) etioporphyrin III oxide ($C_{32}H_{36}N_4OV$ Santa Cruz Biotechnology, CAS number 15709-03-2) in 60 mL of acetone.

Two types of nanostructured TiO_2 powder were used, both based on Degussa P25: pure TiO_2 and N-TiO_2/Cu. This last compound was obtained by a plasma treatment of Degussa P25 in a nitrogen atmosphere in the presence of metallic copper [12]. Figure 1 shows the XPS analysis as well as the X-ray diffraction patterns of the N-TiO_2/Cu material. X-ray diffraction exhibits the well-known proportion of 80% anatase and 20% rutile in titania Degussa P25 but it does not have the sensitivity to detect the presence of copper in the material. However there are small differences between both spectra that can be observed; some peaks are slightly displaced while others are wider or higher, but all of them are closely related to the ones observed in untreated Degussa P25 (see Figure 1(a)). These small changes can be related to changes in the nanoparticles' size due to the copper impregnation process.

In contrast, XPS measurements are able to detect the presence of copper in N-TiO_2/Cu (see Figure 1(b)); in these measurements two bands associated with copper, as well as the characteristic bands of TiO_2 (Degussa P25) and a band related to nitrogen, can be observed. Additional analyses have shown that the plasma-treated samples contain about 4.4 wt% of nitrogen and 0.4% of copper [12].

Using the COE and COEW extracts, a set of samples was prepared by adding 25 mg of TiO_2 or N-TiO_2/Cu, labeled COE-TiO_2, COE-(N-TiO_2/Cu), COEW-TiO_2, and COEW-(N-TiO_2/Cu), respectively. These samples were submitted to an additional mixing process using a Sonics ultrasonic vibrating mixer cell operated at 10 W for 2 minutes and left to settle for 60 minutes with the samples covered to prevent evaporation. For all the solutions, COE, COEW, COE-TiO_2, COEW-TiO_2, COE-(N-TiO_2/Cu), and COEW-(N-TiO_2/Cu) aliquots of about 10 mL were taken from the beakers and labeled as "time zero" experiments. The remaining solution in each one of the beakers was then poured into an Erlenmeyer flask integrated with a cooling system and placed at 400 rpm using magnetic stirring. For the photodegradation studies, the light of a 1000 W Xenon lamp (Oriel 6269), operated at 400 W, was used to illuminate the Erlenmeyer reaction vessel from above. This lamp provided 370 W/m^2 on the surface of the sample, with most of the intensity in the visible region

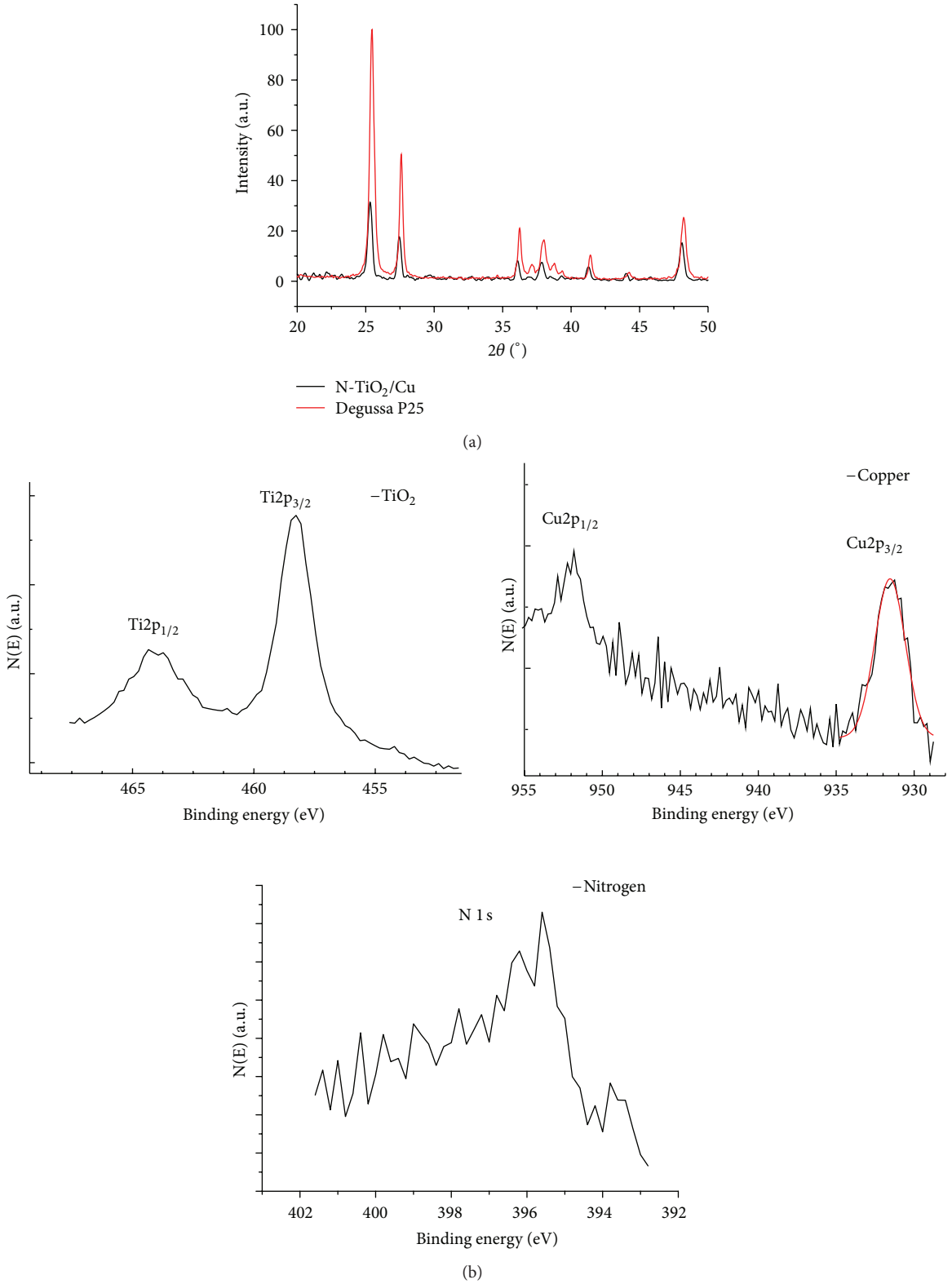

FIGURE 1: (a) X-ray diffraction spectra of TiO_2 (Degussa P25) and N-TiO_2/Cu. (b) XPS of N-TiO_2/Cu.

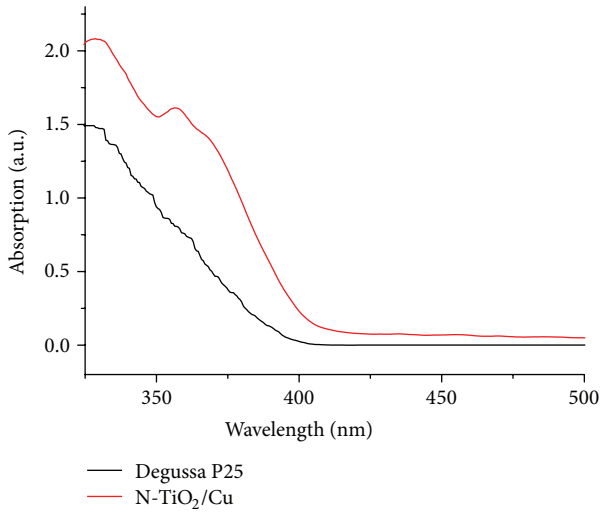

FIGURE 2: Absorption of TiO_2 and N-TiO_2/Cu obtained from diffuse reflectance measurements using the Kubelka-Munk method.

of light, a good emission of UVA and UVB light, and a very low fraction of UVC. During irradiation the samples in the jacketed flask were maintained at a temperature of 30°C using a circulating water system. Aliquots of 10 mL were taken from the Erlenmeyer flask every hour for five hours and transmission optical spectra for the samples were measured in quartz cuvettes using a fiber UV-Vis spectrophotometer in the range from 200 nm to 1100 nm using an AvaSpec-2048 fiber optic spectrometer with a deuterium lamp as the light source.

3. Results and Discussion

Figure 2 shows the absorption spectra, obtained from diffuse reflectance measurements on the powder by applying the Kubelka-Munk method, of the Degussa P25 and N-TiO_2/Cu powders used in the experiments, and an absorption increment for N-TiO_2/Cu in visible light can be observed.

The COE and COEW samples were illuminated over a period of 5 hours, and Figure 3 shows the corresponding UV-Vis spectra obtained before illumination (time zero) and after every hour. Before irradiation the spectra for COE and COEW samples show a broad band from 220 nm to 450 nm with three small peaks at 300 nm, 350 nm, and 400 nm and also a shoulder at 250 nm. Additionally, two smaller bands can be observed at 530 nm and 569 nm. The spectra remain largely unchanged upon irradiation; however, as illustrated in the insets, the peaks at 530 nm and 569 nm disappear upon prolonged illumination indicating a degradation process.

The COE-TiO_2 and COEW-TiO_2 as well as the COE-(N-TiO_2/Cu) and COEW-(N-TiO_2/Cu) samples show the same bands as the samples without TiO_2; however, the shoulder at 250 nm appears more clearly, as illustrated in Figures 4 and 5. Similar to the samples without TiO_2, the two bands at 530 nm and 569 nm are also observed.

It is well known that crude oil contains petroporphyrins [13] so it is possible that the small bands at 530 nm and 569 nm correspond to such type of compounds. Comparing the experimental UV-Vis spectra from the crude oil extracts with databases of spectra for petroporphyrins, we conclude that the vanadium etioporphyrins are the best fit for our crude oil samples. In Figure 6, the UV-Vis spectrum of a standard solution of vanadium etioporphyrin in acetone is presented. In this spectrum, the wide band from 200 nm to 270 nm is due to acetone [14] while a narrow band appearing at 414 nm can be identified as the Soret band. Additionally, two smaller bands are clearly observed at 530 nm and 569 nm. From these results, it can be inferred that the peaks of the spectra of our extracts appearing at 530 nm and 569 nm correspond to vanadium etioporphyrins as previously reported for crude oil from the same geographic location [9].

The UV-Vis spectrum of petroporphyrins show bands that correspond to a strong electronic transition to the second excited state ($S_0 \rightarrow S_2$) at about 400 nm (the Soret or B band) and a weak transition to the first excited state ($S_0 \rightarrow S_1$) at about 550 nm (the Q band). Internal conversion from S_2 to S_1 is rapid and, as a consequence, fluorescence is only detected from S_1. The B and the Q bands both arise from π-π^* transitions and can be explained by considering the four frontier orbitals (HOMO and LUMO orbitals) (the Gouterman four orbital model) [15]. Gouterman's "four-orbital" model of the π-π^* transitions in porphyrins is firmly established as a simple unifying theory of porphyrin spectra. It provides parametric expressions for the frequencies and intensities of the α-β (Q) and Soret (B) bands of the porphyrin chromophore. Spectral shifts caused by systematic variation of ring substituents and changes of the encapsulated metal ion, axial ligation, or even dimer formation have successfully been rationalized based on these grounds [16, 17]. The electronic transition to the higher energy mixed state, the S_2 state, is strongly allowed, whereas the electronic transition to the lower energy mixed state, the S_1 state, is only weakly allowed. The band in the UV-Vis absorption spectrum due to a transition to the S_2 state is the Soret band, and the band due to a transition to the vibrationless S_1 state is the α band. The greater the degree of mixing, the less intense the α band relative to the Soret band. In the UV-visible spectrum of porphyrin, there is also a vibronic band, the β band, which appears at slightly lower wavelengths than the α band. The β band is due to transitions to higher vibrational levels in the S_1 state and serves as a normalization band in porphyrin absorption spectra [15]. In summary, the three characteristic bands appearing in the spectra of the nonirradiated samples correspond to the bands of vanadium etioporphyrins: at 407 nm the Soret band and the β and α bands at 533 nm and 572 nm, respectively [18]. When the intensity of the α band is larger than that of the β band, the metal forms a stable square-planar complex with the porphyrin [19].

In order to determine the concentration of vanadium etioporphyrins in our samples, we prepared dilutions of the standard solution (vanadium IV etioporphyrin III oxide) and determined the absorbance as a function of concentration. The relationship between the absorbance (A) and concentration (C), according to the Lambert-Beer law, is given by $A = \varepsilon d C$, where d (cm) and ε ($L\,cm^{-1}\,mg^{-1}$) are the thickness and extinction coefficient of the sample,

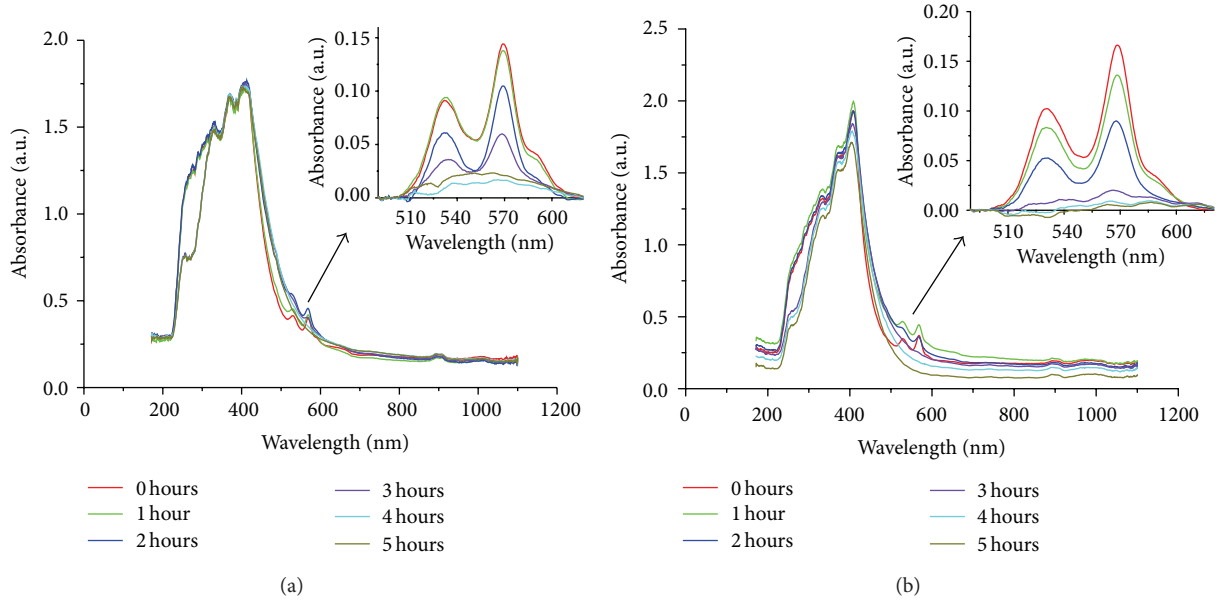

Figure 3: UV-Vis absorbance spectra as a function of illumination time of the crude oil extracts: (a) COE and (b) COEW. The insets show the bands observed at 530 nm and 569 nm with the background subtracted.

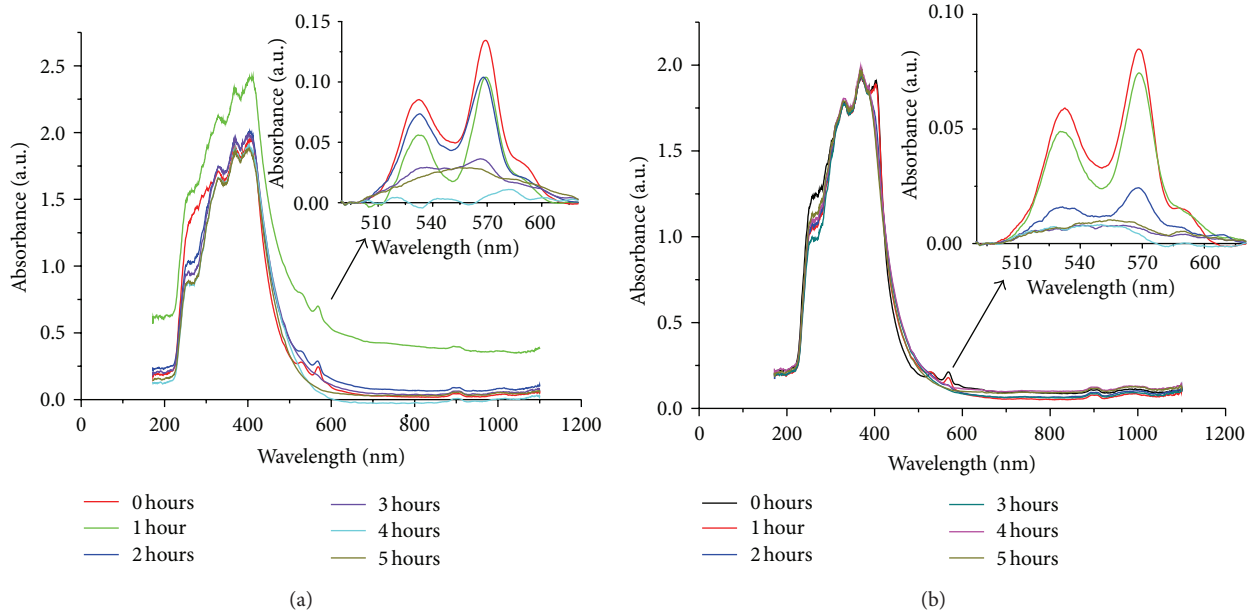

Figure 4: UV-Vis absorbance spectra as a function of illumination time in the presence of the TiO_2 nanomaterial with the crude oil extracts: (a) COE-TiO_2 and (b) COEW-TiO_2. The insets show the bands observed at 530 nm and 569 nm.

respectively. In Figure 7, the absorbance maximum of the α peak versus concentration is presented, in which the fit of the experimental data provides a value of 0.116 L cm^{-1} mg^{-1} for the extinction coefficient.

Using these results, the concentration of the vanadium etioporphyrin in our COE can be estimated as being 3.8 mg/L, which is in agreement with generally observed concentrations in crude oil from the oil from the same geographical location [9].

Due to the UV-Vis irradiation treatment, there are changes in intensity in various bands in the spectra; however, we will focus our attention on the bands in the range from 500 nm to 620 nm because they are associated directly with the vanadium etioporphyrins. In order to perform a nonambiguous analysis of the bands appearing in all spectra, we separated the α and β bands absorbance from the main background absorbance by fitting a cubic spline in the smooth region from 425 nm to 750 nm, excluding

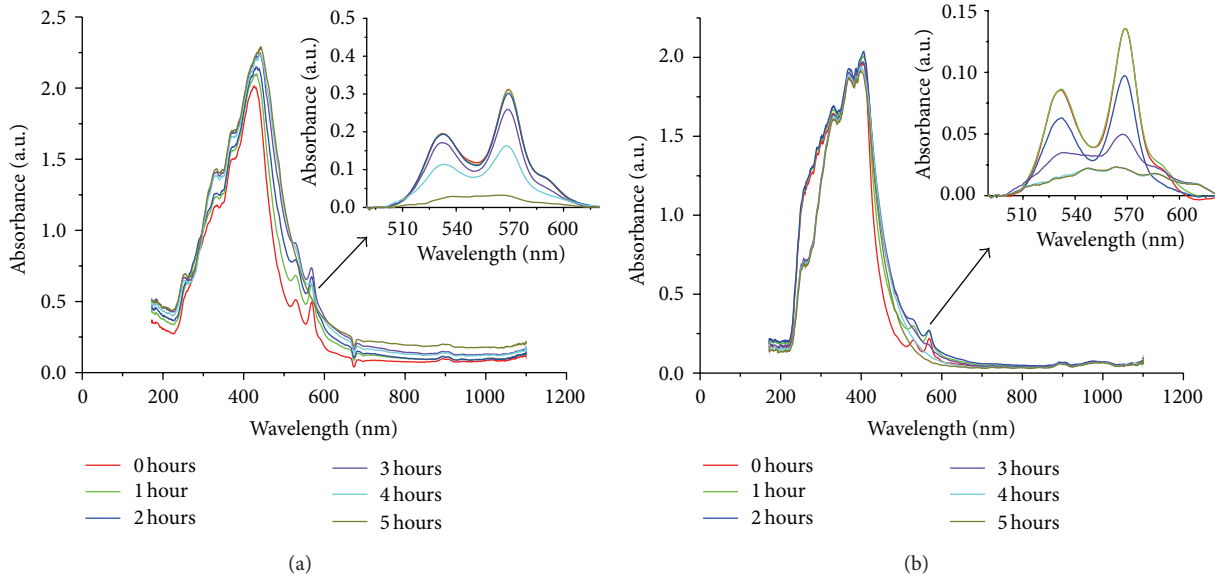

Figure 5: UV-Vis absorbance spectra as a function of illumination time in the presence of the N-TiO_2/Cu nanomaterial with the crude oil extracts: (a) COE-(N-TiO_2/Cu) and (b) COEW-(N-TiO_2/Cu). The insets show the bands observed at 530 nm and 569 nm with the background subtracted.

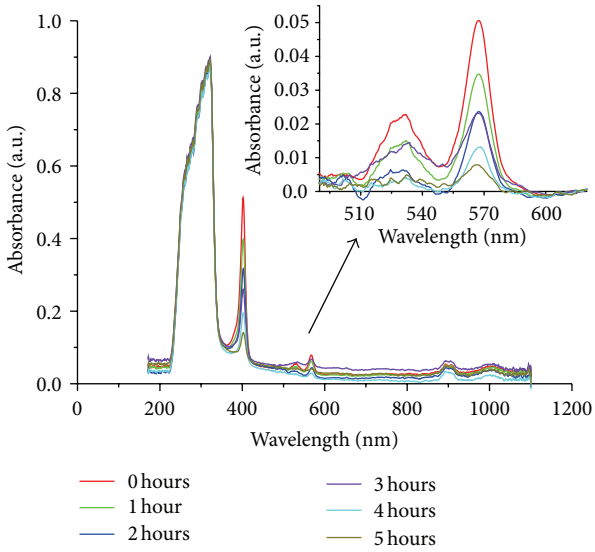

Figure 6: UV-Vis absorbance spectra as a function of irradiation time of the standard vanadium etioporphyrins solution in acetone. The insets show the bands observed at 530 nm and 569 nm with the background subtracted.

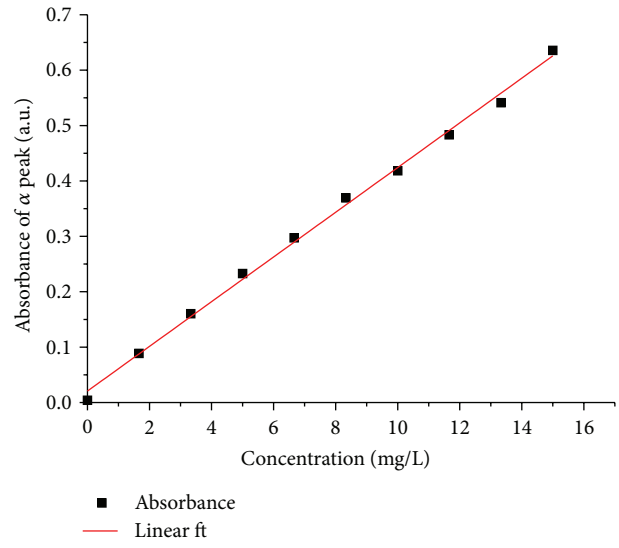

Figure 7: Calibration curve for the vanadium (IV) etioporphyrin III oxide solution in acetone using the height of the absorbance of the α peak as a function of the concentration.

the region from 500 nm to 625 nm and then subtracting this background from the measured absorbance. The result of this background removal is shown in the insets of Figures 3 to 6. After one hour of UV-Vis irradiation, a noticeable decrease in intensity of the α and β bands in all the samples is observed; however, the kinetics depend on the extraction method and the presence and type of catalyst. In order to characterize the results obtained when irradiating with UV-Vis light, the area under the curves of the α and β bands was determined. Figure 8 shows the areas under the peaks versus the irradiation time. It can be seen that in all cases the α and β peaks disappear after several hours of irradiation, but that the time needed for this degradation process depends strongly on the presence of water, TiO_2, and N-TiO_2/Cu. As a general trend, it can be observed that the presence of water shortens the degradation time of the vanadium etioporphyrins, both for the measurements with and those without TiO_2 or N-TiO_2/Cu.

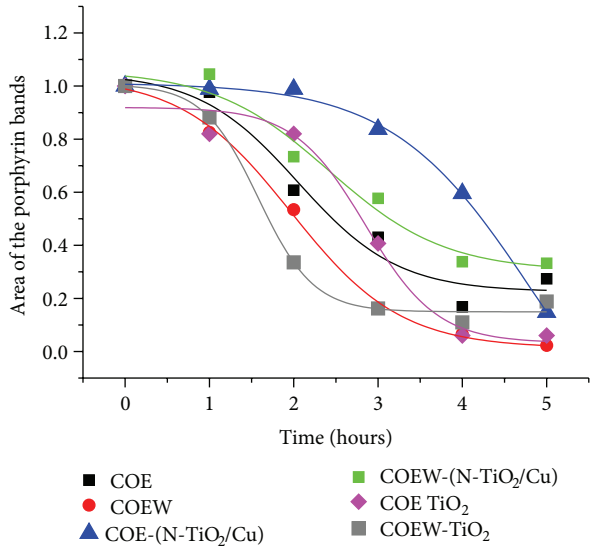

Figure 8: Time evolution of the area of the α and β bands as a consequence of the photodegradation.

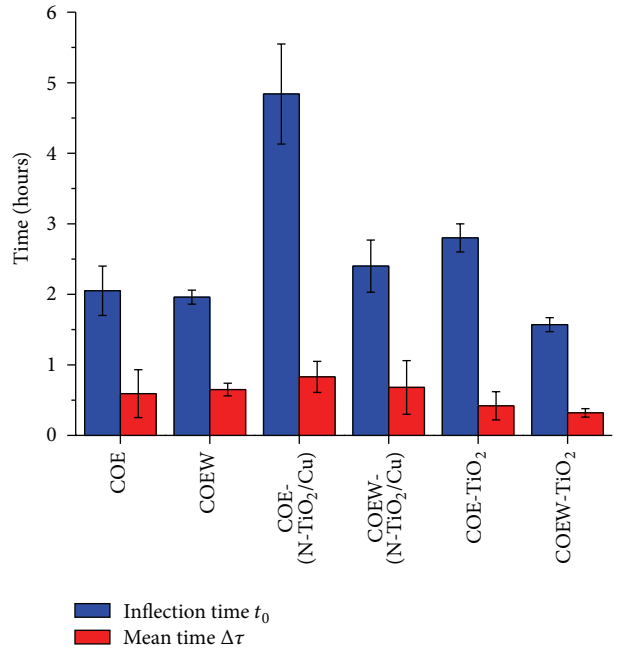

Figure 9: The time parameters of the logistic curve establishing the differences induced in the crude oil extracts by UV-Vis illumination.

The results for samples of crude oil extracts to which N-TiO_2/Cu was added (COE-(N-TiO_2/Cu) and COEW-(N-TiO_2/Cu)) show interesting effects: the samples without water, COE-(N-TiO_2/Cu), show the smallest degradation rate of all samples. In the case of the COEW-(N-TiO_2/Cu) samples, the degradation rate is faster than for the COE-(N-TiO_2/Cu) samples, but slower than for all other samples. Total disappearance of the α and β peaks in this case takes more than 5 hours of irradiation.

The experimental data of the area under both bands corresponding to the petroporphyrins can be analyzed using a sigmoidal fit of the following form:

$$\text{Area} = B_2 + \frac{(B_1 - B_2)}{1 + e^{(t-t_0)/\Delta\tau}}, \quad (1)$$

where B_1 is the initial (maximum) value and B_2 is the final (minimum) value. The time t_0 corresponds to the point at which the slope of the curve changes (inflection point) corresponding to where the maximum rate of change of the process is reached; t_0 measures the time at which half of the process has occurred and is useful to determine if a given factor delays or impedes the process. In this sense it is useful in defining the start of a given kinetic process. The parameter $\Delta\tau$ measures the duration of the process around t_0, in such a way that for an interval $4\Delta\tau$, 95% of the process has occurred. Based on this, the time for the photodegradation resulting from a given treatment, T, can be found using the formula $T = t_0 + 2\Delta\tau$. The continuous lines in Figure 8 correspond to the results of the fits of the experimental data to (1), and the results for the parameters are presented in Figure 9.

Comparing the samples COE, COE-(N-TiO_2/Cu), and COE-TiO_2 with the corresponding samples to which water was added, it can be observed that, in all cases, the addition of water shortens the time t_0, being clearly different for samples with N-TiO_2/Cu and those with TiO_2. This indicates that water shortens the time at which the photodegradation rate reaches its maximum. However, by analyzing the behavior of $\Delta\tau$, it can be observed that the total time it takes is very similar with or without water. Hence, for a given treatment, water shortens the time to initiate photodegradation but once this process is induced, the duration of this last stage for samples with or without water is very similar. As a consequence, the time t_0 mainly corresponds to an induction time.

On the other hand, comparing all the samples with the different treatments, t_0 is around 5 hours for COE-(N-TiO_2/Cu) and 2.5 hours for COE-TiO_2, indicating that the presence of copper induces a delay in the initiation of the degradation. In contrast, $\Delta\tau$ is not very different for both types of samples, which indicates that once the photodegradation process starts, the duration of this last stage is similar for samples with TiO_2 and N-TiO_2/Cu.

This behavior can be a direct consequence of the fact that titania impregnated with copper has a stronger optical absorption in the UV; therefore, adding this material to the oil extract solutions could have the effect of obstructing partially the UV radiation, slowing down photolysis. On the other hand, the impregnation of titania with copper has shown diverse effects on the photocatalytic activity, when degrading methylene blue [12]. Even though the chemical processes induced by light are completely different for methylene blue and extracts of crude oil, our results agree with the ones previously found.

In particular, preliminary results obtained by us and others [20] indicate that a higher concentration of copper does not improve the photocatalytic properties of Cu-TiO_2;

therefore, if the photodegradation of the porphyrins would be the objective, a possible solution could be to use nanoparticles with a lower content of copper concentration. Additionally, t_0 and $\Delta\tau$ are smaller for COEW-TiO_2 than for COEW samples. This implies that Degussa P-25 TiO_2 is showing photocatalytic activity in presence of water. In contrast, this is harder to observe in samples without water, where t_0 is 2 hours for COE-TiO_2 and 2.7 hours for COE; although there is a slight tendency for $\Delta\tau$ to being shorter for COE-TiO_2 than for COE, the spread in the values as represented by the error bars does not allow to unequivocally state that there is a difference between the values. Hence, it appears that direct absorption of UV-light by the crude oil extracts is capable of the photodegradation of petroporphyrins and that adding a TiO_2-based catalyst, in the absence of water, does not significantly accelerate photodegradation. However, the presence of water results in a faster initiation of the photodegradation processes.

4. Conclusions

The effects of UV-Vis illumination on crude oil extracts containing petroporphyrins have been monitored as a function of time. Analysis of the UV-Vis spectra showed that the UV-Vis illumination induces the systematic reduction of the size of the α and β bands, corresponding to the degradation of the petroporphyrins. It has been shown that this reduction can be parameterized as a second-order kinetics process. The analysis of the parameters of the degradation kinetics allows inferring that the addition of water to the crude oil extracts shortens the time to induce the photodegradation. However, once this process has initiated, the duration of the last stage of the photodegradation for samples with or without water is very similar. It has also been shown that the use of N-TiO_2/Cu induces an important delay in the initiation of the process of photodegradation of the porphyrins. Additionally, it has been shown that the presence of TiO_2 in the samples extracted with water induces a small reduction in the duration of the photodegradation; hence, Degussa P-25 can catalyze the degradation of petroporphyrins.

Conflict of Interests

The authors declare that there is no conflict of interests regarding the publication of this paper.

Acknowledgments

Debra Jene Kirkconnell Reyes and Andrés García Saravia thank Conacyt for a scholarship. The authors wish to thank J. Ordoñez-Miranda, J. M. Yañez-Limón, C. Vales-Pinzón, D. Macías, J. Bante-Guerra, Gaspar Euan, N.W. Pech-May, and B.E. Heredia-Cervera for their useful suggestions and enlightening discussions during the development of this work. This work was partially funded by Conacyt projects 105816, 178510 and 193850 and FOMIX-Yucatán project 170120.

References

[1] IUPAC, *Compendium of Chemical Terminology*, The, "Gold Book", Blackwell Scientific Publications, Oxford, UK, 2nd edition, 1997.

[2] J. R. Payne and C. R. Phillips, "Photochemistry of petroleum in water," *Environmental Science and Technology*, vol. 19, no. 7, pp. 569–579, 1985.

[3] X. Xia, G. Li, Z. Yang, Y. Chen, and G. H. Huang, "Effects of fulvic acid concentration and origin on photodegradation of polycyclic aromatic hydrocarbons in aqueous solution: importance of active oxygen," *Environmental Pollution*, vol. 157, no. 4, pp. 1352–1359, 2009.

[4] T. Saeed, L. N. Ali, A. Al-Bloushi et al., "Effect of environmental factors on photodegradation of polycyclic aromatic hydrocarbons (PAHs) in the water-soluble fraction of Kuwait crude oil in seawater," *Marine Environmental Research*, vol. 72, no. 3, pp. 143–150, 2011.

[5] Z. Zhou, Z. Liu, and L. Guo, "Chemical evolution of Macondo crude oil during laboratory degradation as characterized by fluorescence EEMs and hydrocarbon composition," *Marine Pollution Bulletin*, vol. 66, pp. 164–175, 2013.

[6] R. L. Ziolli and W. F. Jardim, "Photochemical transformations of water-soluble fraction (WSF) of crude oil in marine waters. A comparison between photolysis and accelerated degradation with TiO_2 using GC-MS and UVF," *Journal of Photochemistry and Photobiology A*, vol. 155, no. 1–3, pp. 243–252, 2003.

[7] H. W. Hagemann and A. Hollerbach, "The fluorescence behaviour of crude oils with respect to their thermal maturation and degradation," *Organic Geochemistry*, vol. 10, no. 1–3, pp. 473–480, 1986.

[8] J. M. E. Quirke, T. Dale, E. D. Britton, R. A. Yost, J. Trichet, and H. Belayouni, "Preliminary characterisation of porphyrins from the Gafsa Basin, Tunisia: evidence for metal-free benzo porphyrins from an immature sediment," *Organic Geochemistry*, vol. 15, no. 2, pp. 169–177, 1990.

[9] M. Espinosa Pena, A. Manjarréz, and A. Campero, "Distribution of vanadyl porphyrins in a Mexican offshore heavy crude oil," *Fuel Processing Technology*, vol. 46, no. 3, pp. 171–182, 1996.

[10] X. Chen and S. S. Mao, "Titanium dioxide nanomaterials: synthesis, properties, modifications and applications," *Chemical Reviews*, vol. 107, no. 7, pp. 2891–2959, 2007.

[11] M. J. García-Martínez, I. Da Riva, L. Canoira, J. F. Llamas, R. Alcántara, and J. L. R. Gallego, "Photodegradation of polycyclic aromatic hydrocarbons in fossil fuels catalysed by supported TiO_2 ," *Applied Catalysis B*, vol. 67, no. 3-4, pp. 279–289, 2006.

[12] R. Trejo-Tzab, J. J. Alvarado-Gil, P. Quintana, and P. Bartolo-Pérez, "N-doped TiO_2 P25/Cu powder obtained using nitrogen (N_2) gas plasma," *Catalysis Today*, vol. 193, no. 1, pp. 179–185, 2012.

[13] P. Chen, Z. Xing, M. Liu, Z. Liao, and D. Huang, "Isolation of nine petroporphyrin biomarkers by reversed-phase high-performance liquid chromatography with coupled columns," *Journal of Chromatography A*, vol. 839, no. 1-2, pp. 239–245, 1999.

[14] J. Workman and J. R. . Neenah, "Applied Spectroscopy," in *Optical Spectrometers*, Kimberly-Clark Corporation, Analytical Science and Technology, Wisconsin, 1997.

[15] M. Prushan, "Absorption and Fluorescence Spectroscopy of Tetraphenylporphyrin and Metallo-Tetraphenylporphyrin," 2005, http://www.lasalle.edu/.

[16] M. Gouterman, G. H. Wagnière, and L. C. Snyder, "Spectra of porphyrins. Part II. Four orbital model," *Journal of Molecular Spectroscopy*, vol. 11, no. 1–6, pp. 108–127, 1963.

[17] A. Ceulemans, W. Oldenhof, C. Görller-Walrand, and L. G. Vanquickenborne, "Gouterman's "four-orbital" model and the MCD spectra of high-symmetry metalloporphyrins," *Journal of the American Chemical Society*, vol. 108, no. 6, pp. 1155–1163, 1986.

[18] H. Xu, G. Que, D. Yu, and J. R. Lu, "Characterization of petroporphyrins using ultraviolet-visible spectroscopy and laser desorption ionization time-of-flight mass spectrometry," *Energy and Fuels*, vol. 19, no. 2, pp. 517–524, 2005.

[19] L. R. Milgrom, *The Colours of Life: An Introduction to the Chemistry of Porphyrins and Related Compounds*, Oxford University Press, 1997.

[20] B. Xin, P. Wang, D. Ding, J. Liu, Z. Ren, and H. Fu, "Effect of surface species on Cu-TiO_2 photocatalytic activity," *Applied Surface Science*, vol. 254, no. 9, pp. 2569–2574, 2008.

Hindawi Publishing Corporation
International Journal of Photoenergy
Volume 2014, Article ID 219317, 9 pages
http://dx.doi.org/10.1155/2014/219317

Research Article

Application of Glass Fiber-Based N-Doped Titania under Visible-Light Exposure for Photocatalytic Degradation of Aromatic Pollutants

Wan-Kuen Jo,[1] Seung-Ho Shin,[1] and Ho-Hwan Chun[2]

[1] *Department of Environmental Engineering, Kyungpook National University, Daegu 702-701, Republic of Korea*
[2] *Department of Naval Architecture and Ocean Engineering, Pusan National University, 63 Jangjeon-dong, Geumjeong-gu, Busan 609-735, Republic of Korea*

Correspondence should be addressed to Wan-Kuen Jo; wkjo@knu.ac.kr

Received 5 February 2014; Revised 13 March 2014; Accepted 13 March 2014; Published 31 March 2014

Academic Editor: Jiaguo Yu

Flexible glass fiber-supported nitrogen-doped titanium dioxide (GF-N-TiO_2) photocatalysts with different N/Ti ratio were prepared using a dip-coating method followed by a low-temperature heat-treatment process. In addition, their photocatalytic activities were evaluated for the degradation of aromatic volatile organic compounds (VOCs) under visible-light irradiation. The prepared GF-N-TiO_2 photocatalysts were characterized using scanning electron microscopy, energy-dispersive X-ray spectroscopy, X-ray diffraction spectroscopy, and UV-visible spectroscopy. A control photolysis test performed using an uncoated GF displayed no detectable degradation of the target compounds under visible-light irradiation. The outlet-to-inlet concentration ratios of the target pollutants obtained using the GF-N-TiO_2 photocatalysts were lower than that obtained using the GF-TiO_2 photocatalyst. The photocatalytic activity of GF-N-TiO_2 photocatalyst increased as the N-to-Ti ratio increased from 0.06 to 0.08 but decreased gradually as the N-to-Ti ratio increased further to 0.12, suggesting the existence of optimal N/Ti ratios. The outlet-to-inlet concentration ratio of all the target compounds displayed an increasing trend as both air flow rate and inlet concentration increased. Overall, the GF-N-TiO_2 photocatalysts could be applied effectively for the degradation of aromatic VOCs under visible-light irradiation when operation conditions are optimized.

1. Introduction

A significant amount of concern has been directed to volatile organic compounds (VOCs) due to not only their widespread presence in various environments but also their environmental health hazards. Particularly, monocyclic aromatic VOCs, including toluene, ethyl benzene, and xylene (TEX), which originate mainly from traffic emissions in urban environments, industrial combustion processes, solvent and petroleum handling, and other industrial processes, are frequently measured at high concentration levels [1]. Ambient-air TEX can infiltrate buildings, exacerbating indoor air pollution [2]. Indoor air quality can be worsened due to TEX emissions from various indoor sources, such as building finishing materials, furniture, and household products [3, 4]. Moreover, TEX even at sub-ppm concentrations are potentially toxic to human beings [5], necessitating the development of control tools to lower health risks to building occupants from indoor air exposure.

Titanium dioxide (TiO_2) is a representative semiconductor photocatalyst that has been extensively used for environmental pollutant purifications. However, it has a major drawback in its practical application in that it is functional under only UV exposure conditions because of its wide band gap [6]. To address this drawback of TiO_2, several strategies have been applied by a great deal of research groups; these strategies have included nonmetal deposition [7, 8], metal deposition [9, 10], dye sensitization [11], semiconductor coupling [12], and carbon materials coupling [13, 14]. Among them, nonmetal N-doping has received special attention for environmental applications, mainly because N can be easily incorporated into two different sites of the

bulk phase of TiO_2 owing to its atomic size comparable with oxygen and small ionization energy [15, 16]. Even though there are certain questions that remain to be answered to understand the photocatalytic mechanism and behavior of N-doped TiO_2 (N-TiO_2) under visible-light exposure [17–20], several research groups found that N-TiO_2 photocatalysts had superior photocatalytic activity to unmodified TiO_2 under visible-light irradiation for decomposition of a variety of gaseous and aqueous environmental pollutants [8, 15, 21, 22].

Application of nanomaterials for environmental treatments necessitates a supporting substrate to minimize the separation of suspended powders in aqueous media or their uncontrolled dispersion in treated air, problems encountered in water, and air applications, respectively [23, 24]. A range of substrates as a nanomaterial support have been investigated for the photocatalytic degradation of environmental pollutants, including activated carbon powders [25], activated carbon fiber [26, 27], glass beads [28, 29], glass tubes [21], and polymer materials [30, 31]. Among these substrates, glass fiber has received particular attention primarily because of its flexibility, which enables the materials to be fitted in various geometrical-shape photocatalytic reactors [32, 33]. Moreover, Panniello et al. [32] reported that glass fiber-supported Fe-doped TiO_2 prepared by a combined hydrolysis and dip-coating method displayed superior photocatalytic performance to a reference P25 TiO_2 for degradation of aqueous orange dye. However, the feasibility of other types of photocatalysts, including N-TiO_2, which are supported by glass fiber for the treatment of environmental pollutants, is another recent topic of research that requires further examination. Consequently, in this study, the feasibility of applying glass fiber-supported N-TiO_2 (GF-N-TiO_2) under visible-light exposure to degradation of TEX at sub-ppm concentrations typically associated with indoor air quality issues was investigated.

2. Experimental

2.1. Preparation and Characterization of GF-N-TiO_2 and GF-TiO_2. GF (11.5 × 22.0 cm, Hyundai Fiber) was thermally pretreated and then cleaned using methanol and distilled water. The GF was heated at 350°C for 4 h in an electric furnace to burn away organic residues on the GF surface. The pretreated GF was washed sequentially with 2-propanol, acetone, and distilled water, after which it was dried at 125°C for 2 h in a dry oven. The dried GF was further treated with NaOH (98%, Sigma-Aldrich) and distilled water and then dried at 125°C for 2 h in the dry oven.

N-TiO_2 powder was prepared using commercially available P25 TiO_2 powder and urea as a N source. Briefly, 10 g of TiO_2 powder was added to specified amounts of urea solution (0.7 M, Sigma-Aldrich) in a Pyrex flask and then rigorously stirred for 2 h under room temperature conditions. Urea solutions of 19, 25, 31, and 37 mL were used to synthesize N-TiO_2 powders having N-to-Ti ratios of 0.06, 0.08, 0.10, and 0.12, respectively. The flask was wrapped with aluminum foil to prevent transmission gain of light from laboratory fluorescent lamps and then kept for 24 h. Subsequently, the mixture in the flask was dried for 48 h under reduced pressure conditions to give a white powder. This powder was calcined at 550°C for 5 h in an electric furnace, after which it was washed with diluted H_2SO_4 (10%, Sigma-Aldrich), and then distilled water until the pH value of washed water reached 7. The washed powder was vacuum-dried for 12 h and then pulverized using an agate mortar to obtain N-TiO_2 powder (Figure 1).

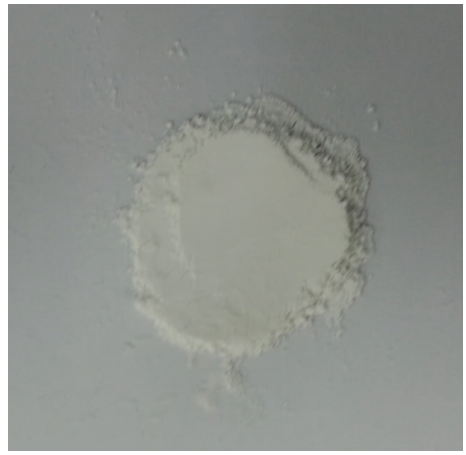

Figure 1: Photograph of as-prepared N-TiO_2 powder.

The GF-N-TiO_2 photocatalyst was prepared using a dip-coating method followed by a low-temperature heat-treatment process. Specifically, 50 mL titanium (IV) isopropoxide (TTIP, 97%, Sigma-Aldrich) was added to 10 mL glacial acetic acid (99%, Sigma-Aldrich) with stirring. This solution was mixed with 1000 mL distilled water followed by addition of 10 mL nitric acid (98%, Sigma-Aldrich) to this solution. Subsequently, the mixture was stirred, until a white precipitate was observed, and then heated at 80°C for 5 h in an oil bath to obtain a transparent sol. The previously prepared N-TiO_2 powder (2 g) was added to this sol, after which this mixture was sonicated for 1 h to obtain the final coating solution. The previously cleaned GF was dipped into the coating solution (500 mL) in a home-made glass container (12 cm × 23 cm × 2 cm) for 10 min, taken out slowly, and dried at room temperature for 2 h. These dip-coating and drying processes were conducted in triplicate to give high coating amounts. GF-N-TiO_2 powders having N-to-Ti ratios of 0.06, 0.08, 0.10, and 0.12 were named as GF-N-TiO_2-0.06, GF-N-TiO_2-0.08, GF-N-TiO_2-0.10, and GF-N-TiO_2-0.12, respectively. In addition, a reference photocatalyst, GF-TiO_2, was prepared using P25 TiO_2 instead of N-TiO_2, following the same coating procedure as used for the preparation of GF-N-TiO_2. The characteristics of as-prepared GF-N-TiO_2, GF-TiO_2, and pretreated GF were determined using scanning electron microscopy (SEM, Hitachi S-4300 FE-SEM), energy-dispersive X-ray spectroscopy (EDX, Hitachi EDX-350), X-ray diffraction spectroscopy (XRD, Rigaku D/max-2500 diffractometer), and UV-visible spectroscopy (Varian CARY 5G). For the EDX analysis, the sample was pretreated using a Pt-coating system (Hitachi E-1030).

2.2. Determination of Aromatic VOC Degradation Efficiencies. The degradation efficiencies of aromatic VOCs were

investigated using GF-N-TiO_2, GF-TiO_2, and GF, which were placed in a cylindrical photocatalytic reactor. The reactor was prepared using a Pyrex tube (a length of 26.5 cm and an inner diameter of 3.8 cm), where a cylindrical-shaped daylight lamp (F8T5DL, Youngwha Lamp Co.) with a spectral range of 400–720 nm was inserted. The light intensities provided by the daylight lamp were 3.2 mW cm^{-2} at a distance from the light source to the surface of photocatalysts. The inner surface of the Pyrex tube was covered by a GF-Fe-TiO_2, GF-TiO_2, or GF sheet. Zero-grade dried air was supplied by an air cylinder and was allowed to flow through a carbon filter for repurification. The dried air stream flowed through two water-containing impingers in tandem, which were partially immersed in a water bath, for air humidification. The relative humidity (RH) levels were adjusted by controlling the mixing ratio of dried with humidified air flows. Standard compounds were prepared by adjusting the mixing ratio of the humidified air with TEX prepared by vaporizing liquid standards, which were injected into a heated glass chamber via a syringe pump (KDS 210, KD Scientific). Lastly, the prepared standard compounds were transferred to the reactor for photocatalytic decomposition efficiency tests. The degradation efficiency tests were conducted under different operational conditions by controlling two important factors: air flow rate (AFR: 1.0, 2.0, 3.0, and 4.0 L min^{-1}) and initial concentration (IC: 0.1, 0.5, 1.0, and 2.0 ppm). When evaluating a specific factor, the other factor was held constant at the following values: IC, 0.1 ppm, and AFR, 1.0 L min^{-1}. In addition, the RH was fixed at 45%, which represents a comfortable value for typical indoor life.

Air measurements were carried out at the inlet and outlet ports of the cylindrical reactor by drawing air through a stainless steel tubing trap containing Tenax GC adsorbent. Gaseous species collected in the adsorbent trap were analyzed using a gas chromatograph/mass spectrometer (Perkin Elmer Clarus SQ 8) (GC/MS) coupled to a thermal desorbing device (Perkin Elmer ATD 350). The gases were qualitatively analyzed based on both their retention times and mass spectra (Wiley 275 software library). Each chemical species was qualitatively analyzed based on calibration curves, which were determined using five concentrations standardized to an internal standard chemical. For the quality control program, a laboratory blank and spiked standard trap samples were analyzed. The entire experimental procedure was repeated three times to give more reliable data and the average values are presented in this paper.

3. Results and Discussion

3.1. Characteristics of As-Prepared Photocatalysts. The surface characteristics of a representative GF-N-TiO_2 with a N-to-Ti ratio of 0.08 (GF-N-TiO_2-0.08) as well as a reference photocatalyst (GF-TiO_2) were examined using SEM, EDX, XRD, and UV-visible absorption analyses. Based on the SEM micrographs (Figure 2), GF-N-TiO_2-0.08 showed a better coating of N-TiO_2 on GF relative to GF-TiO_2. The enhanced coating efficiency for GF-N-TiO_2-0.08 was ascribed to the strong agglomerating nature of N-TiO_2 [17]. Consistently, previous researchers [22, 34] have found a higher aggregation

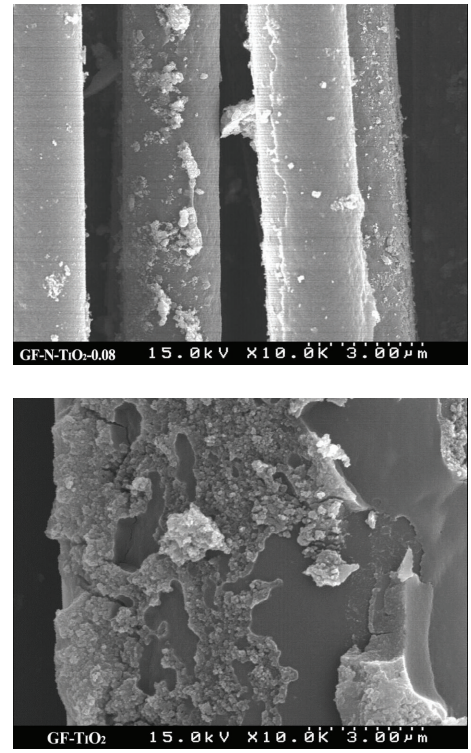

Figure 2: Scanning electron microscopy of GF-N-TiO_2 with a N-to-Ti ratio of 0.08 (GF-N-TiO_2-0.08) and GF-TiO_2.

property of N-TiO_2 as compared to pure TiO_2 by SEM analysis.

As illustrated in Figure 3, the EDX spectrum of GF-N-TiO_2-0.08 showed peaks of Ti, O, and N atoms, whereas the spectrum of GF-TiO_2 showed only Ti and O atom bands; those bands assigned to Ti and O atoms were associated with TiO_2, while the N atom band was ascribed to N atoms embedded in the TiO_2 lattice. Therefore, EDX spectra analysis demonstrated that N atoms could be successfully incorporated into TiO_2 to allow the prepared photocatalyst be activated under visible-light irradiation conditions. In agreement with our results, Gurkan et al. [22] found the existence of N atoms for N-TiO_2 synthesized using a wet incorporation process through EDX analysis. The undesignated peaks in the EDX spectra were attributed to Pt, which was used for sample coating prior to EDX analysis; no other evident impurities were observed in the samples.

Figure 4 illustrates the XRD spectra of GF-N-TiO_2-0.08 and the reference GF-TiO_2 photocatalyst. Both photocatalysts displayed an anatase phase with a major band at 25.3° 2θ and a rutile phase with a major band at 27.3° 2θ. These diffractograms were similar to those of Degussa P25 TiO_2 reported in other studies [22, 35], indicating that N incorporated into TiO_2 for the GF-N-TiO_2-0.08 photocatalyst did not alter the crystal structures of TiO_2. Gurkan et al. [22] also reported that the XRD patterns of N-TiO_2 were similar to those of pure P25 TiO_2. However, any N dopant-associated bands were not found in the spectrum of GF-N-TiO_2-0.08. These findings suggest that N atoms would not chemically

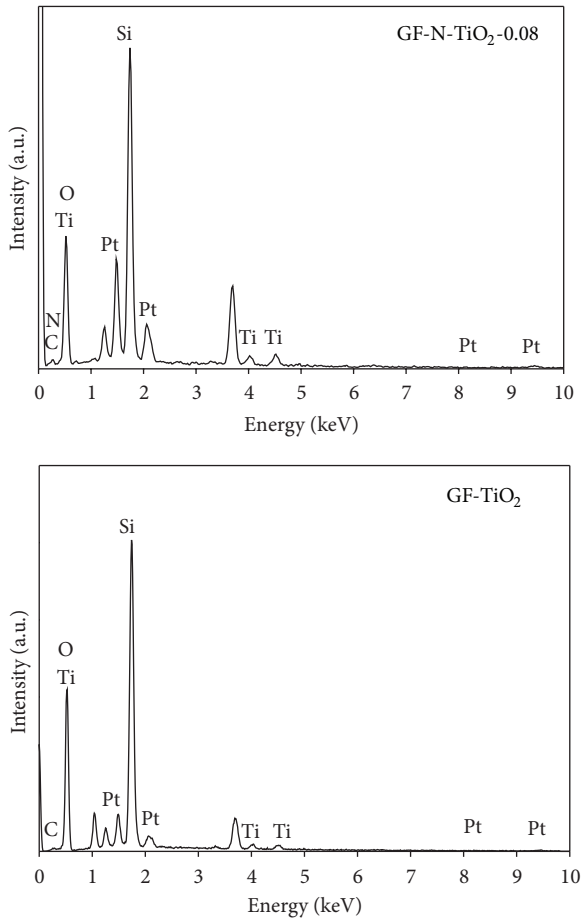

Figure 3: Energy-dispersive X-ray images of GF-N-TiO_2 with a N-to-Ti ratio of 0.08 (GF-N-TiO_2-0.08) and GF-TiO_2.

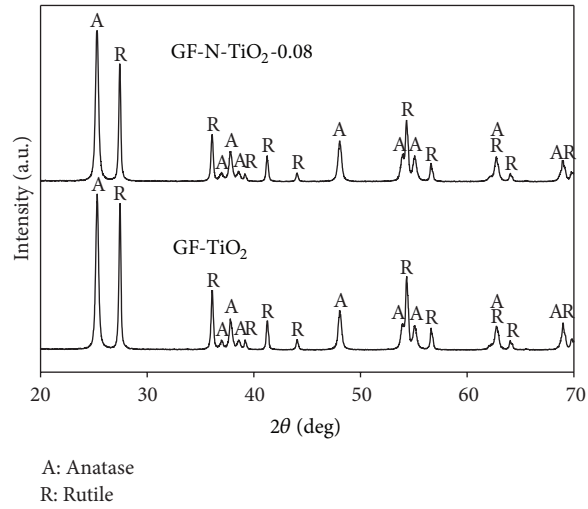

Figure 4: X-ray diffraction patterns of GF-N-TiO_2 with a N-to-Ti ratio of 0.08 (GF-N-TiO_2-0.08) and GF-TiO_2.

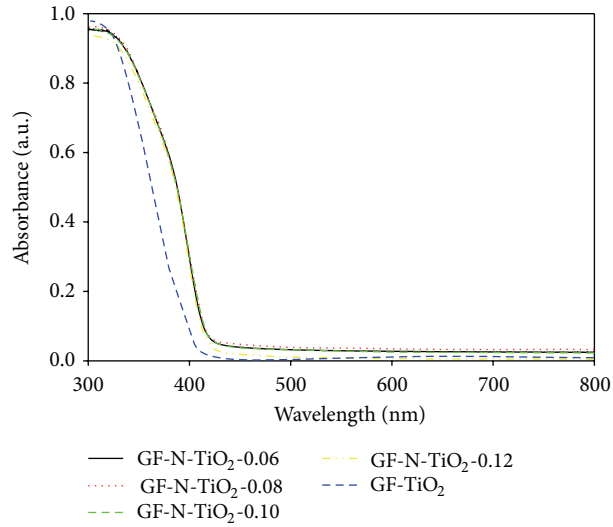

Figure 5: UV-visible spectra of GF-N-TiO_2-0.06, GF-N-TiO_2-0.08, GF-N-TiO_2-0.10, GF-N-TiO_2-0.12, and GF-TiO_2.

react to produce new crystalline structures, such as TiN, but are rather incorporated interstitially and substitutionally into the TiO_2 structure [15]. Otherwise, low amounts of N atoms impregnated into TiO_2 in GF-N-TiO_2-0.08 could not be detected by XRD possibly due to its limited measurement sensitivity.

The sizes of crystal phases of the GF-N-TiO_2 photocatalysts and reference GF-TiO_2 were estimated based on the Scherrer formula [36]. The anatase crystallite size of GF-N-TiO_2-0.08 (36.61 nm) was smaller than that of GF-TiO_2 (39.31 nm), while the crystallite sizes of GF-N-TiO_2-0.06, GF-N-TiO_2-0.10, and GF-N-TiO_2-0.12 were 36.49, 36.72, and 37.04 nm, respectively. Gurkan et al. [22] also reported a smaller crystallite size for N-TiO_2 powder relative to that of pure TiO_2 powder. The reduction in the crystallite size observed for GF-N-TiO_2-0.08 was ascribed to the formation of compressive strain in the crystallite structure, which would likely be due to the transformation of electronic structure resulting from N dopant ion incorporation into TiO_2 [22].

Figure 5 shows the UV-visible spectra of the GF-N-TiO_2 photocatalysts and reference GF-TiO_2. The reference GF-TiO_2 exhibited an absorption edge at a wavelength of around 420 nm, which was in good agreement with that reported in previous studies [22, 34]. In contrast, the UV-visible spectra of GF-N-TiO_2 photocatalysts were highly shifted toward the visible region, which was consistent with the results reported by Gurkan et al. [22]. These shifts toward the visible region of the spectrum were attributed to the generation of a narrowed band gap level, which is located between the valence and conduction bands of TiO_2. Overall, it was suggested that the prepared GF-N-TiO_2 photocatalysts could be functional under visible-light irradiation as well.

3.2. Photocatalytic Degradation of Aromatic VOCs. The photocatalytic degradation of TEX was conducted using the prepared GF-N-TiO_2 photocatalysts with different N-to-Ti ratios and GF-TiO_2 under visible-light irradiation following three-hour adsorption process. As shown in Figure 6, a control photolysis test performed using an uncoated GF displayed no degradation of TEX at all under visible-light irradiation,

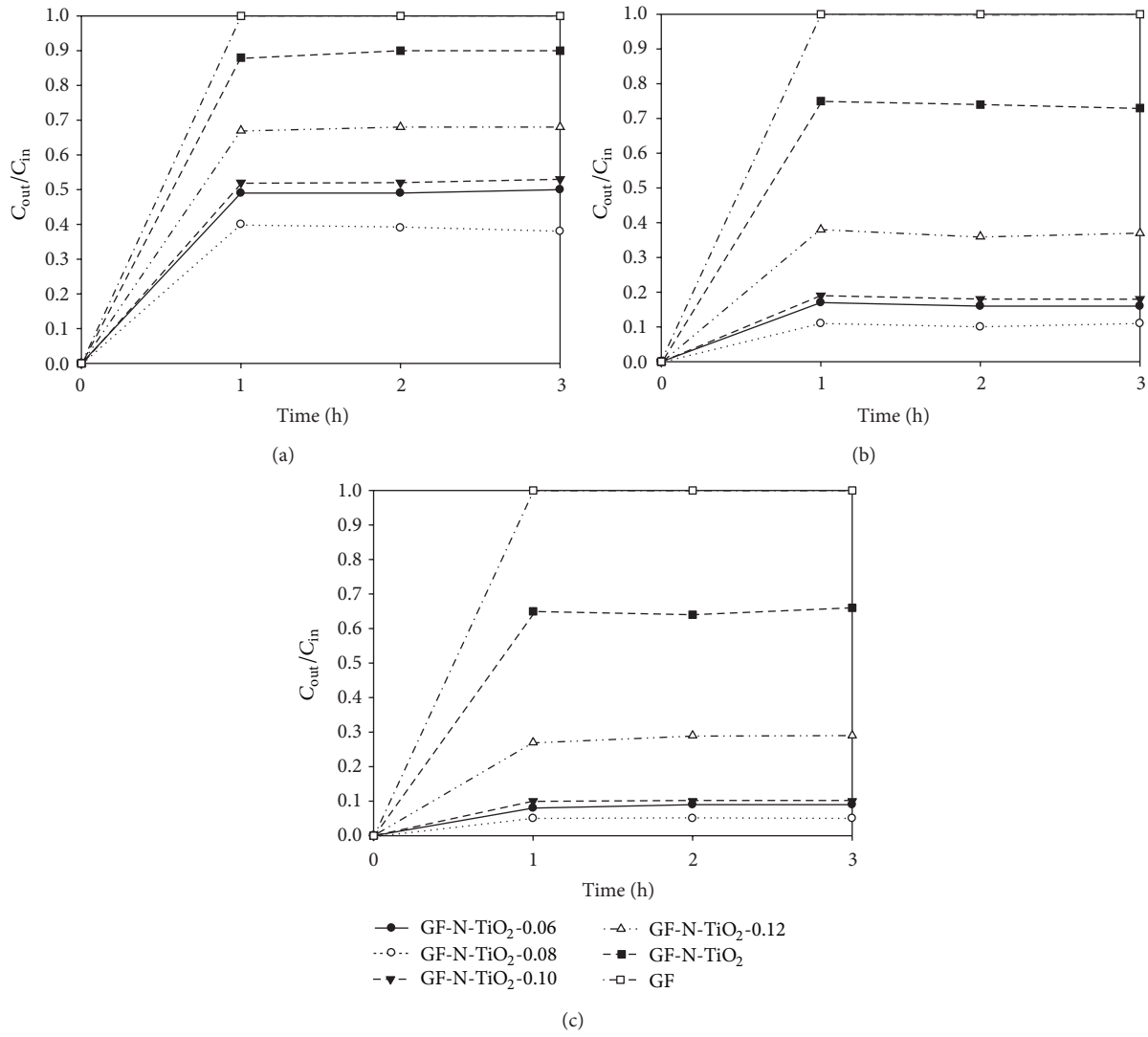

Figure 6: Time-series ratios (C_{out}/C_{in}) of outlet-to-inlet concentrations of (a) toluene, (b) ethyl benzene, and (c) o-xylene as obtained using GF-N-TiO_2 photocatalysts with different N-to-Ti ratios (GF-N-TiO_2-0.06, GF-N-TiO_2-0.08, GF-N-TiO_2-0.10, and GF-N-TiO_2-0.12), GF-TiO_2, and GF.

which was demonstrated by similar values for inlet and outlet concentrations of TEX. In addition, Figure 5 shows the outlet to inlet concentrations of TEX determined for four GF-N-TiO_2 photocatalysts (GF-N-TiO_2-0.06, GF-N-TiO_2-0.08, GF-N-TiO_2-0.10, and GF-N-TiO_2-0.12) and the reference GF-TiO_2 photocatalyst over three-hour photocatalytic process. The outlet-to-inlet concentration ratios of the three target pollutants obtained using the GF-N-TiO_2 photocatalysts were lower than that of the GF-TiO_2 photocatalyst, indicating that GF-N-TiO_2 photocatalysts had higher photocatalytic activity toward the degradation of TEX. For example, the average outlet-to-inlet concentration ratios of TEX for GF-N-TiO_2-0.06 were 0.51, 0.18, and 0.09, respectively, while those of the GF-TiO_2 photocatalyst were 0.90, 0.76, and 0.67, respectively. Similarly, Gurkan et al. [22] demonstrated a higher photocatalytic activity for the degradation of cefazolin in the aqueous phase relative to undoped TiO_2 under sunlight irradiation. Jo and Kim [21] also reported that daylight lamp-irradiated N-TiO_2, which was coated directly onto the inner wall of a Pyrex tubing reactor, showed superior performance for the degradation of aromatic VOCs compared to unmodified TiO_2. The superior photocatalytic activity of the GF-N-TiO_2 photocatalysts under visible-light irradiation was ascribed to their predisposition for visible-light absorbance owing to large specific surface area and the reduced impurity level localized in the top of valence band, as demonstrated from their UV-visible spectra (Figure 5), since the photocatalytic reaction rates are proportional to the amount of photon absorption by the photocatalysts [6, 37–40]. The smaller crystallite size of GF-N-TiO_2 photocatalysts relative to the GF-TiO_2 photocatalyst would also enhance their photocatalytic activity. Consequently, it was suggested that GF-N-TiO_2 photocatalysts with visible-light activation can be applied to effectively degrade aromatic VOCs.

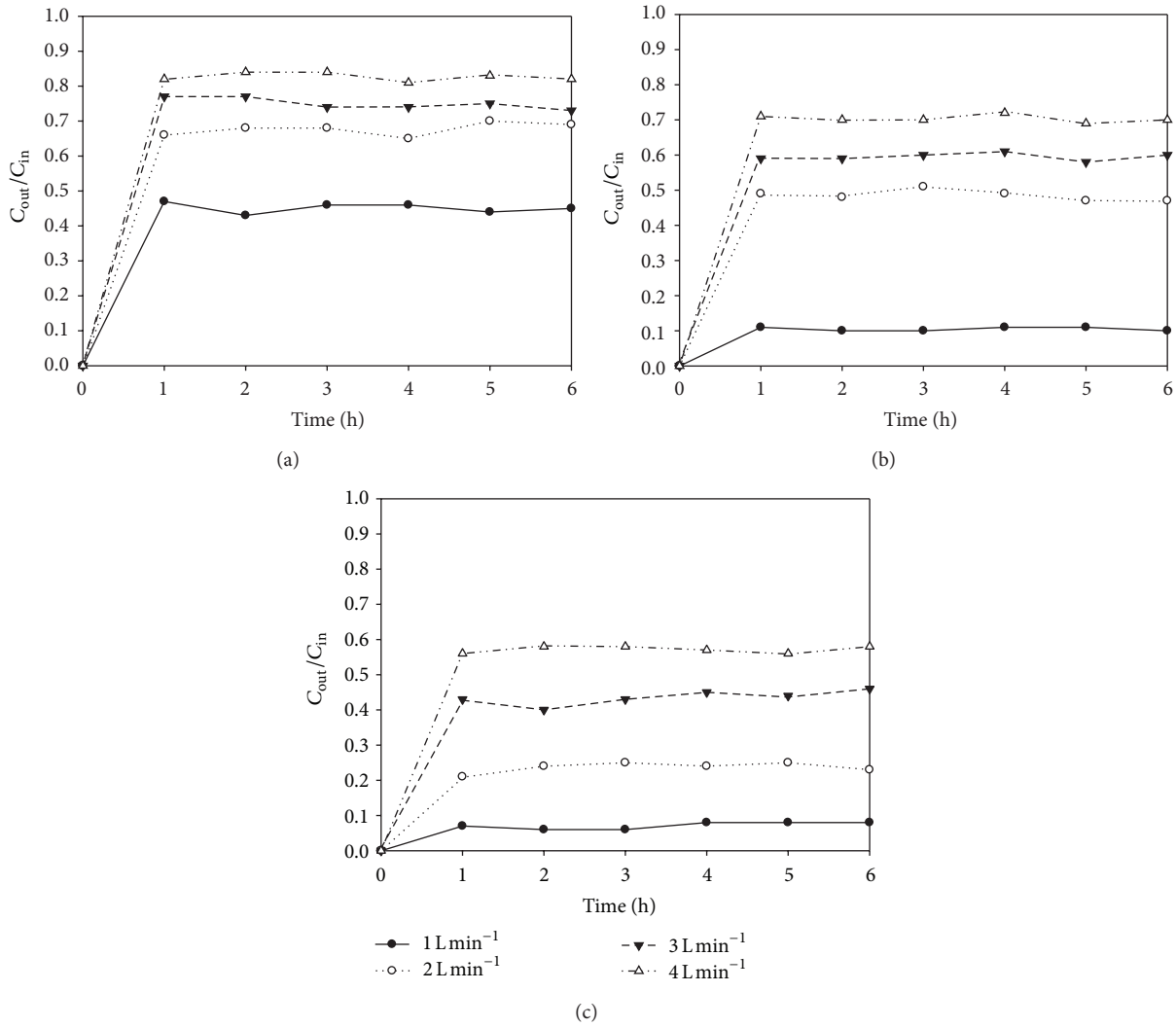

FIGURE 7: Time-series ratios (C_{out}/C_{in}) of outlet-to-inlet concentrations of (a) toluene, (b) ethyl benzene, and (c) o-xylene as obtained using GF-N-TiO_2-0.08 according to air-stream flow rates.

As also demonstrated in Figure 6, the photocatalytic activity of the GF-N-TiO_2 photocatalyst increased as the N-to-Ti ratio increased from 0.06 to 0.08, but then decreased gradually as the N-to-Ti ratio increased further to 0.12. These results indicate that there is an optimal N-to-Ti ratio range for the synthesis of GF-N-TiO_2 photocatalysts. The decreasing pattern for high N-to-Ti ratios was attributed to increased particle aggregation due to high amounts of N dopant, which results in the reduction in photocatalyst surface area [22]. The high amounts of N dopant might also decrease the separation distance of charge carriers, which result in an increase in the recombination of electron-hole pairs.

Figure 7 illustrates the outlet-to-inlet concentration ratios of TEX obtained using GF-N-TiO_2-0.08 according to AFRs. The outlet-to-inlet concentration ratio of all the target compounds displayed an increasing trend as AFR increased, indicating that the photocatalytic activity of GF-N-TiO_2-0.08 decreased with increasing AFRs. Particularly, the average ratios of TEX increased from 0.47 to 0.82, 0.11 to 0.71, and 0.09 to 0.59, respectively, as the AFR increased from 1 to 4 L min^{-1}. In agreement with our results, Jeong et al. [41] reported that the photocatalytic activity of Degussa P25 TiO_2 for the degradation of benzene and toluene under UV irradiation showed a decreasing trend with increasing AFRs. These results might be ascribed to the mass transfer rate of the pollutant molecules from the air stream to the photocatalyst surface as well as photocatalytic reaction kinetics [42]. Unlike batch reactors, the mass transfer rates of gas-phase compounds in continuous-flow photocatalytic reactors are closely associated with the linear face velocities of the air stream [43]. In the present study, the linear face velocities increased as the AFR increased: the linear face velocities for AFRs of 1, 2, 3, and 4 L min^{-1} were 4.8, 9.6, 14.4, and 19.2 cm s^{-1}, respectively. These results suggested that the photocatalytic activity of the GF-N-TiO_2-0.08 would increase as the AFR increased, owing to high mass-transfer rates; rather, the photocatalytic activity of GF-N-TiO_2-0.08 decreased with increasing AFR. As such, the low photocatalytic activity of GF-N-TiO_2-0.08 at

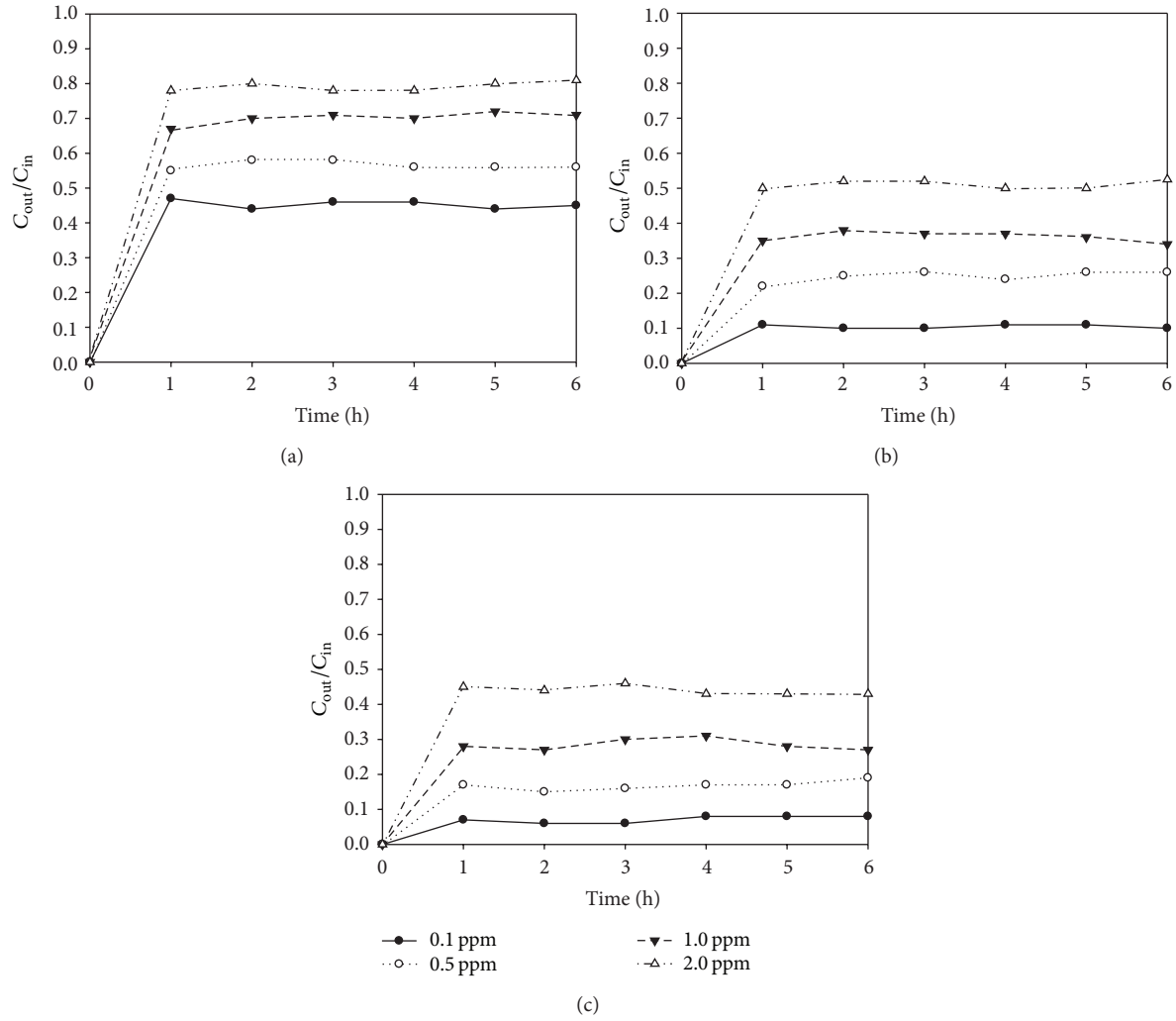

Figure 8: Time-series ratios (C_{out}/C_{in}) of outlet-to-inlet concentrations of (a) toluene, (b) ethyl benzene, and (c) o-xylene as obtained using GF-N-TiO_2-0.08 according to inlet concentrations.

high AFRs was attributed to an insufficient reaction time in the photocatalytic reactor, suggesting that the photocatalytic activity of GF-N-TiO_2-0.08 was likely limited by reaction kinetics on the photocatalyst surfaces. The reaction times for AFRs of 1, 2, 3, and 4 L min^{-1}, which were calculated by dividing the empty-space reactor volume by the AFRs, were 6.1, 3.1, 2.0, and 1.5 s, respectively.

Figure 8 shows the outlet-to-inlet concentration ratios of TEX obtained using GF-N-TiO_2-0.08 according to ICs. For all target compounds, the outlet-to-inlet concentration ratio increased as IC increased, indicating that the photocatalytic activity of GF-N-TiO_2-0.08 decreased with increasing ICs. At the lowest IC (0.1 ppm), the average ratios of TEX were 0.41, 0.10, and 0.07, respectively, whereas those at the highest IC (2.0 ppm) were 0.79, 0.49, and 0.42, respectively. Devahasdin et al. [44] also found that the photocatalytic degradation efficiencies of unmodified TiO_2 for degradation of NO under UV irradiation decreased from 70–15% when IC was increased from 5–60 ppm. In addition, Jeong et al. [41] reported that the photocatalytic degradation efficiency of toluene determined using Degussa P25 TiO_2 decreased gradually as IC increased from 0.6–10 ppm. The descending trend in photocatalytic activity with increasing IC was ascribed to competitive adsorption among TEX molecules on the catalyst surface; adsorption of chemical molecules onto the catalyst surface is known to be a crucial factor influencing the photocatalytic degradation of organic compounds [6].

4. Conclusions

This study investigated the applicability of glass fiber-based N-doped titania (GF-N-TiO_2) under visible-light exposure for the photocatalytic degradation of aromatic VOCs. SEM results indicated the formation of aggregates for the GF-N-TiO_2 photocatalyst, while EDX spectral analysis demonstrated that N elements were successfully incorporated into the TiO_2 crystal lattice. The UV-visible spectra suggested that GF-N-TiO_2 photocatalysts could be functional under visible-light exposure. The prepared GF-N-TiO_2 photocatalysts showed superior photocatalytic performances to the

reference GF-TiO_2 photocatalyst for degradation of aromatic VOCs under visible-light irradiation. The prepared GF-N-TiO_2 photocatalysts also showed a different dependence of N-to-Ti ratios on photocatalytic degradation of aromatic VOCs, indicating that there is optimal range of N-to-Ti ratios for the synthesis of GF-N-TiO_2 photocatalysts. In addition, AFR and IC were both found to be major influential factors on the photocatalytic performance of the GF-N-TiO_2 photocatalysts. Overall, the GF-N-TiO_2 photocatalysts could be applied effectively for the degradation of aromatic VOCs under visible-light irradiation at optimal operation conditions.

Conflict of Interests

The authors declare that there is no conflict of interests regarding the publication of this paper.

Acknowledgments

This work was supported by the National Research Foundation of Korea (NRF) Grant funded by the Korea government (MEST) (no. 2011-0027916) and through the GCRC-SOP (no. 2011-0030013).

References

[1] M. Leuchner and B. Rappenglück, "VOC source-receptor relationships in Houston during TexAQS-II," *Atmospheric Environment*, vol. 44, no. 33, pp. 4056–4067, 2010.

[2] O. O. Hänninen, E. Lebret, V. Ilacqua et al., "Infiltration of ambient PM2.5 and levels of indoor generated non-ETS PM2.5 in residences of four European cities," *Atmospheric Environment*, vol. 38, no. 37, pp. 6411–6423, 2004.

[3] K.-D. Kwon, W.-K. Jo, H.-J. Lim, and W.-S. Jeong, "Characterization of emissions composition for selected household products available in Korea," *Journal of Hazardous Materials*, vol. 148, no. 1-2, pp. 192–198, 2007.

[4] S. H. Shin and W. K. Jo, "Longitudinal variations in indoor VOC concentrations after moving into new apartments and indoor source characterization," *Environmental Science and Pollution Research*, vol. 20, pp. 3696–3707, 2013.

[5] IARC (International Agency for Research on Cancer), "List of classifications by alphabetical order," 2013, http://monographs.iarc.fr/ENG/Classification/index.php.

[6] M. A. Henderson, "A surface science perspective on TiO_2 photocatalysis," *Surface Science Reports*, vol. 66, no. 6-7, pp. 185–297, 2011.

[7] T. Ohno, M. Akiyoshi, T. Umebayashi, K. Asai, T. Mitsui, and M. Matsumura, "Preparation of S-doped TiO_2 photocatalysts and their photocatalytic activities under visible light," *Applied Catalysis A: General*, vol. 265, no. 1, pp. 115–121, 2004.

[8] C.-C. Hu, T.-C. Hsu, and S.-Y. Lu, "Effect of nitrogen doping on the microstructure and visible light photocatalysis of titanate nanotubes by a facile cohydrothermal synthesis via urea treatment," *Applied Surface Science*, vol. 280, pp. 171–178, 2013.

[9] H. Guo, M. Kemell, M. Heikkilä, and M. Leskelä, "Noble metal-modified TiO_2 thin film photocatalyst on porous steel fiber support," *Applied Catalysis B: Environmental*, vol. 95, no. 3-4, pp. 358–364, 2010.

[10] S. Kment, H. Kmentova, P. Kluson et al., "Notes on the photo-induced characteristics of transition metal-doped and undoped titanium dioxide thin films," *Journal of Colloid and Interface Science*, vol. 348, no. 1, pp. 198–205, 2010.

[11] X. Chen, W. Wang, H. Xiao et al., "Accelerated TiO_2 photocatalytic degradation of Acid Orange 7 under visible light mediated by Peroxymonosulfate," *Chemical Engineering Journal*, vol. 193-194, pp. 290–295, 2012.

[12] Y. Wang, J. Zhang, L. Liu, C. Zhu, X. Liu, and Q. Su, "Visible light photocatalysis of V_2O_5/TiO_2 nanoheterostructures prepared via electrospinning," *Materials Letters*, vol. 75, pp. 95–98, 2012.

[13] W.-K. Jo, "Coupling of titania with multiwall carbon nanotubes for decomposition of gas-phase pollutants under simulated indoor conditions," *Journal of Air & Waste Management Association*, vol. 63, pp. 963–970, 2013.

[14] W.-K. Jo and H.-J. Kang, "Titanium dioxide-graphene oxide composites with different ratios supported by Pyrex tube for photocatalysis of toxic aromatic vapors," *Powder Technology*, vol. 250, pp. 115–121, 2013.

[15] R. Asahi, T. Morikawa, T. Ohwaki, K. Aoki, and Y. Taga, "Visible-light photocatalysis in nitrogen-doped titanium oxides," *Science*, vol. 293, no. 5528, pp. 269–271, 2001.

[16] M. Pelaez, N. T. Nolan, S. C. Pillai et al., "A review on the visible light active titanium dioxide photocatalysts for environmental applications," *Applied Catalysis B: Environmental*, vol. 125, pp. 331–349, 2012.

[17] C. di Valentin, E. Finazzi, G. Pacchioni et al., "N-doped TiO_2: theory and experiment," *Chemical Physics*, vol. 339, no. 1–3, pp. 44–56, 2007.

[18] C. di Valentin, G. Pacchioni, A. Selloni, S. Livraghi, and E. Giamello, "Characterization of paramagnetic species in N-doped TiO_2 powders by EPR spectroscopy and DFT calculations," *Journal of Physical Chemistry B*, vol. 109, no. 23, pp. 11414–11419, 2005.

[19] N. Serpone, "Is the band gap of pristine TiO_2 narrowed by anion- and cation-doping of titanium dioxide in second-generation photocatalysts?" *Journal of Physical Chemistry B*, vol. 110, no. 48, pp. 24287–24293, 2006.

[20] A. V. Emeline, V. N. Kuznetsow, V. K. Rybchuk, and N. Serpne, "Visible-light-active titania photocatalysts: the case of N-doped TiO_2s—properties and some fundamental issues," *International Journal of Photoenergy*, vol. 2008, Article ID 258394, 19 pages, 2008.

[21] W.-K. Jo and J.-T. Kim, "Application of visible-light photocatalysis with nitrogen-doped or unmodified titanium dioxide for control of indoor-level volatile organic compounds," *Journal of Hazardous Materials*, vol. 164, no. 1, pp. 360–366, 2009.

[22] Y. Y. Gurkan, N. Turkten, A. Hatipoglu, and Z. Cinar, "Photocatalytic degradation of cefazolin over N-doped TiO_2 under UV and sunlight irradiation: prediction of the reaction paths via conceptual DFT," *Chemical Engineering Journal*, vol. 184, pp. 113–124, 2012.

[23] A. Y. Shan, T. I. M. Ghazi, and S. A. Rashid, "Immobilisation of titanium dioxide onto supporting materials in heterogeneous photocatalysis: a review," *Applied Catalysis A: General*, vol. 389, no. 1-2, pp. 1–8, 2010.

[24] C. L. Bianchi, C. Pirola, E. Selli, and S. Biella, "Photocatalytic NO_x abatement: the role of the material supporting the TiO_2 active layer," *Journal of Hazardous Materials*, vol. 211-212, pp. 203–207, 2012.

[25] J. Matos, E. García-López, L. Palmisano, A. García, and G. Marcì, "Influence of activated carbon in TiO_2 and ZnO mediated photo-assisted degradation of 2-propanol in gas-solid regime," *Applied Catalysis B: Environmental*, vol. 99, pp. 170–180, 2010.

[26] W. K. Jo, S. H. Shin, and E. S. Hwang, "Removal of dimethyl sulfide utilizing activated carbon fiber-supported photocatalyst in continuous-flow system," *Journal of Hazardous Materials*, vol. 191, no. 1–3, pp. 234–239, 2011.

[27] J.-W. Shi, H.-J. Cui, J.-W. Chen et al., "TiO_2/activated carbon fibers photocatalyst: effect of coating procedures on the microstructure, adhesion property, and photocatalytic ability," *Journal of Colloid and Interface Science*, vol. 388, pp. 201–208, 2012.

[28] T. E. Agustina, H. M. Ang, and V. K. Pareek, "Treatment of winery wastewater using a photocatalytic/photolytic reactor," *Chemical Engineering Journal*, vol. 135, no. 1-2, pp. 151–156, 2008.

[29] S. W. Verbruggen, S. Ribbens, T. Tytgat et al., "The benefit of glass bead supports for efficient gas phase photocatalysis: case study of a commercial and a synthesised photocatalyst," *Chemical Engineering Journal*, vol. 174, no. 1, pp. 318–325, 2011.

[30] A. K. Alves, F. A. Berutti, F. J. Clemens, T. Graule, and C. P. Bergmann, "Photocatalytic activity of titania fibers obtained by electrospinning," *Materials Research Bulletin*, vol. 44, no. 2, pp. 312–317, 2009.

[31] C. Prahsarn, W. Klinsukhon, and N. Roungpaisan, "Electrospinning of PAN/DMF/H2O containing TiO_2 and photocatalytic activity of their webs," *Materials Letters*, vol. 65, no. 15-16, pp. 2498–2501, 2011.

[32] A. Panniello, M. L. Curri, D. Diso et al., "Nanocrystalline TiO_2 based films onto fibers for photocatalytic degradation of organic dye in aqueous solution," *Applied Catalysis B: Environmental*, vol. 121-122, pp. 190–197, 2012.

[33] S. Lin, X. Zhang, Q. Sun, T. Zhou, and J. Lu, "Fabrication of solar light induced Fe-TiO_2 immobilized on glass-fiber and application for phenol photocatalytic degradation," *Materials Research Bulletin*, vol. 48, pp. 4570–4575, 2013.

[34] J. Senthilnathan and L. Philip, "Photocatalytic degradation of lindane under UV and visible light using N-doped TiO_2," *Chemical Engineering Journal*, vol. 161, no. 1-2, pp. 83–92, 2010.

[35] M. M. Joshi, N. K. Labhsetwar, D. V. Parwate, and S. S. Rayalu, "Efficient photocatalytic hydrogen generation by silica supported and platinum promoted titanium dioxide," *Materials Research Bulletin*, vol. 48, pp. 3545–3552, 2013.

[36] B. D. Cullity and S. R. Stock, *Elements of X-Ray Diffraction*, Prentice Hall, Upper Saddle River, NJ, USA, 3rd edition, 2001.

[37] Q. Xiang, J. Yu, and M. Jaroniec, "Nitrogen and sulfur co-doped TiO_2 nanosheets with exposed {001} facets: synthesis, characterization and visible-light photocatalytic activity," *Physical Chemistry Chemical Physics*, vol. 13, no. 11, pp. 4853–4861, 2011.

[38] Q. Xiang, J. Yu, W. Wang, and M. Jaroniec, "Nitrogen self-doped nanosized TiO_2 sheets with exposed {001} facets for enhanced visible-light photocatalytic activity," *Chemical Communications*, vol. 47, no. 24, pp. 6906–6908, 2011.

[39] Z. Lin, A. Orlov, R. M. Lambert, and M. C. Payne, "New insights into the origin of visible light photocatalytic activity of nitrogen-doped and oxygen-deficient anatase TiO_2," *Journal of Physical Chemistry B*, vol. 109, no. 44, pp. 20948–20952, 2005.

[40] P. Zhou, J. Yu, and Y. Wang, "The new understanding on photocatalytic mechanism of visible-light response N-S codoped anatase TiO_2 by first-principles," *Applied Catalysis B: Environmental*, vol. 142-143, pp. 45–53, 2013.

[41] J. Jeong, K. Sekiguchi, W. Lee, and K. Sakamoto, "Photodegradation of gaseous volatile organic compounds (VOCs) using TiO_2 photoirradiated by an ozone-producing UV lamp: decomposition characteristics, identification of by-products and water-soluble organic intermediates," *Journal of Photochemistry and Photobiology A: Chemistry*, vol. 169, no. 3, pp. 279–287, 2005.

[42] K. Demeestere, J. Dewulf, and H. van Langenhove, "Heterogeneous photocatalysis as an advanced oxidation process for the abatement of chlorinated, monocyclic aromatic and sulfurous volatile organic compounds in air: state of the art," *Critical Reviews in Environmental Science and Technology*, vol. 37, no. 6, pp. 489–538, 2007.

[43] L. Yang, Z. Liu, J. Shi, H. Hu, and W. Shangguan, "Design consideration of photocatalytic oxidation reactors using TiO_2-coated foam nickels for degrading indoor gaseous formaldehyde," *Catalysis Today*, vol. 126, no. 3-4, pp. 359–368, 2007.

[44] S. Devahasdin, C. Fan Jr., K. Li, and D. H. Chen, "TiO_2 photocatalytic oxidation of nitric oxide: transient behavior and reaction kinetics," *Journal of Photochemistry and Photobiology A: Chemistry*, vol. 156, no. 1–3, pp. 161–170, 2003.

Hindawi Publishing Corporation
International Journal of Photoenergy
Volume 2014, Article ID 524135, 14 pages
http://dx.doi.org/10.1155/2014/524135

Review Article

An Overview: Recent Development of Titanium Oxide Nanotubes as Photocatalyst for Dye Degradation

Chin Wei Lai,[1] Joon Ching Juan,[1] Weon Bae Ko,[2] and Sharifah Bee Abd Hamid[1]

[1] *Nanotechnology & Catalysis Research Centre (NANOCAT), Institute of Postgraduate Studies (IPS), University of Malaya, 3rd Floor, Block A, 50603 Kuala Lumpur, Malaysia*
[2] *Department of Chemistry, Sahmyook University, Seoul 139-742, Republic of Korea*

Correspondence should be addressed to Chin Wei Lai; cwlai@um.edu.my and Weon Bae Ko; kowbsahmyook@syu.ac.kr

Received 25 December 2013; Revised 14 January 2014; Accepted 15 January 2014; Published 27 February 2014

Academic Editor: Jiaguo Yu

Today, organic dyes are one of the largest groups of pollutants release into environment especially from textile industry. It is highly toxic and hazardous to the living organism; thus, the removal of these dyes prior to discharge into the environment is essential. Varieties of techniques have been employed to degrade organic dyes and heterogeneous photocatalysis involving titanium dioxide (TiO_2) appears to be the most promising technology. In recent years, TiO_2 nanotubes have attracted much attention due to their high surface area and extraordinary characteristics. This paper presents a critical review of recent achievements in the modification of TiO_2 nanotubes for dye degradation. The photocatalytic activity on dye degradation can be further enhanced by doping with cationic or anionic dopant.

1. Introduction

1.1. Overview of Organic Dye Degradation. Nowadays, global warming poses one of the most serious threats to the global environment ever faced in human history. The environment pollutions will cause an unprecedented onslaught of deadly and costly weather disasters, such as severe storms, droughts, heat waves, and rising seas and floods all over the world [1–3]. One of the major water pollutions is the residual dyes from different sources (e.g., textile industries, paper and pulp industries, dye and dye intermediates industries, pharmaceutical industries, tannery, and craft bleaching industries, etc.) which are considered a wide variety of persistent organic pollutants introduced into the natural water resources or wastewater treatment systems [4]. Dyeing and finishing industry produces as much as 50–100 L wastewater/kg of finished textile products [5]. As shown in Figure 1, World Bank has estimated that textile industries in many countries contribute to 17 to 20% of global industrial water pollution [6]. There are about 10–15% of 700 thousand tons of 10 thousand types of dyes that have been discharged without any proper physicochemical treatment [7].

There are more than 100 000 commercially available dyes and an annual worldwide production of synthetic dyes of nearly 1 million tons [8–10]. Reactive dyes have been estimated to contribute the most to the discharge of dye wastewater, as much as 57 thousand tons (Figure 2) because of their low fixation rate. As shown in Table 1, the reactive dye has a very poor fixation rates. The fixation rate is influenced by the extent of hydrolysis of the dye [11], signifying the vulnerability of reactive dyes to hydrolysis in dye bath.

The release of the persistent organic dyes structure with toxicity property may cause negative effects on the environment and human health. These negative impacts mainly attributed to the nonbiodegradable nature of the persistent organic dyes as well as their high colour intensity and are able to reduce aquatic diversity by blocking the passage of sunlight through the water [12]. In particular, the discharge of persistent organic dye effluents into the natural water resources or wastewater treatment systems is undesirable because most of these organic dyes released and their breakdown products are very toxic, carcinogenic, or mutagenic to life forms mainly due to the carcinogens, such as benzidine, naphthalene, and other aromatic compounds in the structure of persistent

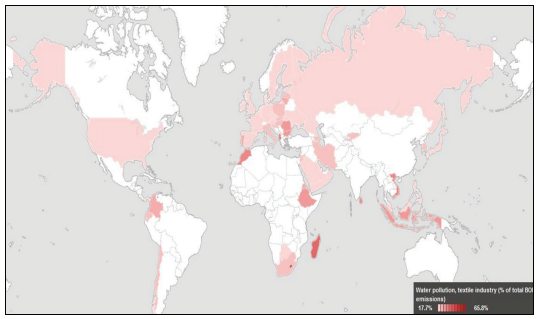

Figure 1: Water pollution caused by textile industrial from various countries. The darker icon signifies higher level of water pollution which is based on percentage of total biochemical oxygen demand (BOD) emissions [20].

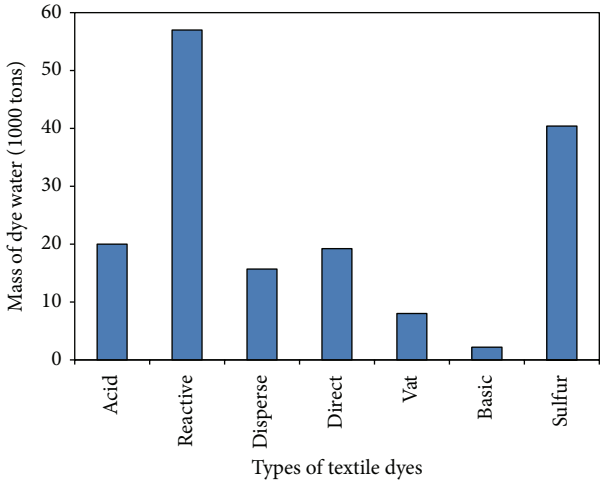

Figure 2: Mass loss of global dyes into the wastewater [21].

organic dyes [5, 13, 14]. These pollutants can cause irritation of the eyes, skin, respiratory tract, sore throat, asthma, and allergic contact dermatitis [15]. The persistent organic dye effluent will remain in the environment for a long period of time if incomplete or inadequate treatments during the water cleaning stage [5]. For instance, the half-life of hydrolyzed Reactive Blue 19 is about 46 years at pH 7 and 25°C [16].

Wastewater containing dyes is very difficult to treat, since the dyes are recalcitrant organic molecules, resistant to aerobic digestion, and are stable to light. Many traditional textile wastewater treatment studies have been applied at many textile mills. However, a synthetic dye in wastewater can not be efficiently decolorized by these traditional methods. This is because of the high cost and disposal problems for treating dye wastewater at large scale in the textile and paper industries [17]. As such, several wastewater treatments for colour removal can be divided into 3 categories, which include physical, chemical, and biological treatments [18, 19]. Nevertheless, most of the conventional dye removal techniques will have their respective limitations in textile industry.

Table 1: General fixation rates for different dye classes [22].

Dye class	Fixation rate (%)	Fibers
Acid	83 to 93	Wool, nylon
Basic	90 to 96	Acrylic
Direct	70 to 95	Cellulose
Disperse	80 to 92	Synthetic
Pigments	95 to 98	Wool
Reactive	50 to 80	Cellulose
Sulphur	60 to 70	Cellulose
Vat	80 to 95	Cellulose

1.2. Dye Removal Techniques. The most popular method for the removal of pollutants from wastewater is using liquid-phase adsorption. In fact, liquid-phase adsorption provides an attractive alternative for the treatment of contaminated waters, especially if the sorbent is cheap and does not require an additional pretreatment step before its application. The adsorption is a well-known equilibrium separation process and an effective method for water decontamination applications due to the water reuse in terms of initial cost, flexibility and simplicity of design, ease of operation, and insensitivity to toxic pollutants [23]. Adsorption and ion exchange reactions play an important role in decolonization [24, 25]. This decolorization process is strongly dependent on the physiochemical factors (e.g., interaction between dye and sorbent, active surface area of sorbent, particle size, reaction time, environment temperature, and pH) [26]. The most important aspect of the adsorption technique is that no harmful substance will be generated and released throughout the reactions. Besides, the adsorption process using activated carbons has been widely used to remove persistent organic dyes from wastewaters [27, 28]. However, commercially available activated carbon is still far from being a potential candidate in dyes removal applications due to the high production cost and regeneration problems [2]. The regeneration activated carbons involve restoring the adsorptive capacity of saturated activated carbon by desorbing adsorbed dyes on its surface. In addition, the adsorption involves a phase transfer of pollutants to other secondary wastes that subsequently require additional treatment of proper disposal procedure.

In general, several types of filtration technology (physical methods) have been widely used for wastewater and textile effluents treatment, such as membrane-filtration processes (microfiltration, ultrafiltration, nanofiltration, and reverse osmosis) and adsorption techniques [23, 29–33]. However, major disadvantages of the membrane-filtration processes are that they are only applied in small wastewater flow rate, require higher production cost of membrane and cost of periodic replacement, require high working pressure to push the wastewater flow through membrane filtration, and are unable to reduce dissolved solid content. In addition, this technique requires frequent cleaning and replacement of the modules to maintain effectiveness in removing organic dyes.

Besides, biodegradation of organic dyes is often the most economical alternative as compared to physical and chemical processes. The possible microorganisms used for

Table 2: Oxidation potential of several powerful oxidants [34].

Oxidant	$^{\bullet}OH$ (hydroxyl radical)	O_3 (ozone)	H_2O_2 (hydrogen peroxide)
Oxidation potential (V)	2.80	2.07	1.77

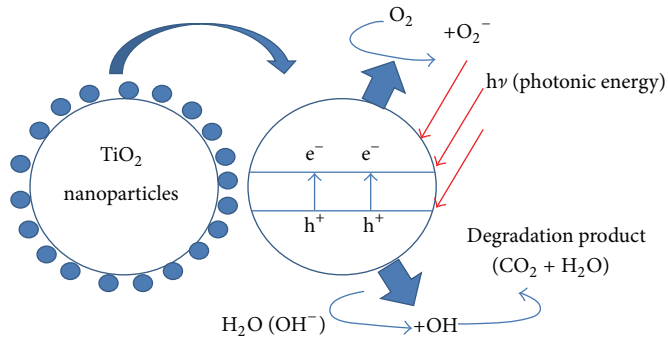

Figure 3: Overall mechanism of the photocatalytic degradation of organic dye compounds using TiO_2-based nanomaterial.

biodegradation dyes are fungi, bacteria, yeasts, and algae. They are involved in fungal decolourization, microbial degradation, and adsorption by (living or dead) microbial biomass and bioremediation systems that are commonly applied to the treatment of industrial effluents [9, 35]. However, the limitations of this technique are often restricted because of technical constraint. The high toxicity of some chemicals could decrease the numbers of active organisms used in the aerobic biological process and long hydraulic retention time [36]. In addition to that, biodegradation of organic dyes normally is incapable of obtaining satisfactory colour elimination with current conventional biodegradation processes [37]. In this manner, many other organic dyes are recalcitrant due to their complex chemical structure and synthetic organic origin [38]. In this case, azo dyes are not totally degraded or show slow degradation because of their xenobiotic nature [39].

The chemical treatment includes coagulation and flocculation for separation of dyes. The major disadvantages of these techniques are high cost of coagulating or flocculating agent and pH dependency for effective dye removal as well as disposal problem resulted from accumulation of concentrated sludge. In addition, secondary pollution problems will arise due to the excessive chemical used. Meanwhile, the main reaction involved in chemical wastewater treatment is ion exchange, which is ineffective in removing several types of persistent organic dyes. The low removal in the case of anionic dyes (disperse dyes), diffusion limitation that can affect reaction rate while the use of organic solvent for regeneration is very expensive [18] and thus, they are commercially unattractive.

1.3. Photocatalytic Degradation of Organic Dye by Titanium Dioxide. In recent years, photocatalysis system has attracted great interest from science community as the most promising way to solve the environmental problems, especially getting rid of residual dyes pollutants from wastewater stream [2, 40–42]. In this manner, photocatalysis system is considered to be ideal green environmental solution to realize our green economy future. In this case, TiO_2-based nanomaterials have been broadly studied as the most promising photocatalyst for environmental remediation such as air purification, water purification, heavy metals degradation, and hazardous waste remediation [3, 43–49]. The reasons mainly attributed to the nontoxicity, cost effective, long-term stability, widespread availability, and high stability against photocorrosion with great capacity for oxidation and high photocatalytic property. The development of the nanoarchitecture of TiO_2 assemblies with precisely controllable nanoscale features has gained significant scientific interest [42–54].

According to Ibhadon and Fitzpatrick (2013) [34], the principle behind the photocatalysis involves the photoexcitation of the metal oxides with light energy (Figure 3). In this case, only UVL ($\lambda \leq 387$ nm) greater than the band gap of the anatase TiO_2 ($E_{bg} = 3.2$ eV) generates electron-hole pairs as shown in (1). The photoinduced electrons and holes diffuse to the particle surface of the TiO_2, in which they can be exploited for various redox processes analogous to those of an electrochemical cell. The positive holes react with water, an electron donors, to produce the most crucial and powerful oxidizing free radicals, $^{\bullet}OH$ ((2) and Table 2). Thus, any organic compound adsorbed on the surface of the photocatalysts is oxidized by $^{\bullet}OH$ (3). The photoexcited negative electrons react with oxygen to become superoxide radicals, $O_2^{-\bullet}$, and perform the similar oxidative attack on organic compounds. Consider

$$TiO_2 + h\nu \longrightarrow TiO_2\left(h^+_{VB}\right) + TiO_2\left(e^-_{CB}\right) \quad (1)$$

where $TiO_2(h^+_{VB})$ is the positive hole in valence band (VB) and $TiO_2(e^-_{CB})$ is the photoexcited electron in conduction band (CB) (Figure 4). Consider

$$TiO_2\left(h^+_{VB}\right) + H_2O_{ads} \longrightarrow TiO_2 + {}^{\bullet}OH + H^+ \quad (2)$$

$$^{\bullet}OH + \text{dye} \longrightarrow CO_2 + H_2O \quad (3)$$

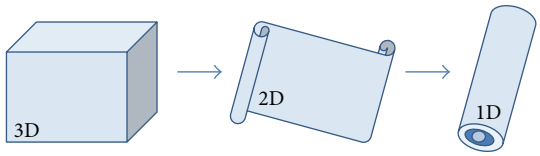

Figure 4: A schematic model for the formation of TiO_2 nanotubes [55].

$$TiO_2\,(e^-_{CB}) + O_{2ads} \longrightarrow TiO_2 + O_2{}^{\bullet-}_{ads} \quad (4)$$

$$O_2{}^{-\bullet} + \text{dye} \longrightarrow CO_2 + H_2O \quad (5)$$

In this manner, TiO_2 can act as an ideal semiconductor material for photocatalysis because it is nontoxic, relatively cheap, and highly photostable. It is interesting to note that TiO_2 exists in six different polymorphs, namely, rutile (tetragonal), anatase (tetragonal), brookite (orthorhombic), TiO_2 (B) (monoclinic), TiO_2 (II) (alpha-PbO_2), and TiO_2(H) (hollandite) [56, 57]. TiO_2 nanoparticle has been widely used as an active photoelectrode applied in variety of environment and energy system since the discovery by Fujishima and Honda [58]. In particular, the particulate TiO_2 in the form of suspension requires appropriate substrates as support to form compacted film [44, 59]. TiO_2 possessing a large bandgap energy of 3.2 and 3.02 eV for anatase and rutile, respectively. Thus, they only can be excited under UV light irradiation. When TiO_2 is excited by UV light irradiation, electrons from valence band will jump to the conduction band leaving behind positive holes (h^+) [34]. The electrons and holes diffuse to the particle surface of the TiO_2 in which they can be exploited for various redox processes analogous to those of an electrochemical cell. The holes react with water, an electron donor, to produce the most crucial and powerful oxidizing free radicals capable of degrading the organic dyes.

However, the major drawback of such nanoparticle TiO_2 is the random pathway of photoinduced electrons during photocatalytic reactions, which will eventually lead to the recombination through trapping/detrapping of electron/hole pairs as well as longer electron transporting time in the particulate TiO_2. In addition to that, the probability of recombination losses of photoinduced charge carriers will be increased significantly due to the presence of defects or trapping sites, more grain boundaries, and disordered contact areas [50, 60–63]. Meanwhile, it was found that two-dimensional TiO_2 thin film is able to eliminate the reusability of photocatalyst issues and ease the filtration procedure after photoreaction [47, 50]. In order to further maximize specific surface area of TiO_2 thin film for better photons absorption from illumination, design and development of TiO_2-based nanostructure assemblies have gained significant interest and triggered enormous effort in physics, chemistry, and material science [45–47, 50, 51, 60]. In this paper, the nanotubular structure of TiO_2 is extensively reviewed. This is because TiO_2 nanotubes are becoming more popular due their high photocatalytic activity for various types of dye degradation.

2. Preparation of TiO_2 Nanotubes

TiO_2 nanotubes can be produced by several methods such as using a template of nanoporous alumina [64], sol-gel transcription process using organogelator templates [65], seeded growth mechanisms [66], and hydrothermal techniques [67–69]. However, none of these methods offer superior control on the nanotube dimensions than the electrochemical anodization technique [52, 70, 71]. In the following sections, several techniques to prepare TiO_2 nanotubes were discussed.

2.1. Sol-Gel Transcription Synthesis. Sol-gel transcription process is a wet-chemical technique used to synthesize oxides at relatively low temperature. The process consists of hydrolysis of precursor species and subsequently polycondensation to form solid network which is known as gel. The common precursors employed in sol-gel processing are metal alkoxides and metal chlorides. This sol-gel template processing making use of porous alumina, polymer fibers or super molecular compound as a template, and their diameters was normally larger than 50 nm [72–74]. The walls of the TiO_2 nanotubes, prepared by deposition in porous alumina membrane, consisted of anatase nanoparticles and contained mesopores arising from the spaces between the anatase particles [75, 76]. Hoyer's research team firstly reported the formation of the pore diameter of 70–100 nm TiO_2 nanotubes via sol-gel transcription process in 1996.

Sol-gel transcription process in formation of high-ordered TiO_2 nanotubes was reported by Kang et al. (2009) [77]. In this report, titanium isopropoxide, $Ti(OC_3H_7)_4$, in ethanol was used as precursor. The TiO_2 nanotubes were grown on an alumina template. Then, the resultant sample was dried at room temperature for 12 hours in an ambient environment and calcined at 500°C to convert into crystalline phase. After that, the isolated TiO_2 nanotubes were obtained by removing the alumina template. However, the main drawback of sol-gel method is that it is difficult to form aligned and well-ordered nanotubular structure. Besides that, this method is time consuming because it is relatively difficult to remove the solvent and organic by-products and not practical from the economic point of view due to high chemical and energy consumption. Furthermore, raw materials used in this experimental works are expensive and caused many research groups to try to find an alternative way to produce TiO_2 nanotubes.

2.2. Hydrothermal Synthesis. Hydrothermal synthesis can be defined as a heterogeneous reaction in the presence of aqueous solvents or mineralizers under high pressure and temperature. This is an important technique to produce big, pure, and dislocation-free single crystals [78–80]. The crystal growth is performed in a steel pressure vessel known as autoclave where nutrient is supplied along with water. A temperature gradient needs to be maintained in the growth chamber so that the hotter end dissolves the nutrient whereas the cooler end causes seeds to take additional growth. The growth rate of the seeds will increase with increasing

Table 3: Comparison of the most widely used synthesis methods for preparing TiO_2 nanotubes.

Synthesis method	Characteristics
Sol-gel transcription process	(a) Ordered arrays (b) Advantages: the scale of nanotubes can be controlled by the applied template (c) Disadvantages: the nanotubular structure can be damaged or destroyed during the after removal of the templates; raw materials used are expensive
Hydrothermal synthesis	(a) Random alignment (b) Advantages: easy route to obtain nanotubes in relatively large amount (c) Disadvantages: difficulty in producing uniform size of nanotubular; long reaction duration; and random distribution of nanostructured tubes
Electrochemical anodization	(a) Oriented arrays with high aspect ratio (b) Advantages: self-organized anodic oxides in the form of nanotubular structures with almost perfect vertical, relatively simple alignment and can be adopted for large-scale industrial production (c) Disadvantages: fabrication apparatuses are costly; massive organic waste will be produced after the anodization process

concentration of solvent, crystallization temperature, and temperature gradient [76, 81, 82].

In a typical hydrothermal experiment, the TiO_2 nanoparticle powder is processed in alkaline solution such as NaOH in a Teflon-lined autoclave at a temperature up to 150°C for time range from 15 h and above [69]. TiO_2 nanoparticles will transform to nanotubes when the reactive Na^+ and OH^- species react with TiO_2 and forms Ti–O–Na and Ti–OH bonds. At this stage, the particles will be transformed to lamellar structure and finally roll up to form tubular structure to reduce the high energy [68, 83]. Figure 4 shows the schematic model for the formation of TiO_2 nanotubes. However, the main drawback of hydrothermal technique is the inability to form nanostructured tubes which are well aligned and ordered. Besides that, hydrothermal treatment required long reaction duration and addition of highly concentrated NaOH having difficulty in obtaining uniform size of TiO_2 nanotubes.

2.3. Electrochemical Anodization Synthesis. Highly ordered and vertically oriented TiO_2 nanotubes can be fabricated by potentiostatic anodization of Ti metal under suitable electrolyte and processing conditions. TiO_2 nanotubes are gained after the process which initially involves the formation of barrier layer and followed by rather well-defined nanoporous structure [51, 53, 84, 85]. The Ti metal was used as substrate for TiO_2 nanotubes to grow. The amorphous TiO_2 nanotubes can be obtained at the end of the anodization process. This amorphous phase of nanotubes needs to be crystallized via high temperature annealing process [70, 86, 87].

Electrochemical anodization is an electrolytic process that creates a protective or decorative oxide layer over a metallic surface [88]. Synthesis of TiO_2 nanotubes using electrochemical anodization method is preferred due to the simplicity in preparation and handling and being more controllable than the other methods [58]. Generally, vertically oriented nanotubes offer large specific surface area, which have tube-like structures with circular nanotubular opening that serve as a scaffold to anchor light-harvesting assemblies [50, 51]. The diameter of the opening ranges from 20 nm to 350 nm and the length of the tube can vary from 0.2 μm to 1000 μm depending on the processing parameter. The bottom part of the nanotubes which are in the form of domes is called barrier layer with typical shape of hexagonal or pentagonal [89–91].

In anodizing cell, Ti is used as an anode and it is connected to positive terminal of power source, whereas platinum is used as cathode being connected to negative terminal of power source [84, 92]. There are few other candidates for cathode, which consist of carbon, lead, nickel, or stainless steel. The cathode has to be an inert electrode and nonreactive in the electrolyte bath [90, 93]. Generally, the geometrical feature of the nanotubes is controlled by a variety of parameters such as anodization potential, electrolyte composition, and properties such as conductivity and viscosity, as well as anodization time and temperature. From theoretical perspective, an anodic oxide layer growth involved field-assisted oxidation of anodic Ti film. The high electric field across the anodic oxide layer will induce the Ti–O bond polarization. Then, Ti–O polarization will lead to the pit formation. These random pits will then etch into nanotubular structure in the presence of fluoride ions via chemical dissolution reaction. The comparison between the unique features of sol-gel transcription process, hydrothermal synthesis, and electrochemical anodization techniques is summarized in Table 3.

3. Titanium Dioxide Nanotubes for Dye Degradation

In this manner, one-dimensional TiO_2 nanotubes are considered a promising candidate because of their inner and outer wall surface area of nanotube that greatly increases the active sites available for photon absorption [43, 48, 50, 80, 94]. One-dimensional TiO_2 with well-aligned nanotube arrays provides unique electronic properties, such as high electron mobility, low quantum confinement effects, and high mechanical strength [95–97]. Furthermore, vertical charge transport in well-aligned TiO_2 nanotube structure greatly contributes to better photocatalytic efficiency due to the

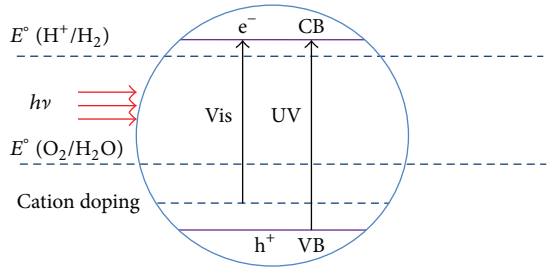

FIGURE 5: Band structure of a cationic loaded on wide band gap of semiconductor photocatalyst with visible light response [105].

grains of TiO_2 that are stretched in the tube growth direction and low recombination losses at grain boundaries as compared to randomly oriented particulate TiO_2 [47, 50, 63, 97]. Quan et al. (2005) [98] have reported that TiO_2 nanotubes give a higher kinetics constant than TiO_2 nanoparticles for photoelectrochemical degradation of pentachlorophenol. In terms of dye degradation in TiO_2 nanotubes, it is also performed far much better as compared to that of TiO_2 nanoparticles. Xu et al. (2011) [99] show that TiO_2 nanotubes efficiency was two times much better than nano-TiO_2 in degrading Acid Orange 7 dye.

3.1. Cationic Doping on Titanium Dioxide Nanotubes. TiO_2 nanotube is considered the noble photocatalyst in organic dye degradation because of its many intrinsic properties [88, 100], but it has its own limitations which are critical to photocatalytic techniques such as recombination of photogenerated electron-hole pairs, fast backward reaction, and inefficient visible light utilization. These drawbacks are very much related to the wide band gap of TiO_2 nanotubes. In fact, TiO_2 nanotube can only effectively function under the UV region ($\lambda < 400$ nm) and it only contains about 4-5% of UV rays from our solar energy. Thus, the efficient use of visible light from our solar energy is essential for effectively degrading organic dye. These drawbacks can not be overcome by only optimizing the dimensions of TiO_2 nanotube itself. Therefore, considerable efforts that have been exerted to solve these drawbacks by modifying TiO_2 nanotubes with the addition of electron donors (hole scavengers), carbonates salts, metal ion doping [101], anion doping [102], and dye sensitization [62] have been investigated. Among these, doping of TiO_2 using metal ions (Fe, Cr, V, Nb, Si, Al, Li, Na, K, Cu, Mn, Co, and Gd) and nonmetal (C, N, S, and P) has reported to show a promising result under visible light irradiation though the mechanism under which this process occurs still remains controversial. The following are some of the attempts made to modify the electronic structures of TiO_2 nanotubes to improve their effectiveness under visible light.

In 2004, Komornicki et al. [103] proposed that binary oxide photocatalysts are promising candidates with enhanced properties for photocatalytic system. Such photocatalysts may benefit from the combination of the best properties of their pure components and modification of the electronic structure of the system could be expected. Later, in 2006, Higashimoto et al. [104] suggested that binary oxide photocatalyst can promote better charge carriers separation by accumulating electrons and holes in two different semiconductor layers with suppression of charge carriers recombination. The useful features of the individual components in the mixed oxide systems can be complementary with each other, while alleviating the disadvantages at the same time. Generally, numerous studies have proved that visible light absorption of TiO_2 photocatalyst could be improved and recombination of charge carriers could be suppressed by coupling with another cationic species [43, 105–107]. The replacement of cationic ions within the crystal lattice may create impurity energy levels that facilitate better absorption in the visible light region, as depicted in Figure 5. Furthermore, different redox energy levels for their corresponding conduction and valence bands provide another attractive approach to achieve much more efficient charge carrier separation to minimize the recombination losses. When TiO_2 photocatalyst is loaded with sufficient content of cationic species in lattice, the electrons would be injected from the semiconductor with a more negative CB level to the positive one, while holes would be transferred from the semiconductor with a more positive VB level to the negative one. Thus, separation of charge carriers could be achieved; as a consequence, the lifetime of the charge carriers and the efficiency of the interfacial charge transfer to water are increasing significantly [49, 100, 108].

Based on the literature, majority of the cationic species-loaded TiO_2 photocatalysts studied were prepared using the coprecipitation, incipient wet impregnation method and sol-gel method. Details of the cationic species-loaded TiO_2 photocatalysts by several researchers and their findings are summarized in Table 4. Transitional metal and rare earth metal ions have been tried as dopants to improve the photocatalytic efficiency of TiO_2 in the visible light region. However, performances of those binary oxide photocatalysts were strongly dependent on the content of cationic dopants. The impurity levels created by cationic dopants in the binary oxide photocatalyst are usually discrete, which would appear disadvantageous for the migration of the charge carriers if the content of cationic dopants exceeds the optimum value [43, 47, 109]. Furthermore, there are a few drawbacks of cationic species doping such as different morphological and crystalline properties of the photocatalyst due to different methods of doping and the shift of the absorption edge in the metal ion doped system may have a complex origin, due to either homogeneous substitution of Ti^{4+} or segregated M_xO_y clusters.

Although cationic species doping can improve the visible spectrum response, the photogenerated electron-hole pair lifetime decreases causing the overall efficiencies to be at similar level [126]. This reason might be attributed to the doped sites that often behave as recombination centers for photogenerated charged carriers due to the substitution of Ti^{4+} with metallic ions. Also, transition metal species-loaded TiO_2 samples often suffer from thermal instability. These cause the photocatalytic activity of cationic species-loaded TiO_2 to often decrease because of the thermal instability or an increase in carrier recombination centers [127, 128]. Thus,

Table 4: Summary of the works reported on the different cationic-loaded TiO_2 photocatalyst.

Cationic	Author (year)	Findings	Reference
Cu	Li et al. (2008)	Cu ions on TiO_2 nanotubes effectively acted as electron trappers prohibiting the recombination of photoexcited electrons and holes in Cu-loaded TiO_2 nanotubes, hence improving the photocatalytic degradation of Rhodamine B under UV light irradiation within 50 min. The catalytic performance is also better than the undoped TiO_2 nanotubes.	[110]
Pd	Mohapatra et al. (2008)	Self-organized TiO_2 nanotubes with Pd nanoparticles were found to be an excellent photocatalyst that can decompose nonbiodegradable azo dyes (methyl red and methyl orange) due to the fact that lifetime of the charge carriers has been increased significantly	[111]
Ru	Khan et al. (2009)	Doping of Ru by the ion exchange method to the hydrothermally synthesized TiO_2 nanotube was found to be an effective photocatalyst active under visible light for degradation of methylene blue dye	[112]
Fe	Deng et al. (2009)	The methyl orange was completely degraded using 0.5% Fe-doped TiO_2 nanotubes under UV light irradiation within 3 h	[113]
Nd	Xu et al. (2009)	Nd-doped TiO_2 nanotubes showed a high photocatalytic activity by degrading 99.6% of methyl orange within 20 min under UV irradiation	[114]
W	Xiao et al. (2009)	5 wt% of W-loaded TiO_2 nanotubes enhanced photocatalytic activity of RhB degradation compared to the pure TiO_2 nanotubes due to the better charge separation efficiency and the extension of the wavelength range of photoexcitation	[115]
Co	Hsieh et al. (2009)	Codoped TiO_2 nanotubes showed a promising candidate in a photocatalysis degradation of basic Violet 10 Dye under visible light irradiation	[116]
W	Paramasivam et al. (2010)	The improvement of the photocatalytic degradation of Rhodamine B was observed for the addition of low WO_3 content (0.2 at.% W) to the Ti nanotubes	[59]
W	Sajjad et al., (2010)	4% WO_x-TiO_2 nanotubes composite demonstrated the best reactivity under visible light in degradation of acid Orange 7 Dye	[117]
La	Wu et al. (2010)	La-doped TiO_2 nanotubes have been tested by using methyl orange dye under UV light irradiation.	[118]
Cu	Ma et al. (2010)	Cu-doped TiO_2 nanotube has been employed to degrade methyl orange. However, only 21% of methyl orange was removed using Cu-doped TiO_2 nanotube arrays after 240 min of UV illumination	[119]
W	Das et al. (2011)	The high efficiency of photodegradation of Rhodamine B is observed for the 0.2 at.% W content	[120]
Pt	Su and Deng (2011)	The Pt-doped TiO_2 nanotubes possess high photocatalytic activity for degrading methyl orange under UV and visible light irradiation	[121]
Fe	Pang and Abdullah (2012)	The Fe-doped TiO_2 nanotubes were evaluated based on oxidation of Rhodamine B under ultrasonic irradiation	[122]
Fe	Wu et al. (2012)	The incorporation of Fe into TiO_2 nanotubes has increase the efficiency of methylene blue degradation under visible light region	[123]
Cu	Sreekantan et al. (2014)	Cu loaded on TiO_2 nanotube arrays demonstrates the highest photocatalytic activity with 84% degradation of methyl orange under visible light	[124]

Table 4: Continued.

Cationic	Author (year)	Findings	Reference
Bi	Natarajan et al. (2013)	Bismuth-doped TiO_2 nanotubes were successfully synthesized and capable of degrading Rhodamine B completely under direct sunlight	[125]

making intuitive prediction is impossible, and conducting a focused research is challenging. It is important to fine-tune the content of the cationic substitution into TiO_2 photocatalysts to develop an efficient visible light driven photocatalyst.

3.2. Anionic Doping on Titanium Dioxide Nanotubes. Anion doping is another type of elemental doping to modify the band gap of TiO_2 nanotubes. It has been proven that anion-doped TiO_2, such as nitrogen-, carbon-, phosphorus-, or sulphur-doped TiO_2, exhibits visible photoresponse and reduced the band gap of native TiO_2. According to Tang and Li (2008), this is because the atomic orbitals of nonmetal elements (e.g., N_{2p}, S_{3p}, and C_{2p}) have higher potential energy than O_{2p} [129]. This will form a new VB instead of a pure O_{2p} atomic orbital which reduce the band gap energy without affecting the conduction band level. This doping required the creation of surface oxygen vacancies where the anions will incorporate into the anatase as well as rutile by substitution in oxygen lattice sites [130].

The nonmetal ion doped catalysts are better for extending the photocatalytic activity of TiO_2 into visible region compared to metal cationic species loading methods because their impurity states are near the VB edge and their roles as recombination centers may be minimized. Table 5 shows the characteristics of anion-doped TiO_2. However, the photocatalytic activity of conventional TiO_2 doped with nonmetal elements is still limited or at early stage. It is expected that a combination of doping elements could result in a marked increase in the photocatalytic activity of TiO_2 under both UV and visible light. Most of the researchers have doped the TiO_2 with nitrogen in order to enhance the photocatalytic activity and expand the photoactivity response toward the visible light region. In addition, codoped species may be more appropriate for extending the photocatalytic activity of TiO_2 into the visible light region. For example, nonmetal codoping of TiO_2 such as F-B-codoping, C-N-codoping, and S-N-codoping was studied to further enhance the visible light activity.

The purpose of the modification of TiO_2 is believed to improve the performance of TiO_2 nanotubes by introducing new energy level into the forbidden gap, therefore causing the effect of band gap narrowing and provide site that slow down the recombination process. This improved the performance of the TiO_2 nanotubes in photocatalytic degradation of organic dyes [131]. The following sections are some of the attempts made to modify the electronic structure of TiO_2 nanotube to improve its effectiveness under visible light. The electronic structure of TiO_2 by the substitution of metal ions or anions to harvest visible light response is shown in Figure 6. The various schemes illustrating the possible band gap electronic structure and excitation processes of visible-light-responsive TiO_2 materials are shown in Figure 7.

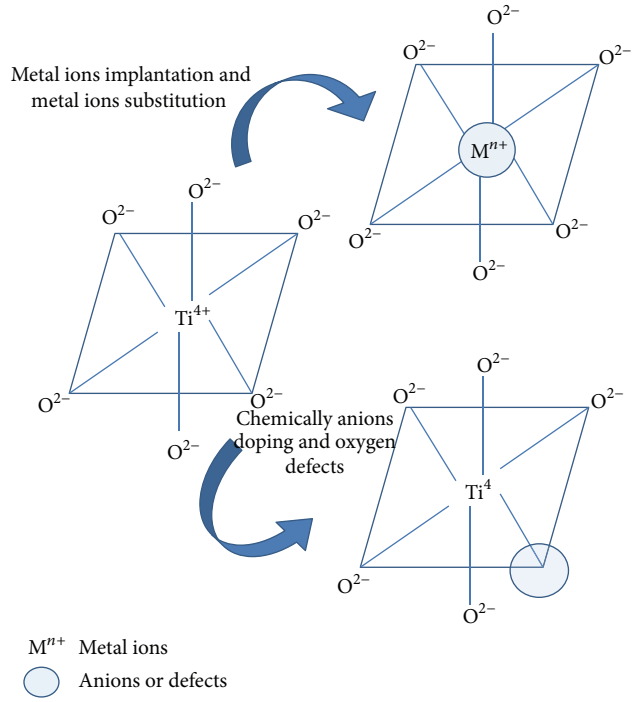

Figure 6: Electronic structure of TiO_2 by the substitution of metal ions or anions to harvest visible light response [101].

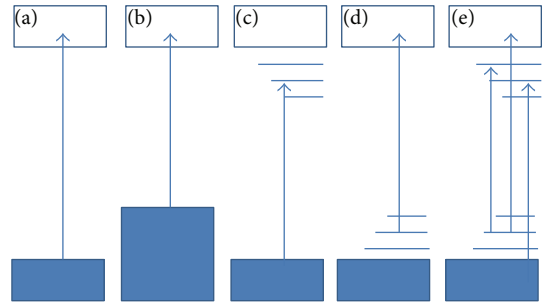

Figure 7: Various schemes illustrating the possible band gap electronic structure and excitation processes of visible-light-responsive TiO_2 materials: (a) pure TiO_2; (b) band gap narrowing model for nonmetal-doped TiO_2; (c) oxygen-deficient TiO_2; (d) localized mid-gap level model for nonmetal-doped TiO_2; (e) oxygen vacancy and nonmetal-doped mid-gap levels are considered together [41].

Table 5: Summary of the works reported on the different anionic-doped TiO_2 photocatalysts.

Anionic	Authors	Findings	Reference
N	Dong et al. (2009)	N-doped TiO_2 nanotubes exhibit enhanced photocatalytic degradation of methyl orange under visible light irradiation by narrowing the band gap energy	[132]
N and C	Liu et al. (2009)	The C–N doping shifts the absorption edge of TiO_2 nanotubes to the visible light regions and promotes the charge carrier transfer from the TiO_2 surface to the electrolyte. The C–N doped TiO_2 higher photocatalytic activity in the degradation of methyl orange than the undoped TiO_2 nanotubes	[133]
N	Lai et al. (2010)	The N-doped titanium dioxide nanotubes exhibited higher photocatalytic activity in degrading methyl orange under UV and simulated sunlight irradiation	[134]
N	Peng et al. (2010)	N-doped titanate nanotubes completely degraded methyl orange within 240 minutes under 15 W fluorescent lamps	[135]
N and Zr	Liu et al. (2010)	N/Zr-codoped TiO_2 nanotubes significantly improved the photocatalytic efficiency of TiO_2 nanotube arrays under both UV and visible light irradiation	[136]
N	Z. He and H. Y. He (2011)	The N-doped TiO_2 nanotubes with 25.7 at.% nitrogen content were capable of degrading methyl orange under visible and sunlight irradiation	[137]
N and C	Wang et al. (2011)	The photocatalytic activity of the codoped TiO_2 nanotubes with C and N shows a superior photocatalytic activity in degradation of Rhodamine B under visible light irradiation	[102]
N	Wang et al. (2012)	N-doped TiO_2 nanotubes associated with iron oxide photocatalyst successfully decomposed methyl orange in air under visible light irradiation	[138]
N	Lv et al. (2012)	N-doped TiO_2 nanotubes showed further enhancement in photodegradation activity of methylene blue in the visible region	[139]
N and F	Lee at al. (2012)	F–N-codoped TiO_2 nanotubes effectively photodegraded the aniline blue dye within 200 min under visible light irradiation	[140]
F and S	Liao et al. (2012)	The binary F- and S-doped TiO_2 nanotubes were capable of degrading methyl orange using xenon lamp to simulate natural sunlight	[141]
N	Dang et al. (2012)	N-doped TiO_2 nanotube array films effectively degraded 81% of methyl orange in 150 min under visible light irradiation	[142]
N and S	Wang et al. (2013)	Thiourea-doped TiO_2 nanotubes composed of N and S successfully decomposed 81.5% of methyl orange under visible light illumination within 90 min	[143]
N	Yuan et al. (2013)	The N-doped TiO_2 exhibited higher photocatalytic degradation of methyl orange as compared to undoped TiO_2 under UV and visible light irradiation	[144]

4. Conclusion and Future Works

Nanosize TiO_2 especially TiO_2 nanotubes seems to be the most promising photocatalyst for organic dye degradation. It is very obvious that many researchers have been trying to synthesize not only higher active surface area of nanotubes but also sunlight-driven photocatalyst for effective dye degradation. The industrial application of TiO_2 nanotubes is anticipated for the future due to its high photocatalytic activity, photostability, and nontoxicity. Nevertheless, further modifications are essential to improve its photocatalytic activity under the direct sunlight irradiation. Thus, various potential cationic and anionic elements have been employed to increase TiO_2 nanotubes efficiency for organic dye degradation under sunlight irradiation. It is believed that TiO_2 nanotubes still permit extensive and in-depth study on the electronic and lattice structure in order to truly understand the effect of different doping method and elements on TiO_2

nanotubes. This is crucial because it is obvious that same elements with different doping methods demonstrated a different photocatalytic activity on dye degradation.

Conflict of Interests

The authors declare that there is no conflict of interests regarding the publication of this paper.

Acknowledgments

This research is supported by High Impact Research Chancellory Grant UM.C/625/1/HIR/228 (J55001-73873) from the University of Malaya. In addition, authors would like to thank University of Malaya for sponsoring this work under EScience MOSTI (06-02-10 SF0130).

References

[1] J. A. Turner, "A realizable renewable energy future," *Science*, vol. 285, no. 5428, pp. 687–689, 1999.

[2] D. Mohan and C. U. Pittman Jr., "Arsenic removal from water/wastewater using adsorbents—a critical review," *Journal of Hazardous Materials*, vol. 142, no. 1-2, pp. 1–53, 2007.

[3] H.-J. Oh, J.-H. Lee, Y.-J. Kim, S.-J. Suh, J.-H. Lee, and C.-S. Chi, "Synthesis of effective titania nanotubes for wastewater purification," *Applied Catalysis B*, vol. 84, no. 1-2, pp. 142–147, 2008.

[4] C. Zaharia and D. Suteu, "Textile organic dyes—characteristics, polluting effects and separation/elimination procedures from industrial effluents—a critical overview," in *Organic Pollutants Ten Years after the Stockholm Convention—Environmental and Analytical Update*, T. Puzyn, Ed., InTech, 2012.

[5] B. Manu and S. Chaudhari, "Anaerobic decolorisation of simulated textile wastewater containing azo dyes," *Bioresource Technology*, vol. 82, no. 3, pp. 225–231, 2002.

[6] S. H. S. Chan, T. Y. Wu, J. C. Juan, and C. Y. Teh, "Recent developments of metal oxide semiconductors as photocatalysts in advanced oxidation processes (AOPs) for treatment of dye waste-water," *Journal of Chemical Technology and Biotechnology*, vol. 86, no. 9, pp. 1130–1158, 2011.

[7] R. Vinu and G. Madras, "Kinetics of sonophotocatalytic degradation of anionic dyes with nano-TiO_2," *Environmental Science and Technology*, vol. 43, no. 2, pp. 473–479, 2009.

[8] C. I. Pearce, J. R. Lloyd, and J. T. Guthrie, "The removal of colour from textile wastewater using whole bacterial cells: a review," *Dyes and Pigments*, vol. 58, no. 3, pp. 179–196, 2003.

[9] G. McMullan, C. Meehan, A. Conneely et al., "Microbial decolourisation and degradation of textile dyes," *Applied Microbiology and Biotechnology*, vol. 56, no. 1-2, pp. 81–87, 2001.

[10] A. K. Sinha, M. Pradhan, S. Sarkar, and T. Pal, "Large-scale solid-state synthesis of Sn–SnO_2 nanoparticles from layered SnO by sunlight: a material for dye degradation in water by photocatalytic reaction," *Environmental Science & Technology*, vol. 47, no. 5, pp. 2339–2345, 2013.

[11] W. J. Epolito, Y. H. Lee, L. A. Bottomley, and S. G. Pavlostathis, "Characterization of the textile anthraquinone dye Reactive Blue 4," *Dyes and Pigments*, vol. 67, no. 1, pp. 35–46, 2005.

[12] R. Koswojo, R. P. Utomo, Y.-H. Ju et al., "Acid green 25 removal from wastewater by organo-bentonite from Pacitan," *Applied Clay Science*, vol. 48, no. 1-2, pp. 81–86, 2010.

[13] D. Suteu, C. Zaharia, and T. Malutan, "Removal of orange 16 reactive dye from aqueous solutions by waste sunflower seed shells," *Journal of the Serbian Chemical Society*, vol. 76, no. 4, pp. 607–624, 2011.

[14] C. Zaharia, D. Suteu, A. Muresan, R. Muresan, and A. Popescu, "Textile wastewater treatment by homogeneous oxidation with hydrogen peroxide," *Environmental Engineering and Management Journal*, vol. 8, no. 6, pp. 1359–1369, 2009.

[15] S. Merouani, O. Hamdaoui, F. Saoudi, M. Chiha, and C. Pétrier, "Influence of bicarbonate and carbonate ions on sonochemical degradation of Rhodamine B in aqueous phase," *Journal of Hazardous Materials*, vol. 175, no. 1–3, pp. 593–599, 2010.

[16] O. J. Hao, H. Kim, and P.-C. Chiang, "Decolorization of wastewater," *Critical Reviews in Environmental Science and Technology*, vol. 30, no. 4, pp. 449–505, 2000.

[17] S. M. Ghoreishi and R. Haghighi, "Chemical catalytic reaction and biological oxidation for treatment of non-biodegradable textile effluent," *Chemical Engineering Journal*, vol. 95, no. 1, pp. 163–169, 2003.

[18] N. J. Robinson, S. K. Whitehall, and J. S. Cavet, "Microbial metallothioneins," *Advances in Microbial Physiology*, vol. 44, pp. 183–213, 2001.

[19] D. Acemoglu, S. Johnson, and J. A. Robinson, "The colonial origins of comparative development: an empirical investigation," *American Economic Review*, vol. 91, no. 5, pp. 1369–1401, 2001.

[20] The World Bank, "Water pollution, textile industry (% of total BOD emissions)," 2013, http://data.worldbank.org/indicator/EE.BOD.TXTL.ZS/countries/1W?display=map.

[21] S. Vanhulle, M. Trovaslet, E. Enaud et al., "Decolorization, cytotoxicity, and genotoxicity reduction during a combined ozonation/fungal treatment of dye-contaminated wastewater," *Environmental Science and Technology*, vol. 42, no. 2, pp. 584–589, 2008.

[22] E. Matyjas and E. Rybicki, "Novel reactive red eyes," *Autex Research Journal*, vol. 3, no. 2, pp. 90–95, 2003.

[23] A. Dąbrowski, "Adsorption—from theory to practice," *Advances in Colloid and Interface Science*, vol. 93, no. 1–3, pp. 135–224, 2001.

[24] Y. M. Slokar and A. M. le Marechal, "Methods of decoloration of textile wastewaters," *Dyes and Pigments*, vol. 37, no. 4, pp. 335–356, 1998.

[25] A. Kandelbauer, A. Erlacher, A. Cavaco-Paulo, and G. M. Guebitz, "Laccase-catalyzed decolorization of the synthetic azo-dye Diamond Black PV 200 and of some structurally related derivatives," *Biocatalysis and Biotransformation*, vol. 22, no. 5-6, pp. 331–339, 2004.

[26] V. Kumar, L. Wati, P. Nigam et al., "Decolorization and biodegradation of anaerobically digested sugarcane molasses spent wash effluent from biomethanation plants by white-rot fungi," *Process Biochemistry*, vol. 33, no. 1, pp. 83–88, 1998.

[27] B. H. Hameed, A. T. M. Din, and A. L. Ahmad, "Adsorption of methylene blue onto bamboo-based activated carbon: kinetics and equilibrium studies," *Journal of Hazardous Materials*, vol. 141, no. 3, pp. 819–825, 2007.

[28] K. Selvi, S. Pattabhi, and K. Kadirvelu, "Removal of Cr(VI) from aqueous solution by adsorption onto activated carbon," *Bioresource Technology*, vol. 80, no. 1, pp. 87–89, 2001.

[29] V. Kumar, N. Talreja, D. Deva, N. Sankararamakrishnan, A. Sharma, and N. Verma, "Development of bi-metal doped micro- and nano multi-functional polymeric adsorbents for the removal of fluoride and arsenic(V) from wastewater," *Desalination*, vol. 282, pp. 27–38, 2011.

[30] A. Aouni, C. Fersi, B. Cuartas-Uribe, A. Bes-Pia, M. I. Alcaina-Miranda, and M. Dhahbi, "Reactive dyes rejection and textile effluent treatment study using ultrafiltration and nanofiltration processes," *Desalination*, vol. 297, pp. 87–96, 2012.

[31] E. Ellouze, N. Tahri, and R. B. Amar, "Enhancement of textile wastewater treatment process using Nanofiltration," *Desalination*, vol. 286, pp. 16–23, 2012.

[32] H. K. Shon, S. Phuntsho, D. S. Chaudhary, S. Vigneswaran, and J. Cho, "Nanofiltration for water and wastewater treatment—a mini review," *Drinking Water Engineering and Science*, vol. 6, pp. 47–53, 2013.

[33] R. A. Al-Juboori and T. Yusaf, "Biofouling in RO system: mechanisms, monitoring and controlling," *Desalination*, vol. 302, pp. 1–23, 2012.

[34] A. O. Ibhadon and P. Fitzpatrick, "Heterogeneous photocatalysis: recent advances and applications," *Catalysts*, vol. 3, pp. 189–218, 2013.

[35] Y. Fu and T. Viraraghavan, "Fungal decolorization of dye wastewaters: a review," *Bioresource Technology*, vol. 79, no. 3, pp. 251–262, 2001.

[36] K. G. Bhattacharyya and A. Sarma, "Adsorption characteristics of the dye, Brilliant Green, on Neem leaf powder," *Dyes and Pigments*, vol. 57, no. 3, pp. 211–222, 2003.

[37] T. Robinson, G. McMullan, R. Marchant, and P. Nigam, "Remediation of dyes in textile effluent: a critical review on current treatment technologies with a proposed alternative," *Bioresource Technology*, vol. 77, no. 3, pp. 247–255, 2001.

[38] M. N. V. R. Kumar, T. R. Sridhari, K. D. Bhavani, and P. K. Dutta, "Trends in color removal from textile mill effluents," *Colourage*, vol. 45, no. 8, pp. 25–34, 1998.

[39] W. S. Pereira and R. S. Freire, "Azo dye degradation by recycled waste zero-valent iron powder," *Journal of the Brazilian Chemical Society*, vol. 17, no. 5, pp. 832–838, 2006.

[40] D. A. Tryk, A. Fujishima, and K. Honda, "Recent topics in photoelectrochemistry: achievements and future prospects," *Electrochimica Acta*, vol. 45, no. 15-16, pp. 2363–2376, 2000.

[41] A. Fujishima, X. Zhang, and D. A. Tryk, "TiO_2 photocatalysis and related surface phenomena," *Surface Science Reports*, vol. 63, no. 12, pp. 515–582, 2008.

[42] A. Kubacka, M. Fernández-García, and G. Colón, "Advanced nanoarchitectures for solar photocatalytic applications," *Chemical Reviews*, vol. 112, no. 3, pp. 1555–1614, 2012.

[43] Y.-C. Nah, I. Paramasivam, and P. Schmuki, "Doped TiO_2 and TiO_2 nanotubes: synthesis and applications," *ChemPhysChem*, vol. 11, no. 13, pp. 2698–2713, 2010.

[44] C. W. Lai and S. Sreekantan, "Preparation of hybrid WO_3–TiO_2 nanotube photoelectrodes using anodization and wet impregnation: improved water-splitting hydrogen generation performance," *International Journal of Hydrogen Energy*, vol. 38, pp. 2156–2166, 2013.

[45] X. Chen and S. S. Mao, "Titanium dioxide nanomaterials: synthesis, properties, modifications and applications," *Chemical Reviews*, vol. 107, no. 7, pp. 2891–2959, 2007.

[46] Z. Su and W. Zhou, "Formation, morphology control and applications of anodic TiO_2 nanotube arrays," *Journal of Materials Chemistry*, vol. 21, no. 25, pp. 8955–8970, 2011.

[47] A. Ghicov and P. Schmuki, "Self-ordering electrochemistry: a review on growth and functionality of TiO_2 nanotubes and other self-aligned MO_x structures," *Chemical Communications*, no. 20, pp. 2791–2808, 2009.

[48] M. Kitano, M. Matsuoka, M. Ueshima, and M. Anpo, "Recent developments in titanium oxide-based photocatalysts," *Applied Catalysis A*, vol. 325, no. 1, pp. 1–14, 2007.

[49] C. W. Lai and S. Sreekantan, "Optimized sputtering power to incorporate WO_3 into C-TiO_2 nanotubes for highly visible photoresponse performance," *NANO*, vol. 7, no. 6, Article ID 1250051, 2012.

[50] L. Sun, S. Zhang, X. Sun, and X. He, "Effect of the geometry of the anodized titania nanotube array on the performance of dye-sensitized solar cells," *Journal of Nanoscience and Nanotechnology*, vol. 10, no. 7, pp. 4551–4561, 2010.

[51] C. A. Grimes, "Synthesis and application of highly ordered arrays of TiO_2 nanotubes," *Journal of Materials Chemistry*, vol. 17, no. 15, pp. 1451–1457, 2007.

[52] S. Sreekantan, L. C. Wei, and Z. Lockman, "Extremely fast growth rate of TiO_2 nanotube arrays in electrochemical bath containing H_2O_2," *Journal of the Electrochemical Society*, vol. 158, no. 12, pp. C397–C402, 2011.

[53] C. W. Lai and S. Sreekantan, "Effect of applied potential on the formation of self-organized TiO_2 nanotube arrays and its photoelectrochemical response," *Journal of Nanomaterials*, vol. 2011, Article ID 142463, 7 pages, 2011.

[54] C. W. Lai and S. Sreekantan, "Photoelectrochemical performance of smooth TiO_2 nanotube arrays: effect of anodization temperature and cleaning methods," *International Journal of Photoenergy*, vol. 2012, Article ID 356943, 11 pages, 2012.

[55] Y. Q. Wang, G. Q. Hu, X. F. Duan, H. L. Sun, and Q. K. Xue, "Microstructure and formation mechanism of titanium dioxide nanotubes," *Chemical Physics Letters*, vol. 365, no. 5-6, pp. 427–431, 2002.

[56] M. Latroche, L. Brohan, R. Marchand, and M. Tournoux, "New hollandite oxides: TiO_2(H) and K0.06TiO_2," *Journal of Solid State Chemistry*, vol. 81, no. 1, pp. 78–82, 1989.

[57] D. W. Meng, X. L. Wu, F. Sun et al., "High-pressure polymorphic transformation of rutile to α-PbO_2-type TiO_2 at $\{0\ 1\ 1\}_R$ twin boundaries," *Micron*, vol. 39, no. 3, pp. 280–286, 2008.

[58] A. Fujishima and K. Honda, "Electrochemical photolysis of water at a semiconductor electrode," *Nature*, vol. 238, no. 5358, pp. 37–38, 1972.

[59] I. Paramasivam, Y.-C. Nah, C. Das, N. K. Shrestha, and P. Schmuki, "WO_3/TiO_2 nanotubes with strongly enhanced photocatalytic activity," *Chemistry—A European Journal*, vol. 16, no. 30, pp. 8993–8997, 2010.

[60] J. Yan and F. Zhou, "TiO_2 nanotubes: structure optimization for solar cells," *Journal of Materials Chemistry*, vol. 21, no. 26, pp. 9406–9418, 2011.

[61] A. Kudo and Y. Miseki, "Heterogeneous photocatalyst materials for water splitting," *Chemical Society Reviews*, vol. 38, no. 1, pp. 253–278, 2009.

[62] B.-X. Lei, J.-Y. Liao, R. Zhang, J. Wang, C.-Y. Su, and D.-B. Kuang, "Ordered crystalline TiO_2 nanotube arrays on transparent FTO glass for efficient dye-sensitized solar cells," *Journal of Physical Chemistry C*, vol. 114, no. 35, pp. 15228–15233, 2010.

[63] A. E. R. Mohamed and S. Rohani, "Modified TiO_2 nanotube arrays (TNTAs): progressive strategies towards visible light responsive photoanode, a review," *Energy and Environmental Science*, vol. 4, no. 4, pp. 1065–1086, 2011.

[64] A. Michailowski, D. Almawlawi, G. Cheng, and M. Moskovits, "Highly regular anatase nanotubule arrays fabricated in porous anodic templates," *Chemical Physics Letters*, vol. 349, no. 1-2, pp. 1–5, 2001.

[65] S. Kobayashi, N. Hamasaki, M. Suzuki, M. Kimura, H. Shirai, and K. Hanabusa, "Preparation of helical transition-metal oxide tubes using organogelators as structure-directing agents," *Journal of the American Chemical Society*, vol. 124, no. 23, pp. 6550–6551, 2002.

[66] Z. R. Tian, J. A. Voigt, J. Liu et al., "Complex and oriented ZnO nanostructures," *Nature Materials*, vol. 2, no. 12, pp. 821–826, 2003.

[67] D. V. Bavykin, V. N. Parmon, A. A. Lapkin, and F. C. Walsh, "The effect of hydrothermal conditions on the mesoporous structure of TiO_2 nanotubes," *Journal of Materials Chemistry*, vol. 14, no. 22, pp. 3370–3377, 2004.

[68] H.-K. Seo, G.-S. Kim, S. G. Ansari et al., "A study on the structure/phase transformation of titanate nanotubes synthesized at various hydrothermal temperatures," *Solar Energy Materials and Solar Cells*, vol. 92, no. 11, pp. 1533–1539, 2008.

[69] S. Sreekantan and L. C. Wei, "Study on the formation and photocatalytic activity of titanate nanotubes synthesized via hydrothermal method," *Journal of Alloys and Compounds*, vol. 490, no. 1-2, pp. 436–442, 2010.

[70] G. K. Mor, O. K. Varghese, M. Paulose, and C. A. Grimes, "Transparent highly ordered TiO_2 nanotube arrays via anodization of titanium thin films," *Advanced Functional Materials*, vol. 15, no. 8, pp. 1291–1296, 2005.

[71] C. W. Lai, S. Sreekantan, and Z. Lockman, "Photoelectrochemical behaviour of uniform growth TiO_2 nanotubes via bubble blowing synthesised in ethylene glycol with hydrogen peroxide," *Journal of Nanoscience and Nanotechnology*, vol. 12, pp. 4057–4066, 2012.

[72] J. H. Jung, H. Kobayashi, K. J. C. van Bommel, S. Shinkai, and T. Shimizu, "Creation of novel helical ribbon and double-layered nanotube TiO_2 structures using an organogel template," *Chemistry of Materials*, vol. 14, no. 4, pp. 1445–1447, 2002.

[73] J. H. Jung, T. Shimizu, and S. Shinkai, "Self-assembling structures of steroidal derivatives in organic solvents and their sol-gel transcription into double-walled transition-metal oxide nanotubes," *Journal of Materials Chemistry*, vol. 15, no. 35-36, pp. 3979–3986, 2005.

[74] Q. Ji, R. Iwaura, and T. Shimizu, "Regulation of silica nanotube diameters: sol-gel transcription using solvent-sensitive morphological change of peptidic lipid nanotubes as templates," *Chemistry of Materials*, vol. 19, no. 6, pp. 1329–1334, 2007.

[75] H. Imai, Y. Takei, K. Shimizu, M. Matsuda, and H. Hirashima, "Direct preparation of anatase TiO_2 nanotubes in porous alumina membranes," *Journal of Materials Chemistry*, vol. 9, no. 12, pp. 2971–2972, 1999.

[76] Z.-Y. Yuan and B.-L. Su, "Titanium oxide nanotubes, nanofibers and nanowires," *Colloids and Surfaces A*, vol. 241, no. 1–3, pp. 173–183, 2004.

[77] T.-S. Kang, A. P. Smith, B. E. Taylor, and M. F. Durstock, "Fabrication of highly-ordered TiO_2 nanotube arrays and their use in dye-sensitized solar cells," *Nano Letters*, vol. 9, no. 2, pp. 601–606, 2009.

[78] M. Yoshimura and K. Byrappa, "Hydrothermal processing of materials: past, present and future," *Journal of Materials Science*, vol. 43, no. 7, pp. 2085–2103, 2008.

[79] M. Yada, Y. Inoue, M. Uota et al., "Formation of sodium titanate nanotube films by hydrothermal transcription," *Chemistry of Materials*, vol. 20, no. 2, pp. 364–366, 2008.

[80] A. Nakahira, T. Kubo, and C. Numako, "Formation mechanism of TiO_2-derived titanate nanotubes prepared by the hydrothermal process," *Inorganic Chemistry*, vol. 49, no. 13, pp. 5845–5852, 2010.

[81] F. Huang, H. Zhang, and J. F. Banfield, "The role of oriented attachment crystal growth in hydrothermal coarsening of nanocrystalline ZnS," *Journal of Physical Chemistry B*, vol. 107, no. 38, pp. 10470–10475, 2003.

[82] J.-N. Nian and H. Teng, "Hydrothermal synthesis of single-crystalline anatase TiO_2 nanorods with nanotubes as the precursor," *Journal of Physical Chemistry B*, vol. 110, no. 9, pp. 4193–4198, 2006.

[83] N. Viriya-Empikul, N. Sano, T. Charinpanitkul, T. Kikuchi, and W. Tanthapanichakoon, "A step towards length control of titanate nanotubes using hydrothermal reaction with sonication pretreatment," *Nanotechnology*, vol. 19, no. 3, Article ID 035601, 2008.

[84] J. M. Macak and P. Schmuki, "Anodic growth of self-organized anodic TiO_2 nanotubes in viscous electrolytes," *Electrochimica Acta*, vol. 52, no. 3, pp. 1258–1264, 2006.

[85] J. M. Macak, H. Tsuchiya, A. Ghicov et al., "TiO_2 nanotubes: self-organized electrochemical formation, properties and applications," *Current Opinion in Solid State and Materials Science*, vol. 11, no. 1-2, pp. 3–18, 2007.

[86] V. K. Mahajan, M. Misra, K. S. Raja, and S. K. Mohapatra, "Self-organized TiO_2 nanotubular arrays for photoelectrochemical hydrogen generation: effect of crystallization and defect structures," *Journal of Physics D*, vol. 41, no. 12, Article ID 125307, 2008.

[87] C. W. Lai and S. Sreekantan, "Higher water splitting hydrogen generation rate for single crystalline anatase phase of TiO_2 nanotube arrays," *The European Physical Journal—Applied Physics*, vol. 59, no. 2, Article ID 20403, 2012.

[88] C. W. Lai and S. Sreekantan, "Photoelectrochemical properties of TiO_2 nanotube arrays: effect of electrolyte pH and annealing temperature," *Journal of Experimental Nanoscience*, vol. 9, no. 3, pp. 230–239, 2014.

[89] M. Paulose, H. E. Prakasam, O. K. Varghese et al., "TiO_2 nanotube arrays of 1000 μm length by anodization of titanium foil: phenol red diffusion," *Journal of Physical Chemistry C*, vol. 111, no. 41, pp. 14992–14997, 2007.

[90] G. K. Mor, O. K. Varghese, M. Paulose, K. Shankar, and C. A. Grimes, "A review on highly ordered, vertically oriented TiO_2 nanotube arrays: fabrication, material properties, and solar energy applications," *Solar Energy Materials and Solar Cells*, vol. 90, no. 14, pp. 2011–2075, 2006.

[91] S. K. Mohapatra, M. Misra, V. K. Mahajan, and K. S. Raja, "Design of a highly efficient photoelectrolytic cell for hydrogen generation by water splitting: application of $TiO_{2-x}C_x$ nanotubes as a photoanode and Pt/TiO_2 nanotubes as a cathode," *Journal of Physical Chemistry C*, vol. 111, no. 24, pp. 8677–8685, 2007.

[92] J. M. Macak, H. Hildebrand, U. Marten-Jahns, and P. Schmuki, "Mechanistic aspects and growth of large diameter self-organized TiO_2 nanotubes," *Journal of Electroanalytical Chemistry*, vol. 621, no. 2, pp. 254–266, 2008.

[93] N. K. Allam and C. A. Grimes, "Effect of cathode material on the morphology and photoelectrochemical properties of vertically oriented TiO_2 nanotube arrays," *Solar Energy Materials and Solar Cells*, vol. 92, no. 11, pp. 1468–1475, 2008.

[94] S. So, K. Lee, and P. Schmuki, "Ultrafast growth of highly ordered anodic TiO_2 nanotubes in lactic acid electrolytes,"

Journal of the American Chemical Society, vol. 134, pp. 11316–11318, 2012.

[95] S. K. Mohapatra, M. Misra, V. K. Mahajan, and K. S. Raja, "A novel method for the synthesis of titania nanotubes using sonoelectrochemical method and its application for photoelectrochemical splitting of water," *Journal of Catalysis*, vol. 246, no. 2, pp. 362–369, 2007.

[96] D. R. Baker and P. V. Kamat, "Disassembly, reassembly, and photoelectrochemistry of etched TiO_2 nanotubes," *Journal of Physical Chemistry C*, vol. 113, no. 41, pp. 17967–17972, 2009.

[97] P. Roy, S. Berger, and P. Schmuki, "TiO_2 nanotubes: synthesis and applications," *Angewandte Chemie—International Edition*, vol. 50, no. 13, pp. 2904–2939, 2011.

[98] X. Quan, S. Yang, X. Ruan, and H. Zhao, "Preparation of titania nanotubes and their environmental applications as electrode," *Environmental Science and Technology*, vol. 39, no. 10, pp. 3770–3775, 2005.

[99] S. Xu, J. Ng, X. Zhang, H. Bai, and D. D. Sun, "Adsorption and photocatalytic degradation of acid orange 7 over hydrothermally synthesized mesoporous TiO_2 nanotube," *Colloids and Surfaces A*, vol. 379, no. 1–3, pp. 169–175, 2011.

[100] D. Y. C. Leung, X. Fu, C. Wang et al., "Hydrogen production over titania-based photocatalysts," *ChemSusChem*, vol. 3, no. 6, pp. 681–694, 2010.

[101] H. Shon, S. Phuntsho, Y. Okour et al., "Visible light responsive titanium dioxide (TiO_2)," *Journal of the Korean Industrial and Engineering Chemistry*, vol. 19, no. 1, pp. 1–16, 2008.

[102] J. Wang, B. Huang, Z. Wang, X. Qin, and X. Zhang, "Synthesis and characterization of C, N-codoped TiO_2 nanotubes/nanorods with visible-light activity," *Rare Metals*, vol. 30, no. 1, pp. 161–165, 2011.

[103] S. Komornicki, M. Radecka, and P. Sobaś, "Structural, electrical and optical properties of TiO_2-WO_3 polycrystalline ceramics," *Materials Research Bulletin*, vol. 39, no. 13, pp. 2007–2017, 2004.

[104] S. Higashimoto, M. Sakiyama, and M. Azuma, "Photoelectrochemical properties of hybrid WO_3/TiO_2 electrode. Effect of structures of WO_3 on charge separation behavior," *Thin Solid Films*, vol. 503, no. 1-2, pp. 201–206, 2006.

[105] R. M. Navarro Yerga, M. C. Álvarez Galván, F. del Valle, J. A. Villoria de la Mano, and J. L. G. Fierro, "Water splitting on semiconductor catalysts under visiblelight irradiation," *ChemSusChem*, vol. 2, no. 6, pp. 471–485, 2009.

[106] J. H. Bang and P. V. Kamat, "Solar cells by design: photoelectrochemistry of TiO_2 nanorod arrays decorated with CdSe," *Advanced Functional Materials*, vol. 20, no. 12, pp. 1970–1976, 2010.

[107] J. Zhang, Y. Wu, M. Xing, S. A. K. Leghari, and S. Sajjad, "Development of modified N doped TiO_2 photocatalyst with metals, nonmetals and metal oxides," *Energy and Environmental Science*, vol. 3, no. 6, pp. 715–726, 2010.

[108] C. W. Lai, S. Sreekantan, and S. E. Pei, "Effect of radio frequency sputtering power on W-TiO_2 nanotubes to improve photoelectrochemical performance," *Journal of Material Research*, vol. 27, no. 13, pp. 1695–1704, 2012.

[109] K. Maeda, A. Xiong, T. Yoshinaga et al., "Photocatalytic overall water splitting promoted by two different cocatalysts for hydrogen and oxygen evolution under visible light," *Angewandte Chemie—International Edition*, vol. 49, no. 24, pp. 4096–4099, 2010.

[110] H. Li, X. Duan, G. Liu, and L. Li, "Synthesis and characterization of copper ions surface-doped titanium dioxide nanotubes," *Materials Research Bulletin*, vol. 43, no. 8-9, pp. 1971–1981, 2008.

[111] S. K. Mohapatra, N. Kondamudi, S. Banerjee, and M. Misra, "Functionalization of self-organized TiO_2 nanotubes with Pd nanoparticles for photocatalytic decomposition of dyes under solar light illumination," *Langmuir*, vol. 24, no. 19, pp. 11276–11281, 2008.

[112] M. A. Khan, D. H. Han, and O.-B. Yang, "Enhanced photoresponse towards visible light in Ru doped titania nanotube," *Applied Surface Science*, vol. 255, no. 6, pp. 3687–3690, 2009.

[113] L. Deng, S. Wang, D. Liu et al., "Synthesis, characterization of Fe-doped TiO_2 nanotubes with high photocatalytic activity," *Catalysis Letters*, vol. 129, no. 3-4, pp. 513–518, 2009.

[114] Y.-H. Xu, C. Chen, X.-L. Yang, X. Li, and B.-F. Wang, "Preparation, characterization and photocatalytic activity of the neodymium-doped TiO_2 nanotubes," *Applied Surface Science*, vol. 255, no. 20, pp. 8624–8628, 2009.

[115] M. Xiao, L. Wang, X. Huang, Y. Wu, and Z. Dang, "Synthesis and characterization of WO_3/titanate nanotubes nanocomposite with enhanced photocatalytic properties," *Journal of Alloys and Compounds*, vol. 470, no. 1-2, pp. 486–491, 2009.

[116] C.-T. Hsieh, W.-S. Fan, W.-Y. Chen, and J.-Y. Lin, "Adsorption and visible-light-derived photocatalytic kinetics of organic dye on Co-doped titania nanotubes prepared by hydrothermal synthesis," *Separation and Purification Technology*, vol. 67, no. 3, pp. 312–318, 2009.

[117] A. K. L. Sajjad, S. Shamaila, B. Tian, F. Chen, and J. Zhang, "Comparative studies of operational parameters of degradation of azo dyes in visible light by highly efficient WO_x/TiO_2 photocatalyst," *Journal of Hazardous Materials*, vol. 177, no. 1–3, pp. 781–791, 2010.

[118] H.-H. Wu, L.-X. Deng, S.-R. Wang et al., "The preparation and characterization of la doped TiO_2 nanotubes and their photocatalytic activity," *Journal of Dispersion Science and Technology*, vol. 31, no. 10, pp. 1311–1316, 2010.

[119] Q. Ma, S. J. Liu, L. Q. Weng, Y. Liu, and B. Liu, "Growth, structure and photocatalytic properties of hierarchical Cu-Ti-O nanotube arrays by anodization," *Journal of Alloys and Compounds*, vol. 501, no. 2, pp. 333–338, 2010.

[120] C. Das, I. Paramasivam, N. Liu, and P. Schmuki, "Photoelectrochemical and photocatalytic activity of tungsten doped TiO_2 nanotube layers in the near visible region," *Electrochimica Acta*, vol. 56, no. 28, pp. 10557–10561, 2011.

[121] Y. Su and Y. Deng, "Effect of structure on the photocatalytic activity of Pt-doped TiO_2 nanotubes," *Applied Surface Science*, vol. 257, no. 23, pp. 9791–9795, 2011.

[122] Y. L. Pang and A. Z. Abdullah, "Effect of low Fe^{3+} doping on characteristics, sonocatalytic activity and reusability of TiO_2 nanotubes catalysts for removal of Rhodamine B from water," *Journal of Hazardous Materials*, vol. 235-236, pp. 326–335, 2012.

[123] Q. Wu, J. Ouyang, K. Xie, L. Sun, M. Wang, and C. Lin, "Ultrasound-assisted synthesis and visible-light-driven photocatalytic activity of Fe-incorporated TiO_2 nanotube array photocatalysts," *Journal of Hazardous Materials*, vol. 199-200, pp. 410–417, 2012.

[124] S. Sreekantan, C. W. Lai, and S. M. Zaki, "The influence of lead concentration on photocatalytic reduction of Pb(II) ions assisted by Cu-TiO_2 nanotubes," *International Journal of Photoenergy*, vol. 2014, Article ID 839106, 7 pages, 2014.

[125] T. S. Natarajan, K. Natarajan, H. C. Bajaj, and R. J. Tayade, "Enhanced photocatalytic activity of bismuth-doped TiO_2 nanotubes under direct sunlight irradiation for degradation of Rhodamine B dye," *Journal of Nanoparticle Research*, vol. 15, no. 5, article 1669, 2013.

[126] K. Shankar, G. K. Mor, A. Fitzgerald, and C. A. Grimes, "Cation effect on the electrochemical formation of very high aspect ratio TiO_2 nanotube arrays in formamide-water mixtures," *Journal of Physical Chemistry C*, vol. 111, no. 1, pp. 21–26, 2007.

[127] T. Hathway, E. M. Rockafellow, Y.-C. Oh, and W. S. Jenks, "Photocatalytic degradation using tungsten-modified TiO_2 and visible light: kinetic and mechanistic effects using multiple catalyst doping strategies," *Journal of Photochemistry and Photobiology A*, vol. 207, no. 2-3, pp. 197–203, 2009.

[128] C. W. Lai and S. Sreekantan, "Single step formation of C-TiO_2 nanotubes: influence of applied voltage and their photocatalytic activity under solar illumination," *International Journal of Photoenergy*, vol. 2013, Article ID 276504, 8 pages, 2013.

[129] X. Tang and D. Li, "Sulfur-doped highly ordered TiO_2 nanotubular arrays with visible light response," *Journal of Physical Chemistry C*, vol. 112, no. 14, pp. 5405–5409, 2008.

[130] Y. Zhang, W. Fu, H. Yang et al., "Synthesis and characterization of P-doped TiO_2 nanotubes," *Thin Solid Films*, vol. 518, no. 1, pp. 99–103, 2009.

[131] J. J. Fan, L. Zhao, J. Yu, and G. Liu, "The effect of calcination temperature on the microstructure and photocatalytic activity of TiO_2-based composite nanotubes prepared by an in situ template dissolution method," *Nanoscale*, vol. 4, pp. 6597–6603, 2012.

[132] L. Dong, G. X. Cao, Y. Ma, X. L. Jia, G. T. Ye, and S. K. Guan, "Enhanced photocatalytic degradation properties of nitrogen-doped titania nanotube arrays," *Transactions of Nonferrous Metals Society of China*, vol. 19, no. 6, pp. 1583–1587, 2009.

[133] S. Liu, L. Yang, S. Xu, S. Luo, and Q. Cai, "Photocatalytic activities of C-N-doped TiO_2 nanotube array/carbon nanorod composite," *Electrochemistry Communications*, vol. 11, no. 9, pp. 1748–1751, 2009.

[134] Y.-K. Lai, J.-Y. Huang, H.-F. Zhang et al., "Nitrogen-doped TiO_2 nanotube array films with enhanced photocatalytic activity under various light sources," *Journal of Hazardous Materials*, vol. 184, no. 1–3, pp. 855–863, 2010.

[135] Y.-P. Peng, S.-L. Lo, H.-H. Ou, and S.-W. Lai, "Microwave-assisted hydrothermal synthesis of N-doped titanate nanotubes for visible-light-responsive photocatalysis," *Journal of Hazardous Materials*, vol. 183, no. 1–3, pp. 754–758, 2010.

[136] H. Liu, G. Liu, and X. Shi, "N/Zr-codoped TiO_2 nanotube arrays: fabrication, characterization, and enhanced photocatalytic activity," *Colloids and Surfaces A*, vol. 363, no. 1–3, pp. 35–40, 2010.

[137] Z. He and H. Y. He, "Synthesis and photocatalytic property of N-doped TiO_2 nanorods and nanotubes with high nitrogen content," *Applied Surface Science*, vol. 258, no. 2, pp. 972–976, 2011.

[138] Y. Wang, G. Zhang, F. Zhang, and X. Fan, "Modified N doped TiO_2 nanotubes with magnetic γ-Fe_2O_3 as visible light photocatalysts," *Advanced Materials Research*, vol. 532-533, pp. 20–24, 2012.

[139] X. Lv, H. Zhang, and H. Chang, "Improved photocatalytic activity of highly ordered TiO_2 nanowire arrays for methylene blue degradation," *Materials Chemistry and Physics*, vol. 136, pp. 789–795, 2012.

[140] S. Lee, H. J. Oh, and C. S. Chi, "Effects of anodic voltages of photcatalytic TiO_2 and doping in H_2SO_4 solutions on the photocatalytic activity," *Korean Journal of Materials Research*, vol. 22, pp. 439–444, 2012.

[141] H. Liao, W. Zhang, X. Sun, L. Shi, and M. Qin, "Synthesis and photoelectrocatalytic property of two-nonmetal-codoped TiO_2 nanotube arrays with high aspect ratio," *Advanced Materials Research*, vol. 412, pp. 219–222, 2012.

[142] M. Dang, Y. Zhou, H. Li, and C. Lv, "Preparation and photocatalytic activity of N-doped TiO_2 nanotube array films," *Journal of Materials Science: Materials in Electronics*, vol. 23, no. 1, pp. 320–324, 2012.

[143] J. Y. Wang, Z. H. Zhao, J. M. Fan, and L. X. Zhu, "One-pot hydrothermal synthesis of N-(S, F) co-doped titanium nanotubes and its visible light responsive photocatalytic properties," *Journal of Functional Materials*, vol. 44, pp. 1502–1506, 2013.

[144] B. Yuan, Y. Wang, H. Bian, T. Shen, Y. Wu, and Z. Chen, "Nitrogen doped TiO_2 nanotube arrays with high photoelectrochemical activity for photocatalytic applications," *Applied Surface Science*, vol. 280, pp. 523–529, 2013.

Hindawi Publishing Corporation
International Journal of Photoenergy
Volume 2014, Article ID 673712, 9 pages
http://dx.doi.org/10.1155/2014/673712

Research Article

Manipulation of MWCNT Concentration in MWCNT/TiO_2 Nanocomposite Thin Films for Dye-Sensitized Solar Cell

Huda Abdullah,[1] Mohd Zikri Razali,[1] Sahbudin Shaari,[2] and Mohd Raihan Taha[3]

[1] *Department of Electrical, Electronic & System, Faculty of Engineering and Built Environment, Universiti Kebangsaan Malaysia, 43600 Bangi, Selangor, Malaysia*
[2] *Institute of Microengineering and Nanoelectronics (IMEN), Universiti Kebangsaan Malaysia, 43600 Bangi, Selangor, Malaysia*
[3] *Department of Civil and Structural Engineering, Faculty of Engineering and Built Environment, Universiti Kebangsaan Malaysia, 43600 Bangi, Selangor, Malaysia*

Correspondence should be addressed to Huda Abdullah; huda@eng.ukm.my

Received 28 December 2013; Accepted 13 January 2014; Published 24 February 2014

Academic Editor: Jiaguo Yu

Dye-sensitized solar cell (DSSC) using multiwalled carbon nanotube/titanium dioxide (MWCNT/TiO_2) was successfully synthesized using sol-gel method. In this method, it has been performed under various acid treatments MWCNT concentration level at (a) 0.00 g, (b) 0.01 g, (c) 0.02 g, and (d) 0.03 g. Atomic force microscopy (AFM) was used to study surface roughness of the MWCNT/TiO_2 thin films. The average roughness results for 0.00 g, 0.01 g, 0.02 g, and 0.03 g were 10.995, 18.308, 24.322, and 25.723 nm, respectively. High resolution transmission electron microscopy (HR-TEM) analysis showned the inner structural design of the MWCNT/TiO_2 particles. The TiO_2 nanoparticles covered almost all the area of MWCNT particles. Field emission scanning electron microscopy (FESEM) gave the morphological surface structure of the thin films. The thin films formed in good distribution with homogenous design. The DSSC with MWCNT/TiO_2 electrode containing 0.03 g MWCNT were resulted in the highest efficiency of 2.80% with short-circuit current density (J_{sc}) of 9.42 mA/cm^2 and open-circuit voltage (V_{oc}) of 0.65 V.

1. Introduction

Dye-sensitized solar cell (DSSC) is considered as a relatively new type of solar cell being discovered, in 1991, by Grätzel et al. DSSC shows greater promise compared to Si solar cells due to low cost, environmental friendly and simple manufacturing process. DSSC has attracted a lot of attention worldwide. Nevertheless, Grätzel's cell has a solar conversion efficiency of ~13% [1], which is significantly lower than that of Si solar cells. To improve the performance of DSSC devices, a number of aspects are considered. Electron transport across a TiO_2 electrode is one of the most important factors affecting the conversion efficiency of DSSC; the greater electron mobility is, the higher the DSSC efficiency will be [2]. On the other hand, charge recombination processes generally inhibited injected electrons from TiO_2 to the conducting glass substrate, thus decreasing the performance of DSSC. Therefore, the rapid photo induced electron transport in the working electrode, TiO_2, and the suppression of charge recombination processes can ensure a higher conversion efficiency of DSSC [3, 4].

In recent years, multiwalled carbon nanotube MWCNT has attracted considerable attention worldwide due to its excellent mechanical properties and electrical and thermal conductivity making it a high potential candidate in various applications, for example, field emission display [5], photo catalysis, photovoltaic devices, and DSSC [6]. Several researches [7, 8] reported the incorporation of MWCNT within nanocrystalline TiO_2 working electrodes to enhance the solar energy conversion efficiency of DSSC. Furthermore, some studies [9] have revealed that the better performance of DSSC fabricated using MWCNT/TiO_2 electrodes is because of the higher electron mobility at the electrodes than that of conventional TiO_2 electrodes. This resulted in a higher short-circuit photocurrent (J_{sc}) of DSSC. However, the performance of DSSC dropped when high MWCNT content

was applied to the MWCNT/TiO_2 electrode, possibly due to a severe aggregation of MWCNT in the nanocomposite electrode [10, 11].

In this study, we aim to synthesize and fabricate MWCNT/TiO_2 dye-sensitized solar cell using sol-gel method with different concentrations of MWCNT. The different MWCNT concentrations were the main key in order to get better photovoltaic efficiency. We investigate the MWCNT concentration effect on the solar cell in terms of their photo-conversion efficiency performance. The samples were analyzed using FESEM, TEM, AFM, and IV curve analysis to see the effect of MWCNT doped into TiO_2 photoelectrode.

2. Methodology

2.1. Materials. Titanium (IV) tetraisopropoxide (TTIP) (98%) was purchased from Sigma-Aldrich, Belgium, and used as the main material. MWCNT, 98% carbon basis with length of 6 to 13 nm, was purchased from Sigma-Aldrich, USA. The MWCNT will go through the acid treatment process before being used. The MWCNT will be sonicated for 2 h in a beaker containing 50 mL of concentrated nitric acid and boiled at 90°C on a hotplate. The MWCNT powder achieved after filtering was washed several times using distilled water to remove residual acid and dried in oven for 24 h. In this study, other chemicals were used as ethanol anhydrous I_2 (99.5%), ruthenium 620-1H3TBA dye obtained from Solaronix SA, adult MPN-100 purchased from Solaronix SA, nitric acid (95%), and electrode substrate fluorine tin oxide (FTO) glasses, 30 Ω, obtained from Solaronix SA and used as received.

2.2. Preparation of MWCNT/TiO_2 Solution. TiO_2 nanoparticles are produced from titanium (IV) tetraisopropoxide that acts as a precursor solution. The TTIP solution mixed with anhydrous ethanol solution in the ratio of (0.1/2) using magnetic bar stirrer for 30 min. The acid treatment MWCNT powder with different weights of (a) 0.00 g, (b) 0.01 g, (c) 0.02 g, and (d) 0.03 g was added into the TiO_2 colloidal solution paste and dispersed using an ultrasonic horn machine for 60 min. MWCNT/TiO_2 nanocomposite stirred vigorously for another 2 h to get homogeneous solution. The MWCNT/TiO_2 paste coated onto the fluorine tin oxide (FTO) conductive glass using doctor-blade technique to generate 0.25 cm^2 active area is followed by evaporation of ethanol in air at room temperature for a few minutes. All the MWCNT/TiO_2 thin films were annealed in a dry furnace at 300°C for 30 min forming noncrack and uniform thin film electrode. Figure 1 shows the flowchart of this preparation.

2.3. Fabrication of Dye-Sensitized Solar Cell. The annealed MWCNT/TiO_2 electrode thin films were then being immersed in 0.5 M N719 ruthenium dye for 1 day to make sure that all the MWCNT/TiO_2 particles were covered with the N719 dye particle. The electrodes were then sandwiched with another electrode glass called counter electrode which was covered with platinum (Pt) thin film on top of the FTO glass. Both electrodes separated using parafilm barrier to place electrolyte between the electrodes. DSSC based MWCNT/TiO_2 nanocomposite is completed and is ready to be analyzed. Figure 2 shows the flowchart of this preparation.

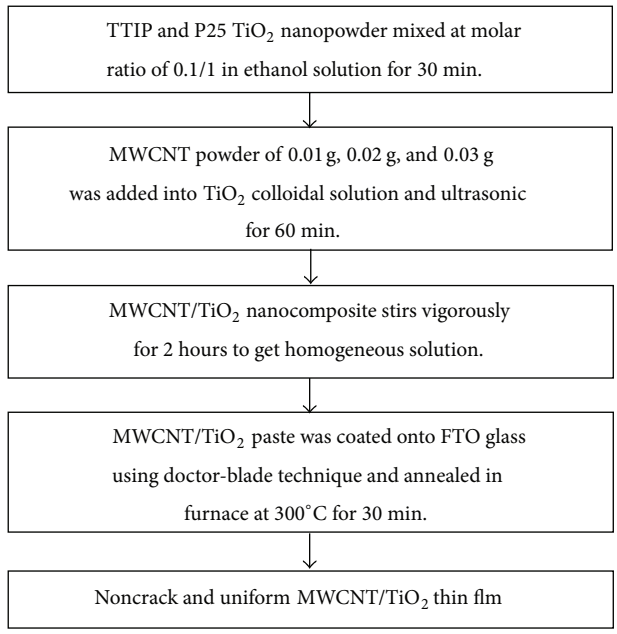

Figure 1: Flowchart diagram for synthesis MWCNT/TiO_2 nanocomposite thin film.

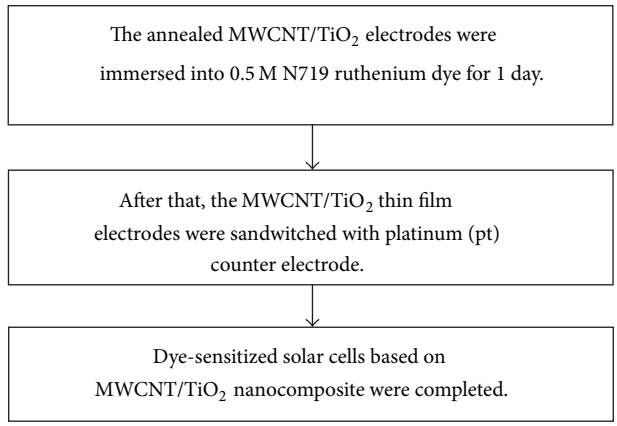

Figure 2: Flowchart diagram for fabrication of MWCNT/TiO_2 dye-sensitized solar cell.

2.4. Characterization. Field emission scanning electron microscopy (FESEM, Zeisz Supra-15KV) was used to analyze the morphological structure of the MWCNT/TiO_2 thin film. Transmission electron microscopy (TEM, CM12 Philips, 1990) is a device used to see the internal structure of a sample. This microscopy has expanded until 660,000x with resolution around 100 nm at 120 keV. Atomic force microscopy (AFM) analysis showed the roughness of thin film in 3D images. Photovoltaic analysis (GAMRY Instruments G300) was assessed as simulated AM 1.5 xenon illumination with

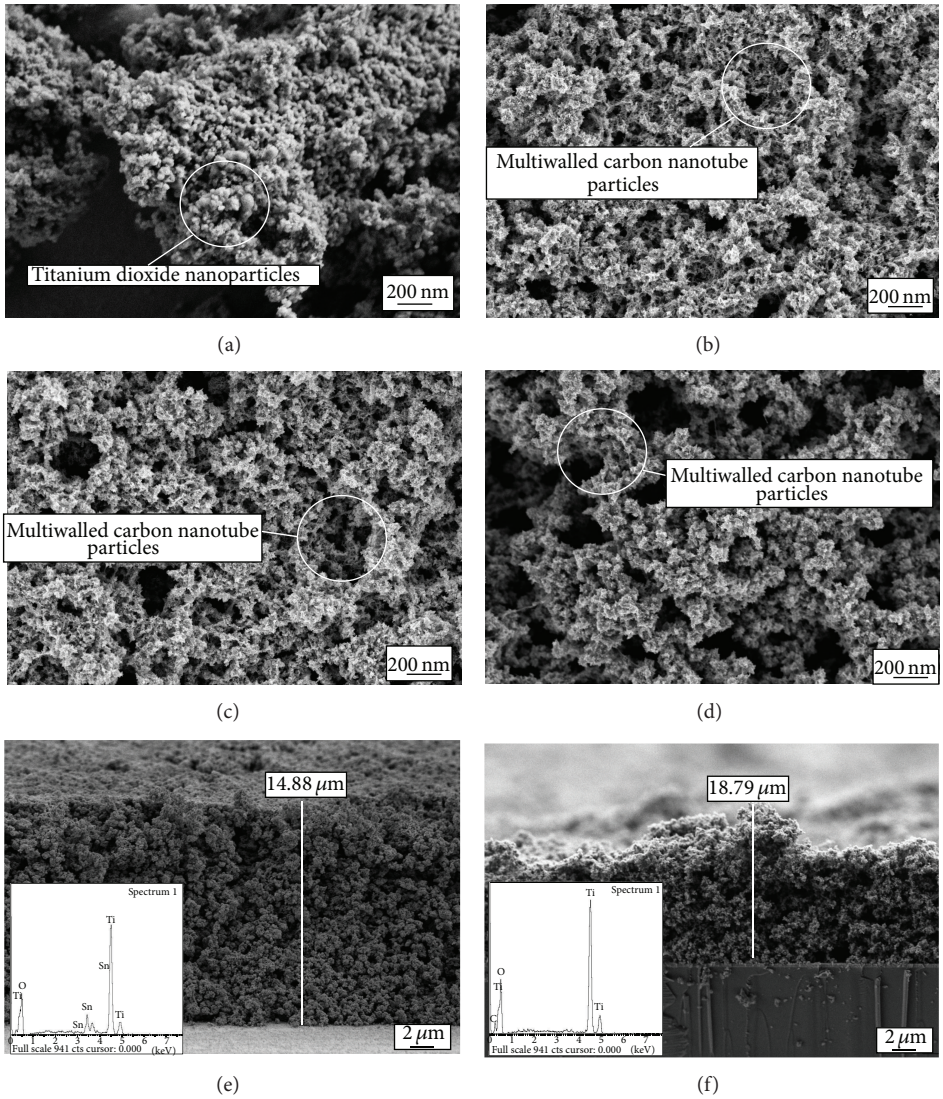

Figure 3: The FESEM images of undoped (a) 0.00 g, (b) 0.01 g, (c) 0.02 g, and (d) 0.03 g added MWCNT; while image (e) and (f) show the average thickness of the thin films with EDX graph.

a 100 mW/cm^2 light output. All experimental results were characterised by good repeatability.

3. Results and Discussions

3.1. Field Emission Scanning Electron Microscopy (FESEM). By referring to other researches and studies [12], we expect to improve the solar cell energy conversion efficiency with the presence of the MWCNT as favorable electrical conductivity on the metal oxide nanocomposite. MWCNT nanoparticles can extend the electron lifetime and enhance the electron transport rate in the photovoltaic metal oxide electrode. In addition, we notice that the MWCNT nanoparticles that go through acid treatment process in the concentrated nitric acid could produce MWCNT with terminal COOH group. This phenomenon can improve the solar cell electron collection due to better interconnection between MWCNT and TiO_2 nanoparticles.

Figure 3: (a) 0.00 g, (b) 0.01 g, (c) 0.02 g, and (d) 0.03 g show the morphological images of MWCNT/TiO_2 thin films, where else for (e) and (f) images show the film cross-section and EDX graph. From FESEM images, we found that the MWCNT and TiO_2 nanoparticles there are in good contact. MWCNT nanoparticles are well dispersed and highly compact after annealing at 300°C for 30 min. The porosity can be observed from the morphological structure of all thin films. The thin films are connected randomly which in lack dissemble long range order for the pore arrangement. We also found that, with every additional MWCNT, the porosity of the thin film became bigger and larger, while the TiO_2 nanoparticles become smaller and thinner [13, 14]. The thin films also show, with increasing the amount of MWCNT, the structural morphology of TiO_2 nanoparticles changes from spherical

Table 1: Weight percentage parameter from EDX analysis.

Sample	MWCNT added	Carbon (%)	Oxygen (%)	Titanium (%)
(a)	TiO_2—nanoparticles	0.00	40.09	59.91
(b)	MWCNT/TiO_2—0.01 g	4.15	40.14	55.71
(c)	MWCNT/TiO_2—0.02 g	5.25	39.64	55.11
(d)	MWCNT/TiO_2—0.03 g	6.55	38.84	54.61

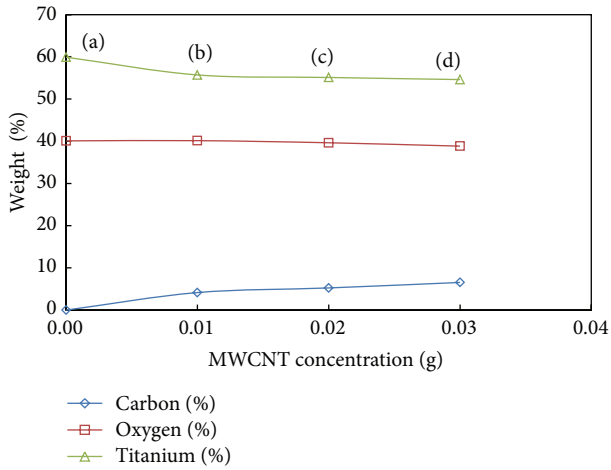

Figure 4: Carbon weight percentage graph from EDX spectroscopy analysis.

to oval nanoparticles structure, which existed around the long range MWCNT nanoparticles. The average thickness of TiO_2 and MWCNT/TiO_2 thin film samples around 14.88 μm and 18.79 μm, respectively. The addition of MWCNT can improve the structural and morphological design of the films. However, the amount of MWCNT added must be controlled and optimized to produce high quality electrode thin film. The amount of MWCNT can affect the films in terms of large crack and inhomogeneous arrangement. Referring to others [15], with the increase in the amount of MWCNT, the number of cracks on the surface of the films is increased subsequently. It is thought that the cracks generated on the surface could be reducing the number of adsorption sites on TiO_2 film as well as causing the discrimination in the conversion efficiency of DSSC.

Table 1 shows the data collected for energy dispersive X-ray (EDX) spectroscopy analysis. The EDX data prove that every additional MWCNT added into the samples, the carbon weight percentage in the samples increased from 0.00%, 4.15%, and 2.25% to 6.55% of samples (a) 0.00 g, (b) 0.01 g, (c) 0.02 g, and (d) 0.03 g, respectively. These results confirm that the sample (d) 0.03 g MWCNT added has a larger MWCNT weight percentage compared to the other samples. Figure 4 shows the MWCNT weight percentage in graphical diagram. Both oxygen and titanium compound weight percentage data were decreased in small amounts from 40.09% to 38.84% and from 59.91% to 54.61%, correspondingly.

Table 2: Average length of MWCNT/TiO_2 nanocomposite and TiO_2 nanoparticles parameter.

Type	Size/nm
MWCNT inner structure	4.49
MWCNT outer structure	17.71
TiO_2 attached at MWCNT	3.91
TiO_2 nanoparticles	12.00

3.2. High Resolution Transmission Electron Microscopy (HR-TEM). In Figure 5, the HR-TEM images of TiO_2 nanoparticles (a) 0.00 g, (b) 0.01 g (c) 0.02 g, and (d) 0.03 g MWCNT/TiO_2 nanocomposite are shown. Images in Figures 5(a), 5(b), 5(c), and 5(d) are carried out to show the comparison between undoped TiO_2 nanoparticles and TiO_2 doped MWCNT nanocomposite in terms of their inner structure design. HR-TEM investigation on selected MWCNT partially covered by TiO_2 aggregates indicates that simple or multiple connections of aggregates of TiO_2 nanoparticles to MWCNT are possible. In Figure 3(a), TiO_2 nanoparticles with low grain density and compact agglomerate configuration were observed. The TiO_2 nanoparticles sizes vary compared to the TiO_2 attached to MWCNT particles. From images (b, c, and d), by using chemical treatment process, we can see the MWCNT particles successfully formed in nanotube structure. From these images, we can find out that the type of CNT used in this research is MWCNT not SWCNT [16, 17]. This can be confirmed by the multiple thin walls formed along the CNT. The TiO_2 nanoparticles and TiO_2 sphere-like shape are formed and positioned mostly around the MWCNT particles. Another researcher [18] also implies that there is a good contact between MWCNTs and TiO_2 particles. MWCNTs are directly coupled with the uniform anatase shell, which are together embedded in the TiO_2 aggregates. Such a structural feature is beneficial for efficient electron transfer and hole-electron separation, as if there is a "conducting wire" acting as a readily accessible electron-transfer channel.

Table 2 illustrates the data size parameter for TiO_2 doped MWCNT nanocomposite and TiO_2 nanoparticles alone. The MWCNT inner and outer structure diameters were approximately 4.49 nm and 17.71 nm in length, respectively. The diameter size for TiO_2 doped MWCNT was slightly smaller with only 3.91 nm compared to the TiO_2 nanoparticles with 12.00 nm. This might be due to the combination with MWCNT nanoparticles that reduce the TiO_2 size and hence produce highly porous thin film as presented and shown in

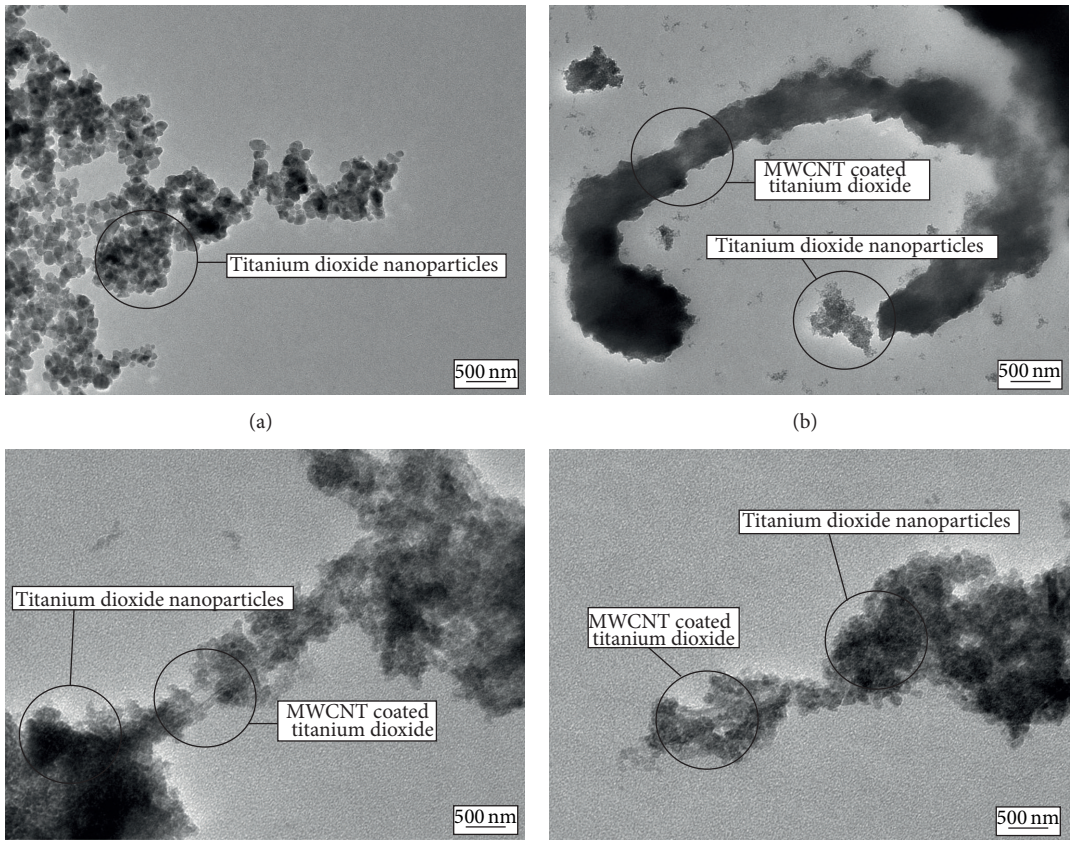

Figure 5: HR-TEM images of undoped (a) 0.00 g, (b) 0.01 g, (c) 0.02 g, and (d) 0.03 g MWCNT/TiO_2 nanocomposite.

the FESEM analysis. HR-TEM images suggest a good affinity between the TiO_2 and the MWCNT, which is important in view of limiting the MWCNT loading required to improve DSSC performance. MWCNT improves the roughness factor of the electrode and limits the charge recombination of electron/hole (e^-/h^+) pairs [19]. Another advantage of combining MWCNT with TiO_2 was to get higher photo response due to decrease in resistivity of the thin film and resulting in a higher current collection at the electrode thin film [20, 21].

Nevertheless, a high loading of MWCNT causes light-harvesting competition that affects the light absorption of the dye sensitizer and consequently reduces the cell efficiency. Moreover, an excess of MWCNT can result in a less compact TiO_2 layer, in which large pores are formed at the micron scale [22] or in the formation of quite disconnected aggregates of MWCNT covered in conformance by TiO_2 nanoparticles.

3.3. Atomic Force Microscopy (AFM). The MWCNT/TiO_2 thin films upper texture prepared using doctor-blade technique are observed by AFM instrument. Images in Figure 6: (a) 0.00 g, (b) 0.01 g, (c) 0.02 g, and (d) 0.03 g demonstrate that, with increasing MWCNT concentration in the MWCNT/TiO_2 sample, the texture of the thin films became rougher and the particle arrangement became compact. This condition can be appointed from the root mean square (rms) value. The AFM analysis results unveil that the nonadded MWCNT 0.00 g has roughness average value of only 10.995 nm. The roughness average slightly increases with additional MWCNT added with 18.308 nm for 0.01 g, 24.322 nm for 0.02 g, and 25.723 nm for 0.03 g. These image data also reveal that rms value drastically increases for each sample. The rms values of the MWCNT/TiO_2 thin film are listed in Table 3 and the data are illustrated with graphical diagram in Figure 7.

Table 3: Average roughness parameter for all samples.

Sample	MWCNT added	Root mean square (rms)/nm
(a)	0.00 g	10.995
(b)	0.01 g	18.308
(c)	0.02 g	24.322
(d)	0.03 g	25.723

AFM measurement investigates the surface morphological roughness of the film. By AFM roughness analysis, roughness factors obtained are increased as increasing the content of MWCNT in TiO_2 film with the maximum value in 0.03 g carbon-content TiO_2 as listed in Table 1. This

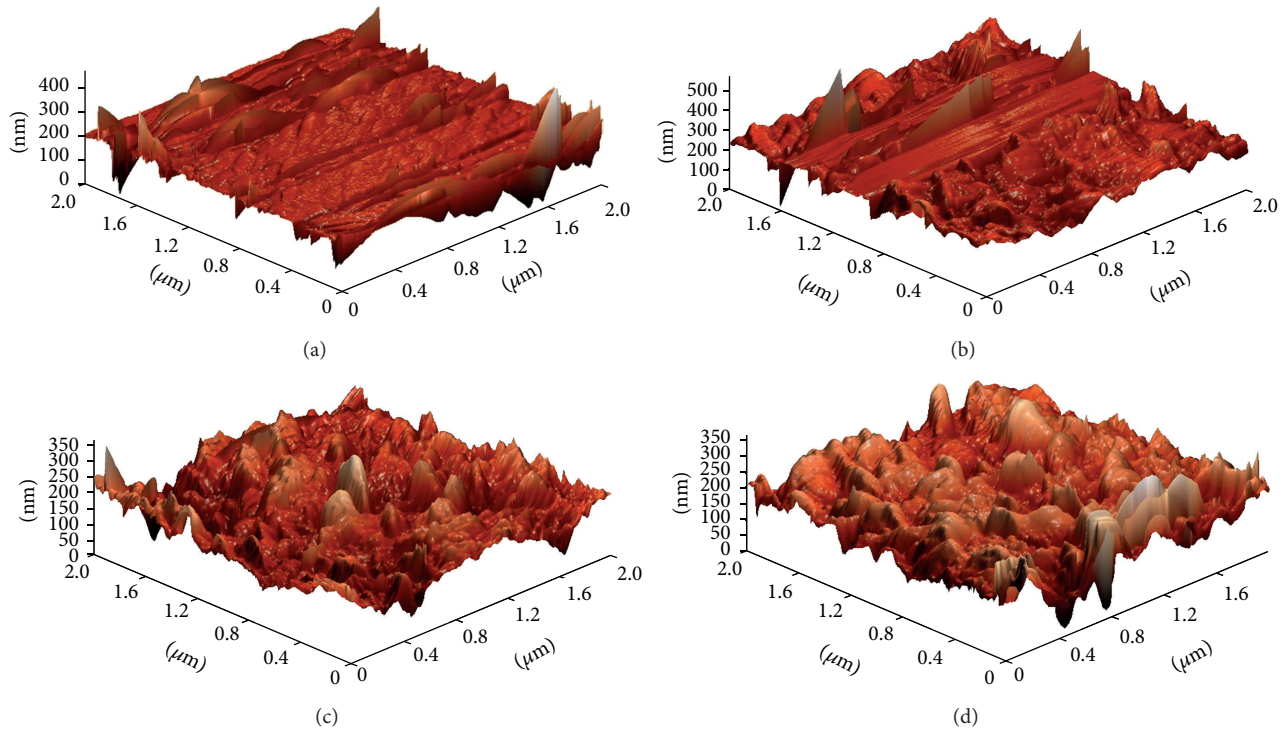

Figure 6: Surface roughness images of MWCNT/TiO_2 thin film with different MWCNT concentrations of undoped (a) 0.00 g, (b) 0.01 g, (c) 0.02 g, and (d) 0.03 g added MWCNT.

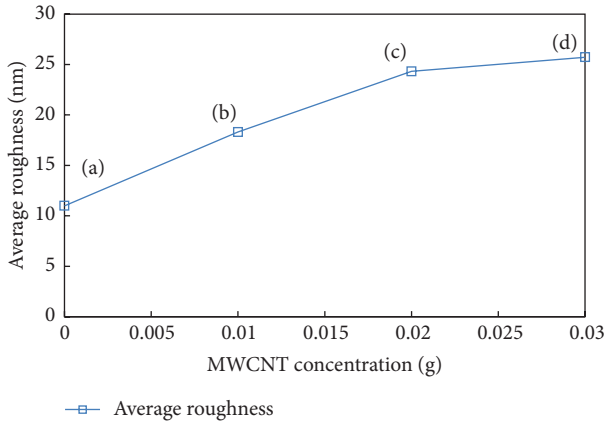

Figure 7: Graphical diagram for MWCNT/TiO_2 thin film roughness of undoped (a) 0.00 g, (b) 0.01 g, (c) 0.02 g, and (d) 0.03 g added MWCNT.

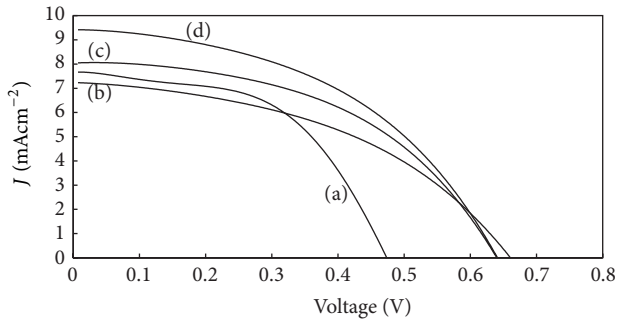

(a) 0.00 g (c) 0.02 g
(b) 0.01 g (d) 0.03 g

Figure 8: Efficiency percentage graphical diagram for MWCNT/TiO_2 DSSC of undoped (a) 0.00 g, (b) 0.01 g, (c) 0.02 g, and (d) 0.03 g added MWCNT.

characterization is an important characteristic to investigate the surface reflection phenomenon in DSSC [23]. Due to the increase in roughness average, the enlargement for surface texture angle in the thin film will bounce the light on surface films and causing the light to reflect indirectly back to the electrode surface. This phenomenon can increase the light absorption in the metal oxide photovoltaic and improve the light of electrical conversion energy because the light reflectance had been reduced [24].

3.4. I-V Curve Efficiency. Figure 8 shows the *I-V* curve graph of MWCNT/TiO_2 thin film photoelectrode dye-sensitized solar cell. This process is performed under 100 mW/cm^2 illuminations using xenon lamp. The measurement of light to electrical process was executed after completing the sandwich-look DSSC between electrode and counter electrode part. The parameters included in Table 4 were open-circuit voltage (V_{oc}), short-circuit photocurrent density (J_{sc}), fill factor (FF), and energy conversion efficiency (η) [25]. As stated in Table 4, open-circuit voltage (V_{oc}) data increased

Table 4: Solar cell efficiency parameter of MWCNT/TiO_2 with different MWCNT concentrations.

Sample	MWCNT added	V_{oc}/V	J_{sc}/mAcm^{-2}	Fill factor (FF)	η/%
(a)	0.00 g	0.49	7.60	0.38	1.43
(b)	0.01 g	0.67	7.25	0.43	2.12
(c)	0.02 g	0.64	8.11	0.47	2.46
(d)	0.03 g	0.65	9.42	0.45	2.80

from 0.49 V to 0.67 V but decreased to 0.64 V for samples (a) 0.00 g, (b) 0.01 g, and (c) 0.02 g MWCNT. At the end, the (V_{oc}) data slightly increased back to 0.65 V for sample (d) 0.03 g MWCNT. Short-circuit photocurrent density (J_{sc}) data for sample (a) 0.00 g is 7.60 mAcm^{-2}. The data for samples (b) 0.01 g and (c) 0.02 g decreased from 7.25 mAcm^{-2} to 8.11 mAcm^{-2}. However, data for sample (d) 0.03 g increased rather large about 19% from sample (c) 0.02 g from 8.11 mAcm^{-2} to 9.42 mAcm^{-2} successively. The fill factor percentage data for (a) 0.00 g, (b) 0.01 g, (c) 0.02 g, and (d) 0.03 g MWCNT are 38%, 43%, 47%, and 45% in that order. An increase in gas values implied enhanced electron transfer in DSSC [26]. The V_{oc} and J_{sc} data gradually increased for sample (d) 0.03 g, which might be attributed from enlargement of thin film porosity and alignment of MWCNT in the photoelectrode thin film. As referred to other researches [27], MWCNT particles might cause a significant change in efficiency via the fluctuation of the short-circuit photocurrent and the open-circuit voltage for the DSSC. Incorporating MWCNT into TiO_2 nanoparticles electrode might also affect the quantity of dye adsorption and the e^-/h^+ recombination process in this dye-sensitized solar cell.

The efficiency data for samples (a) 0.00 g, (b) 0.01 g, (c) 0.02 g, and (d) 0.03 g MWCNT are 1.43%, 2.12%, 2.46%, and 2.80%, respectively. Sample (d) 0.03 g CNT gives the highest efficiency percentage 2.80% with 0.65 V (V_{oc}), 9.42 mAcm^{-2} (J_{sc}), and 45% fill factor. Table 4 demonstrates the solar cell performance trend. It showed that, with every additional MWCNT powder, the efficiency of the solar cell exponentially increased. The MWCNT/TiO_2 nanocomposite combination tends to improve the electrical conductivity of the photoelectrode and also helps to enhance the interconnectivity between the TiO_2 and MWCNT nanoparticles, thus increasing the short-circuit current density and providing an alternative route for efficient electron transfer between the TiO_2 nanoparticles. It shows that the MWCNT can operate as an electrochemical catalyst to improve the energy conversion efficiency of DSSC [28]. The overall light to electrical effectiveness of the dye-sensitized solar cell can be efficiently enhanced with every additional MWCNT added. By referring to another researcher [29], the advantages of adding MWCNT in the photoelectrode are that the MWCNT can absorb over almost the entire visible light spectrum and act as photo sensitizers, providing the MWCNT/TiO_2 nanocomposites with an electron transfer mechanism similar to that of DSSC based TiO_2. As a result, the MWCNT/TiO_2 samples can transfer excited electrons from the MWCNT to the conduction band of TiO_2 when illuminated with visible light, thereby increasing the photocurrent. Second, the conductivity of MWCNTs is superior to that of TiO_2; therefore, we can expect a high transport rate of electrons in the CNT/TiO_2 composites.

However, the concentration of MWCNT should be maintained ~0.03 g optimum MWCNT to avoid MWCNT agglomeration within the films. This is because higher concentration of MWCNT can cause light-harvesting competition between the dye and MWCNT particles. Thus, increases the charge transport resistance and consequently reduces the solar cell efficiency [30]. Besides, excess MWCNT may cause aggregation of TiO_2 grains (as observed in the FESEM result), leading to a decrease amount of dye being adsorbed on the working electrode. In addition, as reported by another researcher [31], excessive amount of MWCNT may cause the working electrode to be less transparent, which leads to reduced efficiency of DSSCs. Furthermore, this condition will decrease the crystallinity of the TiO_2 samples, thereby inhibiting the transport of electrons and increasing the probability of electron trapping by the crystal defects. Moreover, the shielding and scattering effects of excess MWCNT might have prevented the photo absorption of other visible light-active species. Nevertheless, the optimum amount of MWCNT needs to be considered for fabrication of MWCNT/TiO_2 working electrodes being used in DSSC applications.

4. Conclusion

The MWCNT/TiO_2 nanocomposite DSSC was successfully fabricated using sol-gel method and doctor-blade technique. The films were uniform and highly adherent. Photochemical and structural properties of the thin film were improved by incorporate MWCNT powder into TiO_2 nanoparticles. The 0.03 g is the best and optimum concentration of CNT added to this research. Excessive amount of CNT may cause the working electrode to be less transparent, which leads to reduced efficiency of DSSC. FESEM morphological analysis indicated that the TiO_2 and MWCNT/TiO_2 thin films were in compact alignment and highly porous with thickness around 14.88 μm and 18.79 μm. HR-TEM inner structural analysis confirms that the thin film is composed of TiO_2 nanoparticles that existed around the multiwalled carbon nanotube particle. The average thickness for MWCNT and TiO_2 nanocomposite was about 17.71 nm and 3.91 nm, respectively. AFM analysis proved that the roughness factor can significantly improve the photoelectrode performance in the solar cell. The AFM topography reveals a very compact and rough surface; the rms values of all films are in the range of 10–25 nm. From I-V analysis, the highest efficiency

(η) wassuccessfully obtained from sample (c) 0.03 g added MWCNT with 2.80% efficiency, 0.65 V open-circuit voltage (V_{oc}), 9.42 mAcm^{-2} short-circuit photocurrent density (J_{sc}), and 45% fill factor (FF). This result indicated that the solar cell efficiency can be enhanced by adding optimum concentration of MWCNT into TiO_2 photoelectrode solar cell.

Conflict of Interests

The authors declare that there is no conflict of interests regarding the publication of this paper.

Acknowledgment

The authors would like to thank the Laboratory of Photonic Institute of Microengineering and Nanoelectronic (IMEN), Universiti Kebangsaan Malaysia, for providing the facilities.

References

[1] J. Burschka, N. Pellet, S. J. Moon et al., "Sequential deposition as a route to high-performance perovskite-sensitized solar cells," *Nature*, vol. 499, pp. 316–319, 2013.

[2] G. N. Fursey, D. V. Novikov, G. A. Dyuzhev, A. V. Kotcheryzhenkov, and P. O. Vassiliev, "The field emission from carbon nanotubes," *Applied Surface Science*, vol. 215, no. 1–4, pp. 135–140, 2003.

[3] M. L. Chen, F. J. Zhang, and W. C. Oh, "Synthesis, characterization, and photocatalytic analysis of CNT/TiO_2 composites derived from MWCNTs and titanium sources," *New Carbon Materials*, vol. 24, no. 2, pp. 159–166, 2009.

[4] H. Lin, F. Hao, C. F. Lin, J. B. Li, and N. Wang, "Highly catalytic active nanostructured Pt electrodes for dye-sensitized solar cells prepared by low temperature electrodeposition," *Functional Materials Letters*, vol. 4, no. 1, pp. 7–11, 2011.

[5] A. Chindaduang, T. Sawatsuk, W. Wongsukkab, C. Sae-Kung, G. Tumcharern, and S. Pratonetep, "Electron microscopy and optical spectroscopy analyses of carbon nanotube composite electrodes for dye-sensitized solar cells," *Journal of Microscopy*, vol. 22, pp. 23–25, 2008.

[6] S. Chaveanghong, S. M. Smith, J. Sudchanham, and T. Amornsakchai, "Enhancement of power conversion efficiency of dye-sensitized solar cells by using multi-walled carbon nanotubes/TiO_2 electrode," *Journal of the Microscopy Society of Thailand*, vol. 4, no. 1, pp. 36–40, 2011.

[7] K. M. Lee, C. W. Hu, H. W. Chen, and K. C. Ho, "Incorporating carbon nanotube in a low-temperature fabrication process for dye-sensitized TiO_2 solar cells," *Solar Energy Materials and Solar Cells*, vol. 92, no. 12, pp. 1628–1633, 2008.

[8] C. Y. Yen, Y. F. Lin, S. H. Liao et al., "Preparation and properties of a carbon nanotube-based nanocomposite photoanode for dye-sensitized solar cells," *Nanotechnology*, vol. 19, no. 37, Article ID 375305, 2008.

[9] S. R. Jang, R. Vittal, and K. J. Kim, "Incorporation of functionalized single-wall carbon nanotubes in dye-sensitized TiO_2 solar cells," *Langmuir*, vol. 20, no. 22, pp. 9807–9810, 2004.

[10] T. Y. Lee, P. S. Alegaonkar, and J. B. Yoo, "Fabrication of dye sensitized solar cell using TiO_2 coated carbon nanotubes," *Thin Solid Films*, vol. 515, no. 12, pp. 5131–5135, 2007.

[11] Y. Wang, Y. Tan, B. Liu, and B. Liu, "Dual-function layer of mesoporous structure anatase TiO_2 for high performance dye-sensitized solar cells," *Functional Materials Letters*, vol. 5, no. 1, Article ID 12500178, 2012.

[12] K. M. Lee, C. W. Hu, H. W. Chen, and K. C. Ho, "Incorporating carbon nanotube in a low-temperature fabrication process for dye-sensitized TiO_2 solar cells," *Solar Energy Materials and Solar Cells*, vol. 92, no. 12, pp. 1628–1633, 2008.

[13] Y. Ao, J. Xu, D. Fu, X. Shen, and C. Yuan, "Low temperature preparation of anatase TiO_2-coated activated carbon," *Colloids and Surfaces A*, vol. 312, no. 2-3, pp. 125–130, 2008.

[14] H. Abdullah, M. Z. Razali, S. Shaari, and M. R. Taha, "Enhancement of dye-sensitised solar cell efficiency using carbon nanotube/TiO_2 nanocomposite thin film at various annealing temperature," *Electronic Materials Letters*, 2013.

[15] T. Y. Lee, P. S. Alegaonkar, and J. B. Yoo, "Fabrication of dye sensitized solar cell using TiO_2 coated carbon nanotubes," *Thin Solid Films*, vol. 515, no. 12, pp. 5131–5135, 2007.

[16] H. Abdullah, A. Omar, M. A. Yarmo, S. Shaari, and M. R. Taha, "Structural and morphological studies of zinc oxide incorporating single-walled carbon nanotubes as a nanocomposite thin film," *Journal of Materials Science: Materials in Electronics*, vol. 24, no. 9, pp. 3603–3610, 2013.

[17] A. Omar, H. Abdullah, S. Shaari, and M. R. Taha, "Characterization of zinc oxide dye-sensitized solar cell incorporation with single-walled carbon nanotubes," *Journal of Materials Research*, vol. 28, no. 13, pp. 1–8, 2013.

[18] J. Yu, T. Ma, and S. Liu, "Enhanced photocatalytic activity of mesoporous TiO_2 aggregates by embedding carbon nanotubes as electron-transfer channel," *Physical Chemistry Chemical Physics*, vol. 13, no. 8, pp. 3491–3501, 2011.

[19] G. Xue, Y. Guo, T. Yu et al., "Degradation mechanisms investigation for long-term thermal stability of dye-sensitized solar cells," *International Journal of Electrochemical Science*, vol. 7, no. 2, pp. 1496–1511, 2012.

[20] E. R. Morales, N. R. Mathews, D. Reyes-Coronado et al., "Physical properties of the CNT: TiO_2 thin films prepared by sol-gel dip coating," *Solar Energy*, vol. 86, no. 4, pp. 1037–1044, 2012.

[21] W. Zhou, K. Pan, Y. Qu et al., "Photodegradation of organic contamination in wastewaters by bonding TiO_2/single-walled carbon nanotube composites with enhanced photocatalytic activity," *Chemosphere*, vol. 81, no. 5, pp. 555–561, 2010.

[22] C. Y. Yen, Y. F. Lin, S. H. Liao et al., "Preparation and properties of a carbon nanotube-based nanocomposite photoanode for dye-sensitized solar cells," *Nanotechnology*, vol. 19, no. 37, Article ID 375305, 2008.

[23] S. Uk Lee, W. Seok Choi, and B. Hong, "A comparative study of dye-sensitized solar cells added carbon nanotubes to electrolyte and counter electrodes," *Solar Energy Materials and Solar Cells*, vol. 94, no. 4, pp. 680–685, 2010.

[24] N. P. Ariyanto, H. Abdullah, and N. S. A. Ghani, "Surface morphology characterisation of Sn-doped ZnO films for antireflective coating," *Materials Research Innovations*, vol. 13, no. 3, pp. 157–160, 2009.

[25] N. Ikeda and T. Miyasaka, "Plastic and solid-state dye-sensitized solar cells incorporating single-wall carbon nanotubes," *Chemistry Letters*, vol. 36, no. 3, pp. 466–467, 2007.

[26] K. M. Lee, C. W. Hu, H. W. Chen, and K. C. Ho, "Incorporating carbon nanotube in a low-temperature fabrication process for dye-sensitized TiO_2 solar cells," *Solar Energy Materials and Solar Cells*, vol. 92, no. 12, pp. 1628–1633, 2008.

[27] W. Feng, Y. Feng, Z. Wu, A. Fujii, M. Ozaki, and K. Yoshino, "Optical and electrical characterizations of nanocomposite film of titania adsorbed onto oxidized multiwalled carbon nanotubes," *Journal of Physics Condensed Matter*, vol. 17, no. 27, pp. 4361–4368, 2005.

[28] B. Munkhbayar, S. Hwang, J. Kim et al., "Photovoltaic performance of dye-sensitized solar cells with various MWCNT counter electrode structures produced by different coating methods," *Electrochimica Acta*, vol. 80, pp. 100–107, 2012.

[29] F. J. Zhang, M. L. Chen, and W. C. Oh, "Fabrication and electrophotolysis property of carbon nanotubes/titanium composite photocatalysts for methylene blue," *Bulletin of the Korean Chemical Society*, vol. 30, no. 8, pp. 1798–1804, 2009.

[30] J. Yu, J. Fan, and B. Cheng, "Dye-sensitized solar cells based on anatase TiO_2 hollow spheres/carbon nanotube composite films," *Journal of Power Sources*, vol. 196, no. 18, pp. 7891–7898, 2011.

[31] S. Chaveanghong, S. M. Smith, J. Sudchanham, and T. Amornsakchai, "Enhancement of power conversion efficiency of dye-sensitized solar cells by using multi-walled carbon nanotubes/TiO_2 electrode," *Journal of the Microscopy Society of Thailand*, vol. 4, no. 1, pp. 36–40, 2011.

Hindawi Publishing Corporation
International Journal of Photoenergy
Volume 2014, Article ID 503516, 9 pages
http://dx.doi.org/10.1155/2014/503516

Research Article

Role of Platinum Deposited on TiO_2 in Photocatalytic Methanol Oxidation and Dehydrogenation Reactions

Luma M. Ahmed,[1] Irina Ivanova,[2] Falah H. Hussein,[3] and Detlef W. Bahnemann[2]

[1] *Chemistry Department, College of Science, Karbala University, 56001 Karbala, Iraq*
[2] *Institut für Technische Chemie, Leibniz Universität Hannover, Callin Strasse 3, 30167 Hannover, Germany*
[3] *Chemistry Department, College of Science, University of Babylon, 51002 Hilla, Iraq*

Correspondence should be addressed to Falah H. Hussein; abohasan_hilla@yahoo.com

Received 30 November 2013; Revised 4 January 2014; Accepted 5 January 2014; Published 20 February 2014

Academic Editor: Jiaguo Yu

Titania modified nanoparticles have been prepared by the photodeposition method employing platinum particles on the commercially available titanium dioxide (Hombikat UV 100). The properties of the prepared photocatalysts were investigated by means of the Fourier transform infrared spectroscopy (FTIR), X-ray diffraction (XRD), atomic force microscopy (AFM), and UV-visible diffuse spectrophotometry (UV-Vis). XRD was employed to determine the crystallographic phase and particle size of both bare and platinised titanium dioxide. The results indicated that the particle size was decreased with the increasing of platinum loading. AFM analysis showed that one particle consists of about 9 to 11 crystals. UV-vis absorbance analysis showed that the absorption edge shifted to longer wavelength for 0.5% Pt loading compared with bare titanium dioxide. The photocatalytic activity of pure and Pt-loaded TiO_2 was investigated employing the photocatalytic oxidation and dehydrogenation of methanol. The results of the photocatalytic activity indicate that the platinized titanium dioxide samples are always more active than the corresponding bare TiO_2 for both methanol oxidation and dehydrogenation processes. The loading with various platinum amounts resulted in a significant improvement of the photocatalytic activity of TiO_2. This beneficial effect was attributed to an increased separation of the photogenerated electron-hole charge carriers.

1. Introduction

Titanium dioxide is regarded to be one of the most common photocatalysts, having a wide range of properties, such as a strong resistance to chemical and photocorrosion, strong oxidation capability, low operational temperature, low-cost, being and nontoxic [1]. These properties make TiO_2 an attractive candidate for its utilization as a photocatalyst in the photocatalytic processes. TiO_2 has been extensively studied and demonstrated to be suitable for numerous applications such as, destruction of microorganisms [2–5], inactivation of cancer cells [6, 7], protection of the skin from the sun [8–11], photocatalytic water splitting to produce hydrogen gas [12–14], manufacture of some drug types [15–17], degradation of toxic organic pollutants in water [18–20], and self-cleaning of glass and ceramic surfaces [21]. Even though TiO_2 is the most used semiconductor material, it exhibits some disadvantages, such as low surface area and fast recombination rate between the photogenerated charge carriers and the maximum absorption in the ultraviolet light region.

Different attempts have been performed to improve the efficiency of TiO_2 depressing the recombination process of the photoelectron-hole pairs. Some of them include the modification of TiO_2 surface with other semiconductors to alter the charge-transfer properties between TiO_2 and the surrounding environment [22, 23], sensitizing TiO_2 with colored inorganic or organic compounds improving its optical absorption in the visible light region [24–28], bulk modification by cation and anion doping [29–38], and fabrication of TiO_2 surface from polyhedral to produce hallow TiO_2

[39, 40]. TiO_2 nanoparticles are considered to be more active photocatalysts as compared with the bulk powder. The ratio of surface area to volume of nanoparticles has a significant effect on nanoparticles properties. This leads to a higher chemical activity and loss of magnetism and dispersibility [41].

This work was focused on the characterization of the prepared Pt-loaded TiO_2 (Hombikat UV 100) samples. Moreover, the photocatalytic oxidation and photocatalytic dehydrogenation of methanol have been studied employing both the bare and Pt-loaded TiO_2 in the O_2 and N_2 atmosphere. The methanal formation was determined using Nash method at a wavelength of 412 nm.

2. Materials and Methods

A known weight (2 g) of TiO_2 (Hombikat UV 100, Sachtleben, Germany) was suspended under continuous stirring at 250 rpm in a solution containing 40 cm^3 of 40% aqueous methanal (Chemanol), 10 cm^3 of methanol (Hayman), and the appropriate volume of hexachloroplatinic acid (Riedel-De-Haen AG) dissolved in HCl. The reaction mixture was maintained at 303 K, purged with nitrogen gas (20 cm^3/min) and irradiated by UV-A light employing Philips Hg lamp (90 W) with the light intensity of 3.49 mW/cm^2 (Efbe-Schon 6 lamps) for 4 h. This period of irradiation time was found to be the most sufficient time for the complete photodeposition process of metallic platinum. The concentration of platinum was monitoring by the atomic absorption spectroscopy (Shimadzu-AA-6300, Japan). The milky white suspension turns to the pale grey colour with the deposition of Pt. The suspension solution was filtered and washed by absolute methanol, throwing in a desecrater overnight. At the end the product was dried in an oven at 100°C for 2 h [31, 32]. Band gap energies of bare and Pt (0.5)-loaded on TiO_2 surface were determined, via the measurement of reflectance data R by (Cary 100 Scan) UV-visible spectrophotometer system. It is equipped, with using a Labsphere integrating sphere diffuse reflectance accessory for diffuse reflectance spectra over a range of 300–500 nm by employing $BaSO_4$ as reference material.

In all photocatalytic experiments, 100 cm^3 of 40 mM aqueous methanol solution (HPLC grade, Sd fine-CHEM limited) was mixed with certain weight of bare TiO_2 or platinized TiO_2 and was suspended using a magnetic stirrer at 500 rpm. At different time of intervals 2.5 cm^3 of reaction mixture was collected in a plastic test tube and centrifuged (4000 rpm, 15 minutes) in an 800 B centrifuge. The supernatant solution was carefully removed by a syringe to a new plastic test tube and centrifuged again to remove the fine particles of bare TiO_2 or platinized TiO_2. The concentration of formed methanal was determined spectrophotometrically at 412 nm following Nash method [42, 43] using UV-visible spectrophotometer (T80+, PG Instruments Limited, England).

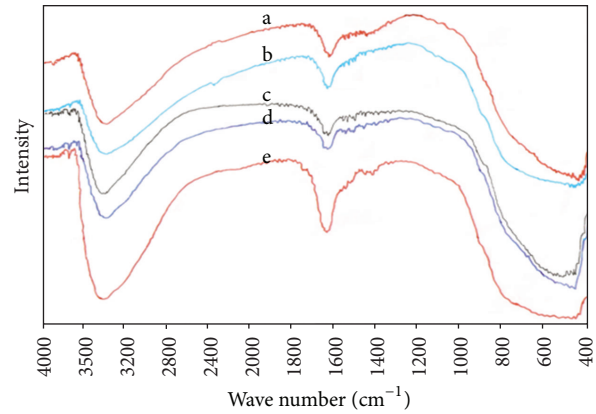

Figure 1: FT-IR spectra for bare and different percentages of Pt-loaded on TiO_2, at (a) bare TiO_2, (b) Pt (0.25)/TiO_2, (c) Pt (0.50)/TiO_2, (d) Pt (0.75)/TiO_2, and (e) Pt (1.00)/TiO_2.

3. Results and Discussion

3.1. Characterisation of Bare and Platinized TiO_2

3.1.1. FTIR Analysis. The Fourier transform infrared spectra of bare and platinized TiO_2 are depicted in Figure 1. The illustrated peaks at 3350–3450 cm^{-1} correspond to the stretching vibration mode of O–H bonds of free water molecules and at 1620–1630 cm^{-1} correspond to the bending vibration mode of O–H bond of chemisorbed water molecules. The absorption intensity of surface O–H groups in TiO_2 is regularly increased with the increasing of the percentage of metals content. These findings are in a good agreement with the literature data [44–46]. The broad intense band below 1200 cm^{-1} is due to Ti–O–Ti bridging stretching mode in the crystal. This peak appeared as unsymmetrical valley with the increasing of metal loading (or content) on TiO_2 exhibiting a maximum at 580 cm^{-1}. This change is related to the formation of Ti–O–M vibrations [47, 48]. The intense bands at 3621, 3645, and 3696 cm^{-1} in all spectra are attributed to the characteristic tetrahedral coordinated vacancies of $_4Ti^{4+}$–OH besides two bands at 3765 and 3840 cm^{-1}. These revealed that the octahedral vacancies designated as $_6Ti^{3+}$–OH are found. In the presence of metal loaded on TiO_2 the peaks of $_6Ti^{3+}$–OH are not observed. This is because the metal acts as an electron trapper, mainly preventing the formation of Ti^{3+}–OH species [49]:

$$Ti^{4+}\text{–OH} + e^- \longrightarrow Ti^{3+}\text{–OH} \quad (1)$$

$$M + e^- \longrightarrow M^- \quad (2)$$

3.1.2. XRD Analysis. The XRD patterns of different TiO_2 samples (bare and platinum loaded) are shown in Figure 2. The mean crystallite size (L) of samples was calculated by Scherrer's equation (3) and the crystallite size ($\acute{L}$) of samples can be estimated from plotting the modified Scherrer's

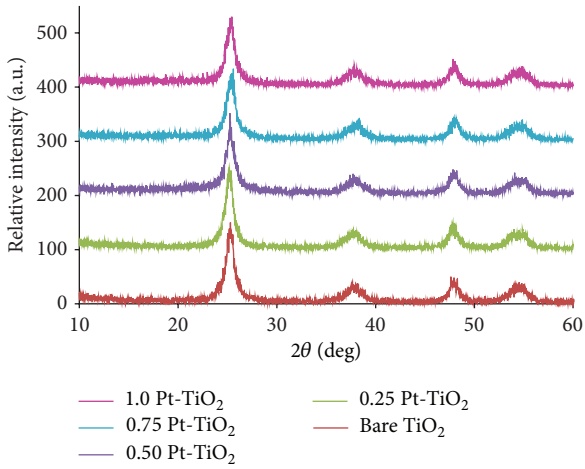

Figure 2: XRD patterns of bare and different percentage of Pt loaded on TiO_2 surface.

formula (4) [50] as shown in Figure 3. The corresponding values are listed in Table 1:

$$L = \frac{k\lambda}{\beta \cos\theta}, \tag{3}$$

$$\ln\beta = \ln\left(\frac{k\lambda}{\acute{L}}\right) + \ln\left(\frac{1}{\cos\theta}\right). \tag{4}$$

In (3) and (4), k is Scherer's constant depending on shape of particles (0.94), λ is the wavelength of the X-ray radiation (0.15418 nm for CuK_α), β is the full width of half maximum (FWHM) intensity (in degree which converted to radian), and θ is the diffraction (Bragg) angle [50, 51].

No peak was observed for Pt (0.25 wt%)/TiO_2 sample at $\theta = 46.5^\circ$. This result is in good agreement with the previous findings [52]. However, $\theta = 46.6^\circ$ which is related to Pt appeared very weak band with Pt (0.5%) loading and increased for Pt (1.0%) as shown in Figure 2. The mean crystallite size of both bare and platinized TiO_2 decreased from 11.487 nm to 9.355 nm, respectively. The crystallite size of bare TiO_2 was found to be equal to 10.132 nm. This value was decreased with the increasing of Pt content on TiO_2. The decreasing of the mean particle size of platinized TiO_2 is attributed to the location and incorporation of Pt(IV) with Ti(III) in TiO_2 lattice. Moreover, the ionic radius of Pt(IV) (0.63 Å) is relatively smaller than that of Ti(III) (0.67 Å) [53, 54].

3.1.3. AFM Analysis. Figure 4 shows the three-dimensional AFM images of bare and Pt-loaded TiO_2 surface which were used to measure the particle sizes. AFM images indicate that the shapes of both bare and platinized TiO_2 are spherical. The results summarized in Tables 1 and 2 indicate that the particle sizes for all samples are found to be bigger than the values found for crystallite size. This indicates that each particle consists of several crystals (polycrystals) [55]. The values of crystal size and particle size for bare TiO_2 are more than those values for metalized TiO_2. This is related to the

Table 1: Mean crystallite sizes and crystallite sizes of bare TiO_2 and Pt-loaded on TiO_2.

Crystal components	Pt %	Mean crystallite sizes (L)/nm	Crystallite sizes ($\acute{L}$)/nm
TiO_2 Hombikat (UV 100)	0.000	11.487	10.132
Pt-TiO_2	0.250	10.799	10.021
Pt-TiO_2	0.500	9.355	9.503
Pt-TiO_2	0.750	10.221	9.589
Pt-TiO_2	1.000	10.475	8.262

increasing of the number of located of Pt^{4+} ions in TiO_2 lattice, which depresses the growth of TiO_2 Hombikate (UV 100) nanocrystals [54]. The results show that each particle consists of about 9 to 11 crystals, according to the results obtained from the calculation of Crystallinity Index values by employing the following equation [56]:

$$\text{Crystallinity Index} = \frac{D_p}{L \text{ or } \left(\acute{L}\right)}, \tag{5}$$

where D_p is the particle size which is measured by AFM analysis and L and $\acute{L}$ are the corresponding mean crystallite size and the crystallite size calculated by the Scherrer equation and the modified Scherrer equation employing XRD data, respectively.

The maximum value of average Crystallinity index for Pt (0.5)/TiO_2 is found to be 8.168. That referred to the suppression of the crystal defects number through decreasing the amorphous phase present in TiO_2 and overall enhancing the photocatalytic activity of TiO_2 [57].

3.1.4. UV-Visible Diffuse Reflectance Spectra. The UV-vis absorbance spectra of the bare TiO_2 and platinized TiO_2 (0.5% Pt) powders were also measured to confirm the Pt-loading trend and to measure the effect of Pt loading. The results from UV-visible reflectance spectra as plotted in Figure 5 clearly show the shift of absorption edge towards longer wavelength for platinized TiO_2. These results indicate that the excitation of metalized TiO_2 occurs with the narrowing and red shift of the band gap energy (E_g) peak [58]. These results were subsequently agreed with the increasing of the average Crystallinity Index [57].

3.2. Effect of the Metal Loading on Photocatalytic Activity of Methanol Solution. The photocatalytic activity of the platinized titanium dioxide was first increased with the increasing of the metal loading until a maximum was reached with the following decrease in the activity. Figures 6 and 7 show the results obtained with the samples containing different amount of platinum. The highest photocatalytic activity was observed with the Pt loading of 0.5 wt%. This loading percentage may give the most efficient separation of photogenerated electron-hole pairs [59]. The presence of Pt on the TiO_2 surface leads to an increase of the surface barrier and the space charge region becomes narrower. As a result of

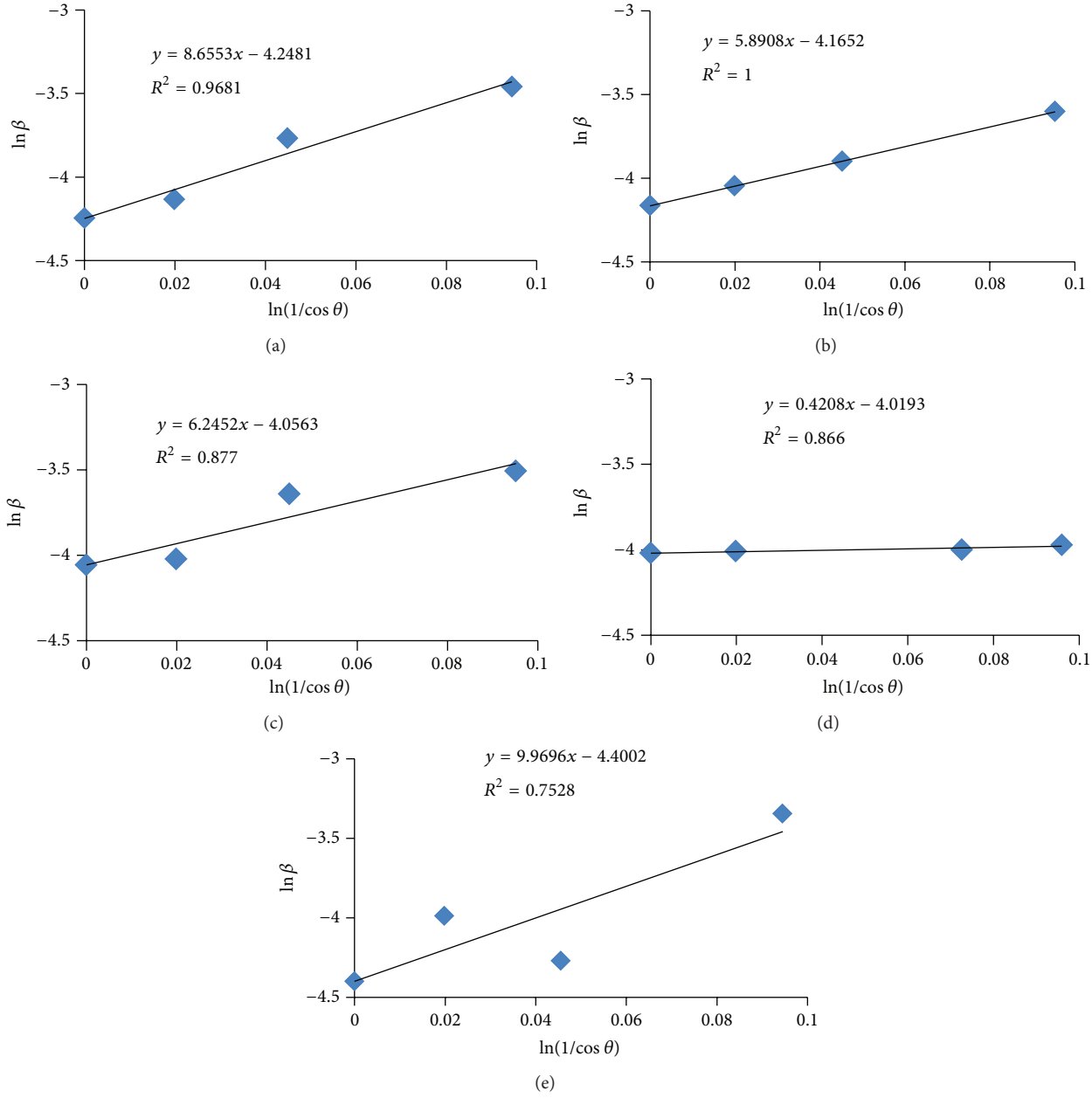

Figure 3: Modified Scherrer equation plot of (a) bare TiO_2, (b) 0.25% Pt loaded on TiO_2, (c) 0.50% Pt loaded on TiO_2, (d) 0.75% Pt loaded on TiO_2, and (e) 1.00% Pt loaded on TiO_2.

Table 2: Particle size measured by AFM and Crystallinity values of bare TiO_2 and platinized TiO_2.

Samples	Particle size/nm	*Crystallinity Index	**Crystallinity Index	Average Crystallinity Index
TiO_2	80.940	7.046	7.988	7.517
Pt(0.25)/TiO_2	63.600	5.889	6.346	6.117
Pt(0.50)/TiO_2	77.020	8.233	8.104	8.168
Pt(0.75)/TiO_2	54.890	5.370	5.724	5.547
Pt(1.00)/TiO_2	73.130	6.981	8.851	7.916

*Crystallinity Index calculated by divided particle size on mean crystallite size and **Crystallinity Index calculated by divided particle size on crystallite size.

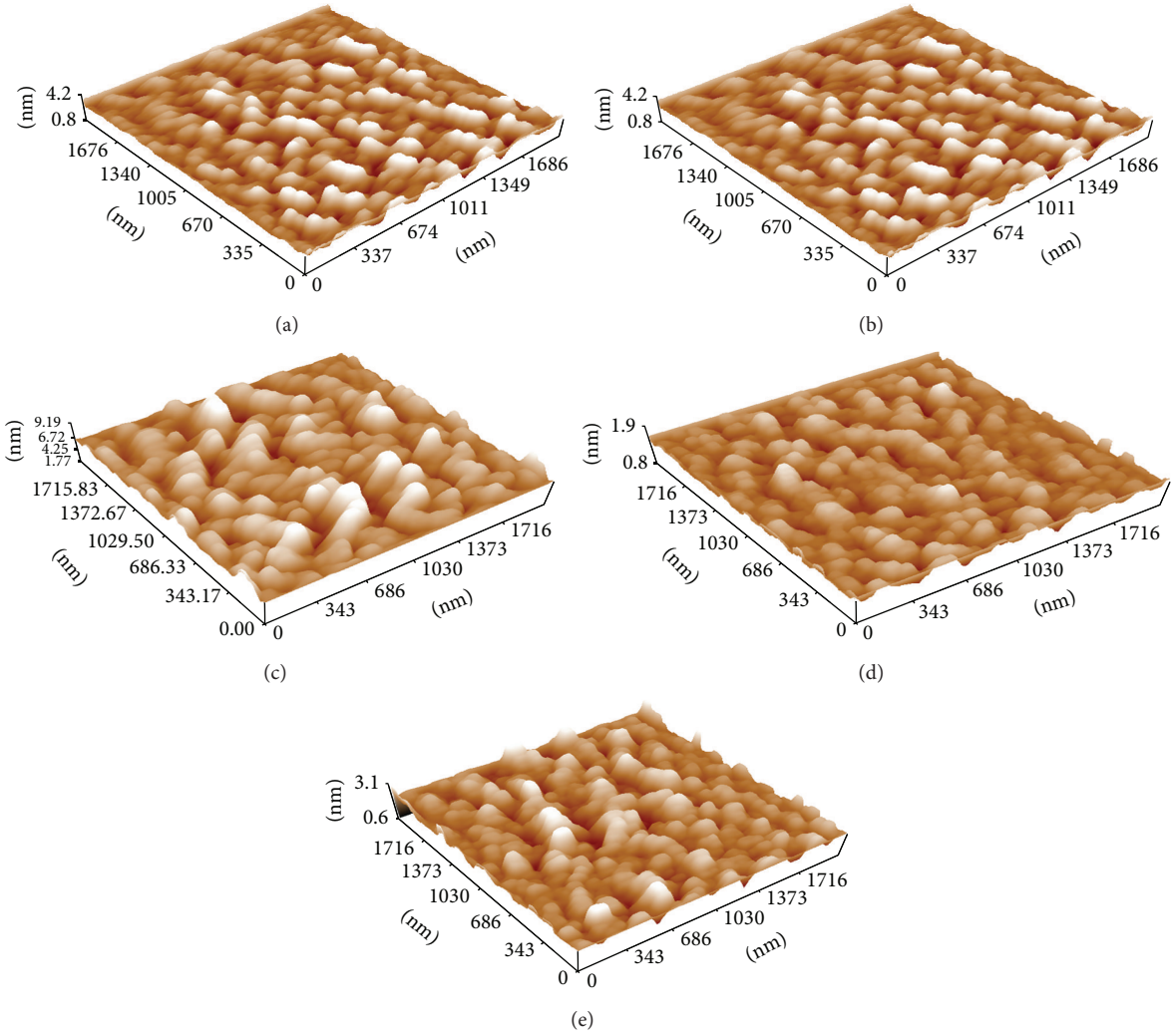

FIGURE 4: Three-dimensional AFM image of (a) bare TiO_2, (b) 0.25% Pt loaded on TiO_2, (c) 0.50% Pt loaded on TiO_2, (d) 0.75% Pt loaded on TiO_2, and (e) 1.00% Pt-loaded on TiO_2.

the metal loading the space charge region becomes narrower leading to an increase of the efficiency of the electron-hole separation [60] and formation of the Schottky barrier by the electron transfer from the conduction band of TiO_2 to the conduction band of Pt. Thereby the recombination process is suppressed according to the following equations [31, 32, 61]:

$$\mathrm{Pt/TiO_2} + h\nu \longrightarrow \mathrm{h^+_{VB}} + \mathrm{e^-_{CB}} \quad (6)$$

$$\mathrm{Pt}_n + \mathrm{e^-_{CB}} \longrightarrow \mathrm{Pt^-}_n \quad (7)$$

$$\mathrm{O_2} + \mathrm{Pt^-}_n \longrightarrow \mathrm{O_2^{-\bullet}} + \mathrm{Pt}_n. \quad (8)$$

Platinum acts as electron scavenger hindering the recombination of the charge carriers and ultimately exhibiting the enhancement of the photoreactivity as shown in the following equation [31, 32, 62, 63]:

$$\mathrm{Pt^-}_n + \mathrm{h^+_{VB}} \longrightarrow \mathrm{Pt}_n. \quad (9)$$

However, when the percentage of the metal reached maximum, the additional amount leads to making the space charge layer very narrow. As a result the penetration depth of light exceeds the space charge layer. The recombination of the electron-hole pairs will be favorable and the photocatalytic activity will be reduced [60]. Moreover, the presence of metal on the TiO_2 surface reduces the number of the surface hydroxyl groups leading to the reduction of the photoreactivity [64]. This means that the metal on the TiO_2 surface acts both as an efficient trap site and as a recombination center at the same time [65]. Hence the rate of the methanal (HCHO) formation will be slower while the conversion of methanal to formic acid (HCOOH) is a faster process. On the other hand, with the increasing of the metal amount, TiO_2 samples will become more grey in color. Thus, the changed optical properties of the samples could lead to the screening of the light towards the TiO_2 and suppression of the electrons excitation to the conduction band [31, 66].

Two mechanisms for the photocatalytic oxidation (in the presence of O_2) and photocatalytic dehydrogenation (in the presence of N_2) of methanol with Pt (0.5)/TiO_2 are suggested as shown in Scheme 1. The scheme shows the differences

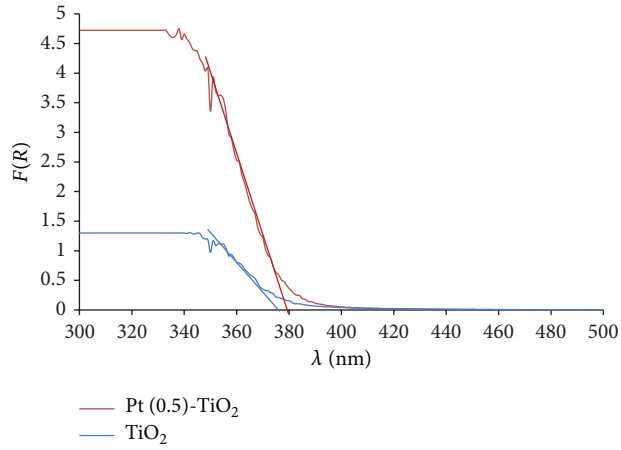

Figure 5: UV-visible diffuse reflectance spectra of bare and Pt-loaded on TiO_2 surface.

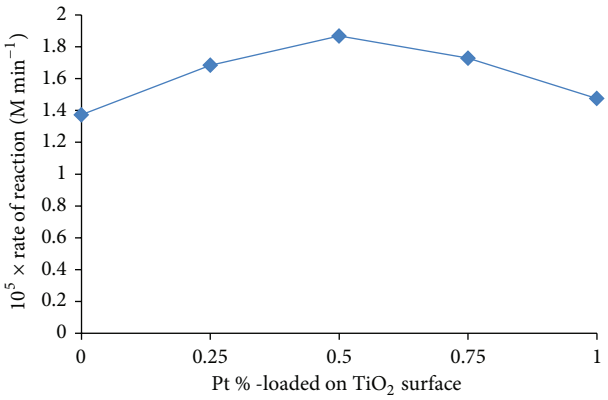

Figure 6: Rate of methanal formation as function of bare and different percentage of Pt on TiO_2 surface, under purged O_2.

between the mechanism of photooxidation and photodehydrogenation of methanol on platinized titanium dioxide. The formation of $CaCO_3$ in photooxidation process was indicated by passing the outlet gas in $Ca(OH)_2$ solution. However, no CO_2 formation was indicated in photodehydrogenation of methanol.

Differences in experimental conditions, such as, experimental equipment, type of photocatalyst, position of band edges of semiconductor compared to redox potential of $O_2/O_2^{-\bullet}$ and $^{-}OH/^{\bullet}OH$, and type and concentration of organic pollutant, cause difficulties in the comparison of photocatalytic activity of different materials. Xiang et al. [67] measured the formation rates of hydroxyl free radical for various semiconductor photocatalysts at the same experimental conditions. They discussed the difference of rates formation of hydroxyl free radical on various semiconductors. In another study Xiang et al. [68] showed that hydroxyl radicals are one of active species and indeed participate in photocatalytic reactions. They also found that the photocatalytic activity of Ag-TiO_2 exceeds that of P25 by a factor of more than 2. Our results are in good agreement with these findings.

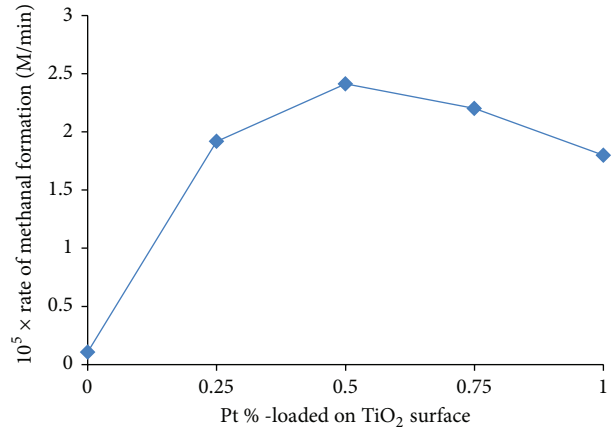

Figure 7: Rate of methanal formation as function of bare and different percentage of Pt on TiO_2 surface, under purged N_2.

The different yields that are suggested in the two mechanisms are HCOH and H_2O in the absence of oxygen (photocatalytic dehydrogenation of methanol) and HCOOH in the presence of oxygen (photocatalytic oxidation of methanol). The pH of the reaction suspension after one hour of irradiation was found 6.93 in dehydrogenation process while it was 4.82 in photooxidation process. This indicates the further oxidation of the formed formaldehyde to formic acid.

4. Conclusions

This study is focused on the elucidation of the mechanism of the methanol formation by the photocatalytic oxidation and/or photocatalytic dehydrogenation of aqueous methanol solution with bare and platinized TiO_2. The main conclusions can be summarized as follows.

(1) The FT-IR spectra show that the peaks at 3450 cm^{-1} and 1630 cm^{-1} related to the surface O–H groups of TiO_2 are increased with the increasing of the platinum amount loaded on TiO_2 surface. The intense bands at 3621, 3645, and 3696 cm^{-1} have been observed in all spectra which are characteristics for the tetrahedral coordinated vacancies designated as $_4Ti^{4+}$–OH. Additionally, a disappearance of two bands at 3765 and 3840 cm^{-1} attributed to $_6Ti^{3+}$–OH has been observed as well.

(2) The XRD data have been used to calculate the crystallite size of the bare and Pt-loaded TiO_2. The values obtained for the crystallite size of the bare TiO_2showed a decrease with the increasing of platinum amount on TiO_2.

(3) AFM images indicate that the shapes of both bare and platinized TiO_2 are spherical.

(4) One particle consists of about 9 to 11 crystals.

(5) In photoreaction, no reaction occurred with using bare TiO_2 under inert gas (N_2); however, in the presence of metal, the photoreaction occurred; that is, the existence of the metal substituted the needed

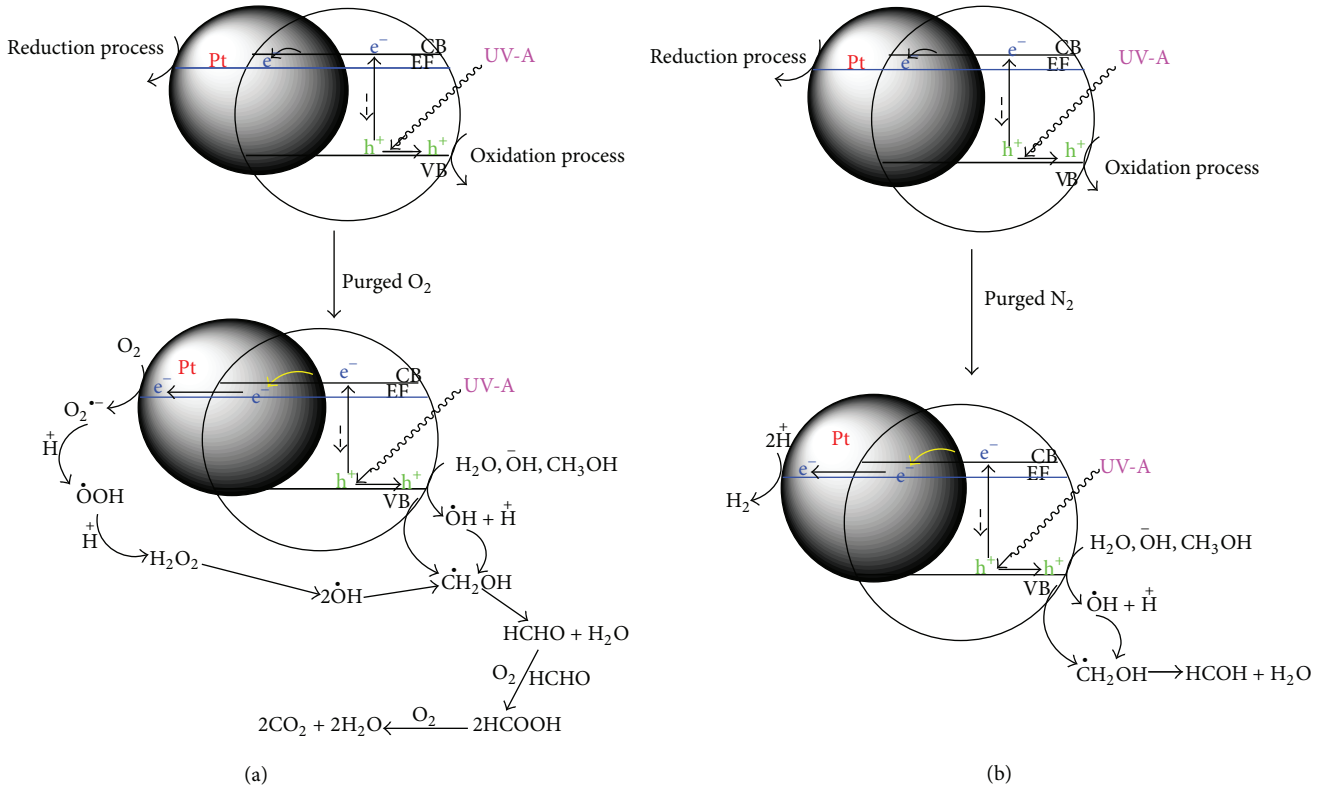

Scheme 1: General mechanism of photocatalytic of methanol with platinized TiO_2 under (a) passing O_2 and (b) passing N_2.

for the O_2. In the existence of O_2 the reaction was carried on to form formic acid as a result of further oxidation of methanol while, in the absence of the O_2, dehydrogenation of methanol occurred, and no further photooxidation occurred.

Conflict of Interests

The authors declare that there is no conflict of interests regarding the publication of this paper.

References

[1] H. Yang, S. Zhu, and N. Pan, "Studying the mechanisms of titanium dioxide as ultraviolet-blocking additive for films and fabrics by an improved scheme," *Journal of Applied Polymer Science*, vol. 92, no. 5, pp. 3201–3210, 2004.

[2] J. A. Ibáñez, M. I. Litter, and R. A. Pizarro, "Photocatalytic bactericidal effect of TiO_2 on *Enterobacter cloacae*. Comparative study with other Gram (−) bacteria," *Journal of Photochemistry and Photobiology A*, vol. 157, no. 1, pp. 81–85, 2003.

[3] M. Haghi, M. Hekmatafshar, B. Mohammad Janipour et al., "Antibacterial effect of TiO_2 nanoparticles on pathogenic strain of *E. coli*," *International Journal of Advanced Biotechnology and Research*, vol. 3, no. 3, pp. 621–624, 2012.

[4] L. Zhang, J. Yan, M. Zhou, and Y. Liu, "Photocatalytic inactivation of bacteria by TiO_2-based compounds under simulated sunlight irradiation," *International Journal of Material Science*, vol. 2, no. 2, pp. 43–46, 2012.

[5] R. Liu, H. Wu, R. Yeh, C. Lee, and Y. Hung, "Synthesis and bactericidal ability of TiO_2 and Ag-TiO_2 prepared by coprecipitation method," *International Journal of Photoenergy*, vol. 2012, Article ID 640487, 7 pages, 2012.

[6] A.-P. Zhang and Y.-P. Sun, "Photocatalytic killing effect of TiO_2 nanoparticles on Ls-174-t human colon carcinoma cells," *World Journal of Gastroenterology*, vol. 10, no. 21, pp. 3191–3193, 2004.

[7] T. Sungkaworn, W. Triampo, P. Nalakarn, I. Tang, Y. Lenburg, and P. Picha, "The Effects of TiO_2 nanoparticales on tumor cell colonies: fractal dimension and morphological properties," *International Journal of Biological and Life Sciences*, vol. 2, no. 1, pp. 67–74, 2007.

[8] A. Popov, *TiO_2 Nanoparticles as Uv Protectors in Skin*, Oulun Yliopisto, Oulu, Finland, 2008.

[9] C.-C. Lin and W.-J. Lin, "Sun protection factor analysis of sunscreens containing titanium dioxide nanoparticles," *Journal of Food and Drug Analysis*, vol. 19, no. 1, pp. 1–8, 2011.

[10] S. Singh and A. pal, "Review: emergence of novel nanoparticles as Uv absorber in sunscreen and their application," *International Journal of Pharmaceutical Research & Development*, vol. 4, no. 3, pp. 207–216, 2012.

[11] A. P. Popov, A. V. Zvyagin, J. Lademann et al., "Designing inorganic light-protective skin nanotechnology products," *Journal of Biomedical Nanotechnology*, vol. 6, no. 5, pp. 432–451, 2010.

[12] E. Selli, G. L. Chiarello, E. Quartarone, P. Mustarelli, I. Rossetti, and L. Forni, "A photocatalytic water splitting device for separate hydrogen and oxygen evolution," *Chemical Communications*, no. 47, pp. 5022–5024, 2007.

[13] J. Oudenhoven, F. Scheijen, and M. Wollfs, "Fundamental of photocatalytic water splitting by visible light," *Chemistry of Catalytic System 2: Photocatalysis*, pp. 1–22, 2004.

[14] A. Fujishima and K. Honda, "Electrochemical photolysis of water at a semiconductor electrode," *Nature*, vol. 238, no. 5358, pp. 37–38, 1972.

[15] M. Del Arco, S. Gutiérrez, C. Martín, V. Rives, and J. Rocha, "Synthesis and characterization of layered double hydroxides (LDH) intercalated with non-steroidal anti-inflammatory drugs (NSAID)," *Journal of Solid State Chemistry*, vol. 177, no. 11, pp. 3954–3962, 2004.

[16] H. Zhang, K. Zou, S. Guo, and X. Duan, "Nanostructural drug-inorganic clay composites: structure, thermal property and in vitro release of captopril-intercalated Mg-Al-layered double hydroxides," *Journal of Solid State Chemistry*, vol. 179, no. 6, pp. 1792–1801, 2006.

[17] S.-J. Xia, Z.-M. Ni, Q. Xu, B.-X. Hu, and J. Hu, "Layered double hydroxides as supports for intercalation and sustained release of antihypertensive drugs," *Journal of Solid State Chemistry*, vol. 181, no. 10, pp. 2610–2619, 2008.

[18] F. Hussein, "Comparison between solar and artificial photocatalytic decolorization of textile industrial wastewater," *International Journal of Photoenergy*, vol. 2012, Article ID 793648, 10 pages, 2012.

[19] S. Devipriya, S. Yesodharan, and E. Yesodharan, "Solar photocatalytic removal of chemical and bacterial pollutants from water using Pt/TiO_2-coated ceramic tiles," *Journal of Photoenergy*, vol. 2012, Article ID 970474, 8 pages, 2012.

[20] Y. Tan, C. Wong, and A. Mohamed, "An overview on the photocatalytic activity of nano-doped-TiO_2 in the degradation of organic pollutants," *Materials Science*, vol. 2011, Article ID 261219, 18 pages, 2011.

[21] D. Verhovšek, N. Veronovski, U. L. štangar, M. Kete, K. žagar, and M. Čeh, "The synthesis of anatase nanoparticles and the preparation of photocatalytically active coatings based on wet chemicalMethods for self-cleaning applications," *International Journal of Photoenergy*, vol. 2012, Article ID 329796, 10 pages, 2012.

[22] H.-X. Tong, Q.-Y. Chen, Z.-L. Yin, H.-P. Hu, D.-X. Wu, and Y.-H. Yang, "Preparation, characterization and photo-catalytic behavior of WO_3-TiO_2 catalysts with oxygen vacancies," *Transactions of Nonferrous Metals Society of China*, vol. 19, no. 6, pp. 1483–1488, 2009.

[23] M. Kim, J. Choi, T. Toops et al., "Coating SiO_2 support with TiO_2 or ZrO_2 and effects on structure and CO oxidation performance of Pt catalyst," *Catalysts*, vol. 3, no. 1, pp. 88–103, 2013.

[24] F. Hussein and A. Halbus, "Rapid decolorization of cobalamin," *International Journal of PhotoenergyInternational Journal of Photoenergy*, vol. 2012, Article ID 495435, 9 pages, 2012.

[25] E. Adamek, W. Baran, J. Ziemianska, and A. Sobczak, "The comparison of photocatalytic degradation and decolorization processes of dyeing effluents," *International Journal of Photoenergy*, vol. 2013, Article ID 578191, 11 pages, 2013.

[26] F. Hussein and T. Abass, "Photocatalytic treatment of textile industrial wastewater," *International Journal of Chemical Sciences*, vol. 8, no. 3, pp. 1353–1364, 2010.

[27] F. Hussein and T. Abass, "Solar photocatalysis and photocatalytic treatment of textile industrial wastewater," *International Journal of Chemical Sciences*, vol. 8, no. 3, pp. 1409–1420, 2010.

[28] F. Hussein, M. Obies, and A. Drea, "Photocatalytic decolorization of bismark brown R by suspension of titanium dioxide," *International Journal of Chemical Sciences*, vol. 8, no. 4, pp. 2736–2746, 2010.

[29] L. Wen, B. Liu, X. Zhao, K. Nakata, T. Murakami, and A. Fujishima, "Synthesis, characterization, and photocatalysis of Fe-doped TiO_2: a combined experimental and Theoretical Study," *International Journal of Photoenergy*, vol. 2012, Article ID 368750, 10 pages, 2012.

[30] M. Shaddad, A. Al-Mayouf, M. Ghanem, M. AlHoshan, J. Singh, and A. Al-Suhybani, "Chemical deposition and electrocatalytic activity of platinum nanoparticles supported on TiO_2 Nanotubes," *International Journal of Electrochemical Science*, vol. 8, pp. 2468–2478, 2013.

[31] L. Ahmed, F. Hussein, and A. Mahdi, "Photocatalytic dehydrogenation of aqueous methanol solution by bare and platinized TiO_2 nanoparticles," *Asian Journal of Chemistry*, vol. 24, no. 12, pp. 5564–5568, 2012.

[32] F. H. Hussein and R. Rudham, "Photocatalytic dehydrogenation of liquid propan-2-ol by platinized anatase and other catalysts," *Journal of the Chemical Society, Faraday Transactions 1: Physical Chemistry in Condensed Phases*, vol. 80, no. 10, pp. 2817–2825, 1984.

[33] F. H. Hussein and R. Rudham, "Photocatalytic dehydrogenation of liquid alcohols by platinized anatase," *Journal of the Chemical Society, Faraday Transactions 1: Physical Chemistry in Condensed Phases*, vol. 83, no. 5, pp. 1631–1639, 1987.

[34] W. Shi, W. Yang, Q. Li, S. Gao, P. Shang, and J. Shang, "The synthesis of nitrogen/sulfur co-doped TiO_2 nanocrystals with a high specific surface areaand a high percentage of 001 facets and their enhanced visible-light photocatalytic performance," *Nanoscale Research Letters*, vol. 7, pp. 1–9, 2012.

[35] V. Štengl and T. M. Grygar, "The simplest way to iodine-doped anatase for photocatalysts activated by visible light," *International Journal of Photoenergy*, vol. 2011, Article ID 685935, 13 pages, 2011.

[36] A. A. Ismail, D. W. Bahnemann, L. Robben, V. Yarovyi, and M. Wark, "Palladium doped porous titania photocatalysts: impact of mesoporous order and crystallinity," *Chemistry of Materials*, vol. 22, no. 1, pp. 108–116, 2010.

[37] K. Cheng, W. Sun, H. Jiang, J. Liu, and J. Lin, "Sonochemical deposition of Au nanoparticles on different facets-dominated anatase TiO_2 single crystals and resulting photocatalytic performance," *The Journal of Physical Chemistry C*, vol. 117, pp. 14600–14607, 2013.

[38] G. Dai, S. Liua, Y. Lianga, H. Liua, and Z. Zhong, "A simple preparation of carbon and nitrogen co-doped nanoscaled TiO_2 with exposed 0 0 1 facets for enhanced visible-light photocatalytic activity," *Journal of Molecular Catalysis A*, vol. 368-369, pp. 38–42, 2013.

[39] S. Liu, J. Yu, and M. Jaroniec, "Tunable photocatalytic selectivity of hollow TiO_2 microspheres composed of anatase polyhedra with exposed 001 facets," *Journal of the American Chemical Society*, vol. 132, no. 34, pp. 11914–11916, 2010.

[40] J. Yu, W. Liu, and H. Yu, "A one-pot approach to hierarchically nanoporous titania hollow microspheres with high photocatalytic activity," *Crystal Growth and Design*, vol. 8, no. 3, pp. 930–934, 2008.

[41] A. H. Lu, E. L. Salabas, and F. Schüth, "Magneticnanoparticles: synthesis, protection, functionalization, and application," *Angewandte Chemie International Edition*, vol. 46, no. 8, pp. 1222–1244, 2007.

[42] T. Nash, "The colorimetric estimation of formaldehyde by means of the Hantzsch reaction," *The Biochemical journal*, vol. 55, no. 3, pp. 416–421, 1953.

[43] C. Castell and B. Smith, "Measurement of formaldehyde in fish muscle using TCA extraction and Nash reagent," *Journal Fisheries Research Board of Canada*, vol. 30, no. 1, pp. 91–98, 1973.

[44] M. Hamadanian, A. Reisi-Vanani, and A. Majedi, "Sol-gel preparation and characterization of Co/TiO_2 nanoparticles: application to the degradation of methyl orange," *Journal of the Iranian Chemical Society*, vol. 7, no. 1, pp. S52–S58, 2010.

[45] J. Cai, J. Huang, H. Yu, and L. Ji, "Synthesis, characterization, and photocatalytic activity of TiO_2 microspheres functionalized with porphyrin," *International Journal of Photoenergy*, vol. 2012, Article ID 348292, 10 pages, 2012.

[46] K. Rahulan, S. Ganesan, and P. Aruna, "Synthesis and optical limiting studies of Au-doped TiO_2 nanoparticles," *Advances in Natural Sciences: Nanoscience and Nanotechnology*, vol. 2, pp. 1–6, 2011.

[47] K. Jackson, "7. A guide to identifying common inorganic fillers and activators using vibrational spectroscopy," *The Internet Journal of Vibrational Spectroscopy*, vol. 3, no. 3, pp. 1–12, 2004.

[48] P. M. Kumar, S. Badrinarayanan, and M. Sastry, "Nanocrystalline TiO_2 studied by optical, FTIR and X-ray photoelectron spectroscopy: correlation to presence of surface states," *Thin Solid Films*, vol. 358, no. 1, pp. 122–130, 2000.

[49] J. J. Murcia, M. C. Hidalgo, J. A. Navío, V. Vaiano, P. Ciambelli, and D. Sannino, "Photocatalytic ethanol oxidative dehydrogenation over Pt/TiO_2: effect of the addition of blue phosphors," *International Journal of Photoenergy*, vol. 2012, Article ID 687262, 2012.

[50] A. Monshi, M. Foroughi, and M. Monshi, "Modified Scherrer equation to estimate more accurately nano-crystallite size using XRD," *World Journal of Nano Science and Engineering*, vol. 2, pp. 154–160, 2012.

[51] D. Moore and R. Reynolds, *X-Ray Diffraction and the Identification and Analysis of Clay Minerals*, Oxford University Press, Oxford, UK, 2nd edition, 1997.

[52] B. Kouakou, L. Ouattara, A. Trokourey, and Y. Bokra, "Characterization of thermal prepared platinized tin dioxide electrodes: application to methanol electro-oxidation," *Journal of Applied Sciences and Environmental Management*, vol. 12, no. 4, pp. 103–110, 2008.

[53] U. M. űller, *Inorganic Structural Chemistry*, John Wiley & Sons Ltd, England, UK, 2nd edition, 2006.

[54] B. Yarmand and S. K. Sadrnezhaad, "Structural and optical properties of Pd^{2+}-doped mesoporous TiO_2 thin films prepared by sol-gel templating technique," *Optoelectronics and Advanced Materials, Rapid Communications*, vol. 4, no. 10, pp. 1572–1577, 2010.

[55] D. Ozkaya, "Particle size analysis of supported platinum catalysts by TEM," *Platinum Metals Review*, vol. 52, no. 1, pp. 61–62, 2008.

[56] X. Pan, I. Medina-Ramirez, R. Mernaugh, and J. Liu, "Nanocharacterization and bactericidal performance of silver modified titania photocatalyst," *Colloids and Surfaces B*, vol. 77, no. 1, pp. 82–89, 2010.

[57] K. Eufinger, D. Poelman, H. Poelman, R. De Gryse, and G. Marin, "TiO_2 thin films for photocatalytic applications," in *Thin Solid Films: Process and Applications*, S. Nam, Ed., pp. 189–227, 2008.

[58] N. Venkatachalam, M. Palanichamy, and V. Murugesan, "Sol-gel preparation and characterization of nanosize TiO_2: its photocatalytic performance," *Materials Chemistry and Physics*, vol. 104, no. 2-3, pp. 454–459, 2007.

[59] Y. Wang, H. Cheng, L. Zhang et al., "The preparation, characterization, photoelectrochemical and photocatalytic properties of lanthanide metal-ion-doped TiO_2 nanoparticles," *Journal of Molecular Catalysis A*, vol. 151, no. 1-2, pp. 205–216, 2000.

[60] A.-W. Xu, Y. Gao, and H.-Q. Liu, "The preparation, characterization, and their photocatalytic activities of rare-earth-doped TiO_2 nanoparticles," *Journal of Catalysis*, vol. 207, no. 2, pp. 151–157, 2002.

[61] B. K. Vijayan, N. M. Dimitrijevic, J. Wu, and K. A. Gray, "The effects of Pt doping on the structure and visible light photoactivity of titania nanotubes," *Journal of Physical Chemistry C*, vol. 114, no. 49, pp. 21262–21269, 2010.

[62] J. Galvez and S. Rodriguez, *Solar Detoxification*, United Nations Educational, Scientific and Cultural Organization, Spine, 1st edition, 2003.

[63] J. S. Jang, P. H. Borse, J. S. Lee et al., "Photocatalytic hydrogen production in water-methanol mixture over iron-doped $CaTiO_3$," *Bulletin of the Korean Chemical Society*, vol. 32, no. 1, pp. 95–99, 2011.

[64] W. Choi, A. Termin, and M. R. Hoffmann, "The role of metal ion dopants in quantum-sized TiO_2: correlation between photoreactivity and charge carrier recombination dynamics," *Journal of Physical Chemistry*, vol. 98, no. 51, pp. 13669–13679, 1994.

[65] L. Wang and T. Egerton, "The effect of transition metal on the optical properties and photoactivity of nanoparticulate titanium dioxide," *Journal of Materials Science Research*, vol. 1, no. 4, pp. 17–27, 2012.

[66] B. Neppolian, H. Jung, and H. Choi, "Photocatalytic degradation of 4-chlorophenol using TiO_2 and Pt-TiO_2 nanoparticles prepared by sol-gel method," *Journal of Advanced Oxidation Technologies*, vol. 10, no. 2, pp. 369–374, 2007.

[67] Q. Xiang, J. Yu, and P. K. Wong, "Quantitative characterization of hydroxyl radicals produced by various photocatalysts," *Journal of Colloid and Interface Science*, vol. 357, no. 1, pp. 163–167, 2011.

[68] Q. Xiang, J. Yu, B. Cheng, and H. C. Ong, "Microwave-hydrothermal preparation and visible-light photoactivity of plasmonic photocatalyst Ag-TiO_2 nanocomposite hollow spheres," *Chemistry: An Asian Journal*, vol. 5, no. 6, pp. 1466–1474, 2010.